Distinguishing The Geochemical Effects Of Sedimentary Processes And Source Region Characteristics In Gale Crater, Mars.

Thesis

Distinguishing the geochemical effects of sedimentary processes and source region characteristics in Gale crater, Mars.

Candice Ceilidh Bedford

MSci Geosciences with international year of study

(Royal Holloway, University of London, UK)

School of Physical Sciences

A thesis submitted to The Open University for the degree of Doctor of Philosophy

Submitted January 2019, resubmitted June 2019

Abstract

The NASA *Curiosity* rover has investigated a diverse stratigraphic record at Gale crater, Mars, ranging from poorly-sorted conglomerates to cross-bedded sandstones and thinly-laminated mudstones. This stratigraphic record is indicative of deposition in multiple paleoenvironments (fluvial, lacustrine and aeolian), within which variable degrees of mineral sorting, chemical weathering and post-depositional aqueous alteration occurred. This study delineates the geochemical effects of these different sedimentary processes using major element data from the Chemistry and Camera (ChemCam) instrument suite and mineralogical data provided by the Chemistry and Mineralogy (CheMin) instrument suite to identify source region characteristics, mineral sorting regimes, variations in chemical weathering, and the impact of diagenesis on the geochemistry of the host rock. Delineating the different geochemical effects of these sedimentary processes on the lithified units will better constrain our understanding of the geological record and paleoenvironmental conditions in Gale crater, along with the extent of geochemical variation in the surrounding Martian crust.

Here, I show that four previously identified compositional endmembers (subalkaline basalt, trachybasalt, trachyte and rhyolite), and one new endmember (silica-rich basalt) contributed to Gale crater's stratigraphic groups. The previously identified endmembers' influence extends throughout Gale crater's stratigraphic record beyond where they were initially identified. The silica-rich basalt source region is the main contributor to the lower Mt Sharp Group, including the Vera Rubin Ridge, whose hardness likely results from a later diagenetic event precipitating additional hematite in sedimentary pore spaces. This thesis further supports that Martian fluviolacustrine deposits are more enriched in felsic material relative to mafic material with distance from the sediment source. Meanwhile, aeolian deposits become preferentially enriched in mafic materials.

Geochemically identifying the ancient aeolian mineral sorting trend has also constrained the prevailing wind direction at the time of deposition as SW-NE, which is the reverse of the current prevailing wind direction within Gale crater today.

“A famous explorer once said, that the extraordinary is in what we do, not who we are. I’d finally set out to make my mark; to find adventure. But instead adventure found me…”

- *Lara Croft*

Acknowledgements

I am incredibly grateful for having had the opportunity to embark on this PhD journey to help unravel the geochemical mysteries buried in the breath-taking stratigraphy preserved in Gale crater. To my supervisors Dr. Susanne P. Schwenzer, Prof. John C. Bridges, Prof. Simon Kelley, and Prof. Iain Gilmour, I wish to thank you for guiding me in my scientific development, and being supportive, understanding and patient when I've needed it most. I would also like to thank the Mars Science Laboratory Science and Engineering teams, specifically the scientists within the ChemCam and CheMin instrument teams for the acquisition of the datasets, without which this PhD would not be possible. In particular. I thank MSL science team members Dr. Roger C. Wiens, Dr. J. Frydenvang, Dr. Steve Banham and Dr. Elizabeth B. Rampe for their much valued feedback and support in my research, in addition to the many stimulating discussions on the intricacies of sediment geochemistry and mineralogy on Mars. Further thanks go to Dr. Matt Balme for his insight and advice into the eclectic world of academia.

I'm sure many can agree that a PhD is not easy. But even in my most difficult moments, I have remained strong, determined and undoubting of my career choice in planetary science thanks to the amazing community of scientists, friends and family who have supported me along the way. To my dear friends and colleagues Alex, Anton, Chris, Frances, Jack, Isra, Laura, Matt, Paul, Pegg, Peter, Rachael, Rhian, and Robert, thank you all for putting up with my over-enthusiasm for coffee, climbing and sourdough. I hope I have helped and inspired you, as much as you have all helped and inspired me to keep going. To all the members of the DPS House Band and MK Monkeys, I cannot thank you enough for reinvigorating my love of performing and climbing, and gifting me with all the great moments we have shared together. To my long-serving friends outside of science; Charlie, Katie and Nicole, thank you for entertaining my love of rocks and volcanoes, and not judging me when I nerd out during our epic adventures. Furthermore, a special mention

goes to Tom, who has stood by my side no matter what trials life has thrown at us, and to my familiar, Sukhi, who has sat by my side through the long working days.

Last, but by no means least, I am indebted to my parents who have both given me the inspiration and motivation to make my mark on this world and those beyond. I could not have come this far without their love, support and belief in myself as a person, and without them instilling within me their curiosity for all things and their want for adventure.

Table of Contents

List of Figures

List of Tables

1. Introduction

The geological record on Mars is diverse, particularly that relating to its sedimentary record which has been generated by fluvial, lacustrine, glacial and aeolian processes (e.g., Stack et al., 2014a; Hynek and Phillips, 2003; Hynek and Phillips, 2001; Malin and Edgett, 2000). Throughout geological time, these processes have shaped the Martian surface along with impacts and volcanism to generate sediments by the chemical and physical erosion of impact-generated, igneous and pre-existing sedimentary rocks. These eroded materials have then been redeposited, including in Gale crater, as sedimentary units. Understanding the origin of these sediments can potentially provide information on Mars' crustal compositions, and the igneous processes therein (Mangold et al., 2017; McSween et al., 2009), granting a window into the crustal record that is obscured from orbit by dust, ice, dunes, regolith and other sedimentary deposits.

The Martian crustal record is of interest to geologists on the Earth, as both planets formed at roughly the same time (~4.5 Ga) during the stage of planetary accretion in the early solar system (McLennan et al., 2012; Carr and Head, 2010). However, the initiation and continuation of plate tectonics and subduction on the Earth has resulted in a loss of almost all of its ancient (older than 3 Ga) crustal record (e.g., Griffin et al., 2014; Vezier and Jansen, 1979). As Mars' ancient crustal record is largely intact, understanding the geochemical complexity of its crust, by analogy, can provide a window into the possible geology and geochemistry of the early Earth (McLennan et al., 2012). Ancient sediments on Mars, along with the sedimentary processes and paleoenvironments that produced them are also of interest as they can provide clues to the habitability of Mars in the past, and whether it could be habitable today (Ehlmann et al., 2010; 2008).

Distinguishing the past habitability of Gale crater throughout its geological history is the main aim of the Mars Science Laboratory (MSL) *Curiosity* rover which landed on

Mars in 2012. Before *Curiosity*, Martian meteorites, orbiter data and in situ geochemical analyses obtained from previous rover and lander missions were the sole methods with which to obtain information about magma differentiation and sedimentary processes on Mars. MSL has traversed over 20 km as of December 2018, and accumulated the most in-depth chemostratigraphic record of another planet to date thanks to the multitude of rapid analyses conducted with the Chemistry and Camera (ChemCam) instrument suite. Data from ChemCam coupled with mineralogical information from the rover's X-Ray Diffraction instrument CheMin (Chemistry and Mineralogy) have permitted studies to be conducted on Gale crater's ancient Martian sediments, leading to an unparalleled insight into the geochemical complexity of the Martian crust.

1.1. The Martian crust

1.1.1. Physical Characteristics

The surface of Mars can be divided into two main regions; the Ancient Southern Highlands and the Young Northern Lowlands (Fig. 1.1; Carr and Head, 2010). These two global regions are divided by a dichotomy that encircles the planet (Nimmo and Tanaka, 2005). Currently, there are two main hypotheses to explain the formation of the dichotomy (Nimmo and Tanaka, 2005); the exogenic and endogenic hypotheses. The exogenic hypothesis suggests that the dichotomy is the result of one or more large impacts occurring early in Mars' history that resurfaced the upper portion of the Martian crust (Golabek et al., 2011; Carr and Head, 2010; Andrews-Hanna et al., 2008; Wilhelms and Squyres, 1984), and potentially initiated volcanism in the Tharsis Plateau (Reese et al., 2004; Schultz and Glicken, 1979). The endogenic hypothesis discusses an internal origin whereby the crust formed non-uniformly, likely through mantle convection (McGill and Dimitriou, 1990),

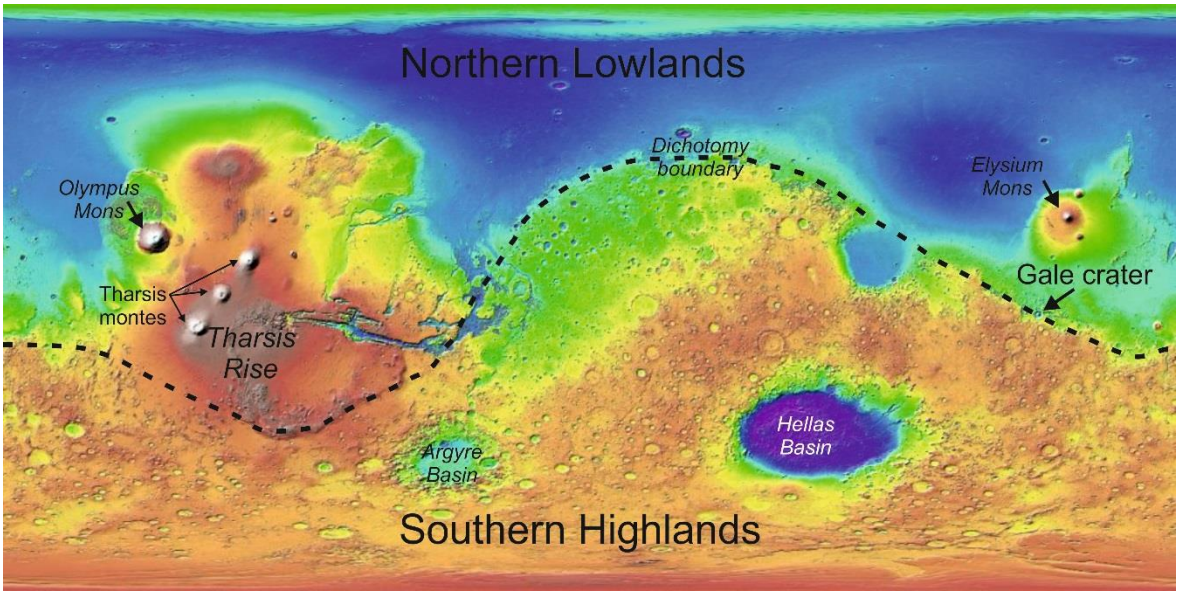

Figure 1.1: An annotated, topographic, shaded relief map of Mars from the Mars Orbiter Laser Altimeter (MOLA) instrument on-board Mars Global Surveyor (MGS). Labels show the main geographical regions of Mars and the location of Gale crater. The dashed, black line marks the approximate location of the dichotomy boundary. Image credit: NASA Planetary Data System (PDS) Geosciences Node.

which may have been initiated by strongly depth-dependent viscosities (Zhong and Zuber, 2001). In either case, the formation of this dichotomy resulted in the Borealis Basin which constitutes the Northern Lowlands (Golabek et al., 2011; Andrews-Hanna et al., 2008). This basin then provided a sink for sediments (Tanaka et al., 2005; Lucchitta et al., 1986) transported by ancient fluvial (Davis et al., 2016; Hynek and Phillips, 2003; Clifford and Parker, 2001; Baker et al., 1991), massive flood (Carr, 2000) and more recent aeolian (Hayward et al., 2014; Tsoar et al., 1979) processes. Some authors also hypothesised that a Martian ocean may have existed here in the past (Chan et al., 2018; Mouginot et al., 2012; Baker et al., 2001; Clifford and Parker, 2001; Parker, 1998), though the existence of a former Martian ocean has been debated against by others (Turbet and Forget, 2019; Carr and Head, 2003; Carr, 2000; Malin and Edgett, 1999).

The Southern Highlands of Mars are heavily cratered (Carr and Head, 2010; Carr, 2000) and are situated on average 5 km higher than the Northern lowlands (Carr, 2000) despite being heavily eroded (Craddock and Howard, 2002; Hynek and Phillips, 2001;

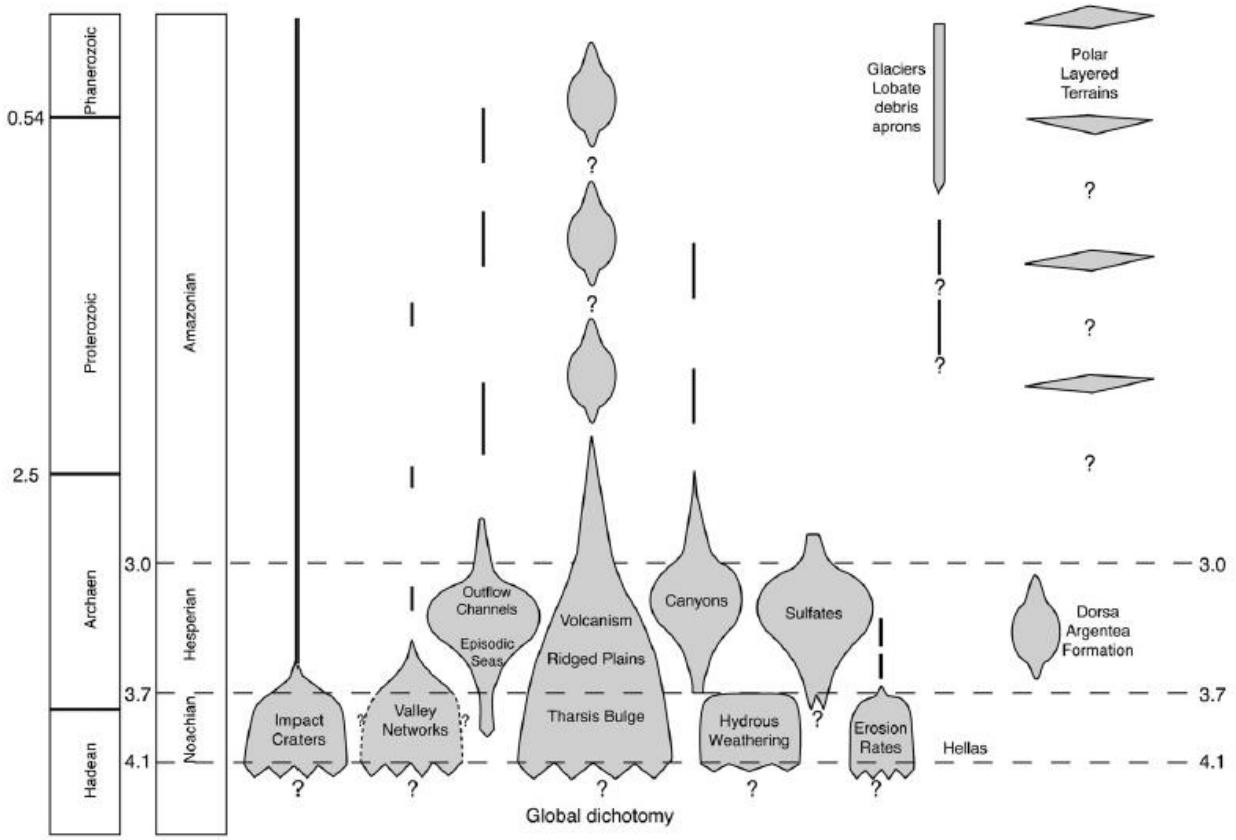

Figure 1.2: An illustration (Figure 1 by Carr and Head, 2009) of the dominant geological processes that define the different geological epochs of Mars, with a comparison to the main geological epochs of the Earth. Y-axis is in Ga.

Craddock and Maxwell, 1993). They also contain areas of remnant magnetism from Mars' former magnetic field (McEnroe et al., 2004; Acuňa et al., 2001; Acuňa et al., 1998). The evidence of the ancient magnetic field on Mars is limited to these areas as large impacts, such as those that generated Hellas and Argyre (Fig. 1.1), demagnetised the crust in the past and potentially weakened the internal dynamo (Acuňa et al., 1998).

The geological record of Mars' crust is divided into three Epochs (Fig. 1.2); Noachian (4.1–3.7 Ga), Hesperian (3.7–3.0 Ga) and Amazonian (3.0 Ga – present) based on intersection relations and superimposed impact crater counts (Carr and Head, 2010; Tanaka, 1986). Noachian terrains are relicts from the heavy bombardment and demonstrate high rates of cratering, erosion and valley formation (Carr and Head, 2010). This period was also very volcanically active, accumulating the majority of the Tharsis volcanic bulge

(Williams et al., 2008; Anguita et al., 2001). The Noachian is associated with a widespread abundance of phyllosilicates suggesting a warm, wet climate with a thicker atmosphere compared to that on Mars today (Ehlmann et al., 2013; Ehlmann et al., 2010; Bibring et al., 2006).

Extensive volcanism continued from the Noachian into the Hesperian but at rates diminished in relation to the Noachian (Fig 1.2; Williams et al., 2008; Anguita et al., 2001). The number of impacts became much scarcer in this period with the end of the heavy bombardment 3.7 Gyr (Carr and Head, 2010). The formation of extensive canyon networks such as *Valles Marineris* (Mangold et al., 2004; Baker et al., 1991), large outflow channels (Harrison and Grimm, 2005; Baker et al., 1991) and the development of widespread sulfate deposits (Ehlmann et al., 2010; Bibring et al., 2006; Gendrin et al., 2005) dominate this time period. So does a contemporaneous reduction in the rates of erosion and alteration identified through a comparison between erosion rates calculated for Mars Exploration Rover (MER) landing sites (Golombek et al., 2006) and the variable erosion of impact craters in the ancient highland terrain (e.g., Craddock and Maxwell, 1993). These features, calculated erosion rates and mineralogical assemblages of Hesperian terrain suggests a climatic change from the previous warm and wet Noachian into the drier, cooler Mars observed today (Ehlmann et al., 2013; Ehlmann et al., 2010; Bibring et al., 2006; Harrison and Grimm, 2005; Mangold et al., 2004).

Towards the end of the Hesperian and during the transition into the Amazonian, rates of volcanism, canyon formation and large flood events diminished (Fig 1.2), though volcanism persisted in certain areas such as the western flanks of Tharsis (Williams et al., 2008). The decrease in frequency of these features in younger terrains indicates a dramatic overhaul in climatic conditions towards that of a global cryosphere (Carr and Head, 2010; Head et al., 2010; Head et al., 2006). Aside from the areas where volcanism still occurred,

such as Tharsis, the dominant characteristics of the Amazonian are features formed by the accumulation and migration of ice across Mars' surface, especially towards the Polar Regions, through variations in orbital parameters (Carr and Head, 2010; Head et al., 2010).

1.1.2. Chemical and Mineralogical Characteristics of the Martian crust

The Shergottite, Nakhlite and Chassignite (SNC) meteorites are an essential part of studying the geochemistry of the Martian crust. In the late 1970's, the SNC meteorites were recognised as Martian (McSween and Stolper, 1980; McSween et al., 1979). Their remarkable mineral and chemical similarities to terrestrial basalts, and relatively young ages <1.1 Ga compared to asteroid-derived meteorites such as the eucrites (4.4–4.6 Ga crystallisation age, McSween and Stolper, 1980) implied relatively recent melting of a large, differentiated body similar to the Earth, that had also undergone large impacts (McSween and Stolper, 1980; McSween et al., 1979). Proof of their Martian origin came when isotopes of trapped gases in shergottite shock-melted glass were found to be equivalent to those analysed by the Viking landers for the Martian atmosphere (Nyquist et al., 2001; Swindle et al., 1986; Bogard and Johnson, 1983).

SNC meteorites are samples of Martian volcanic and plutonic rocks that are dominantly tholeiitic basalt (Fig. 1.3; McSween et al., 2009; Bridges and Warren, 2006; Nyquist et al., 2001). Most SNC meteorites have crystallisation ages (~1.3 Ga – 165 Ma; Nyquist et al., 2001) indicative of young Martian crust derived from relatively recent magmatic activity such as that from the Tharsis or Elysium volcanic plateaus (Cassanelli and Head, 2018; McLennan et al., 2012; Wilson et al., 2001). ALH 84001, a cumulate orthopyroxenite, has an ancient crystallisation age (~4.5 Ga based on $^{40}Ar/^{36}Ar$ radiometric

dating; Nyquist et al., 2001; Bogard and Garrisson, 1999) that suggests an origin in the Southern Highlands (McLennan et al., 2012; Nyquist et al., 2001). Although ALH 84001 is a cumulate igneous rock that formed through crystal accumulation from a basaltic magma (Mittlefehldt, 1994), a Martian polymict breccia meteorite and its pairs have also been identified in recent years – NWA 8114 (MacArthur et al. 2019), NWA 7034 (Santos et al., 2015), NWA 7475 (Wittmann et al., 2014), and NWA 7533 (Hamayun et al., 2013). Despite these meteorites containing clasts derived from multiple sources, many are predominately basaltic in composition (Wittman et al., 2014; Hamayun et al., 2013), similar to igneous rocks analysed by the *Spirit* MER rover (Hamayun et al., 2013). These Martian breccias are associated with ancient Martian crust– with zircons dated to 4.4 Ga using U-Pb geochronology (Hamayun et al., 2013) – that had been brecciated by multiple impact events (Santos et al., 2015; Wittman et al., 2014; Hamayun et al., 2013, MacArthur et al. 2019).

The orbital mapping with Mars Global Surveyor (MGS) and Mars Odyssey (MO) near infrared data has also shown that the mineralogy of Mars' surface is dominated by primary mafic igneous minerals such as olivine and pyroxenes (Chervrier and Mathé, 2007; Bandfield et al., 2000), with olivine detected across many locations (Hanna et al., 2016; Hamilton and Christensen, 2005). Further evidence of a predominately basaltic Martian crust came when Adirondack Class basalts were analysed by the Mars Exploration Rover (MER) *Spirit* at Gusev crater and revealed an olivine-rich mineralogy (McSween et al., 2006a). The geochemistry of the Adirondack Class basalts is therefore thought to be derived from unfractionated, primitive melt of a depleted Martian mantle source (McSween et al., 2006b), similar to the SNC meteorites discussed above (Fig. 1.3; McLennan et al., 2012; McSween et al., 2009).

Chapter 1. Introduction

With the majority of Martian geochemical and petrological studies revealing Mars' crust as mostly basaltic in composition, Martian rocks were previously not considered to show the same range in geochemistry as crustal rocks studied on the Earth. However, orbital data have also detected silica-rich material on the NW flank of Syrtis Major (Bandfield et al. 2004), though it is debated whether this relates to evolved crustal material (Bandfield 2006; Bandfield et al. 2004) or late-stage aqueous alteration (Smith and Bandfield 2012). Further evidence for evolved Martian crustal compositions came in the form of occurrences of silica-rich and alkali-rich material that has been observed in Martian samples such as in Martian meteorites NWA 6963 (Filiberto et al. 2014), NWA 7034 (Agee et al. 2013) and NWA 7533 (Humayun et al. 2013). Silica-rich and alkali-rich rocks have been identified at the surface by previous landed missions such as the silica-rich compositions from NASA *Pathfinder* (Wänke et al., 2001; Rieder et al., 1997), relatively alkali-rich basalts at Gusev crater (McSween et al., 2006b), trachybasalt float (Edwards et al., 2017) and tridymite-rich rocks (Morris et al., 2016) in Gale crater. These evolved compositions at the surface and those detected in meteorites have indicated that evolved magmatic compositions could be more widespread than is indicated from orbit. Several factors have impeded the remote detection of these evolved compositions on the surface, for instance; hydrothermal alteration of the Martian crust (Ehlmann et al., 2013; Bibring et al., 2006), global dust obscuring much of the planet (McSween et al. 2009), and widespread, mixed Martian basaltic soil identified from ground-based observations (Chevrier and Mathé 2007).

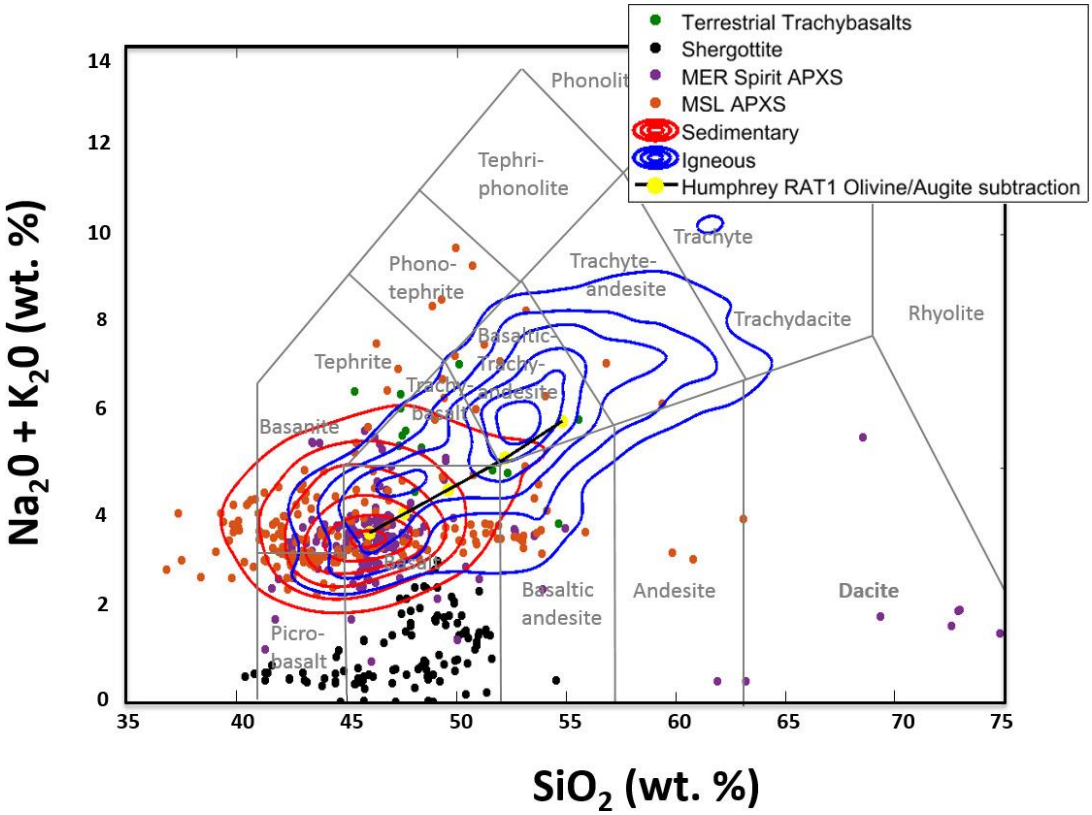

Figure 1.3: Taken from Edwards et al. (2017), this figure shows the range in geochemical compositions of crustal igneous rocks on Mars with a total alkali (Na_2O + K_2O) versus silica (SiO_2) plot. Data for igneous rocks on Mars include Martian shergottite meteorites (black dots), as well as the landed MER Spirit (purple dots), and Mars Science Laboratory (MSL)APXS data up to sol 1000. MSL ChemCam data of igneous float and clasts are shown as dark blue density contour lines whereby the highest data density is at the focus. The black line shows a trachybasalt fractional crystallisation line (Edwards et al., 2017) and the green dots provide reference terrestrial trachybasalt compositions. MSL ChemCam and APXS data of sedimentary rocks in Gale are also shown as red contour lines and dots respectively.

1.2. Exploration of the Martian surface and the search for life

So far, every mission sent to Mars since the 1960's has changed our view of its geologic and climatic processes. Mars was initially thought to be dry and geologically inactive from images and atmospheric data returned by the early *Mariner 4* (July, 1965), *6* (July, 1969) and *7* (August, 1969) fly-by missions (Jones, 2008; Chapman, Pollack and Sagan, 1968; Tanaka, 1986). These images from the early missions were limited to

resolving large impact craters on the Martian surface (Chapman, Pollack and Sagan, 1968; Tanaka, 1986). It was not until later missions such as the NASA *Mariner 9* orbiter (1971–1972) that the on-board cameras managed to resolve a geologically diverse planet dominated by vast canyon-networks, volcanic systems and alluvial plains (Jones, 2008; Malin and Edgett, 2001; Hammond, 1972; Masursky et al., 1972; McCauley et al., 1972). Topographic features from *Mariner 9*'s TV images such as the Martian valley networks with gullies and ravines, and sinuous, multichannel features indicated that running water and former river systems existed on the surface of Mars in the past (McCauley et al., 1972). Further evidence for previous water-rock interactions at the Martian surface came in the form of spectral data of soils analysed by the later *Viking* landers (1976–1980) which were inferred to contain palagonite and salts (Arvidson et al., 1989; Adams, Smith and Johnson., 1986; Allen et al., 1981; Toulmin et al., 1977). These palagonite and salt soil components were interpreted to have formed as a result of water interacting with the regolith via hydrothermal reactions (Arvidson et al., 1989; Allen et al., 1981; Toulmin et al., 1977).

With the overwhelming body of evidence suggesting that water existed on the surface of Mars in the past, and the astrobiological implications this brings in terms of whether life could have existed there, NASA and the planetary science community redefined the scientific theme in 1996 for Mars exploration to "Follow the Water" (Soderblom and Bell, 2008; McCleese et al., 2001). This new theme bore fruition with the later *Mars Global Surveyor* (MGS), *Mars Odyssey* and *Mars Reconnaissance Orbiter* (MRO) missions revealing hydrous-bearing mineral assemblages across the surface of the planet (Ehlmann et al., 2013; Ehlmann et al., 2010; Murchie et al., 2009; Mustard et al., 2008; Bibring et al., 2006; Poulet et al., 2005). Hydrous minerals detected using the MGS *Observatoire pour la Mineralogie L'Eau, les Glaces et l'Activité* (OMEGA) and MRO *Compact Reconnaissance Imaging Spectrometer for Mars* (CRISM) NIR instruments

revealed a remarkable diversity over a wide variety of geological and geochemical settings (Murchie et al., 2009). These hydrous mineral assemblages likely formed through the dissolution of Mars' predominately basaltic crust by aqueous fluids over a variety of pH and temperature settings (Ehlmann et al., 2013; 2010).

Mineralogical and chemical analyses of the Martian SNC meteorites also showed various pre-impact aqueous alteration assemblages (Giesting and Filiberto, 2016; Lee et al., 2015; Hicks et al., 2014; Bridges and Schwenzer, 2012; Hallis et al., 2012; Changela and Bridges, 2010; Bridges et al., 2001; Treiman et al., 1993) which supports clay minerals identified at the surface with MGS and MGO. Aside from detailed petrological studies that demonstrated a pre-terrestrial origin for SNC alteration assemblages (e.g., Treiman et al., 1993), additional proof that SNC alteration was Martian, and did not occur after their arrival to the Earth, came in their analysed deuterium/hydrogen ratios (D/H; Hallis et al., 2012). SNC D/H ratios were shown to be elevated compared to the Earth's, reflecting the high D/H values of the Martian atmosphere (Hallis et al., 2012). Alteration assemblages within the SNC meteorites include clay minerals such as the iron-rich smectites and serpentine in veins within the Lafayette meteorite (Lee et al., 2015; Hicks et al., 2014; Treiman et al., 1993) and evaporites including gypsum and halite within the Nakhla meteorite (Bridges et al., 2001; Bridges and Grady, 2000). Thermochemical modelling of the alteration assemblages in the Nakhlite meteorites has demonstrated that the original Martian fluid was likely to have been an alkaline, dilute brine at a habitable temperature range (Bridges and Schwenzer, 2012).

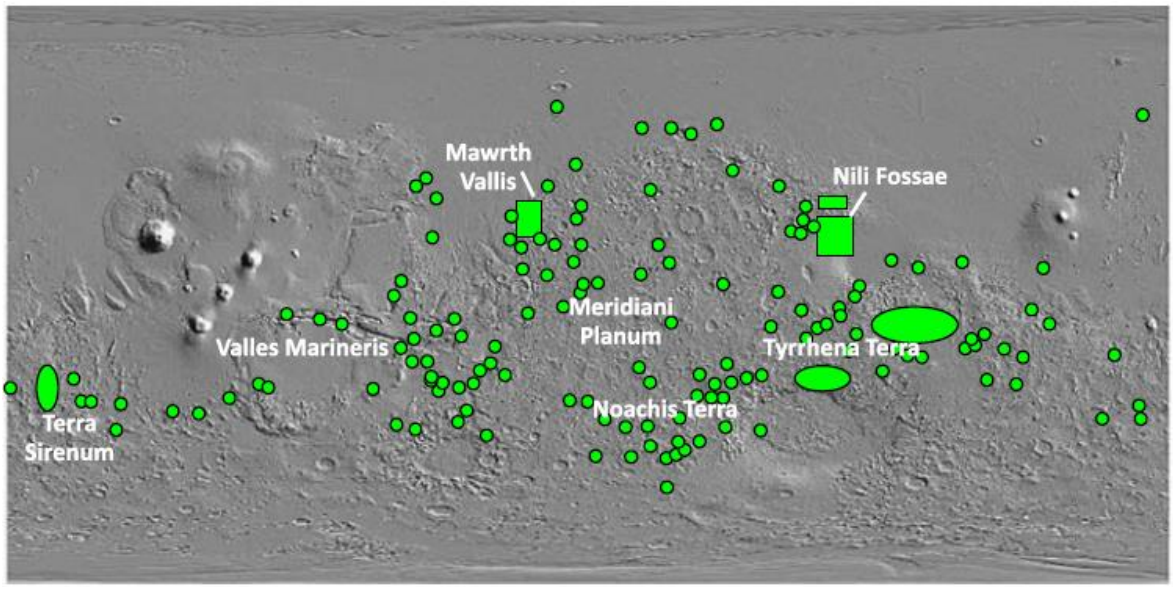

Figure 1.4: A schematic map from Ehlmann et al. (2013) showing the distribution of clay minerals across the Martian surface as detected by the OMEGA and CRISM instruments onboard the respective MGS and MGO orbiting spacecraft.

On the surface of Mars, clay minerals are detected in the greatest quantities within the *Nili Fossae* and *Mawrth Vallis* regions (Poulet et al., 2008), though many isolated occurrences are also seen in the Noachian highlands (Mustard et al., 2008) and within large craters across both hemispheres (Ehlmann et al., 2013; Carter et al., 2010). These clays identified from orbit predominately consist of Fe/Mg smectites – similar to the Martian meteorite clay assemblages – which are indicative of long-term interaction of rocks with neutral to alkaline solutions (Ehlmann et al., 2013; Murchie et al., 2009; Mustard et al., 2008). Rarer occurrences of higher temperature alteration phases such as illite or muscovite have also been detected within craters (Ehlmann et al., 2013; 2010) which may have resulted from post-impact hydrothermalism such as that modelled by Schwenzer and Kring (2009).

Other hydrated minerals detected at the surface include salts i.e., chlorides and sulfates, though these are not commonly seen in the same geological units as the clays (Ehlmann et al., 2013; Milliken et al., 2009). The presence of salts is more indicative of short-term aqueous alteration in acidic environments (Ehlmann et al., 2013). Salt deposits

become more common than clay mineral assemblages in younger terrains (Ehlmann et al., 2010; Bibring et al., 2006) and have been identified alongside detections of crystalline ferric minerals within craters, along with layered deposits such as *Valles Marineris* (Murchie et al., 2009).

In addition to identifying surficial alteration assemblages across Mars, orbital spacecraft such as MGS and MRO also provided the basis for determining the landing sites of the subsequent lander and rover missions. These orbital spacecraft also continue to be used to assess the potential landing sites of future missions such as the NASA *Mars2020* (Schulte et al., 2018, *Mars Sample Return*) and ESA *ExoMars* (Bridges et al., 2017a) missions which will continue the search for life on Mars over the next few decades. The *Mars2020* Jezero crater and *ExoMars* Oxia Planum landing sites were selected due to the detection of hydrated minerals from orbit such as Mg-carbonate in Jezero crater (Schulte et al., 2018; Goudge et al., 2017; Ehlmann et al., 2008) and Fe/Mg phyllosilicates in both Jezero and Oxia (Quentin et al., 2018). These hydrated minerals, and the fluviodeltaic interpretation of the proposed landing sites have strong implications for the habitability of the paleoenvironmental conditions and the detection of organics therein (Schulte et al., 2018; Quentin et al., 2018; Bridges et al., 2017a; Goudge et al., 2017; Ehlmann et al., 2008). Currently, the MSL mission (2011–present) is the most recent to have successfully landed on the surface at a site which contained a long-lived fluviolacustrine system (Grotzinger et al., 2015; 2014), and it is the data returned from this mission that forms the basis of this study.

1.3. The Geological record in Gale crater and the MSL mission

The MSL *Curiosity* rover landed in Gale crater in August 2012. Gale crater is a ~155 km diameter crater situated just south of the global dichotomy that, at this location, marks a boundary between the late Noachian Highlands to the South, and early Hesperian fretted terrain to the North (Fig. 1.1; Thomson et al., 2011; Anderson and Bell, 2010; Milliken et al., 2010; Irwin et al., 2004; Malin and Edgett, 2000).

The primary mission aim of MSL is to explore a region on Mars' surface and investigate its potential as a habitat for past or present life (Grotzinger et al., 2012). Gale was selected as the landing site for MSL due to its low elevation and the ~5 km high, stratified sedimentary mound *Aeolis Mons* (Malin and Edgett, 2000) situated within. This mound was informally named "Mt Sharp" (Grotzinger et al., 2012) and was identified as a location of interest to meet the "Follow the Water" 1996 NASA guidelines due to the hydrated clay-, hematite-, and sulfate-bearing units on its lower slopes that had been identified from orbit (Fig. 1.5; Fraeman et al., 2013; Grotzinger et al., 2012; Milliken et al., 2010). In addition, these layered, hydrated units made Gale a good candidate site to better understand the role water played in Mars' early history, and to determine whether Gale crater was habitable at some point in its past (Grotzinger et al., 2012), fulfilling the MSL primary mission objective.

In order to achieve its mission aim, the MSL *Curiosity* rover was sent to Mars with a series of science instruments to investigate the geology and geochemistry of Gale's preserved geological record, both in situ and through remote observations (Grotzinger et al. 2012). As such, the MSL campaign presents an opportunity to geochemically identify sedimentary processes recorded in Gale crater's stratigraphy such as; changes in source

regions, mineral sorting regimes and aqueous alteration trends. Determining the controls on host rock geochemistry within Gale crater further constrains the sedimentary processes that formed them (such as mineral sorting regimes in Chapters 3 and 4), and provide insights about the geochemical complexity of the crust, including its alteration (Chapters 3 and 5). The research for this PhD thesis aims to determine the main causes of geochemical variation observed across the stratigraphic units in Gale crater using data from the ChemCam (Laser-Induced Breakdown Spectroscopy) and CheMin (X-ray Diffraction) MSL instrument suites (outlined in detail in Chapter 2.1.1. and 2.1.3.). The ChemCam instrument aboard *Curiosity* has analysed >2000 sedimentary targets throughout the duration of the mission while CheMin has analysed 19 drilled and 3 scooped samples to date (December, 2018), providing a wealth of geochemical and mineralogical information for the sedimentary units analysed along the traverse. The next sections place Gale crater into regional and local geological context and describe the stratigraphic units analysed by *Curiosity* along its traverse up the slopes of Mt Sharp.

1.3.1.Regional Context

Gale crater is a complex crater that formed as a result of an impact approximately ~3.8 ± 0.3 Ga ago (Thomson et al., 2011; Anderson and Bell, 2010). This impact would have been large enough to generate a central peak, a melt sheet that is estimated to have a maximum thickness of 0.3 to 1.7 km, and initiate a hydrothermal system within the crater that may have lasted for approximately 300 ka (Schwenzer et al., 2012). However, since formation, Gale's impact crater morphology has been subject to erosion and burial underneath sedimentary materials that constitute the ~5 km thick sequence of layered deposits in Mt Sharp and on the crater floor (Borlina et al., 2015; Grotzinger et al., 2014; Thomson et al., 2011; Anderson and Bell, 2010). Gale crater is situated in the *Aeolis Mensae* region of Mars on the Southern edge of *Elysium Planitia* (Fig. 1.1, Malin and

Edgett, 2000; Thomson et al., 2011; Anderson and Bell, 2010) within a zone of "fretted terrain" where the cratered topography has been incised by multiple valley networks to generate a knobby and mantled appearance (Grotzinger et al., 2012; Thomson et al., 2011; Anderson and Bell, 2010). The valley networks indicate that former aqueous flows have carved the landscape around Gale crater as they flowed from the Southern Highlands to the Northern Lowlands (Grotzinger et al., 2012). The northern rim of Gale crater has been heavily eroded and lies several kilometres lower in elevation compared to the southern crater rim and central mound (Fig. 1.6; Thomson et al., 2011; Irwin and Watters, 2010). Previous studies have shown that this may be the result of either the aforementioned South to North regional drainage of river channels (Irwin and Watters, 2010; Irwin et al., 2004; Malin and Edgett, 2000), or the fact that Gale crater is superimposed on the global dichotomy boundary which is naturally lower in elevation in the North compared to the South (Anderson and Bell, 2010).

Drainage features such as alluvial fans, fluvial channels and inverted channels occur within Gale crater itself (Fig. 1.5) showing that multiple rivers flowed into Gale crater in the past (Anderson and Bell, 2010; Thomson et al., 2008). These drainage features, coupled with the 5 km layered deposits of Mt Sharp, and CRISM detections of hydrated mineral assemblages (Miliken et al., 2010) indicate that Gale crater acted as a sediment sink for an extensive period of time (Grotzinger et al., 2012; Anderson and Bell, 2010; Malin and Edgett, 2000). Lobes of deltaic fans extending from the crater wall such as *Aeolis Palus* (Fig. 1.5) also imply that material at the crater rim was eroded and deposited within Gale's sedimentary assemblage (Miliken et al., 2010). This makes Gale crater a prime field site for potentially identifying the geochemical variability of the surrounding ancient crust.

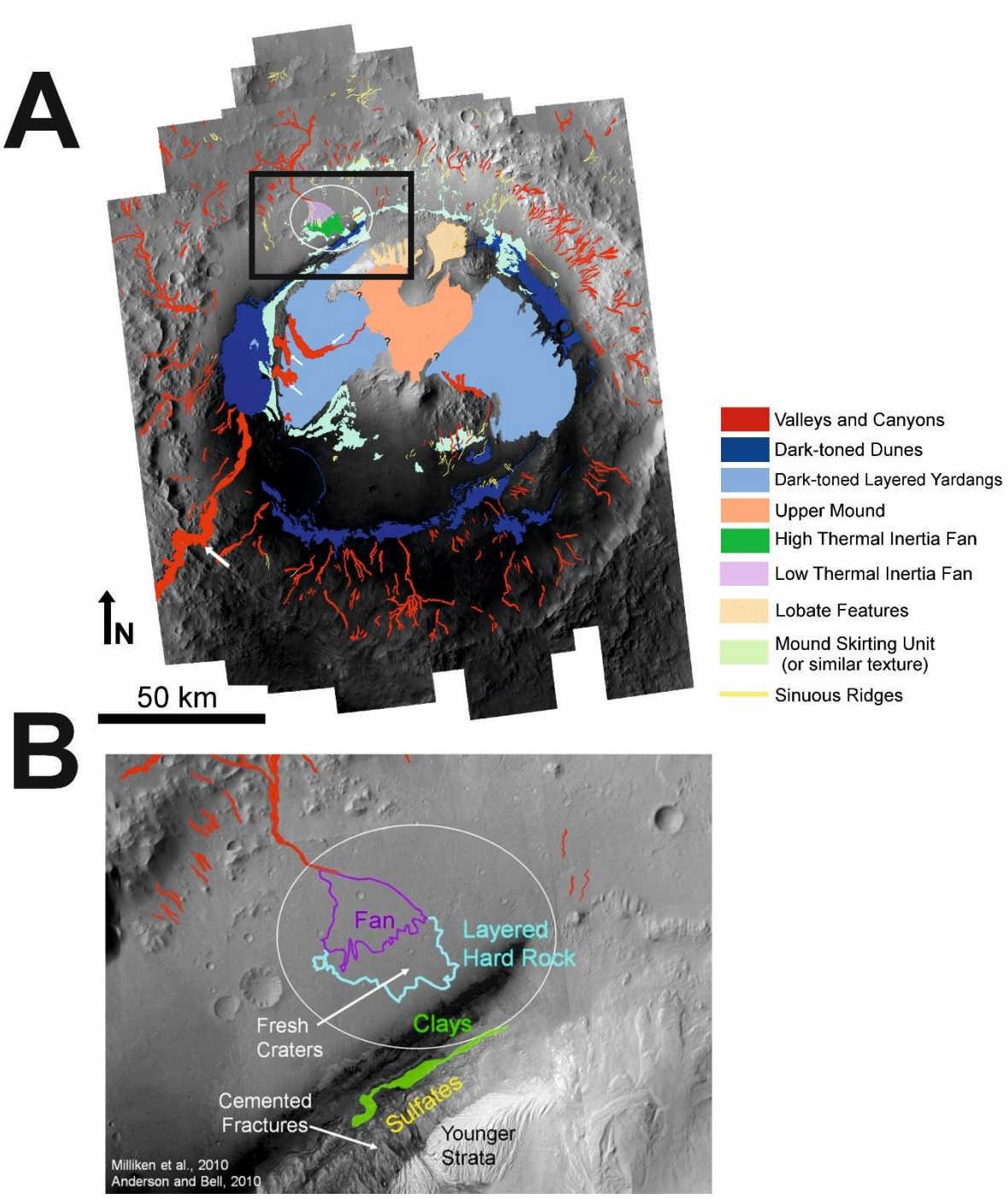

Figure 1.5: A) A geological map of the ~155 km diameter Gale crater produced by Anderson and Bell (2010). The central mound is Mt Sharp, the large fan in the NW is Aeolus Palus, the landing ellipse is displayed as a white circle (20 km x 25 km). The black box in A) outlines the annotated area in B) which shows the key features of interest to explore by MSL as determined by Milliken et al. (2010) and Anderson and Bell (2010) (image credit: NASA/JPL/Caltech).

1.3.1.1. The deposition and exhumation of Mt Sharp's layered deposits

The greater elevation of Mt Sharp compared to the northern rim and absence of tapering in the layers seen from orbital data suggests that Mt Sharp's layered sedimentary units once extended further into Gale crater (Fig. 1.6 B & C) and have since been eroded, exposing the layers of the central mound seen today (Fig. 1.6 D; Grotzinger et al., 2015; Anderson and Bell, 2010; Malin and Edgett, 2000). The sedimentary processes that deposited Mt Sharp's layered units also likely eroded and buried Gale's central peak (Fig. 1.6 A; Grotzinger et al., 2014) which formed through dynamic uplift in the early stages of impact formation (Schwenzer et al., 2012; Pike, 1980). So far, two hypotheses of formation for Mt Sharp have been proposed; the "infill and erosion" or "modification" hypothesis (Grotzinger et al., 2015; 2014; Andrews-Hanna et al., 2010; Malin and Edgett, 2000), and the "mounds-grew-as-mounds" or "growth" hypothesis (Gabasova and Kite, 2018; Kite et al., 2016; 2013).

The modification hypothesis is based on the notion that Gale crater was once completely infilled by sediments (Grotzinger et al., 2015; 2014; Andrews-Hanna et al., 2010; Malin and Edgett, 2000). Infilling of the crater floor by sedimentary units after its formation has been supported by more recent stratigraphic analysis conducted by MSL post-landing. Sedimentological studies based on data returned by *Curiosity*'s science cameras have revealed that the basal Mt Sharp units were likely deposited at the end of a similar fluviolacustrine distributory system that also deposited the crater floor sedimentary units (Fig. 1.6 D; Grotzinger et al., 2015). From orbit, most of the Upper Mt Sharp consists of anhydrous bearing strata (Milliken et al., 2011; Thomson et al., 2011) and is therefore unlikely to have been entirely deposited by fluvial processes (Bennett and Bell, 2016).

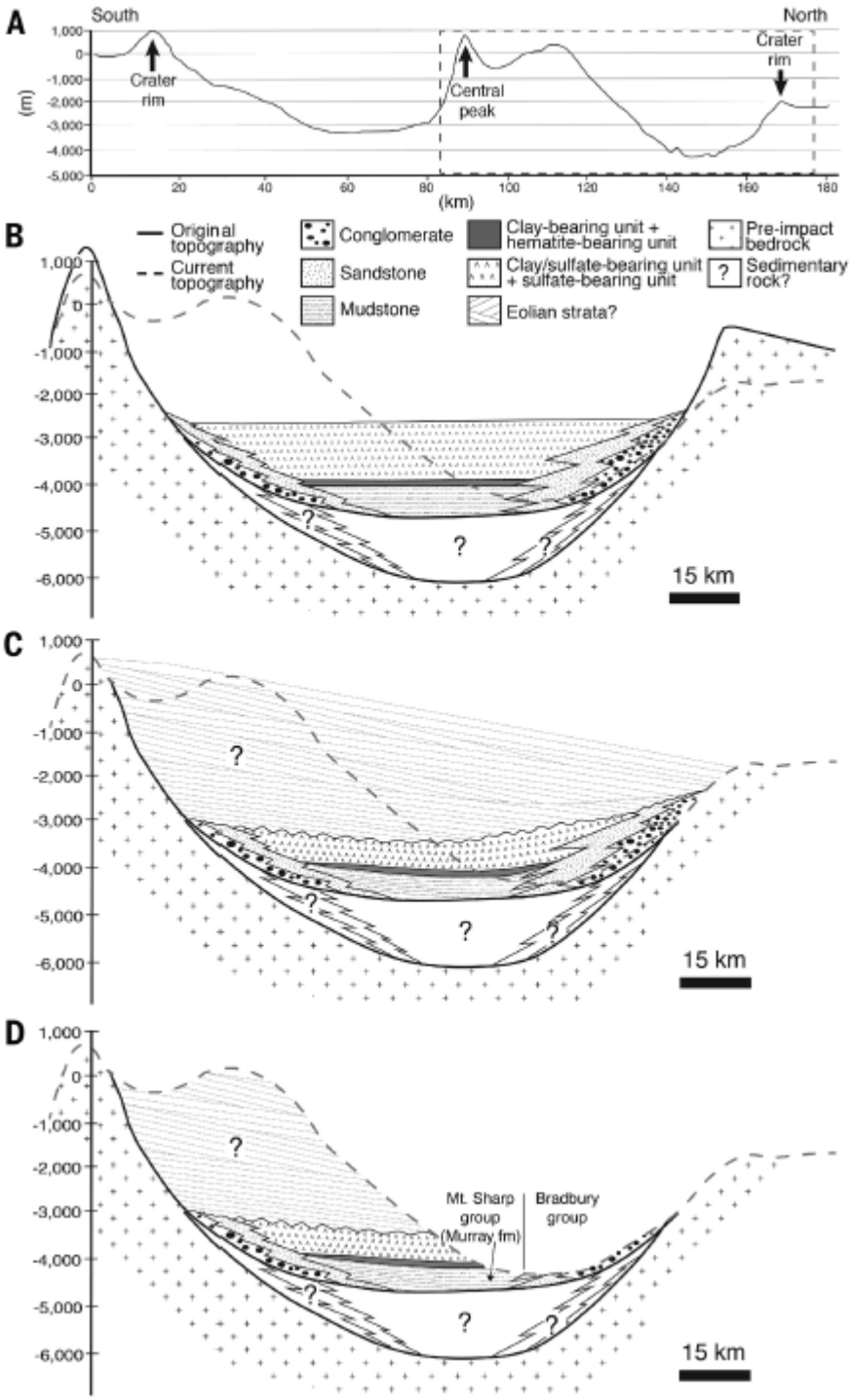

Figure 1.6: A schematic diagram by Grotzinger et al. (2015) that shows A) a cross-section through Gale crater followed by the geological history of the northern part of the crater starting with B) infilling of sediments by a fluviolacustrine system and subsequent erosion of the northern crater rim, C) continued sedimentary deposition in Gale, this time by aeolian processes, and D) exhumation of the sedimentary deposits, likely by aeolian abrasion, to form the current topography for the northern part of the crater.

Instead, the Mt Sharp Group sediments were most likely brought into the crater via fluvial activity, then later by air fall dust and aeolian processes that were cemented by ice during periods of high-obliquity (Bennett and Bell, 2016). As no outlet channel has yet been identified around Gale crater, and as Gale crater's rim is still relatively intact, these suggest that the sediments have been exhumed from Gale crater via suspension (Bennett and Bell, 2016; Day et al., 2016; Anderson and Bell, 2010). The widespread occurrence of yardangs (Day et al., 2016; Anderson and Bell, 2010), and ventifacts (Day and Kocurek, 2016; Bridges et al., 2014) in Gale crater's lithified sedimentary deposits also supports an aeolian exhumation hypothesis of Mt Sharp, as aeolian abrasion and erosion has clearly played a considerable role throughout its more recent geological history (Grotzinger et al., 2015; Anderson and Bell, 2010).

In the modification hypothesis, the regional dip away from the central mound is explained through the presence of a central peak and variations in grain size between the sedimentary units that constitute the crater floor and those of Mt Sharp (Grotzinger et al., 2015; 2014). The grain size variation between sedimentary units may have additionally played a role in aeolian processes, preferentially eroding material at the crater rim. Greater compaction of the finer Mt Sharp Group sediments may have made them more resilient to erosion compared to the coarser crater floor material (Grotzinger et al., 2015), generating the exposed stratigraphic record and topographic profile of Mt Sharp seen today. In addition, the presence of the central peak may have also influenced the compaction gradient between Mt Sharp's sediments and the sedimentary deposits closer to the rim. The central peak may also explain the gentle, regional northward dip in the stratigraphy away from Mt Sharp (Grotzinger et al., 2015).

The growth hypothesis for Mt Sharp's formation (Kite et al., 2016; 2013) discusses the accumulation of the central mound into its present form as a result of aeolian

deposition, without the complete infill and exhumation of the crater (Kite et al., 2016; 2013). Kite et al. (2013) argued that compaction of sedimentary units in a sedimentary basin such as Gale would result in a regional dip towards the centre of the crater, not towards the rim. Their model suggests that wind-blown sediment accrete towards the centre of the crater, away from the katabatic winds at the crater-wall, until the topographic relief of the developing mound becomes such that mound-flank slope winds predominantly start to erode material (Kite et al., 2016; 2013). However, this model does not take into account the presence of a central peak (Kite et al., 2016; 2013), and Gale's central mound is not situated directly in the centre of the crater as would be predicted by the model (Bennett and Bell, 2016; Thomson et al., 2011; Anderson and Bell, 2010). Furthermore, when a complex crater topography was included in a more recent model by Gabasova and Kite (2018), and substantial (~10 km thick) fluviolacustrine sediments were considered for lower Mt Sharp, the desired ~4° outward dip was achieved, but with a > 3 km thick, torus-shaped past overburden. This model provides a promising compromise to the growth and modification endmember hypotheses. Although, as it is unclear what geological process could produce the torus/donut-shaped past overburden structure required for the model to work, uncertainties still exist for the growth hypothesis (Gabasova and Kite, 2018). Hence, the modification hypothesis of Grotzinger et al. (2015) remains the preferred explanation for Mt Sharp's formation.

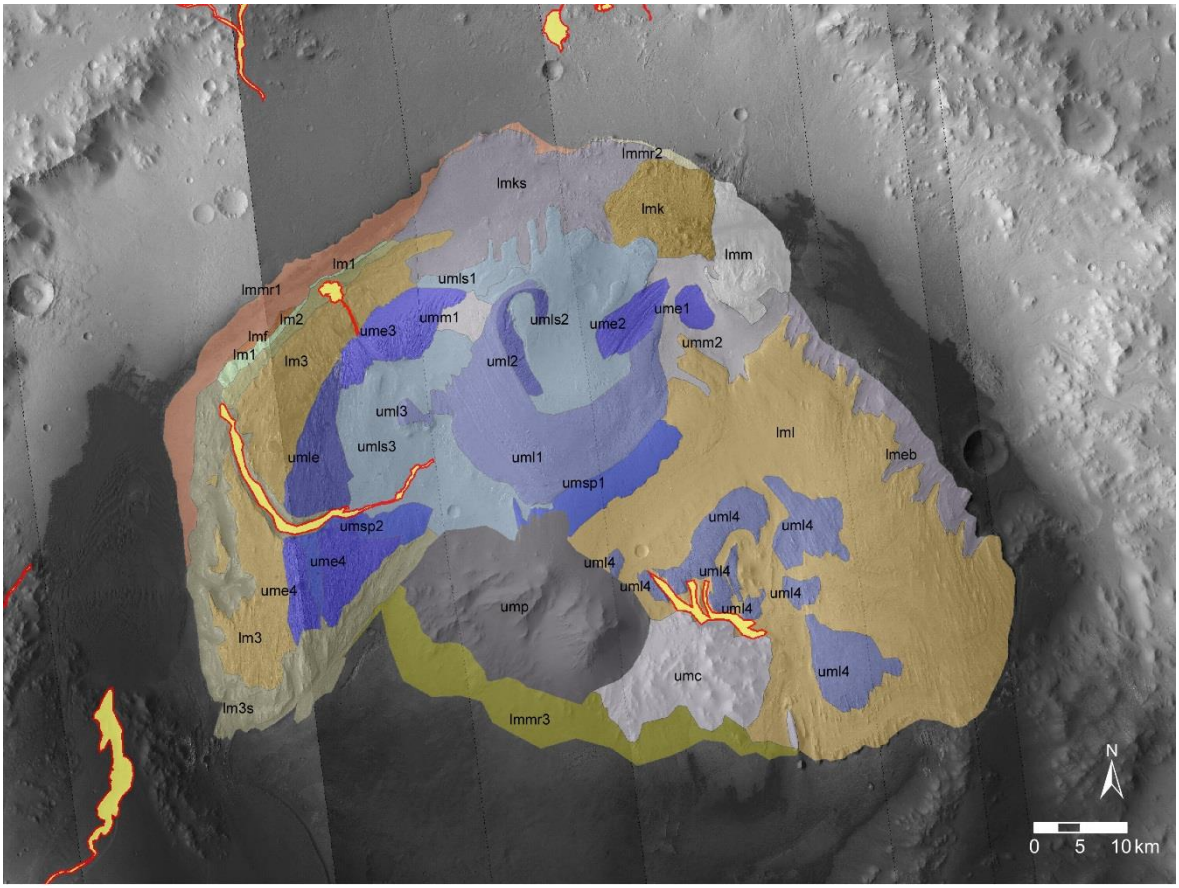

Geologic Map Key

Lower mound (Lm) formation

- lm1 Lower mound 1 unit
- lm2 Lower mound 2 unit
- lm3 Lower mound 3 unit
- lm3s Lower mound subdued 3 unit
- lmmr1 Lower mound marginal 1 unit
- lmmr2 Lower mound marginal 2 unit
- lmmr3 Lower mound marginal 3 unit
- lml Lower mound eastern layered unit
- lmf Lower mound fractured unit
- lmk Lower mound knobby unit
- lmm Lower mound mantled unit
- channel and inverted channel material

Upper mound (Um) formation

- ume1-3 Upper mound etched 1-3 units
- uml1-4 Upper mound layered 1-4 units
- umls1-3 Upper mound subdued layered 1-3 units
- umle Upper mound layered etched unit
- umsp1-2 Upper mound smooth plains 1-2 units
- ump Upper mound mountainous unit
- umc Upper mound chaotic unit
- umm1-2 Upper mound mantled 1-2 units
- lmeb Lower Mound embayed unit
- lmks Lower Mound subdued knobby unit

Figure 1.7: Mt Sharp Geological map from Fig. 3 of Thomson et al. (2011). The Lower Mt Sharp units (orange to tan units to the NW of the mound) are well layered with variable thermal inertia and hydrated mineral spectral signatures identified by CRISM (clays and sulfates, Thomson et al., 2011; Fraeman et al., 2016). Upper Mt Sharp units (purple, blue and yellow units) display cross bedding and do not show a hydrate mineral (Thomson et al., 2011; Anderson and Bell, 2010),

Prior to *Curiosity*'s landing in the late Noachian/Early Hesperian Gale crater (Thomson et al., 2011), Gale's layered deposits were subdivided into stratigraphic units based on their orbital characteristics such as variations in thermal inertia, surface roughness, albedo and textural morphology (Fraeman et al., 2016; Fraeman et al., 2013; Thomson et al., 2011; Anderson and Bell, 2010; Milliken et al., 2010). A distinct unconformity divides Mt Sharp into two main stratigraphic units according to geology and mineralogy: Lower Mt Sharp and Upper Mt Sharp (Fig. 1.7; Thomson et al., 2011; Anderson and Bell, 2010; Milliken et al., 2010). The Lower Mt Sharp Group contains approximately parallel beds of variable thickness, albedo and surface texture with hydrated mineral assemblages identified from orbit by CRISM. Meanwhile, the Upper Mt Sharp Group has steeper dipping beds with more homogeneous orbital characteristics and anhydrous mineral detections (Thomson et al., 2011; Milliken et al., 2010).

The hydrated lower units of the Lower Mt Sharp Group show a transition from predominately clay-bearing units to sulfate-bearing units (Fig. 1.5 B and 1.7; Milliken et al., 2010), in addition to multiple features (i.e., valleys and canyons) indicative of fluvial erosion (Fig 1.5 A; Anderson and Bell, 2010). This strongly suggests that the sedimentary units below the Mt Sharp unconformity were deposited during a period of Mars' history where aqueous processes were widespread (Fraeman et al., 2016; Fraeman et al., 2013; Anderson and Bell, 2010; Milliken et al., 2010). Alternatively, the minimal erosion of the Upper unit, and more steeply dipping, truncating beds indicative of large cross-sets (Wray, 2013; Anderson and Bell, 2010) indicates that the Upper Mt Sharp Group was deposited in dry, aeolian conditions and potentially represents large, preserved sand dunes (Anderson and Bell, 2010). Therefore, understanding Mt Sharp's preserved stratigraphy may contribute to our understanding of why Mars' climate transitioned from an ancient warm and wet environment to the present dry cryosphere.

1.3.2. Local geological context of the *Curiosity* rover's landing site

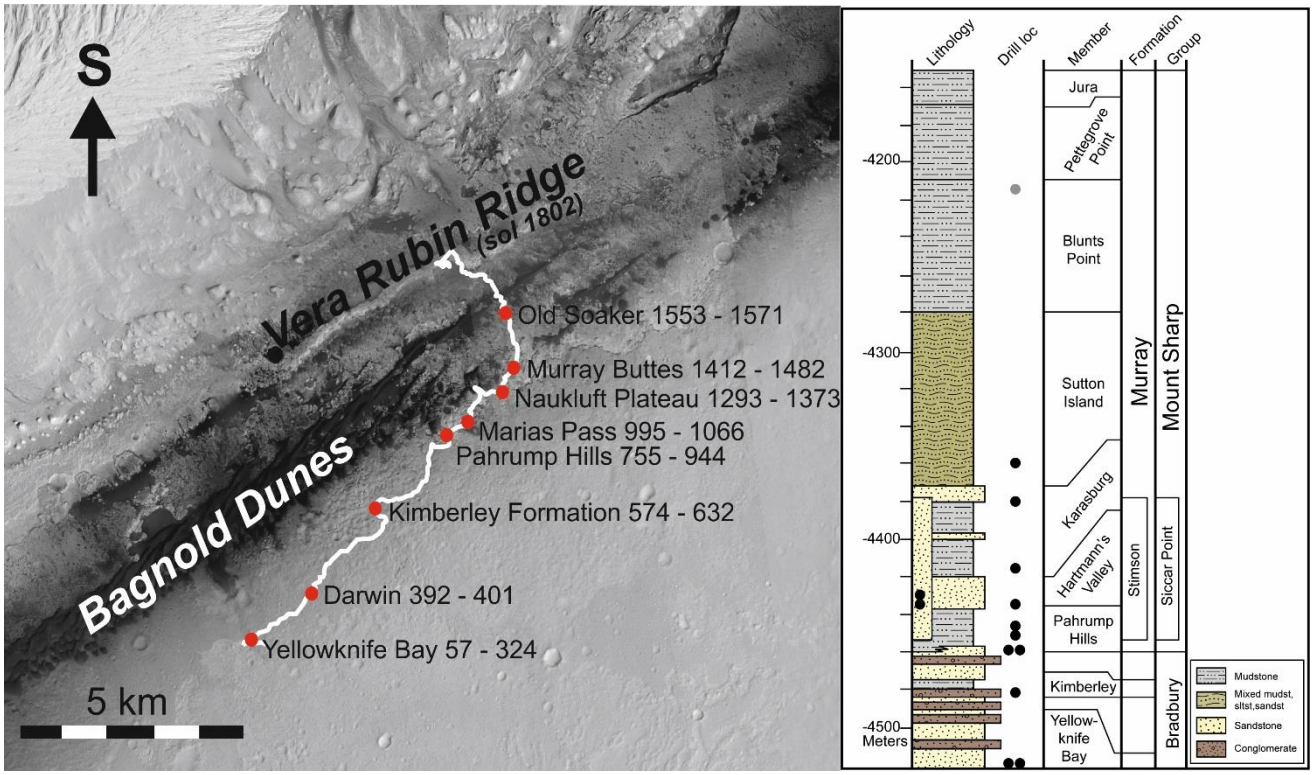

Figure 1.8: Merged HiRISE orthophoto mosaic base map (Calef and Parker, 2016) of the NW lower slopes of Mt Sharp annotated with the Curiosity rover traverse up to sol 2108 (white line) and key localities (red dots). Next to the traverse map is the Gale crater summary stratigraphic log of the geological units traversed by Curiosity (image credit: The MSL Science Team sedimentology and stratigraphy working group).

At the time of writing (December, 2018), *Curiosity* has successfully traversed the Hummocky plains of the crater floor from its landing site at the base of the large alluvial fan *Aeolis Palus* (Fig. 1.5; Grotzinger et al., 2014) and is currently exploring the most ancient units exposed at the base of NW Mt Sharp's stratigraphy (Fraeman et al., 2016; Grotzinger et al., 2015). The Gale crater succession so far consists of mudstone, fine to coarse sandstone, and conglomerate-rich units (Fig. 1.8), and has been divided into three main stratigraphic Groups (Fraeman et al., 2016; Grotzinger et al., 2015; 2014) that were deposited following the formation of the crater in the late Noachian/early Hesperian (Thomson et al. 2011). These stratigraphic groups are;

- The Bradbury Group (Fig. 1.9 C), which constitutes the sedimentary units located on the crater floor from the base of *Aeolis Palus* to the foothills of Mt Sharp. Defined pre-landing orbital units within this Group developed by Grotzinger et al. (2014) from the work of Anderson and Bell (2010) are the Bedded Fractured unit, Hummocky Plains, Rugged Terrain and the Striated unit. The Bradbury Group consists of predominately fluvially-deposited conglomerate and sandstone, associated with deposition during delta progradation and sampled by the rover during sols 1–750 (Grotzinger et al., 2015; 2014).
- The Mt. Sharp Group (Fig. 1.9 B) encompasses the sedimentary units deposited as part of the original Mt Sharp succession. The Mt Sharp Group traversed by *Curiosity* so far was originally defined in Anderson and Bell (2010) as the Mound Skirting unit (Fig. 1.5 A). *Curiosity* has analysed this lowermost exposed stratigraphy of Mt Sharp from sol 755, now named the Murray formation (Fraeman et al., 2016; Grotzinger et al., 2015). The Murray formation is largely finely-laminated mudstone interpreted to have been deposited within the standing water body located at the end of Gale crater's ancient fluviolacustrine system (Stack et al., 2018; Fraeman et al., 2016; Grotzinger et al., 2015).
- The Siccar Point Group (Fig. 1.9 A) is a lithified aeolian capping unit that unconformably overlies and truncates the Mt Sharp Group (Banham et al. 2018; Fraeman et al. 2016). This Group has been analysed in situ from sol 990–1352 by *Curiosity* as the Stimson formation and was originally identified by Rubin et al. (2014) within Anderson and Bell's (2010) Mound Skirting unit (Fig. 1.5 A). The Stimson formation has been investigated in detail at the Emerson and

Naukluft Plateaus (Banham et al., 2018) and is interpreted to have been deposited in a dry aeolian dune field (Banham et al., 2018).

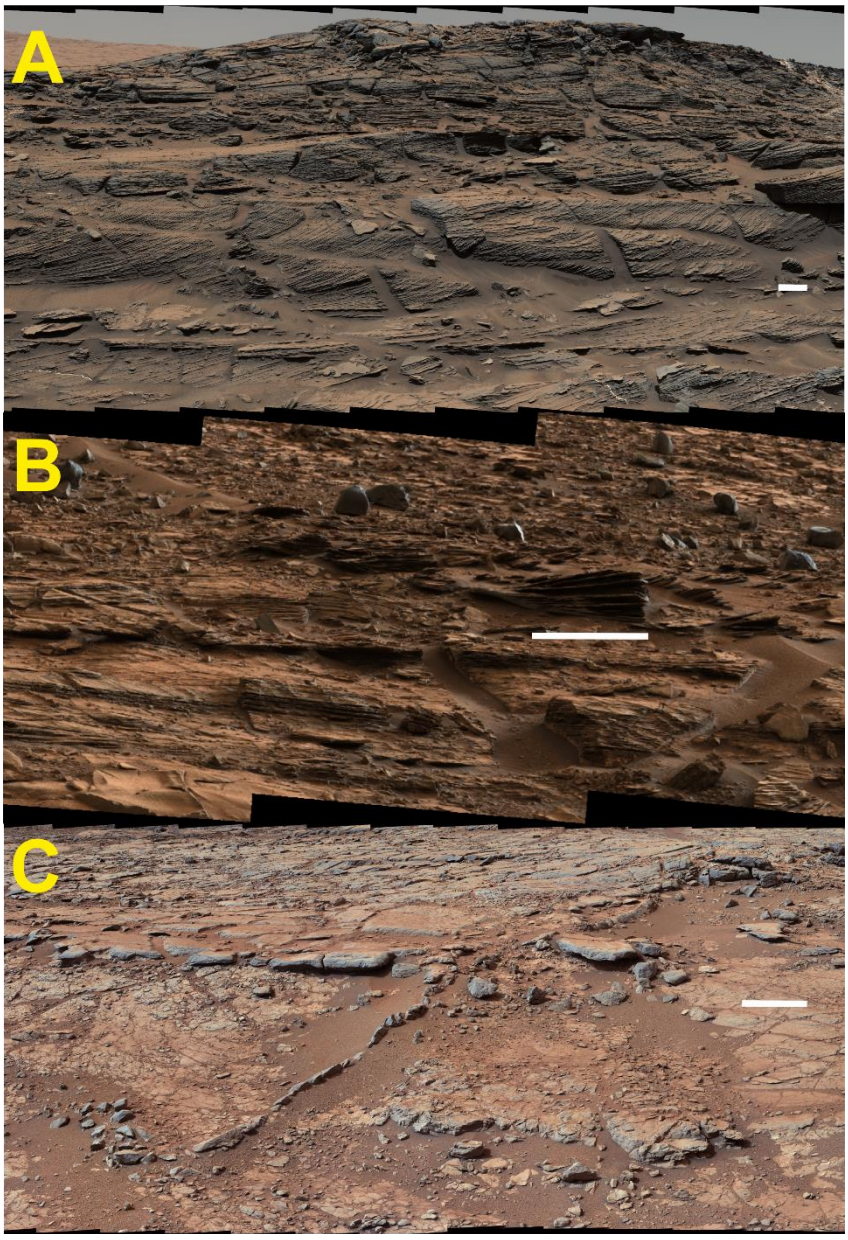

Figure 1.9: MastCam images of the three stratigraphic groups. A) The Stimson Formation (Siccar Point Group) with large-scale cross bedding (Williams Peak ML_mcam04777, sol 1099). B) The Murray Formation (Mt Sharp Group) with laminated mudstone and some interstratified fine-sandstone (Chinle Peak, ML_mcam03617, sol 821). C) The Yellowknife Bay formation with Sheepbed member mudstone capped by Gillespie Lake member sandstone and conglomerate (ML_mcam00817, sol 137). White scale bar measures 50 cm.

This study aims to expand upon the key areas investigated by the *Curiosity* rover within the Bradbury (Yellowknife Bay formation, Darwin waypoint, Kimberley formation), Mt Sharp (Pahrump Hills, Marias Pass, Murray Buttes localities), and Siccar Point (Emerson and Naukluft Plateaus) Groups that have provided a basis for previous studies into sediment source regions (Banham et al., 2018; Stack et al., 2018; Edwards et al. 2017; Hurowitz et al. 2017; Mangold et al. 2017; Rampe et al. 2017; Siebach et al. 2017a; Le Deit et al. 2016; Mangold et al. 2016; Morris et al. 2016; Anderson et al. 2015; Mangold et al. 2015; McLennan et al. 2014; Vaniman et al., 2014). These previous studies show that the sediments are largely basaltic in nature, though alkali- and silica-enrichments have also been identified in certain units, possibly relating to distinct, evolved magmatic source regions (Siebach et al., 2017a; Le Deit et al., 2016; Morris et al., 2016; Thompson et al., 2016; Treiman et al., 2016). The next sections define these key areas in greater detail for each stratigraphic group.

1.3.3.The Bradbury Group

From orbit, the Bradbury Group consists of high-thermal inertia terrain compared to the lower Mt. Sharp Group (Grotzinger et al., 2014; Milliken et al., 2010) and was initially divided into the Bedded Fractured unit, Hummocky Plains, Rugged Terrain and Striated units according to orbital characteristics (Grotzinger et al., 2014; Alexander and Bell, 2010). The Bedded Fractured unit has a higher thermal inertia compared to surrounding units, with extensive metre- to decimetre-scale fracture networks (Grotzinger et al., 2014; Thomson et al., 2011) and includes the Yellowknife Bay formation that was investigated by *Curiosity* from sols 57–324 (Fig. 1.8 & 1.10).

The Rugged Terrain unit comprises the majority of the outcrops analysed from *Curiosity*'s traverse from the Yellowknife Bay area to the Kimberley locality and gets its

rugged orbital texture from a high degree of scattered float material (Stack et al., 2016). The Hummocky Plains unit is tonally smooth and lower in thermal inertia than the Yellowknife Bay formation's Bedded Fractured unit (Grotzinger et al., 2014). The key outcrop of interest within the Hummocky Plains unit is the Darwin outcrop investigated from sols 392–401, and for the Rugged Terrain is the Cooperstown locality studied between sols 426–469 (Fig. 1.8 & 1.11).

The orbitally identified Striated unit lies close to the Bradbury/Mt Sharp boundary (Stack et al., 2016; Grotzinger et al., 2015) and was investigated at the Kimberley outcrop by *Curiosity* over sols 574–632 (Fig. 1.11). In situ analysis by *Curiosity* revealed that the source for the striations were east by northeast to west by northwest trending clinoform sandstone units that dip towards the south (Stack et al., 2016; Grotzinger et al., 2015). At the Pahrump Hills waypoint where the boundary between the Bradbury and Mt Sharp Groups was encountered by *Curiosity*, this clinoform unit was seen to interfinger with the basal Mt Sharp Group's Murray formation (Fig. 1.6 and 1.8; Stack et al., 2018; Grotzinger et al., 2015). The interfingering stratigraphic relationship was interpreted as the coeval deposition of fluvial sandstones and lacustrine mudstones (Fig. 1.8) at which point the rivers transporting material from the crater rim reached a perennial lake environment (Grotzinger et al., 2014; 2015).

Overall, ground based observations made by *Curiosity* revealed that the previously identified orbital units were comprised of mudstones in addition to medium- to coarse-grained, trough cross-bedded sandstones and poorly-sorted conglomerates, (see stratigraphic column, Fig. 1.8), supporting the fluviolacustrine environment hypothesised by previous orbital studies for Gale crater's sedimentary succession (Grotzinger et al., 2015; 2014).

1.3.3.1. The Yellowknife Bay formation

Yellowknife Bay (sols 57–324) has a sedimentary succession 4–6 m thick of lacustrine mudstone (Sheepbed Member, Fig. 1.10 A) overlain by cross-bedded, fluvial sandstone and conglomerate (Gillespie Lake and Glenelg Members; Fig. 1.10 B and C). Widespread diagenetic features – which are discussed in more detail in section 1.3.6. – were identified in the sedimentary succession at this waypoint, such as; raised ridges (Leveille et al., 2014; Fig. 1.17 A), filled and hollow nodules (Stack et al., 2014b; Fig. 1.17 B) and sulfate veins (Rapin et al., 2016; Fig. 1.17 C). Two samples (John Klein and Cumberland) were drilled from the Sheepbed mudstone and delivered to CheMin for mineralogical analysis (Vaniman et al. 2014).

The main lithology present in Yellowknife Bay is the laminated, smectite-bearing Sheeped Member mudstone deposited in roughly decimetre-scale beds (Fig. 1.10 A; Grotzinger et al., 2013). Geochemical and mineralogical analyses of this unit showed that it was likely to have been deposited at a neutral to slightly alkaline pH with low salinity, variable redox conditions, and an availability of key bioessential elements C, H, O, S, N and P (Grotzinger et al., 2014). The Sheepbed Member constitutes the first geological unit identified to have been deposited in an environment that was habitable for life as we know it, specifically chemolithoautotrophic organisms (Grotzinger et al., 2014). Detections of organic molecules chlorobenzene (C_6H_5Cl) at 150–300 ppbw and trace levels of dichloroalkanes have also been made with the Sample Analysis at Mars (SAM) instrument (Freissinet et al., 2015). These chlorinated hydrocarbons are hypothesised to result from the breakdown of Martian chlorine and organic carbon potentially derived from Martian or exogenous sources (Freissinet et al., 2015). A biological source for the chlorinated hydrocarbons is possible, but hydrocarbon sources derived from non-biological sources such as Martian igneous, hydrothermal or atmospheric processes, or meteoritic, cometary or interplanetary dust particles are also likely (Freissinet et al., 2015).

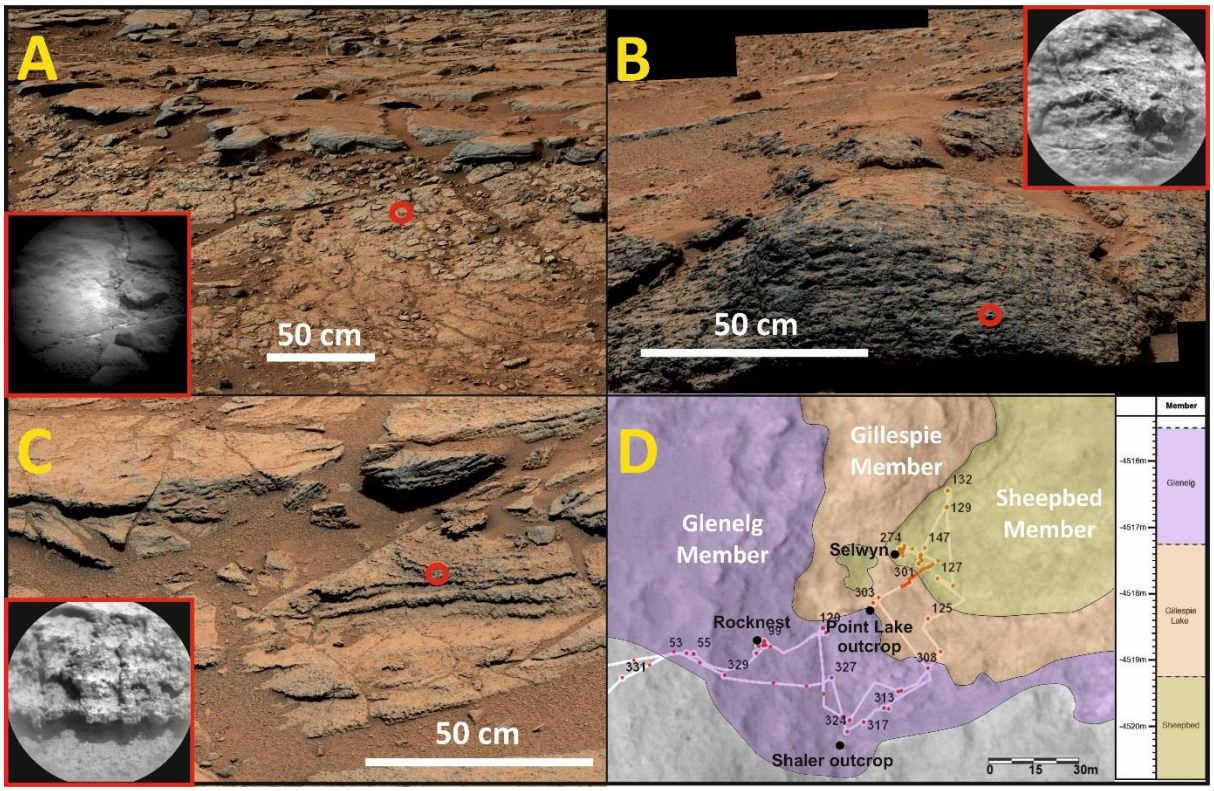

Figure 1.10: Mastcam and Remote Micro-Imager (RMI) images showing the representative outcrops and ChemCam targets of the Yellowknife Bay formation. Red circles show the ChemCam's target on the Mastcam images. A) The Selwyn ChemCam target of the Sheepbed Mudstone Member (sol 154, mcam00817). B) Knob Lake ChemCam target in the Point Lake outcrop which is representative of the Gillespie Lake area (sol 302, mcam00784). C) Cartwright ChemCam target acquired in the Glenelg member (sol 319, mcam01306). D) A geological map based on Grotzinger et al. (2014) of the Yellowknife Bay area, subsequent stratigraphic members, representative outcrop areas (black dots) and rover traverse (white line with red dots showing sol numbers).

The Gillespie Lake and Glenelg Members stratigraphically overlie the Sheepbed Member and consist of interstratified, coarse-grained sandstones and pebbly units separated by finer-grained, recessive units (see Figures 1.10 B and 1.10 C; Grotzinger et al., 2014). Gillespie Lake and Glenelg targets were analysed on the sols leading up to, and away from the Sheepbed Member area (sols 124–125 and 302–205 for Gillsepie Lake, and sols 57–123 and 309–323 for the Glenelg Member). Two key locations in the Glenelg member are the Rocknest and Shaler areas (Figure 1.10 D). The Rocknest location was one of the first outcrop sites to be studied and consists of a very fine-grained, laminated

sandstone with shrinkage cracks (Le Deit et al., 2016; Blaney et al., 2014; Grotzinger et al., 2014). Several float targets were also analysed at the Rocknest locality in addition to a sand shadow. This sand shadow was scooped and passed to CheMin for the first XRD mineralogical analyses of an aeolian deposit on Mars (Bish et al., 2013).

The Shaler outcrop (analysed by ChemCam from sols 309–324) was selected as a location of interest due to its distinctive cross-stratified sandstones (Fig. 1.10 C) identified in the panoramic images of the surrounding area at Rocknest (Anderson et al., 2015; Grotzinger et al., 2014). Images taken closer to Shaler show that this outcrop consists of thinly layered, interstratified, pebbly sandstones in addition to the recessive, fine-grained, cross-stratified sandstones identified from further away (Anderson et al., 2015; Grotzinger et al., 2014). Shaler has since been shown to have facies representing deposition in a high-energy, fluvial environment with evidence of low chemical weathering and a slightly alkali-rich basaltic composition compared to Shergottite meteorites (Anderson et al., 2015).

1.3.3.2. The Darwin and Cooperstown outcrops

From Yellowknife Bay, the rover embarked upon a ~8 km traverse to the base of Mt Sharp across the Hummocky Plains and Rugged Terrain orbital units (Grotzinger et al., 2015; 2014). Outcropping units of the Darwin and Cooperstown outcrops are similar (Fig. 1.11 A and B), consisting of river-deposited conglomerates with heterogeneous plagioclase-rich pebbles (Mangold et al., 2016), and some cross-bedded sandstone of varying grain sizes and resistant properties (Grotzinger et al., 2015). The coarse grain sizes and presence of polymict, pebble-sized clasts give evidence for deposition in a high energy fluvial environment with material derived from multiple source rocks (Mangold et al., 2016; Grotzinger et al., 2015).

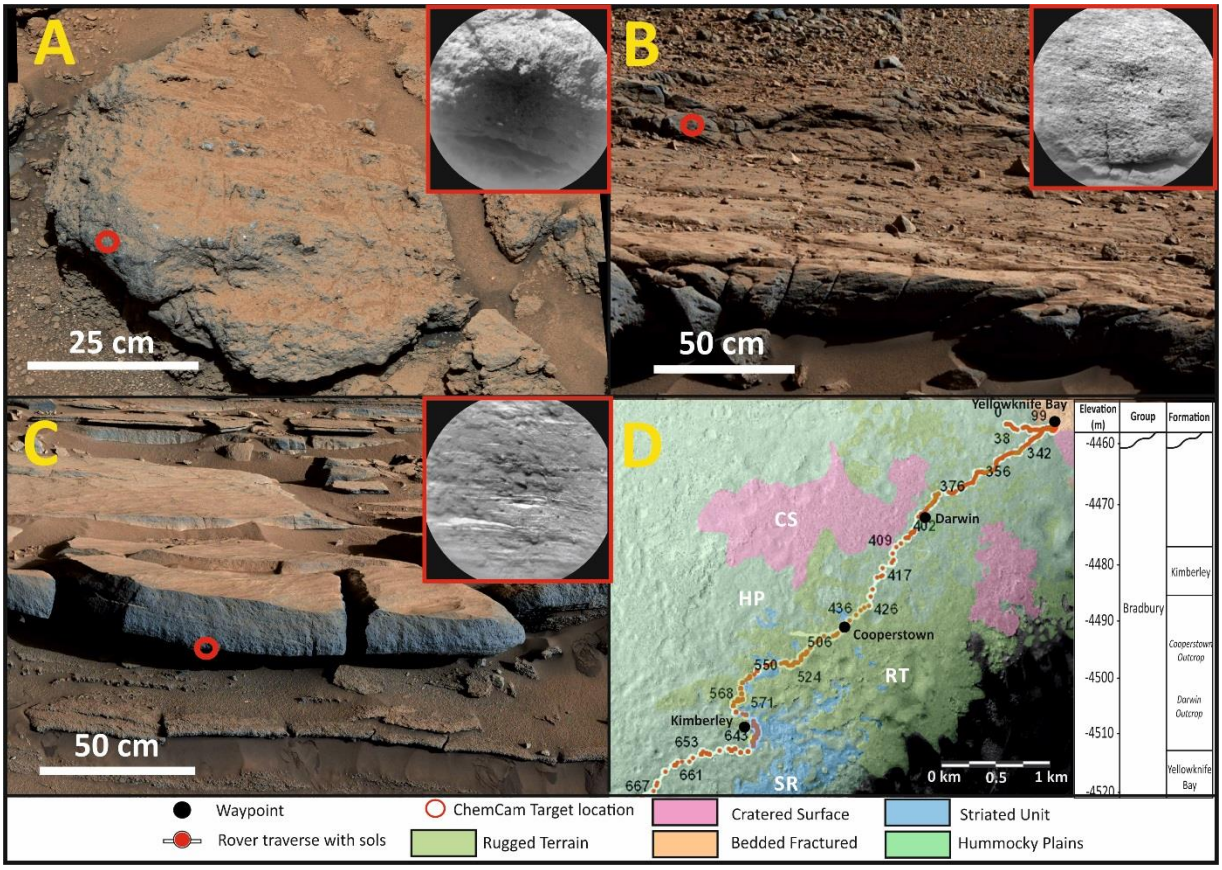

Figure 1.11: Mastcam and RMI images showing representative ChemCam targets for outcrops: A) Darwin (Bardin Bluffs2 ChemCam target, sol 392, mcam01619), B) Cooperstown (The Palisades target analysed on sol 453, mcam01793) and C) The Kimberley (The Square Top target from sol 576, mcam02368). The rover's traverse is shown in D) with orbital units and approximate stratigraphic thicknesses, outcrop locations and sols modified from Grotzinger et al., (2014). The stratigraphic column provides estimated thicknesses of each unit up to the interfingering boundary with the Murray formation (shown as a wavy line in the group and formation columns).

The Darwin outcrop (sols 392–401) of the Hummocky Plains unit is comprised of multiple exposures of conglomerate and sandstone bedrock, overlain by sand drifts and dark float accumulations (Mangold et al. 2016; Vasavada et al. 2014). Exposures of these conglomerates were also identified on the traverse leading up to and beyond the Kimberley formation described below (Mangold et al. 2016). Several clasts of igneous rock were seen at this locality within conglomerate units, or as igneous float scattered on top (Cousin et al. 2017; Mangold et al. 2016). Igneous float and clasts are discussed in more detail in section 1.3.7.

From orbit, the Cooperstown outcrop (Fig. 1.11 B) is situated within the distinct Rugged Terrain mapped unit, named as such from an increased abundance of scattered float with igneous textures and trachybasalt or basalt compositions (Edwards et al., 2017; Sautter et al., 2015) and dark-toned resistant outcrops giving the surface a rugged appearance (Le Deit et al., 2016; Grotzinger et al., 2014). It is divided into three units; a basal, cross-bedded sandstone unit, a thick (~50 cm), homogeneous sandstone unit and an uppermost resistant ledge unit of coarse sandstone with pebbles and voids (Le Deit et al., 2016). Potassium enrichment in the clastic sedimentary units was first noted at the Cooperstown outcrop with ChemCam (Le Deit et al., 2016) and associated with the potential presence of either potassic feldspar or illite (Le Deit et al., 2016). No CheMin analyses were conducted at this locality, but from this location, potassium-enrichment continued along the traverse to The Kimberley formation where it became over 5 times greater than the average for Mars (Le Deit et al., 2016). As potassium-enrichment is not associated with changes in grain size/texture and instead correlates with elevation, it likely relates to a change in sediment source region and not to physical sorting processes (Siebach et al., 2017a).

1.3.3.3. The Kimberley formation

The Kimberley formation (Fig. 1.11 C, sols 574–632), situated at the boundary between the Hummocky Plain, Striated and Rugged Terrain units, is the stratigraphically youngest key waypoint of the Bradbury Group (Grotzinger et al. 2015). Kimberley constitutes a fining upwards sequence of polymict conglomerate to fine to medium grained sandstone, capped by a massive coarse sandstone member (Thompson et al. 2016; Treiman et al. 2016). This formation was subdivided into the Point Coulomb and Liga conglomerates, Square Top fluvial sandstone, Dillinger trough cross-bedded sandstone,

and Mt. Remarkable massive sandstone Members (Fig. 1.12). These Members span at least two of the orbitally mapped units with the Point Coulomb, Liga and Square Top Members situated within the Striated unit, and the Dillinger and Mount Remarkable Members parts of the Rugged unit. Members of the Kimberley formation were analysed by ChemCam and APXS (Le Deit et al., 2016; Thompson et al., 2016; Grotzinger et al., 2015), and the Windjana sample was drilled from the Dillinger Member and delivered to CheMin (Treiman et al. 2016). No in situ analyses have been directly acquired from the uppermost Beagle Member (Treiman et al., 2016, Fig. 1.12). Inferences on the Beagle Member's sedimentology and geochemistry have instead been drawn from studying nearby float material with similar characteristics (Treiman et al., 2016).

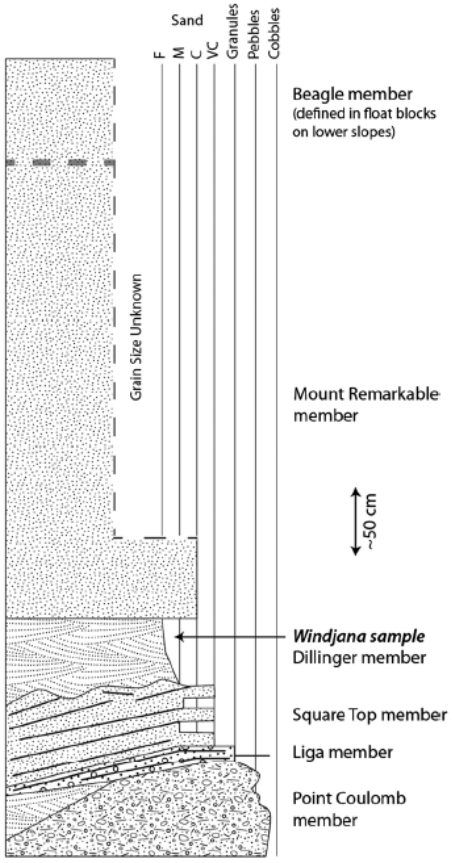

Figure 1.12: A stratigraphic log (Figure 2 from Treiman et al., 2016) detailing the different members of the Kimberley formation and where in the stratigraphy the Windjana drilled sample was acquired. Grain size is given at the top of the column and ranges from fine (F) medium (M), coarse (C) and very coarse (VC) sand, to granules, pebbles and cobbles.

Potassium concentrations in the Kimberley formation generally increase up-section with the lowest abundances in the Point Coulomb and Liga Members, and the highest abundances in the Dillinger and Mt Remarkable Members (Le Deit et al., 2016). The Dillinger Member Windjana drill hole analysis detected a high abundance of high order sanidine (21 ± 3 wt% total crystalline component) that has been associated with a trachytic igneous source region (Treiman et al., 2016). The Windjana drill CheMin analysis also showed mafic igneous minerals, such as olivine, indicating that the Dillinger sandstone is likely a poorly sorted sandstone derived from multiple igneous source regions; both mafic basalt and evolved trachyte (Treiman et al., 2016).

1.3.4.The Mt Sharp Group

The lower Murray formation (lowermost unit of the Mt. Sharp Group from the Pahrump Hills to Marias Pass; Fig. 1.8, 1.9 B and 1.13) is a laminated, fine-grained mudstone that appears stratigraphically ~20 m above the Kimberley formation (Fig. 1.8; Grotzinger et al., 2015). *Curiosity* has gained approximately 400 m in elevation during its traverse of this largely mudstone formation (Fedo et al., 2018). Here, elevation is considered to correspond to thickness due to the subhorizontal layering (Fedo et al., 2018). The Murray formation has been subdivided into five Members that are separated by conformable contacts (Fedo et al., 2018): The Pahrump Hills Member is the basal Member that is approximately 25 m thick, this is followed by the 25 m thick Hartmann's Valley Member, 37 m thick Karasburg Member, 98 m thick Sutton Island Member and >100 m thick Vera Rubin (Hematite) Ridge Member. Drilled samples from the lower Pahrump Hills Member include Confidence Hills, Mojave 2, and Telegraph Peak (Rampe et al., 2017), along with Buckskin from the Marias Pass locality (Morris et al. 2016).

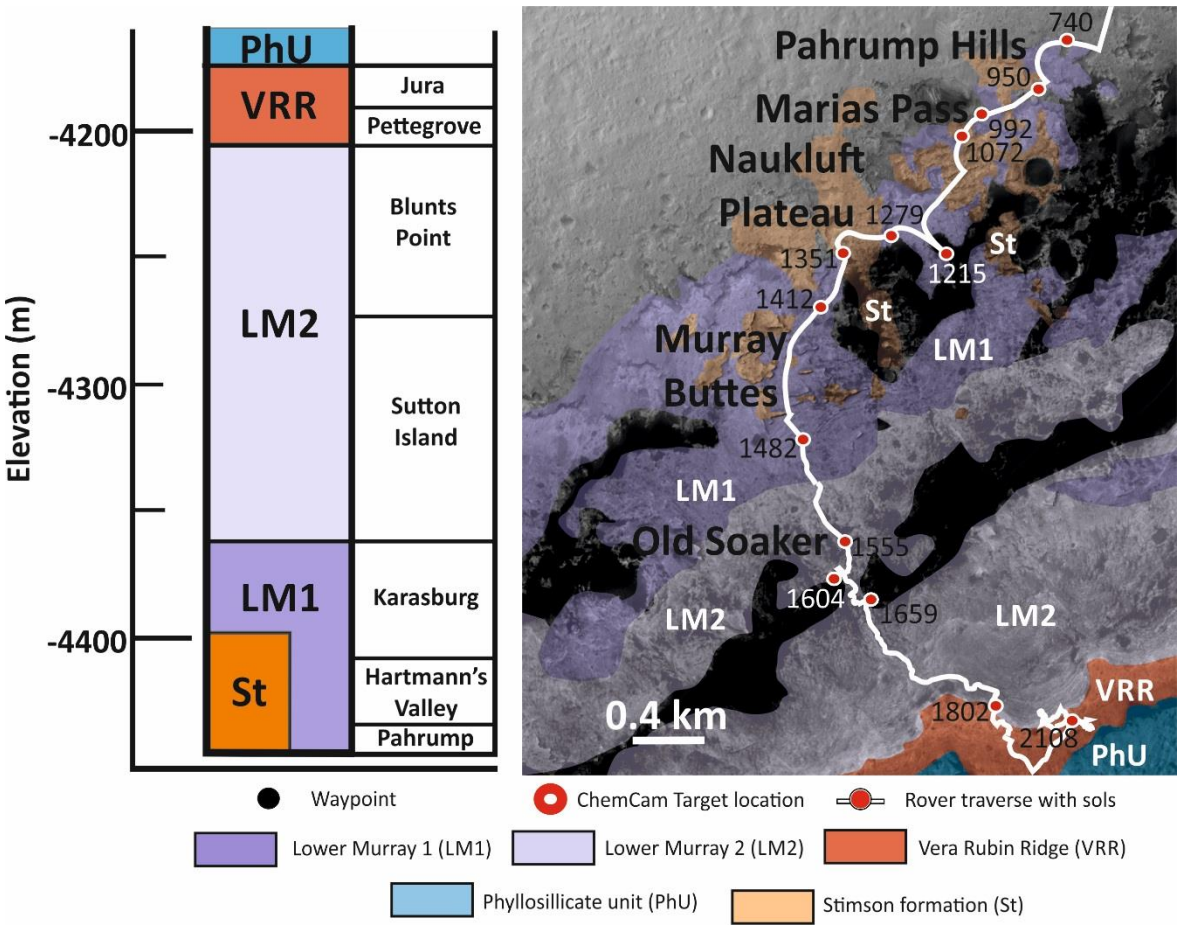

Figure 1.13: A geological map of the Lower Mt. Sharp orbitally derived stratigraphic units based on Fraeman et al. (2016), annotated with the Curiosity rover traverse and key waypoints (red dots) and sols. To the left is a stratigraphic column with the orbital units (Fraeman et al., 2016) alongside the ground-based members defined by Fedo et al. (2018).

The change from the Bradbury Group to the Mt. Sharp Group was marked by a transition from fluvial sandstone and conglomerate detected at the base (e.g., Bald Mountain, sols 775–778), to thinly laminated mudstone with extensive diagenetic features such as erosion resistant nodules, raised ridges and dark and light mineral veins (Nachon et al. 2017). The Murray formation also contains cross-laminated mudstone/siltstone – best preserved in the Hartmann Valley Member (Gwizd et al., 2018) –, interstratified fine-grained sandstone facies identified in the Pahrump Member (Hernández-Rivera et al., 2019; Fedo et al., 2018; Stack et al., 2018), and a heterolithic mudstone and sandstone unit in the Sutton Island Member (Fig. 1.8; Fedo et al., 2018). Despite these localities

exhibiting variations in grain size, overall grain size varies much less than in the Bradbury Group (Hernández-Rivera et al., 2019; Hurowitz et al., 2017; Rampe et al., 2017; Siebach et al., 2017a; Grotzinger et al., 2015) and the Murray Formation is considered as representative of continuing deposition in a lacustrine environment (Hernández-Rivera et al., 2019; Fedo et al., 2018; Gwizd et al., 2018; Stack et al., 2018).

From orbit, Murray appears homogeneous, at least up to the Vera Rubin Ridge Member, and has intermittent areas with notable orbital infrared signatures of Fe/Mg clay and sulfate (Fraeman et al., 2016; 2013). From rover observations, a mineralogical distinction can be made within the Murray formation between Murray units containing abundant hematite, and Murray units with high abundances of magnetite and crystalline silica (Hurowitz et al., 2017; Rampe et al., 2017; Morris et al., 2016). The CheMin samples which were drilled from the Murray formation encountered after the Naukluft plateau (sols 1373–1482) are Oudam and Marimba 2 (Bristow et al., 2018).

Moving up the Mt. Sharp stratigraphic succession towards the Murray Buttes, Murray becomes punctuated by a section of trough cross-bedded, fine-grained sandstone and siltstone, followed by a return to well-laminated mudstone, with some interstratified sandstone (Fig. 1.8; Fedo et al., 2018).

1.3.4.1. The Pahrump Hills locality

The Pahrump Hills area was investigated from sols 750–940. The main lithology present is the parallel, finely-laminated (~2.2 mm thick) lacustrine mudstone typical of the Murray formation and consistent with deposition in a lacustrine environment (Stack et al., 2018; Grotzinger et al., 2015). A change from thinly laminated mudstone to more thickly laminated mudstone/siltstone has been detected throughout (Stack et al., 2018; Hurowitz et al., 2017; Grotzinger et al., 2015). Cross-laminated, interstratified sandstones are also

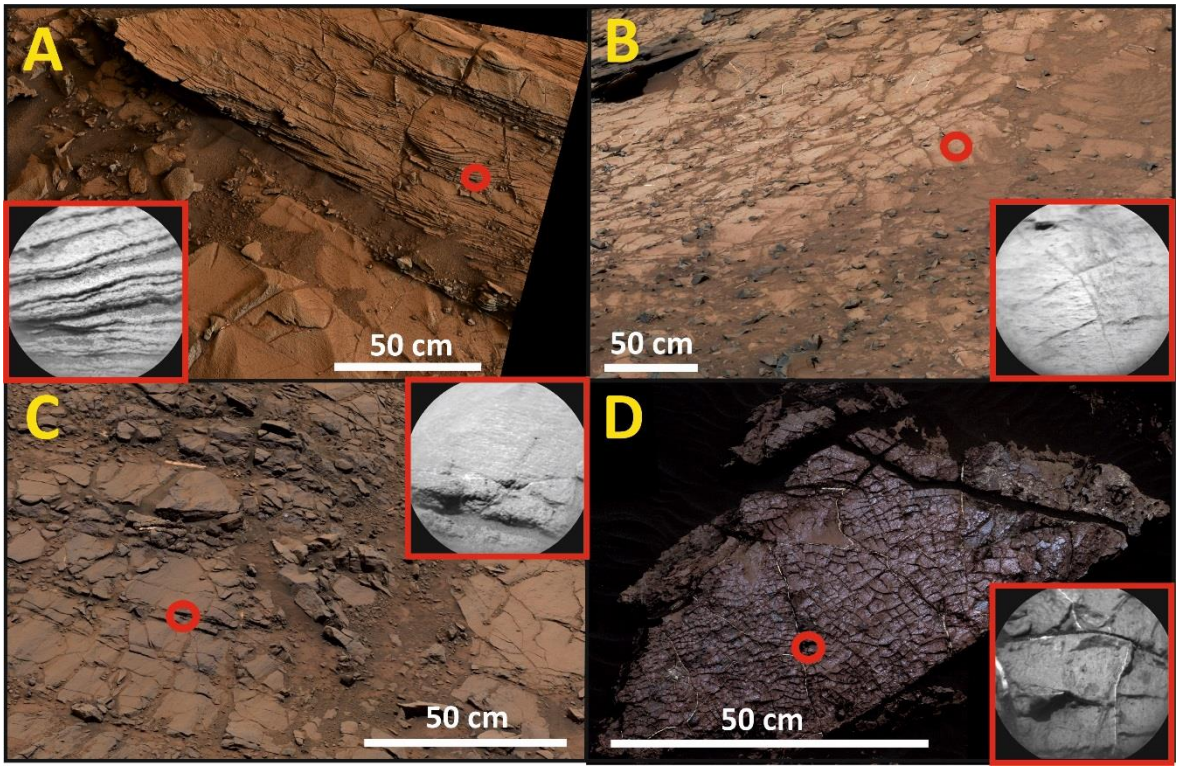

Figure 1.14: ChemCam targets showing examples of Murray bedrock in Mastcam and RMI images at key locations in the Lower Murray formation. A) Sespe target in the Chinle outcrop at Pahrump Hills (sol 794, mcam03457). B) The Buckskin pre-drill Murray formation target acquired on sol 1053 in the Lions Outcrop at Marias Pass (mcam04625). C) The Swakopmund ChemCam target in the Murray Buttes area (sol 1414, mcam06925). D) ChemCam target Somes Sound (sol 1555, mcam07981) of the Old Soaker outcrop.

present higher up in the Pahrump Hills section (Hernández-Rivera et al., 2019; Grotzinger et al., 2015), and are interpreted as basin-ward progradation of a fluvio-deltaic system into the lake body (Stack et al., 2018). The Pahrump Hills area is the northernmost exposure of the Murray formation and represents the lowermost 13 m of the Pahrump Hills Member (Fedo et al., 2018; Stack et al., 2018; Nachon et al., 2016; Grotzinger et al., 2015). Prevalent local alteration features cross-cutting the stratigraphy also exists here, such as dark-toned resistant ridges, magnesium-rich dendritic aggregates, and dark-toned, sulfate veins (Nachon et al., 2016).

Three drilled samples have been acquired and analysed by CheMin at this locality (Hurowitz et al., 2017; Rampe et al., 2017). These include the Confidence Hills, Mojave 2

and Telegraph Peak drilled samples. A mineralogical transition between samples Confidence Hills and Mojave containing abundant hematite and phyllosilicate (HP) to Telegraph Peak, and the later Buckskin drill of the Marias Pass area that is rich in magnetite and silica (MS) has been identified by Hurowitz et al. (2017). These mineralogical transitions are hypothesised to relate to either varying redox conditions in the lake, whereby the more oxidised assemblage was deposited closer to the shoreline (Hurowitz et al., 2017), or the interaction of the basal units with mildly acidic groundwaters (Rampe et al., 2017).

1.3.4.2. The Marias Pass locality

Marias Pass (Fig. 1.14 B) was encountered from sols 992–1072 and was found to contain bedrock with some of the highest silica abundances observed by ChemCam and APXS within the MSL mission. Marias Pass mudstone is approximately 2–3 m thick and is composed of the same parallel and finely laminated mudstone facies observed at the base of Pahrump Hills (Stack et al., 2018), with the exception of any cross-bedded sandstones or fluvial facies (Morris et al., 2016). The similarity in mudstone facies to that identified in the Pahrump locality indicates that they both relate to the Pahrump Hills Member of the Murray formation (Fedo et al., 2018). High silica observations are generally lighter-toned in colour relative to darker, low-SiO_2 analyses (Frydenvang et al., 2017), though due to the level of dust coverage, this is not always apparent. The CheMin Buckskin drill conducted at the Lion's outcrop sampled abundant tridymite – a high-temperature silica polymorph associated with evolved igneous assemblages (Morris et al., 2016). This is the only location so far where this mineral has been identified in abundance by CheMin.

The Stimson formation of the Siccar Point Group unconformably overlies the Murray formation at this locality (see also section 1.3.5. and Fig. 1.16). In general, the

Murray formation is finer grained, lighter in colour and does not possess cross-bedding or cross-laminations unlike the Stimson formation (Banham et al., 2018; Watkins et al., 2016). Additionally, the unconformity is marked by the presence of Ca-sulfate cement and Murray intraclasts in the basal beds of the Stimson sandstone (Newsom et al., 2018). Largely as a result of these basal Murray intraclasts and the difference in dip of the beds between the Murray and Stimson formation, the unconformity has been interpreted as erosional in nature (Banham et al., 2018; Watkins et al., 2016).

Silica-enrichment associated with light-toned, diagenetic halos surrounding fractures cross-cut both the Murray and Stimson formations in this area (Frydenvang et al., 2017). As the Stimson formation was deposited and lithified long after the deposition of the Murray formation after climatic conditions in Gale had changed to those dominated by dry aeolian processes, these diagenetic halos represent some of the most recent groundwater activity that post-dates the existence of a lake (Frydenvang et al., 2017). Two hypotheses on the nature of these silica-rich halos exist; one invokes passive silica-enrichment in the bedrock from migrating acidic groundwaters (Hausrath et al., 2018; Yen et al., 2017), while the other suggests silica-remobilisation from the detrital silica in the Marias Pass Murray formation through neutral to alkaline groundwaters moving up through the succession under pressure (Frydenvang et al., 2017). The co-location of the detrital silica unit with these features, as well as no obvious signs of leaching (i.e., enrichment in TiO_2 or Al_2O_3) and an absence of low pH indicator minerals such as jarosite better supports the silica-remobilisation hypothesis by Frydenvang et al. (2017). However, so far, no hydrous alteration model for neutral to alkaline solutions has been able to replicate this diagenesis (Frydenvang et al., 2017).

1.3.4.3. The Murray Buttes locality

The Murray Buttes area was traversed from sols 1414–1455 once the rover had descended the Naukluft Plateau (Fig. 1.14 C). Here, *Curiosity* encountered an area with multiple Buttes consisting of Murray outcrop capped with the Stimson draping unit. As the Stimson unit was located towards the tops of the Buttes, it was not analysed in situ at this locality unlike in the Marias Pass area. The Murray formation of the Murray Buttes locality is ~30 m thick and once again consists of parallel, finely-laminated lacustrine mudstones (Bristow et al., 2018), but this time differs in colour, with a greater purple hue compared to previous Murray. In addition, Murray at the Murray Buttes has a greater abundance of large concretions (Fedo et al., 2018). This variation in colour and diagenetic features distinguished Murray Buttes Murray from the previous Pahrump Hills and Hartmann Valley Members, placing it in the Karasburg Member (Fedo et al., 2018). Abundant calcium-sulfate mineral veins, calcium-sulfate cement (Newsom et al., 2017) and dark-toned vein features were also encountered in this area.

Two drilled samples were analysed in the Murray Buttes area; Marimba and Quela. These two samples are mineralogically similar to one another and possess abundant hematite and clays (Bristow et al., 2018). The detected phyllosilicates in Marimba and Quela include 1:1 and 1:2 proportions of dioctahedral to trioctahedral smectites (Bristow et al., 2018). These results fit with a possible trend of increasing dioctahedral smectite abundances in the Gale crater mudstone mineral assemblages, suggesting more oxidising conditions about the time of sediment deposition (Bristow et al., 2018).

1.3.4.4. The Old Soaker and Squid Cove outcrops

The Old Soaker and Squid Cove outcrops were encountered within the Sutton Island Member on Sol 1555 and are the first outcrops with sedimentological evidence of desiccation within the Murray formation (Stein et al., 2018). These outcrops consist of red mudstone with prominent polygonal arcuate ridges (Fig. 1.14 D) interspersed with $CaSO_4$ veins that both follow and cross-cut the ridges (Stein et al., 2018). Though $CaSO_4$ veins are common within the outcrop, the prominent ridges terminate at and are largely comparable in composition to the underlying grey bed (Stein et al., 2018). Both outcrops are geochemically similar to the average Murray bedrock, but with enrichments in Cl and Br (Stein et al., 2018). These observations show that the Old Soaker and Squid Cove outcrops have recorded a period of desiccation in the ancient lake, likely as a result of oscillating lake levels resulting in a period of exposure (Stein et al., 2018).

1.3.4.5. Vera Rubin Ridge

Vera Rubin Ridge (Fig. 1.15), previously known as Hematite Ridge in Fraeman et al. (2013), is a prominent ridge ~250 m wide that was identified from CRISM to have a spectral signature indicative of high hematite abundances relative to the surrounding units (Fraeman et al., 2016; Fraeman et al., 2013; Milliken et al., 2010). High abundances of hematite usually occur in the geological record at redox interfaces (Fraeman et al., 2013). Fe^{2+} is relatively soluble in anoxic aqueous solutions, whereas Fe^{3+} is insoluble. Therefore, substantial iron is precipitated out of solution when it meets more oxidising conditions (Fraeman et al., 2013). Before *Curiosity* reached Vera Rubin Ridge (VRR), three hypotheses of formation were put forward, either; (1) iron oxidisation occurred during the in-place alteration of local materials, (2) through the interaction of Fe-rich anoxic groundwater fluids with an oxidising atmosphere or (3) through the interaction of Fe-rich

anoxic groundwater fluids with oxidising groundwater fluids (Fraeman et al., 2016; 2013). In either case, hematite would precipitate in abundance as pore-filling cement, but in the alteration scenario would additionally occur as a coating and be spatially associated with leached material (Fraeman et al., 2013).

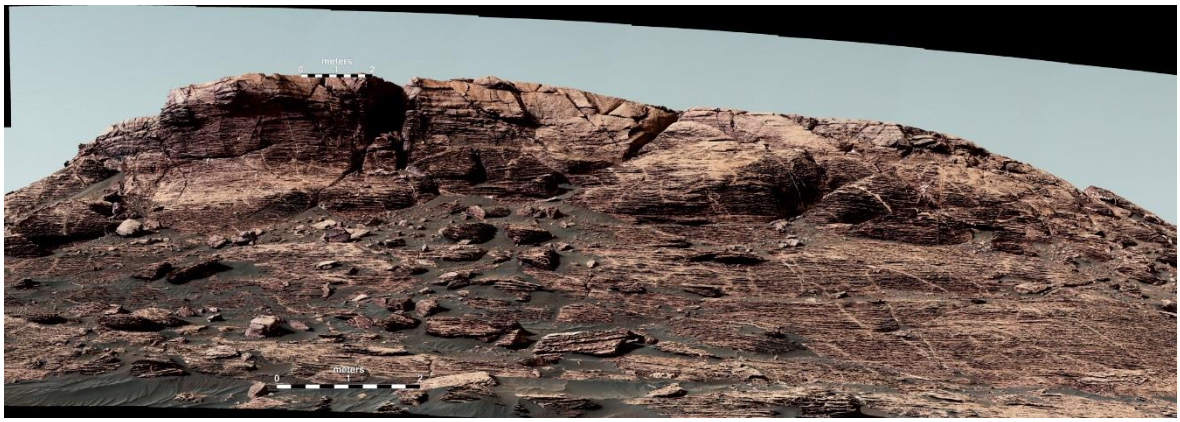

Figure 1.15: Coloured RMI mosaic of a portion of the Vera Rubin Ridge imaged during the approach on sol 1785. Scale bars measure 2 m. Image courtesy of NASA/JPL-Caltech/MSSS.

Curiosity arrived at the VRR on sol 1720 after traversing across the Sutton Island and Blunts Point Murray Members. So far, the lithology at the VRR appears consistent with the Murray formation mudstones analysed previously (Fedo et al., 2018; Heydari et al., 2018), and no substantial evidence for higher abundances of hematite or iron have been identified with the rover's on-board geochemical and mineralogical instrument suites (Frydenvang et al., 2018a; Thompson et al., 2018a). The notable difference between Murray encountered on the VRR compared to that investigated earlier is evidence for an increased hardness that may be attributed to greater proportions of a cement component (Bennett et al., 2018; Heydari et al., 2018).

At present, the VRR stratigraphy has been divided into the lower Pettegrove Point and upper Jura Members based on an apparent conformable boundary that follows the ridge, in addition to changes in diagenetic features and APXS derived bulk geochemistry (Fedo et al., 2018*;* Thompson et al., 2018a. Generally, Pettegrove Point has fewer

diagenetic features (nodules, mineral veins, fractures and erosion resistant features), and is lower in Al_2O_3, SiO_2, and higher in FeO_T than the Jura Member. Both members are generally red/purple (Bennett et al., 2018), though the Jura Member also contains patches of grey bedrock with Fe-rich nodules, sticks and gypsum pseudomorph features (L'Haridon et al., 2018a).

1.3.5.The Siccar Point Group (Stimson Formation)

Murray is capped by the Stimson formation (Siccar Point Group; Fig. 1.9 A & 1.16) – a draping unit composed of thickly laminated, cross-bedded sandstone with NE-SW trending ridges (Banham et al., 2018; Watkins et al., 2016; Grotzinger et al., 2015). The undulating unconformity separating these two stratigraphic formations represents an erosive boundary, further evidenced by the presence of Murray clasts in basal Stimson at certain areas such as Marias Pass and Bridger Basin (Banham et al., 2018; Newsom et al., 2018; Watkins et al., 2016). This draping unit was deposited post-exhumation of the Murray formation as ancient aeolian sand dunes migrated across the surface (Banham et al., 2018) which suggests that it is significantly younger than the Bradbury and Mt. Sharp Groups (Banham et al., 2018). Stimson is substantially less altered than Murray and is darker in colour (Banham et al., 2018; Watkins et al., 2016). However, this unit does exhibit light-toned, SiO_2-rich alteration halos around fracture zones that cross-cut both the Murray and Stimson formations (Frydenvang et al., 2017; Yen et al., 2017). Two pairs of samples (Big Sky/Greenhorn and Okoruso/Lubango) were collected from halos in the Stimson formation where one sample of each pair (Big Sky and Okoruso) was collected from outside the halo, and the other from inside (Yen et al., 2017). Calcium-sulfate mineral veins and nodules are also observed in Stimson suggesting that these diagenetic features

formed late in the geological history of Gale crater, post-lithification of Stimson (Frydenvang et al., 2017).

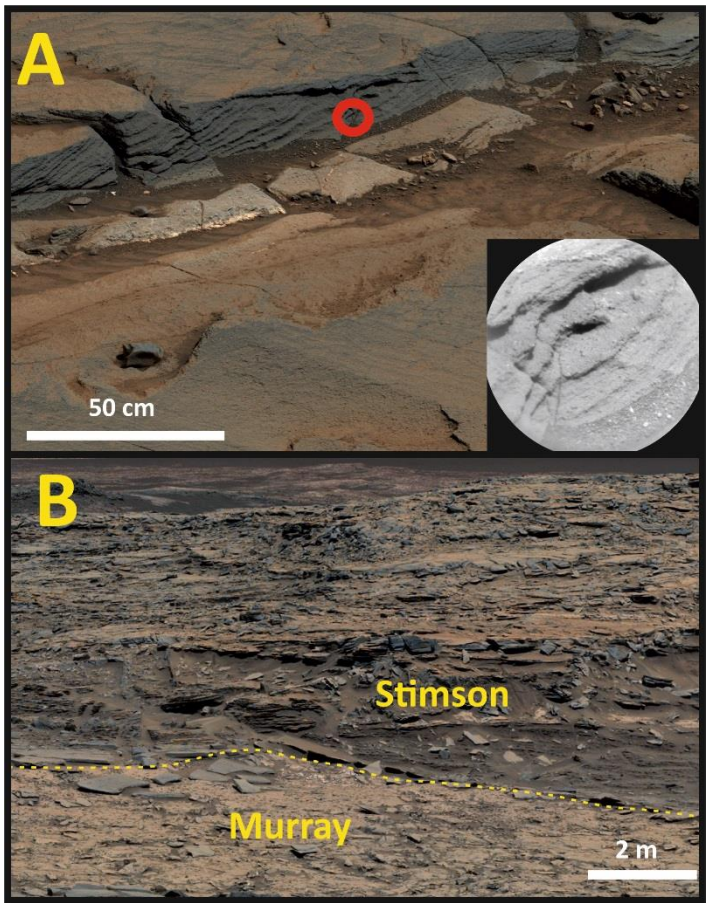

Figure 1.16: A) Representative Mastcam and RMI images of the Stimson formation. Circled in yellow is the Gordon ChemCam target (sol 1085, mcam04769). B) Shows an annotated Mastcam image of the Murray-Stimson contact studied at the East Glacier outcrop area (sol 1030, mcam04393). Here, the colour variation across the boundary along with its undulatory nature is highlighted by the dashed yellow line.

1.3.6. Alteration features and diagenesis in Gale crater

The variety of alteration features seen within the Gale crater stratigraphy – especially in the mudstone members – suggests that aqueous alteration occurred after deposition and lithification of the sediments (Frydenvang et al., 2017; Nachon et al., 2017; Rapin et al., 2016; Schwenzer et al., 2016a; Bridges et al., 2015a; Leveille et al., 2014; Nachon et al., 2014). Some features were identified throughout the stratigraphic record, such as calcium-sulfate mineral veins (Rapin et al., 2016; Nachon et al., 2014). Meanwhile

others were seen in specific areas (Fig. 1.17) i.e., raised ridges in Yellowknife Bay (Leveille et al. 2014), Mg-rich dendritic concretions at Pahrump Hills (Kah et al. 2015), dark mineral veins at Garden City (Nachon et al. 2017), and alteration halos between Marias Pass and Bridger Basin (Frydenvang et al. 2017; Yen et al. 2017).

ChemCam analyses taken across diagenetic features show that chemical remobilisation appears localised to weaknesses in the lithological units such as fractures (Frydenvang et al. 2017; Nachon et al. 2017). These weaknesses were exploited by the groundwater causing the dissolution and precipitation of soluble minerals and mobile elements along them. Hence, the low permeability of the units appears to have limited the open system alteration in bulk rock compositions away from the structural weaknesses of the bedrock (Anderson et al. 2015; McLennan et al. 2014).

In addition to the obvious diagenetic features, so far all Gale crater CheMin analyses of host rock and soil targets have contained a substantial proportion (16–60 wt%) of an amorphous and phyllosilicate (AP) component (Rampe et al., 2017; Treiman et al., 2016; Dehouck et al., 2014; Vaniman et al., 2014; Bish et al., 2013; Blake et al., 2013). A best estimate of the AP abundance and composition can be modelled using a full-pattern FULLPAT fitting method which compares known terrestrial natural and synthetic amorphous and clay samples to Mars CheMin analyses (Chipera and Bish 2013, 2002). Then AP compositions are calculated through a mass balance calculation using the bulk sample geochemistry analysed by the APXS instrument combined with the modelled FULLPAT sample phase abundances (Morrison et al., 2018). The amorphous component in the lithified sedimentary units – whether basaltic or silicic – has largely been hypothesised to relate to diagenetic cement derived from the aqueous alteration of the volcanic minerals or glass that constitute Gale's sedimentary units (Rampe et al., 2017; Treiman et al., 2016; Vaniman et al., 2014). In general, the calculated chemical

composition of the AP component has been associated with material initially derived from a basaltic source (Dehouck et al., 2014; Vaniman et al., 2014; Bish et al., 2013; Blake et al., 2013), except for the high-silica amorphous component in the Buckskin drill hole that was instead associated with an evolved volcanic source and/or enhanced leaching (Frydenvang et al. 2017; Morris et al. 2016).

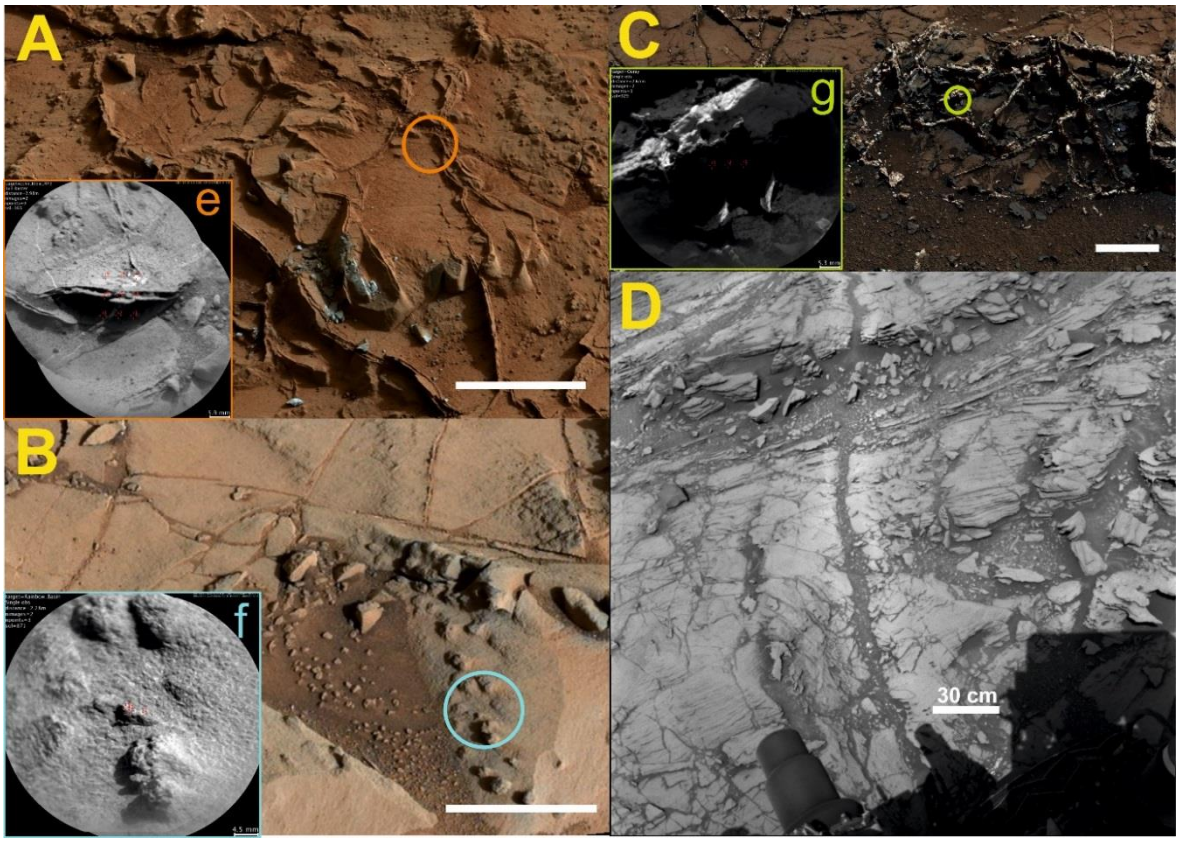

Figure 1.17. Mastcam, Navcam and RMI examples of identified alteration targets A) Raised ridge target John Klein RP3 (sol 165, mcam00885) in the Bradbury Group Sheepbed Member, B) Nodule target Rainbow Basin (sol 871, mcam03804) in the Mt Sharp Group Pahrump Hills locality, C) vein target Ouray (sol 929, mcam04068) in the Mt Sharp Group Garden City locality, and D) Alteration halo target Whitewater (sol 1094, ncam00354) at the Mt Sharp group, Marias Pass waypoint. Scale bar measures 10 cm, except for D which measures 30 cm. Images e), f), and g) are the RMI mosaics for the respective alteration feature footprints highlighted by the circles.

1.3.7. Gale crater igneous float and clasts

The *Curiosity* rover has identified evidence for fractionated crustal compositions in over 60 targets within Gale crater that occur as clasts in conglomerate units or scattered float (Cousin et al. 2017; Edwards et al. 2017; Mangold et al. 2016; Sautter et al. 2014). Igneous float and clasts were recognised according to identifiable igneous textures (porphyritic, aphanitic, vitreous and vesicular) from the rover's on-board science cameras (Cousin et al., 2017; Edwards et al., 2017; Mangold et al., 2016; Sautter et al., 2014). Their ChemCam derived compositions range from basalt (most abundant) to trachybasalts (Edwards et al. 2017). The variation between igneous float and clast geochemistry is attributed to olivine-dominated crystal fractionation of a subalkaline melt, similar in composition to the Adirondack Class basalts in Gusev crater (Edwards et al., 2017, Fig. 1.3). These igneous float and clasts were likely derived from the crust surrounding Gale crater that had been eroded, possibly by fluvial processes (Mangold et al., 2016; Sautter et al., 2014), due to the large clast/float size and poor sorting in conglomerates requiring minimal transport distance (Mangold et al., 2016).

1.3.8. A summary of Gale crater's geological record

After its formation ~3.8 ± 0.3 Ga ago (Thomson et al., 2011), Gale has since become a substantial sediment sink for material transported into the crater by fluvial and aeolian processes (Grotzinger et al., 2012; Anderson and Bell, 2010; Malin and Edgett, 2000). The sedimentary units that were deposited in Gale likely buried and eroded the original impact morphology of the crater (Grotzinger et al., 2015; Grotzinger et al., 2014; Schwenzer et al., 2012) before these sedimentary units were subsequently eroded themselves by aeolian processes to form Mt Sharp. At the time of writing (December, 2018) the MSL *Curiosity* rover had traversed across the crater floor to the lower units of

Mt Sharp's stratigraphy that was identified from orbit to contain hydrous bearing minerals (Fraeman et al., 2016; 2013; Thomson et al., 2011; Milliken et al., 2011). The geological units that were analysed by *Curiosity* on the floor of Gale crater are situated within the Bradbury Group and largely consist of fluvial sandstones and conglomerates (such as those analysed at the Darwin and Kimberley localities, Fig. 1.8 & 1.11; Grotzinger et al., 2014). Some lacustrine mudstones were also identified in the Bradbury Group at the Yellowknife Bay locality (Fig. 1.10) where the mineralogy and geochemistry suggests that they were deposited in a neutral to alkaline lake environment, with the chemical components necessary to support life (Grotzinger et al., 2014). This discovery completed one of the main *Curiosity* science goals to determine if Mars was habitable in the past (Grotzinger et al., 2014; 2012).

Curiosity then traversed up the foothills of Mt Sharp where the phyllosilicate and sulfate detections were seen from orbit (Fraeman et al., 2016; Milliken et al., 2011) in order to investigate these hydrous mineral signatures and reach the Vera Rubin Ridge – one of the initial mission aims (Fraeman et al., 2013; Grotzinger et al., 2012, Fig 1.5 & 1.8). The lowermost layers of Mt Sharp which derive the Murray formation and the Mt Sharp Group (Fraeman et al., 2016; Grotzinger et al., 2015) were seen to largely consist of laminated mudstone that was likely deposited in a lacustrine environment (Stack et al., 2018; Grotzinger et al., 2015). These mudstones continue throughout the Mt Sharp geological record and constitute the Vera Rubin Ridge which the rover is currently investigating. So far, just one outcrop, Old Soaker, shows evidence of desiccation suggesting that the lake was long-lived and perennial, where fluctuations in the shoreline likely related to seasonal variations (Stein et al., 2018). Ancient aeolian dune deposits were also seen to unconformably overlie the lake-deposited Murray formation at the Marias Pass, Bridger Basin, Naukluft Plateau and Murray Buttes localities (Banham et al., 2018; Watkins et al., 2016; Fraeman et al., 2016). These aeolian deposits comprise the Stimson

formation of the Siccar Point Group which were deposited after the transition from a warm and wet environment that could sustain a perennial lake, to the dry, arid conditions seen on Mars today (Banham et al., 2018).

1.4. Thesis Aims

The overarching research aim of this thesis is to identify the main sedimentological influences on Gale crater stratigraphic unit geochemistry and how this may have changed with time. Several processes such as source region composition, mineral sorting, chemical weathering, diagenesis and aqueous alteration can change the geochemical composition and mineralogy of sediments (Siebach et al., 2017; Fedo et al., 2015; Mangold et al., 2015; Tolosana-delgada et al., 2012; Weltje et al., 2012; Nesbitt and Wilson, 1992). Delineating the geochemical effects of each of these processes can therefore constrain the original geochemistry of the host rock they were sourced from and the environmental conditions under which they were transported, deposited and altered. Currently, there is a debate in the Mars community to what extent chemical weathering and post-depositional aqueous alteration masked the original geochemical composition of the sedimentary units in Gale crater (e.g., Mangold et al., 2019; Siebach et al., 2017). If the source region characteristics can be constrained, not only will we get information about the diversity of the Martian crust surrounding Gale crater, but we can use this as a basis to better understand the processes of aqueous alteration and mineral sorting regimes.

This PhD research aims to answer the following questions about Gale crater's chemostratigraphic record:

1. To what extent are the source region characteristics of Gale crater's sedimentary record preserved, or have they been overprinted by chemical weathering, mineral sorting and post-depositional aqueous alteration?
2. What are the geochemical trends of the main alteration features present in Gale crater's stratigraphic record?
3. How have sediment source regions changed with time?

The following objectives are employed to answer the above research questions:

1. Generate "constrained bulk rock datasets" through a detailed image analysis of each ChemCam observation point that have sampled relatively alteration feature-free sedimentary host rock and don't exceed the total oxide range of 95–105 wt% (see section 2.1.1). This bulk rock dataset is then subdivided according to stratigraphic group in order to model their respective minimally altered bulk compositions via multivariate density estimation (see section 2.4.1).
2. Derive the effect of grain size and ancient sediment sorting regimes on stratigraphic unit geochemical variation through a grain size-dependent comparison of constrained stratigraphic unit ChemCam data using qualitative (density contour analysis, section 2.4.1.) and quantitative (linear regression models, section 2.4.2., cluster analysis, section 2.4.3, and equivalence test, section 2.4.5.) techniques,
3. Constrain the degree of open-system weathering that has occurred between stratigraphic units and groups through a density contour and linear regression analysis of sedimentary host rock Chemical Index of Alteration values (see

section 2.4.2.), comparing the results to CheMin derived mineralogy of drilled host rock samples,

4. Determine the extent to which post-depositional aqueous alteration has occurred in the main stratigraphic groups of Gale crater and how this may have affected source region characteristics. This is achieved through a geochemical comparison of ChemCam observation points that have targeted obvious alteration features in the host rock (see section 1.3.6) and estimated, constrained bulk ChemCam compositions of analyses taken away from these features.
5. Estimate the dominant sediment source region geochemical characteristics using density contour plots of constrained ChemCam analyses (see section 2.2.1.) once the effects of chemical weathering, aqueous alteration and mineral sorting has been ascertained through objectives a) to e). This delineates the geochemical characteristics of the main sediment source regions in Gale crater from the sedimentological processes outlined in (1) and constrain how these may differ between the fluvial, lacustrine and aeolian units.

Active dune deposits are present within Gale crater today with orbital data indicating that mineral sorting has created a variation in mafic and felsic minerals across the dune field relative to the prevailing wind direction (Rampe et al., 2019; Lapotre et al., 2017). On the basis of this evidence and that acquired from terrestrial studies of basaltic dune mineral sorting regimes (e.g., Baratoux et al., 2011; Mangold et al., 2011; Mountney and Russell, 2004), I also aim to answer whether the geochemical signature of the aeolian mineral sorting regime of the ancient, aeolian Stimson formation can be identified and used to determine the prevailing wind direction at the time of deposition. In order to answer this research question, the following objective was taken for data relating to the Stimson formation in addition to those discussed above:

1. Isolate ChemCam analyses in the Stimson formation that have targeted more "mafic" or "felsic" minerals through a cluster analysis (section 2.4.3.), determine the relative enrichment of these mineral groups between the two localities using density contour analyses (sections 2.3.1.), and compare it to the aeolian mafic-felsic mineral sorting regime determined for basaltic environments.

Finally, due to the *Curiosity* rover's recent campaign at the Vera Rubin Ridge and its importance to understanding the continued geological record and habitability of Gale crater (Fraeman et al., 2018; Fraeman et al., 2013), I also aim to answer what the relationship is of this ridge to the underlying Murray formation and which hypothesis for its formation and the high hematite orbital spectral signature is more likely based on the geochemistry analysed in situ by *Curiosity*. To achieve this, I have fulfilled the following objective:

1. Conduct a comparative study of estimated Vera Rubin Ridge bulk rock compositions compared to the underlying Murray formation bulk composition, in addition to a geochemical analysis of alteration features specific to the ridge (such as grey and red patches).

1.5. Thesis Structure

The structure of this thesis is as follows:

- Chapter 2 provides a detailed outline of the methods used in this study including the target classification scheme, how I constrained the ChemCam dataset and the statistical methods used throughout to analyse and interpret each database group.

- Chapter 3 investigates the constrained bulk rock geochemistry of the main fluviolacustrine stratigraphic groups in Gale crater; Bradbury and Mt Sharp in relation to their diagenetic features, degree of chemical weathering, mineral sorting processes, and source region characteristics. This chapter has formed the main base of the paper "**Alteration trends and geochemical source region characteristics preserved in the fluviolacustrine sedimentary record of Gale crater, Mars.**" C. C. Bedford, J. C. Bridges, S. P. Schwenzer, E. B. Rampe, R. C. Wiens, J. Frydenvang, P. J. Gasda. This paper has been published in *Geochimica et Cosmochimica Acta* (https://doi.org/10.1016/j.gca.2018.11.031).
- Chapter 4 analyses the constrained bulk rock geochemistry of the Stimson formation in order to understand the influence of lithification on the preserved dune formation relative to the modern Bagnold dunes, determine the geochemical effect of aeolian mineral sorting regimes on the preserved dune formation, and discuss potential sediment source regions, comparing them to those determined for the fluviolacustrine groups in Chapter 3. Work from this Chapter is anticipated to form the basis for a paper with the working title "**The Geochemistry of the Stimson ancient aeolian formation in Gale crater, Mars.**" C. C. Bedford, J. C. Bridges, S. P. Schwenzer, R. C. Wiens, S. Banham, J. Frydenvang, P. J. Gasda, E. B. Rampe, which I expect to submit to *Earth and Planetary Science Letters* within a month after thesis submission (i.e., February 2019).
- Chapter 5 compares the bulk geochemical composition of the Vera Rubin Ridge to the underlying Murray formation to draw preliminary conclusions on its sediment source regions, diagenesis and discuss possible origins relating to previous hypotheses drawn from orbital data. After submission, work from this

chapter will contribute to the ChemCam team paper of the *JGR* special issue on the Vera Rubin Ridge campaign led by Dr. Jens Frydenvang.

- Chapter 6 synthesises the results and conclusions of the previous chapters, whether the main science aims have been achieved, and discuss the main conclusions of this thesis in relation to the wider scientific picture of the geological history of Gale crater and Mars, including the future landing sites of the Mars2020 and ExoMars rovers.

2. Methods

In this chapter, I detail the methods used throughout this thesis to constrain the geochemical effects of Ancient Mars' sedimentary processes and delineate these from the crustal source region characteristics of the lithified units in Gale crater. The following section 2.1 briefly describes the instruments on-board the *Curiosity* rover, along with their various sampling techniques, from which data are derived for this PhD project. I next detail the various methods under which these data are analysed (sections 2.2 & 2.4) along with the comparison datasets (section 2.3) that are also used in order to accomplish the research aims and objectives described in Chapter 1.4.

2.1. MSL Instruments and sampling techniques

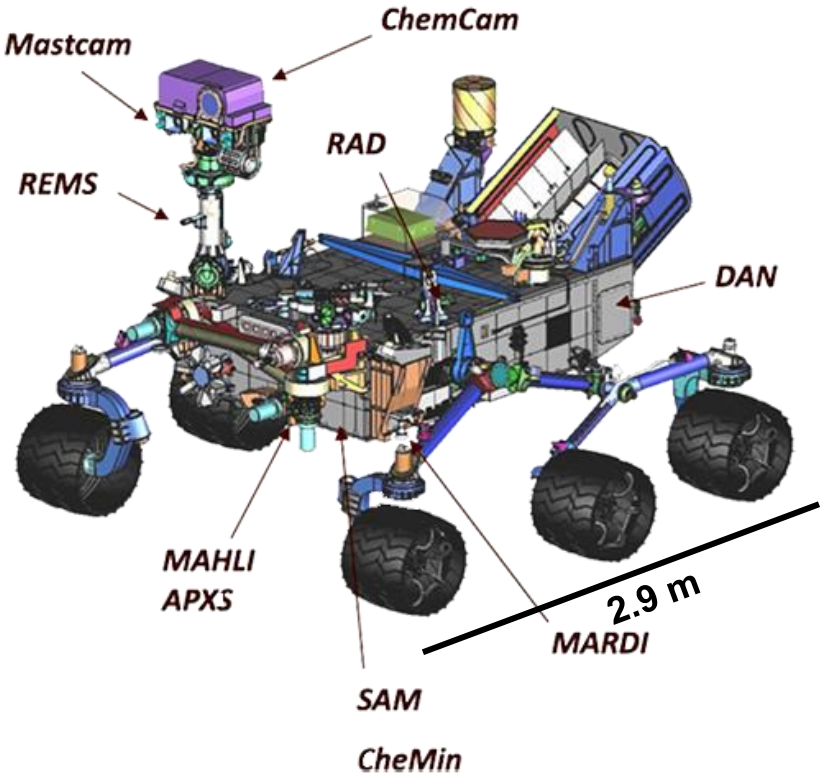

Figure 2.1: Schematic diagram of the MSL Curiosity rover instrument suites. Image credit: NASA/JPL-Caltech.

Fig. 2.1. shows a schematic diagram of the *Curiosity* rover's instrument suites. Data for this project are acquired from the ChemCam, APXS, CheMin, Mastcam, MAHLI, Navcam and Hazcam instruments and are pre-processed by the subsequent instrument teams. In this section, I briefly outline the sampling techniques of each instrument suite whose data are used in this thesis. Team-calibrated data were downloaded from the NASA Planetary Data System and Jet Propulsion Laboratory's MSL science team database.

2.1.1. The ChemCam instrument and LIBS technique

I have used data from the ChemCam instrument in this thesis as the basis for geochemical analyses. ChemCam (Fig. 2.2) is located in the *Curiosity* rover's mast and body units (Maurice et al., 2012; Wiens et al., 2012; Sallé et al., 2007) and consists of a telescopic imager situated in the mast unit, with three spectrometers housed in *Curiosity*'s body unit (Maurice et al., 2012; Wiens et al., 2012). The Laser-Induced Breakdown Spectroscopy (LIBS) technique is based on the Stoichiometric Ablation hypothesis which states that material excited by short pulses of a high-powered laser generates a plasma with the same composition as the sample (Sallé et al., 2007). This technique enables multi-element analyses over a variety of sample types up to 7 m from the rover mast. These capabilities have allowed ChemCam to generate a dataset of over 750,000 spectral analyses (as of December 2018) for a variety of geological targets, with some targets that would otherwise have been at a location not reachable by the rover's on-board instruments. The LIBS method also removes soil coatings and weathering rinds from the first few laser shots of targeted samples and analyses a small area with high precision (sample footprint <1 mm). These precise target analyses can then be placed into geological context as a result of ChemCam's baseline operation sequence that includes target imaging by the Remote Micro-Imager (RMI) before and after sample acquisition (Maurice et al., 2012;

Wiens et al., 2012). Target analyses can also be placed into geological context using images from Mastcam and MAHLI (Maurice et al., 2012; Wiens et al., 2012). These have contributed to the capability of this study to accurately assess Gale crater's sediment compositions by permitting fine-scale target classification, and the analysis of soil, dust, and coating-free rock along the rover traverse.

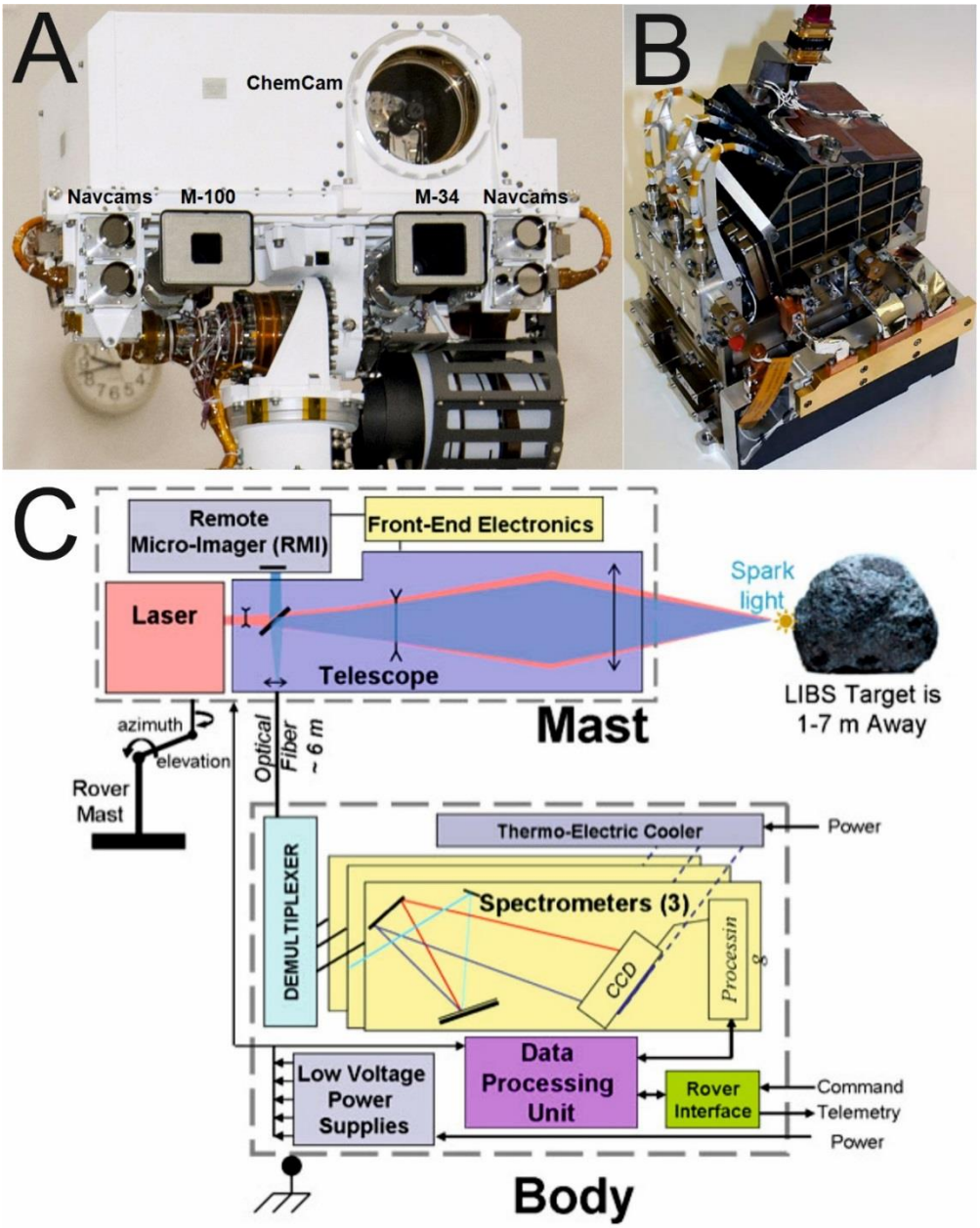

Figure 2.2: Images of A) the mast unit instruments with ChemCam, Mastcam and Navcam highlighted, B) The ChemCam body unit, and C) A diagrammatic overview of the ChemCam instrument and its division between the body and mast units of the Curiosity rover. Image credit NASA/JPL-Caltech/LANL/IRAP/CNES.

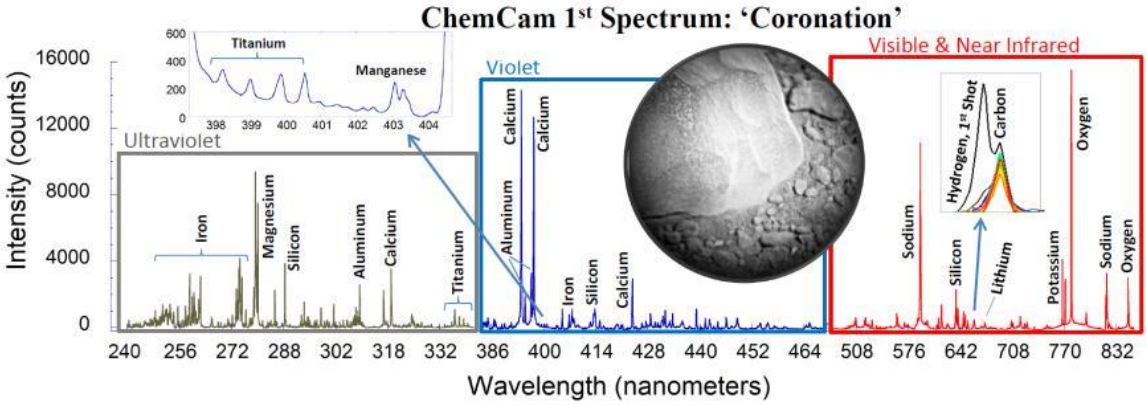

Figure 2.3: A composite diagram of the first 30 spectral analyses taken by the ChemCam instrument across the three spectrometers housed in Curiosity's body unit. Image credit: NASA/JPL-Caltech/LANL/CNES/IRAP.

LIBS analyses are conducted as a series of short, 14 mJ laser pulses directed at an observation point on the incident sample (Maurice et al., 2016; Maurice et al., 2012; Wiens et al., 2012). These laser pulses induce a short-lived plasma within the host rock or soil, exciting the electrons in the atoms and ions of the sample. The excited electrons then emit photons at diagnostic wavelengths upon their decay to lower energy levels which are subsequently detected by the telescopic imager and passed to three spectrometers in the ultra-violet light (UV; 240–340 nm), violet (VIO; 380–470 nm), and visible and near infra-red (VNIR; 470–900 nm) spectral ranges (Wiens et al., 2012). Spectral analyses are then pre-processed to remove continuum-effects that can reduce the quality of the analysis such as Bremsstrahlung and Recombination effects (Wiens et al., 2013). Next, quantitative analysis is attained by comparing the spectra to a ground-based calibration set of over 400 standards, through the combination of Partial Least Squares (PLS) sub-models and an Independent Component Analysis (ICA) algorithm (Clegg et al., 2017).

The calibration library of standards includes an extensive range of natural geological samples of igneous, sedimentary and metasedimentary origins ranging from Archaean to Triassic in age. Synthetic samples have also been included to increase the compositional range of certain major elements, such as TiO_2 (Clegg et al., 2017; Wiens et

al., 2013), and account for a variety of salts and oxides to simulate various mineral vein fills and cements (Lanza et al., 2010), such as the calcium sulfate veins identified within Gale crater (Clegg et al., 2017; Rapin et al., 2016). The igneous standards used are also representative of a wide range in compositions – from mugearite to andesite – and contain varying degrees of alteration (Clegg et al., 2017; Wiens et al., 2013). This provides eight major element oxide abundances as wt % (SiO_2, TiO_2, Al_2O_3, FeO_T, MgO, CaO, Na_2O, and K_2O). A set of on-board calibration targets, e.g. Ti Metal, are regularly checked for any instrument drift during the mission (Blaney et al., 2014; Vaniman et al., 2012). Non-normalised major element compositions have been used in this study to account for minor element contributions such as S, P, F, Cl, and H. See Fig. 2.3 for an example of a ChemCam laser spectrum with characteristic emission lines of the various elements.

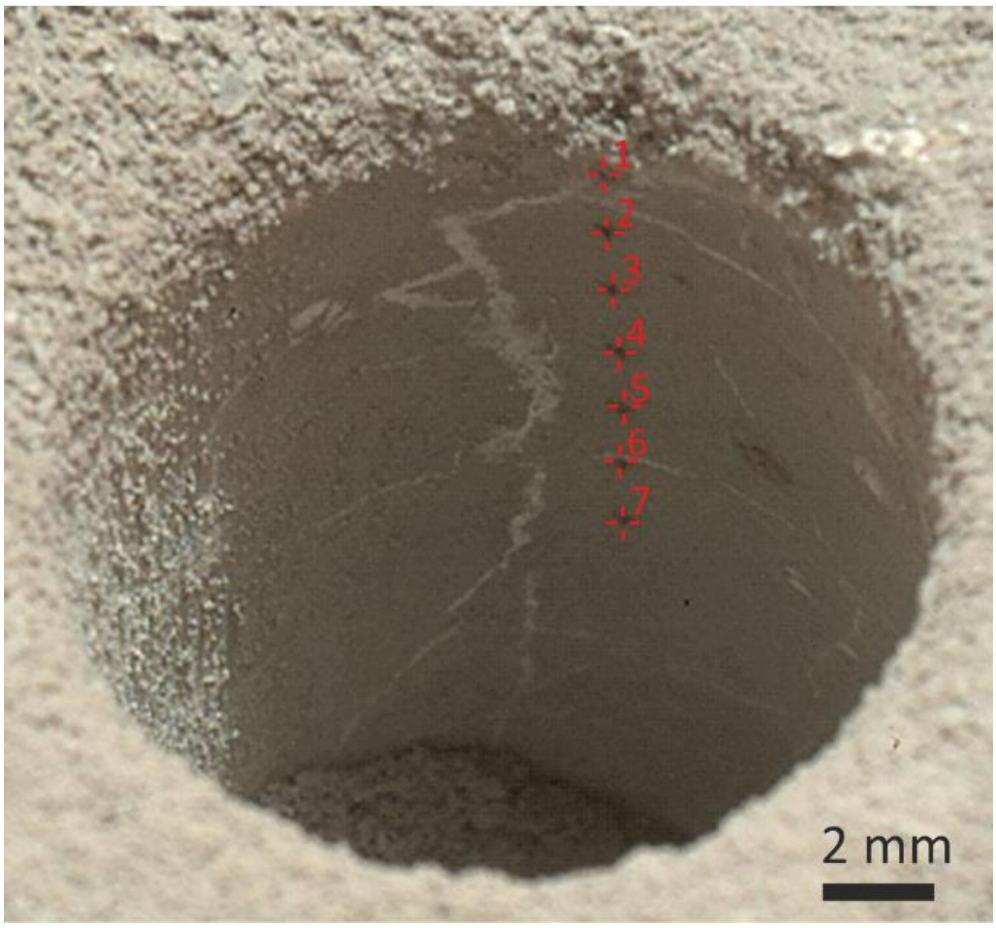

Figure 2.4: Example of a linear, 7x1 ChemCam raster conducted on the John Klein drill hole (sol 165) where each red cross shows the location of the observation points (MAHLI sol 270, image credit: NASA/JPL-Caltech/MSSS).

Each ChemCam LIBS observation point consists of 30–50 spectral analyses and is acquired as part of a target raster. Raster geometries are conducted as either a matrix (3x3 or 5x5) or a linear (5x1, 7x1, or 10x1) configuration of observation points (See Fig 2.4 for an example) that range in size between 350–550 µm depending on distance from the rover mast and the sample material properties (Maurice et al., 2012; Wiens et al., 2012). Observation point analyses are averages of the spectral analyses taken at a point in the target raster, with the first five laser pulses removed to minimise surface dust contamination (Wiens et al., 2013; 2012). These observation point analyses are what I have used to calculate target type and stratigraphic unit compositions (see Section 2.2), and examine the geochemical trends distinguishing alteration and sedimentary processes from endmember source region compositions.

ChemCam uncertainty has been presented as accuracy and precision (Wiens et al., 2012) and shown in Table. 2.1. Accuracy represents the root mean square error product (RMSEP) of samples across all abundance ranges for the eight major elements that had been left-out of the calibration model. ChemCam instrument precision relates to the 'error' presented with APXS results (Blaney et al., 2014).

Table 2.1: ChemCam precision and mean accuracy, values given in wt %.

	SiO_2	TiO_2	Al_2O_3	FeO_T	MgO	CaO	Na_2O	K_2O
Precision, cal. targets[a]	1.5	0.14	0.57	1.8	0.49	0.42	0.49	0.14
Accuracy*[,b]	5.1	0.6	3.5	3.7	2.0	1.7	0.7	0.8

**Root mean square error product (RMSEP) of ChemCam test samples of known composition that had been left out of the calibration model. [a]Blaney et al. (2014); [b]Clegg et al. (2017).*

2.1.2. The Alpha Particle X-ray Spectroscopy technique

The Alpha Particle X-ray Spectroscopy (APXS) instrument uses a ^{244}Cm alpha particle source to irradiate a 1.7 cm diameter area of a sample host rock or soil, and acquire its bulk geochemical composition (Gellert and Clark, 2015). Bombarding a sample's surface with alpha particles and X-Rays from a radioactive source causes characteristic X-rays to be emitted from the sample via Rutherford Backscattering, Particle Induced X-Ray Emission (PIXIE), and X-Ray fluorescence (Gellert and Clark, 2015; Rieder et al., 2003). Analyses can take roughly 20 minutes for the MSL *Curiosity* rover, and several hours or overnight for the MER *Spirit* and *Opportunity* rovers depending on what elements are being sampled (Gellert and Clark, 2015). This is due to those elements with a low alpha sensitivity (such as carbon) requiring longer periods of analysis in order to generate sufficient counting statistics (Rieder et al., 2003). Once the sample's X-ray spectrum has been detected by the X-ray detector it is then de-convoluted according to a non-linear least-squares fitting program, GUAPX (Perrett et al., 2017; Campbell et al., 2010). GUAPX has been calibrated using a series of 53 homogeneous geochemical reference materials that range in composition from minerals such as albite and glauconite, to igneous rocks (basalt to dacite) and sedimentary rocks (Perrett et al., 2017; Campbell et al., 2010; Gellert et al., 2006).

The APXS instrument has flown on four Mars missions to date, permitting the geochemical cross comparison of multiple landing sites (Gellert and Clark, 2015). Combining APXS analyses of drill tailings with CheMin analyses has also been useful for constraining the composition of detected minerals and amorphous materials or clays in the MSL mission (Rampe et al., 2017; Morris et al., 2016; Treiman et al., 2016; Vaniman et al., 2014). Thus, APXS analyses are used as a reference against the ChemCam modal bulk compositions modelled within this PhD to constrain mineral mixing in ChemCam analyses,

the geochemical influence of an amorphous component on ChemCam sediment samples, and compare hypothesised sediment source region compositions with the primary igneous rocks analysed by the MER *Spirit* rover in Gusev Crater (section 2.3).

When comparing APXS analyses with that of ChemCam, it is important to bear in mind that the two geochemical instruments on-board *Curiosity* analyse different aspects of a geological sample (Clegg et al., 2017). The larger analytical area of APXS means that APXS analyses are more representative of the bulk composition of target rocks, while ChemCam analyses are more likely to be representative of individual minerals, particularly for coarse-grained targets, which generates greater scatter in the compositions (Cousin et al., 2017a). As the APXS instrument is calibrated using a smaller set of homogeneous standards, it is also more prone to the matrix effect in heterogeneous samples which increases the instrument error (Campbell et al., 2006), though this remains lower than the ChemCam instrument precision (Clegg et al., 2017). APXS analyses also require a calibration to remove dust contamination, as the instrument does not possess depth profiling capabilities (Rieder et al., 2003), though on MSL the dust removal tool (DRT) is used to remove as much dust from the APXS target's surface as possible prior to analysis (Gellert and Clark, 2015).

2.1.3. The Chemistry and Mineralogy instrument, CheMin

The CheMin instrument on-board the *Curiosity* rover is housed within the body unit and generates diffraction patterns of sieved, drilled or scooped samples using X-ray diffraction (XRD). These diffraction patterns are used to identify the mineral, clay and amorphous components of the sample, their relative abundances, as well as the unit-cell parameters of major crystalline phases (Morrison et al., 2018; Bish et al., 2014). So far, CheMin has analysed 3 scooped samples of the Rocknest sand shadow, Namib dune and

linear dunes, as well as 15 drilled samples of mudstones and sandstones spanning all three stratigraphic groups (Bristow et al., 2018; Achilles et al., 2017; Rampe et al., 2017; Morris et al., 2016; Treiman et al., 2016; Vaniman et al., 2014; Bish et al., 2013). CheMin derived mineral abundances of these samples enable the geochemical compositions acquired by ChemCam to be placed in mineralogical context. Comparison between these two data sets is therefore a crucial part of this thesis, and forms the basis of the discussion in Chapters 3, 4, and 5.

CheMin analysis was undertaken by the CheMin team using a Co X-ray source on scooped and drilled rock material that has been sieved to <150 μm prior to delivery (Morrison et al., 2018; Bish et al., 2014). The instrument has 27 reusable sample cells which are positioned in pairs at the ends of tuning forks (Morrison et al., 2018; Bish et al., 2014). During sample analysis, these tuning forks are vibrated to resonance using a piezoelectric actuator, which drives the sample material at random grain orientations through the collimated 70 μm diameter X-ray beam (Morrison et al., 2018). The resulting diffracted X-rays of the sample are then detected by an X-ray sensitive Charge-Coupled Device (CCD), which collects two-dimensional images over 10–40 hours of analysis (Morrison et al., 2018). These two-dimensional images are converted to one-dimensional patterns using the GSE_ADA software (Dera et al. 2013), to which a Rietveld refinement method was applied to acquire the crystalline abundances and major crystalline phase unit-cell parameters (Dera et al., 2013). XRD-determined abundance of clay minerals and the amorphous component was determined using a full-pattern FULLPAT fitting method, which quantitatively analyses the entire diffraction pattern to calculate all phases present in a sample (Chipera and Bish 2013, 2002). It is these data products derived by the CheMin team that I have used in my analysis and discussion of the ChemCam data.

2.1.4. The on-board scientific cameras

As well as utilising the images from the ChemCam RMI (see section 2.1.1) to characterise targets according to the sample type, morphology and stratigraphic position (see section 2.2), I also used images taken from *Curiosity*'s 16 other on-board science (Mastcam and MAHLI) and engineering (Navcam and Hazcam) camera suites. I did not use data from the Mars Descent Imager (MARDI) camera, as this is situated under *Curiosity*, facing the floor, and as such is rarely used to image targets (Mangold et al., 2017; Malin et al., 2009). The Mastcam and engineering cameras place ChemCam analyses in geological context at the scale of the outcrop, and were particularly useful in identifying large float targets, bedding, and assessing any alteration of the target outcrop that may be missed at the mm-scale of the RMI target mosaics or MAHLI images (Mangold et al., 2017).

2.1.4.1. The Mastcam instrument

The Mast camera (Mastcam) instrument comprises two, fixed-focal length, multispectral, colour CCD imagers (Bell et al., 2017; Malin et al., 2010). These cameras are situated on *Curiosity*'s mast unit 24.2 cm apart (Fig. 2.2.A), and are positioned ~2 m from the surface with their associated electronics situated in the body unit (Bell et al., 2017). The left Mastcam (M-34) has a focal length of 34 mm, with a field of view (FOV) of 20° x 15°, and a pixel scale of 0.22 mrad/pixel, while the right Mastcam (M-100) has a 100 mm focal length, a FOV of 6.8° x 5.1°, and a 0.074 mrad/pixel scale of sampling (Bell et al., 2017; Malin et al., 2010). The Mastcam instrument can acquire images at a range of 2–5 m from the rover mast, be rotated 360° in azimuth and ±90° in elevation, and detect grain size greater than coarse-sand (Bell et al., 2017; Mangold et al., 2017). Data from this instrument suite was used to analyse geological targets at the scale of the outcrop, and to

acquire Bayer pattern red, green and blue true colour images using the eight-position filter wheel within each camera (Bell et al., 2017; Malin et al., 2010). The Mastcam instrument can also acquire multispectral (400-1000 nm), stereoscopic images (Bell et al., 2017; Malin et al., 2010), though these were not used for the purposes of this PhD project.

2.1.4.2. The Mars Hand Lens Imager, MAHLI

In this study, I used images taken by MAHLI of ChemCam targets to support those from the ChemCam RMI. MAHLI is situated on the turret at the end of the *Curiosity* rover's arm, and uses a 2-megapixel colour CCD camera to analyse the textures, structures and morphologies present at *Curiosity*'s field site (Edgett et al., 2012). MAHLI utilises a focusable macro lens to take images of the target from 2.1 cm to infinity (Edgett et al., 2012). The minimum working distance is ~2.1 cm, for which a standard MAHLI 1600 x 1200 pixels image covers a FOV of roughly 2.3 by 1.7 cm, and a pixel size of ~0.014 mm/pixel (Edgett et al., 2012). This science camera has the capability to detect the finest grain size 0.0042 mm (silt) in geological samples of all the camera instruments on-board *Curiosity* (Mangold et al., 2017), however, as it is located on the rover arm and has a relatively small FOV, it does not always take direct images of ChemCam targets. Instead, images taken by this camera are best used to characterise outcrops and rocks that the ChemCam instrument has analysed.

2.1.4.3. The MSL engineering cameras

The *Curiosity* rover has a total of 12 Navigation cameras (Navcam) and Hazard Avoidance Cameras (Hazcam) to aid with; navigating the rover on the Martian surface, deploying the rover arm and placing samples into the rover sample processing system

(Maki et al., 2012). The Navcams have a 45° x 45° FOV, a pixel scale of 0.82 mrad/pixel, and are mounted to a pan/tilt mast. Meanwhile, the Hazcams have a 124° x 124° FOV with a pixel scale of 2.1 mrad/pixel and are situated on the front and rear of the rover chassis (Maki et al., 2012). All engineering cameras use a 1024 x 1024 pixel detector as well as red/near IR bandpass filters centred at 650 nm (Maki et al., 2012).

In this study, I used images returned from these engineering cameras to help characterise the stratigraphic position of ChemCam in situ targets, as well as identifying gross outcrop features such as diagenetic halos and bedding planes (see section 2.2).

2.2. ChemCam Target classification

As the aim of this PhD is to delineate the geochemical effects of aqueous alteration and diagenesis from that of Gale crater's sediment source regions, it is imperative that these ChemCam targets are sorted and grouped according to geological context to derive meaningful conclusions from the dataset. For that reason, I have analysed the ChemCam RMI images taken before and after each target acquisition, as well as any Mastcam, Navcam and MAHLI image taken of the ChemCam target in question, in order to identify what type of geological material was sampled and group them accordingly. I acquired the ChemCam RMI mosaics from both the ChemCam team website (http://msl-chemcam.com/index.php) and the MSL analysts notebook team site. Navcam, MAHLI and individual Mastcam images were also acquired from the MSL analysts notebook, with Mastcam mosaics taken from the MSL team's the Malin Space Science Systems Mastcam mosaics website. Images that have been publically released by the team will be on the ChemCam team site, MSL analysts notebook public site (https://an.rsl.wustl.edu/msl/mslbrowser/Account/login.aspx) and the NASA MSL

Planetary Data System (PDS) Geosciences Node (http://pds-geosciences.wustl.edu/missions/msl/) for the respective instruments. Images that are not publically available at the time of the thesis publication will become available on the MSL PDS and public websites after 3 months of acquisition.

ChemCam observation points have been grouped into host rock, secondary diagenetic features, unconsolidated sediments, and float datasets (see Fig. 2.5). Classification has been done on individual ChemCam observation points as many targets sample both unaltered host rock and alteration features (see section 2.1.1). By focusing on what each observation point has analysed, the analysis becomes more precise and the geochemical compositions become more representative of the various features/sedimentary units.

2.2.1. Host rock target definition

Host rock is defined here as that in which the sediments exist as an indurated, lithified unit, commonly containing sedimentary structures such as bedding or laminations, and secondary structural features (e.g., bedrock fractures). The minimum grain size that MSL cameras can identify requires a resolution of at least 3 pixels (Mangold et al., 2017). Therefore, at the optimum MAHLI working distance (~2 cm), grains coarser than very fine sand (<0.062 mm) are resolvable when the target is not obscured by too much dust or soil. Grain size estimates for the ChemCam analyses used in this study have been acquired from the literature (see Table 2.3 for a comprehensive list of references for each grain size and stratigraphic unit or waypoint). The extent of induration for a suspected host rock target can be ascertained from the depth of the LIBS pit (Wiens et al., 2012), with harder – and hence more indurated targets – possessing a shallower LIBS crater than those of softer sedimentary units or unconsolidated material.

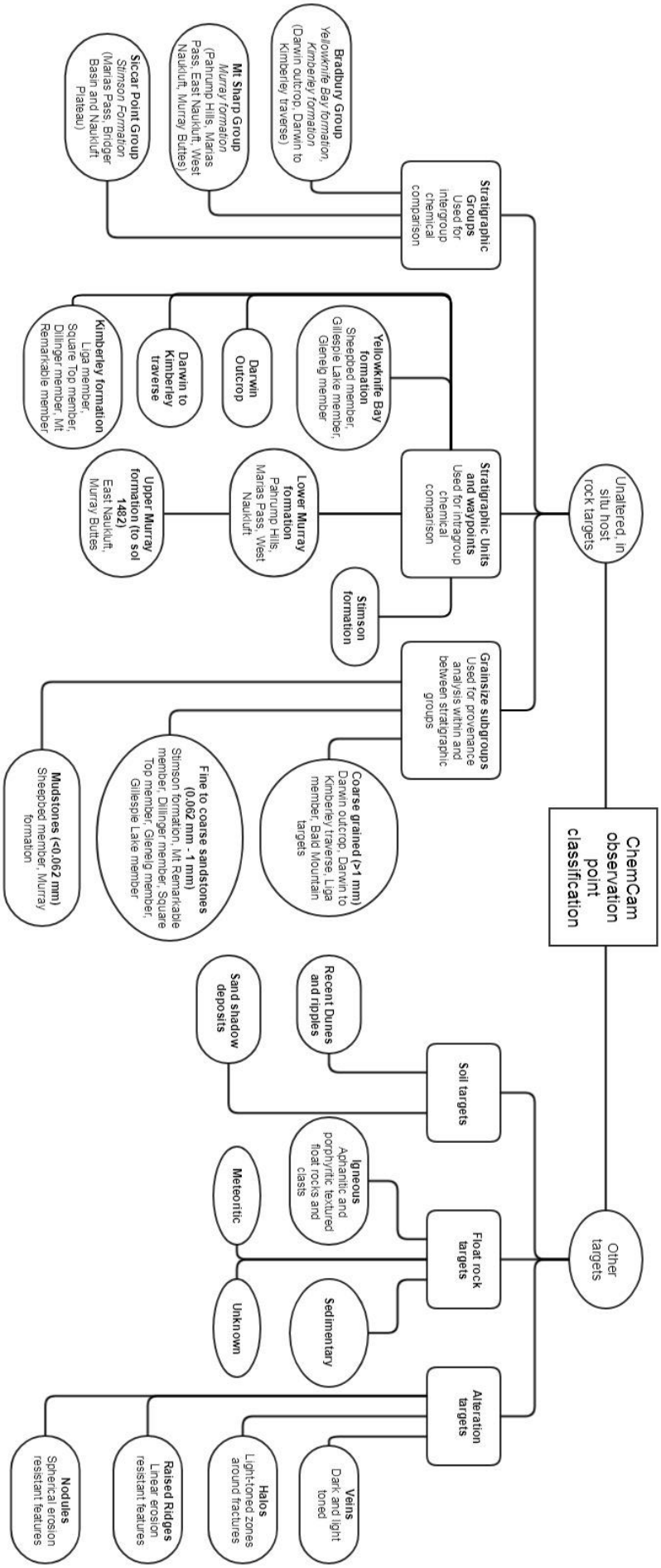

Figure 2.5: Flowchart diagram showing the breakdown of ChemCam observation point analyses classification criteria used in this study.

For some targets with extensive soil cover, it is not clear whether they are in situ host rock, or float. This uncertainty can be improved upon by knowing the direction of bedding and whether the unknown target conforms to the regional dip direction. If it is still not obvious whether a target is in situ host rock or float, it is classified as "unknown" and placed into its own data subset. It is possible that with a better understanding of average geochemical compositions for each stratigraphic group and unit, these unknown targets that are clearly identifiable as sedimentary can be assigned a geological position within the stratigraphy. For now, however, they are excluded from the current study. Once host rock targets have been identified, they are then constrained using the methods in the following sections to generate the constrained bulk rock dataset.

2.2.1.1. Constraining the bulk rock dataset

In order to isolate the effects of post-depositional alteration in the ChemCam database, observation points seen to have hit any obvious diagenetic feature have been removed and placed into their own dataset (see section 2.2.2.). As Gale crater's host rock targets are all sedimentary units, aqueous alteration and diagenesis will have occurred at a microscopic scale undetectable to the rover's on-board cameras in the form of cementation and compaction. Fine-grained sedimentary units (i.e., mudstone and siltstone) are most affected by aqueous alteration at these scales, however, provided this alteration occurred in a closed-system (where the system is defined as the stratigraphic unit or group under question), source region characteristics can still be determined with a bulk rock analysis. Sediments affected by extensive open-system alteration become enriched in volatile elements S and H, depending on whether the alteration is acid-sulfate or hydrolytic (Morris et al., 2001). As ChemCam cannot detect these volatile elements, any observation point

that has sampled substantially altered samples will show a depletion in the non-normalised total sum of oxides (e.g. Fig 2.6).

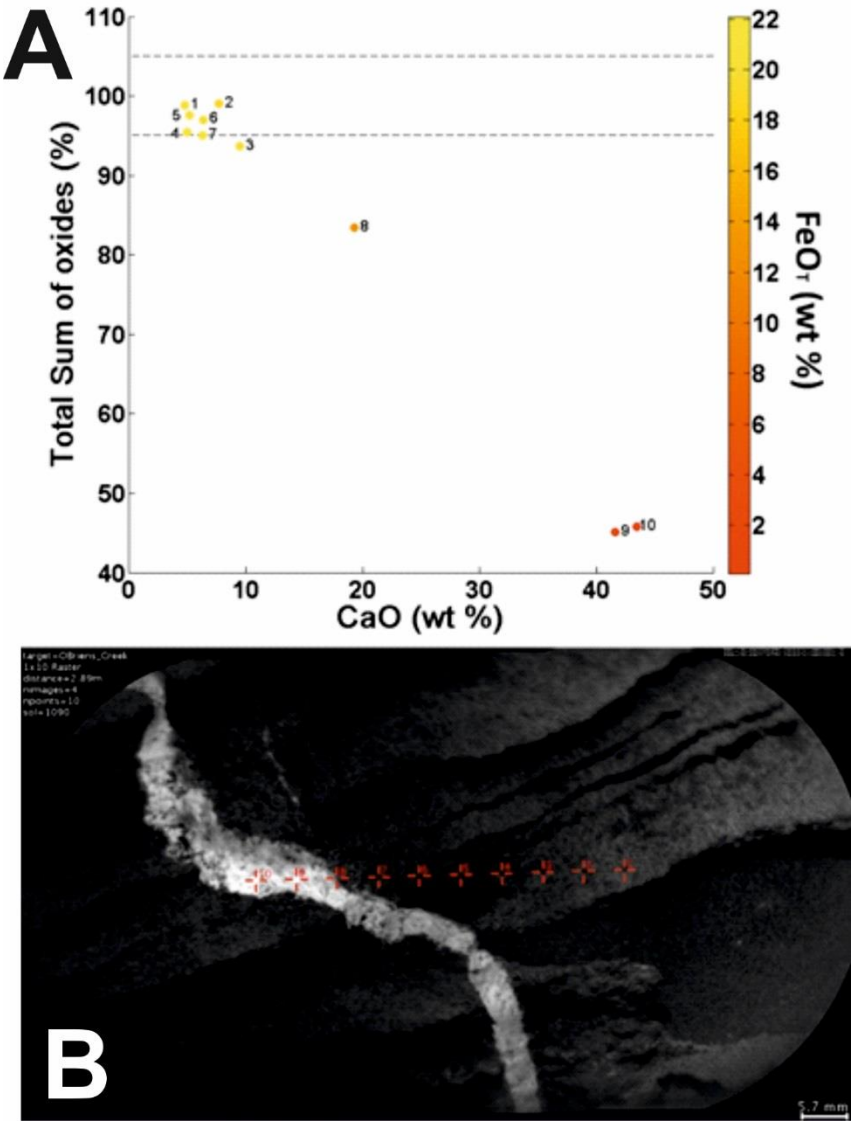

Figure 2.6: A) Scatter plot of OBriens Creek (sol 1090) observation point compositions in the Murray formation with total sum of oxides plotted against CaO compositions in wt%. Dashed grey lines represent the cut-off bounds for the low and high totals used in this study, the observation point colour corresponds to total iron concentrations with yellow showing high iron, and red, low iron concentrations. FeO_T was chosen as a reference major element to demonstrate the mineral vein alteration trend as Gale crater sediments have relatively uniform FeO_T compositions (Chapters 3, 4 & 5). The ChemCam target OBriens Creek is shown underneath in B) with observation point locations presented as a red cross. Observation points 8–10 are seen in the RMI image to have hit a mineral vein. This correlates with a strong depletion in total sum of oxides and iron, along with a strong enrichment in CaO in A).

An investigation into the effect of ChemCam observation point totals against major element oxide concentrations was conducted to determine a suitable range to rule out the geochemical effect of volatile addition on the sedimentary target analyses. ChemCam analyses from the Stimson formation were used to test this range as it has a relatively small number of data points and Stimson does not show evidence of widespread diagenesis (e.g., there are no clays and few sulfate veins, see Chapter 4.3.1; Banham et al., 2018; Yen et al., 2017). SiO_2, Al_2O_3 and Na_2O compositions appear to be most affected by low total sum of oxides due to their strong positive Pearson correlation coefficients of 0.75, 0.75 and 0.65 (see section 2.4.2. for a description of Pearson correlation coefficients). Owing to these high correlations of SiO_2, Al_2O_3 and Na_2O with total sum of oxides, I have restricted the acceptable total sum of oxide range to 95–105 %. This total range has been selected as the variation in these elements does not exceed the instrument accuracy (5.0 wt%, 3.6 wt% and 0.6 wt%) according to the linear regression models (Fig. 2.7 and Table 2.2). For this reason, observation points with total sum of oxides outside of the range 95–105 % are removed from the host rock dataset that is used to estimate the constrained bulk rock compositions. This method also has the added benefit of removing targets that have been contaminated by Martian surface dust and soil due to their high concentrations of volatiles (Ehlmann et al., 2017; O'Connell-Cooper et al., 2017; Bish et al., 2013; Meslin et al., 2013).

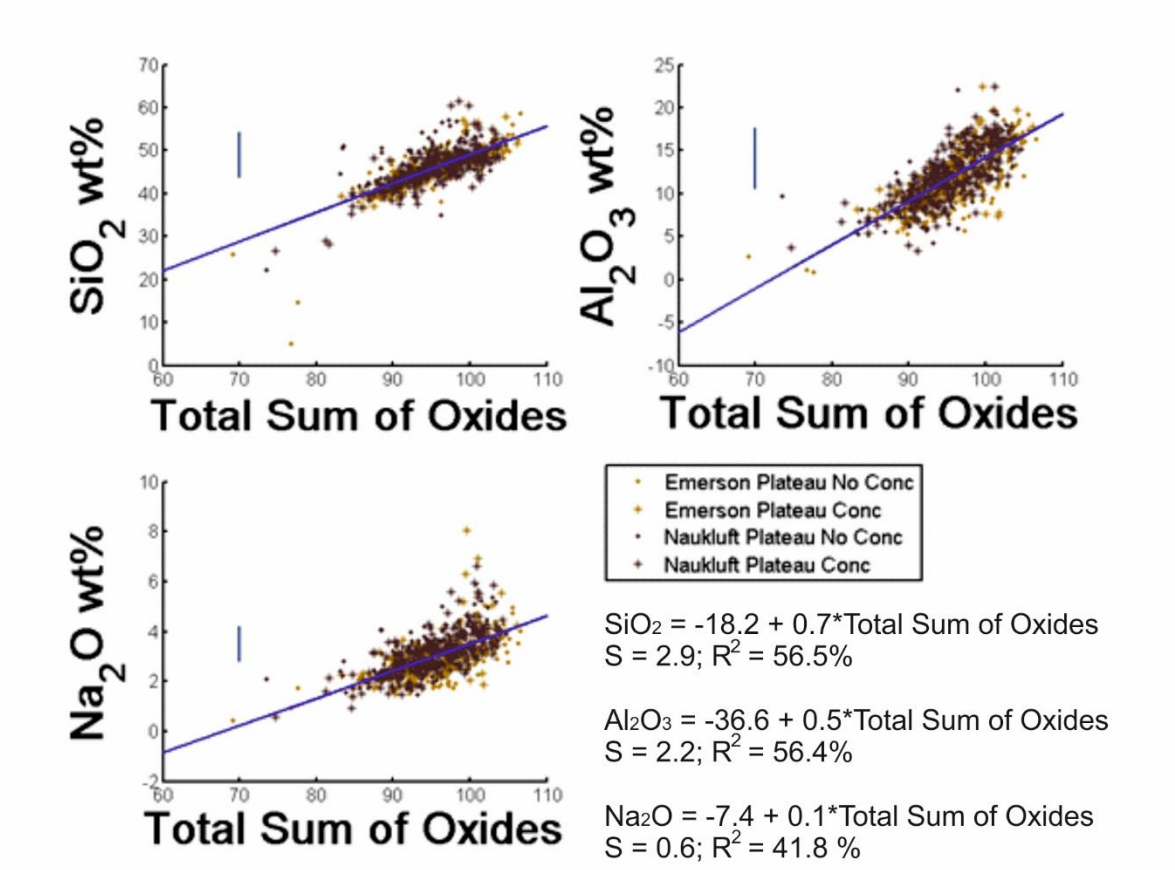

Figure 2.7: SiO_2, Al_2O_3 and Na_2O major element compositions plotted against total sum of oxides for all Stimson analyses with calculated regression line in blue. Dark blue vertical line represents the ChemCam RMSEP (instrument accuracy). S is the calculated model standard error.

Table 2.2: The table shows the predicted variation for each major element oxide according to totals. Values in red are outside of the +/- ChemCam instrument accuracy range. The total sum of oxide range of 95–105 % was selected as the variation in SiO_2, Al_2O_3 and Na_2O with variation in total sum of oxides was within the ChemCam instrument accuracy.

Total Sum of Oxides (%)	90	95	100	105	110	ChemCam accuracy
SiO_2 (wt %)	42.35	45.70	49.06	52.42	55.79	5.0
Al_2O_3 (wt %)	9.09	11.62	14.16	16.70	19.24	3.6
Na_2O (wt %)	2.43	2.98	3.52	4.07	4.62	0.6

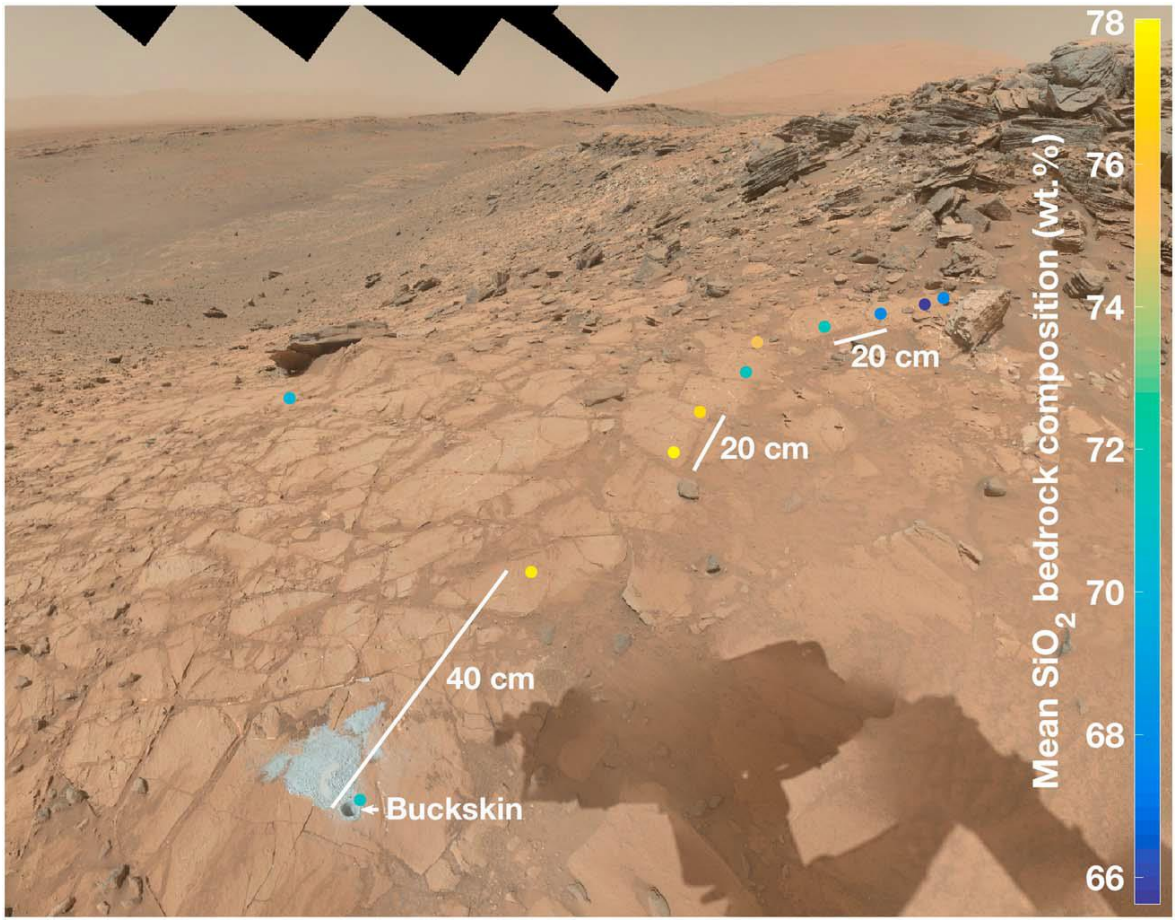

Figure 2.8: Figure 2 from Frydenvang et al. (2017) that shows the silica enrichment at the Lion outcrop area of Marias with ChemCam detected silica concentrations ranging from 66 w t% SiO_2 (blue) to 78 wt % SiO_2 (yellow).

ChemCam targets of Murray formation and Stimson targets sampled at the Marias Pass locality have required an extra level of care to remove the potential effects of secondary alteration. Silica-enrichment in this area is a prominent feature (Fig. 2.8) and may relate to either the CheMin detected detrital tridymite and cristobalite derived from a highly fractionated, igneous endmember (Morris et al., 2016), or diagenesis similar to that seen in the fracture-associated halos (Frydenvang et al., 2017). To minimise the influence of alteration in Marias Pass targets, ChemCam observation points taken only at the Lion outcrop where the Buckskin drill hole was conducted and tridymite detected (Morris et al., 2016) have been included for endmember analysis. As silica-rich diagenetic halos are also

accompanied by a strong, light-coloured change in the bedrock (Frydenvang et al., 2017), dark-toned bedrock targets at these localities have also been incorporated into the constrained bulk rock dataset.

Other targets removed from the constrained bulk rock dataset are those that have been disturbed by the rover (e.g., drill cuttings and dump piles formed during CheMin analysis) so that the constrained bulk rock dataset represents as clean an analysis of the host rock as can be provided.

2.2.2. Sub-classification of the constrained bulk rock dataset

Once I had determined and constrained all observation point analyses that clearly constitute bedrock, I further sub-classified them according to grain size and stratigraphic position (Fig. 2.5). The reasons for analysing Gale crater's sedimentary units according to grain size is two-fold: The first is to remove the geochemical variation inherent within samples of different grain sizes, which for terrestrial sediments have been shown to strongly correlate with one another (Bloemsma et al., 2012; Weltje, 2012; Pettijohn, 1954), and the second is to minimise the effects of hydrodynamic mineral sorting during sediment transportation and deposition (Siebach et al., 2017a; Fedo et al., 2015). Average grain sizes for Gale crater's geological units and key waypoints have been obtained from literature studies that have utilised MAHLI, RMI, and Mastcam images to establish the grain size category for each geologically distinguished unit (Mangold et al., 2017; Siebach et al., 2017a; Mangold et al., 2016; Treiman et al., 2016; Anderson et al., 2015; Grotzinger et al., 2015; Grotzinger et al., 2014; Meslin et al., 2013). As grain size analysis is currently dependent on rover-based imagery, it is not distinguishable to a great degree of accuracy, particularly for targets masked by Martian regolith or with substantially weathered surfaces (Mangold et al., 2017). Grain size for stratigraphic units is therefore an approximate

average and has been categorised into three specific classes; coarse-grained, sandstone, and mudstone categories (Table 2.3). Coarse-grained targets are defined as those with grain sizes greater than 1 mm (Mangold et al., 2017; Mangold et al., 2016) which in Gale crater typically consists of clast-supported conglomerates. Sandstone targets have a grain size between 0.062 mm and 1 mm and can typically be resolved in RMI and MAHLI images as well as Mastcam to some extent for grains greater than 0.15 mm in diameter (Mangold et al., 2017). Sedimentary units that constitute the mudstone category are finer than very fine sand (<0.062 mm) and unresolvable in RMI and MAHLI imagery (Mangold et al., 2017).

Table 2.3: Grain size definitions with Mastcam and RMI image examples. Yellow circle shows the field of view for the RMI image.

	Mudstone (< 0.062 mm)	Sandstone (0.062 - 1 mm)	Coarse grained (> 1 mm)
MastCam image (Left)	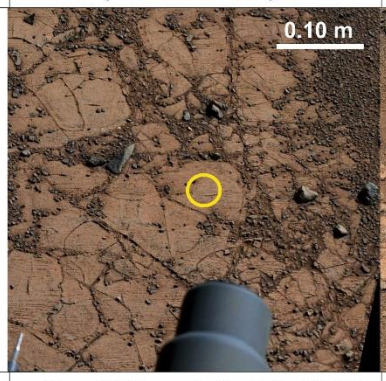	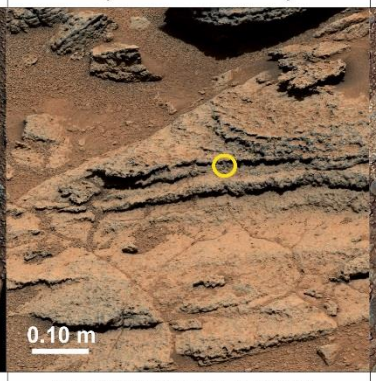	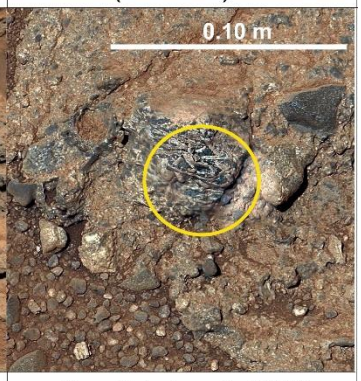
	Target Telegraph Peak (sol 903) mcam03953	Target Cartwright (sol 318) mcam01302	Target Harrison (sol 512) mcam02012
RMI image	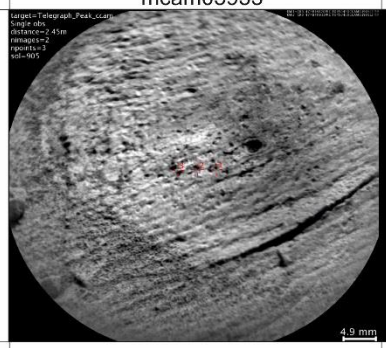	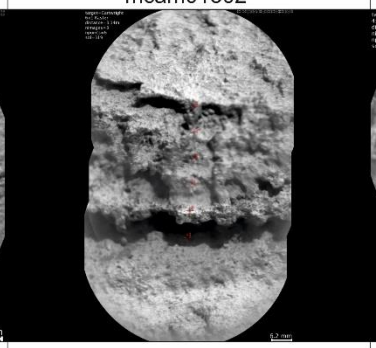	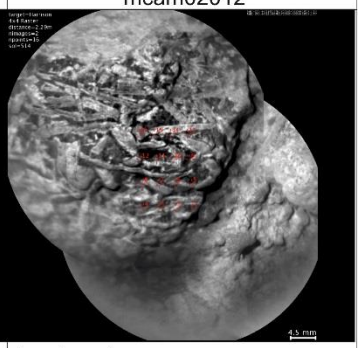
Stratigraphic units and targets	Yellowknife Bay formation (Sheepbed Member) Murray formation (Pahrump Hills, Marias Pass, Bridger Basin, West Naukluft plateau, East Naukluft plateau, Murray Buttes)	Yellowknife Bay formation (Glenelg member, Gillespie Lake member) Kimberley formation (Mt Remarkable member, Dillinger member, Square Top member) Stimson formation (pre-Naukluft, Naukluft plateau)	Darwin outcrop Darwin to Kimberley traverse Kimberley formation (Liga member) Bald_Mountain target
Refs	*Grotzinger et al., 2014; Grotzinger et al., 2015; Nachon et al., 2016; Rampe et al., 2017; Hurowitz et al., 2017.*	*Grotzinger et al., 2014; Anderson et al., 2015; Grotzinger et al., 2015; Treiman et al., 2016; Banham et al., 2017*	*Grotzinger et al., 2014; Grotzinger et al., 2015; Mangold et al., 2016; Treiman et al., 2016; Mangold et al., 2017; Nachon et al., 2016;*

Along with grain size, the host rock dataset has been further sub-classified in relation to the stratigraphic groups, units and key waypoints based on stratigraphic nomenclature derived from the literature (Banham et al., 2018; Ehlmann et al., 2017; Hurowitz et al., 2017; Rampe et al., 2017; Fraeman et al., 2016; Mangold et al., 2016; Treiman et al., 2016; Anderson et al., 2015; Grotzinger et al., 2015; 2014). Key waypoints are either those in which Gale crater endmember studies have already been conducted or localities where an extensive scientific campaign has taken place such as the Yellowknife Bay, Darwin outcrop, Kimberley formation, Pahrump Hills, Marias Pass, Naukluft Plateau, Murray Buttes areas (Hurowitz et al., 2017; Rampe et al., 2017; Siebach et al., 2017a; Yen et al., 2017; Le Deit et al., 2016; Mangold et al., 2016; Morris et al., 2016; Treiman et al., 2016; Anderson et al., 2015; Grotzinger et al., 2015; 2014; Vaniman et al., 2014). Grouping the dataset according to stratigraphy permits the geochemical analysis of ChemCam's in situ host rock targets in relation to geological time, and makes it easier to compare the results of this study with that of the literature. Hence, stratigraphic group divisions (Bradbury, Mt Sharp, Siccar Point, Fig. 2.5, section 1.3) are used to study the average geochemical variation between distinct paleoenvironmental settings on the largest geological scale possible. A more detailed study of stratigraphic group and grain size compositional variation is then provided with the analysis of stratigraphic units and waypoints, such as those outlined in the introduction, section 1.3 and described in Fig. 2.5 and Table 2.3.

Table 2.3 presents the average grain sizes assigned to each stratigraphic unit and key waypoint, and Table 2.4 shows the total number of observation points included for each stratigraphic unit and area.

Table 2.4: Number of ChemCam observation points acquired at each locality along with the number of observation points included in the constrained bulk rock dataset. SB = Sheepbed Member, GL = Gillespie Lake Member, G = Glenelg Member, D = Darwin Waypoint, DK = Darwin to Kimberley traverse targets, Kim = Kimberley Formation, PH = Pahrump Hills locality, MP = Marias Pass locality, EN = East Naukluft Plateau locality, WN = West Naukluft Plateau locality, MB = Murray Buttes locality, VRR = Vera Rubin Ridge locality.

	SB	GL	G	D	DK	K	PH	MP	EN	WN	MB	VRR
Area obs. points	886	106	648	127	454	608	627	488	825	459	808	3301
No. of Obs. points used	319	45	177	78	61	164	292	130	227	163	282	1274

2.2.3. Diagenetic feature classification and identification

A wide variety of diagenetic features associated with secondary alteration processes are present within Gale crater's stratigraphic record (see section 1.3.6) and have been isolated from the host rock dataset into a dataset of their own. These have been carefully documented and grouped according to the major types; mineral veins, fracture-associated halos, erosion resistant raised ridges and nodules (Fig. 1.17) and will be compared against the constrained bulk rock dataset to determine whether aqueous alteration relating to these features has influenced the surrounding host rock targets.

Erosion resistant raised ridges and nodules have been identified in the Bradbury group as linear or circular expressions of topographic relief (Fig. 1.17 A) and are most common in the Sheepbed member mudstone (Nachon et al., 2017; Leveille et al., 2014; Stack et al., 2014b) though some are found in the Kimberley formation. Erosion resistant raised ridges are narrow (<1 mm), mostly aligned at fracture margins, and can be darker in colour than the surrounding bedrock (Nachon et al., 2017). The erosion resistant raised ridges of Yellowknife Bay also contain multi-layered fracture fillings (Leveille et al., 2014), which may indicate a separate formation pathway. Due to the different

morphologies in different locations, raised ridges have also been subdivided according to stratigraphic unit (Sheepbed mudstone and Kimberley formation) to enable a more detailed analysis of these structures.

Nodules can be millimetre to centimetre in scale, are roughly spherical in shape, and can either be hollow or filled (Fig. 1.17 B; Nachon et al., 2017; Wiens et al., 2016; Grotzinger et al., 2014; Stack et al., 2014b). Nodules also possess morphological variations according to stratigraphic unit, with those identified at the Pahrump Hills locality being overall larger in size and possessing a wider range in morphologies (dendritic and clusters, as well as the usual spherical appearance). Nachon et al. (2017) separated the clusters and dendritic aggregates from the other enhanced relief features in the Murray formation. However, for the sake of simplicity, and as their geochemistry is similar to the other nodular features in the Murray formation, I have given dendritic aggregates the same classification as clusters, with analysis conducted according to stratigraphic group, similar to the raised ridges.

Mineral veins (Fig. 1.17 C) can either be light- or dark-toned and are present in all stratigraphic groups so far identified with a wide variety of widths and lengths. They are commonly associated with bedrock fractures, though some veinlets (veins >1 mm wide) can occur at a variety of orientations within the bedrock, around mineral grains, or other diagenetic features (e.g., nodules). They commonly present a glassy lustre and can also be distinguished in ChemCam analyses as a drop in total sum of oxides due to the majority of veins consisting of bassanite ($CaSO_4 \cdot 0.5[H_2O]$) (Rapin et al., 2016).

Fracture-associated halos (Fig. 1.17 D) are identified within the Gale crater stratigraphy as white discoloration surrounding large bedrock fractures. This diagenetic feature is most common in the Marias Pass and Bridger Basin localities, spanning both the Mt Sharp and Siccar Point stratigraphic groups, and has been associated with strong silica-

enrichment for ChemCam analyses (Frydenvang et al., 2017), though one halo target has been identified in the Bradbury Group (Williams et al., 2014).

2.2.4. Characterising unconsolidated sediment and float targets

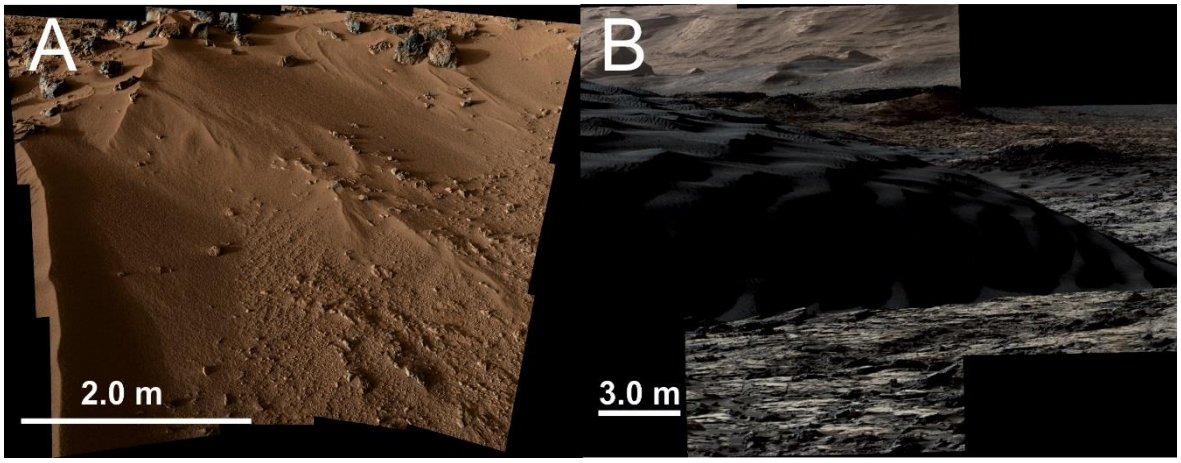

Figure 2.9: Representative Mastcam mosaic images of two unconsolidated sediment bedforms A) The Rocknest sand shadow (sol 55, mcam00254) and B) The Namib dune (sol 1192, mcam05410).

Unconsolidated sedimentary material includes soil and dune targets. Soil targets are defined as fine-grained accumulations of sand- to silt-grained particles, such as the Rocknest sand shadow (sols 56–102; Bish et al., 2013). Soils have been identified across the *Curiosity* rover traverse, with soil accumulations distinguishable from sedimentary host rock due to their "softness" determined by ablation pit depth (Wiens et al., 2012), lack of obvious cement or association with surrounding bedrock, and the occasional ripple feature indicating recent aeolian remobilisation (Fig 2.9). Soil accumulations are more common around the Bagnold dune fields (Achilles et al., 2017; Cousin et al., 2017; Ehlmann et al., 2017, Fig. 2.9 B), but are distinguishable from the dunes themselves due to their smaller scale (<1 m across; see Fig. 2.9 A).

The *Curiosity* rover has encountered two large, active, aeolian dune fields, and analysed them in individual campaigns (Bagnold 1 & 2; Lapotre and Rampe, 2018; Bridges and Ehlmann, 2017). The aeolian dunes occur as large bedforms ~15 m across, are dark in colour, and possess a similar apparent softness when targeted with the LIBS laser to their soil counterparts. For comparison with the ancient, lithified aeolian dunes (Stimson formation), ChemCam observation points that have targeted the dunes have been placed into their own dataset. Due to soil and dune targets in Gale crater being generally more enriched in volatiles than host rock targets (particularly S and H; O'Connell-Cooper et al., 2017; Bish et al., 2013), their dataset has not been constrained to exclude targets outside the range of 95–105 wt % unlike that of the host rock targets. Instead, targets with total sum of oxides below 80 % have been excluded to limit the effect of sulfate adsorbed onto the grains, or mixed into the dunes from local bedrock material (Ehlmann et al., 2017; Bish et al., 2013), and permit a better comparison with the constrained dataset of the ancient, lithified, aeolian Stimson formation.

Float targets in Gale crater are defined as pebble to boulder size fragments of lithified rocks which are either sedimentary, igneous, or meteoritic in origin (Fig. 2.10). Sedimentary float are classified on the same morphological characteristics of the sedimentary host rock outlined earlier in section 2.2.1. with the exception that these are not seen to exist as part of the in situ stratigraphic sequence. Igneous float targets have been identified in the literature (Cousin et al., 2017b; Edwards et al., 2017; Mangold et al., 2016) based on identifiable igneous textures (i.e., porphyritic, aphanitic or vesicular). I have placed igneous float and conglomerate unit igneous clast targets into their own dataset for later geochemical comparison to the sedimentary bulk rock dataset (see below and Fig. 2.5). Meteorite targets have been identified according to the literature (Johnson et al., 2014; Meslin et al., 2017) and removed from the database as these possess extreme compositions that have not been calibrated for ChemCam analyses (Meslin et al., 2017).

As meteorites are non-native to the planet their compositions are also unrelated to the Martian crust and therefore are not part of this study.

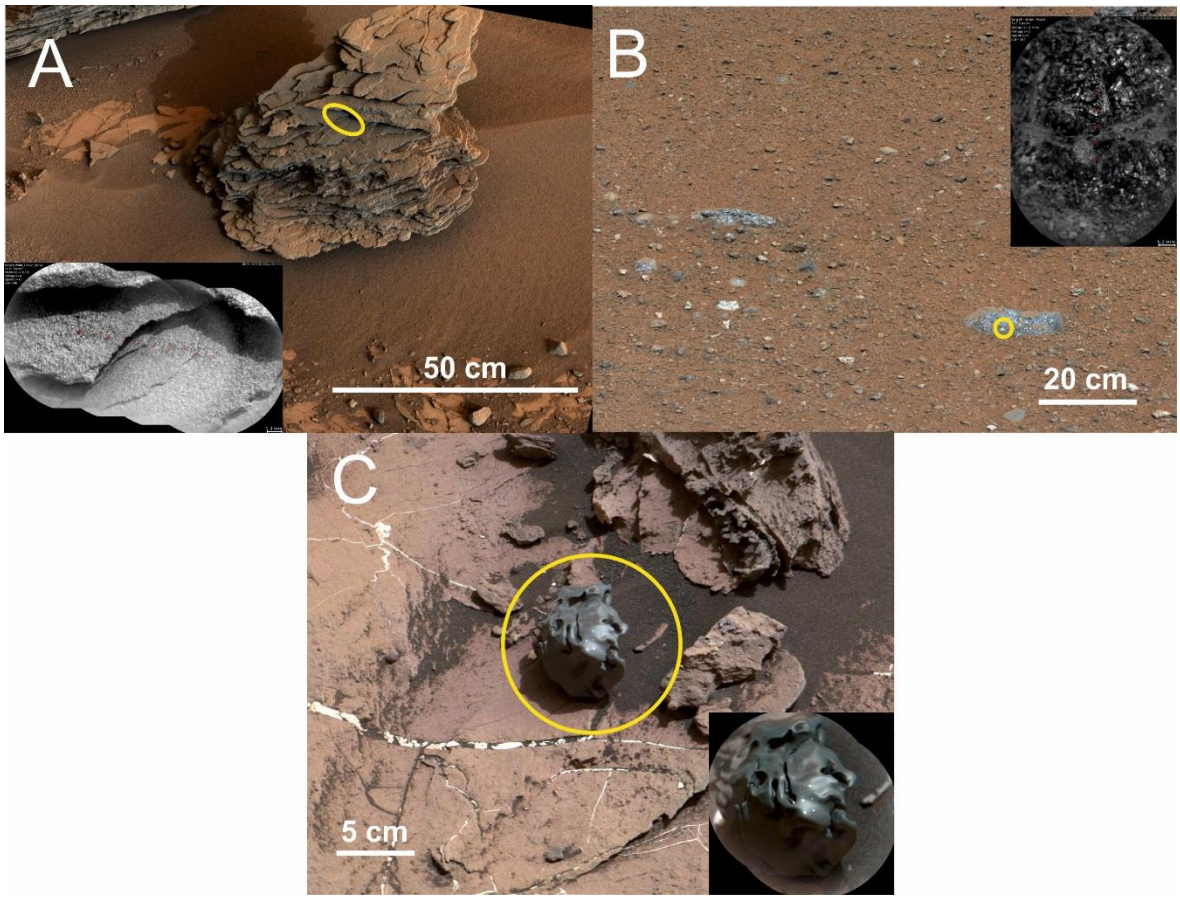

Figure 2.10: Target examples of the three different classes of float rock identified in Gale crater; A) sedimentary float target Wild Horse Mesa (sol 792, mcam03472), B) igneous float target Robin Hood (sol 365, mcam01481), and C) iron meteorite target Egg Rock (sol 1505, mcam07625).

2.3. Comparison datasets

Several comparison datasets have been acquired from the literature and used to place ChemCam major element oxide analyses into mineralogical (CheMin), local (igneous float and clast analyses) and regional (Adirondack class basalts) context. CheMin analyses of drilled and scooped samples provide the mineralogical datasets for Gale crater's bulk rock (Rampe et al., 2017; Morris et al., 2016; Treiman et al., 2016; Vaniman et al., 2014), sand shadow (Bish et al., 2013) and dunes (Rampe et al., 2018; Achilles et al.,

2017). Data have been acquired from the NASA PDS, as well as several studies which have also combined CheMin mineralogical data with APXS measurements to constrain the geochemistry of the amorphous and phyllosilicate (AP) component inherent in all Gale crater samples (Bristow et al., 2018; Rampe et al., 2017; Yen et al., 2017; Morris et al., 2016; Treiman et al., 2016; Dehouck et al., 2014; Vaniman et al., 2014). Major element compositions of the CheMin derived minerals have been determined by Morrison et al. (2018) and have been plotted alongside the constrained bulk rock compositions to highlight possible mineralogical endmembers for the sedimentary units.

Datasets used to help place *Curiosity* ChemCam analyses into local crustal context are those of the igneous float and clasts identified within pebble-rich units and scattered across the surface of Gale crater (Cousin et al., 2017; Edwards et al., 2017; Mangold et al., 2016). Igneous float and clasts were identified according to morphology, with several exhibiting porphyritic, aphanitic and vesicular textures indicative of an igneous origin (Cousin et al., 2017; Edwards et al., 2017; Mangold et al., 2016). The literature that identified these igneous float and clast targets was used to isolate the igneous float and clast targets into a dataset of their own. The separation was done so that a comparison between Gale crater's "igneous" geochemical compositions and sedimentary unit constrained bulk compositions could be achieved. This comparison can then potentially identify whether there is a link between the subalkaline basalt and trachybasalt endmembers identified in Gale crater's igneous and float targets (Edwards et al., 2017) and that of Gale crater's sedimentary units analysed here.

A final comparison dataset of the MER *Spirit* Adirondack Class basalts analysed in Gusev crater has been used to place Gale crater's sediment geochemistry into regional crustal context. The Adirondack Class basalts represent ancient Martian igneous rocks, analysed in situ using *Spirit*'s Alpha-Particle X-ray Spectrometer (McSween et al., 2006a),

and the Adirondack class basalt compositions have been acquired from the NASA PDS. Comparing the datasets mentioned in this subsection to those of Gale crater's sediment compositions and hypothesised source regions, can aid in the determination of the chemical heterogeneity of Mars' upper crust, and comparing Gale crater's geochemistry to other known examples of Martian crustal compositions.

2.4. Statistical analysis of the ChemCam datasets

Due to the number of ChemCam analyses taken throughout the duration of the mission (over 16000 observation points for the period up to sol 2163) on a variety of geological targets and stratigraphic groups/units, a statistical approach is required to identify and delineate the geochemical trends and bulk compositions associated with each. Using this method, I can determine the cause of geochemical variation within Gale crater's host rock, and whether this relates to source region compositions or secondary alteration, assuming substantial geochemical variation exists between the stratigraphic groups. The statistical methods applied here include a simple univariate description of the data in the form of basic statistics (i.e., mean, mode, range) and histogram plots, along with multivariate density contour plots (section 2.4.1.), simple and multiple linear regression models (section 2.4.2.), cluster analysis (section 2.4.3.) and equivalence tests (section 2.4.4.).

2.4.1. Density contour analysis

Density contour plots are a form of multivariate data visualisation that, much like a scatterplot, display the data population distribution across two variables. Contour plots show the major element distribution as isolines (contours) of x and y, representative of the

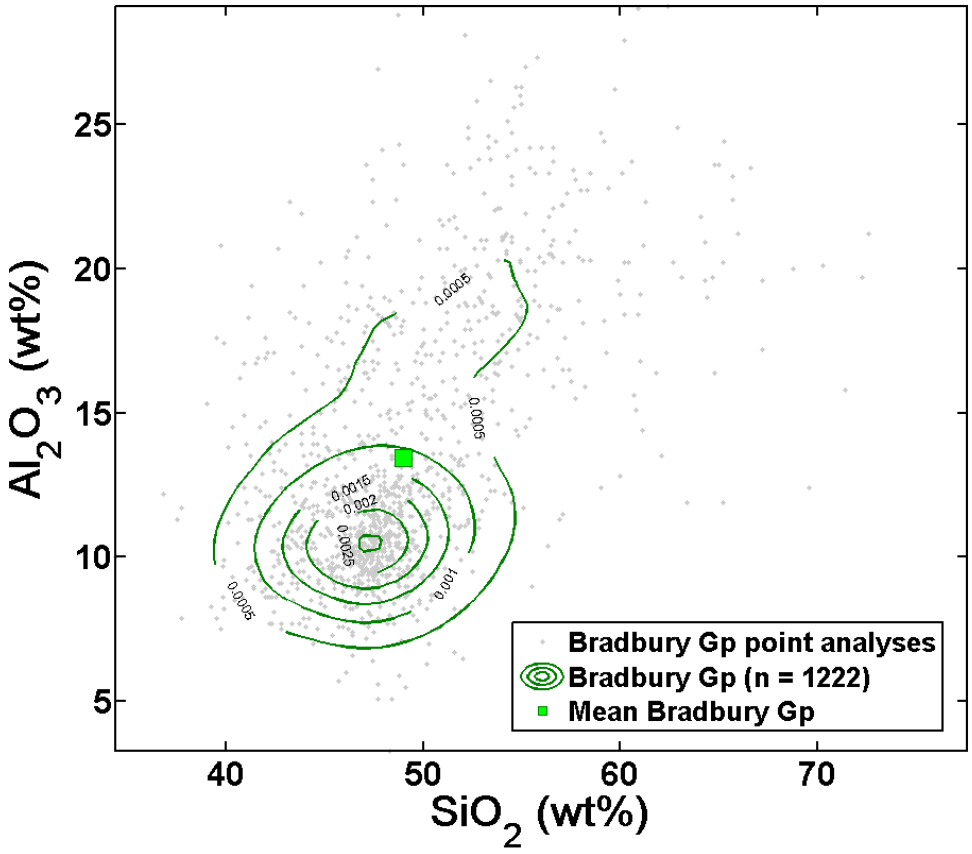

Figure 2.11: Density contour plot of the constrained Bradbury Group Al_2O_3 versus SiO_2. Contour level steps are shown (0.0005 in the outermost contour, 0.0025 in the innermost contour), along with calculated mean compositions and scatter points of Bradbury Group observation point analyses. The x-y boundaries of this plot are defined by the Bradbury group maximum and minimum values for SiO_2 and Al_2O_3.

proportion of data point density within each 'pixel', or 100 x 100 grid, and smoothed according to the methods of Eilers and Goemann (2004) – discussed further in section 2.4.1.1. Density contours can be considered similar to how contours on a map show the same difference in elevation, but in the case of this study the contours show increasing population density between variables x and y for the constrained ChemCam observation point dataset. Each contour level is representative of the proportion of smoothed data points per x-y bin (or pixel). The average number of smoothed data points per pixel represented by the contour can be calculated by multiplying the sample number *n* by the

level step *ls* and contour level *c*. For example, in Fig. 2.11. the average number of smoothed data points per pixel for contour level 3 is:

$$N = n * (ls * c) = 1222 * (0.0005 * 3) = 1.83 \quad (2.1)$$

Using density contour plots generates a better approximation of the bulk composition as the focal composition is not skewed by extreme outlying values, unlike the mean composition (Fig. 2.11). Smoothed density contours also allow for a better visualisation of large datasets for qualitative analyses.

This method has proven useful to illustrate the compositional foci and geochemical trends across each of the stratigraphic groups and has the additional benefit of effectively simulating bulk rock compositions at the stratigraphic scale of analysis. Due to the small sampling footprint of the ChemCam LIBS laser (350–750 μm for distances of 3–7 m from the rover mast; Maurice et al., 2016), target analyses are often not representative of whole rock compositions, particularly if the target is coarse-grained (grain diameter >1 mm) as in this case individual mineral grains are more likely to be analysed (Cousin et al., 2017a).

Edwards et al. (2017) used density contours for ChemCam igneous float and clast analyses to determine volcanic/magmatic endmember compositions according to the contour foci. This study adopts a similar approach to analyse ChemCam observation point compositions across the sedimentary units. Although, here the focal compositions relate more to stratigraphic group whole-rock compositions which can be used as a standard of comparison between stratigraphic units, isolated alteration features, and comparison datasets. As such, density contours have provided a beneficial exploratory tool for Gale crater's chemostratigraphy and will be initially displayed as a series of Harker biplots with SiO_2 on the x-axis. SiO_2 was selected as the comparator major element oxide as it exhibits a wide range of values (34.4 wt% – 78.8 wt%) for Gale crater's sedimentary rocks that, in previous studies, has been associated with changes in sediment provenance, chemical

weathering and aqueous alteration (e.g., Frydenvang et al., 2017; Hurowitz et al., 2017; Yen et al., 2017; Morris et al., 2016).

2.4.1.1. Generating density contours with MATLAB

For this study, I generated density contours for stratigraphic groups (Bradbury and Mt Sharp) in the constrained ChemCam bulk rock dataset, as well as the Stimson formation of the Siccar Point Group and "Igneous float and clast" datasets using the MATLAB `dscatter` algorithm (MathWorks Inc, 2003-2004). The `dscatter` algorithm uses a method of density estimation based on two-dimensional histograms and linear algebra (Eilers and Goeman, 2004) to plot the contours according to the following code:

1) First, the algorithm divides the (x,y) space of the plot into an appropriate number of bins [`nbins`] for the dataset according to the number of unique values present therein. If there are more than 200 unique values, the algorithm sets the number of bins to 200 unless specified by the user.

```
nbins = [min(numel(unique(X)),200) ,min(numel(unique(Y)),200)];
```

For univariate histograms, the number of bins is highly important as it dictates bin width which determines the amount of smoothing inherent in the subsequent plot. For this algorithm, bin size (and hence bin width) is less important at this stage as a smoothing function is applied later to account for the random error present within the plots (see section 2.2.1.1.1.). Instead, for large databases keeping the number of bins relatively high allows me to fully account for the population distribution of a heterogeneous dataset and avoids overly smoothing the data at this initial step. To

make comparisons between the density distributions of the two stratigraphic groups Bradbury and Mt Sharp which are of an approximately equal sample size I have used a set total bin number of 100 x 100 (unless stated otherwise). For the Stimson formation and "Igneous float and clasts" datasets that are much smaller in sample size, I selected a bin number of 50 x 50. This value contributed to a suitable contour level step between the calculated dataset population densities (Fig. 2.12) which resulted in less noise and an appropriate level step for each contour (e.g., a density >1 point per 2 pixels for the outermost contour).

2) Once an appropriate bin size has been established, the algorithm creates linearly spaced vectors between the minimum [`minx`, `miny`] and maximum [`maxx`, `maxy`] values of the dataset x and y variables that are being plotted.

```
edges1 = linspace(minx, maxx, nbins(1)+1);
edges2 = linspace(miny, maxy, nbins(2)+1);
```

3) The linearly spaced vectors calculated in step (2) are then used to define the (x,y) co-ordinates of the density contours according to the (x,y) range of the dataset and defined bin sizes.

```
ctrs1 = edges1(1:end-1) + .5*diff(edges1);
ctrs2 = edges2(1:end-1) + .5*diff(edges2);
```

4) Then, the variables `edges1` and `edges2` are redefined to replace the previous maximum and minimum values in `edges1` and `edges2` with -∞ and ∞ to include all non-`NaN` (Not a Number) values.

```
edges1 = [-Inf edges1(2:end-1) Inf];
edges2 = [-Inf edges2(2:end-1) Inf];
```

5) From (4) the number of observation points are assigned to each bin using the MATLAB function `histc`, and then placed into the empty matrix `bin`, with bin number assigned to row, and x, y variables assigned to the columns. This is used to generate the matrix of counts for a two-dimensional histogram `H`, which is then

smoothed according the smoothing function `smooth1D` (discussed in section 2.2.1.1.1.).

```
[n,p] = size(X);
bin = zeros(n,2);
[dum,bin(:,2)] = histc(X,edges1);
[dum,bin(:,1)] = histc(Y,edges2);
H = accumarray(bin,1,nbins([2 1])) ./ n;
G = smooth1D(H,nbins(2)/lambda);
F = smooth1D(G',nbins(1)/lambda)';
```

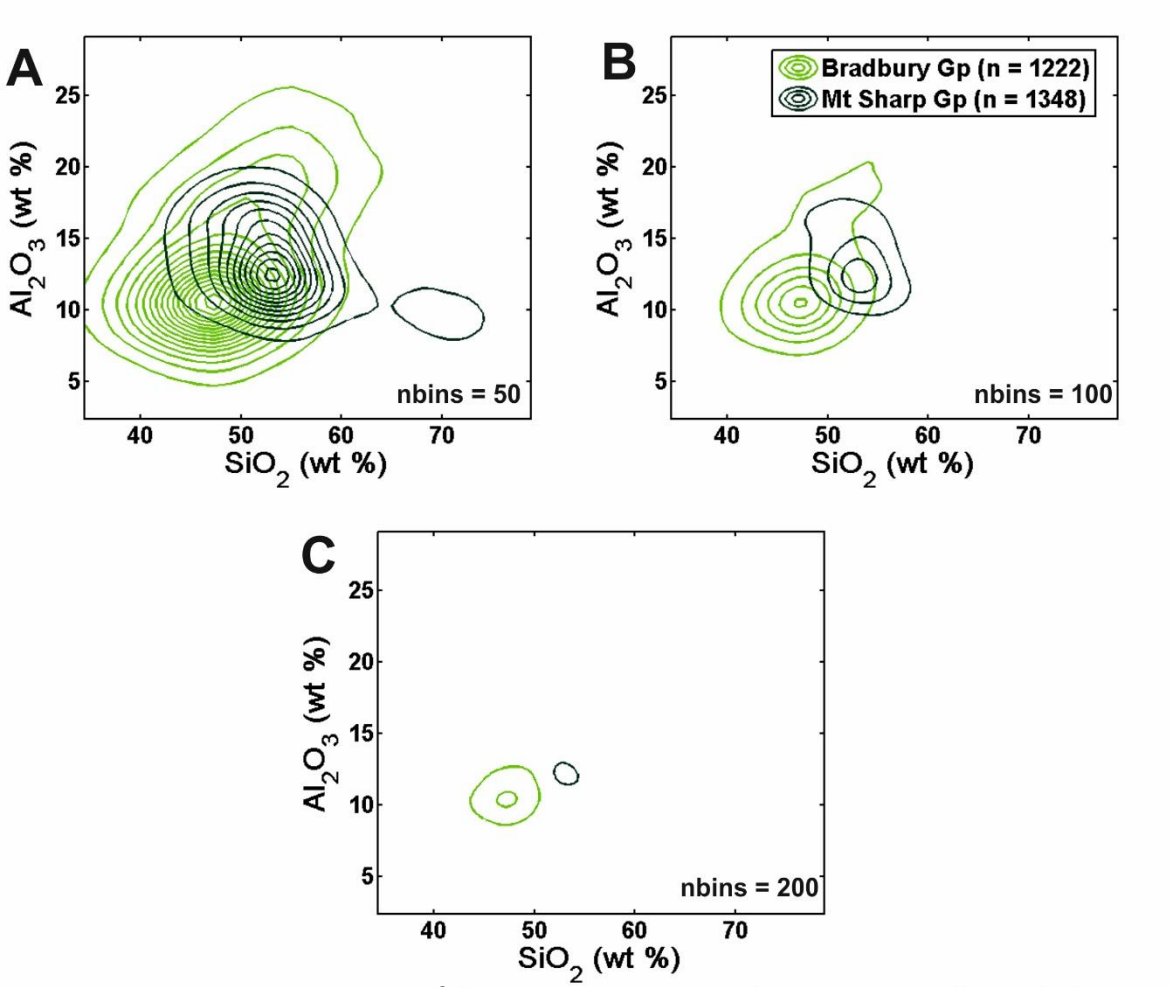

Figure 2.12: Density contours of the two main stratigraphic groups Bradbury (light green) and Mt Sharp (dark green) with varying bin numbers (nbins). A) bin size is 50, B) bin size is 100 and C) bin size is 200. The level step was kept at 0.0005 for all groups and plots. The chosen bin number is 100 as this gives the best fit of the contours to the data for the selected sample sizes.

6) Finally, the contour plot is made with `ctrs1` and `ctrs2` as the subsequent x and y coordinates, and the values generated by the smoothed density estimator `F` plotted as the z coordinates which the MATLAB function `contour` uses to draw the density contour lines.

```
[dummy, h] = contour(ctrs1,ctrs2,F);
```

2.4.1.1.1. The density contour smoothing function

The smoothing function applied in the `dscatter` algorithm is derived from the Eilers and Goeman (2004) smoothing method for two-dimensional histogram analysis, a method used to make two-dimensional histograms "more informative (and attractive)" (Eilers and Goeman, 2004). This smoothing function computes the degree of scatter between the residuals of a column *y* of the histogram count matrix `H`, and that of smoothed column *z*, in order to smooth the scatter of the residuals using a method based in partial least squares (Eilers and Goeman, 2004):

$$S = \sum_i (y_i - z_i)^2 = |y - z|^2, \quad (2.2)$$

where scatter is determined by the sum of squares of the residual differences:

$$R = \sum_i (\Delta z_i)^2 = |D_1 z|^2 \quad (2.3)$$

for which,

$$\Delta z_i = z_i - z_{i-1}. \quad (2.4)$$

Then, S and R, calculated from (2.1) and (2.2), are combined into one penalised least squares function Q:

$$Q = S + \lambda R = |y - z|^2 + \lambda |D_1 z|^2, \quad (2.5)$$

from which the vector $\hat{z}$ can be determined that minimises Q using the following equations:

$$(2.6) \qquad (I + \lambda D'_1 D_1)\hat{z} = y,$$

where *I* is the identity matrix and λ is the smoothing factor used by the density estimator that determines the fit of the data to *y* and the "roughness" of *z* (i.e., roughness increases in the plot, with a lower λ and a better fit to the data).

A second-order difference matrix $D_2 = \Delta^2 z$ is obtained from (2.4) using the following equation:

$$(2.7) \qquad \Delta^2 z_i = \Delta(\Delta z_i) = (z_i - z_{i-1}) - (z_{i-1} - z_{i-2})$$
$$= z_i - 2z_{i-1} + z_{i-2},$$

To which λ is now λ^2. In order to counteract the negative values inherent in using the second-order differences, Eiler and Goeman (2004) use both a first- and second-order penalty that translates the penalised least squares function into:

$$(2.8) \qquad Q = |y - z|^2 + \lambda^2 |D_2 z|^2 + 2\lambda |D_1 z|^2,$$

for which α = 2 is the impulse response used to keep *Q* positive, found by trial and error by Eilers and Goeman et al. (2004).

Hence, the smoothing of the matrix Y, to get Z becomes:

$$(2.9) \qquad (I + 2\lambda D'_1 D_1 + \lambda^2 D'_2 D_2)\hat{Z} = Y,$$

Which is applied to all columns of `H` (from step 5) using the MATLAB code:

```
function Z = smooth1D(Y,lambda)
[m,n] = size(Y);
E = eye(m);
D1 = diff(E,1);
D2 = diff(D1,1);
P = lambda.^2 .* D2'*D2 + 2.*lambda .* D1'*D1;
Z = (E + P) \ Y;
```

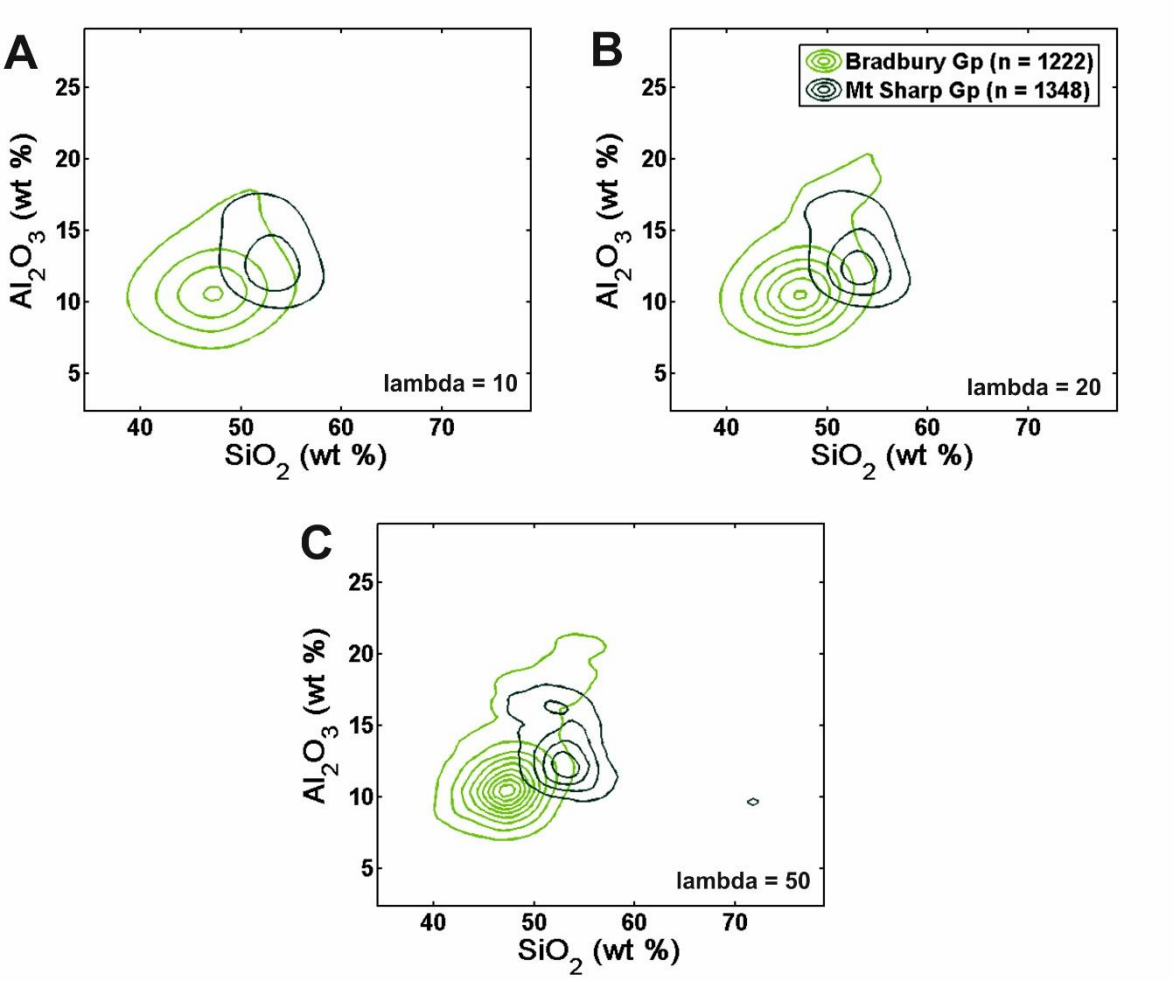

Figure 2.13: Contour plots of the Bradbury (light green) and Mt Sharp (dark green) stratigraphic groups with a set level step of 0.0005 and bin number 100 x 100. Each plot shows a different value for the smoothing factor (lambda) with A) at 10, B) at 20 and C) at 50. The chosen value for the main stratigraphic groups is 20 as this neither over nor under smoothed the contours. Contour shape does not vary significantly between 20 and 30, so the lower value is chosen in line with the default setting recommended by Eilers and Goeman (2004).

For the purposes of this study, I have deemed a λ value of 20 as appropriate as it produces enough smoothing to illustrate the compositional characteristics of the stratigraphic groups, but not too much to mask trends and focal compositions (such as in Fig. 2.13 A). For the smaller datasets (Stimson formation and "Igneous Float and Clasts") I selected a value of 30 for λ to provide a higher precision, but for it to still be comparable to the larger datasets.

2.4.1.1.2. Contour error propagation

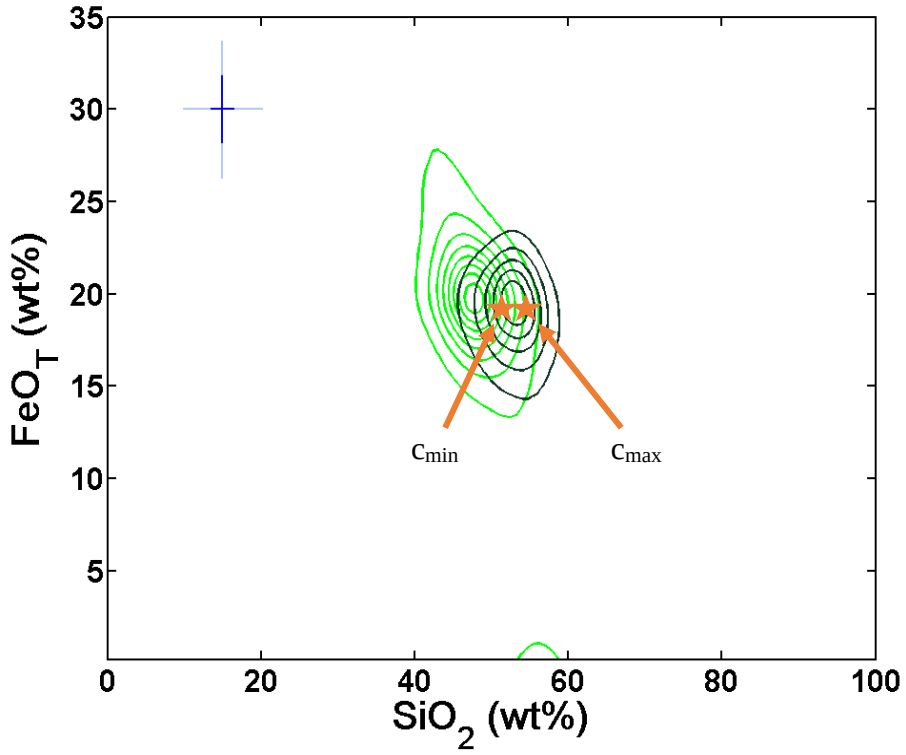

Figure 2.14: An example of where the c_{max} and c_{min} values are acquired for the x-axis variable of the Mt Sharp Group.

In order to acquire the precise focal compositions for each variable used to generate the contours, I plotted each variable against one another and determined the maximum (c_{max}) and minimum (c_{min}) extent of the contour focus (e.g., Fig. 2.14) for a set level step and bin size (e.g., For the Bradbury and Mt Sharp study in Chapter 3, the level step used ls = 0.0005 and bin size 100 x 100). Then, once the maximum and minimum extent of the focal compositions had been derived, I calculated the mean composition for all values across each variable combination to derive the exact focal composition.

To then propagate the error for this process, I took the ChemCam standard deviation for each stratigraphic group constrained dataset and applied equations (2.10) and (2.11) to the values for each dataset variable.

$$(2.10) \qquad \sigma_x = \sqrt{\sigma^2 + \sigma^2 + \sigma^2 \ldots + \sigma_n^2}\,,$$

$$(2.11) \qquad \sigma_y = \left|\frac{1}{n}\right| . \sigma_x\,,$$

Table 2.5: Mt Sharp maximum and minimum values for contour foci when plotted against each y variable. Average compositions that correlate to the exact focal composition, and the standard deviation (sd) of the contour cmax and cmin are given in the right hand columns.

Mt Sharp		y variable									
x variable		SiO2	TiO2	Al2O3	FeOT	MgO	CaO	Na2O	K2O	Average	sd
SiO2	cmax	0.0	54.6	54.6	54.6	53.8	54.6	54.2	54.7		
	cmin	0.0	51.6	51.2	51.2	52.9	51.6	52.5	50.8	53.1	1.5
TiO2	cmax	1.1	0.0	1.1	1.1	1.1	1.1	1.1	1.1		
	cmin	0.9	0.0	0.9	0.9	0.9	0.9	0.9	0.9	1.0	0.1
Al2O3	cmax	13.5	13.0	0.0	13.5	13.5	12.7	13.4	12.7		
	cmin	11.2	11.7	0.0	10.9	11.2	11.2	10.9	11.2	12.2	1.1
FeOT	cmax	20.7	19.9	21.1	0.0	19.9	20.7	19.6	20.7		
	cmin	18.2	19.0	18.2	0.0	19.0	18.6	19.4	17.8	19.5	1.1
MgO	cmax	4.7	5.4	5.4	5.0	0.0	5.5	5.2	5.0		
	cmin	4.5	4.1	3.7	4.1	0.0	3.7	3.8	4.1	4.6	0.7
CaO	cmax	2.8	2.7	2.7	2.8	2.8	0.0	2.8	3.2		
	cmin	1.8	2.0	1.8	1.8	1.8	0.0	1.8	1.6	2.3	0.6
Na2O	cmax	3.0	3.0	3.1	3.0	3.1	3.1	0.0	3.1		
	cmin	2.8	2.8	2.5	2.8	2.8	2.7	0.0	2.6	2.9	0.2
K2O	cmax	1.5	1.4	1.3	1.5	1.2	1.6	1.5	0.0		
	cmin	0.9	1.0	1.0	0.8	0.9	0.8	0.8	0.0	1.2	0.3

where σ_x is the propagated error value, σ is the standard deviation for the variable in question, σ_n is the nth standard deviation for *n* values used to calculate the average focal composition from the c_{min} and c_{max} values. In this ChemCam study, one major element out of the 8 analysed will always be on the x-axis, with two values (c_{min} and c_{max}) taken to determine the focus. Therefore, the value of n will always be n = 14 in equation 2.16 for the ChemCam major element oxide dataset presented here.

2.4.2. Linear regression models

I have used both multiple and simple linear regression models to explore and define the geochemical correlations inherent in the datasets. Due to the large size of the dataset, and high number of variables (8 major element oxides) from which to conduct linear regression models, I constructed a matrix table of Pearson correlation coefficients for each stratigraphic group and diagenetic feature subclass. Pearson correlation coefficients are useful to "sieve" the dataset in order to find variables with notable correlations that can then be explored further with regression analysis (Kutner et al., 2004).

The Pearson correlation coefficient measures the extent a linear relationship exists between two variables, and is calculated using the following equation:

$$(2.12) \qquad \rho = \frac{\sum_{i=1}^{n}(x_i-\bar{x})(y_i-\bar{y})}{(n-1)\sigma_x\sigma_y},$$

Where $\bar{x}$ and $\bar{y}$ are the sample means for the first and second variables respectively, σ_x and σ_y are the subsequent x and y standard deviations, and n is the column length. Pearson correlation coefficients range from between -1 and +1 depending on the direction and strength of the correlation (Pearson, 1896; Kutner et al., 2004). Showing the Pearson correlation coefficients in a matrix of variables (major element oxides) permits a simultaneous comparison of all variable correlation coefficients with each other (e.g., Appendix Table A.3.2; Pearson, 1896; Kutner et al., 2004). Correlation coefficients are shown to be statistically significant through the calculation of the student's t-test:

$$(2.13) \qquad t = r\sqrt{\frac{n-2}{1-r^2}},$$

In this case, the student's t-test tests the null hypothesis that there is no correlation between the two variables (H_0:$\rho = 0$), against the alternative hypothesis that there is a correlation (H_A:$\rho \neq 0$) (Montgomery et al., 2012). *r* is the observed value of the correlation

coefficient calculated in (2.12) for a cut off value $\alpha = 0.05$. *p* is calculated for (2.12) using a t-distribution for n-2 degrees of freedom with the equation:

$$(2.14) \quad p - value = 2P(T > |t|) ,$$

Once the variables with notable correlations ($r > 0.5$) have been identified, I then conduct simple linear regression models to confirm the relationship, and generated a scatter plot to graphically display the fit to the model compared to the degree of residual scatter around it. Simple linear regression is conducted in Minitab 17 based on the following model (Kutner et al., 2004; Montgomery et al., 2012):

$$(2.15) \quad Y = \beta_0 + \beta_1 X_1 + e$$

In this model, *Y* is the response for the population, β_k is the k^{th} population regression coefficient. X_k is the k^{th} predictor, and *e* is the error term ~ N(0, 1). Minitab 17 generates the fitted response $\hat{y}$ with regression estimates β_0 by b_0 and β_1 by b_1, to develop the following model (Kutner et al., 2004; Montgomery et al., 2012):

$$(2.16) \quad \hat{y} = b_0 + b_1 x_1.$$

In equation 2.16, the fitted value of the response $\hat{y}$ is calculated using the estimated coefficients (b_k) and their predictors (Kutner et al., 2004; Montgomery et al., 2012):

$$(2.17) \quad b_1 = \frac{\sum(x_i - \bar{x})(y_i - \bar{y})}{\sum(x_i - \bar{x})^2}$$

If the relationship between two variables and their relative stratigraphic position is to be explored further, stratigraphic unit may be added as a categorical predictor to the models for which Minitab 17 then displays separate regression equations for each level of the categorical variables.

Multiple linear regression models are also generated using Minitab 17 and are used to show how the response (*Y*) relates to more than one predictor (Montgomery et al., 2012):

$$(2.18) \qquad Y = \beta_0 + \beta_1 X_1 + \cdots + \beta_k X_k + e \ ,$$

The model Minitab uses for multiple regression is the matrix terms of (2.15) and estimates b_k instead of β_k to determine the fitted value of the dataset **y**:

$$(2.19) \qquad \boldsymbol{y} = \boldsymbol{xb} + \boldsymbol{e} \ .$$

In turn, the formula for determining multiple regression coefficients is also a matrix derivation of the simple linear regression equation (2.17) (Montgomery et al., 2012):

$$(2.20) \qquad \boldsymbol{b} = (\boldsymbol{x}'\boldsymbol{x})^{-1}\boldsymbol{x}'\boldsymbol{y}.$$

Minitab output for the regression model consists of four sections; an ANOVA analysis of the model's fit to the data, a model summary, a table of coefficients and their associated statistics, and the calculated regression equation. Appendix Table A.2.1. summarises the model output functions and provides a brief description on how they apply to the suitability of the model to the data.

I conducted multiple linear regression models for the stratigraphic groups, with Al_2O_3 as a response to all other major elements. Al_2O_3 is used as the response due to its use in calculating the Chemical Index of Alteration (CIA) of sedimentary and igneous samples (Nesbitt and Wilson, 1992; Nesbitt and Young, 1982; section 3.2.1.3.). CIA values are a method of quantifying the extent of chemical alteration in a sample based on the principles of feldspar dissolution (Nesbitt and Wilson, 1992; Nesbitt and Young, 1982). Feldspar is a common component of terrestrial sediments with Al_2O_3, CaO, Na_2O and K_2O in its crystal structure. When feldspar undergoes dissolution is a geological system CaO, Na_2O and K_2O

are leached from the sample, enriching it in the relatively immobile Al_2O_3 (Nesbitt and Wilson, 1992; Nesbitt and Young, 1982). Therefore, calculating the proportion of Al_2O_3 against CaO, Na_2O, K_2O, including MgO and FeO_T for basaltic sediments with mafic components (Babechuk et al., 2014; Nesbitt and Wilson, 1992), can give insight on the extent of chemical weathering in a sample (Nesbitt and Wilson, 1992; Nesbitt and Young, 1982). In modelling Al_2O_3 as a response to all other major element predictors, this can statistically distinguish which major elements contribute the most to aluminium's variation and help ascertain whether or not this is indeed related to chemical weathering regimes, or source region characteristics. The relationship of SiO_2 variation according to chemical weathering or variations in source region compositions is a particularly notable topic of debate for Martian sediments (Mangold et al., 2019; Hurowitz et al., 2017; McLennan, 2003) as silica is seen to vary across much of the planet (McLennan, 2003). As such, multiple linear regression models of SiO_2 against all other major element predictors have also been conducted.

2.4.3. Cluster analysis method

The smaller dataset relating to Siccar Point Group observation point analyses compared with the Bradbury and Mt Sharp Groups permits a cluster analysis to be performed on the dataset. I used a cluster analysis for the Siccar Point Group as it is a useful method of distinguishing previously undefined groups that exist within a multivariate dataset (Schuenemeyer and Drew, 2011), in this case, that relating to the ancient aeolian dune deposits (Banham et al., 2018). Identifying the main geochemical components, and how they vary between the two ancient dune locailities can aid in constraining the geochemical effect of mineral sorting and lithification, as well as whether sediment source regions have varied since the Siccar Point Group was deposited and the

Bagnold dunes were formed. Analysing the ancient deposits with this method also provides another means of validating the hypothesis that source region compositions are the main causes of geochemical variation within Gale crater's sedimentary units and can aid in determining Martian aeolian mineral sorting regimes for the past and present. Furthermore, calculating the natural clusters inherent in the dataset provides additional means of testing whether the current interpretation for what constitutes these sedimentary units (felsic and mafic minerals, amorphous component and sulfate mineral veins) is correct.

Minitab 17 conducts Cluster Observations analysis using an agglomerative hierarchical algorithm. This algorithm defines each data point as a cluster, then combines the two closest clusters into a new one at each step (Schuenemeyer and Drew, 2011). In Minitab v17, the similarity (s_{ij}) between two clusters (i and j) is calculated as:

$$(2.21) \qquad S_{ij} = \frac{100(1-d_{ij})}{d_{max}},$$

Where d_{ij} is the distance between clusters i and j, and d_{max} is the maximum value in the original distance matrix **D**.

The distance of clusters is calculated according to the measure of association and distance method defined by the user. For the constrained Stimson dataset, I used the Complete Linkages (d_{mj}) measure of association for Manhattan distances $d(i,k)$, with all major element oxides as variables (k). The formula for which is as follows:

$$(2.22) \qquad d_{mj} = \max(d_{kj}, d_{lj}) ,$$

$$(2.23) \qquad d(i,k) = \sum_j \left| x_{ij} - x_{kj} \right| .$$

The Complete linkages of Manhattan distance was the preferred method due to other measures of association providing a limited number of clusters (less than 2). In addition, as the Manhattan distance is calculated through the sum of absolute distances,

less weight is placed on outlying values compared to the Euclidean distance. Therefore, the Manhattan distance method is more optimal when considering small-scale LIBS analyses on polymineralic and variably altered sedimentary rock. Variables (SiO_2, TiO_2, Al_2O_3, FeO_T, MgO, CaO, Na_2O, K_2O) were standardised in order to minimise the effect of scale differences. Minitab 17 standardises the variables according to:

$$x_{st} = \frac{(x_{ik} - \bar{x}_k)}{\sigma_k} . \quad (2.24)$$

Minitab 17 then generates an output table consisting of; the number of clusters at each iteration, their similarity level, distance level, the number of clusters joined at that iterative step, the number of new clusters formed at each step, and the number of observations in the newly formed cluster at each step (see Appendix Table A.4.1.). The final partition was determined by analysing the changes in similarity levels at each step to "cut" the dendrogram (Schuenemeyer and Drew, 2011). In this study, I identified a new group with an abrupt change in similarity or distance values between steps (i.e., the difference in similarity is greater than 5.00 where previously it was less than 1.00). The cluster analysis graphical summary is presented as a dendrogram that displays the groups formed through the clustering of observations on the x-axis, and the Manhattan distances between each group on the y-axis (Schuenemeyer and Drew, 2011).

Once the appropriate number of groups is determined according to the change in similarity levels outlined above, I then run the cluster analysis again with the final group (or partition) number placed into the Minitab 17 input. Minitab 17 cluster analysis output for the final partition also includes a summary of modelled cluster compositions (based on their cluster centroid position in the variable space), their distance from the grand centroid and distances between cluster centroids. Cluster analysis has the added benefit of each initial observation point analysis being assigned a cluster membership (Schuenemeyer and Drew, 2011), and Minitab 17 prints this as a new column in the data spreadsheet. As

Minitab 17 does not calculate statistical significance for the clusters to the dataset, this cluster membership column is used as the factor, with each cluster pertaining to a factor level, in a one-way analysis of variance (ANOVA) for which each major element oxide (cluster variable) is in turn designated as the response. ANOVA tests the null hypothesis where all means are equal (H_0: $\mu_1 = \mu_2 = \ldots = \mu_r$) against the alternative hypothesis that at least one mean is different (H_A: at least one mean is not equal to the others) for a significance level of $\alpha = 0.05$ (Montgomery et al., 2012; Schuenemeyer and Drew, 2011). ANOVA uses the F-test which is calculated by dividing the mean squares (*MS*) of the factor with the mean squares of the error, and is calculated using the following equations:

$$(2.25) \qquad MS\ (Factor) = \frac{\sum n_i(\bar{y}_i - \bar{y}_{...})^2}{r-1} = \frac{SS\ (Factor)}{DF\ (Factor)},$$

$$(2.26) \qquad MS\ (Error) = \frac{\sum_i \sum_j (y_{ij} - \bar{y}_i)^2}{n_T - r} = \frac{SS(Error)}{DF(Error)},$$

$$(2.27) \qquad F = \frac{MS\ (Factor)}{MS\ (Error)},$$

where *r* is the number of factor levels, *i* is a given factor level, *j* is the given case for a particular factor level, n_i is the number of observations at the given factor level, n_T is the total number of cases, y_i is the total of the observations at the i^{th} factor level, and $\bar{y}_i$ is the mean of observations at the i^{th} factor level.

2.4.4. Equivalence tests

Equivalence tests calculate whether the mean of one group is the same as the mean of the other within a predetermined equivalence interval (Lakens et al., 2017; Welleck, 2010). This equivalence interval for a "two one-sided test" is defined by the lower Δ_L and upper boundaries Δ_U which are set by the tester based on the dataset and conditions under investigation (Lakens et al., 2017; Schuirmann, 1987). Equivalence tests differ from a

standard t-test of the means (such as that conducted to test the statistical significance of Pearson correlation coefficients in section 2.4.2) in that the burden on proof is placed on proving whether one mean differs from the other population mean (H_0: $\mu_1 - \mu_2 < \Delta_L$ or $\mu_1 - \mu_2 > \Delta_U$), instead of proving that they are the same (H_0: $\mu_1 = \mu_2$). Equivalence tests also differ from the standard t-test in that the tester defines the equivalence interval, or range of acceptable values, within which the difference must fall in order for the sample means to have equivalency (Lakens et al., 2017; Welleck, 2010).

I used two-sample equivalence tests in Chapter 4 to statistically determine whether the geochemical composition of the Stimson formation at the Emerson Plateau locality differs from that of the Naukluft Plateau locality. This test was performed to identify whether mineral sorting in the ancient Stimson dune field created an identifiable geochemical signature similar to how it is hypothesised to have changed the proportions of mafic/felsic mineral populations in the active Bagnold dune field (Rampe et al., 2018). In this study, the upper and lower equivalence limits were defined according to 1σ ChemCam instrument precision (Table 2.1) as any geochemical variation within this defined equivalence interval likely relates to the uncertainty of the ChemCam instrument and not the natural geochemical variation of the test population. Equal variance was not assumed as both datasets were taken in separate localities of sedimentary rock that potentially contain varying abundances of minerals and sandstone cement. I selected the Emerson Plateau as the reference level due to it containing fewer diagenetic concretions and no trace quantities of hydrated calcium-sulfates which are stated to be indicative of minor alteration in the Naukluft Plateau drilled Okoruso sample (Yen et al., 2017). For these tests, the null hypothesis was H_0: $-1\sigma \geq \mu_E - \mu_N \geq 1\sigma$ for $\alpha = 0.05$ where μ_E and μ_N are the respective means for the Emerson and Naukluft Plateaus.

I conducted two-sample equivalence tests using Minitab v17 for each major element oxide (SiO_2, TiO_2, Al_2O_3, FeO_T, MgO, CaO, Na_2O, and K_2O) of the constrained Stimson dataset. They are calculated based on the difference (*D*) between the test mean, which in this case in the mean of the Naukluft Plateau μ_N and the reference mean, the mean of the Emerson Plateau μ_E :

$$D = \mu_N - \mu_E, \quad (2.28)$$

Whereby the mean (μ) of the test and reference sample is calculated through:

$$\mu = \frac{\sum_{i=1}^{n_1} x_i}{n_1}, \quad (2.29)$$

with x_i as the observations ($i = 1,\ldots n_1$) and n_1 as the number of observations in the sample.

When equal variance is not assumed, Minitab calculates the standard error of the difference (*SE*) by:

$$SE = \sqrt{\frac{S_1^2}{n_1} + \frac{S_2^2}{n_2}}, \quad (2.30)$$

Where the standard deviation of the test and reference samples are given as S_1 and S_2 respectively, and the number of observations for the test and reference samples are n_1 and n_2. Minitab also calculates the degrees of freedom (*DF*) when unequal variance is assumed as the following:

$$DF = \frac{\left(\frac{S_1^2}{n_1} + \frac{S_2^2}{n_2}\right)^2}{\frac{\left(\frac{S_1^2}{n_1}\right)^2}{n_1 - 1} + \frac{\left(\frac{S_2^2}{n_2}\right)^2}{n_2 - 1}}, \quad (2.31)$$

In order to calculate statistical significance for the defined equivalence intervals, Minitab calculates two t-values, one (t_1) for the upper equivalence limit (Δ_U) for a hypothesis that the test mean > reference mean, $\Delta_U = 0$ (2.32),and one (t_2) for the lower equivalence limit (Δ_L) for a hypothesis that the test mean < reference mean, $\Delta_L = 0$ (2.33).

$$(2.32) \qquad t_1 = \frac{D-\Delta_U}{SE},$$

$$(2.33) \qquad t_2 = \frac{D-\Delta_L}{SE},$$

Finally, the probability (P_{H0})for each null hypothesis used to calculate equations 2.31 and 2.32 is calculated by Minitab by:

$$(2.34) \qquad H_0: D \leq \Delta_U, P_{H_0(T \geq t_1)},$$

$$(2.35) \qquad H_0: D \geq \Delta_L, P_{H_0(T \leq t_2)},$$

Whereby *D* is the difference between the test population and the mean of the reference population (2.28) and *T* is the t-distribution with DF degrees of freedom.

Through using the classification and statistical methods described above for the large and heterogeneous ChemCam dataset, this research will make an important step in understanding how the ChemCam analysed geochemical variability relates to the Martian sediments and main stratigraphic groups along the *Curiosity* rover traverse. This in turn will further the understanding of Martian crustal compositions surrounding Gale crater in addition to mineral sorting regimes across different paleoenvironments, weathering and aqueous alteration processes.

3. Determining the sediment source region characteristics of Gale crater's fluviolacustrine sedimentary record

Terrestrial provenance studies have shown that the mineralogy and geochemistry of fine-grained, clastic, sedimentary units are largely characteristic of their crustal source region, provided the extent of aqueous alteration, transport fractionation, and the effects of grain size variation have been taken into account (Bloemsma et al., 2012; Weltje et al., 2012; Jin et al., 2006; Kroonenberg, 1992; Herron, 1988; Roser and Korsch, 1986). In this Chapter, I explore the hypothesis that Gale crater's sedimentary record can also provide information on the geochemistry of the surrounding crust and the processes that have eroded, weathered, transported and deposited them through using the methods of Chapter 2 that were based on the terrestrial studies outlined above. With the increasing evidence that Mars' crust has more evolved igneous source regions than the widespread basalt identified from orbit (e.g., McSween et al., 2009; Chevrier and Mathé, 2007; Bandfield et al., 2000; section 1.2), and with Gale crater's stratigraphic record largely dominated by primary igneous minerals and a lack of open system weathering products away from alteration features (Hurowitz et al., 2017; Rampe et al., 2017; Siebach et al., 2017a; Treiman et al., 2016; Anderson et al., 2015; Grotzinger et al., 2014; Vaniman et al., 2014), I also hypothesise that the main cause of geochemical variation within Gale crater sediments is likely to be from changes in sediment source region composition. The majority of studies pertaining to Gale crater sediment source regions focus on specific waypoints along the traverse, often neglecting the full extent of the ChemCam dataset, and not discussing the sediment source regions for the majority of the Murray formation outside of the Marias

Pass area. This chapter therefore identifies and interprets the geochemical endmembers of all fluviolacustrine stratigraphic units analysed from the start of the mission until sol 1482.

The results of this analysis have been published in Bedford et al. (2019, Geochimica et Cosmochimica Acta) of which I am the first author. In this manuscript, I conducted the analysis of the ChemCam observation point geochemical dataset, classifying the targets, placing them into geological context and analysing the constrained dataset using the statistical methods outlined in 2.3. I then interpreted the results of the statistical analysis, wrote the first draft of the manuscript and answered the reviewer comments. Co-authors Dr. J. Frydenvang and Dr. P. J. Gasda contributed to the discussion of the ChemCam targets derived from the Marias Pass silica-rich locality. Dr. E. B. Rampe aided in the discussion of the ChemCam dataset in relation to the CheMin analyses and provided Fig. 3.14. Dr. R. C. Wiens contributed to the methods relating to the operation of the ChemCam instrument, data processing and the instrument uncertainties. All co-authors provided additional input into the development of the discussion and the response to reviewer comments throughout the publication process.

3.1. Results: Geochemical characteristics of the fluviolacustrine stratigraphic groups

This subsection outlines the defining geochemical characteristics of the Bradbury and Mt Sharp stratigraphic Groups, which are interpreted to have been deposited in an ancient river and closed basin lake environment (Stack et al., 2018; Grotzinger et al., 2015; 2014; Chapter 1.3.3 & 1.3.4). The following results of the statistical methods outlined in chapter 2.3 are presented to highlight any statistically significant similarities and differences between the two fluviolacustrine stratigraphic groups, the contributions of the

key waypoints to the chemostratigraphic record, and the geochemical characteristics of the dominant diagenetic features identified in this study (see methods section 2.2 for details of the target classification). Defining the geochemical compositions of each group, their major element trends, and how they differ is crucial to delineating whether alteration processes have overprinted the geochemical composition of the sediments or whether the igneous source region characteristics can still be determined.

3.1.1. The Bradbury Group

Overall, the results for the Bradbury Group show that major elements SiO_2, TiO_2, FeO_T, CaO and K_2O display a unimodal distribution in their frequency histograms (Fig. 3.1) and density contour Harker plots (Fig. 3.2). These unimodal distributions are generally asymmetric, particularly for K_2O which is strongly left skewed, SiO_2 and TiO_2 that are weakly left skewed, and FeO_T which is weakly right skewed. The single major element in the Bradbury Group to show a symmetric distribution in its histogram is CaO (Fig. 3.1). The asymmetry of several major element histogram distribution suggests an influence on mean compositions of extreme outliers, particularly for FeO_T, K_2O and TiO_2 (Figs. 3.1, 3.2). Bradbury demonstrates a clear bimodality in its histograms for MgO, Na_2O and Al_2O_3 (Fig. 3.1). Peak MgO compositions occur at 0.8–1.3 wt% and 7.1–7.6 wt%; Na_2O peaks occur at 2.9–3.1 wt% and 5.2–5.4 wt%; and Al_2O_3 peaks at 10.4–11.0 wt% and 17.8–18.3 wt%. The standard deviation of the dataset is relatively large, particularly for Al_2O_3, FeO_T, MgO, Na_2O and K_2O, highlighting the geochemical heterogeneity of the geological samples (Table 3.1).

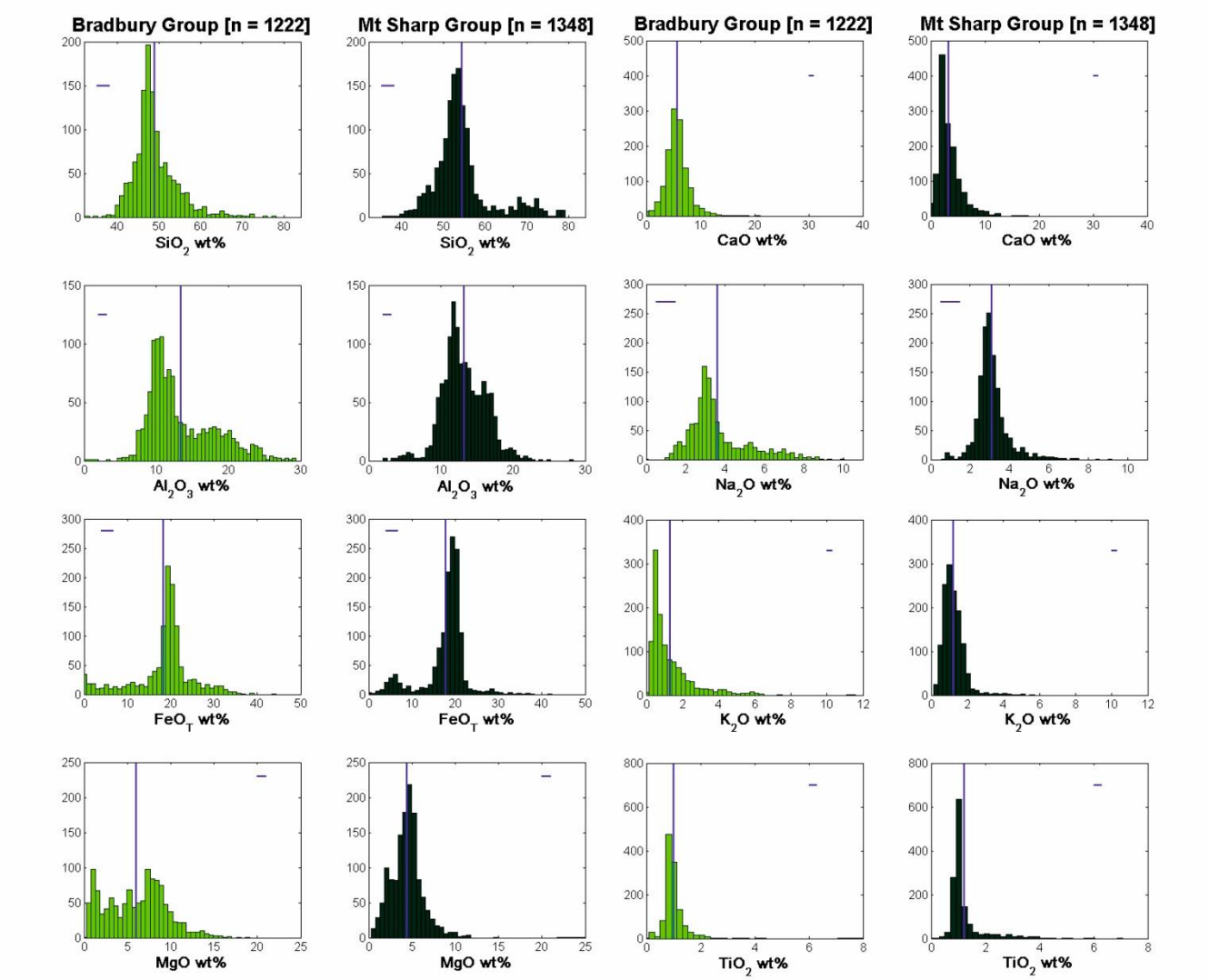

Figure 3.1: Major element histograms for the Bradbury (light green, n = 1222) and Mt Sharp (dark green, n = 1348) stratigraphic groups for the constrained ChemCam dataset of sedimentary outcrop. The mean composition is presented as a blue vertical line while the standard deviation (1σ) is shown as a horizontal line.

Figure 3.2 (next page): Harker density contour plots of constrained ChemCam sedimentary outcrop analyses plotted according to related stratigraphic groups; Bradbury (light green) and Mt Sharp (dark green), with SiO_2 on the x-axis and major element oxide on the y-axis. The light blue cross represents ChemCam accuracy (RMSEP), the dark blue cross shows ChemCam precision (1σ).

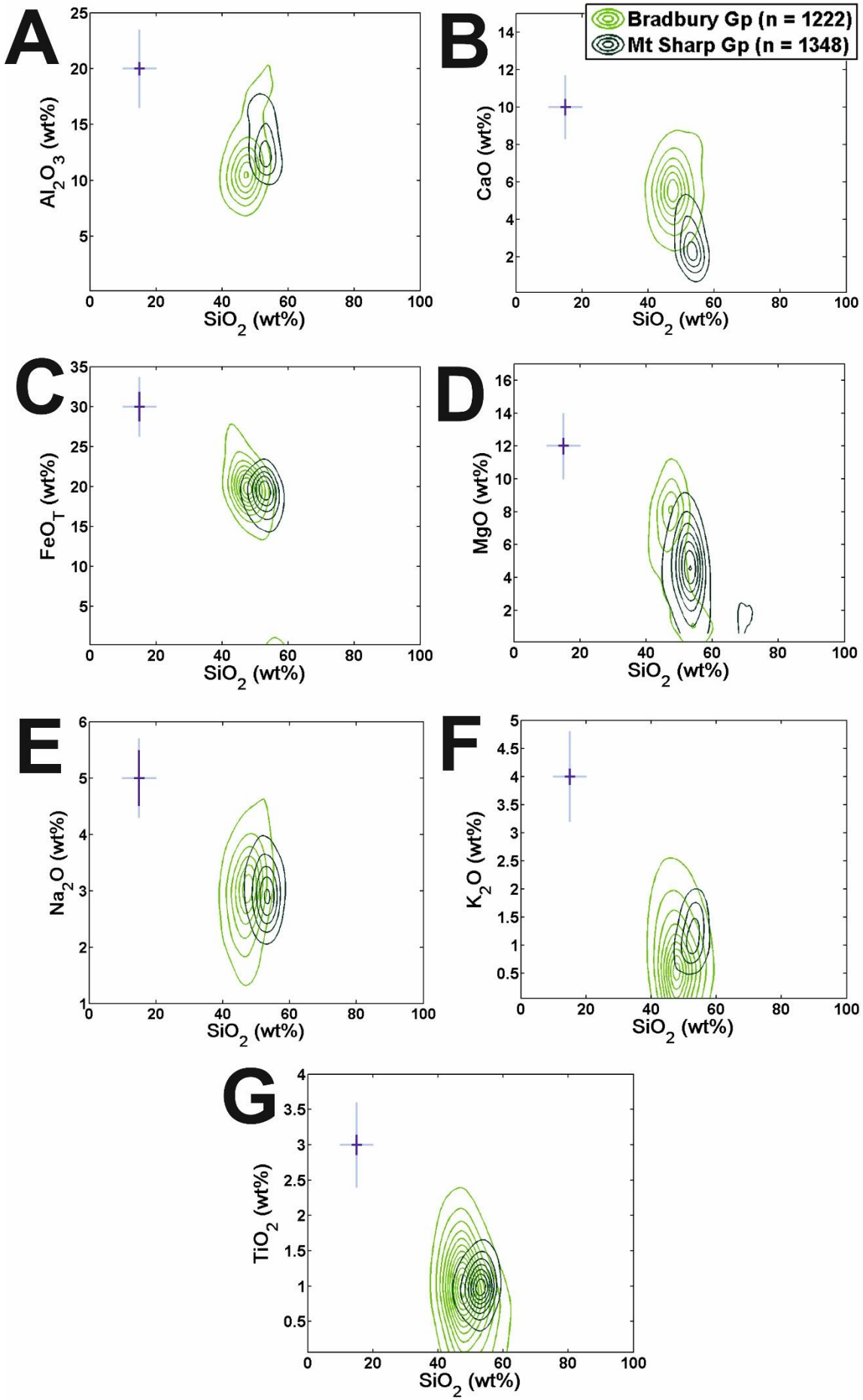
A
B
C
D
E
F
G
Bradbury Gp (n = 1222)
Mt Sharp Gp (n = 1348)
Al2O3 (wt%)
CaO (wt%)
FeOT (wt%)
MgO (wt%)
Na2O (wt%)
K2O (wt%)
TiO2 (wt%)
SiO2 (wt%)

Table 3.1: Basic ChemCam statistics showing the mean, standard deviation (StDev), Minimum, Median, Maximum and Range across each major element oxide for the Bradbury and Mt Sharp stratigraphic Groups.

Variable (wt %)	Unit	Mean	StDev	Minimum	Median	Maximum	Range
SiO_2	Bradbury	49.0	5.2	34.4	48.0	77.6	43.2
	Mt Sharp	54.4	7.0	36.0	53.2	78.8	42.8
TiO_2	Bradbury	1.0	0.6	0.0	0.9	13.1	13.1
	Mt Sharp	1.2	0.7	0.0	1.0	7.0	7.0
Al_2O_3	Bradbury	13.5	4.6	3.3	11.9	29.1	25.8
	Mt Sharp	13.2	3.0	2.4	12.8	27.9	25.5
FeO_T	Bradbury	18.3	7.0	0.0	19.6	43.7	43.7
	Mt Sharp	17.8	5.2	0.1	19.0	41.7	41.6
MgO	Bradbury	6.0	3.5	0.3	6.4	19.0	18.7
	Mt Sharp	4.4	1.8	0.4	4.4	14.8	14.4
CaO	Bradbury	5.7	2.2	0.0	5.6	20.8	20.8
	Mt Sharp	3.4	2.2	0.2	2.7	17.1	16.9
Na_2O	Bradbury	3.6	1.5	1.0	3.2	9.9	8.9
	Mt Sharp	3.1	0.8	0.7	3.0	9.2	8.4
K_2O	Bradbury	1.3	1.2	0.1	0.8	11.4	11.3
	Mt Sharp	1.2	0.6	0.2	1.1	5.5	5.4

Density contours of the Bradbury Group are generally dispersed as concentric ellipses about the mean (Fig. 3.2), but with a slight deviation for the outermost edges towards higher Al_2O_3, FeO_T, Na_2O and K_2O, and lower FeO_T, MgO and Na_2O concentrations (Fig. 3.2). These deviations roughly correspond to the heavy tails in the histograms or the lesser secondary histogram peaks of Al_2O_3 and MgO (Fig. 3.1), and indicate subpopulations, likely associated with the mixing of different endmember proportions. As the level step (0.005) per contour and data size are constant, an increase in contour number equates to an increase in density for the innermost contour. Therefore, the Harker plots that have the highest density of points within their major element foci are TiO_2, K_2O and FeO_T versus SiO_2, with 12, 9 and 8 contours respectively. MgO against

SiO_2 has the lowest number of contours for the dataset, showing that it is more evenly spread in the x-y space between its maximum and minimum values.

Bradbury Group Pearson correlation coefficients (Table 3.2) show strong, statistically significant ($p < 0.05$) negative correlations for FeO_T and SiO_2 ($r = -0.85$), Al_2O_3 and MgO ($r = -0.82$), and MgO and Na_2O ($r = -0.74$). These strong correlations are shown in the density contours and can be modelled with both linear and, in the case of MgO, curvilinear regression lines (e.g., Fig. 3.3). The major element oxides that derive each of the modelled curvilinear regression lines are those that show a bimodal distribution in their histograms (Fig. 3.1) suggesting that distinct subpopulations may be the cause of the curvilinear nature of these correlations.

Table 3.2: Bradbury Group Pearson correlation coefficients and associated p-value (grey numbers). Black outlined boxes are correlations that match with the Mt Sharp Group. Strong, moderate and weak correlations are shaded according to their positive (yellow, orange and light orange) or negative (cyan, blue and light blue) nature.

Bradbury Gp							
	SiO_2	TiO_2	Al_2O_3	FeO_T	MgO	CaO	Na_2O
TiO_2	-0.27						
	0.0000						
Al_2O_3	0.52	-0.16					
	0.0000	0.0000					
FeO_T	-0.85	0.33	-0.68				
	0.0000	0.0000	0.0000				
MgO	-0.41	0.00	-0.82	0.44			
	0.0000	0.9920	0.0000	0.0000			
CaO	-0.07	-0.16	0.13	-0.21	-0.16		
	0.0200	0.0000	0.0000	0.0000	0.0000		
Na_2O	0.57	-0.14	0.86	-0.66	-0.74	-0.03	
	0.0000	0.0000	0.0000	0.0000	0.0000	0.3290	
K_2O	0.13	-0.10	0.13	-0.10	-0.13	-0.23	-0.05
	0.0000	0.0010	0.0000	0.0010	0.0000	0.0000	0.0710

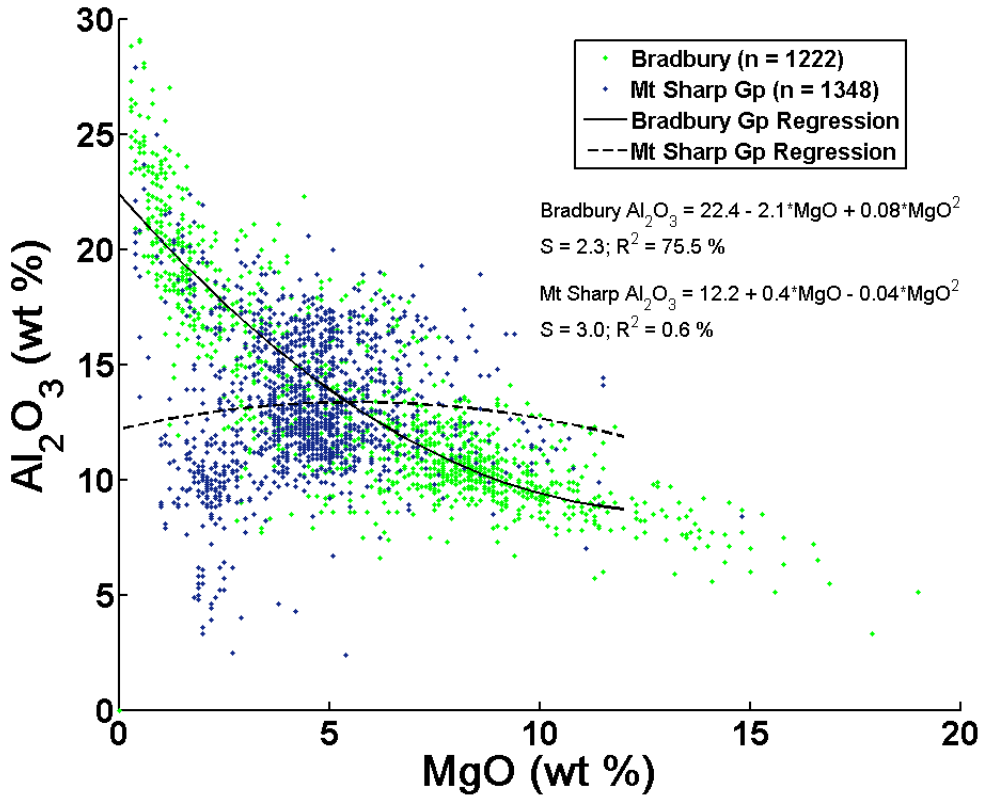

Figure 3.3: Curvilinear regression model for Bradbury (light green) and Mt Sharp (dark blue) stratigraphic groups; MgO (predictor) and Al_2O_3 (response).

For the Bradbury Group, Al_2O_3 against FeO_T (r = -0.68) and FeO_T versus Na_2O (r = -0.66) have moderately strong, statistically significant, negative correlations (Table 3.2). SiO_2 also shows a moderately strong correlation with Al_2O_3 (0.52) and Na_2O (0.57), as well as a moderate, negative correlation with MgO (-0.41). Finally, the strongest correlation within the Bradbury group is between Al_2O_3 and Na_2O which possesses an r value of 0.86. Based on these correlations, one endmember must possess high Al_2O_3, Na_2O and SiO_2, while the other has high MgO and FeO_T.

Results from the Bradbury Group Al_2O_3 Multiple Linear Regression (MLR) models show that the residuals largely fit a normal distribution (Fig. 3.4), though some outliers exist towards extreme compositions, with no correlation of residuals with order (sampling location). Hence, the MLR model is suitable to the constrained ChemCam dataset. In the MLR model (Table 3.3), all predictors (SiO_2, TiO_2, FeO_T, MgO, CaO, Na_2O, K_2O)

contribute to the statistical model ($p < 0.05$), with Na_2O (74.5 %), K_2O (4.7 %) and MgO (4.6 %) contributing the most to Al_2O_3 variation. FeO_T (0.31 %) and TiO_2 (0.04 %) contribute the least in this regression model and are therefore unlikely to substantially relate to the geochemical variation of Al_2O_3 across the Bradbury Group. All predictors have negative coefficients, and therefore correlations in relation to the response, with the exception of Na_2O and K_2O.

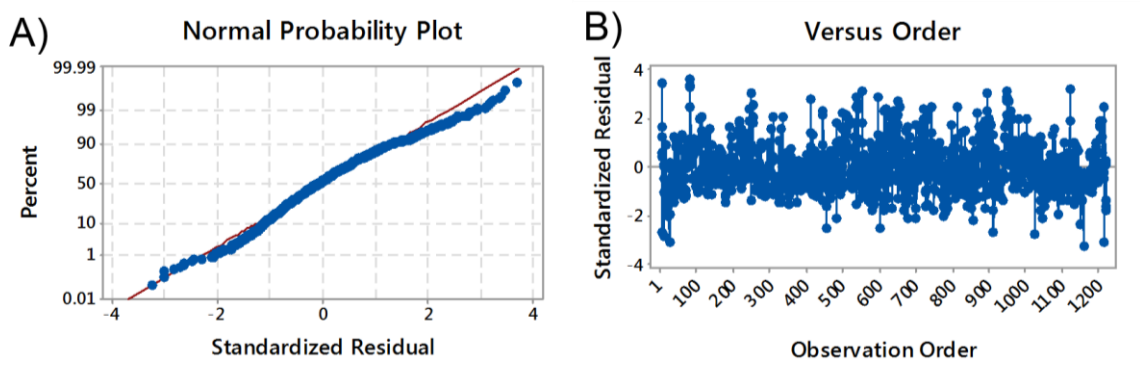

Figure 3.4: Residual Plots for Bradbury Group Multiple Linear Regression Model using Al_2O_3 as a response. A) shows the residuals against the line of normal probability. If residuals fit the model well, they should lie along this line. B) This plot tests whether there is a dependency on sample location to geochemical composition (multicollinearity). As the residuals plot with a random distribution about 0, they do not display multicollinearity.

Table 3.3: Multiple Linear Regression Model output for the Bradbury group (n = 1222) with Al_2O_3 as the response and CaO, Na_2O, K_2O, FeO_T, MgO, SiO_2, and TiO_2 as the predictor variables for a null hypothesis of H_0: $\rho = 0$.

Analysis of Variance

Source	DF	Seq SS	Contribution	Adj SS	Adj MS	F-Value	P-Value
Regression	7	22629.1	87.78%	22629.1	3232.73	1244.13	0.000
CaO	1	407.0	1.58%	42.5	42.47	16.34	0.000
Na2O	1	19211.1	74.52%	543.6	543.65	209.23	0.000
K2O	1	1218.9	4.73%	59.5	59.49	22.89	0.000
FeOT	1	79.4	0.31%	867.2	867.22	333.75	0.000
MgO	1	1185.0	4.60%	1557.6	1557.63	599.46	0.000
SiO2	1	516.3	2.00%	527.6	527.58	203.04	0.000
TiO2	1	11.4	0.04%	11.4	11.37	4.38	0.037
Error	1212	3149.2	12.22%	3149.2	2.60		
Lack-of-Fit	1195	3149.2	12.22%	3149.2	2.64	*	*
Pure Error	17	0.0	0.00%	0.0	0.00		
Total	1219	25778.3	100.00%				

Model Summary

S	R-sq	R-sq(adj)	PRESS	R-sq(pred)
1.61195	87.78%	87.71%	3199.07	87.59%

Coefficients

Term	Coef	SE Coef	95% CI	T-Value	P-Value	VIF
Constant	34.82	1.71	(31.46, 38.17)	20.36	0.000	
CaO	-0.1292	0.0320	(-0.1919, -0.0665)	-4.04	0.000	2.37
Na2O	1.0400	0.0719	(0.8990, 1.1811)	14.46	0.000	5.56
K2O	0.2193	0.0458	(0.1294, 0.3092)	4.78	0.000	1.54
FeOT	-0.3416	0.0187	(-0.3783, -0.3049)	-18.27	0.000	8.09
MgO	-0.6299	0.0257	(-0.6803, -0.5794)	-24.48	0.000	3.82
SiO2	-0.2921	0.0205	(-0.3323, -0.2518)	-14.25	0.000	5.40
TiO2	-0.301	0.144	(-0.584, -0.019)	-2.09	0.037	1.49

Regression Equation

```
Al2O3 = 34.82 - 0.1292 CaO + 1.0400 Na2O + 0.2193 K2O - 0.3416 FeOT
        - 0.6299 MgO - 0.2921 SiO2 - 0.301 TiO2
```

Figure 3.5 (next page): Scatter plot of the Yellowknife Bay formation observation points included in the constrained dataset with the Sheepbed (black), Gillespie Lake (yellow), and Glenelg (brown) Members shown alongside the Bradbury Group density contours. Light blue cross represents ChemCam accuracy (RMSEP), dark blue cross shows the precision (1σ).

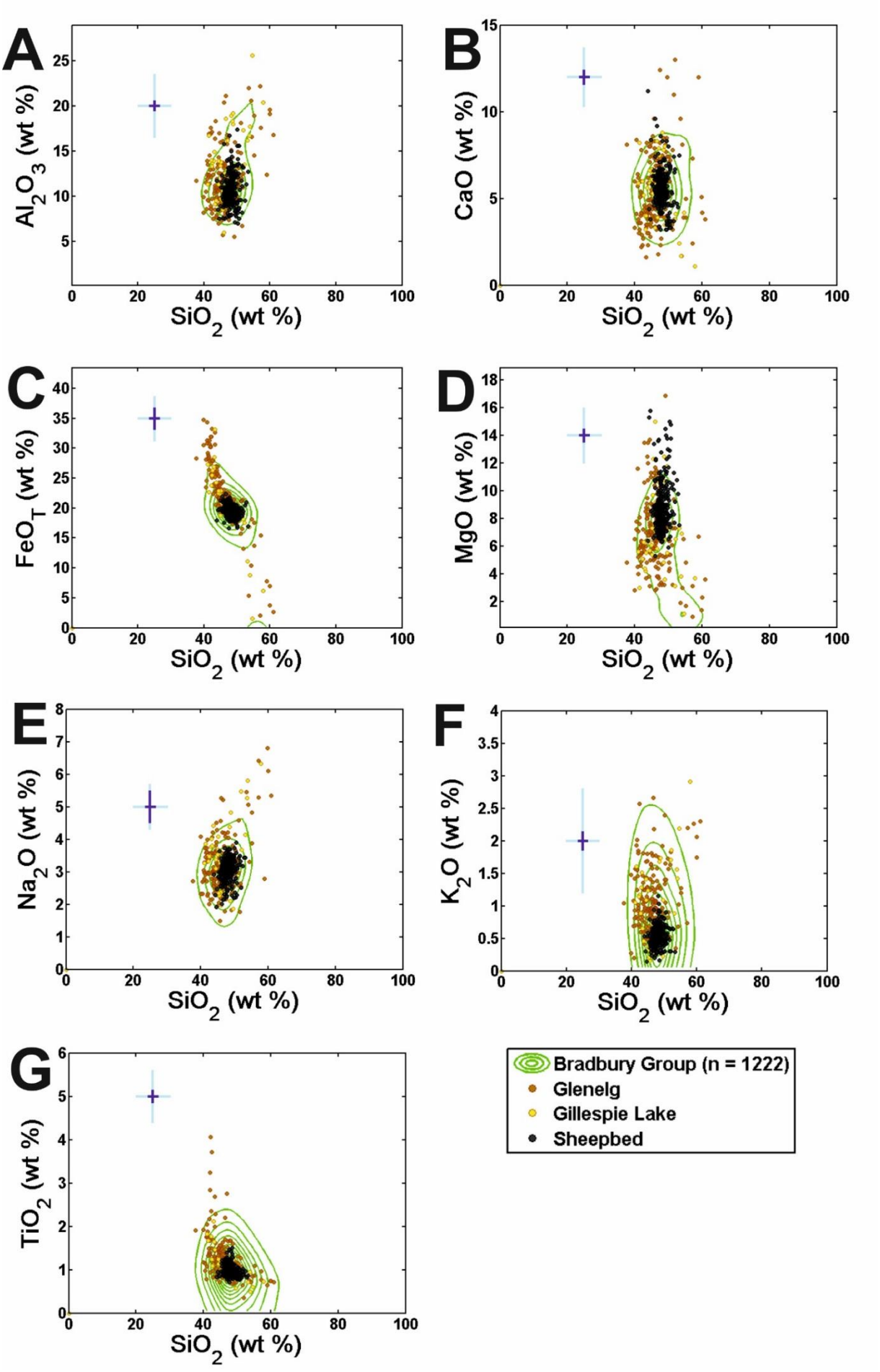
A
Al_2O_3 (wt %)
SiO_2 (wt %)
B
CaO (wt %)
SiO_2 (wt %)
C
FeO_T (wt %)
SiO_2 (wt %)
D
MgO (wt %)
SiO_2 (wt %)
E
Na_2O (wt %)
SiO_2 (wt %)
F
K_2O (wt %)
SiO_2 (wt %)
G
TiO_2 (wt %)
SiO_2 (wt %)
Bradbury Group (n = 1222)
Glenelg
Gillespie Lake
Sheepbed

3.1.1.1. The Yellowknife Bay formation

The Yellowknife Bay formation consists of three stratigraphic members; Sheepbed (oldest), Gillespie Lake, and Glenelg (youngest) (see section 1.3.3.1 for a detailed description of stratigraphy). Overall, the Sheepbed Member mudstone analyses show a uniform geochemistry, comparable to the average chemical composition of the MgO-rich, Bradbury Group subfocus (Fig. 3.5). Scatter plots show that the largest population of Sheepbed targets plot within the focus of the Bradbury Group outcrop, with just MgO showing notable scatter away from the Bradbury focal composition (Fig. 3.5 D).

Similar to the Sheepbed mudstones, the Gillespie Lake sandstone major element compositions lie within the bulk Bradbury group density contours (Fig. 3.5). However, this member is more heterogeneous, spanning a larger range in compositions compared to Sheepbed - as shown in the larger degree of scatter in the Harker plots (Fig. 3.5) – particularly for Al_2O_3, MgO, FeO_T, and Na_2O. The Glenelg Member sandstone analyses show the same major element compositions and trends as the Gillespie Lake Member, but instead with a greater proportion of scatter towards high FeO_T values.

Figure 3.6 (next page): Scatter plot of the constrained ChemCam dataset for observation points acquired at the Darwin waypoint (blue circles) shown alongside the Bradbury Group density contours. Light blue cross represents ChemCam accuracy (RMSEP), dark blue cross shows the precision (1σ).

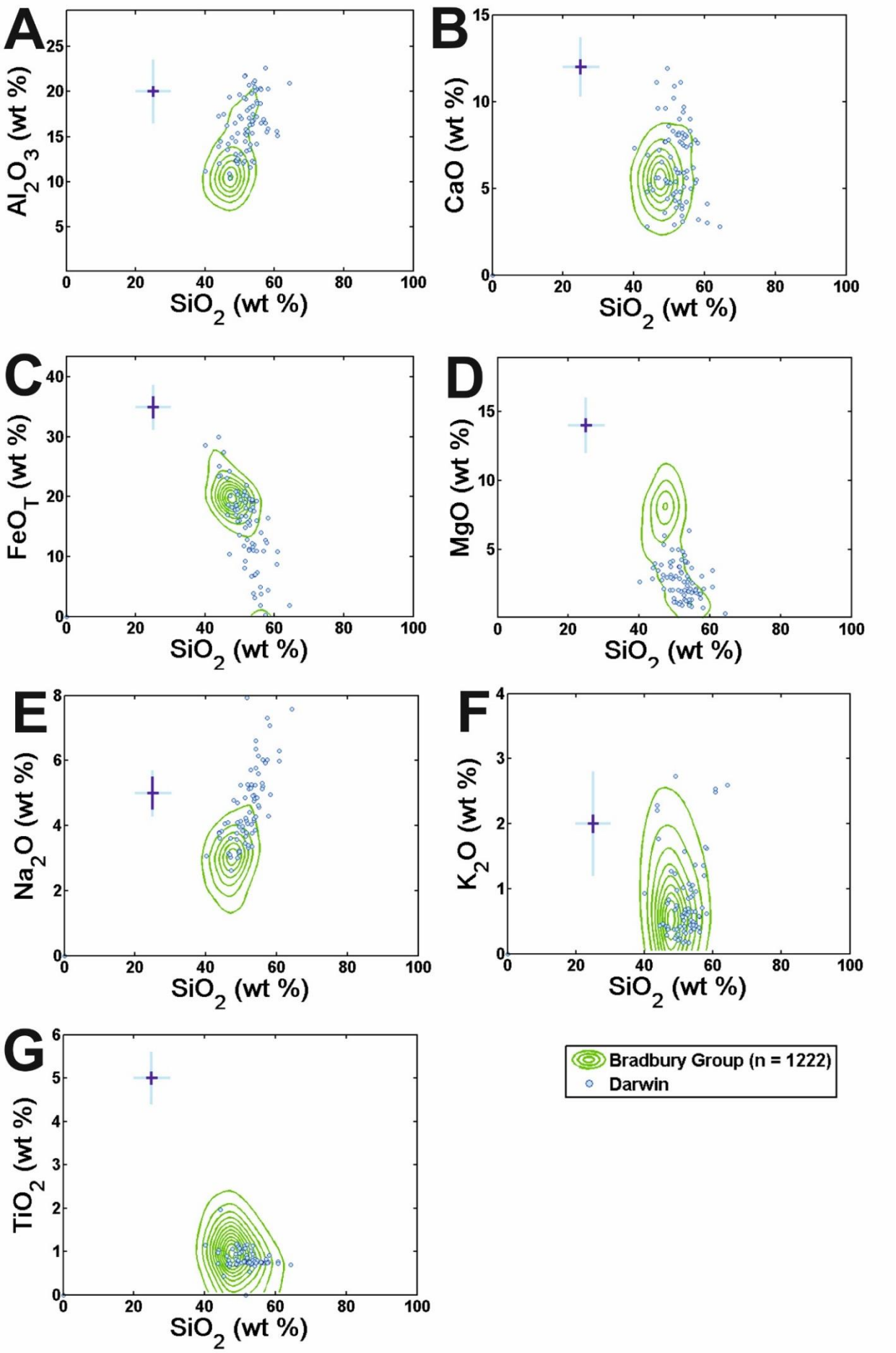
A
Al_2O_3 (wt %)
SiO_2 (wt %)
B
CaO (wt %)
SiO_2 (wt %)
C
FeO_T (wt %)
SiO_2 (wt %)
D
MgO (wt %)
SiO_2 (wt %)
E
Na_2O (wt %)
SiO_2 (wt %)
F
K_2O (wt %)
SiO_2 (wt %)
G
TiO_2 (wt %)
SiO_2 (wt %)
Bradbury Group (n = 1222)
Darwin

3.1.1.2. The Darwin outcrop

The Darwin outcrop marks the next notable waypoint in the *Curiosity* traverse, and largely consists of coarse, poorly-sorted conglomerates (Mangold et al., 2016; Grotzinger et al., 2015). Darwin analyses plot within the high Al_2O_3, low MgO subfocus of the Bradbury Group (Fig. 3.6), and demonstrate notable scatter towards low FeO_T abundances along with high SiO_2 and Na_2O concentrations. K_2O and CaO concentrations plot within the bulk Bradbury Group contours, with a comparable scatter to the Gillespie Lake and Glenelg Members (Fig. 3.5).

3.1.1.3. The Kimberley formation

ChemCam observation point analyses for the Kimberley formation span four Members (discussed in greater stratigraphic detail in section 1.3.3.3); the basal Liga Member (conglomerate), Square Top Member (sandstone), Dillinger Member (sandstone), and Mt Remarkable Member (sandstone). The coarsest member, Liga, has the greatest degree of geochemical scatter in its analyses compared to the rest of the Kimberley formation (Fig. 3.7), with a similar clustering of points around the high SiO_2 and Al_2O_3 Bradbury subfocus to the Darwin conglomerate. The Liga Member differs from the Darwin conglomerate in its overall greater concentration in the alkalis, particularly K_2O and a greater proportion of data points located in the high MgO, low SiO_2 subfocus for the Bradbury Group.

Figure 3.7 (next page): Scatter plot of constrained ChemCam observation points from the Kimberley formation Liga (dark purple), Square Top (light purple), Dillinger (beige) and Mt Remarkable (pink) Members. ChemCam observation points are shown alongside the Bradbury Group density contours. The light blue cross represents ChemCam accuracy (RMSEP) and the dark blue cross shows instrument precision (1σ).

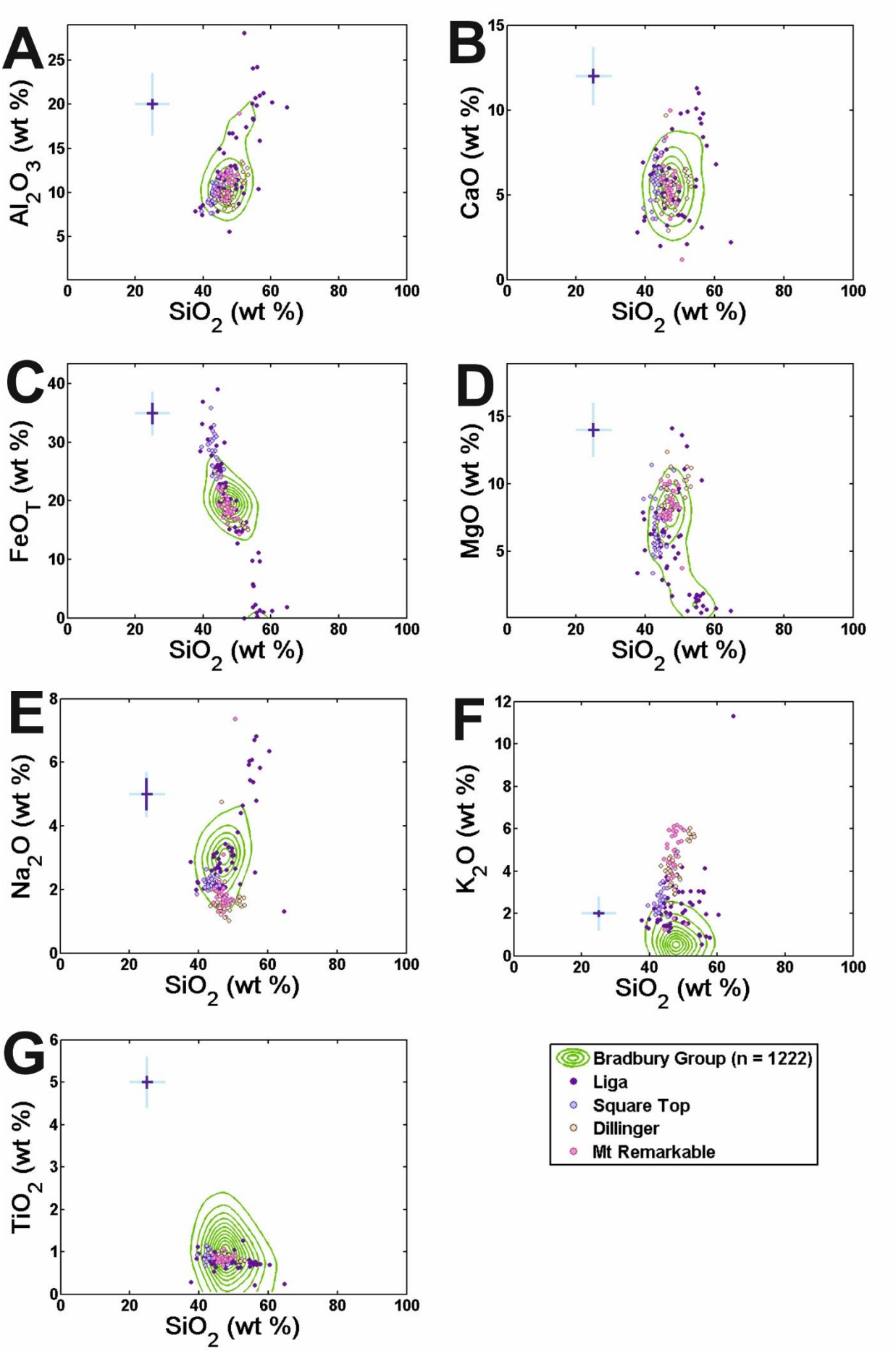
A
Al_2O_3 (wt %)
SiO_2 (wt %)
B
CaO (wt %)
SiO_2 (wt %)
C
FeO_T (wt %)
SiO_2 (wt %)
D
MgO (wt %)
SiO_2 (wt %)
E
Na_2O (wt %)
SiO_2 (wt %)
F
K_2O (wt %)
SiO_2 (wt %)
G
TiO_2 (wt %)
SiO_2 (wt %)
Bradbury Group (n = 1222)
Liga
Square Top
Dillinger
Mt Remarkable

The other sandstone members of the Kimberley formation (Fig. 3.7) all share similar geochemical trends and relationships to the sandstones of the Yellowknife Bay formation (Fig. 3.5). They mostly cluster around the Bradbury low Al_2O_3, high MgO subfocus with the rest of the sediments, but display a similar apparent negative FeO_T–SiO_2 correlation to that seen with the Yellowknife Bay sandstone units. Where the Kimberley sandstone Member compositions differ from those of the rest of the Bradbury group sediments is in regards to the alkalis, whereby they are substantially more enriched in K_2O (particularly Dillinger and Mt Remarkable) and depleted in Na_2O than the Bradbury Group focal composition.

3.1.2. The Mt Sharp Group

The Mt Sharp group discussed here consists of ChemCam analyses from sol 755 to sol 1482 (stratigraphy discussed in detail in section 1.3.4). This group demonstrates a unimodal geochemical composition for FeO_T, K_2O, Na_2O and TiO_2 when plotted against SiO_2 (Fig. 3.2), though slight bimodality is shown in the FeO_T histogram with a small peak at 5.6–6.6 wt%, and a large peak at 18.9–19.9 wt% (Fig. 3.1). Al_2O_3 and SiO_2 density contours and histograms show a slight bimodality (histogram peaks at 53.1–54.1 and 67.7–68.7 wt% SiO_2, 11.5–12.0 and 15.7–16.2 wt% Al_2O_3), as does MgO versus SiO_2 to a lesser extent (Figs. 3.1 & 3.2). The low MgO subpopulation at high SiO_2 in the Harker plot contours deviate from the respective modal compositions (Fig. 3.2 D) and correlate with the minor SiO_2 peak of ~70 wt% shown in Fig. 3.1.

Table 3.4: Mt Sharp Group Pearson correlation coefficients and associated p-value (grey numbers). Black outlined boxes are correlations that match with the Bradbury Group, strong, moderate and weak correlations are shaded according to their positive (yellow, orange and light orange) or negative (cyan, blue and light blue) nature.

Mt Sharp Gp							
	SiO_2	TiO_2	Al_2O_3	FeO_T	MgO	CaO	Na_2O
TiO_2	0.39						
	0.0000						
Al_2O_3	-0.40	-0.35					
	0.0000	0.0000					
FeO_T	-0.49	-0.20	-0.05				
	0.0000	0.0000	0.0570				
MgO	-0.44	-0.32	0.11	0.21			
	0.0000	0.0000	0.0000	0.0000			
CaO	-0.49	-0.18	0.42	-0.09	0.00		
	0.0000	0.0000	0.0000	0.0010	0.8910		
Na_2O	-0.22	-0.16	0.60	0.00	-0.12	0.31	
	0.0000	0.0000	0.0000	0.9030	0.0000	0.0000	
K_2O	0.10	-0.22	0.12	0.21	-0.02	-0.30	0.25
	0.0000	0.0000	0.0000	0.0000	0.5410	0.0000	0.0000

The Mt Sharp Group is more uniform in composition for MgO, Na_2O and K_2O compared to the Bradbury Group according to the associated standard deviations (1.8 wt%, 0.8 wt%, and 0.6 wt% respectively for the Mt Sharp Group; Table 3.1). Similar to Bradbury, contours for this dataset also largely exist as concentric circles about the modal composition (Fig. 3.2), with the notable deviations in contour shape residing in MgO and Al_2O_3 against SiO_2 which are shown to have a bimodal distribution in the histograms (Fig. 3.1). The uniformity in shape of the Mt Sharp Group density contours relative to those of the Bradbury Group are testament to their more uniform geochemical nature.

Calcium oxide contents are notably lower in the Mt Sharp Group than the Bradbury Group with mean, peak and focal compositions all <3.4 wt% (Figs. 3.1 & 3.2 and Table 3.1). Mt Sharp Group total FeO and Na_2O focal compositions are similar to those of the Bradbury Group (Fig. 3.2), but with less variability between these oxides and SiO_2,

indicated by the contours centred more uniformly on the foci. The Mt. Sharp Group has a higher mean SiO_2 content (54.4 wt% vs. 49.0 wt% for the Bradbury Group, Table 3.1), which is reflected in its density contours whose average focal compositions centre around 53.1 ± 1.9 wt% SiO_2 (Fig. 3.2 and Table 3.8). Substantial variation exists for SiO_2 according to the large standard deviation (7.0 wt%; Table 3.1) and bimodality in the SiO_2 frequency histogram at 67.7–68.7 wt% SiO_2 (Fig. 3.1), indicating a lesser subpopulation of high silica analyses. This subpopulation is not clearly identifiable in the contour plots, except for the MgO versus SiO_2 outermost contours, and does not skew the bulk composition due to it consisting of a relatively small number of representative analyses. A lesser subpopulation is also identified at low FeO_T concentrations in the frequency histogram at ~6.0 wt% (Fig. 3.1), but due to the same reasons listed for SiO_2, has also not affected calculated bulk group compositions in the density contours. Though not identified in mean compositions, the density contour plots also show that Mt Sharp Group focal compositions are more elevated in Al_2O_3 (12.1 ± 0.8 wt%) and K_2O (1.2 ± 0.2 wt%) than the Bradbury Group (foci at 10.6 ± 1.2 wt% and 0.5 ± 0.3 wt% respectively). Overall, the Mt Sharp Group has a smaller, more uniform, range in major element compositions than the Bradbury Group (Table 3.1).

According to the Pearson correlation coefficients (Table 3.3), the strongest correlation within the Mt Sharp Group is for Na_2O against Al_2O_3 (0.60). Though a moderately strong, negative correlation between FeO_T and SiO_2 (-0.49) is shared with the Bradbury Group, but is not seen in the Mt Sharp group density contours (Fig. 3.2). Instead the Mt Sharp group analyses cluster at ~ 20.0 wt% FeO_T. Strong positive correlations ($r > 0.5$) for Al_2O_3 and Na_2O also exist in both groups (Fig. 3.8), with the Bradbury Group demonstrating the best fit ($r = 0.86$; Table 3.2) and the Mt Sharp group substantially lower ($r = 0.60$; Table 3.3) due to a higher proportion of scatter that trends towards elevated Na_2O concentrations (Fig. 3.1).

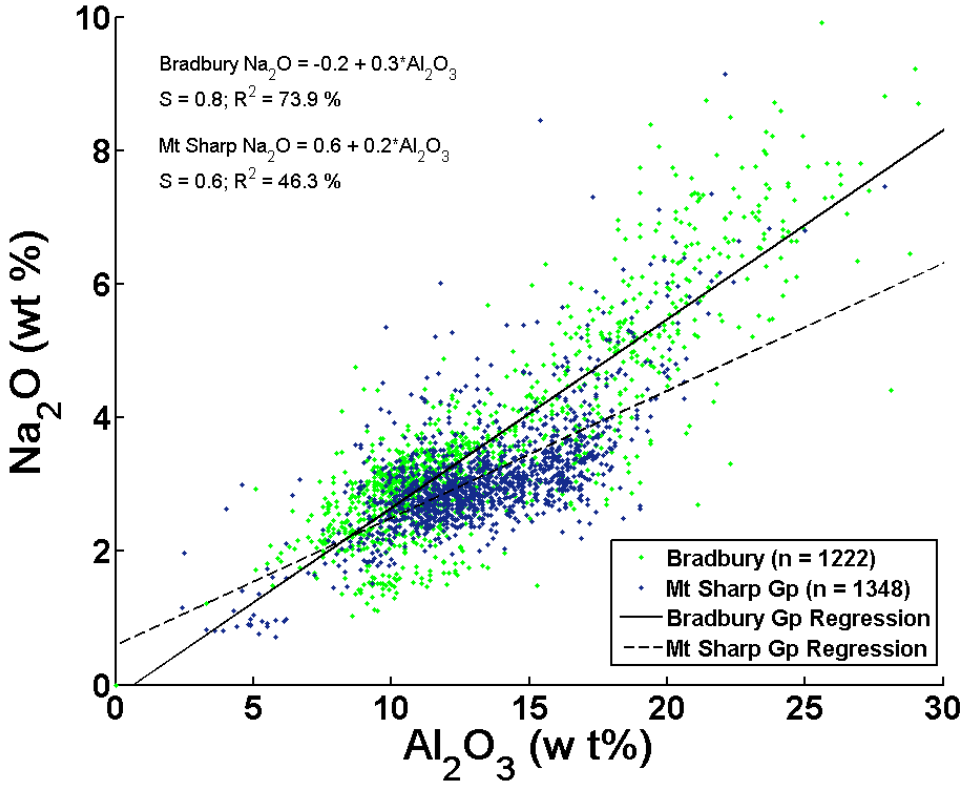

Figure 3.8: Curvilinear regression model for Bradbury (light green) and Mt Sharp (dark green) stratigraphic groups; MgO (predictor) and Al_2O_3 (response).

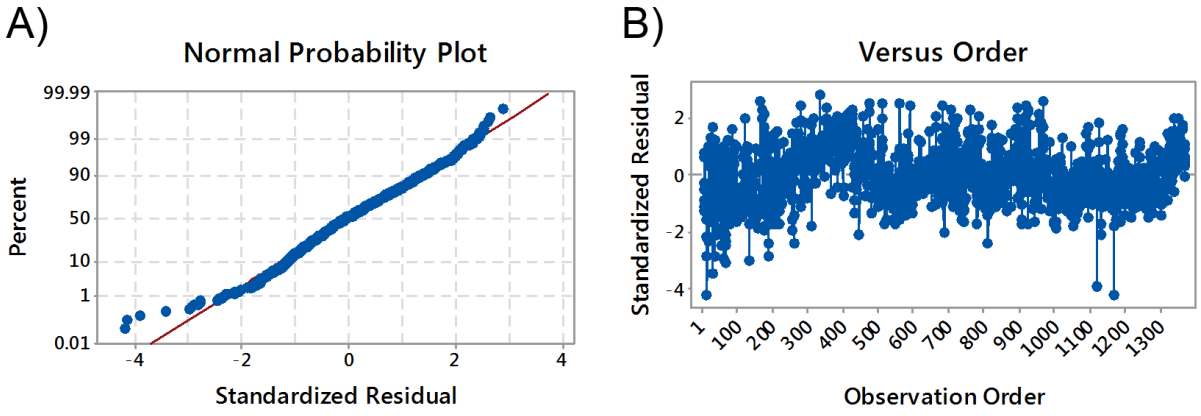

Figure 3.9: Residual Plots for Mt Sharp Group Multiple Linear Regression Model using Al_2O_3 as a response. A) shows the residuals against the line of normal probability. The Mt Sharp Group residuals are shown to fit the model well as they lie along the probability line. B) This plot tests whether there is a dependency on sample location to geochemical composition (multicollinearity). Multicollinearity can be observed for observations 300–400 that are located in the Pahrump Hills area, otherwise residual distribution is random.

All MLR predictors except K_2O (p-value = 0.60) contribute sufficiently to the model, suggesting a weak association of this element with the response, Al_2O_3 (Table 3.5). Removal of K_2O from the model does not significantly improve the fit, so I keep K_2O as a predictor. In the Mt Sharp Group, SiO_2 (22.2 %), FeO_T (20.9 %) and Na_2O (9.9 %) contribute the most to the model, with K_2O (0.01 %) and CaO (3.7 %) providing the smallest contributions. For the Mt Sharp Group, predictor coefficients show that as Al_2O_3 increases, all major elements except Na_2O decrease.

Table 3.5: Model output for the Mt Sharp Group (n = 1348) multiple linear regression model with Al_2O_3 as the response and CaO, Na_2O, K_2O, FeO_T, MgO, SiO_2, and TiO_2 as the predictors. The model is built around the null hypothesis that there is no fit between the response and predictors (H_0: $\rho = 0$).

Analysis of Variance

Source	DF	Seq SS	Contribution	Adj SS	Adj MS	F-Value	P-Value
Regression	7	8341.6	67.51%	8341.63	1191.66	397.73	0.000
SiO2	1	2738.7	22.16%	1293.52	1293.52	431.72	0.000
TiO2	1	657.7	5.32%	240.85	240.85	80.39	0.000
FeOT	1	2580.0	20.88%	1220.58	1220.58	407.38	0.000
MgO	1	685.5	5.55%	211.86	211.86	70.71	0.000
CaO	1	457.5	3.70%	196.01	196.01	65.42	0.000
Na2O	1	1221.3	9.88%	1129.81	1129.81	377.08	0.000
K2O	1	0.8	0.01%	0.82	0.82	0.27	0.601
Error	1340	4014.9	32.49%	4014.87	3.00		
Lack-of-Fit	1329	4014.9	32.49%	4014.87	3.02	*	*
Pure Error	11	0.0	0.00%	0.00	0.00		
Total	1347	12356.5	100.00%				

Model Summary

S	R-sq	R-sq(adj)
1.73094	67.51%	67.34%

Coefficients

Term	Coef	SE Coef	95% CI	T-Value	P-Value	VIF
Constant	40.43	1.58	(37.33, 43.53)	25.57	0.000	
SiO2	-0.3940	0.0190	(-0.4312, -0.3568)	-20.78	0.000	7.86
TiO2	-0.8800	0.0982	(-1.0726, -0.6875)	-8.97	0.000	2.01
FeOT	-0.3960	0.0196	(-0.4345, -0.3575)	-20.18	0.000	4.59
MgO	-0.2469	0.0294	(-0.3044, -0.1893)	-8.41	0.000	1.71
CaO	-0.2699	0.0334	(-0.3354, -0.2045)	-8.09	0.000	2.37
Na2O	1.4039	0.0723	(1.2621, 1.5458)	19.42	0.000	1.69
K2O	-0.0487	0.0933	(-0.2317, 0.1342)	-0.52	0.601	1.41

Regression Equation

```
Al2O3 = 40.43 - 0.3940 SiO2 - 0.8800 TiO2 - 0.3960 FeOT - 0.2469 MgO
- 0.2699 CaO
        + 1.4039 Na2O - 0.0487 K2O
```

3.1.2.1. The Pahrump Hills waypoint

The Pahrump Hills locality was analysed with ChemCam between sols 792–990, and contains the lowermost stratigraphic waypoint of the Murray formation. Overall, Pahrump Hills observation point compositions lie within the high Al_2O_3 Mt Sharp Group subfocus and have bulk Murray compositions for the rest of the major element oxides (Fig. 3.10). Some scatter is present towards high CaO, FeO_T, and Na_2O compositions and low K_2O with some Pahrump Hills observation points demonstrating the apparent negative FeO_T, SiO_2 correlation trend seen in the Bradbury Group sandstone and coarse grained units (Figs. 3.5, 3.6 & 3.7). The scatter in this unit relates to the basal conglomerate within the Murray formation which constitutes the Bald Mountain, Bald Mountain 3, and Mount Powell ChemCam targets. These conglomerate beds within the Mt Sharp Group also correlate to high Al_2O_3 and K_2O concentrations relative to the bulk Mt Sharp Group contour compositions.

3.1.2.2. The Marias Pass waypoint

The Marias Pass locality was analysed by ChemCam from sols 992–1072 and consists of largely pavement-style, light-toned mudstone with fine laminations (for more information see section 1.3.4.2). The Marias Pass ChemCam geochemistry shows that many targets here have high abundances of SiO_2 compared to the bulk Mt Sharp Group focal composition, along with lower concentrations of all other major elements except K_2O and TiO_2. K_2O shows no change from the bulk Mt Sharp group average, whereas TiO_2 is overall higher in concentration (Fig. 3.10).

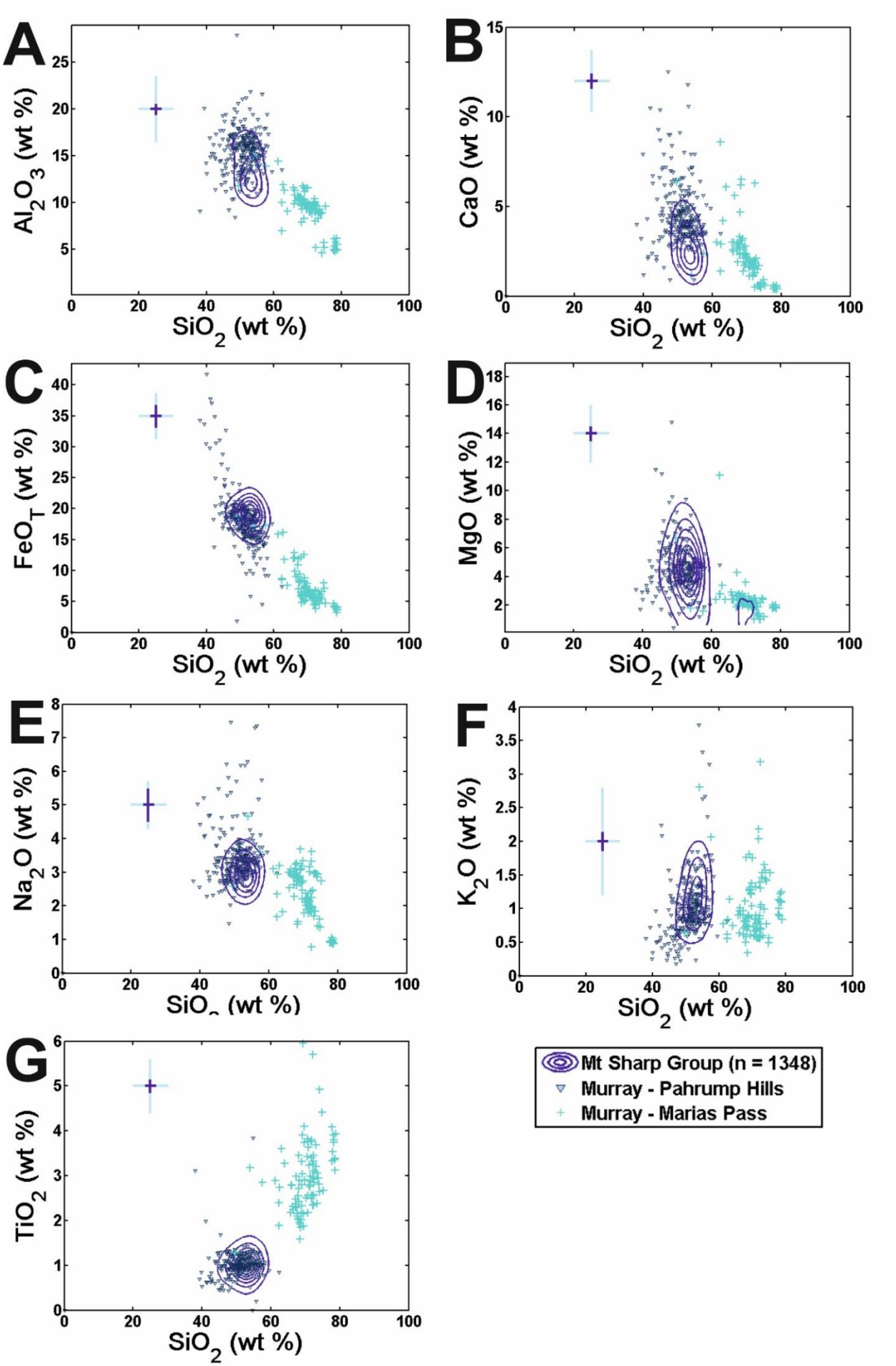
A
Al_2O_3 (wt %)
SiO_2 (wt %)
B
CaO (wt %)
SiO_2 (wt %)
C
FeO_T (wt %)
SiO_2 (wt %)
D
MgO (wt %)
SiO_2 (wt %)
E
Na_2O (wt %)
SiO_2 (wt %)
F
K_2O (wt %)
SiO_2 (wt %)
G
TiO_2 (wt %)
SiO_2 (wt %)
Mt Sharp Group (n = 1348)
Murray - Pahrump Hills
Murray - Marias Pass

Figure 3.10 (previous page): Scatter plot of constrained ChemCam observation points from the Murray formation Pahrump Hills (light blue triangles) and Marias Pass (blue crosses) waypoints. ChemCam observation points are shown alongside the Mt Sharp Group density contours. The light blue cross shows ChemCam instrument accuracy (RMSEP) and the dark blue cross represents ChemCam instrument precision (1σ).

3.1.2.3. East and West Naukluft localities

The East Naukluft plateau locality is defined from the Bridger Basin area (sol 1153) to the Naukluft Plateau (sol 1293) and encompasses bedrock analysed around the Bagnold dunes. The West Naukluft Plateau region is the section of *Curiosity*'s traverse after the rover left the Naukluft Plateau (sol 1373), and before it entered the Murray Buttes waypoint (sol 1412). Few analyses of Murray bedrock were acquired on the Naukluft Plateau itself as this plateau largely consists of the capping aeolian Stimson formation (Banham et al., 2018) that will be discussed in Chapter 4.

Analyses from the East and West Naukluft regions have very uniform geochemical compositions that are situated within the Mt Sharp Group density contour focus (Fig. 3.11). Observation point compositions from the East Naukluft Plateau region largely plot within the low Al_2O_3 focal composition with minimal scatter, while the East Naukluft region shows some scatter towards higher Al_2O_3 compositions though these still plot within the outermost contour. Some scatter is observed for CaO, particularly in the East Naukluft region (Fig. 3.11 B) as well as towards high FeO_T, low SiO_2 compositions, similar to that observed in the Pahrump Hills locality (Fig. 3.10). Targets demonstrating these scattered compositions are not obviously correlated with any identifiable alteration feature in the RMI images.

3.1.2.4. The Murray Buttes Waypoint

The Murray Buttes area was analysed by *Curiosity* between sols 1412 and 1482 of the mission, and possesses uniform compositions for Al_2O_3, SiO_2, FeO_T, and TiO_2 that are all situated within the Mt Sharp group contours (Fig. 3.11). Very few points demonstrate scatter away from the bulk Mt Sharp group composition towards higher CaO, K_2O and Na_2O concentrations, though a notable number of observation points show scatter towards higher MgO, low SiO_2 concentrations (Fig. 3.11 D).

3.1.3. Alteration feature major element variation and correlations

Figures 3.12 and 3.13 highlight the major element trends associated with alteration features identified within each stratigraphic group, and isolated from the constrained bulk rock dataset (see Fig. 1.17 and section 2.2). The stratigraphic group density contours modelled in this thesis are shown with CheMin derived amorphous and phyllosilicate (AP) components and common primary, detrital, silicate minerals (olivine, plagioclase, alkali feldspar and augite) from Morrison et al. (2018) to help distinguish alteration trends from detrital igneous mineral mixing trends. Alteration features (Fig. 1.17) have been identified within each stratigraphic group, and are presented as scatter points over the stratigraphic group density contours (Figs. 3.12–3.13).

Figure 3.11 (next page): Scatter plot of constrained ChemCam observation points from the Murray formation West of Naukluft (dark purple triangles) and East of Naukluft (light purple traingles) and Murray Buttes waypoint (dark blue triangles). ChemCam observation points are shown alongside the Mt Sharp Group density contours. Light blue cross is the ChemCam accuracy, dark blue cross is ChemCam instrument precision.

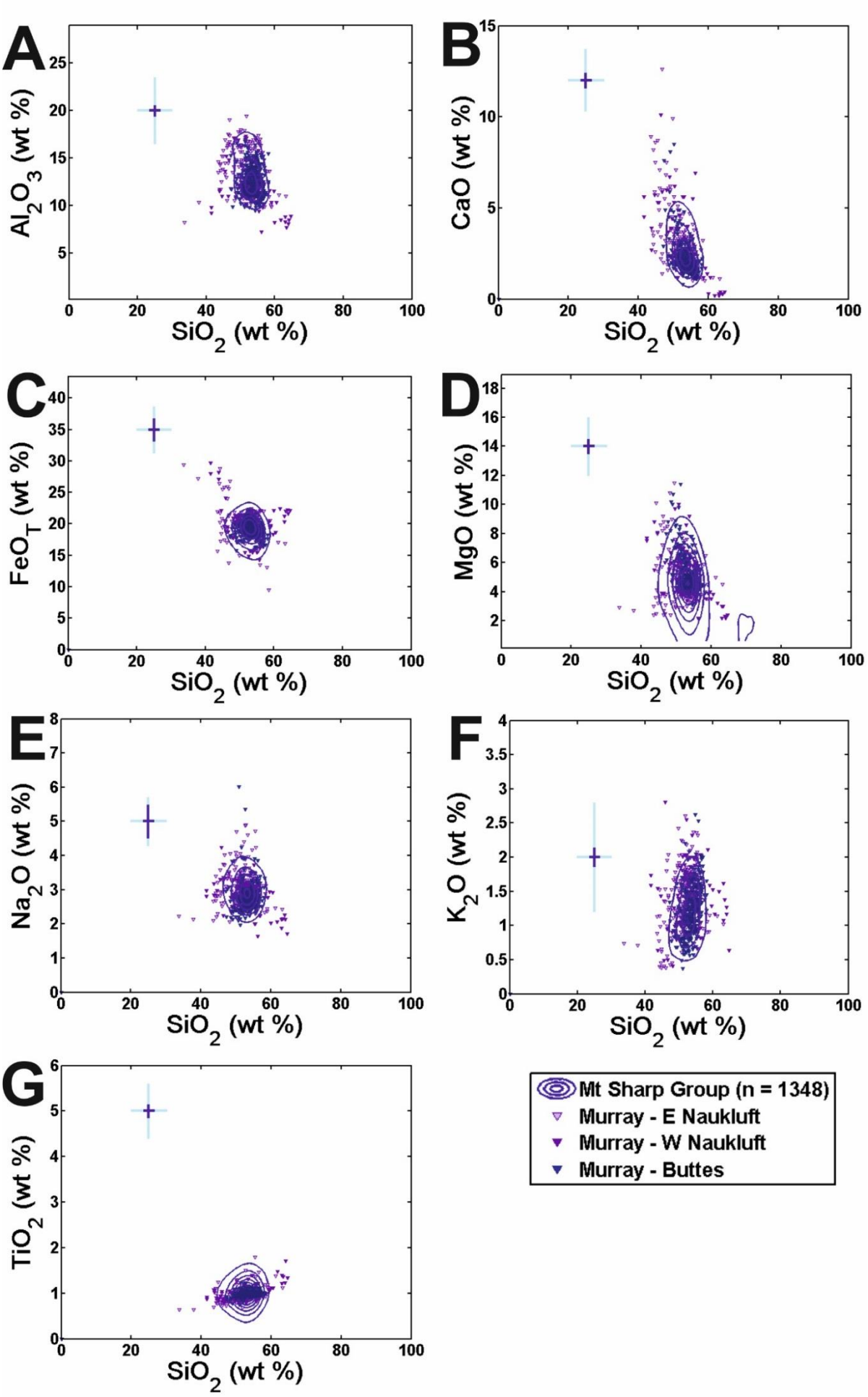
A
Al_2O_3 (wt %)
SiO_2 (wt %)
B
CaO (wt %)
SiO_2 (wt %)
C
FeO_T (wt %)
SiO_2 (wt %)
D
MgO (wt %)
SiO_2 (wt %)
E
Na_2O (wt %)
SiO_2 (wt %)
F
K_2O (wt %)
SiO_2 (wt %)
G
TiO_2 (wt %)
SiO_2 (wt %)
Mt Sharp Group (n = 1348)
Murray - E Naukluft
Murray - W Naukluft
Murray - Buttes

3.1.3.1. Sulfate mineral veins and fracture-associated alteration halos

Sulfate mineral veins (Fig. 1.17 C, pp. 47) exhibit high calcium enrichment (Fig. 3.12 and 3.13), low abundances of other oxides, and low totals. Meanwhile, diagenetic halos, ~50 cm in width (Yen et al. 2017), are associated with an increase in silica content of the host rock (Frydenvang et al. 2017; Yen et al. 2017) and share similar elemental compositions to the high silica targets analysed at the Buckskin drill hole on sol 1057 (Fig. 3.10; Morris et al. 2016). The halos mostly occurred in the Mount Sharp Group, particularly between Marias Pass and Bridger Basin (Frydenvang et al. 2017; Yen et al. 2017). However, one possible halo was observed in the Bradbury Group, with the target Kukri at Darwin, on sol 392 (Williams et al. 2014).

Within fracture-associated alteration halos (Fig. 1.17 D, pp. 47) FeO_T and Na_2O possess the best-defined negative correlations against SiO_2, giving strong Pearson's correlation coefficients of -0.90 and -0.82 respectively (Table A.3.2. in the Appendix). The single element to show a (weak) positive correlation with halo SiO_2 enrichment is TiO_2 ($r = 0.29$, t-test p-value $<\alpha$). Al_2O_3 and Na_2O show the strongest positive correlation ($r = 0.92$), and display the best-defined negative trends when plotted against SiO_2, along with FeO_T (Figs. 3.11, 3.12). MgO concentrations appear to be relatively uniform at ~3.0 wt%, except at SiO_2 >80 wt% where concentrations remain at ~1.0 wt%.

Figure 3.12 (next page): Harker density contour plots of Bradbury Group bulk composition (light green density contours) and alteration trends, with SiO_2 on the x-axis and major element oxide on the y-axis. Each scatter point for the alteration features represents a ChemCam observation point composition for mineral vein, fracture-associated halo, nodule and raised ridge (RR) targets. The light blue cross shows ChemCam accuracy (RMSEP), the dark blue cross shows precision (standard deviation). Calculated CheMin amorphous and phyllosilicate compositions (Vaniman et al., 2014; Treiman et al., 2016) are plotted as squares with modelled Gale crater primary igneous minerals (olivine, augite, plagioclase and sanidine) shown as stars. $CaSO_4$ = calcium-sulfate, Silica = silica-enrichment.

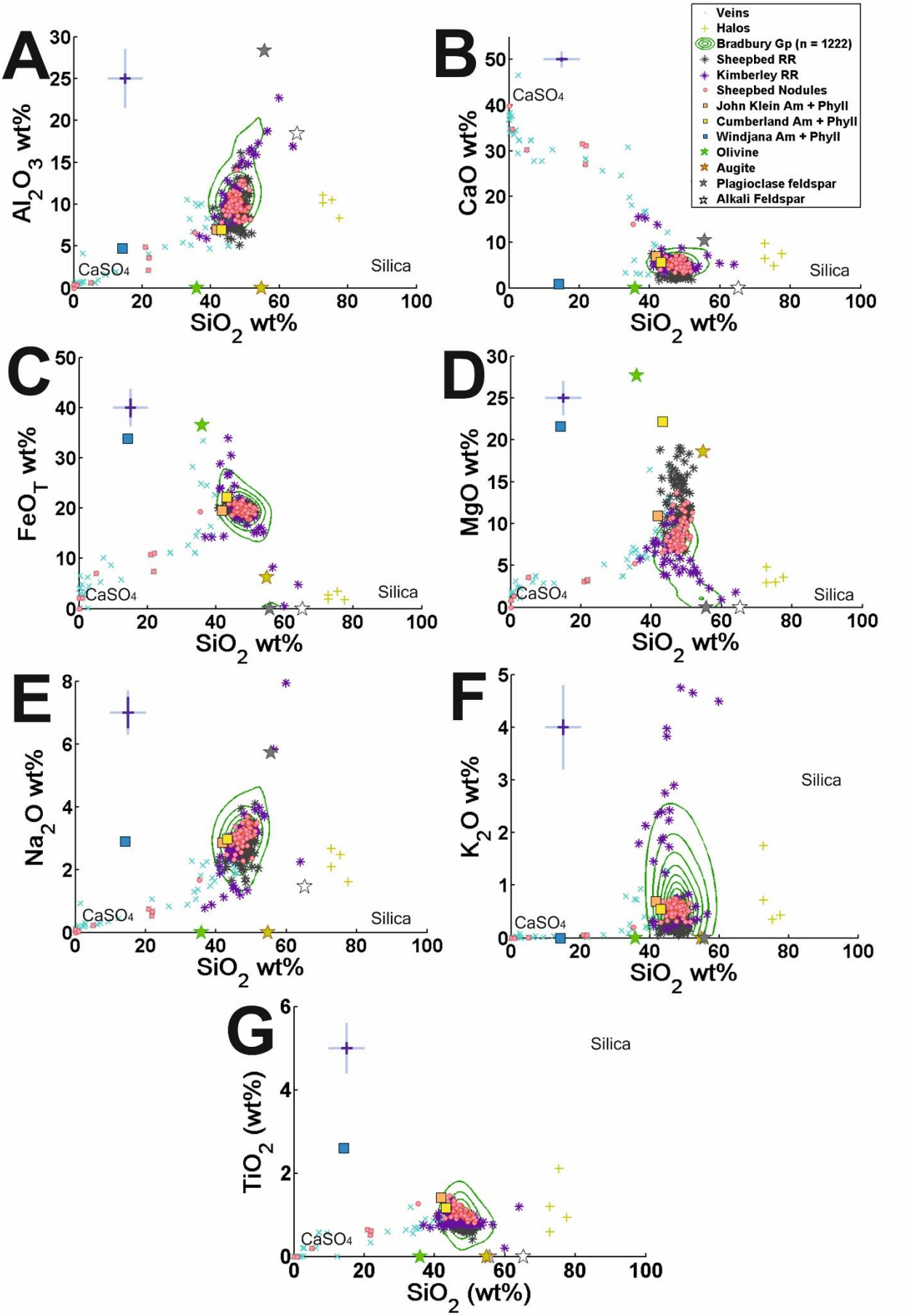
A
B
C
D
E
F
G
Veins
Halos
Bradbury Gp (n = 1222)
Sheepbed RR
Kimberley RR
Sheepbed Nodules
John Klein Am + Phyll
Cumberland Am + Phyll
Windjana Am + Phyll
Olivine
Augite
Plagioclase feldspar
Alkali Feldspar
Al2O3 wt%
CaO wt%
FeOT wt%
MgO wt%
Na2O wt%
K2O wt%
TiO2 (wt%)
SiO2 wt%
SiO2 (wt%)
CaSO4
Silica

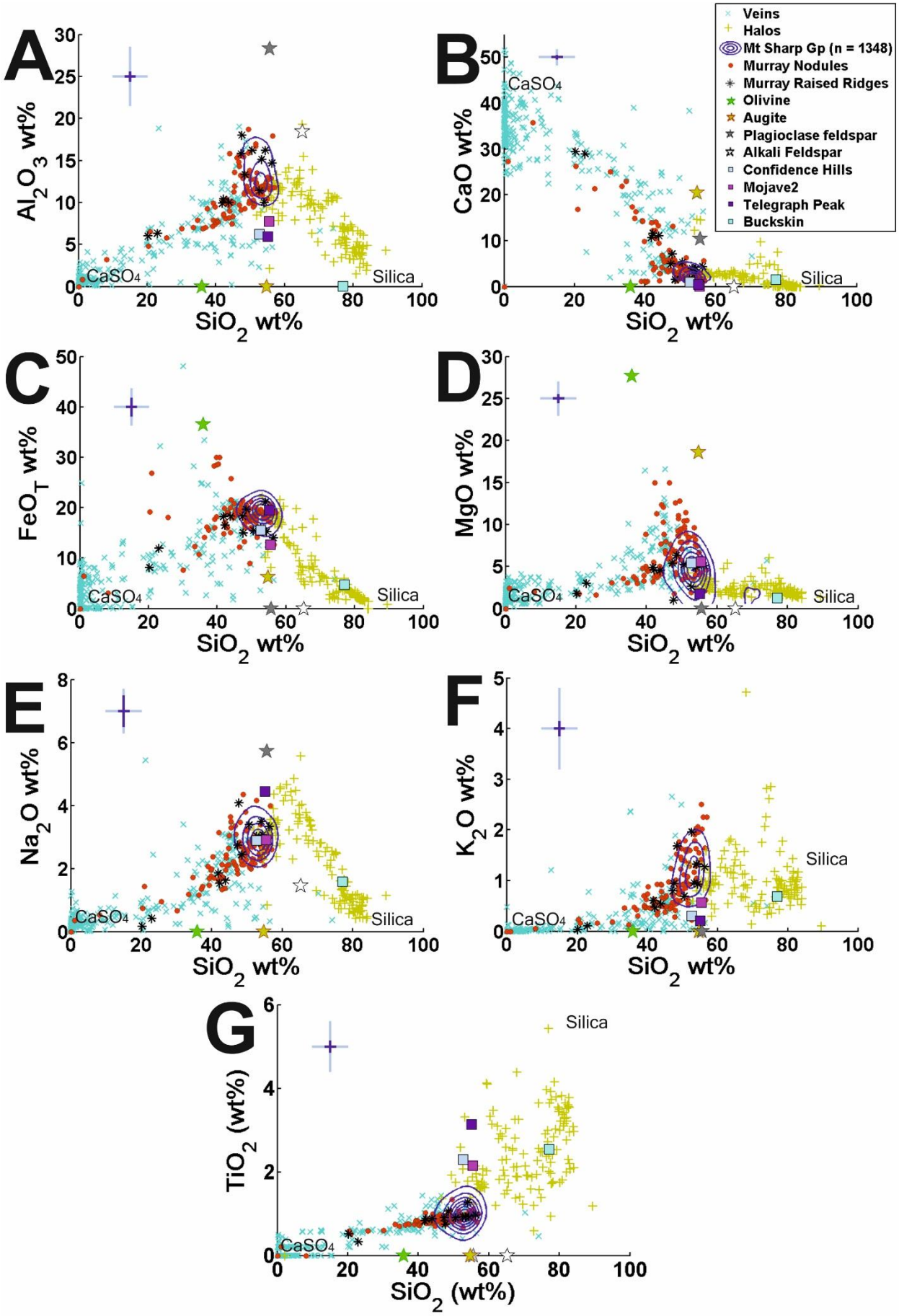
A
B
C
D
E
F
G
Veins
Halos
Mt Sharp Gp (n = 1348)
Murray Nodules
Murray Raised Ridges
Olivine
Augite
Plagioclase feldspar
Alkali Feldspar
Confidence Hills
Mojave2
Telegraph Peak
Buckskin
Al2O3 wt%
CaO wt%
FeOT wt%
MgO wt%
Na2O wt%
K2O wt%
TiO2 (wt%)
SiO2 wt%
SiO2 (wt%)
CaSO4
Silica

Figure 3.13 (previous page): Harker density contour plots of Mt Sharp Group bulk composition (dark green density contours) and alteration trends, with SiO_2 on the x-axis and major element oxide on the y-axis. Each scatter point for the alteration features represents a ChemCam observation point composition for mineral vein, fracture-associated halo, nodule and raised ridge (RR) targets. The light blue cross shows ChemCam accuracy (RMSEP), the dark blue cross shows precision (standard deviation). Calculated CheMin amorphous and phyllosilicate compositions (Rampe et al., 2017) are plotted as squares, modelled Gale crater primary igneous minerals (olivine, augite, plagioclase and sanidine) are shown as stars. $CaSO_4$ = calcium-sulfate, Silica = silica-enrichment.

Stratigraphic group density contours in the constrained bulk dataset do not appear to have been influenced by the silica-rich halos (Fig. 3.11, 3.12). However, despite measures taken to remove the effects of diagenetic silica enrichment in the Marias Pass area, scatter plots of the Marias Pass observation point compositions follow a silica-rich alteration trend (e.g., Fig. 3.10). The Marias Pass observation points were not removed from the bulk dataset as they constitute a small proportion of data points and hence, have not affected the overall stratigraphic group density contour focal compositions.

3.1.3.2. Raised Ridges

Erosion resistant raised ridge features (Fig. 1.17 A, pp. 47) occur across both stratigraphic groups (Fig. 3.12 and 3.13). Bradbury raised ridges (BRR), are present in both the Sheepbed Member and Kimberley formation and show variable Al_2O_3 5.1–22.7 wt% relative to the Bradbury density contour focus at 10.6 ± 1.2 wt%. MgO concentrations can extend up to 20 wt% with BRR features demonstrating a slight depletion in Na_2O, and some scatter towards elevated K_2O concentrations. When the BRR are subdivided into Sheepbed raised ridges and the two raised ridges analysed by ChemCam at the Kimberley formation (targets Roebuck sol 584 and Loadstone sol 625), it is evident that the Sheepbed BRR are more enriched in MgO and depleted in CaO and K_2O compared to the Bradbury host rock (Fig. 3.12). The results for the Sheepbed raised ridges are consistent with the

results of Leveille et al. (2014) who reported similar element enrichments and depletions for raised ridges at this locality. On the other hand, the Kimberley BRR are generally more enriched in K_2O, and depleted in MgO, with substantial scatter for Al_2O_3, CaO, Na_2O and FeO_T relative to bulk rock.

Fewer raised ridges were identified within the Mt Sharp Group (MRR), usually at vein or fracture margins, and either possess similar geochemical compositions to the bulk Mt Sharp Group composition, or they follow the same CaO enrichment trend as the calcium-sulfate mineral veins (Fig. 3.13). The MRR spatial and geochemical association with mineral vein features suggests that these may relate to a similar process, indicating that these are not formed via the same mechanism as those in the Bradbury Group. Due to element enrichments associated with raised ridges plotting away from the host rock density contours, they do not appear to have influenced host rock compositions.

3.1.3.3. Nodules

Bradbury Group nodules were predominately identified in the Sheepbed Member mudstone within "nodule-rich" bedrock (Stack et al., 2014b). Sheepbed nodules are spheroidal, at the mm-scale, and can be divided into three groups (solid, hollow, or filled) depending on their internal structure (Stack et al. 2014b). Solid nodules do not show obvious internal structures, are similar in texture and colour to the host rock and contribute the majority of ChemCam nodule analyses. Hollow nodules possess raised rims and internal depressions. Finally, filled nodules classify those that contain light-toned, sulfate minerals (Stack et al. 2014b). ChemCam targets from the Sheepbed nodule-rich bedrock show minimal deviation from bulk rock composition (Fig. 3.12).

Similar to Bradbury Group nodules, the nodule features identified in the Mt Sharp Group are also mm-scale and of a similar colour to the surrounding bedrock (e.g., Fig. 1.17

B), though these are less frequent and have more irregular shapes (Nachon et al. 2017). Unlike the Sheepbed nodules, Mt Sharp Group nodules do not show any obvious internal structure. Nodules of the Mt Sharp Group have similar geochemical trends to the calcium-sulfate mineral veins with a major element depletion in SiO_2 and the alkalis, plus most points showing Al_2O_3 and FeO_T depletion with CaO enrichment (Fig. 3.13).

3.1.4. Constrained bulk rock dataset summary

In summary, notable geochemical differences exist between the Bradbury and Mt Sharp Groups, as do certain geochemical similarities. Overall Mt Sharp has a higher modelled bulk abundance of SiO_2 (53.1 ± 1.9 wt%) and K_2O (1.2 ± 0.2 wt%) compared to the Bradbury Group (47.4 ± 1.4 wt% SiO_2, 0.5 ± 0.3 wt% K_2O) which in turn, Bradbury has greater concentrations of CaO (5.5 ± 1.6 wt%) and MgO (8.1 ± 0.9 wt%). The Mt Sharp Group also has a more uniform composition than the Bradbury Group (Fig. 3.2) except for the high SiO_2 Marias Pass locality which is geochemically distinct to the rest of the Mt Sharp Group (Fig. 3.10). The dominant negative correlation trend for both stratigraphic groups is FeO_T and SiO_2, with MgO against Al_2O_3, and MgO versus Na_2O. The sole significant positive correlation trends for both groups is Na_2O versus Al_2O_3.

Finally, alteration features in Gale crater do not appear to have influenced the bulk density contour compositions of the constrained ChemCam stratigraphic group datasets. Ca-sulfate veins and diagenetic halos show strong deviations away from bulk focal compositions with high CaO and all other major element oxides at low concentrations for the veins, and high SiO_2 and low concentrations of all other major element oxides for the halos. Nodules and raised ridges show less deviation away from bulk compositions, particularly for the Bradbury Group, where nodules and raised ridges in the Yellowknife Bay formation generally show high MgO abundances, and raised ridges in the Kimberley

formation have high K_2O concentrations. Meanwhile, Mt Sharp Group nodules and raised ridges largely following the Ca-sulfate trend.

3.2. Discussion

3.2.1. Chemical alteration of Gale crater sediments

Chemical weathering on Mars has been relatively low compared to Earth for most of the planet's history as evidenced by the high abundance of ancient unweathered basaltic material on the Martian surface (McSween et al., 2009; Hausrath et al., 2008; Hoefen et al., 2003), and the paucity of chemical weathering products in Amazonian-aged terrains (e.g., Ehlmann et al., 2013). Instead, mechanical and physical weathering processes have dominated sediment generation (McLennan et al., 2014; Christensen et al., 2001; Bandfield et al., 2000). The majority of the constrained ChemCam bulk rock major element correlations presented here point towards the importance of detrital primary minerals in Gale crater's sedimentary record. The dominant negative correlation trend for both stratigraphic groups in the constrained bulk rock dataset is FeO_T against SiO_2. The Bradbury Group also has notably strong negative correlations between MgO against Al_2O_3, and MgO against Na_2O. The sole significant positive correlation for both stratigraphic groups is Na_2O versus Al_2O_3. These correlations extend throughout the stratigraphic succession. They are expressed through the elongation of density contours in the direction of CheMin-derived olivine, augite, and feldspar compositions (Figs. 3.12 and 3.13) and are therefore likely related to mafic versus felsic mineral abundances. The strong positive association of Al_2O_3 in the MLR models with Na_2O (and K_2O for the Bradbury Group), and negative association with FeO_T and MgO also indicates that felsic/mafic mineral proportions are the controlling factors on bulk stratigraphic unit geochemistry.

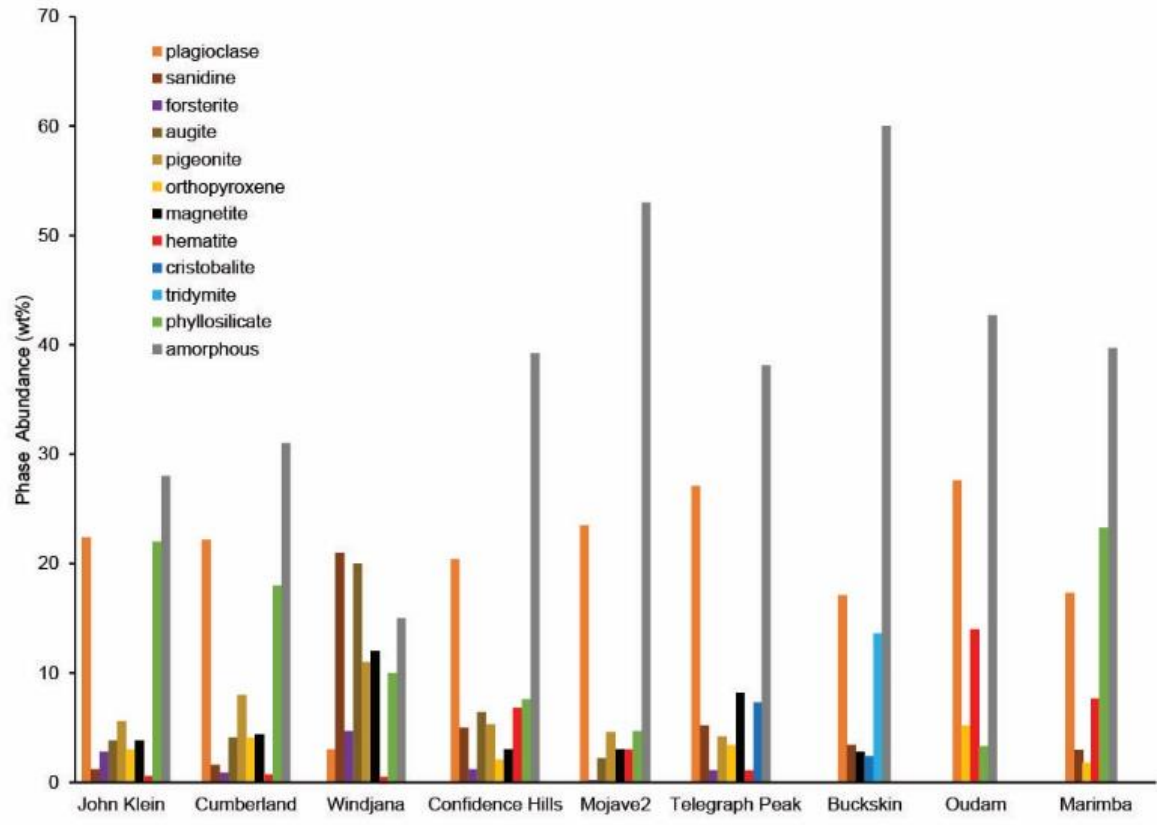

Figure 3.14: Crystalline abundance of minerals in wt % (Morrison et al., 2018; Morris et al., 2016; Treiman et al., 2016; Vaniman et al., 2014) and amorphous abundance (Morrison et al., 2018; Rampe et al., 2017) [y-axis] for each drill hole taken in the Bradbury (John Klein, Cumberland and Windjana) and Mt Sharp (Confidence Hills, Mojave2, Telegraph Peak, Buckskin, Oudam and Marimba) stratigraphic groups.

The minerals that appear to dominate geochemical variation within Gale crater's sedimentary units constitute on average ~40–70% in all CheMin analyses and are of primary igneous origin (for CheMin mineral compositions, see Appendix A.3.1.). The other ~30–60 % in CheMin analyses relate to the amorphous and phyllosilicate component (Fig. 3.14 and discussed in section 3.2.1.2; for compositions see Table A.3.1. of the Appendix). Secondary minerals suggest that chemical weathering is recorded to some extent in the ChemCam target analyses included in our constrained bulk rock dataset. The abundance of alteration features in Gale crater's stratigraphy is also evidence of aqueous alteration, likely the result of diagenetic episodes. Distinguishing alteration trends relating

to these diagenetic episodes and chemical weathering from source rock characteristics is essential before any conclusions on source region chemistry can be made.

3.2.1.1. Element mobility and feature-related alteration

In this section, I have used major element trends of observed diagenetic features to determine the extent of alteration that has occurred in the constrained bulk rock dataset presented in this thesis (Figs. 3.12, 3.13). As described previously (section 3.1.3.), the late-stage diagenetic features (mineral veins and silica-rich halos) which cross-cut stratigraphic units show clear geochemical trends away from all stratigraphic group compositions (Fig. 3.12, 3.13).

For the silica-rich halos, ChemCam analyses plot away from constrained contour compositions suggesting that element mobilisation was restricted to the associated fracture zones (Frydenvang et al. 2017; Yen et al. 2017). The one exception is the Marias Pass area of the Murray formation presented in section 1.3.2.4. and 3.1.2.2. whose compositions follow a similar trend to the silica-rich halos (Fig. 3.10). This could be related to the SiO_2 polymorph grains that are abundant in the Buckskin drill hole (Morris et al. 2016), and which would plot at a similar position on the Harker diagrams to the fracture-associated halo alteration trends (Fig. 3.13). Alternatively, the Marias Pass Lion outcrop (sols 1053–1066) where the Buckskin drill hole was conducted and ChemCam observation points acquired, does possess the near white, light-toned, visual characteristic of the alteration halos. These outcrops are also located near light-toned, fracture-associated halos in the overlying Stimson formation (Frydenvang et al. 2017). Therefore, it is difficult to distinguish whether the Marias Pass target igneous mineralogy and source composition have been overprinted by secondary alteration processes of the fracture-associated halo alteration. As Marias Pass analyses represent a small set of outlying Mt Sharp Group

compositions that plot far from the main Mt Sharp Group contours (Fig. 3.10), this silica-rich endmember and halo diagenesis has not influenced the density contour compositions of the constrained bulk Mt Sharp Group dataset. Hence, I have not recalculated the Mt Sharp Group contours, but have excluded Marias Pass data in the Chemical Index of Alteration analysis of section 3.2.1.3.

Scatter trends associated with the light-toned mineral vein features demonstrate a clear trend away from host rock compositions towards CaO enrichment (Figs. 3.12, 3.13) which supports the interpretation that these are predominately calcium-sulfate mineral veins (L'Haridon et al., 2018a; Rapin et al., 2016; Nachon et al., 2014). They are thought to be dominated by bassanite in ChemCam surface analyses (Rapin et al. 2016) but some appear more hydrated below the surface as exposed by the drill (L'Haridon et al. 2018a; Vaniman et al. 2018). The total sum of oxides also becomes lower as a result of not directly analysing sulfur in the Ca-sulfate veins (Rapin et al. 2016). Overall, the Bradbury Group and Mt Sharp Group density contours do not appear to have been influenced by this set of alteration features (Figs. 3.12, 3.13) indicating that the geochemical influence relating to these diagenetic features was successfully removed from the constrained bulk rock dataset.

Many nodule compositions reflect bulk rock composition, particularly those of the Bradbury Group (Fig. 3.12, Stack et al. 2014b), which could either indicate that these observation point analyses have proportionally sampled more host rock, or that these features have formed by closed system alteration preserving geochemical source characteristics. The nodules that show geochemical variation away from bulk composition, such as those at the base of the Mt Sharp Group, appear to relate to sulfate precipitation (Fig. 3.12 and Nachon et al. 2017). They follow similar major element trends to the mineral veins, but this time with magnesium- as well as calcium-sulfates dominating the

geochemical composition (Figs. 3.12 and 3.13; Nachon et al. 2017). In the Mt Sharp Group, a few nodule analyses show high FeO_T compositions >25.0 wt% (Fig. 3.13.C). I interpret these FeO_T-rich nodule analyses as potentially showing iron-oxides, as they are low in concentration for the other major elements with respect to bulk Mt Sharp. This is in contrast to the high-FeO_T composition of the ChemCam target Hayden Peak (sol 785) that Nachon et al. (2017) interprets to be Na-jarosite due to its high Na_2O compared to other Pahrump diagenetic features. As the nodules of the Bradbury Group do not deviate significantly from the Bradbury density contours, it is likely that they resulted from closed system alteration at the scale of the stratigraphic units. However, the association of sulfates with nodules in the Mt Sharp Group indicates more open system conditions, similar to the sulfate veins, to contribute the excess CaO and MgO. With these nodules removed from the constrained bulk rock dataset, the geochemical effect of open system alteration on the Mt Sharp Group constrained dataset is minimised.

The geochemical compositions of raised ridges in Gale crater vary according to stratigraphic unit (Figs. 3.12 and 3.13). Bradbury Group raised ridges show enrichments in either MgO, or K_2O, Na_2O, and Al_2O_3 (Fig. 3.12), while raised ridges identified in the Mt Sharp Group appear to be geochemically related to calcium-sulfates comparable to the Mt Sharp Group nodules (Fig. 3.13). Aqueous alteration models of raised ridges in the Bradbury Group Sheepbed mudstone show that their high MgO concentrations likely occurred as a result of olivine dissolution in a closed system with a low water-rock ratio (Bridges et al. 2015a; Leveille et al. 2014; McLennan et al. 2014). The enrichment in K_2O, Na_2O, and Al_2O_3 for the Kimberley formation raised ridges could relate to a similar process but with feldspar dissolution, particularly due to the high total mass abundance (26.8 %) of felsic minerals in the Windjana drilled sample (Morrison et al. 2018; Treiman et al. 2016). As the raised ridge features have been removed from the constrained database, the local, post-depositional remobilisation of these elements is minimised.

3.2.1.2. Gale crater amorphous and phyllosilicate components

Due to the lithified nature of the ChemCam host rock targets, some diagenesis will have occurred on a scale smaller than that of MAHLI image resolution (13.9 μm at a standoff distance of 2 cm; Edgett et al., 2012) during the cementation of the mud and sandstone units. For this reason, I compare the geochemical compositions modelled from CheMin and APXS analyses for the amorphous and phyllosilicate (AP) components (Rampe et al., 2017; Treiman et al., 2016; Vaniman et al., 2014) to the constrained bulk rock dataset. Fig. 3.12 and 3.13 show the composition of the X-ray amorphous and phyllosilicate components as a single point for each sample, based on the bulk composition and the calculated composition of the crystalline phases identified by CheMin (for compositions, see Table A.3.1. in the Appendix). In actuality, there is a range of potential AP compositions because of the uncertainties in mineral and amorphous abundances and refined crystal chemistry of major minerals calculated from CheMin data (e.g., Dehouck et al., 2014). I have plotted the best estimate of the AP compositions, rather than the range of potential compositions, to simplify the diagrams.

All of the Bradbury and Mt Sharp Group's 9 drilled samples in the region included here possess varying abundances of an amorphous component, up to 60 % in the Buckskin drill hole (Morris et al., 2016). The origin of this amorphous component in Gale crater has been hypothesised to either relate to detrital, and then subsequently altered soil or aeolian material (Dehouck et al. 2014; Vaniman et al. 2014), diagenetic cement (Treiman et al. 2016), or chemically altered and weathered volcanic glass (Rampe et al., 2017; Bish et al., 2013). Excluding the Marias Pass area, the Mt Sharp Group has ~10–15% greater amorphous component than the Bradbury Group Sheepbed mudstones, which additionally possess a ~10% greater abundance of phyllosilicates than the Mt Sharp mudstones reported here (Murray formation; Fig. 3.14).

Most AP components in mudstone units (John Klein, Mojave 2, Telegraph Peak, Confidence Hills, Marimba, with the exception of Cumberland and Buckskin) are within ChemCam instrument error of their associated stratigraphic group constrained bulk rock geochemistry (Fig. 3.12, 3.13), with some slight variations relative to their Group focus. For the purposes of this study I note that AP in the mudstone units does not demonstrate consistent enrichments in Al_2O_3 or SiO_2, or a consistent loss of divalent and monovalent cations relative to either the constrained ChemCam calculated bulk compositions presented here or in the APXS bulk compositions (Rampe et al. 2017). Hence, Gale crater mudstone AP component may largely reflect local variations in mineralogy of the stratigraphic units that have undergone relatively closed system diagenesis as calculated AP compositions do not show the expected trends for open system aqueous alteration.

MgO-enrichment in the Cumberland AP component of the Sheepbed mudstone relative to the Bradbury bulk rock composition has been attributed to olivine saponitisation (Dehouck et al. 2014; Vaniman et al. 2014). The mean phyllosilicate abundance in the Sheepbed Member is ~20% (Vaniman et al. 2014). Different 001 spacing within CheMin for the John Klein and Cumberland smectites suggests that the elevated MgO component in Cumberland most likely relates to a $Mg(OH)_2$-rich interlayer site in the smectite component that is absent in the collapsed smectite analysed at John Klein (Bristow et al. 2015; Vaniman et al. 2014). In addition, MgO enrichment in the Cumberland AP component follows the trends of enrichment similar to the Sheepbed raised ridges and nodules (Fig. 3.12; Leveille et al. 2014), supporting the conclusions of Vaniman et al. (2014) and Bristow et al. (2015) that the Cumberland drill hole has sampled one of these diagenetic features. Therefore, the greater abundance of Mg^{2+} in the Cumberland phyllosilicates is likely a consequence of the aqueous alteration that formed these diagenetic features. This MgO-rich AP component will have consequently been removed from the constrained bulk rock dataset with the exclusion of raised ridge features.

The other mudstone sample whose AP component demonstrated a distinct composition relative to the bulk Mt Sharp Group focal composition is the Marias Pass Buckskin drilled sample. The Buckskin sample contains no phyllosilicate (Rampe et al., 2017; Morris et al., 2016) and possesses a strong enrichment in SiO_2 and TiO_2, as well as a depletion in FeO_T, relative to the Mt Sharp Group density contours. These major element trends are similar to those of its host rock whose composition may either relate to the silica-rich volcanic source region that formed the tridymite (Morris et al., 2016), or the fracture-associated alteration halos. Hence, this mudstone amorphous component may have also been derived from a similar process (section 3.2.1.1.).

The Windjana drill hole AP composition of the Kimberley formation is distinct from the mudstone and bulk Bradbury geochemistry, likely as a result of its sandstone grain size (Treiman et al. 2016) resulting in greater porosity and enabling a higher permeability and pore water content. Windjana AP possesses strong enrichments in FeO_T and MgO with depletions in SiO_2, CaO, and K_2O relative to the bulk Bradbury Group compositions (Fig. 3.12). The higher pore water content of the Windjana sandstone relative to the mudstone units may have inhibited pressure solution upon compaction, more so than in the finer grained units. This would have restricted extensive element remobilisation within the unit similar to cementation of terrestrial sandstones (Henares et al. 2014; McKinley et al. 2011), making the compositions of the AP component more distinct compared to that of the bulk rock. High concentrations of FeO_T have been observed in all of Gale crater's sedimentary units analysed so far by MSL (Grotzinger et al., 2015; 2014). The iron content of sedimentary units in Gale crater has been suggested to be associated with iron-rich cement (Anderson et al. 2015; Blaney et al. 2014; Grotzinger et al. 2014; Vaniman et al. 2014) that may have formed through isochemical alteration with an iron-rich fluid (Hausrath et al., 2018; Bridges et al., 2015a; Grotzinger et al., 2014). This likely led to the precipitation of magnetite in the Windjana sandstone and an iron-rich AP

component hypothesised to relate to a poorly-crystallised, iron-rich phase such as ferrihydrite and/or an Fe/Mg smectite (Treiman et al. 2016). These hypothesised iron-rich phases for the Windjana AP component are based on CheMin XRD amorphous diffraction intensities and the SAM evolved gas analysis broad water release of the Windjana drilled sample (Treiman et al. 2016).

The presence of alteration phases derived from early stages of alteration e.g., smectites and Fe-oxides (Rampe et al., 2017; Treiman et al., 2016), and lack of secondary mineral phases such as Al-clays indicative of environments subject to extensive leaching (Bristow et al., 2018; Rampe et al., 2017) suggests minimal open system weathering. This, together with the compositions of mudstone AP that do not substantially deviate from the ChemCam constrained bulk rock compositions (except the sandstone Windjana, and potentially altered Cumberland and Buckskin drill holes) suggests isochemical weathering in a closed system for samples in the constrained bulk rock dataset (Fig. 3.12 & 3.13). With obvious diagenetic features e.g., halos, ridges, nodules, veins removed from the constrained ChemCam bulk rock dataset, and by just considering point analyses with total sum of oxides between 95–105 wt% according to the methods outlined in section 2.2, chemical trends across stratigraphic units should be generally representative of detrital source compositions and/or mineral sorting processes.

3.2.1.3. CIA values

As the geochemical effects of diagenesis in the previous sections have been distinguished and isolated, I now proceed to use Chemical Index of Alteration (CIA) values in order to determine the extent of chemical weathering experienced by the ChemCam sedimentary targets included in the constrained dataset. CIA (Nesbitt and Young, 1982) is a method to quantitatively determine how chemically weathered a sample

is according to the susceptibility of silicate minerals to chemical remobilisation, e.g., feldspar to clay alteration. CIA values ($Al_2O_3/(Al_2O_3+CaO+Na_2O+K_2O)$) have been used to gauge the extent of open system chemical weathering at the source or during sediment transportation for Gale crater (e.g., Mangold et al., 2019; Hurowitz et al. 2017; Schieber et al. 2017; Siebach et al. 2017a; Le Deit et al. 2016; McLennan et al. 2015; 2014). On Earth, where carbonates represent a significant fraction of the sedimentary budget, CIA values are corrected to only account for silicate-bound Ca (Nesbitt and Wilson, 1992). Carbonates are more localised on Mars in comparison to Earth (Bridges et al. 2019; Ehlmann et al. 2008), and only traces of carbonates have been found in Gale crater (Archer et al., 2014). Ca-sulfates may, however, have been introduced to the sediment from external sources during burial and diagenesis (Schieber et al. 2017). To correct for this, I have removed targets containing sulfates from the bedrock dataset, as described in method section 2.2, despite indigenous sulfate minerals in the bedrock appearing to be rare for the part of the rover traverse considered in this study (sols 1–1482). Some minor phosphates abundances have been described (Meslin et al., 2018; Rampe et al., 2017; Forni et al., 2015). Because of the possibility of some non-Si-bound Ca in these calculations, the CIA values determined here should be considered as a minimum (Mangold et al., 2019). CIA values for the stratigraphic groups and units (along with equations) are given in Table 3.6 based on both APXS and ChemCam data. Despite Marias Pass targets being included in the constrained bulk rock dataset for the Mt Sharp Group, they are not included in the CIA calculations due to their apparent very different mineralogy (e.g., tridymite; Morris et al. 2016) and/or post-depositional aqueous alteration related to the silica-rich fracture-associated halos (see above, section 3.2.1.1.). CIA values have also been calculated for ChemCam data by Mangold et al. (2019) for various portions of the Murray formation of the Mt. Sharp group.

Table 3.6: Average Chemical Indices of Alteration (CIA; Nesbitt and Young, 1982) values for ChemCam observation point analyses taken at the stratigraphic group and unit scale for the constrained host rock dataset. The equations are also displayed and calculated using molar abundances. SB = Sheepbed; GL = Gillespie Lake; G = Glenelg; D = Darwin; KB = Kimberley; PH = Murray Pahrump Hills; EN = Murray East Naukluft; WN = Murray West Naukluft; B = Murray Buttes.

Group CIA (%)	Bradbury	Mt Sharp
ChemCam	43 ± 9	52 ± 8

$$CIA = \frac{Al_2O_3}{(Al_2O_3 + CaO + Na_2O + K_2O)}$$

Strat. Unit CIA(%)	SB	GL	G	D	KB	PH	EN	WN	B
ChemCam	40 ± 4	45 ± 9	42 ± 8	44 ± 8	39 ± 8	51 ± 6	53 ± 8	54 ± 6	55 ± 5
APXS*	34 ± 2					45 ± 4			

** APXS values reported by Hurowitz et al. (2017)*

Constrained ChemCam bulk rock analyses in the Bradbury Group demonstrate a low average CIA (43 ± 9, Table 3.6) indicative of minimal chemical alteration at the source, a similar conclusion to the CIA values obtained for Bradbury APXS analyses (Hurowitz et al., 2017; Siebach et al., 2017a; McLennan et al., 2012). In contrast, constrained bulk rock analyses for the Mt Sharp Group have a relatively elevated average CIA value (52 ± 8) compared to Bradbury, though it is within error of Bradbury's average (Table 3.6). These similar averages suggest that the difference in chemical weathering for constrained bulk rock analyses has not been strong for either stratigraphic group. However, average CIA values do vary between the different stratigraphic units and waypoints within the Bradbury and Mt Sharp Groups (Table 3.6). Notably, the coarser grained units (Glenelg, Gillespie Lake, Darwin and Kimberley) generally demonstrate higher CIA values, particularly Darwin (CIA 44 ± 8) compared to the fine-grained, mafic Sheepbed mudstone (CIA 40 ± 4). This difference may either reflect contributions from a relatively felsic sedimentary source region, or the mineral sorting regime preferentially preserving felsic minerals over mafic minerals in coarser grained units (Siebach et al., 2017a; Fedo et

al., 2015), as felsic material has higher CIA values compared to sediments rich in mafic minerals (Nesbitt and Wilson, 1992).

Previous CIA studies (Mangold et al., 2019; Hurowitz et al., 2017; Siebach et al., 2017a) on Gale crater sediments have highlighted a variation between the Bradbury Group's Sheepbed Member mudstone and Mt Sharp Group's Murray formation mudstone. APXS analyses (Hurowitz et al. 2017; Siebach et al. 2017a) and ChemCam analysis (Mangold et al., 2019) show the Mt Sharp Group to have notably higher CIA values compared to the Bradbury Group which has led these authors to hypothesise that Murray formation mudstones have undergone more chemical weathering at their source compared to Sheepbed Member mudstones. ChemCam analyses of the constrained bulk rock dataset presented in this thesis also show Murray formation CIA values to be higher than those of the Sheepbed Member (Murray formation CIA = 51 ± 6 to 55 ± 5, Sheepbed Member = 40 ± 4; Table 3.6). Hurowitz et al. (2017) hypothesised that the differences in APXS derived CIA values between the Sheepbed (CIA 34 ± 2) and Murray Pahrump Hills (CIA 45 ± 4) mudstone units reflect modest, short-term paleoclimate fluctuations. According to Hurowitz et al. (2017), the Sheepbed mudstone sediments were eroded and transported during a colder, drier period compared to the Murray formation sediments, and that geochemical variation between these mudstone units is unlikely to be related to a different igneous source. The early stages of chemical weathering in basalts can liberate substantial amorphous silica from primary igneous phases which are susceptible to weathering (McLennan et al., 2014; 2003; Nesbitt and Wilson, 1992). On this basis, Hurowitz et al. (2017) also associated the relatively elevated SiO_2 concentrations in the Murray formation with respect to Sheepbed mudstone as being caused by the greater degree of weathering, particularly as CIA and SiO_2 share a (weak) positive correlation between the two mudstone units for APXS analyses.

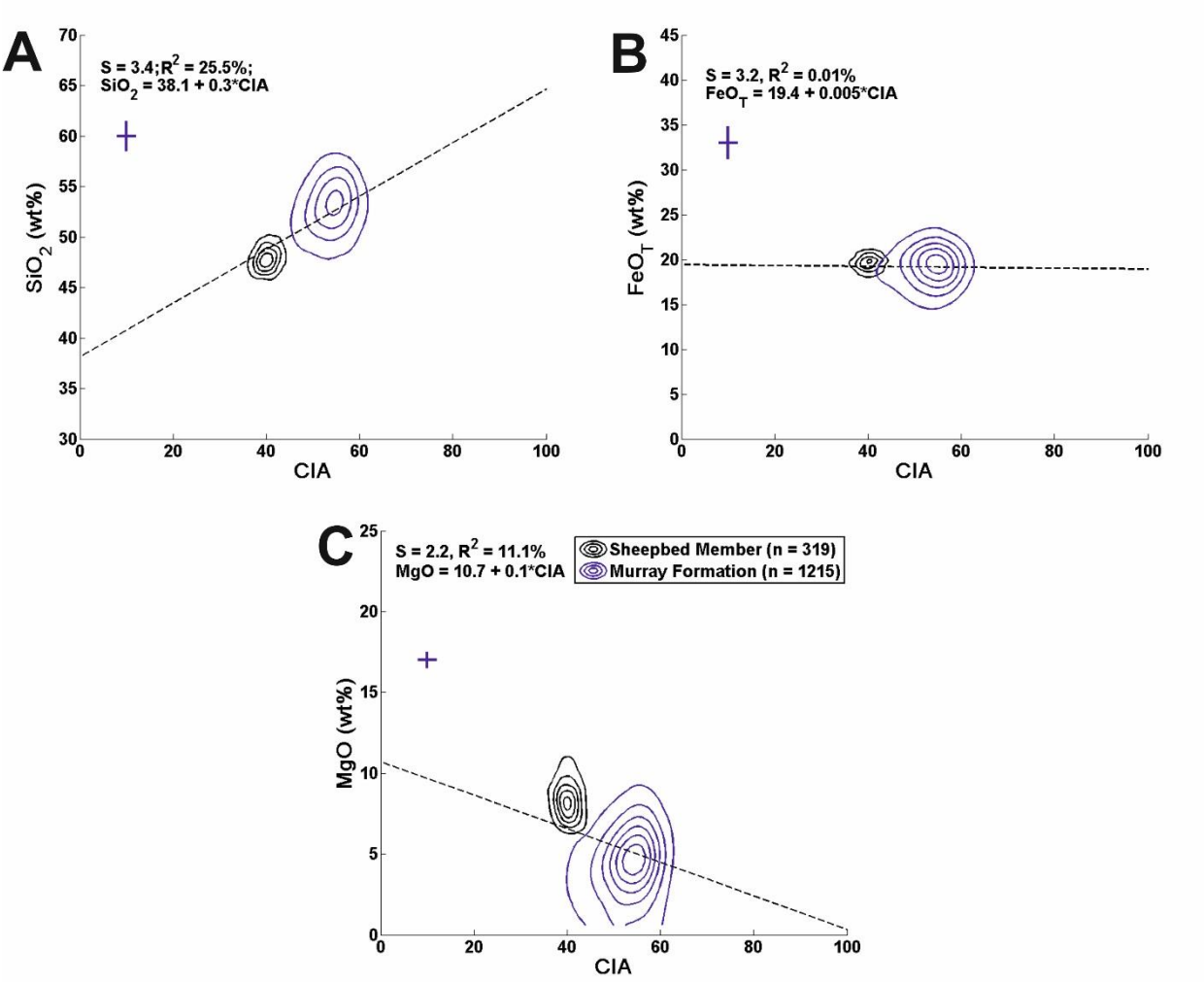

Figure 3.15: Density contours of ChemCam observation point analyses from the Sheepbed Member and Murray formation mudstone (excluding the Marias Pass area). These contours show A) SiO_2, B) MgO, and C) FeO_T, plotted against CIA values (see Table 3.6 for determination of CIA values). ChemCam precision is shown as the respective dark blue lines. The regression line (dashed black line) for the Linear Regression models (see Supplementary information in the Appendix A.3.) were calculated using Minitab v17 to test the linear relationship of the Sheepbed and Murray formation mudstones.

Fig. 3.15 shows calculated CIA values for the constrained ChemCam bulk rock dataset plotted against SiO_2, MgO and FeO_T. I also conducted SLR models of the mudstone dataset for SiO_2, MgO and FeO_T against CIA (Fig. 3.15; Appendix A.3). My results show a minor (r^2=25.5 %), but statistically significant ($p < 0.05$) correlation between CIA and SiO_2 (Fig. 3.15 A). This slight correlation suggests that chemical weathering may

have somewhat increased SiO_2 concentrations between the Murray and Sheepbed mudstones (the model suggests an increase in 2.6 wt% SiO_2 for every 10 % increase in CIA values) prior to Murray formation deposition, but in general the variation in SiO_2 concentrations cannot be explained by CIA values alone. In addition, the regression models show that neither MgO nor FeO_T present a significant correlation with CIA values (Fig. 3.15 B, 3.15 C). The FeO_T regression model does not show a statistically significant correlation with CIA, having high p-values ($p = 0.67$; Appendix Table A.3.7). On the other hand, modelled MgO concentrations do show a very weak negative correlation with CIA ($r^2 = 11.1$ %), for a p-value <0.01 denoting statistical significance (Appendix Table A.3.6), though this still leaves most of the MgO variation between the mudstone units unaccounted for. Hence, chemical weathering does not appear to fully account for chemical differences between the Sheepbed and Murray mudstones. According to these models, the increased SiO_2, and decreased MgO present in the Mt Sharp Group is likely a factor of different source region geochemistry, and not sufficiently explained by different degrees of chemical weathering. Furthermore, the strong association of Na_2O with Al_2O_3 in both stratigraphic groups according to MLR and SLR models (sections 3.1.1., 3.1.2. and Appendix A.3) suggests that feldspar is still the dominant control on this major element oxide across Gale crater samples.

The slightly elevated CIA values in the Murray formation mudstones must therefore be related to the lower CaO, and higher Al_2O_3 contents compared to Sheepbed. A decrease in CaO was also noted by Mangold et al. (2019) to be correlated with CIA within the Mt. Sharp Group members that were studied in that work. In the Sheepbed mudstones, CaO and Al_2O_3 have a Pearson correlation coefficient indicative of a strong correlation ($r = 0.60$; Table A.3.4. in the Appendix), but these elements are poorly correlated in the Murray formation ($r = 0.23$). These correlation coefficients suggest that in the Sheepbed mudstone, CaO is present within Al-bearing mineral phases such as plagioclase feldspar

and pigeonite – which is supported by CheMin derived mineral compositions (Morrison et al. 2018). Although Murray formation pigeonite determined by CheMin possesses little or no CaO, CaO was identified within the plagioclase feldspar component (Morrison et al. 2018). Hence, dissolution of plagioclase feldspar by chemical weathering at the source region or during transport may have liberated some Ca^{2+} and Al^{2+} cations into solution. The most common secondary minerals to form from the chemical weathering of basaltic minerals are smectites and kaolinites, both of which are associated with Al^{2+}, but neither smectites nor kaolinites incorporate significant (>3.5 wt%; Deer et al. 1992) Ca^{2+} into their crystal structure (Deer et al., 1992; Nesbitt and Wilson, 1992). This would result in some Ca^{2+} remaining in solution and being transported away from the system. As plagioclase feldspar is more resilient to chemical weathering than olivine and volcanic glass (Nesbitt and Wilson, 1992), it is likely that these will have also experienced some chemical weathering, liberating Mg and Fe ions into solution that could bond with Al to form Mg- and Fe-bearing smectites.

In addition to the relatively low CaO content in the Murray mudstones potentially relating to chemical weathering, the apparent lack of substantial CaO in Murray pigeonites may also be a product of relatively low CaO at the source. If the source of the Murray mudstones was richer in felsic material through a more evolved magmatic composition (indicated by the pigeonite's intermediate Fe/Mg ratio; Morrison et al., 2018), this would generate naturally higher CIA values than a more mafic source. In this scenario, these naturally higher CIA values may have been accentuated by minor chemical weathering, but not enough to drastically alter or mask source region characteristics. As the CIA values just show a weak correlation with SiO_2 and MgO, no correlation with FeO_T, and average Murray CIA values are not situated considerably above 50 – the CIA value of pure feldspar – I conclude that the degree of chemical weathering of Murray formation source material was not significant enough to mask source region characteristics in the constrained bulk

rock dataset. Therefore, I favour that geochemical variation between the Sheepbed Member and Murray formation mudstones is more likely a factor of different source regions.

3.2.2. Variation of source region characteristics with grain size

3.2.2.1. Endmembers identified in the coarse-grained (>1 mm) units

Coarse-grained targets (Table 2.3; Siebach et al., 2017a; Le Deit et al., 2016; Mangold et al., 2016) were identified within the Darwin Outcrop (sols 392–401), on the Kimberley to Darwin traverse (sols 401–574), at the Kimberley Waypoint (Point Coulomb, Jum Jum target and Liga members; sols 574–632), and at the base of the Mt. Sharp Group at Pahrump Hills (Bald Mountain 1 and 2; sols 775–778; see section 2.2.2). Bulk ChemCam observation point analyses for these pebbly-units plot within the basalt to trachybasalt igneous float and clast density contours, and constitute the majority of point analyses in the Bradbury Group's high aluminium subfocus (Fig. 3.16 A, 3.17 A). Total-alkali versus silica (TAS) plots are commonly applied to terrestrial magmatic rocks in order to distinguish the extent of fractionation that a magma has undergone (Le Bas et al., 1986). On Earth, geochemical variation of coarse sediments (grain size >1 mm) is largely inherited from source rock characteristics (Tolosana-Delado and von Eynatten, 2009). At Gale crater, the number of igneous float and clasts identified within coarse grained units and targets (Edwards et al., 2017; Mangold et al., 2016) suggests that this is also true for Gale crater's conglomerates. Due to the lack of large scale chemical remobilisation in the Bradbury Group (see section 3.2.1 and Siebach et al., 2017a) and presence of primary igneous minerals (Fig. 3.14), this plot is able to reveal likely detrital source compositions and geochemical differences between the groups relating to the alkali contents (Mangold et al., 2017), especially when compared to the Gale crater igneous float and clasts. The foci

of the geochemical contours for the Bradbury Group and igneous float are not coincident with the most abundant primary igneous minerals. Therefore, similar to the results of Cousin et al. (2017), this indicates that a mixture of minerals is analysed by ChemCam at most observation points, including for relatively coarse mineral grains.

Darwin-type conglomerate observation point analyses (Darwin and Darwin to Kimberley traverse analyses) are concentrated within the igneous float and clast high-Al_2O_3 Bradbury subfocus (Fig. 3.16 A), which make it likely that the coarse-sand matrix and small pebbles of Darwin-type conglomerates are derived from the trachybasalt parent rock. Meanwhile, the Kimberley-type conglomerates are relatively more enriched in K_2O than Darwin-type conglomerates (Fig. 3.16 D and 3.17 A) suggesting that a potassium-rich endmember has contributed to this stratigraphic unit. This potassium-enrichment correlates with the presence of sanidine detected at high concentrations (~20 wt %) in the Windjana drill hole within the Dillinger sandstone Member linked to a potassic-igneous source (Treiman et al., 2016). The JumJum conglomerate target (sol 550) representative of the lowermost Point Coulomb member in the Kimberley formation also has elevated K_2O/Na_2O ratios. Hence, during the period of deposition in the sedimentary units leading up to Kimberley, this trachytic endmember grew in significance as a Gale crater source region (Le Deit et al., 2016).

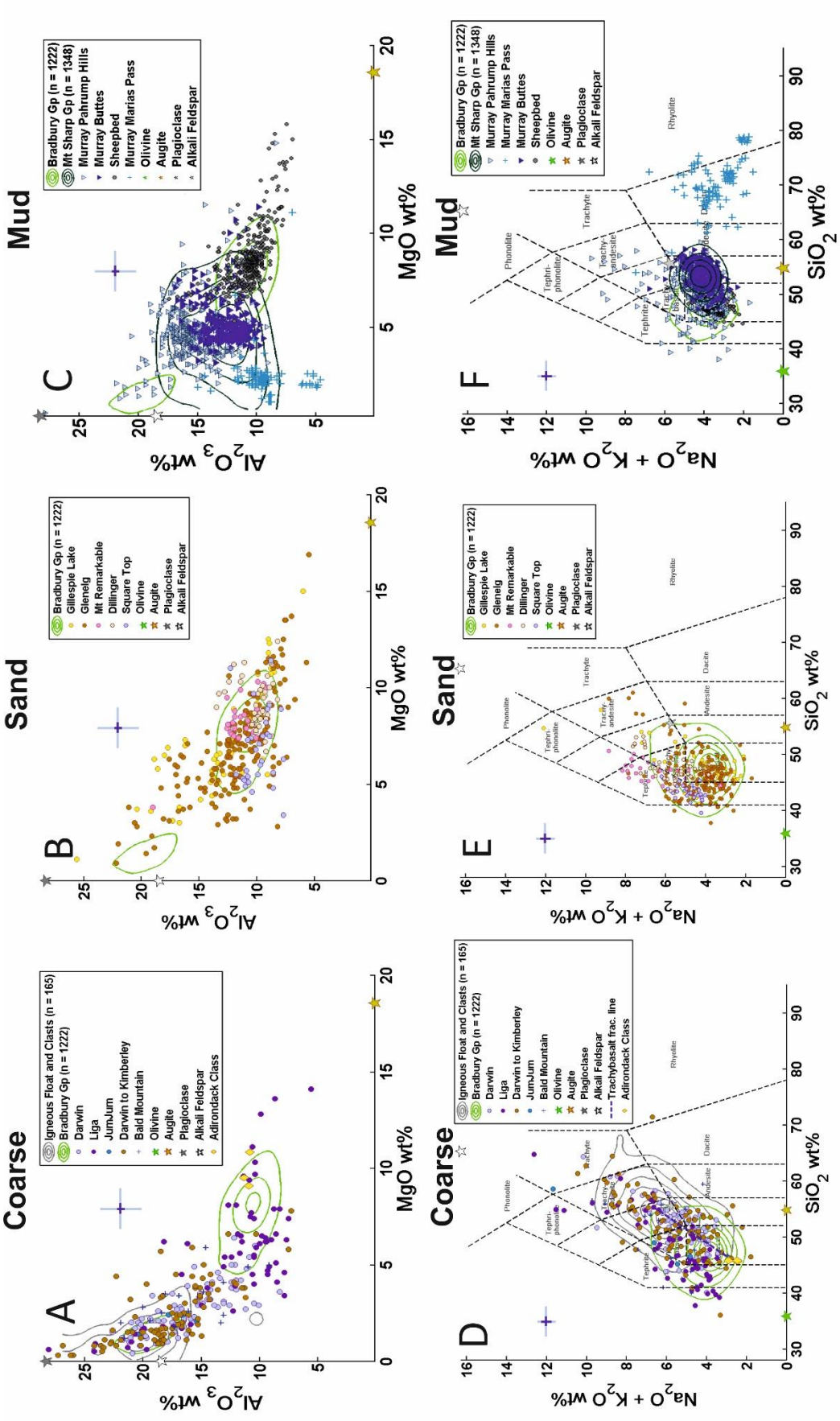

Figure 3.16: ChemCam observation point analyses for Gale crater stratigraphic units and targets shown on Al_2O_3 versus MgO major oxide diagrams and total alkali-silica diagrams. Plots are displayed in accordance to the grain size fraction represented (left column is coarse (>1 mm), middle column sand grain (0.062–1 mm) and the right column is mud grain size (<0.062 mm). Igneous group contours are derived from Gale crater igneous float and clasts data (Edwards et al., 2017; Mangold et al., 2016) and the olivine fractionation line was determined by Edwards et al (2017), CheMin derived Martian mineral compositions for the Rocknest (olivine, plagioclase, augite) and Windjana (alkali feldspar) samples are taken from Morrison et al. (2018), Adirondack Class basalt compositions are from Gellert et al., (2006).

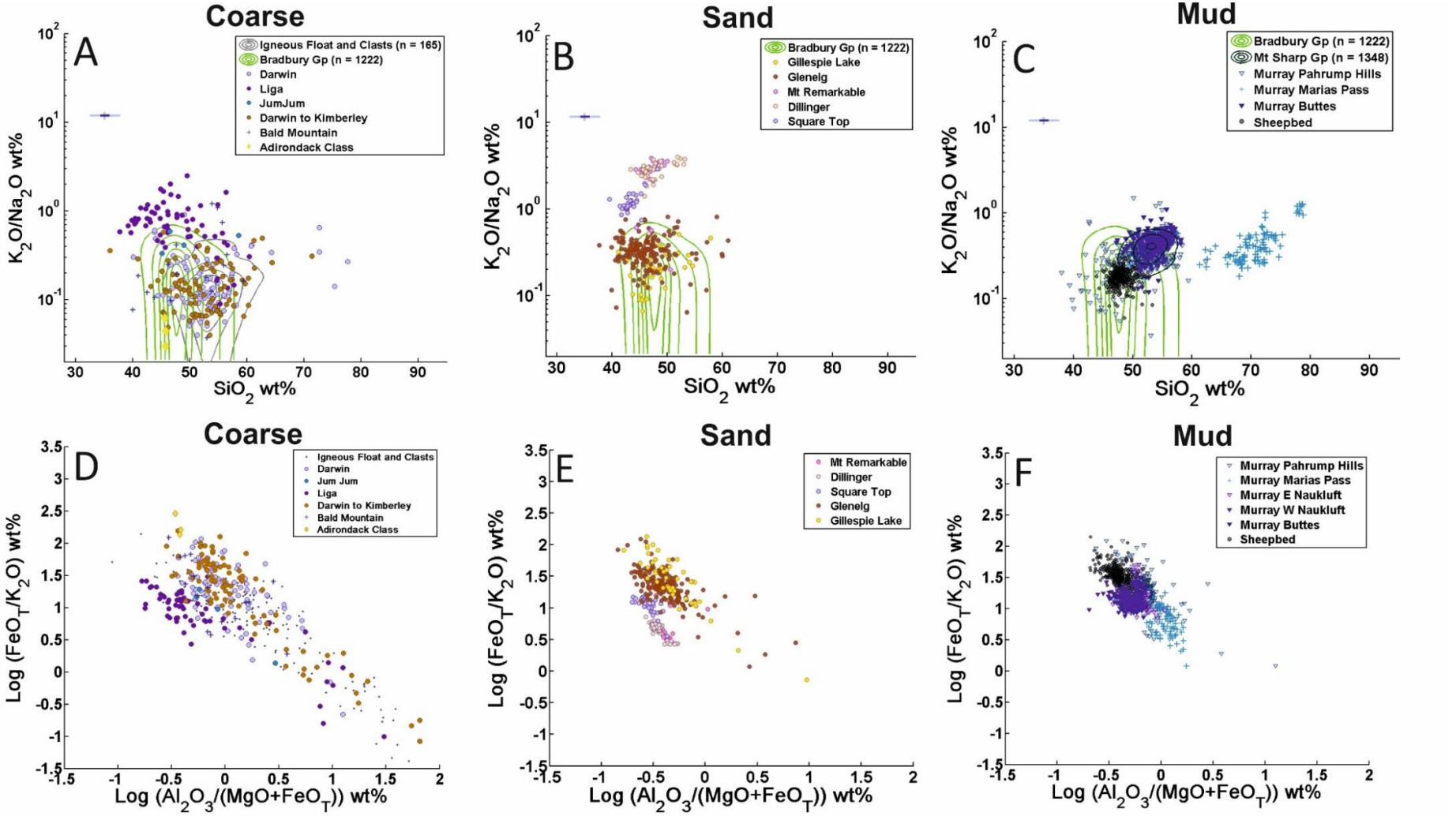

Figure 3.17: ChemCam observation point analyses for Gale crater stratigraphic units and targets shown on K_2O/Na_2O against SiO_2 plots in order to distinguish potential differences in endmember contributions using Roser and Korsch, (1986) and Adapted Herron (1988) log-ratio plot for sediments (see section 3.2.2.2). Plots are displayed in accordance to the grain size fraction represented (left column is coarse (>1 mm), middle column sand grain (0.062 – 1 mm) and the right column is mud grain size (<0.062 mm). The total bins used for the K_2O/Na_2O against SiO_2 plots were 200 x 200 for the Bradbury and Mt Sharp group contours with a reduced level step of $2.5x10^{-4}$ for the Mt Sharp group compared to $5x10^{-4}$ for the Bradbury and Igneous group contours. CheMin derived martian mineral compositions for the Rocknest (olivine, plagioclase, augite) and Windjana (alkali feldspar) samples are taken from Morrison et al. (2018). Igneous group contours are derived from Gale crater igneous float rocks and clasts data (Edwards et al., 2017; Mangold et al., 2016). Adirondack Class basalt data is from Gellert et al. (2006)

Aside from source region variation of the sediments in Gale crater, an alternative hypothesis relating to Martian mineral sorting regimes could explain why both the igneous and high aluminium Bradbury density group contours are co-located between the alkali and plagioclase feldspar compositions (Fig. 3.16 A, 3.17 A). Feldspars have been noted to be more resilient to physical weathering than mafic minerals (Fedo et al., 2015; Nesbitt and Young, 1997), and hence are more concentrated in coarse-grained fluvial sediments eroded from basaltic provenances (Siebach et al., 2017a). The scatter of these observation point analyses towards modelled Gale crater feldspar compositions could suggest that the trachybasalt source signature identified in coarse-sediments may be a result of the concentration of feldspar resulting from this Martian fluvial mineral sorting regime. However, as most conglomerate targets are poorly sorted, and have therefore been derived from multiple source rocks (Grotzinger et al., 2015; 2014), I favour the initial interpretation that the felsic nature of the coarse grained units is considered to be representative of input from the trachybasalt source composition described by Edwards et al. (2017) and potassic source described by Treiman et al. (2016) in the Kimberley formation (Table 3.7).

3.2.2.2. Endmembers identified in the sandstone units (0.062–1 mm)

Fluvial sandstones are present within the Glenelg and Gillespie Lake Members of the Yellowknife Bay formation (Anderson et al. 2015; Grotzinger et al. 2014) as well as the Kimberley formation's Square Top, Dillinger, and Mt. Remarkable Members (Treiman et al. 2016; Grotzinger et al. 2015). On Earth, sandstones and shales have been related to source regions on the basis of their SiO_2/Al_2O_3 and Na_2O/K_2O ratios (Roser and Korsch, 1986; Pettijohn et al., 1972). They are also classified according to their relative abundances of quartz, feldspar and lithic fragments as these mineral populations are abundant in

terrestrial sediments (Weltje, 2012; Dickinson 1988; Pettijohn et al., 1972). On Mars, quartz has not been detected with CheMin at concentrations >1% (Fig. 3.14; Rampe et al. 2017; Yen et al. 2017; Treiman et al. 2016; Vaniman et al. 2014), therefore the SiO_2/Al_2O_3 ratios employed by most terrestrial sediment geochemical classification schemes (Herron 1988; Pettijohn et al. 1972) cannot distinguish key mixing components on Mars. Instead, due to the abundance of mafic minerals (especially clinopyroxene) detected in the CheMin analyses of drilled samples, I use the log-ratio $Al_2O_3/(MgO+FeO_T)$ to distinguish between these mafic and felsic contributions in sandstone and fine-grained units (Fig. 3.17 D-F). The log-ratios FeO_T/K_2O (Fig. 3.17 D-F) and K_2O/Na_2O (Fig. 3.17 A-C and 3.18, plotted against SiO_2 to differentiate between possible igneous rock sources) are employed to distinguish volcanic lithic-fragments and feldspars from evolved (K-rich feldspar) and relatively primitive (Na-rich feldspar) sources.

The majority of Gale crater's sandstone compositions plot within the mafic Bradbury Group subfocus, with some coarse sandstone units trending towards high-Al_2O_3 compositions (Fig.3.16 B). The low-Al_2O_3 subfocus has a similar geochemical composition (though at face value is slightly more K_2O-rich and MgO-poor) compared to the tholeiitic Adirondack Class basalts sampled in Gusev crater by the MER *Spirit* rover (Fig. 3.16 B and 3.16 D). The Adirondack Class basalts are olivine-phyric, primitive basalts representative of primary, basaltic melt (Filiberto et al., 2008; McCubbin et al., 2008; Gellert et al., 2006; McSween et al., 2006a). The similarity in composition between these and the majority of the Bradbury Group sediments indicates that Gale crater's dominant endmember composition is potentially derived from a comparable subalkaline basalt (Edwards et al. 2017; Vaniman et al. 2014). This subalkaline basalt endmember was also identified from ChemCam and CheMin analyses on fluvial sandstone (Treiman et al. 2016), and APXS analyses of Bradbury sediments (Siebach et al. 2017a).

Sandstone units with variations between coarse and fine sandstone (e.g., Glenelg; Anderson et al. 2015) demonstrate scatter that trends towards feldspar (Fig. 3.16 B and 3.16 E). Due to the poor to moderately sorted nature of the sandstone units (Grotzinger et al. 2015; 2014) the mafic-felsic mineral sorting regime outlined in section 3.2.2.1. and described by Siebach et al. (2017a) is also unlikely to have had a significant effect on sandstone compositions. Hence, this scatter may relate to sediment contribution from the trachybasalt endmember identified in the conglomerate units. However, as there is grain size variation within the units themselves, it is not clear to what extent the high proportion of plagioclase feldspar in this unit has been concentrated in the coarser fraction as a result of the mineral sorting regime (Siebach et al. 2017a). Therefore, it is impossible to discern whether these feldspar-rich sediments were related to the trachybasalt source type or feldspar from the low-Al_2O_3, basaltic source that was concentrated in the coarser beds.

A clear difference can be seen between the Yellowknife Bay and Kimberley formation sandstones (Square Top, Dillinger and Mt. Remarkable Members) based on potassium-enrichment (Figs 3.9, 3.16 E and 3.17 B). The upper Dillinger and Mt. Remarkable Members are particularly distinct, forming their own cluster. As the CheMin analysis was conducted within the Dillinger Member, it can be assumed that the less K_2O-rich Square Top member of the Kimberley formation contains a lower abundance of sanidine. The Glenelg and Gillespie Lake Members also possess higher K_2O/Na_2O ratios (cf. Anderson et al., 2015) than the sodic Darwin and Hummocky plains conglomerates (Fig. 3.17 B). If this is attributed to relative proportions of potassic and sodic feldspars this suggests that these coarse sandstone units also contain some sanidine mineral grains. Therefore, the hypothesised potassic-igneous endmember has had an influence on Gale crater's sediment mineral assemblage throughout its depositional history (Table 3.7). But, either due to a change in source region contribution, or increased sandstone maturity

(Treiman et al., 2016; Grotzinger et al., 2015), this endmember is seen to significantly contribute only to the later Dillinger and Mt. Remarkable stratigraphic units.

In summary, the sandstone units within Gale crater are largely derived from a subalkaline basalt source, similar to the Adirondack Class basalts of Gusev crater, with a minor contribution from a potassic volcanic source (Table 3.7; Treiman et al. 2016). Sediment contribution from the potassic volcanic source appears to increase from the Darwin waypoint (Fig. 3.8) to the Kimberley formation (Fig. 3.9; Le Deit et al. 2016) where it is seen to strongly influence the geochemical composition of the Dillinger and Mt Remarkable Members. The trachybasalt endmember described by Edwards et al. (2017) may have also contributed to the sedimentary record within this grain size. However, it is not clear whether the increased abundance of feldspars present within these units are the result of the trachybasalt source region, or grain size variation within units.

Table 3.7: A schematic table showing which endmembers are identified within each grain size population. White = no detection, Yellow = possible contribution, Green = definite contribution

Grainsize	Subalkaline Basalt	Trachybasalt	Trachyte	Rhyolite	Silica-rich Basalt
Coarse fraction (> 1 mm)					
Sand fraction (0.062 - 1 mm)					
Mud fraction (< 0.062 mm)					

3.2.2.3. Endmembers identified within the mudstone units (<0.062 mm)

The Sheepbed Member and Murray formation constitute Gale crater's mudstones (Stack et al., 2018; Grotzinger et al., 2015; 2014). The vast majority of the Mt. Sharp Group's lower Murray formation consists of either mudstone or very fine sandstone, and possess a relatively uniform composition throughout the East and West Naukluft, and

Murray Buttes localities (Figs. 3.11 and 3.17 D & F). This general chemistry is more enriched in Al_2O_3, K_2O, SiO_2 and depleted in CaO, MgO and Na_2O than the Sheepbed mudstone in the Bradbury Group (which plot within the mafic Bradbury contour focus). The very fine grain size of the Sheepbed mudstone and Murray formation results in more homogeneous compositions observed by ChemCam with its small analysis size. With the removal of alteration features and targets potentially exposed to open system weathering (see methods section 2.2.1.1, and sections 3.1.3 and 3.2.1; Fig. 3.12, 3.13 & 3.15), the observed geochemical variation between the Bradbury and Mt. Sharp Group (lower Murray) mudstone units must be representative of either lacustrine mineral sorting processes (section 3.2.2.3.1.), or different endmember mixing proportions (section 3.2.2.3.2).

3.2.2.3.1. The effects of mineral sorting processes within the Gale Lake on sediment geochemistry

A possible explanation for the observed geochemical differences between stratigraphic groups could relate to transport fractionation processes in a lake body. Supposing no change in sediment source region and assuming a homogeneous grain size of input materials, distal lake deposits will possess higher Al_2O_3 and alkali (especially Na_2O) concentrations due to greater, low density felsic and possibly clay-rich mineral abundances (Babechuk et al. 2014; Das et al. 2006; Jin et al. 2006). For Gale crater's Sheepbed mudstone, bed thicknesses and a close association with overlying fluvial sandstone have been interpreted as a depositional environment that was relatively rapid, close to the shoreline and sediment source (Hurowitz et al. 2017; McLennan et al. 2014). It has also been argued by Hurowitz et al. (2017) that hematite-bearing sections of the Murray formation such as the Pahrump Hills were deposited in shallow water potentially near the

shoreline due to high abundances of hematite and Mn-oxide pertaining to an oxidising environment. Trough cross-bedding and interstratified siltstone and fine sandstone near Pahrump also support deposition in shallower waters and/or proximity to the lake shoreline (Hurowitz et al. 2017). Therefore, if both the Sheepbed Member and Pahrump Hills Murray formation mudstones are deposited at near-shore locations in the paleolake, their differences in mineralogy and chemistry must reflect a change in source regions. The Pahrump Hills mudstones located near the interfingering boundary with the Bradbury Group are more Na_2O- and K_2O-rich, and possess greater abundances of plagioclase feldspar than the Sheepbed mudstone (Fig. 3.14 and 3.17 F) which is not what is to be expected based on mineral density and sediment sorting alone.

In contrast, Rampe et al. (2017) noted that the observed secondary mineral assemblages in Pahrump Hills that Hurowitz et al. (2017) attributes to a shallow lake environment could also be produced through diagenesis in short-lived, oxidizing ground waters. However, the morphological evidence for shallower lake conditions for the Mt Sharp Group near Pahrump is significant (thicker laminations, interstratified, cross-bedded, fine sandstones; Hurowitz et al. 2017; Grotzinger et al. 2015). Thus, differing source regions between the Murray formation and Sheepbed Member mudstones are the most plausible explanation for their geochemical differences.

3.2.2.3.2. Endmembers and source region contributions

This section builds on the model above that chemical weathering in source materials, diagenesis and transport processes have not erased the source rock compositions of the mudstones. The Sheepbed Member consistently plots within the dominant, Mg-rich focal composition of the Bradbury Group (Fig. 3.5, Fig. 3.16 C, 3.16 F, 3.17 C) and is similar in composition to the Adirondack Class basalts and subalkaline basalt endmember

determined by Edwards et al. (2017) from Gale crater's igneous pebbles and float (Fig. 3.16 C). Therefore, the Sheepbed mudstone unequivocally relates to the dominant, subalkaline basalt source region that has also contributed sediment to the Bradbury Group's sandstones and conglomerates. In contrast, the Mt Sharp Group MgO composition appears intermediate between those of the Bradbury trachybasalt and subalkaline basalt sub-focal compositions (Fig. 3.2 D and 3.16 C) suggesting similar mixing between a mafic and felsic source. However, the increased K_2O, $Al_2O_3/(MgO + FeO_T)$ and SiO_2 content of the Murray formation compared to the Sheepbed mudstones (Fig. 3.16 C, 3.16 F, 3.17 C, and 3.17 F) requires a greater contribution of felsic minerals and silica-rich material. CheMin analyses (Fig. 3.14) also demonstrate this greater felsic/mafic mineral proportion.

CheMin XRD analyses show sanidine across the Murray formation (except for Mojave 2 and Oudam) with between 4.2% at the Buckskin drill hole, to 7.7% in Marimba 2 (Bristow et al., 2018; Rampe et al., 2017; Morris et al., 2016). These are higher abundances than those of sanidine detected in the Yellowknife Bay formation (2.9–3.4%). On average, Murray alkali feldspars are suggested to possess higher potassium content, more similar to that analysed at The Kimberley (Rampe et al., 2017; Treiman et al., 2016). This shows that the potassic igneous source identified in the Kimberley sandstone by Treiman et al. (2016) is likely a volumetrically significant contributor to Gale's sedimentary record. Though the presence of the potassic igneous endmember may explain some of the elevated potassium contents, it does not fully explain the increase in SiO_2 content for Murray. Hence, for the Mt. Sharp Group to be more silica and potassium enriched – elements not commonly seen on Earth to change significantly with increased lake depth for sediments derived from the same source region (Das et al. 2006; Jin et al. 2006) – I infer, based on the analysis above, the presence of a distinct source region.

On Earth, tholeiitic terrains such as the Eastern Volcanic Zone of Iceland are usually punctuated by periods of silica-rich tholeiitic volcanism (Haddadi et al., 2015; Bindeman et al., 2006; Jakobsson, 1972). These silicic-tholeiites are derived from the fractionation of olivine-normative parent magmas at shallow or mid-crustal depths (less than 15 km) within the crust (Haddadi et al., 2015; Green et al., 1967). All CheMin analyses in the Murray formation have notable silica-enrichment in the amorphous component (Rampe et al., 2017; Morris et al., 2016), which may be volcanic glass or an alteration product thereof (Achilles et al., 2017; Rampe et al., 2017; Dehouck et al., 2014; Bish et al., 2013; Blake et al., 2013). Terrestrial silicic-tholeiites also possess a slightly higher bulk K_2O content than olivine-tholeiites (Bindeman et al. 2006; Green et al. 1967). Along the rover traverse the K_2O content is seen to increase with silica from the Pahrump Hills to the Murray Buttes area (Fig. 3.10, 3.11 & 3.17 C; excluding the Marias Pass silica-rich area). CheMin-determined pigeonite compositions for the Murray formation are also very low in calcium and possess intermediate Fe/Mg (Morrison et al., 2018; Rampe et al., 2017). The latter characteristic especially is the hallmark of a more fractionated, magma source (Deer et al. 1992).

Though not seen throughout the Mt. Sharp stratigraphy, tridymite and cristobalite were detected in abundance at Marias Pass (Morris et al. 2016), and cristobalite in abundance in Telegraph Peak (Rampe et al., 2017). These minerals are high temperature, low pressure silica polymorphs (Shinohara and Kohyama, 2004) that usually form within late-stage, strongly-fractionated magmas on Earth (Morris et al., 2016; Keith and Muffler, 1978). Marias Pass mudstone thus shows influence by a completely distinct source region not detected in the Bradbury Group, and provides strong evidence for a temporally evolving sediment composition. Marias Pass sediments appear derived from a highly fractionated, silica-rich ($\geq$75 wt% SiO_2) endmember which contributed the tridymite and cristobalite. This region also contains a continued – but minor – influence of the potassic

endmember (Fig. 3.14 and 3.17 C). The extreme low density of these silica polymorphs (2.3 g/cm^3) and the fine-grained nature of the material (e.g., Frydenvang et al. 2017) means that this endmember could be located far from the Gale crater catchment area as the tridymite grains are able to be entrained longer in the fluid flow. With more time spent in the fluid flow, mineral sorting will have had a greater effect resulting in the concentration of these endmember mineral grains along with fine-grained amorphous material or detrital clays, at the end of the distributary system. However, aqueous alteration models (i.e., Bridges et al. 2015a), and the lack of clays in the Telegraph Peak and Buckskin drill holes suggest that Gale crater's clay component is primarily authigenic. Concentration due to density-related transport fractionation could explain the localised high abundance of tridymite along with significant amorphous content (60%, Morris et al., 2016) identified by CheMin at the Buckskin drill hole (sol 1061).

Alternative explanations have been proposed by others to explain the presence of the high-silica Marias Pass unit. The first suggests that it was deposited in a temporally isolated event, such as a relatively sudden, volcanic eruption of a highly evolved silicic magma (Morris et al. 2016). This could have generated a thick layer of ash that was later washed downstream into the lake (Morris et al. 2016). Once this eruption had ceased, a return to the mafic sediments deposited prior to the eruption occurred, resulting in the distinct Marias Pass stratigraphic unit within the Murray formation (Frydenvang et al. 2017; Morris et al. 2016). The second explanation for silica-enrichment in Marias Pass discusses that sediments may have been leached in place by short-lived, mildly acidic, late-stage fluids (Rampe et al., 2017). These diagenetic fluids could have dissolved ferromagnesian minerals and created the observed trace element trends (Rampe et al. 2017). As tridymite is strongly suggested to be detrital from a silicic source region (Morris et al. 2016), and as the abundance of magnetite and lack of hematite at this locality is more

indicative of reducing settings (Hurowitz et al. 2017), I prefer a source region and deposition-related hypothesis to explain the presence of this unusual unit.

3.3. Chapter 3 conclusions

Investigation of the ChemCam database from the beginning of the mission through to sol 1482 suggests that the main influences on observed geochemical variation are changing sediment sources (see Table 3.8 for endmember compositions), and mineral sorting regimes once diagenetic features are removed from the database and the effects of chemical weathering have been taken into account. The dominance of primary igneous minerals, and CIA values unrelated to SiO_2 and MgO variations in the constrained dataset, all suggest that chemical weathering processes have not dominated the endmember compositions despite CIA values being higher in the Mt Sharp Group mudstones compared to the Sheepbed mudstone. Instead, bulk compositions for the stratigraphic units and groups are likely determined by varying proportions of primary igneous minerals, with isochemical weathering hypothesised to generate amorphous and phyllosilicate component compositions similar to bulk rock geochemistry. The results presented in this thesis also support the Martian fluvial mineral sorting regime whereby felsic minerals are more abundant in coarse sandstone fractions due to their resilience to diminution during transportation (Siebach et al. 2017a), but are more likely to travel farther into a lake body because of their lower density compared to mafic minerals. As a consequence of the Murray formation and Sheepbed mudstone possessing a possibly similar depositional setting in relatively shallow water and/or close to the shoreline, the geochemical differences between these units likely reflect changes in sediment source region. This change in sediment provenance is particularly notable in the Marias Pass region with the

appearance of the silica-rich endmember, so I propose a silica-rich, subalkaline basalt endmember to be the main source of sediments at the base of Mt Sharp.

In isolating the analysis to grain size dependent subpopulations, four previously identified endmembers and one new endmember are observed throughout Gale crater sediments in this part of the mission, which can be related to specific igneous source regions (Fig. 3.18). These are:

1. A subalkaline basalt endmember (Edwards et al., 2017; Anderson et al., 2015); similar in composition to the Adirondack Class basalts observed by the MER *Spirit* rover at Gusev. This endmember is observed throughout the Bradbury Group stratigraphy and is concentrated within the Sheepbed mudstone Member of Yellowknife Bay. Due to the similarity of this composition to Adirondack basalts it can be surmised that this is most likely a regional endmember composition and contributes significantly to Gale crater's geochemical record.
2. A trachybasalt endmember (Edwards et al. 2017); likely formed during crystal-melt fractionation of the mafic, Adirondack-type basalt that constitutes endmember (1). This is largely identified in clasts within the conglomerate outcrops (especially Darwin), and is characterised by Na_2O and Al_2O_3 enrichment associated with an increase in plagioclase feldspars.
3. A trachyte endmember (Treiman et al. 2016); related to an increased abundance of sanidine in comparison to the more Na-rich plagioclase feldspars from endmember (2). This endmember is recognised to an extent within the Gillespie Lake and Glenelg Members of the Yellowknife Bay formation, plus the later Mt. Sharp Group mudstone. It is seen to contribute significantly to the Kimberley formation sandstones and conglomerates and – due to the detection of pure sanidine – it may

be associated with erosion from a volcanic alkaline or trachytic source (Treiman et al. 2016).

4. A silica-rich (rhyolite) igneous endmember (Morris et al. 2016); identified at the Marias Pass locality within the Mt. Sharp Group, this endmember is thought to resemble the erosion of a late-stage magmatic source, or ash cloud generated from a volcanic event of an evolved magma composition, due to the predominance of high-temperature silica polymorphs.
5. A silica-rich, subalkaline basaltic endmember; proposed by this study, this endmember contributes most to the Mt. Sharp Group and is more SiO_2, Al_2O_3 and K_2O-rich than endmember (1). This endmember is seen to become more prevalent up the stratigraphic succession.

The above source compositions have strongly influenced the geochemistry and mineralogy of the sedimentary rocks which constitute the Bradbury and Mt. Sharp (Murray formation up to sol 1482) fluviolacustrine stratigraphic groups traversed by MSL. Endmembers (1) and (2) are largely associated with the distal alluvial fan deposits seen within the Bradbury Group (Grotzinger et al., 2015; 2014) while endmembers (4) and (5) are solely recognised in the lower Murray formation. Endmember (3) is identified across the fluviolacustrine deposits, predominately in Bradbury Group fluvial sandstone and Murray mudstone, but contributes little to the Yellowknife bay formation. Instead, the Yellowknife bay formation appears to be largely derived from endmember (1) with some local influence of endmember (2).

This study shows that despite temporal and spatial influences on sediments, distinct source region characteristics can still be distinguished within the Martian sedimentary record. This can be achieved through identifying chemical and mineralogical trends that contradict physical sorting processes, as well as analysing sediments according to grain

size. Gale crater stratigraphy therefore shows that the ancient highland crust which contributed to its basin fill is more geochemically complex than previously anticipated for Mars. This is despite the lack of evidence for evolved crustal compositions detected from orbit which I speculate may relate to evolved rocks being volumetrically smaller relative to basalt in Mars' crust.

Table 3.8: A table of the hypothesised sediment endmember compositions in Gale crater identified according to ChemCam. 1σ ChemCam precision is given as the error.

Endmember	SiO_2	TiO_2	Al_2O_3	FeO_T	MgO	CaO	Na_2O	K_2O	Reference
Subalkaline Basalt	47.4 ± 1.4	0.9 ± 0.2	10.6 ± 1.2	19.8 ± 1.9	8.1 ± 0.9	5.5 ± 1.6	3.0 ± 1.4	0.5 ± 0.3	This paper, Edwards et al. (2017)
Trachybasalt	55.2 ± 3.5	0.8 ± 0.2	19.8 ± 2.5	7.7 ± 5.6	1.6 ± 1.0	6.4 ± 2.4	5.4 ± 1.3	1.2 ± 0.9	Edwards et al. (2017)
Trachyte[1,*]	-	-	-	-	-	-	-	-	Treiman et al. (2016)
Silica-rich Basalt	53.1 ± 1.9	1.0 ± 0.2	12.1 ± 0.8	19.5 ± 1.4	4.6 ± 0.6	2.3 ± 0.6	2.9 ± 0.2	1.2 ± 0.2	This thesis
Rhyolite[2,*]	-	-	-	-	-	-	-	-	Morris et al. (2016)
1σ	1.5	0.1	0.6	1.8	0.5	0.4	0.5	0.1	

[1]Endmember determined by the presence of high-order sanidine (Treiman et al., 2016).

[2]Endmember determined by the presence of tridymite (Morris et al. 2016).

** As these endmembers were distinguished according to specific minerals and not related to a host rock, the compositions are left blank.*

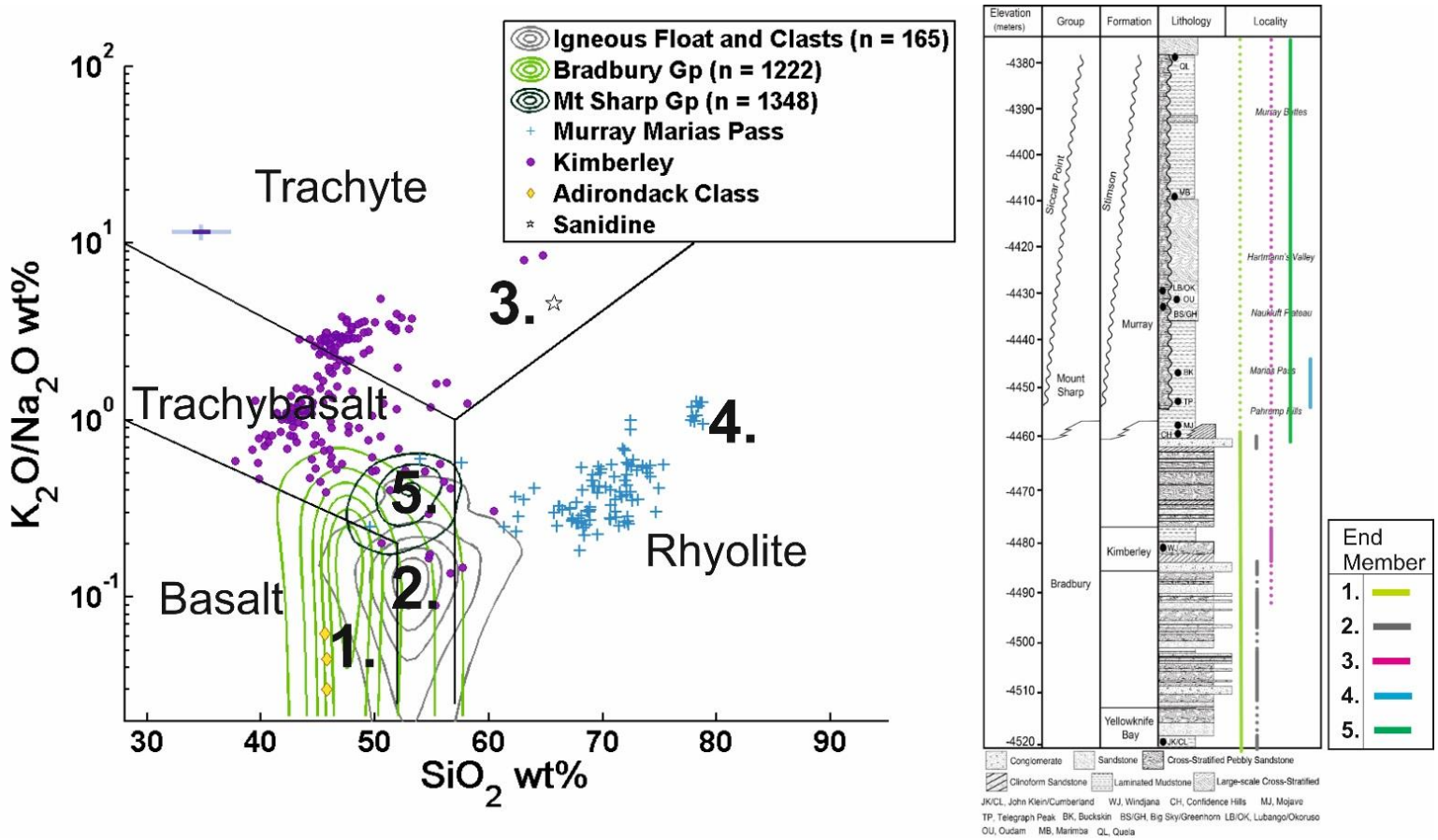

Figure 3.18: A K_2O/Na_2O vs SiO_2 plot of stratigraphic units most influenced by distinct endmembers alongside the Gale crater stratigraphic column, modified to show approximately where each end member is predicted to contribute to the stratigraphic record. Provenance field boundaries for the K_2O/Na_2O vs SiO_2 plot are determined by replotting the basalt, trachybasalt, trachyte and rhyolite TAS silica field boundaries (Le Bas and Maitre, 1986) against terrestrial basalt, trachybasalt, trachyte and rhyolite compositions obtained from the georoc.de database. Geochemically distinctive endmembers are 1. Adirondack-type subalkaline basalt which constitutes the majority of the Bradbury group sediment compositions, and is the most dominant throughout the stratigraphic succession (light green line). 2. A trachybasalt endmember largely recognised in the coarse-grained conglomerate and sandstone units (grey line), 3. A potassium-rich (trachyte) volcanic source region, which is most dominantly expressed in the Kimberley formation sandstones (pink line), 4. A silica-rich (rhyolite) volcanic endmember, most dominant in the Marias Pass locality of the Mt Sharp Group (light blue line), and 5. A silica-rich subalkaline basalt endmember composition present in the Mt Sharp group Murray mudstones (dark green line). Adirondack Class basalt geochemical data are also displayed (Gellert et al., 2006). Dashed lines on the stratigraphic column show where the endmember contributes to a lesser extent, undashed lines show the endmembers that are most dominant in that stratigraphic area.

4. Geochemical variation in the Stimson formation: A comparison with modern Martian dunes and lithified unit provenance.

In addition to the ancient fluviolacustrine stratigraphic Groups - Bradbury and Mt Sharp (analysed in detail in Chapter 3) - *Curiosity* also investigated the chemistry and mineralogy of an ancient aeolian unit informally named the Stimson formation (Banham et al., 2018). The Stimson formation is a part of the Siccar Point Group which can be seen from orbit to unconformably overlie the Mt Sharp Group (Fig. 4.1), hence, the Stimson formation was likely deposited after the warm and wet period ended in Gale crater (Banham et al., 2018; Fraeman et al., 2016; Watkins et al., 2016). Aeolian processes have dominated the geological record of Mars from the start of the Amazonian to the present day (e.g., Hayward et al., 2014; Fenton and Richardson, 2001; Greeley et al., 2001; Edgett and Malin, 2000) and are currently active in Gale crater with the modern Bagnold dune field (Fig. 4.2 B; Ehlmann and Bridges, 2017; Lapotre and Rampe, 2018). In investigating the geochemistry of the ancient aeolian Stimson formation and comparing it with the other ancient and modern sedimentary deposits in Gale crater, I aim to constrain the geochemical effect of sedimentary processes and provenance throughout Gale crater's geological history, particularly that relating to the aeolian processes which have dominated the Martian surface for several billion years. This aim is achieved through combining the ChemCam geochemical dataset for constrained analyses using the methods outlined in Chapter 2, with mineralogy determined from CheMin's Stimson drilled samples. As aeolian processes are highly effective at mineral sorting with distance from the source (e.g., Kocurek, 1991; Pye and Tsoar, 2008; Nichols, 2009), I also hypothesise that this mineral sorting regime can be identified through using a Cluster analysis to sort mafic

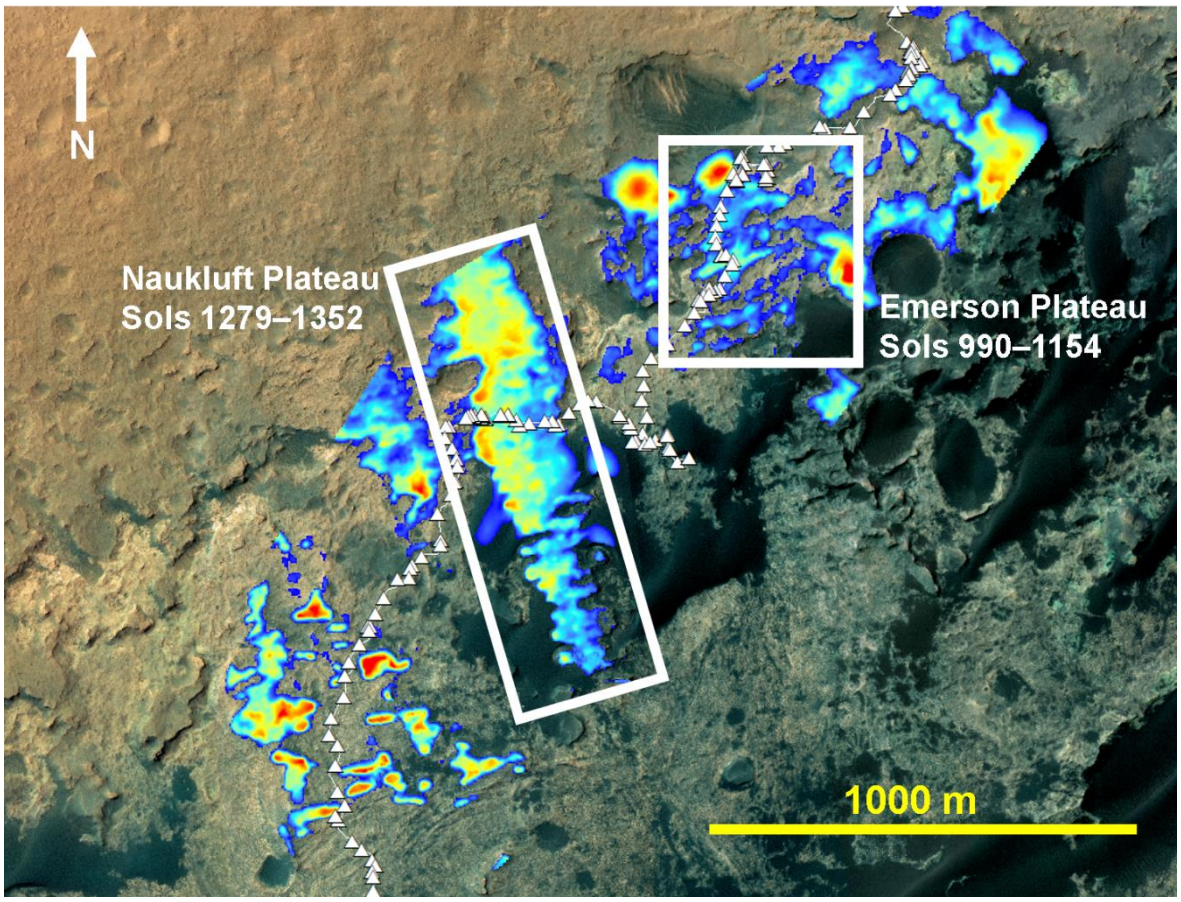

Figure 4.1: Annotated isopach map of the Stimson formation with main localities Emerson Plateau and Naukluft Plateau labelled and outlined in boxes. The thin white line represents the rover traverse with triangles showing stops. The colours on the isopach map show where the Stimson formation is thin (blue) and up to 11 m thick (red) with respect to the Murray-Stimson unconformity. The isopach map was created by Steve Banham using data from Watkins et al. (2016).

clusters from felsic clusters (see section 2.4.3). If the mineral sorting regime can be distinguished, this can also provide information on the ancient prevailing wind direction at the time of the Stimson formation's deposition for comparison to that determined for the modern Bagnold dunes.

This geochemical analysis complements the sedimentological study by Banham et al. (2018) that characterises the Stimson sandstone and depositional setting. In the context of this thesis, this chapter follows from Chapter 3 by continuing the ChemCam geochemical source region study on the main sedimentary groups and units in Gale crater.

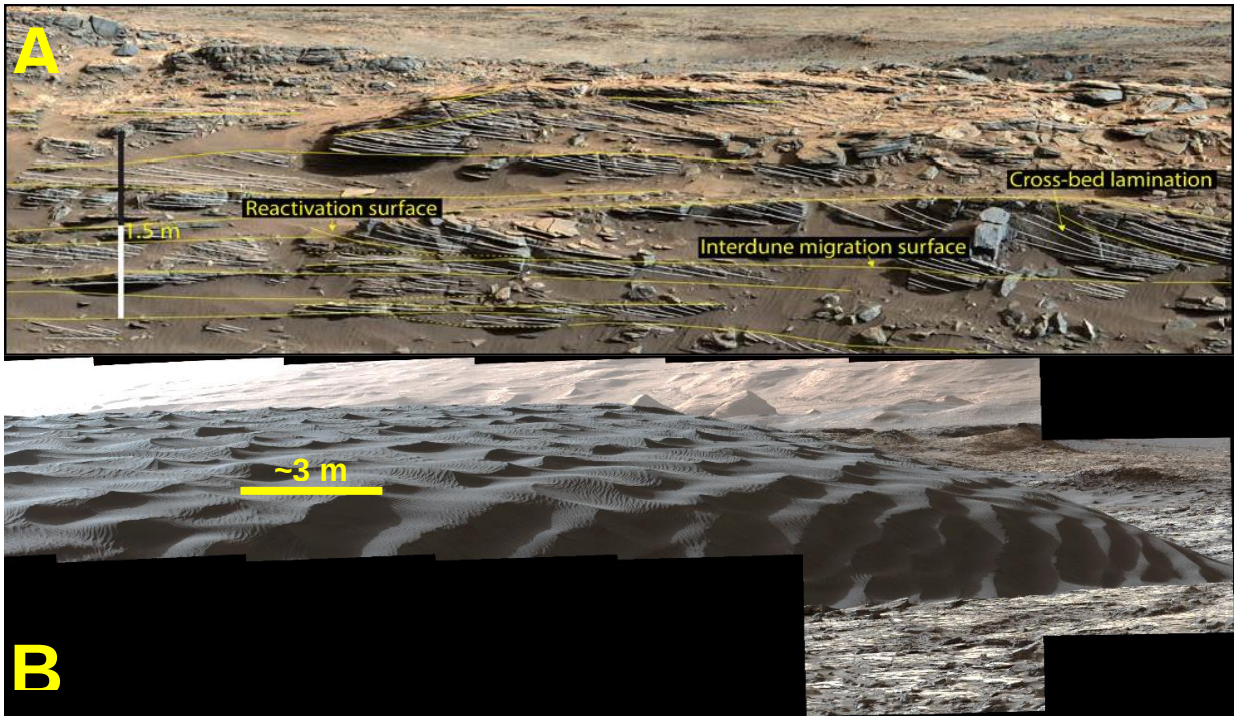

Figure 4.2: A) Annotated Mastcam image taken from Banham et al. (2017) of the Stimson formation in Bridger Basin (mcam04872, sol 1099) showing the bounding surfaces and cross-sets that led to an aeolian interpretation. B) Mastcam mosaic (mcam05410, sol 1192) of the active Namib dune within the Bagnold dune field. A modern Martian analogue to the Stimson formation.

In discussing the Stimson formation now, this research transitions from the fluviolacustrine groups deposited earlier in the stratigraphic record to the aeolian Stimson formation of the Siccar Point Group that was likely deposited once the long-lived fluviolacustrine system ceased (Banham et al., 2018). This Chapter order also follows the timeline of the MSL mission as Stimson was first encountered in the Marias Pass, Naukluft and Murray Buttes localities (Chapter 1.3.5), which was where the analysis of the previous Chapter ended.

4.1. Geochemical diversity across the Stimson formation - Background

The Stimson formation has a total outcrop of 17 km^2 (Calef et al., 2016) though the ChemCam instrument analysed Stimson at only two main areas of outcrop exposure along its traverse (Fig. 4.1): the Emerson Plateau (sols 990–1154) which covers the Marias Pass and Bridger Basin localities, and the Naukluft Plateau (sols 1279–1352). Stimson was also identified at the top of the Murray Buttes. However, at the Murray Buttes it was too far away to analyse in situ with any of the rover's on-board geochemical instruments, so in this Chapter I solely discuss the Stimson at the Emerson and Naukluft Plateaus. Stimson largely consists of a decametre-thick, cross-bedded sandstone and shares an erosive boundary with the underlying Murray formation (Banham et al., 2018; Watkins et al., 2016). A dry, aeolian origin was determined for Stimson due to the high sphericity and roundness of the grains, uniform bimodal grain size distribution with a major modal peak at 250 µm and a minor modal peak at 850 µm, and 1 m thick cross-beds separated by sub-horizontal bounding surfaces representative of dune-migration (Banham et al., 2018; Fig. 4.2 A). The lack of phyllosilicates or fluvial deposits (i.e., conglomerate beds), and large, metre-scale cross-sets also provide further support to the aeolian interpretation.

The erosional unconformity between the lake-deposited Murray mudstones of the underlying Mt Sharp Group (see Chapter 1.3.4 for a detailed stratigraphic description of this formation) and aeolian Stimson sandstone, as well as Murray clasts incorporated into the Stimson sandstone at the base, suggests that Stimson was deposited after the paleoclimate in Gale crater changed from a warm and wet environment that could sustain a perennial lake to the cold, arid conditions which we see at the surface today (Banham et al., 2018; Newsom et al., 2016; Watkins et al., 2016). As such, it is the youngest in situ unit analysed at the time of writing (December 2018) by *Curiosity*. Therefore,

understanding its geochemical composition in contrast to that of the lithified fluviolacustrine groups (described in Chapter 1.3.3 & 1.3.4 and analysed in Chapter 3) and active Bagnold dunes within Gale crater (Fig. 4.2 B) can provide insights into ancient aeolian processes, diagenesis and how sediment provenance has changed after the Bradbury and Mt Sharp Groups were deposited and lithified.

4.1.1. Geochemical variation between the Stimson facies

The Stimson formation has been divided into four facies (Fig. 4.3): (1) metre-scale planar and trough cross-bedded Stimson, (2) decimetre-scale trough cross-bedded Stimson, (3) concretion-rich Stimson and (4) Stimson with Murray intraclasts (Banham et al., 2018; Newsom et al., 2016). Facies (1) and (2) are the most common across the Stimson formation and represent the migration of simple and complex dunes respectively. Facies (3) also consists of the metre- and decimetre-scale cross-bedding, but in this facies these sedimentary features have been overprinted by millimetre- to centimetre-scale concretions. Based on terrestrial studies of concretion formation, the Stimson concretions have been hypothesised to form through preferential cementation of the sandstone (Banham et al., 2018; Siebach et al., 2017b; Clarke and Stoker, 2011). The ChemCam derived geochemistry of this facies is discussed further in section 4.2.2. Facies (4) has been investigated only at the Missoula Outcrop in Marias Pass which has been subjected to multiple stages of aqueous alteration (Newsom et al., in rev.). As such, it has not been included in any density contour analysis that models the constrained bulk composition of the geological unit (for more information on the density contour methods see sections 2.2 and 2.3), but is discussed further in section 4.2.2. in relation to diagenesis.

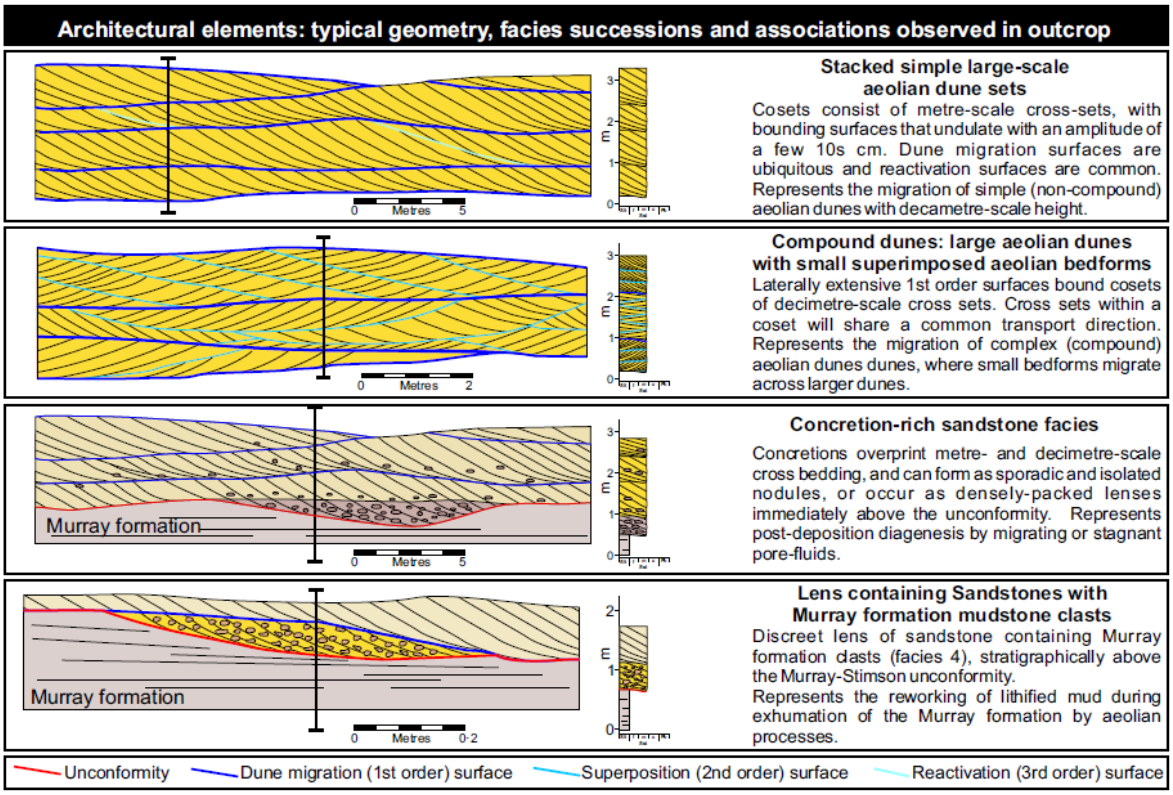

Figure 4.3: Fig. 10 of Banham et al. (2018) of the four facies identified within the Stimson formation.

4.1.2. Diagenetic features in the Stimson formation

In general, Stimson has noticeably fewer aqueous alteration features compared to the fluviolacustrine groups (Newsom et al. in rev.; Banham et al., 2018), though silica-rich halos, calcium-sulfate veins and concretions were still identified at both the Emerson and Naukluft localities as a result of multiple, late-stage diagenetic events (Hausrath et al., 2018; Frydenvang et al., 2017; Yen et al., 2017). After the initial lithification of the Stimson sandstone and formation of the early diagenetic concretions (Banham et al., 2018; Siebach et al., 2017b), two separate events of fluid migration through fractures in the bedrock formed the calcium-sulfate mineral veins and silica-rich alteration halos (Frydenvang et al., 2017; Yen et al., 2017). Calcium-sulfate mineral veins are prevalent throughout Gale crater and likely precipitated from a late-stage diagenetic fluid (Rapin et

al., 2016; Schwenzer et al., 2016a; Nachon et al., 2014). Several hydrous alteration models involving both acidic and alkaline fluids have been proposed to explain the silica-rich alteration halos of the Murray and Stimson formation (Hausrath et al., 2018; Frydenvang et al., 2017; Yen et al., 2017). The "acidic" model invokes the extensive leaching of Mg, Al, Mn, Fe, Ni and Zn and dissolution of pyroxene to explain the silica-enrichment of the bedrock surrounding affected fractures (Hausrath et al., 2018; Yen et al., 2017). Meanwhile, the "alkaline" model hypothesises that the silica-enrichment was caused by the remobilisation of amorphous silica in the tridymite-bearing unit of Marias Pass by alkaline fluids (Frydenvang et al., 2017). Later, these silica-rich, alkaline fluids underwent a change in either pH or temperature and precipitated opaline silica along the fractures in the overlying Stimson formation (Frydenvang et al., 2017). Based on the current evidence and understanding of these features, both hypotheses are plausible, though the alkaline model is preferred as this takes into account the spatial association of the silica-rich halos to the tridymite-bearing unit.

Concretion-rich Stimson makes up a substantial portion of ChemCam analyses across both localities, particularly in the Naukluft Plateau area where 74 % of analyses targeted the concretion-rich facies. APXS analyses of concretions suggest that they are geochemically the same as their host rock which supports that they formed isochemically (Banham et al., 2018; Siebach et al., 2017b). Concretions are on average larger in diameter than the ChemCam analysis footprint (150–350 μm), with several LIBS spots targeting either the concretion itself, or the border of the concretion and the bedrock. Therefore, ChemCam may better identify any geochemical variation that relates to the concretions compared to its surrounding bedrock. In order to investigate the concretion geochemistry, I have isolated concretion-rich Stimson from non-concretionary Stimson in section 4.2.2. Conducting this analysis can show whether concretion-rich Stimson should be included in the Stimson constrained bulk rock dataset.

I have removed ChemCam analyses of obvious alteration features as part of the constrained bulk rock dataset refinement process (see methods 2.2) and placed them into their own category for a comparative analysis against the constrained bulk Stimson. In Chapter 3, subsection 3.2.1.1, I show that the methods outlined in Chapters 2.2, and 2.3 sufficiently removed the effects of geochemical trends associated with aqueous alteration features from the source characteristics of the sediment host rock. Here, I apply the same method to the ChemCam analyses in the Stimson formation to also ensure that the geochemical effects of alteration have been appropriately disentangled from that of the sediment source region characteristics.

4.2. Results

4.2.1. Bulk Stimson geochemistry

Overall, the Stimson formation possesses a uniform geochemical composition with minimal difference between the mean and median compositions (Table 4.1 and Fig. 4.4). Al_2O_3 has a clear bimodal distribution with peaks at 11.3–12.6 wt% and 15.2–16.5 wt% and, despite the bimodality, the mean and median compositions are approximately equal (mean = 13.7 wt%, median = 13.9 wt%). This bimodality within Al_2O_3 could represent subpopulations within the Stimson formation. All other major element oxides (SiO_2, TiO_2, FeO_T, MgO, CaO, Na_2O and K_2O) demonstrate an approximately normal, unimodal distribution, though FeO_T shows skew in the mean composition towards lower values (Fig. 4.4 C), while K_2O is skewed towards higher values (Fig. 4.4 G).

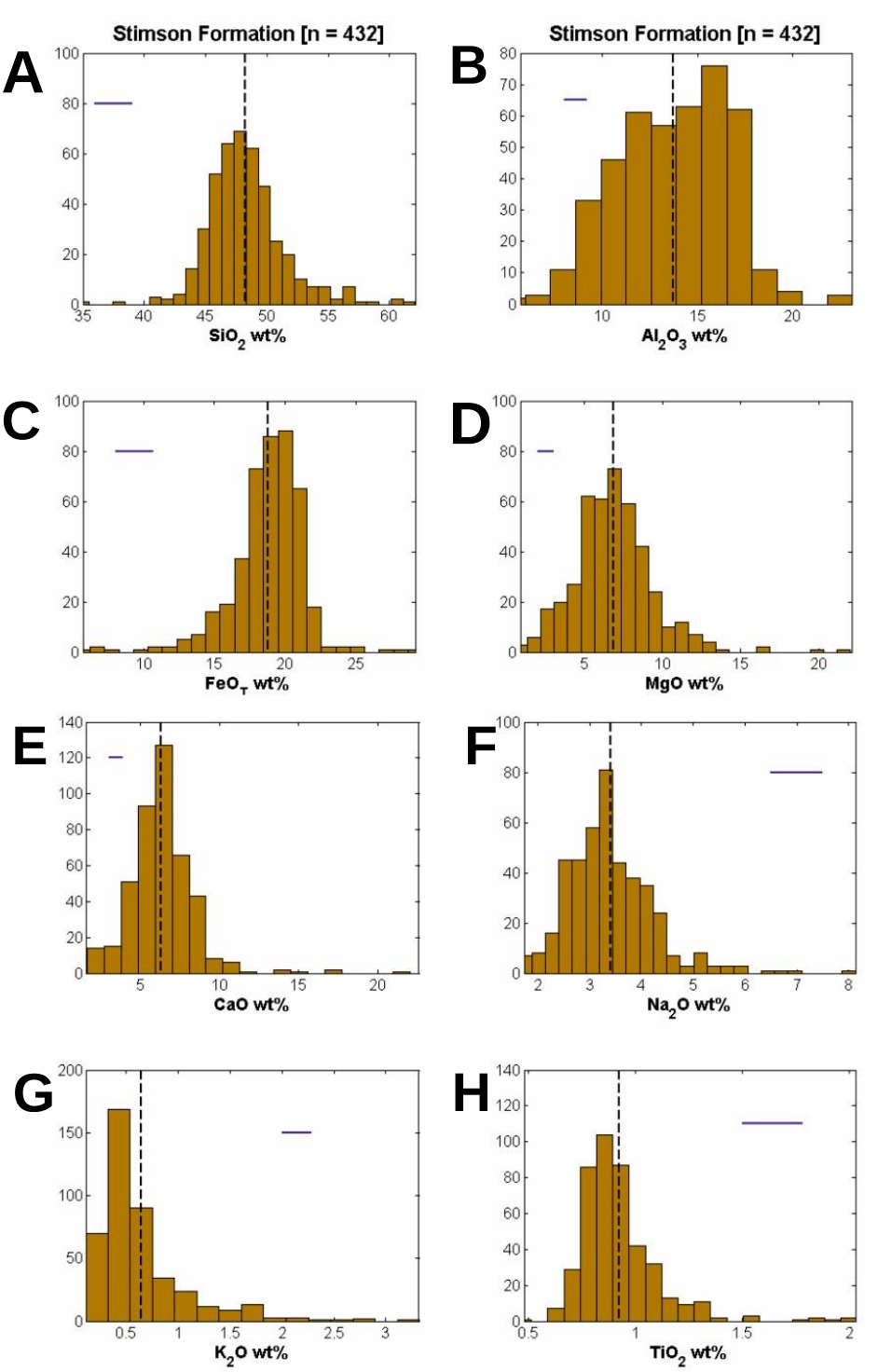

Figure 4.4: Major element histograms of Stimson analyses within 95–105 % sum of oxides, and excluding observation points that analysed obvious diagenetic features. Mean compositions (dashed vertical line) and 1σ precision (horizontal blue line) are also shown.

Table 4.1: Basic statistics of the observation point compositions included in the constrained bulk Stimson formation dataset. Basic statistics include the mean, standard deviation (StDev), minimum (Min), median (Med), maximum (Max), and geochemical range for each major element oxide.

Variable	Mean	StDev	Min	Med	Max	Range
SiO_2	48.3	3.1	35.0	48.0	61.6	26.6
TiO_2	0.9	0.2	0.5	0.9	2.0	1.5
Al_2O_3	13.7	2.9	5.7	13.9	22.5	16.8
FeO_T	18.8	2.6	5.7	19.1	29.2	23.5
MgO	6.9	2.5	0.9	6.8	21.6	20.7
CaO	6.3	2.1	1.6	6.3	21.5	19.9
Na_2O	3.4	0.8	1.7	3.3	8.1	6.3
K_2O	0.6	0.4	0.1	0.5	3.2	3.1

Figure 4.5 (next page): Density contour Harker plots of the constrained Stimson dataset for each major element against SiO_2 with a level step of 0.001, smoothing factor 30 and bin size 50. Alteration feature trends are shown as yellow and red crosses for the light-toned halos, and light blue crosses for the Ca-sulfate veins. Data also included are the Big Sky plagioclase feldspar, K-feldspar, pigeonite and orthopyroxene mineral compositions from Morrison et al. (2018) shown as stars, and the Big Sky and Okoruso amorphous component best estimate from Morrison et al. (2018) shown as squares. The light and dark blue crosses show the ChemCam instrument accuracy and precision respectively to 1σ. Ksp in D) shows the direction of the CheMin derived K-feldspar composition from Morrison et al. (2018) which contains 16.9 wt% K_2O.

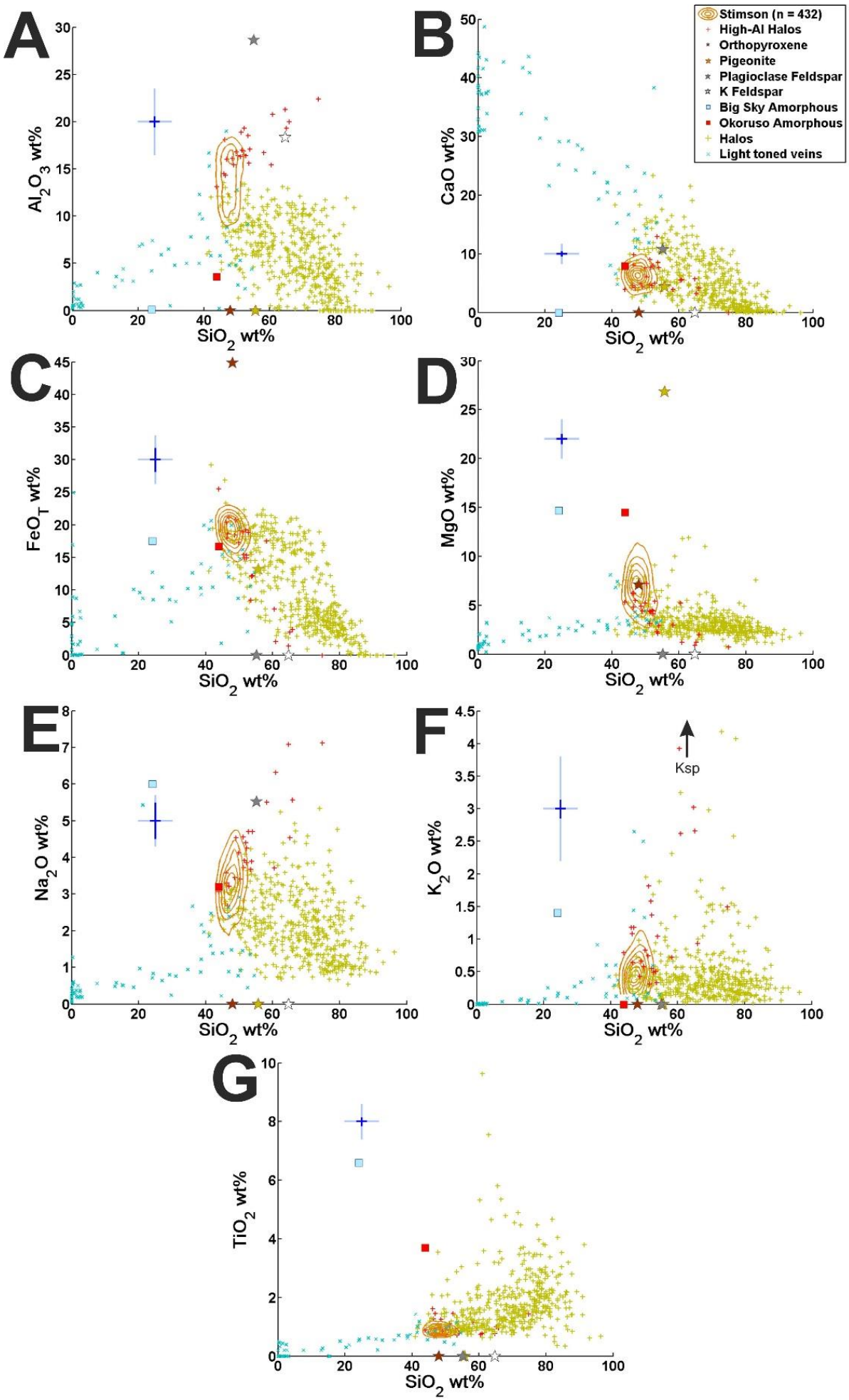
A
B
C
D
E
F
G
Stimson (n = 432)
High-Al Halos
Orthopyroxene
Pigeonite
Plagioclase Feldspar
K Feldspar
Big Sky Amorphous
Okoruso Amorphous
Halos
Light toned veins
Al2O3 wt%
CaO wt%
FeOT wt%
MgO wt%
Na2O wt%
K2O wt%
TiO2 wt%
SiO2 wt%
Ksp

Density contours for the bulk Stimson formation (Fig. 4.5) also highlight the geochemical uniformity present in the histograms, mean and median statistics, with most major elements possessing 6 or 7 contour levels when plotted against SiO_2. Only Na_2O and Al_2O_3 show lower contour numbers due to a greater spread in compositions between the respective major element maximum and minimum values. This spread in Al_2O_3 and Na_2O compositions is also highlighted in the histograms (Figs. 4.4 B & 4.4 F) and by the apparent elongation of the contours along their y-axis compared to the concentric circles distributed about the foci for the other major elements (Figs. 4.5 A & 4.5 E).

4.2.2. Stimson alteration trends

Fig. 4.6 shows boxplots of Emerson Plateau and Naukluft Plateau concretion-rich Stimson against their unaffected host rock equivalents for samples across all total sum of oxide values. All units show similar mean and median compositions, as well as geochemical ranges indicating a uniform geochemistry. Moreover, all units present minimal skews from their mean and median compositions – with the exceptions of TiO_2 and K_2O – and outlying values are not solely restricted to the concretion-rich units. These results suggest that the concretions are not the cause of the outlying values and hence confirm the interpretations of these features as isochemical cement by Banham et al. (2018) and Siebach et al. (2017b). Consequently, facies (1), (2), and (3) can remain within the constrained bulk Stimson dataset, despite facies (3) relating to early-stage diagenesis.

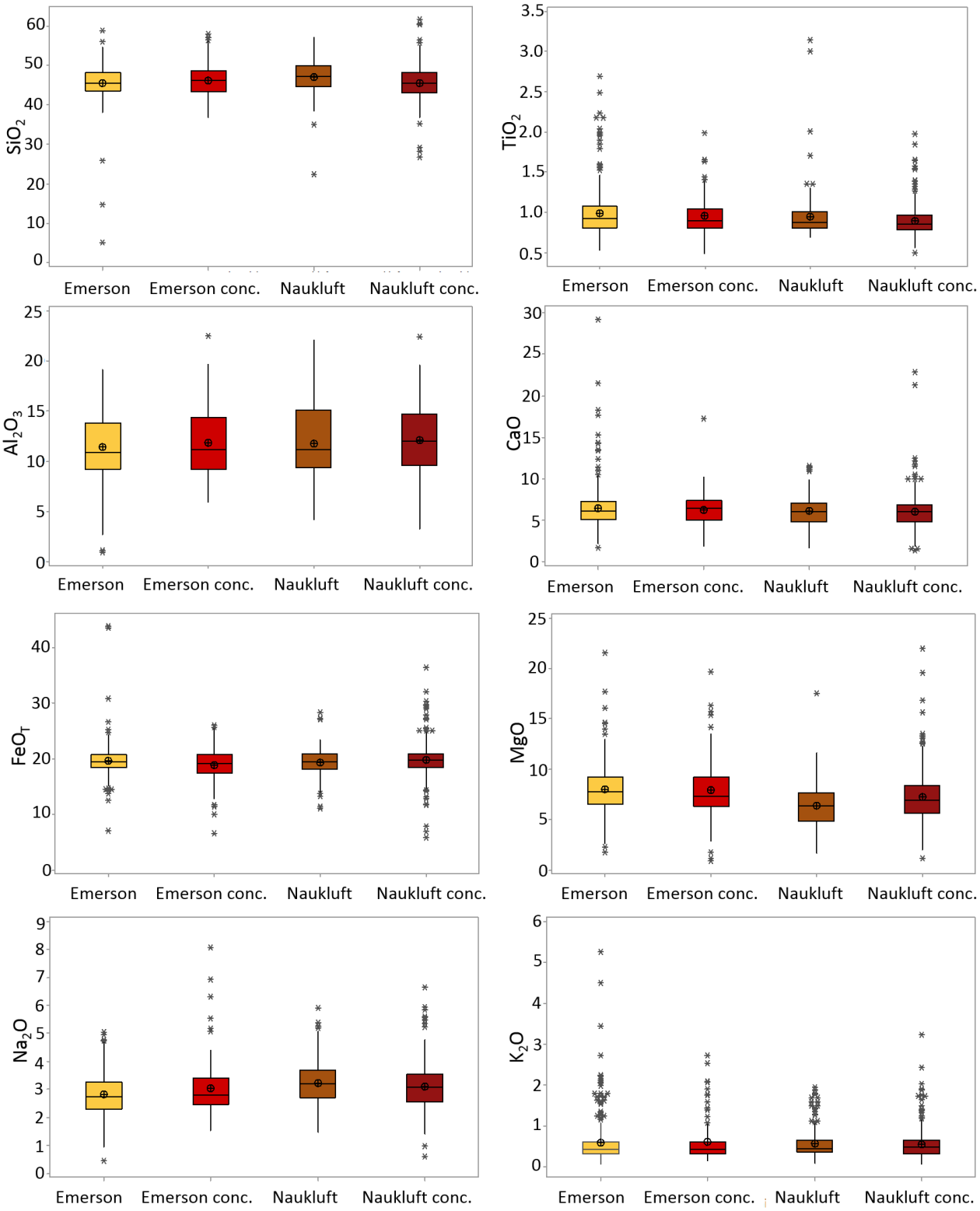

Figure 4.6: Boxplots comparing Stimson analyses from the Emerson Plateau and Naukluft Plateau localities between non-concretion and concretion-rich bedrock for all total sum of oxides. Crossed circles represent mean compositions and asterisks show outlying observation point analyses. The boxes show the interquartile range of the data about the median value (black line). The whiskers show the range of adjacent values (any value that is within 1.5 times the interquartile range) from the upper and lower interquartile values respectively.

Calcium-sulfate veins and halos demonstrate distinct geochemical trends away from bulk Stimson indicative of open-system weathering (Fig. 4.5; Hausrath et al., 2018; Yen et al., 2017; Rapin et al., 2016). Unsurprisingly, calcium-sulfate mineral veins show strong enrichments in CaO relative to Stimson bedrock, similar to the trends outlined for the fluviolacustrine groups (see 3.1.3.1.) with depletions in all other major element oxides and a low total sum of oxides.

Alteration halos (shown in Fig. 4.5 as yellow and red crosses) have a geochemical trend towards high SiO_2 compositions (>80 wt%). The majority of ChemCam halo analyses (Fig. 4.5, yellow crosses) also show low abundances for the other major elements except TiO_2 and some K_2O values, once again reflecting the geochemical trends observed in the Murray formation halos (section 3.1.3.2; Frydenvang et al., 2017). Nevertheless, some Stimson halo analyses show a different trend with an apparent positive correlation for Al_2O_3, Na_2O and K_2O against SiO_2 (Fig. 4.5, red crosses). These high Al_2O_3, Na_2O and K_2O halo analyses trend away from the high Al_2O_3 (~15 wt%) bulk Stimson contour subfocus, and appear to be associated with sampling apparent white grains in the bedrock fracture-related halo features (e.g., target Blaubock point #3, Fig. 4.7).

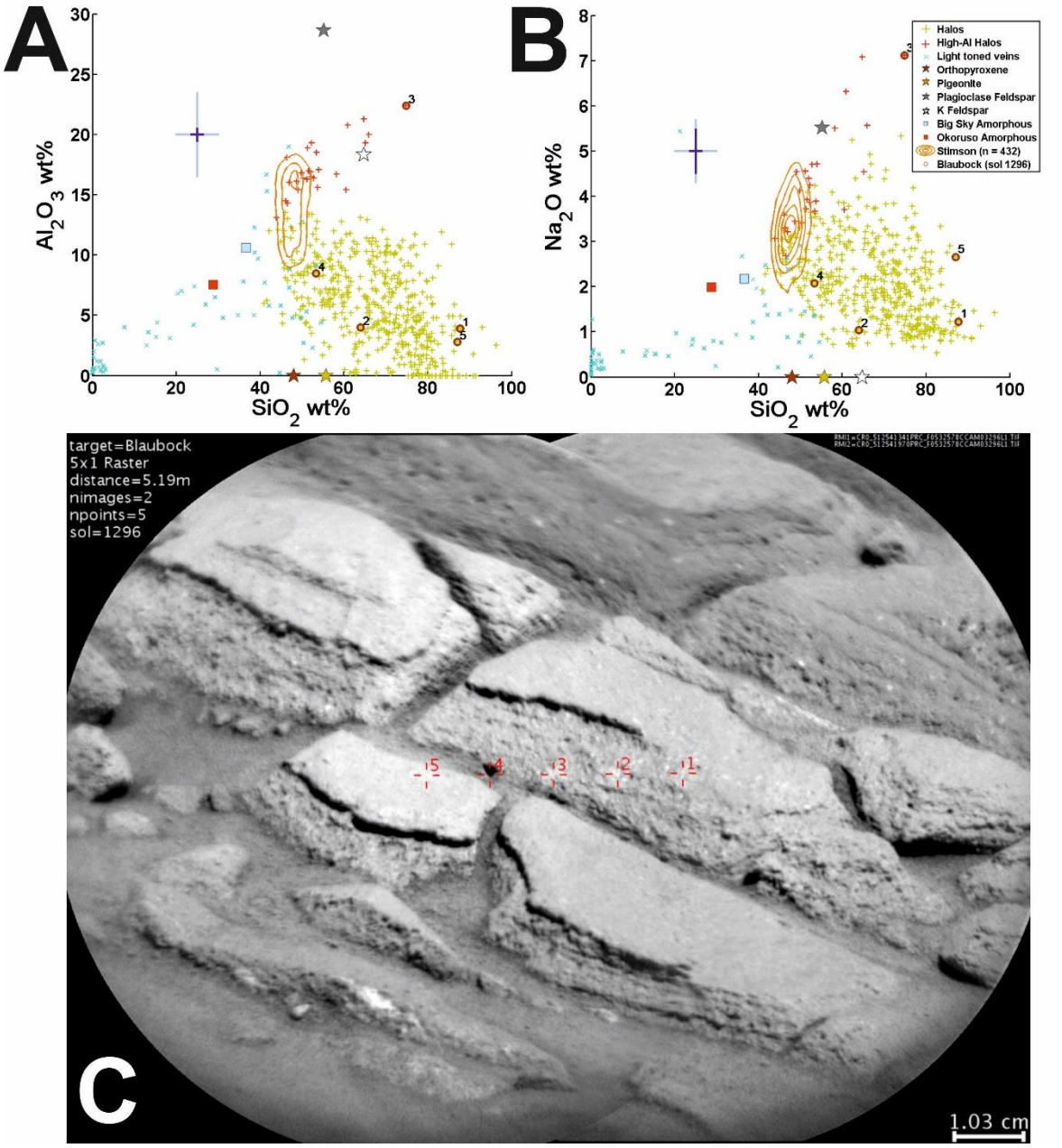

Figure 4.7: Blaubock analyses 1–5 highlighted on Stimson contour and alteration feature (halo, veins and amorphous composition) plots as numbered dots for A) Al_2O_3 and B) Na_2O against SiO_2. Data also included are the Big Sky plagioclase feldspar, K-feldspar, pigeonite and orthopyroxene mineral compositions from Morrison et al. (2018) shown as stars, and the Big Sky and Okoruso amorphous component best estimate from Morrison et al. (2018) shown as squares. The light and dark blue crosses show the ChemCam instrument accuracy and precision respectively to 1σ. Blaubock analyses 1–5 are also annotated on C) the ChemCam LIBS target RMI mosaic. Observation #3 appears to have hit a white grain in the RMI image and shows the highest Al_2O_3 and Na_2O reported in the Stimson formation.

In the fluviolacustrine groups, high-aluminium focal compositions were shown to relate to higher proportions of felsic material (section 3.2.3). The proximity of the high-Al_2O_3 subfocus to the felsic minerals (Fig. 4.5 A), and correlation of analyses with apparent white grains (Fig. 4.7) suggests that this may also relate to felsic material. As such, one possibility is that the halo analyses enriched in Al_2O_3, Na_2O and K_2O could represent felsic minerals that have not been affected by the silica-rich halo alteration process, implying a resilience of feldspars during halo diagenesis such as that hypothesised by Yen et al. (2017). Alternatively, the high Al_2O_3-halo analyses could also be revealing sericitzation of feldspar, as some targets have more Al_2O_3 and Na_2O than the Big Sky plagioclase and sanidine compositions (Fig. 4.7 A & B).

As mentioned in section 4.1.1 and by Newsom et al. (in rev), the Stimson facies (4) identified within the Missoula outcrop is likely to have undergone several stages of aqueous alteration. When plotted against the Stimson alteration trends (Fig. 4.8), it clearly shows that certain observation points in this outcrop have been influenced by calcium–sulfate addition as well as both halo alteration trends. As a result, it remains removed from the bulk Stimson dataset as our results support those of Newsom et al. (in rev.) that this outcrop in particular has undergone multiple stages of diagenesis.

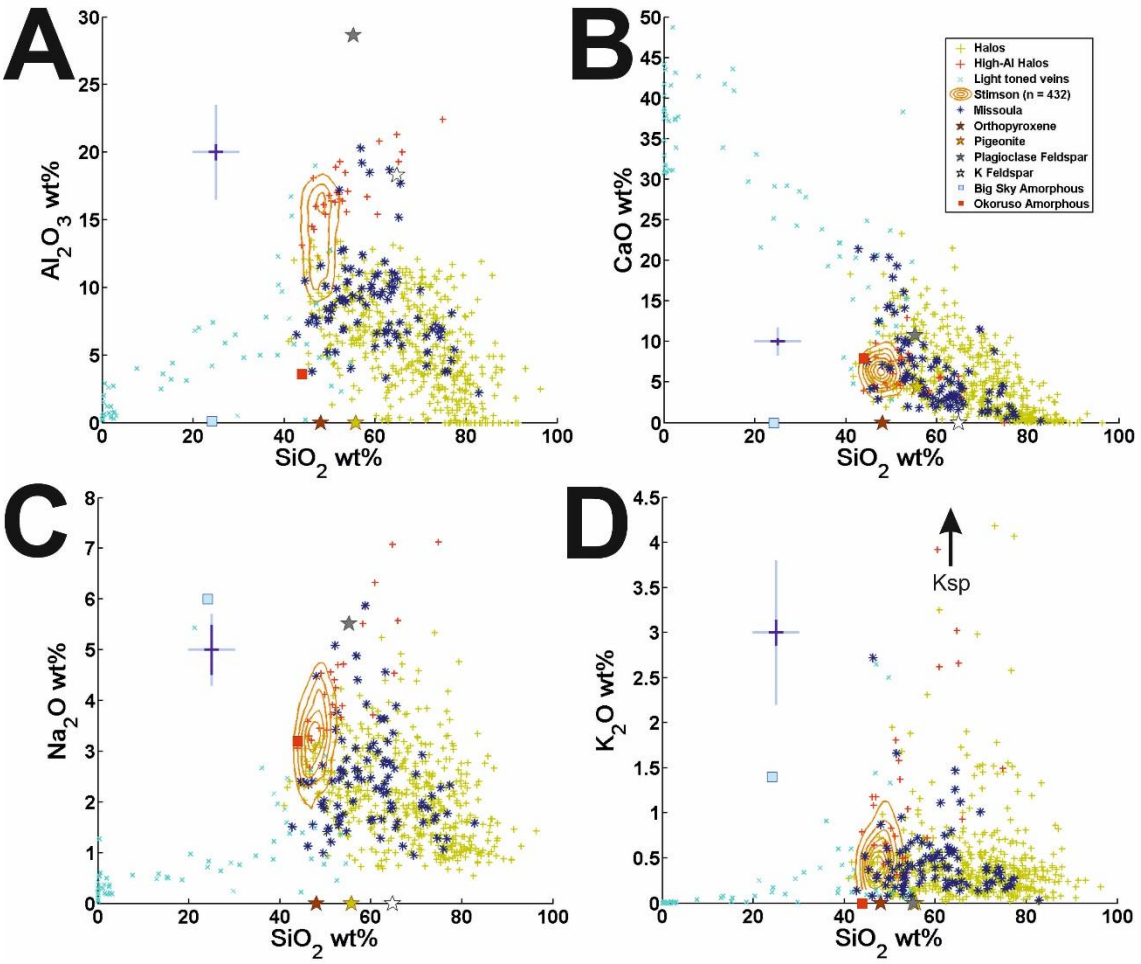

Figure 4.8: Stimson constrained bulk rock density contours and alteration trends (halos shown as yellow and red crosses, Ca-sulfate veins as light blue crosses) with the Missoula outcrop observation point analyses plotted as blue asterisks. Data also included are the Big Sky plagioclase feldspar, K-feldspar, pigeonite and orthopyroxene mineral compositions from Morrison et al. (2018) shown as stars, and the Big Sky and Okoruso amorphous component best estimate from Morrison et al. (2018) shown as squares. The light and dark blue crosses show the ChemCam instrument accuracy and precision respectively to 1σ. Ksp in D) shows the direction of the CheMin derived K-feldspar composition from Morrison et al. (2018) which contains16.9 wt% K_2O.

4.2.3 Cluster analysis results for bulk Stimson

With the results of the density contour analysis confirming that there has been minimal alteration for the constrained Stimson bulk rock dataset, I have conducted an agglomerative, hierarchical cluster analysis using Minitab v17 (Chapter 2.4.3) to identify any unknown groups in the sample set that may not be immediately recognizable using contour analysis. This can better distinguish the endmembers generating the bimodal distributions for Al_2O_3, as well as any other currently unknown groups too fine to distinguish through group- and unit-scale contour analysis alone (see methods section 2.4.3 for details). Results from the multivariate analysis show that seven clusters fit the data best according to the similarity levels and number of observations assigned to each cluster (see methods section 2.4.3.). Each identified cluster is shown to be statistically significant ($p < 0.05$) for the 8 major element oxide variables used to differentiate them (Table 4.2). The model output is provided in the Appendix A.4, and the seven clusters are detailed in Table 4.2 and Fig. 4.9.

According to the dendrogram (Fig. 4.9), Clusters 1 & 4 (similarity level 41.8), 2 & 3 (similarity level 47.8), and 5 & 7 (similarity level 37.7) are closely linked. Cluster 6 is the most distinct to Clusters 1, 4 & 6 with a similarity level of 0.0. Clusters 2, 3, 5 and 7 are more similar to each other than the other clusters, and are distinguished from the rest by a similarity level of 28.9. The cluster with the greatest proportion of observations is Cluster 2 (186), followed by Cluster 3 (159). Clusters 5 and 7 have the fewest observation points associated with them (5 and 4 respectively). Despite the small sample size (<10) associated with Clusters 5 and 7, they are statistically significant according to the calculated p-values of an ANOVA analysis ($p < 0.05$ for all clusters, therefore the clusters are significantly different according to the alternate hypothesis) and possess equivalent average distances to the centroids of the other clusters (~2.00). It is most likely that the

clusters with small observation numbers represent geochemical outliers in the dataset, which is investigated in section 4.3.1.2.

Table 4.2: Mean compositions[1] of the 7 clusters identified in the cluster analysis with the standard deviation, number of observations within each cluster (N), F-values (F) and p-values (p) derived from the F-test statistic[2].

Cluster	1	2	3	4	5	6	7	F	P
SiO_2 (wt%)	47.4 ± 2.8	47.6 ± 2.1	48.9 ± 2.4	54.2 ± 4.6	44.8 ± 4.2	**57.2 ± 2.8**	**41.4 ± 4.4**	22.4	0.000
TiO_2 (wt%)	0.9 ± 0.1	0.9 ± 0.2	0.9 ± 0.2	**1.3 ± 0.4**	**0.7 ± 0.1**	0.9 ± 0.2	0.8 ± 0.1	7.1	0.000
Al_2O_3 (wt%)	**8.5 ± 1.5**	12.3 ± 1.9	15.9 ± 1.7	10.6 ± 1.8	13.0 ± 3.7	**18.3 ± 3.0**	14.2 ± 1.0	107.0	0.000
FeO_T (wt%)	20.2 ± 1.1	19.4 ± 1.5	18.0 ± 2.1	20.0 ± 1.4	15.5 ± 1.5	**9.9 ± 2.9**	**26.4 ± 1.6**	41.3	0.000
MgO (wt%)	**12.2 ± 3.6**	7.7 ± 1.8	5.6 ± 1.5	4.6 ± 1.9	5.8 ± 1.8	**2.2 ± 1.1**	5.3 ± 0.7	55.0	0.000
CaO (wt%)	5.2 ± 1.4	6.5 ± 1.4	6.3 ± 1.8	4.9 ± 1.8	**15.6 ± 1.8**	**3.8 ± 1.7**	5.8 ± 3.6	23.1	0.000
Na_2O (wt%)	**2.2 ± 0.4**	3.0 ± 0.4	3.9 ± 0.7	3.1 ± 0.4	2.5 ± 0.8	**5.8 ± 1.1**	2.9 ± 0.4	67.6	0.000
K_2O (wt%)	**0.3 ± 0.2**	0.6 ± 0.4	0.7 ± 0.4	0.6 ± 0.2	0.4 ± 0.2	**1.8 ± 0.8**	0.5 ± 0.2	15.2	0.000
N	24	186	159	16	5	10	4		

[1]Cluster mean compositions highlighted in yellow are greater than mean bulk Stimson, numbers highlighted in blue are lower than the mean bulk Stimson (given in Table 4.1.) Numbers in bold are the highest compositions in each variable for the derived clusters while those in bold and underlined are the lowest.

[2]P-values were generated using one-way ANOVA on the data assigned to each cluster membership in order to determine statistical significance from one another. Unequal variance was assumed for the ANOVA analysis.

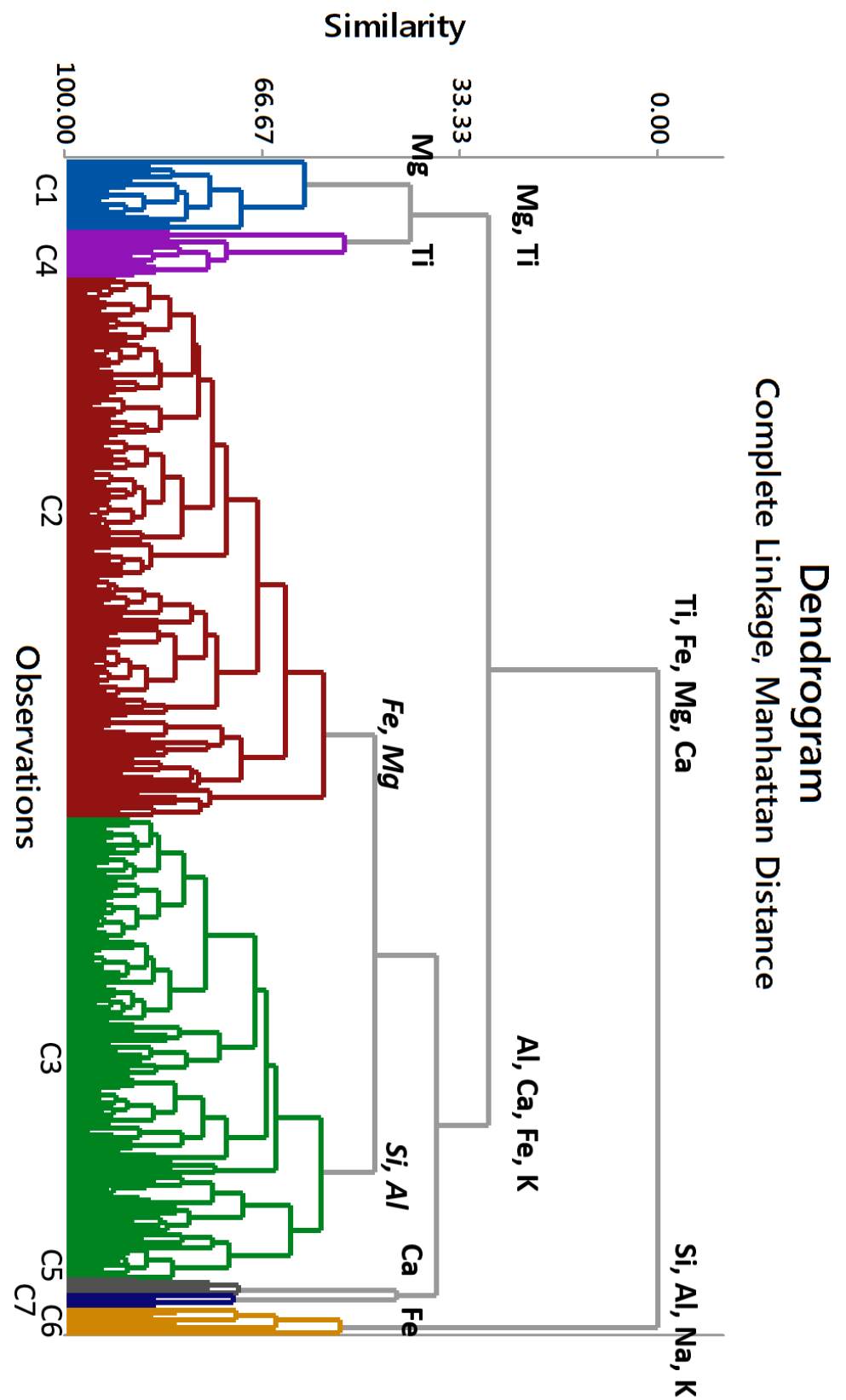

Figure 4.9: Dendrogram derived from the Cluster analysis on bulk Stimson observation points. According to the change in similarity levels, 7 clusters were derived from this formation. Blue = Cluster 1, red = Cluster 2, green = Cluster 3, pink = Cluster 4, grey = Cluster 5, yellow = Custer 6, dark blue = Cluster 7. The geochemical variations that define the different clusters are shown at the branching points with italicised major elements for Clusters 2 and 3 indicating relative major element differences between these two clusters.

After the seven clusters had been identified, each Stimson observation was assigned its cluster membership number, and a one-way analysis of variance (ANOVA) was undertaken to calculate the cluster mean compositions and standard deviations (Table 4.2) that differentiate them in the cluster analysis (Fig. 4.9).

Results suggest that:

- Cluster 1 is defined by high MgO (12.2 ± 3.6 wt%) relative to the other clusters, and low concentrations of Al_2O_3 (8.5 ± 1.5 wt%), Na_2O (2.2 ± 0.4 wt%) and K_2O (0.3 ± 0.2 wt%). Only Al_2O_3 is significantly lower than the bulk Stimson average (13.7 ± 2.9 wt%),
- Cluster 2 is within error of bulk Stimson, but at face value has a slightly higher MgO abundance (7.7 ± 1.8 wt%) and lower Al_2O_3 (12.3 ± 1.9 wt%) compared to the other groups and Stimson average (MgO, 6.9 ± 2.5 wt% and Al_2O_3 13.7 ± 2.9 wt%; Tables 4.1 and 4.2),
- Cluster 3 is also within error of bulk Stimson average compositions, but at face value has moderately elevated, Al_2O_3 (15.9 ± 1.7 wt%), and K_2O (0.7 ± 0.4 wt%), with lower MgO (5.6 ± 1.5 wt%) compared to the other clusters (Table 4.2),
- Cluster 4 possesses moderately high SiO_2 (54.2 ± 4.6 wt%), and high TiO_2 (1.3 ± 0.4 wt%) compared to the other clusters, though these compositions are within error of bulk Stimson due to Cluster 4's high standard deviation (Table 4.2),
- Cluster 5 is most abundant in CaO (15.6 ± 1.8 wt%) relative to the other contours and Stimson average (6.3 ± 2.1 wt%),
- Cluster 6 has the highest SiO_2 (57.2 ± 2.8 wt%), and Na_2O (5.8 ± 1.1 wt%), with the lowest average FeO_T (9.9 ± 2.9 wt%) and MgO (2.2 ± 1.1 wt%) abundances relative to bulk Stimson (Table 4.1), in addition to greater average abundances of

Al_2O_3 (18.3 ± 3.0 wt%), and K_2O (1.8 ± 0.8 wt%) compared to the other clusters, and finally,

- Cluster 7 has high concentrations of FeO_T (26.4 ± 1.6 wt%) compared to bulk Stimson (18.8 ± 2.6 wt%, Table 4.1), and has a lower average SiO_2 (41.4 ± 4.4 wt%) composition relative to the other derived clusters.

4.3. Discussion

4.3.1. Interpretation of the cluster endmembers

Now that a cluster analysis has revealed seven clusters within the Stimson formation, it is fundamental to understand which seven key components these clusters may relate to within the sandstone itself e.g., whether they be varying proportions of common minerals (section 4.3.1.1.) or sandstone cement (section 4.3.1.2.). This must be achieved in order to better understand the implications geographical variations of these clusters may have on mineral sorting, variations in diagenesis across the Stimson formation, or changes in sediment source regions.

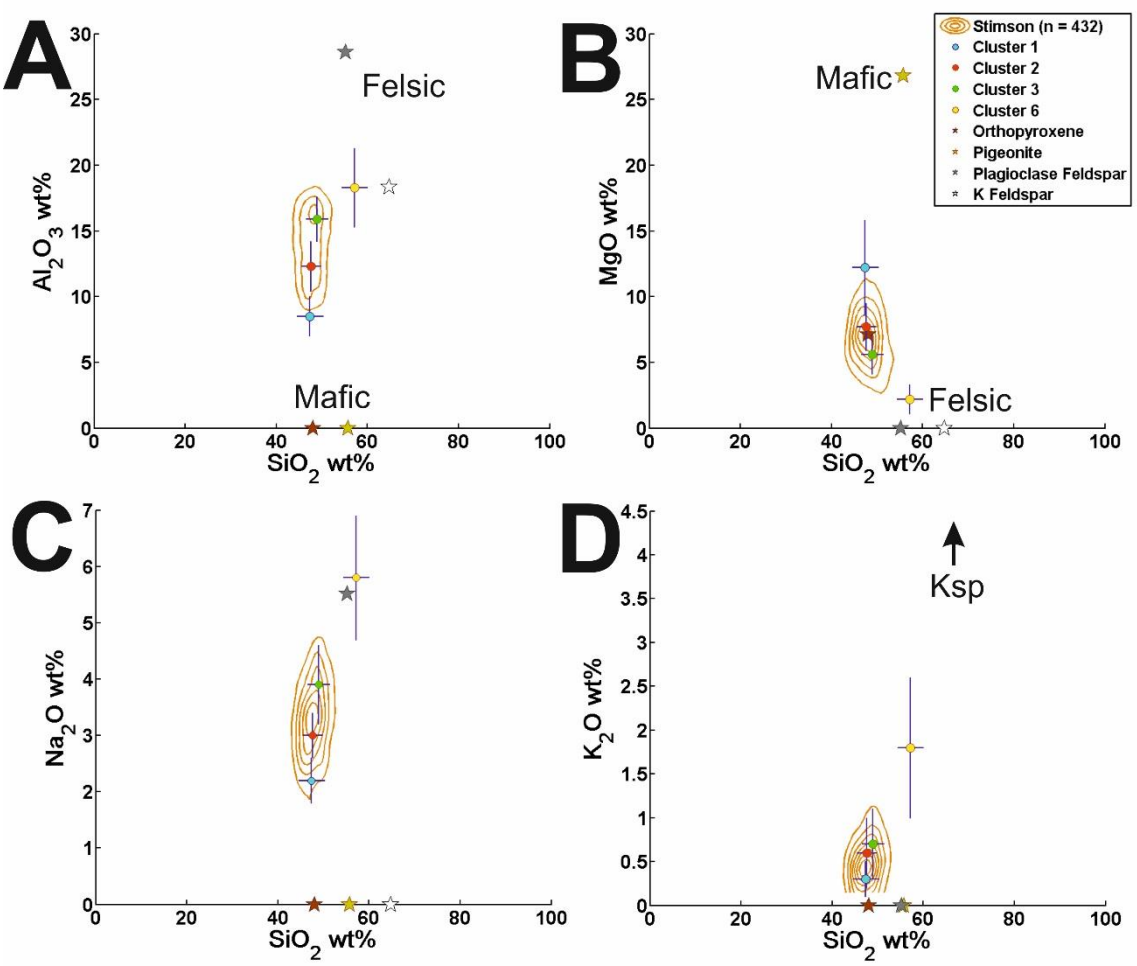

Figure 4.10: Defining major element oxides versus SiO_2 of the Stimson clusters that relate to mineral endmembers (Clusters 1, 2, 3, and 6) plotted with Stimson bulk density contours, and CheMin modelled mineral compositions for Okoruso. Hypothesised endmembers relating to the clusters are labelled as Mafic and Felsic. Data also included are the Big Sky plagioclase feldspar, K-feldspar, pigeonite and orthopyroxene mineral compositions from Morrison et al. (2018) shown as stars. The light and dark blue crosses show the ChemCam instrument accuracy and precision respectively to 1σ

4.3.1.1. Clusters relating to endmember mineral populations

The Stimson sandstone is largely composed of a mixture of primary igneous minerals derived from physical erosion of the source region in addition to the products of diagenesis that cemented the sandstone after its deposition (Banham et al., 2018; Yen et al., 2017). Both Big Sky and Okoruso drilled samples have high crystalline abundances relative to the amorphous component (14.1% Big Sky, 24.6% Okoruso; Morrison et al., 2018; Yen et al., 2017). This makes it likely that the clusters derived from ChemCam

analyses of Stimson sedimentary rock are representative of the different mineral abundances in this sandstone as these are the main components.

Clusters 1 and 6 are the most geochemically distinct from bulk Stimson as they plot the furthest from the density contour focal compositions (Fig. 4.10). They also consistently plot close to the mafic and felsic Big Sky mineral compositions (Fig. 4.10) which respectively constitute 51% and 30% of the total crystalline component, and hence, the majority of the CheMin drilled sample. From this, I interpret Cluster 1 to represent a high proportion of mafic minerals (pigeonite, orthopyroxene) while Cluster 6 represents analyses with a high number of felsic minerals such as feldspar. Out of the seven clusters identified, Clusters 2 and 3 are the most similar in composition to each other and bulk Stimson according to the dendrogram (Fig. 4.9) and when plotted on a density contour diagram (Fig. 4.10). Clusters 2 and 3 also appear to be less extreme variants of Clusters 1 and 6 (Fig. 4.10) and they correlate with the contour subfocal compositions (Fig. 4.10 & 4.11). This suggests that Cluster 2 and 3 analyses have likely targeted a more average Stimson mixing proportion of respective mafic and felsic mineral populations.

When a simple linear regression model is calculated with Al_2O_3 as the response and MgO as the predictor, using only bulk Stimson analyses with Cluster 1, 2, 3, and 6 memberships, a straight line (r^2 = 51.0%; $p < 0.05$) is plotted through the Stimson focus. All Clusters (1, 2, 3 and 6) lie within ChemCam precision of this line (Fig. 4.11). Clusters 2 and 3 are also situated about the focal compositions of the Stimson sandstone. This supports the hypothesis that Clusters 1 and 6 are closest in composition to mineral endmembers with Clusters 2 and 3 correlating with analyses that have targeted a more average Stimson mixing proportion of respective mafic and felsic mineral populations as these are situated within the subfocal compositions (Fig. 4.10 & 4.11).

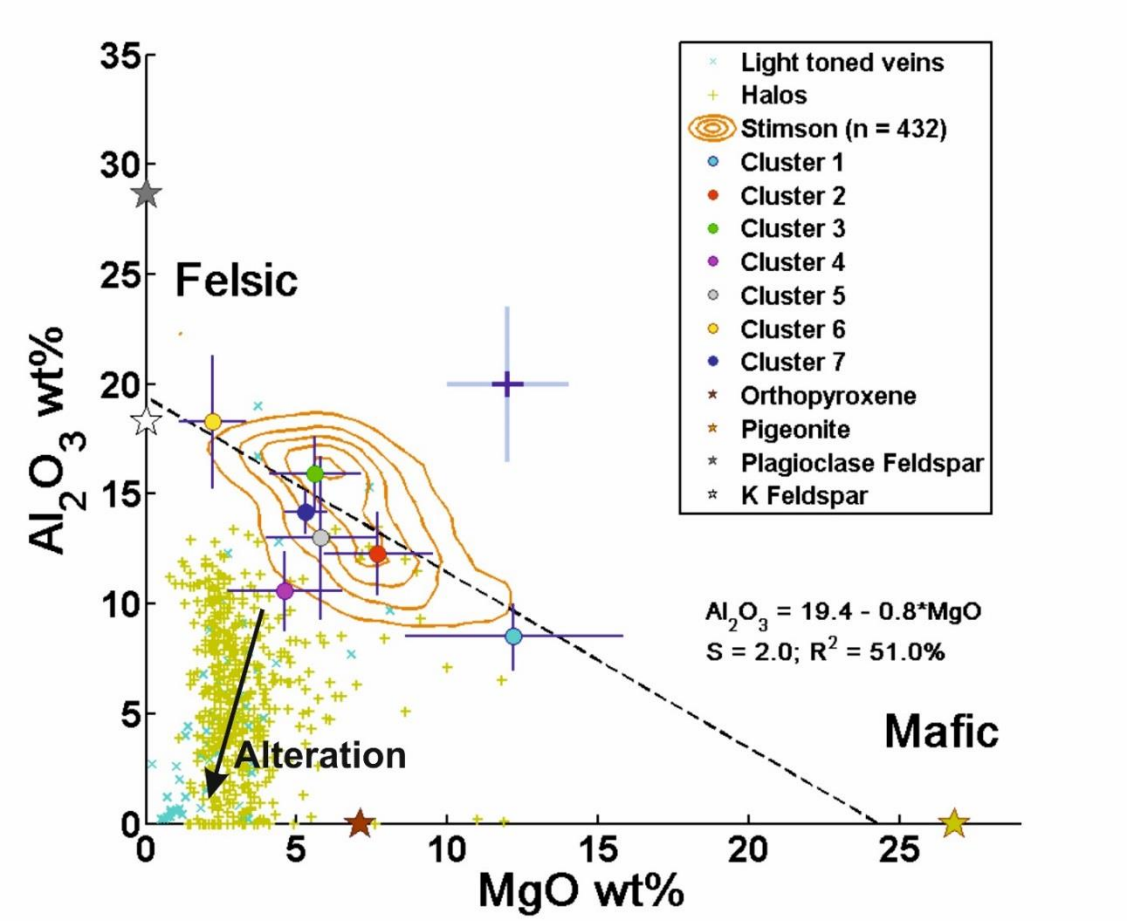

Figure 4.11: A density contour plot of bulk Stimson analyses (level step = $7.5x10^{-4}$) for Al_2O_3 against MgO with Clusters 1–7, Big Sky feldspar, orthopyroxene and pigeonite (Morrison et al., 2018; Yen et al., 2017), Stimson mineral veins and silica-rich halos plotted. Black dashed line is a simple linear regression model for Stimson analyses derived from clusters not associated with alteration or cement (Clusters 1, 2, 3 and 6). Light blue cross-hairs show ChemCam instrument accuracy to compare against calculated CheMin minerals, dark blue show ChemCam precision or cluster standard deviation.

4.3.1.2. Clusters relating to sandstone cement or diagenetic features

Clusters 4, 5 and 7 deviate from the mineral mixing linear regression line detailed in section 4.3.1.1. and plot towards the origin in a plot of Al_2O_3 versus MgO, similar to the $CaSO_4$ mineral vein and halo analyses (Fig. 4.11). These three clusters also show relatively large standard deviations and only differ from the bulk Stimson composition for notably high concentrations in one major element oxide relative to the others (Fig. 4.12). This suggests that these clusters may relate to bulk Stimson that has been geochemically enriched or depleted in certain major elements through a process such as diagenesis.

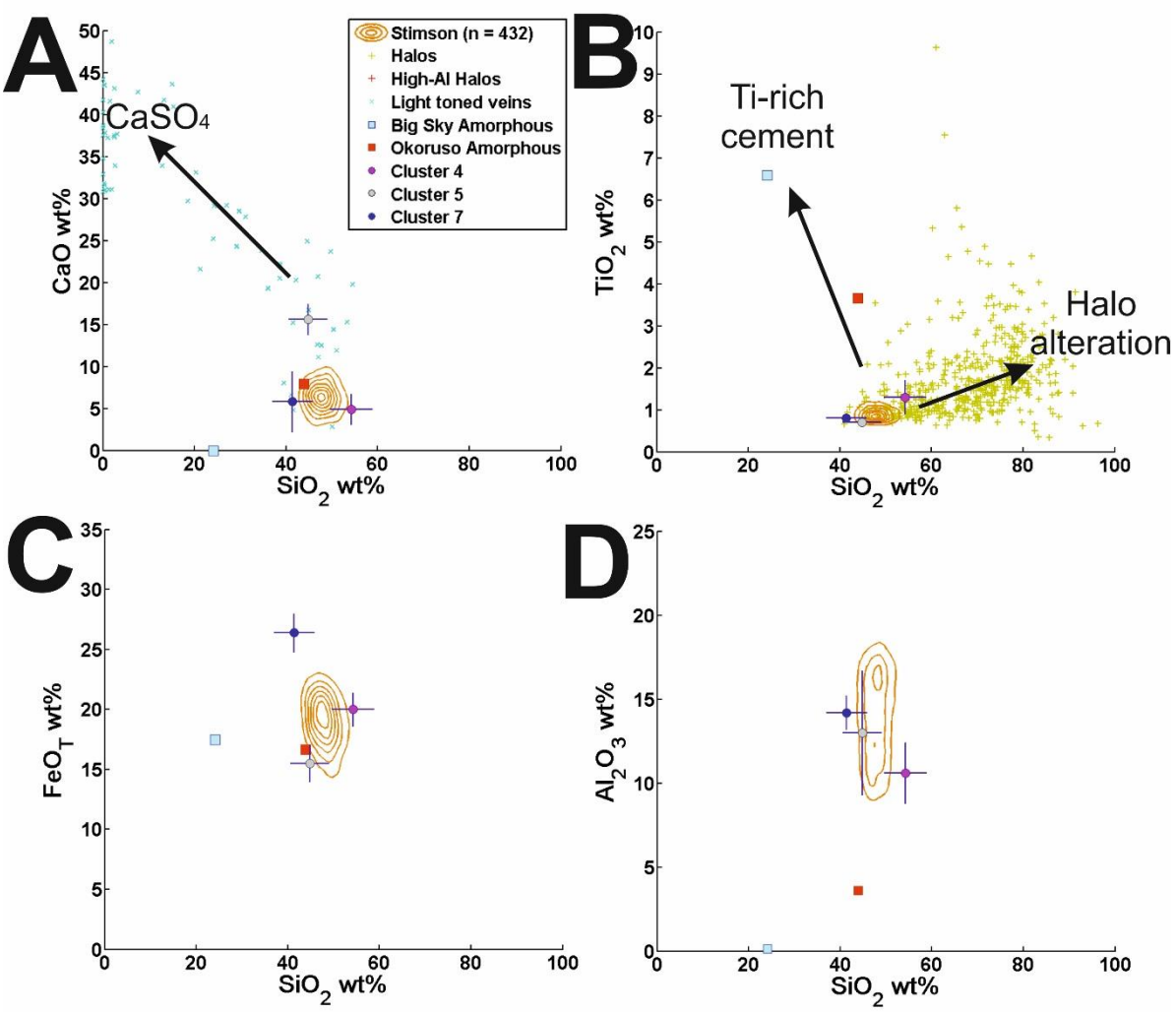

Figure 4.12: Defining major element oxides versus SiO_2 of the Stimson clusters that relate to diagenesis (Clusters 4, 5 and 7) plotted with Stimson bulk density contours, Big Sky and Okoruso amorphous component and calcium-sulfate mineral vein and halo analyses. Possible endmembers relating to the clusters are labelled as $CaSO_4$ (calcium-sulfate cement/grains which may have other hydration states), Ti-rich cement, and halo alteration.

4.3.1.2.1. Ti-rich Cluster 4

Cluster 4 analyses are enriched in TiO_2 relative to bulk Stimson (Fig. 4.12 B). So far, there are two possible explanations for high TiO_2 concentrations: contamination from the silica-rich halos, or a TiO_2-rich cement/amorphous component. None of the observation points that constitute the Cluster 4 group show any association with these alteration halo features in the Mastcam, Navcam or RMI images. Instead, Cluster 4 analyses only constitute one or two observation points per ChemCam target, indicating that

they relate to a much smaller process than the large, metre-scale halo features in the Murray and Stimson formation (Frydenvang et al., 2017; Yen et al., 2017).

The majority of the TiO_2 content within the Stimson Big Sky and Okoruso drilled samples have been allocated to the amorphous component (14–25 wt%) whose compositions were modelled using a FULLPAT analysis by Morrison et al. (2018) and Yen et al. (2017). Therefore, if TiO_2 is present only in the amorphous component it may relate to localised pockets of Ti-enrichment in the Stimson sandstone cement associated with Ti-rich minerals such as titanomagnetite, brookite or anatase. These minerals are common microcrystalline constituents of terrestrial sandstone cements in addition to iron oxides and can form through the diagenesis of Ti-bearing igneous minerals such as ilmenite, pyroxene or biotite (Pe-Piper et al., 2011; Deer, Howie and Zussman, 1992; Morad and Aldahan, 1982). As pyroxene is an abundant mineral in the Stimson sandstone (Yen et al., 2017) and ilmenite has been detected in small quantities in the aeolian Rocknest sand shadow at Gale crater (Bish et al., 2013), diagenesis of these Ti-bearing minerals is my preferred hypothesis to explain the Ti-rich Cluster 4 analyses.

4.3.1.2.2. Ca-rich Cluster 5

The most obvious source of the high-CaO content in Cluster 5 analyses (Fig. 5.12 A) is the calcium-sulfate diagenetic features present throughout Gale crater's known stratigraphy, such as calcium-sulfate mineral veins (L'Haridon et al., 2018a; Schieber et al., 2017; Siebach et al., 2017a; Nachon et al., 2014). Calcium-sulfate has also been considered as a cement component at the base of the Stimson formation in the Marias Pass locality (Newsom et al., in rev; Siebach et al., 2017b, see also Fig. 4.8 and section 4.2.2.) and has been identified with both APXS and ChemCam at this locality. However, the analyses that constitute Cluster 5 are not situated within any obviously veined outcrop, nor

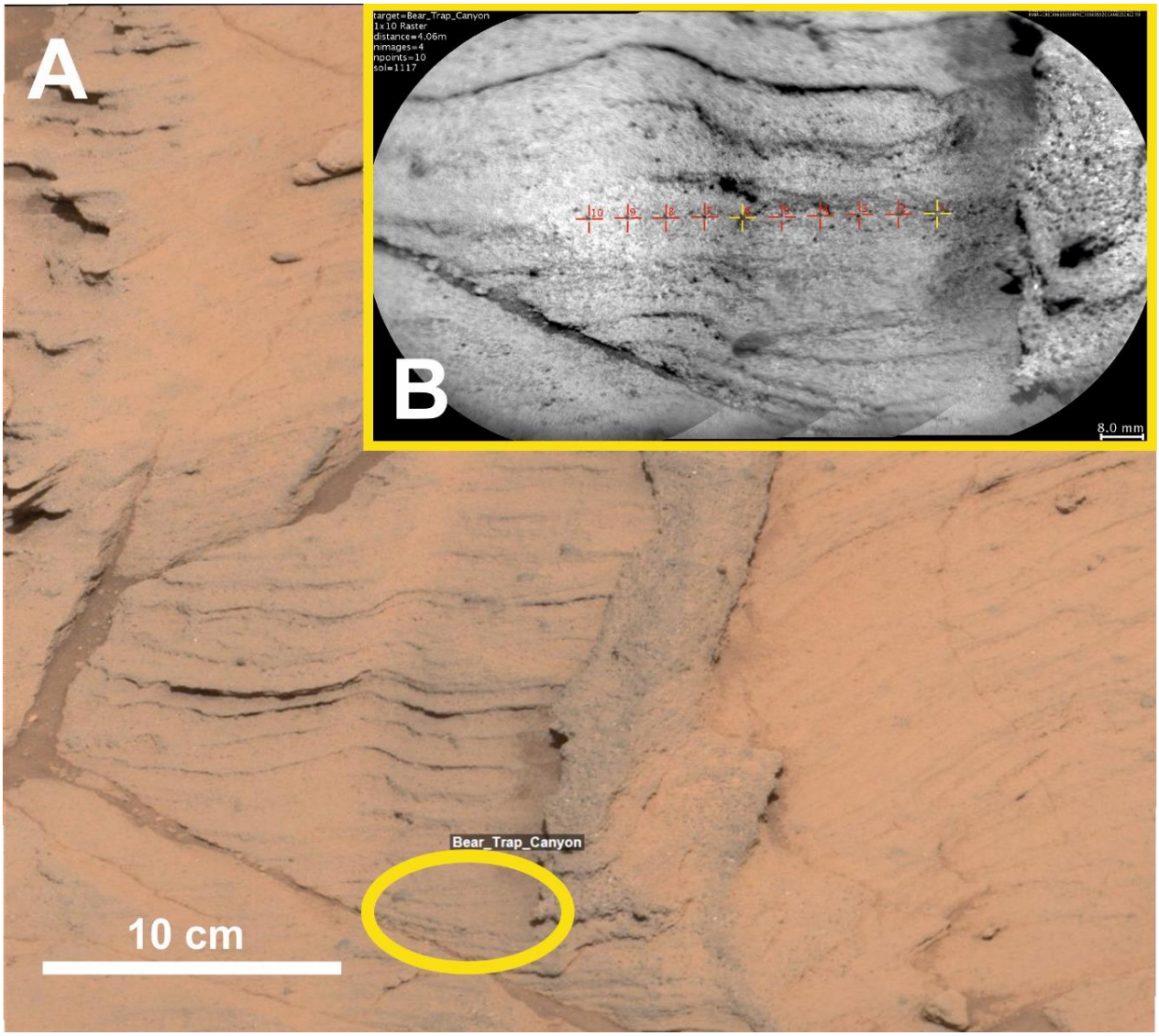

Figure 4.13: A) Mastcam image (mcam004993, sol 1120) and B) RMI mosaic of ChemCam target Bear Trap Canyon (sol 1116). This target has two observation points #1 and #6 (highlighted in yellow crosshairs in the RMI image) that group into the high-CaO Cluster 6 despite no obvious mineral veins, speckled calcium-sulfate cement or white grains targeted.

are they proximal to any calcium-sulfate related feature. The ChemCam LIBS points that have analysed calcium-sulfate cement in the Missoula outcrop generally show a strong CaO content (10–40 wt%) coupled with a substantial depletion in totals (<10 wt%; Newsom et al., in rev.). In RMI and MAHLI images, this cement occurs as rinds around clasts, or has a speckled appearance in the bedrock (Newsom et al., in rev.). These visual characteristics of calcium-sulfate cement have not been observed in the Cluster 5 targets that show elevated CaO-concentrations relative to Stimson bedrock (e.g., Fig. 4.13).

Additionally, if calcium-sulfates accounted for a 9.3 wt% increase in CaO content with respect to bulk Stimson, such as is implied by the cluster analysis, this would require an increase of the calculated difference of SO_3 by 13.3 wt % and 19.3 wt% respectively depending on whether gypsum or anhydrite is assumed to be present. This would skew the totals outside the acceptable 95–105 % range and warrant exclusion from the constrained bulk rock dataset. Therefore, Ca-sulfate can be excluded from the likely phases that host the excess CaO for the constrained ChemCam Stimson dataset presented here.

Alternatively, CaO-rich LIBS analyses may relate to a cement derived from the alteration of Ca-bearing minerals such as plagioclase feldspar rather than the presence of $CaSO_4$ cement. The Okoruso drilled sample contains 7.9 wt% CaO and 0.4 wt% SO_3 in its amorphous component according to the mass balance calculation on APXS and CheMin analyses by Morrison et al. (2018, see also Table 4.3). This is relative to the negligible quantity of CaO calculated in Big Sky's amorphous component (Table 4.3; Morrison et al., 2018; Yen et al., 2017) suggesting that calcium may have been leached from the Ca-bearing minerals into the amorphous component, particularly within the concretion-rich Stimson that the Okoruso drill sampled. The leaching of CaO would provide localised enrichments in the sedimentary units that are not necessarily related to SO_3 and would consequently not show a depletion in ChemCam total sums of oxides. Calculated CaO concentrations in plagioclase feldspar and pigeonite detected at both sites are shown to vary (Morrison et al., 2018), with the concretion-rich Okoruso sample lower in CaO (8.0 wt% for plagioclase and 3.4 wt% for pigeonite) compared to Big Sky (10.8 wt% for plagioclase and 4.4 wt% for pigeonite). Ca^{2+} ions may have been mobilised from plagioclase feldspar and pigeonite during the burial diagenesis that formed the sandstone cement and concretions. As concretions are concentrated pockets of cement, this could explain why CaO is more enriched in the concretion-rich Stimson amorphous component relative to normal Stimson.

Table 4.3: Adapted from Morrison et al. (2018), this table gives the calculated CheMin sample APXS, amorphous (Amorph), and crystalline (Xtal) compositions in wt% whereby the amorphous and crystalline components are normalised to 100%. The proportion (Prop.) is the minimum amount of amorphous material and maximum quantity of crystalline material present in a sample based on mass balance calculations.

	Big Sky			Okoruso		
	APXS	*Xtal*	*Amorph*	*APXS*	*Xtal*	*Amorph*
SiO_2	42.95	46.36	24.13	45.13	45.55	43.91
TiO_2	1.00	0.00	6.59	0.94	0.00	3.65
Al_2O_3	11.52	13.57	0.12	9.64	11.72	3.62
Cr_2O_3	0.51	0.00	3.36	0.41	0.00	1.59
FeO_T	21.55	22.30	17.48	22.40	24.38	16.67
MnO	0.40	0.00	2.64	0.39	0.00	1.52
MgO	7.49	6.21	14.68	8.97	7.04	14.54
CaO	6.12	7.22	0.00	6.37	5.82	7.94
Na_2O	3.08	2.55	6.03	3.08	3.03	3.24
K_2O	0.46	0.29	1.40	0.37	0.50	0.00
P_2O_5	0.72	0.55	1.69	0.75	0.68	0.97
SO_3	3.35	0.89	17.08	0.96	1.15	0.41
Cl	0.73	0.00	4.81	0.50	0.00	1.94
F	--	--	0.05	--	--	0.06
H_2O	--	0.00	--	--	0.08	--
Prop.	--	0.86	0.14	--	0.75	0.25

4.3.1.2.3. Fe-rich Cluster 7

The high FeO_T average composition of Cluster 7 (26.4 ± 1.6 wt%) likely pertains to LIBS points that have targeted a higher proportion of iron oxides in the Stimson sandstone crystalline component (Morrison et al., 2018; Siebach et al., 2017b; Yen et al., 2017). Both Okoruso and Big Sky have high FeO_T contents for their calculated crystalline components (22.3 wt% and 24.4 wt% respectively; Table 4.3) that relates to the high proportions of magnetite and hematite in each sample (16.2 wt% iron oxides in Big Sky and 18.4 wt% iron oxides in Okoruso; Morrison et al., 2018; Achilles et al., 2017; Yen et al., 2017). These iron oxides are more abundant in the ancient Stimson aeolian deposit relative to the modern Bagnold dunes and Gale crater soil deposits (Achilles et al., 2017), as they are part

of the Stimson sandstone cement (Siebach et al., 2017b). An iron oxide cement is also hypothesised for other lithified units in Gale crater (e.g., Treiman et al., 2016; Anderson et al., 2015; Blaney et al., 2014), making it likely that Cluster 7 analyses also relate to observation points that have analysed a high proportion of iron oxide cement component in the Stimson sandstone.

4.3.2. Geographic variations of mafic and felsic clusters and their effect on bulk geochemistry

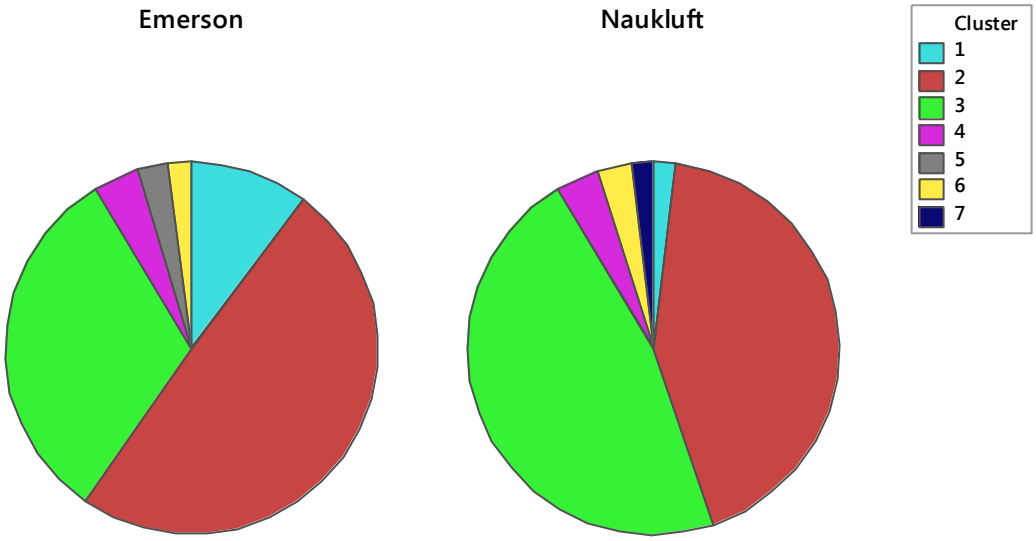

Figure 4.14: Pie Charts showing the proportion of each cluster between the Emerson Plateau and Naukluft Plateau Stimson localities.

Several studies of aeolian mineral sorting of basaltic sediments on the Earth and Mars use major element oxides such as Al_2O_3, SiO_2, MgO and FeO_T as proxies for identifying the extent of mineral sorting a deposit has undergone (e.g., Lapotre et al., 2017; Baratoux et al., 2011; Mangold et al., 2011; Stockstill-Cahill et al., 2007), therefore it is important to know whether the geochemical variation identified in the Stimson formation can be used to the same effect. Overall, the Emerson plateau has a higher proportion of

points within the mafic cluster memberships (Clusters 1 and 2) compared to Stimson analysed at the Naukluft Plateau which in turn has a much greater proportion of points associated with felsic clusters (Clusters 3 and 6). Clusters 1, 2, 3, and 6 are all defined by relative differences in Al_2O_3, MgO, CaO, Na_2O and K_2O. To investigate whether this variation in mafic and felsic mineral clusters between the Emerson and Naukluft Plateaus has significantly influenced their bulk geochemical composition, equivalence tests were used according to the method outlined in Chapter 2.4.4.

Table 4.4: Results of the two-way equivalence tests for all major elements across the Stimson Emerson Plateau and Naukluft Plateau. Table shows the difference and standard error (SE) of the unit means, Equivalence Interval (EI) and the associated T- and P-values of the differences between the equivalence intervals and the confidence intervals from the mean.

	Diff of means	SE of diff	EI	Difference ≤ -EI		Difference ≥ -EI		Equiv
				T-value	P-value	T-Value	P-value	(Y/N)
SiO_2	0.27	0.28	±1.50	6.30	0.00	- 4.40	0.00	Y
TiO_2	0.05	0.02	±0.14	5.70	0.00	-11.75	0.00	Y
Al_2O_3	-0.71	0.30	±0.57	4.34	0.00	0.49	0.69	N
FeO_T	-0.08	0.25	±1.80	6.82	0.00	-7.48	0.00	Y
MgO	-1.27	0.26	±0.49	-2.99	1.00	-6.76	0.00	N
CaO	-0.33	0.17	±0.42	0.50	0.31	-4.39	0.00	N
Na_2O	0.37	0.09	±0.49	10.00	0.00	-1.38	0.09	N
K_2O	0.11	0.05	±0.14	5.19	0.00	-0.66	0.26	N

In this study, the two groups are the two Stimson localities (Emerson and Naukluft Plateau), and the equivalence limits were defined according to 1σ ChemCam precision (listed in the Appendix Tables A.4.2–A.4.9). Despite the apparent uniformity of bulk Stimson as shown in Fig. 4.5, the two-sample equivalence tests of the Emerson Plateau and Naukluft Plateau have identified statistically significant geochemical variation between them in relation to Al_2O_3, MgO, CaO, Na_2O and K_2O (Table 4.4 and Appendix Tables A.4.2–A.4.9). SiO_2, TiO_2, and FeO_T on the other hand were shown to be equivalent

between the localities. Density contours of the two localities support the results of the equivalence tests (Fig. 4.15 D and E, and Fig. 4.16 C). Therefore, geochemical variation does exist between these two localities which may have been influenced by the mineral sorting regime.

According to calculated CheMin mineral compositions by Morrison et al. (2018), Al_2O_3 is determined by the proportion of the felsic minerals plagioclase and K-feldspar, MgO is influenced by the abundances of the mafic minerals pigeonite and orthopyroxene, CaO is situated within plagioclase feldspar and pigeonite, Na_2O is only located within plagioclase feldspar, and K_2O within K-feldspar (Figs. 4.15 and 4.16; see also Morrison et al., 2018; Yen et al., 2017). Histograms of Al_2O_3, MgO, CaO, Na_2O and K_2O for ChemCam data with Cluster 1, 2, 3, and 6 memberships between the Emerson and Naukluft Plateaus all show peaks that approximately align with the modelled CheMin compositions of the Big Sky (Emerson) and Okoruso (Naukluft) crystalline components (Fig. 4.15 and 4.16). These results suggests that, similar to the previous studies of aeolian mineral sorting in basaltic sands, these major element oxides may be usable as proxies to determine the extent of mineral sorting that has occurred in the ancient Stimson dune field. However, as the Stimson formation has been lithified, diagenesis may have reduced the effectiveness of certain major element oxides for use as proxies. The following subsections investigate which major element oxides are most appropriate to use when identifying variations in mafic and felsic minerals across the Stimson formation.

4.3.2.1. Assessing CaO, Na_2O, K_2O and Al_2O_3 as reliable proxies for felsic minerals in the Stimson formation

As discussed in section 4.3.1.2.2., the calculated plagioclase feldspar compositions of the Emerson Big Sky drilled sample and Naukluft Okoruso drilled sample vary between

both sites, particularly in regards to CaO, as burial diagenesis has likely leached Ca^{2+} from the plagioclase feldspars into the amorphous component creating Cluster 5. This is reflected in the constrained ChemCam analyses for Cluster 1, 2, 3 and 6 analyses with Emerson Stimson ChemCam data showing a higher CaO peak concentration at 6.8–7.3 wt% in its histogram compared to Naukluft Stimson (5.8–6.3 wt%), mirroring the Morrison et al. (2018) feldspar compositions. The ChemCam analyses also show a minor secondary peak for CaO identified in the Emerson analyses at 5.8–6.3 wt%, equivalent to the lower CaO Naukluft peak composition. ChemCam derived Na_2O concentrations also differ with peaks in Emerson Stimson at 2.6–2.9 wt% and 3.1–3.4 wt% Na_2O, but only one peak at 3.1–3.4 wt% in the Naukluft Stimson analyses (Fig. 4.15). This change in Na_2O likely relates to the leaching of Ca^{2+} during aqueous alteration as this will cause a decrease in the feldspar anorthite number (Deer, Howie and Zussman, 1992). As a result, CaO and Na_2O concentrations may help to distinguish the abundance of feldspars in the Stimson formation, but as the leaching of Ca^{2+} likely caused a variation in the plagioclase anorthite number, these elements are not the best proxy to use to distinguish mineral sorting in the ancient dune field.

CheMin analysis of the Big Sky and Okoruso drill holes show that K_2O is largely present within the crystalline component. Both Stimson drill holes also contain trace amounts of K-feldspar (2–3 wt%) which is the most likely mineral in the Stimson assemblage to have influenced potassium variations, particularly given that there are no clays detected in this formation (Morrison et al., 2018). Overall, the Naukluft Plateau has a broader peak in the histogram covering a larger range in K_2O compositions than Stimson in the Emerson Plateau (Fig. 4.15; 0.3–0.5 wt% Big Sky compared to 0.3–0.7 wt% Okoruso). For the Big Sky drill hole, K-feldspar with a modelled crystal chemistry of 17 wt% K_2O is expected to provide an average of ~0.3 wt% K_2O. This CheMin modelled K-feldspar contribution is the approximate composition of the Emerson Plateau histogram's peak

ChemCam K_2O (Fig. 4.15). The Okoruso drilled sample has a calculated ~1 wt% greater K-feldspar abundance than Big Sky, which is estimated to provide an average K_2O composition of ~0.5 wt% (Morrison et al., 2018). Once again, this calculated contribution of K_2O from CheMin analyses is similar to the bulk composition of ChemCam analyses in the Naukluft Plateau (Fig. 4.15). Bulk sediment geochemical variation of K_2O between the two localities does therefore relate to variations in K-feldspar mineral proportions, though as K_2O is low in abundance across the Stimson formation, this is also not an ideal geochemical proxy to use when investigating mineral sorting between the two localities.

According to the CheMin derived compositions for the Stimson formation's drilled samples, Al_2O_3 is predominately situated within the crystalline components of both Stimson analyses (13.6–11.7 wt% Al_2O_3), particularly in plagioclase feldspar and K-feldspar (Morrison et al., 2018). ChemCam analyses show bimodal peak concentrations, with low Al_2O_3 peaks (11.5–12.5 wt% for Emerson and Naukluft), similar to the CheMin derived crystalline Al_2O_3 concentrations (Fig. 4.16). Both groups also have high Al_2O_3 peaks (15.5–16.5 wt% for the Emerson Plateau and 16.5–17.5 wt% for the Naukluft Plateau) that lie closer towards the CheMin derived Al_2O_3 composition of pure feldspar (up to 28.6 wt% Al_2O_3). Therefore, these high Al_2O_3 peaks likely relate to ChemCam analyses that have preferentially hit sandstone richer in plagioclase grains (Fig. 4.16). This second histogram peak is also notably higher in Al_2O_3 for the Naukluft Plateau than the Emerson Plateau suggesting that this area has a higher abundance of feldspar-rich targets.

Figure 4.15 (next page): Histograms to show the distribution A) CaO, B) Na_2O, and C) K_2O between the Emerson Plateau and Naukluft Plateau localities. CheMin derived crystalline (Xtal), amorphous component (amorph) compositions and crystal chemistries of plagioclase feldspar (plag), K-feldspar (ksp), pigeonite (pig), and orthopyroxene (opx) from Morrison et al. (2018) are shown for comparison. Also shown are the approximate total crystalline compositions including altered ($Plag_{alt}$) and unaltered ($Plag_n$). Density contour plots of the analyses associated with Clusters 1, 2, 3 and 6 at both Stimson localities (level step = 0.001) for A) CaO and B) K_2O against Na_2O are also shown along with ChemCam precision (1σ) as a dark blue cross and the mean compositions of the entire dataset as diamonds.

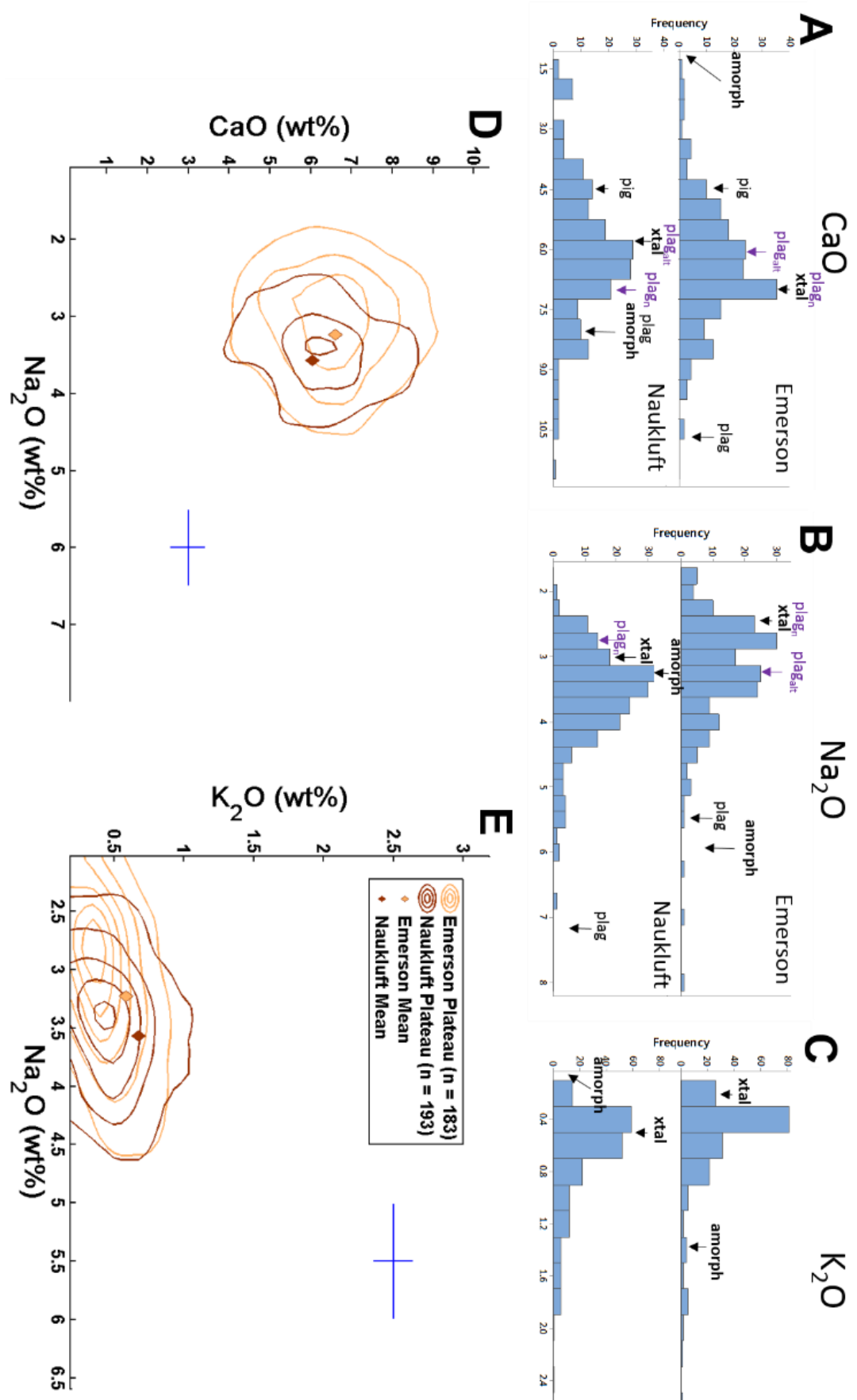
A
CaO
Frequency
amorph
pig
plag_alt
plag_n
xtal
plag
Emerson
Naukluft
B
Na2O
C
K2O
Ksp
D
CaO (wt%)
Na2O (wt%)
E
K2O (wt%)
Emerson Plateau (n = 183)
Naukluft Plateau (n = 193)
Emerson Mean
Naukluft Mean

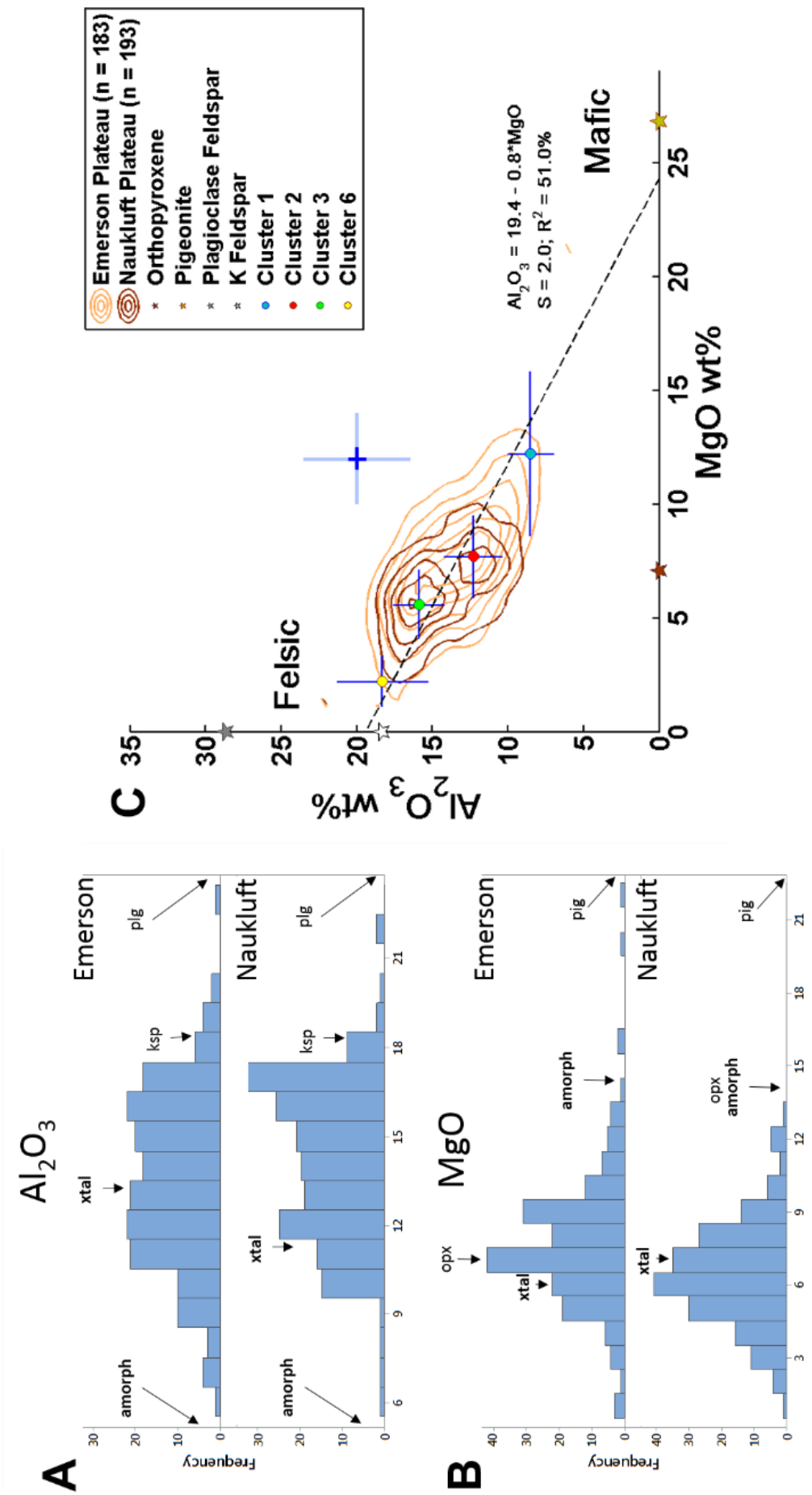
C
Emerson Plateau (n = 183)
Naukluft Plateau (n = 193)
Orthopyroxene
Pigeonite
Plagioclase Feldspar
K Feldspar
Cluster 1
Cluster 2
Cluster 3
Cluster 6
Al2O3 = 19.4 - 0.8*MgO
S = 2.0; R2 = 51.0%
Felsic
Mafic
Al2O3 wt%
MgO wt%
A
Al2O3
Emerson
Naukluft
plg
ksp
xtal
amorph
Frequency
B
MgO
pig
opx
xtal
amorph

Figure 4.16 (previous page): Histogram plots of the two Stimson localities; Emerson Plateau and Naukluft Plateau for A) Al_2O_3 and B) MgO. CheMin derived crystalline (Xtal), amorphous component (amorph) compositions and crystal chemistries of plagioclase feldspar (plag), K-feldspar (ksp), pigeonite (pig), and orthopyroxene (opx) from Morrison et al. (2018) are shown for comparison. Density contours of these two localities for Al_2O_3 against MgO is also given in C) showing their relationship to the mafic-felsic mineral mixing line, Stimson mineral compositions (Morrison et al., 2018) and Clusters 1–3 and 6. ChemCam precision (1σ) is shown as a dark blue cross while accuracy (1σ) for comparison between ChemCam data and CheMin mineral compositions is shown in light blue. For the contours: level step = 0.0005, bin size = 50, smoothing = 30.

4.3.2.2. Using MgO as a proxy for mafic minerals in the Stimson formation

Similar to the previous analyses, the histograms (Fig. 4.16) show that peak compositions for MgO approximate the concentration of MgO provided by the CheMin samples crystalline components. This supports that MgO for the constrained bulk dataset is largely dictated by the main Mg-bearing minerals present in the Stimson formation; pigeonite and orthopyroxene (Morrison et al., 2018). Different histogram distribution patterns are present between the two localities and are mirrored in the density contour plot (Fig. 4.16 C); the Naukluft Plateau shows a relatively normal, unimodal distribution in MgO about a peak of 5.5–6.5 wt% with few outliers, while Emerson Plateau Stimson is bimodal with peaks at 6.5–7.5 wt% and 8.5–9.5 wt%. Emerson Plateau Stimson also has a heavy tail towards high-MgO compositions (up to 21.6 wt%).

Similar to the cause of bimodality in the Al_2O_3 histograms, the high MgO peak for Emerson Plateau may represent ChemCam analyses that have sampled a higher proportion of mafic minerals compared to felsic ones. Alternatively, MgO is one of the most abundant major elements within the amorphous component (~15 wt% for both drill sites), and has a higher derived MgO composition than the crystalline component for both sites (Fig. 4.16). Therefore, the smaller histogram peak and possible the tail to high MgO concentrations could be from ChemCam sampling a greater proportion of MgO-rich amorphous

component. One Mg-bearing mineral not identified in the Stimson formation is olivine which is unexpected given that strong olivine signatures have been detected from orbit in active dunes at multiple locations across Mars (Lapotre et al., 2017; Bourke et al., 2008; Hayward et al., 2007). Furthermore, the currently active Bagnold dunes contain a notable proportion of olivine in their crystalline components (25.8–18.2 wt%; see Table 4.5) in addition to plagioclase, augite and pigeonite and negligible MgO in the amorphous component (Rampe et al., 2018; Achilles et al., 2017). Hausrath et al. (2018) conducted an aqueous alteration model to test if diagenesis of the Bagnold dune Gobabeb scooped sample, which is rich in olivine, could generate a high abundance of Fe-oxide cement. In their models, olivine dissolution in solutions of pH 6–8 precipitates significant magnetite (~5–6 vol%) with slight depletions in all major elements and slight enrichments in S, Cl, Zn and Br. The MgO and FeO_T from the olivine may now therefore reside in the amorphous component of the Stimson sandstone (Table 4.3). Provided olivine burial diagenesis in the Stimson formation was isochemical, the variation in MgO concentrations can still be used as a reliable proxy for mafic mineral proportions. The next subsection discusses the likelihood that this diagenesis was isochemical through comparing the Stimson formation's bulk geochemistry to that of the first Bagnold dune campaign.

Table 4.5: Calculated crystalline abundances from CheMin XRD analyses of Stimson drilled samples (Big Sky), scooped soil (Rocknest) and scooped dune (Gobabeb and Ogunquit Beach). Abundances reported in wt. %.

	Big Sky[1]	Okoruso[1]	Gobabeb[1]	Ogunquit Beach[2]	Rocknest[1]
augite	0.0	0.0	22.0	15.7	18.1
olivine	0.0	0.0	25.8	18.2	20.7
plagioclase	45.7	41.9	36.5	47.1	40.6
pigeonite	20.2	20.8	10.6	10.2	12.4
orthopyroxene	10.0	11.0	0.0	0.0	0.0
magnetite	12.6	17.3	2.1	2.5	2.8
hematite	3.6	1.1	0.9	2.3	1.5
ilmenite	0.0	0.0	0.0	0.0	1.4
K-feldspar	1.7	2.9	0.0	0.0	0.0
bassanite	0.0	1.2	0.0	0.0	0.0
quartz	1.6	1.2	0.8	1.6	1.0
tridymite	1.8	0.0	0.0	0.0	0.0
fluorapatite	1.3	1.6	0.0	0.0	0.0
anhydrite	1.5	0.8	1.3	2.3	1.0

[1]*Crystalline abundances from Morrison et al. (2018)*

[2]*Crystalline abundances from Rampe et al. (2018)*

4.3.2.2.1. Constraining the amount of olivine in the Stimson formation compared to the Bagnold dunes

The actively migrating Bagnold dunes in Gale crater have been sampled by the *Curiosity* rover in two locations (Fig. 4.17). The first campaign analysed two barchan dunes informally named Namib and High dune (Bridges and Ehlmann, 2018) with a CheMin analysis conducted at Namib on the Gobabeb sample scooped adjacent to the crest of a secondary slip-face ripple (Achilles et al., 2017). The second campaign analysed linear dunes at the Nathan Bridges dune and Mount Desert Island ripple field (Lapotre and Rampe, 2018) with a CheMin scooped sample taken from a ripple trough at Mount Desert Island (Rampe et al., 2018). These campaigns showed that the Bagnold dunes have a basaltic geochemistry (O'Connell-Cooper et al., 2018; Cousin et al., 2017a; O'Connell-Cooper et al., 2017) with the coarse grains composed of primary igneous minerals,

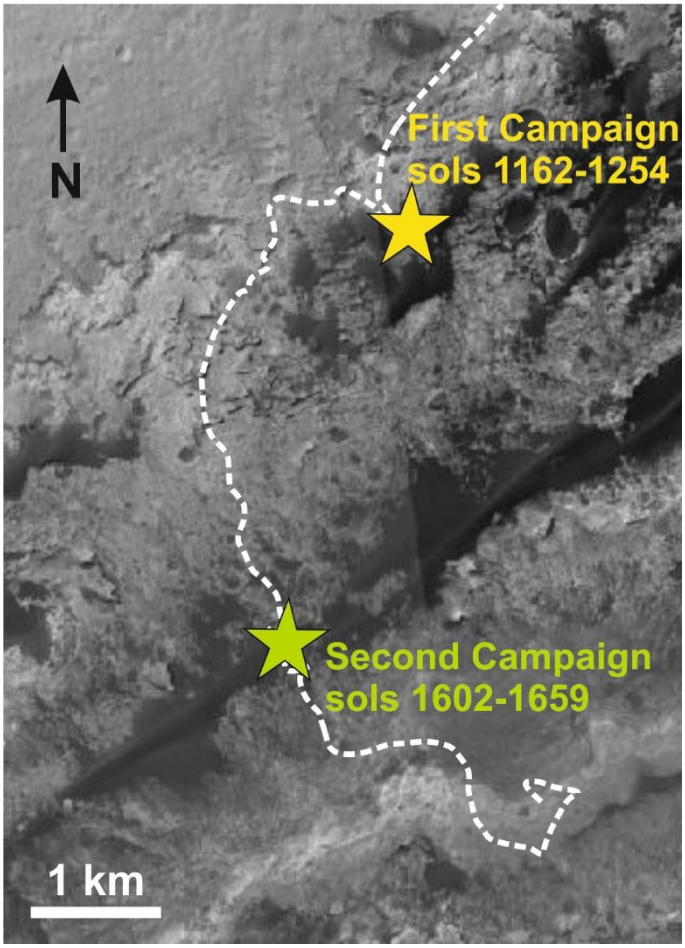

Figure 4.17: Map showing the locations of phase 1 and phase 2 of the Bagnold dune campaigns. The first campaign was conducted on two barchan dunes; High dune and Namib dune, while the second analysed the Nathan Bridges linear dune and Mount Desert Island ripple field. HiRISE image used for the base of the map.

specifically olivine, augite and plagioclase (Rampe et al., 2018; Achilles et al., 2017). In general, the Bagnold dunes along with Gale crater's other aeolian deposits contain a much greater proportion of analyses lower than the acceptable total sum of oxide range used in this study (95–105%, see Appendix) due to higher abundances of S, Cl, H, and other volatiles in the recent sediment deposits relative to the lithified units (Cousins et al., 2017a; O'Connell-Cooper et al., 2017). Although the active aeolian dunes generally have less volatiles compared to Gale crater soils (Cousin et al., 2017a), volatile contents are still substantial enough to complicate a direct comparison of the active dunes and constrained Stimson data. Hence, I have normalised ChemCam dune analyses to 100% for direct comparison with the Stimson formation.

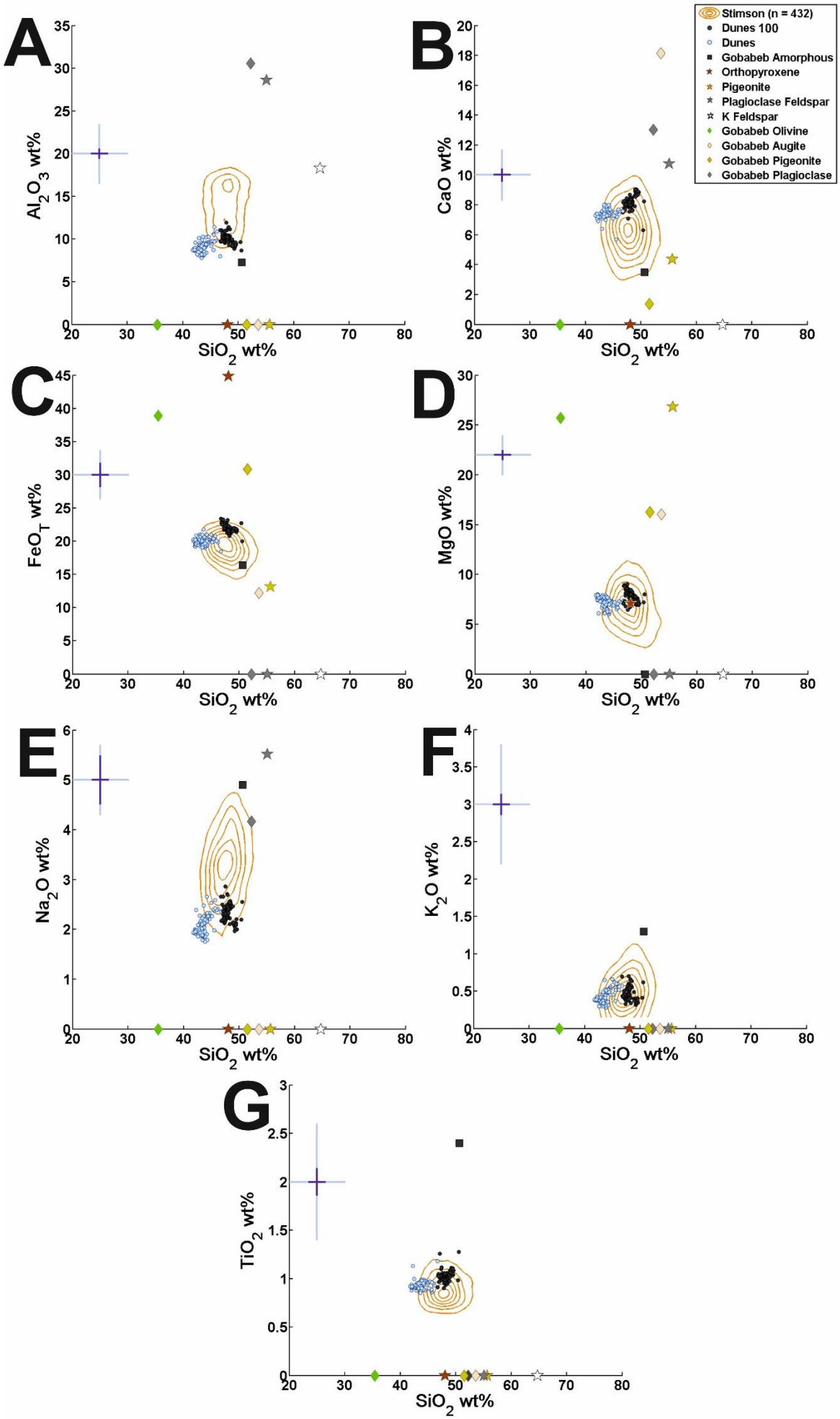
A
B
C
D
E
F
G
Stimson (n = 432)
Dunes 100
Dunes
Gobabeb Amorphous
Orthopyroxene
Pigeonite
Plagioclase Feldspar
K Feldspar
Gobabeb Olivine
Gobabeb Augite
Gobabeb Pigeonite
Gobabeb Plagioclase
Al2O3 wt%
CaO wt%
FeOT wt%
MgO wt%
Na2O wt%
K2O wt%
TiO2 wt%
SiO2 wt%

Figure 4.18 (previous page): Bagnold phase 1 ChemCam analyses plotted over the Stimson formation contours (level step = 0.001, bins = 50, smoothing = 30) alongside CheMin mineral compositions for the main crystalline components from Big Sky and Gobabeb samples (Morrison et al., 2018). ChemCam Bagnold dune compositions corrected to 100% totals are also shown (black circles) alongside the uncorrected dune compositions (light blue circles).

Normalised Bagnold dune analyses show similar SiO_2, MgO, K_2O and TiO_2 with slightly lower Al_2O_3 and Na_2O, and higher CaO and FeO_T compared to bulk Stimson (Fig. 4.18). Normalised dune compositions also plot closer to the mafic-felsic mineral line of Stimson, but offset from it slightly (Fig. 4.19). These variations all relate to different minerals and mineral compositions that most likely reflect variation in source region (e.g., Gobabeb has a high abundance of augite and no orthopyroxene compared to Stimson which has no augite but abundant orthopyroxene and pigeonite; Table 4.5), which are discussed further in section 4.3.4. Some of the S volatile component could have paired with Ca in the amorphous component to make $CaSO_4$ causing certain Bagnold ChemCam analyses to lie off the mafic-felsic mixing line towards the origin of Fig. 4.19 and to higher CaO concentrations than bulk Stimson (Fig. 4.18 B). However, this can also be explained by the Bagnold dune crystalline component having a high-Ca pyroxene (augite) and plagioclase feldspar. The similarity of bulk Stimson to normalised Bagnold MgO suggests a previous abundance of olivine and Mg-bearing minerals in Stimson that mirrors that of the modern Bagnold dunes analysed in the first campaign (25.8 wt% crystalline abundance, Achilles et al., 2017), supporting the model assumptions and results of Hausrath et al. (2018) and indicating that diagenesis must have been isochemical. Therefore, MgO can still be regarded as a good geochemical proxy for determining mafic mineral proportions in the ancient Stimson sandstone.

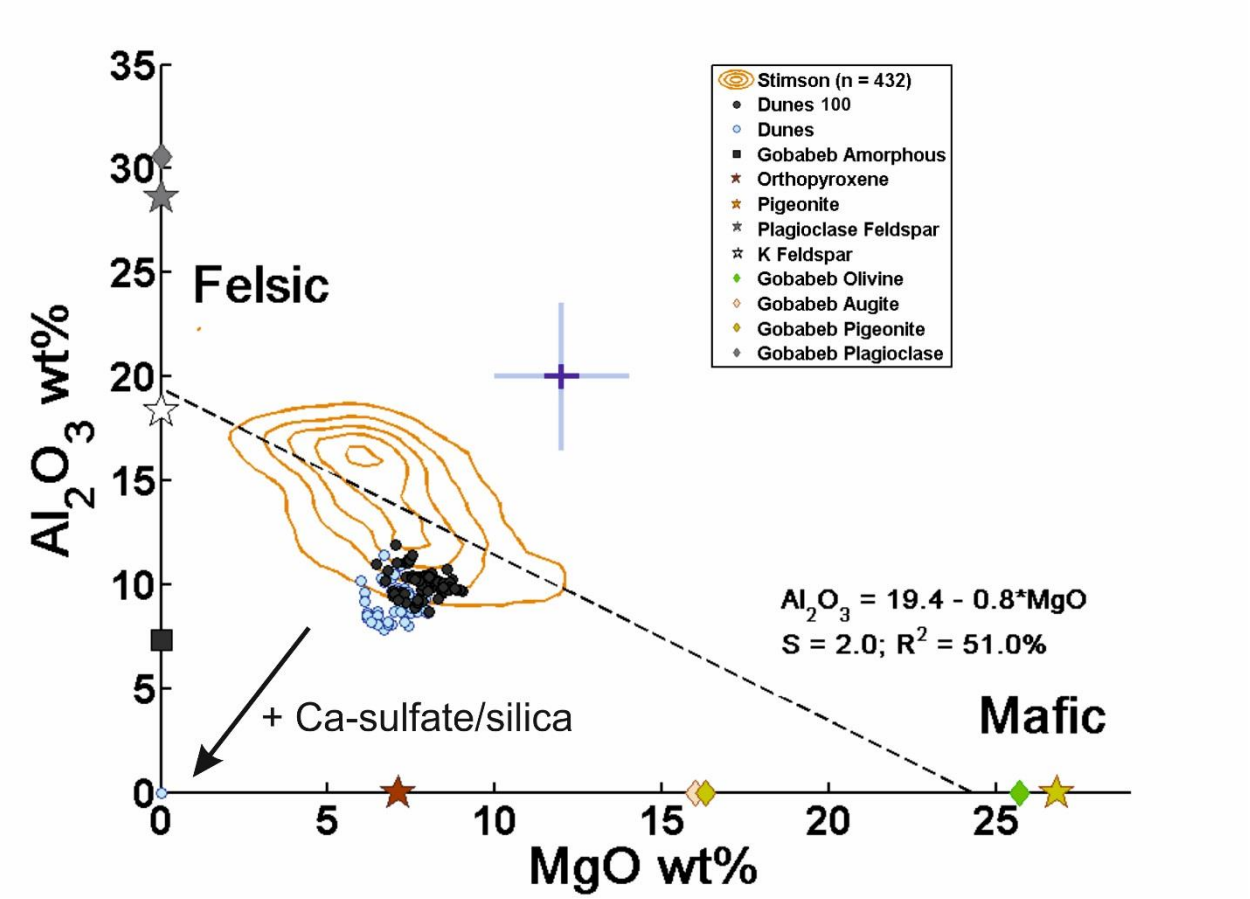

Figure 4.19: Bulk Stimson contours (level step = 0.00075, bins = 50, smoothing = 30), ChemCam corrected (black) and uncorrected (light blue) observation points are given for Al_2O_3 against MgO. Calculated Stimson mafic-felsic mixing line is shown as a dashed line with CheMin minerals of both the Stimson Big Sky (stars), Bagnold Gobabeb (diamond) samples and Gobabeb amorphous component (square). The trend towards the origin from calcium sulfate and silica-rich halo alteration (seen in Fig. 4.14) is also labelled. 1σ ChemCam precision and accuracy are shown as the respective dark and light crosses.

In summary, equivalence tests for both localities show statistically significant geochemical variation between the Emerson and Naukluft Plateaus for Al_2O_3, MgO, CaO, Na_2O and K_2O, which are largely controlled by different proportions of mafic and felsic minerals between these two sites. Although the elemental abundances of CaO and Na_2O largely relate to plagioclase feldspar minerals, these cannot be used to definitively prove a variation in feldspar abundance between sites as these elements can be affected by burial diagenesis. In addition, despite the variation in K_2O likely being a factor of the abundance of K-feldspar between localities, the trace quantities of K-feldspar in the sandstone makes

this an unreliable proxy to use. Therefore, the geochemical variation between the Emerson and Naukluft Plateaus relating to the mineral sorting of mafic and felsic minerals are distinguishable only in MgO and Al_2O_3 concentrations. The Emerson Plateau has higher concentrations of MgO relative to Al_2O_3 and K_2O, which likely results from a greater proportion of mafic minerals. Furthermore, the average compositions of Clusters 2 and 3 are situated within the focal compositions of the Naukluft Plateau which supports that they may be representative of Stimson dominated by a higher proportion of mafic minerals (Cluster 2) or felsic minerals (Cluster 3).

4.3.3. Mineral sorting within the dune or dune field

Aeolian processes are highly effective at mineral sorting, both over long distances and within the dune itself (e.g., Nichols, 2009, Pye and Tsoar, 2008; Kocurek, 1991). Mineral sorting of primary igneous minerals has been identified in active aeolian deposits such as dunes, sand sheets and megaripples on the Earth in volcanic plateaus such as Iceland (Baratoux et al., 2011; Mangold et al., 2011; Mountney and Russell, 2004), and on Mars according to orbital (e.g., Lapotre et al., 2017; Bourke et al., 2008; Stockstill-Cahill et al., 2008; Hayward et al., 2007) and ground-based data (e.g., Ehlmann et al., 2017; Sullivan et al., 2005). Variation in the feldspar and olivine ratio between the two Bagnold dune localities sampled by Curiosity also suggests that mineral sorting has preferentially enriched mafic minerals in the distal Namib dune relative to the more felsic Mount Desert Island ripple field (Rampe et al., 2018).

Terrestrial studies of aeolian mineral sorting regimes in Icelandic sand sheets and aeolian deposits show that the minerals incorporated into the aeolian deposits themselves can provide information on what material was eroded (e.g., glass-rich hyaloclastite and pillow basalts or crystalline, subaerial lava; Baratoux et al., 2011; Mangold et al., 2011;

Mountney and Russell, 2004). The mineral grains transported in aeolian environments can further provide a representative average composition, characteristic of the source region the material is derived from (Baratoux et al., 2011; Mangold et al., 2011; Mountney and Russell, 2004) which is promising for studies on sediment provenance. However, on both planets, aeolian mineral sorting regimes preferentially enrich deposits in olivine relative to plagioclase the further the sediment has been transported from its source (Johnson et al., 2017; Lapotre et al., 2017; O'Connell-Cooper et al., 2017; Baratoux et al., 2011; Mangold et al., 2011; Mountney and Russell, 2004). This is a result of the high Mohs hardness of olivine (6.5–7) and its capacity to form single, rounded grains that are ideal for transportation in aeolian processes (Mangold et al., 2011; Baratoux et al., 2011). These physical properties allow it to saltate effectively over long distances in contrast to other basaltic minerals, such as the elongate feldspar minerals whose shape limits their saltation capacity (Mangold et al., 2011; Mountney and Russell, 2004), and clinopyroxene phenocrysts that are more susceptible to mechanical breakdown (Lapotre et al., 2017; Baratoux et al., 2011; Mangold et al., 2011).

Although this aeolian mineral sorting regime may complicate derivation of source region characteristics, it can also provide information on the paleo-net transport direction, and therefore the prevailing wind direction that shaped the dune field. The next sections investigate whether the geochemical variation between the Stimson localities associated with the mafic and felsic clusters derived in section 4.3.1. relate to the preserved mineral sorting regime in order to derive the paleo-net transport direction of the ancient Stimson sand dunes and compare it to modern day wind direction of the Bagnold dunes.

4.3.3.1. Within dune mineral sorting, stratigraphic position and the likelihood of sampling bias

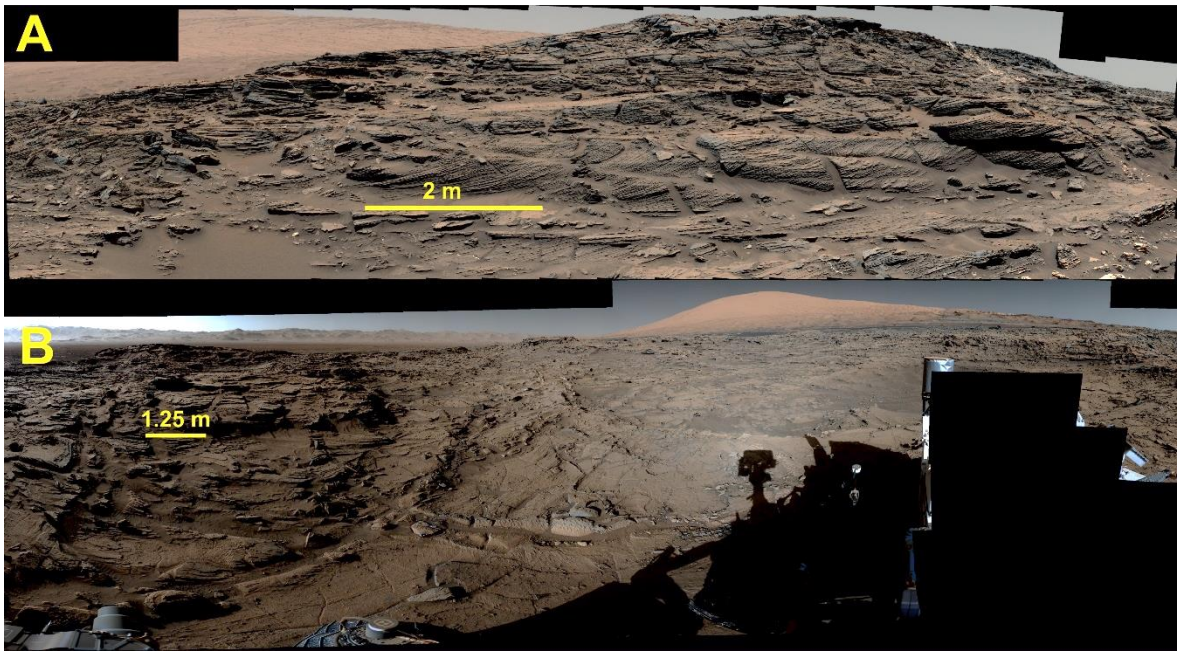

Figure 4.20: Mastcam mosaics of A) The Williams outcrop of the Emerson Plateau (mcam04777, sol 1099) and B) The terrain while crossing the Naukluft Plateau (mcam06191, sol 1302). Most analyses of the Stimson formation in the Emerson Plateau were taken from the side of the Stimson outcrop, whereas Naukluft analyses were conducted from the top of the Stimson outcrop.

Overall, the clusters identified from the statistical analysis in section 4.2.3., Clusters 1–4 and 6 occur in both Stimson localities (Fig. 4.14). The Emerson plateau also has a higher proportion of points within the mafic cluster memberships (Clusters 1 and 2) compared to Stimson analysed at the Naukluft Plateau which in turn has a much greater proportion of points associated with felsic clusters (Clusters 3 and 6). Sampling bias was considered as a possible cause of variation between mafic and felsic minerals as Emerson Plateau analyses were acquired from the side of the lithified dune outcrop, whereas Naukluft analyses were taken from the top of the dune formation (Fig. 4.20). On Mars, the proportion of olivine/feldspar is shown to vary from ripple and dune troughs to crests (Johnson et al., 2017; Lapotre et al., 2017; O'Connell-Cooper et al., 2017) with crests being more enriched in the coarser mafic material relative to the troughs (O'Connell-

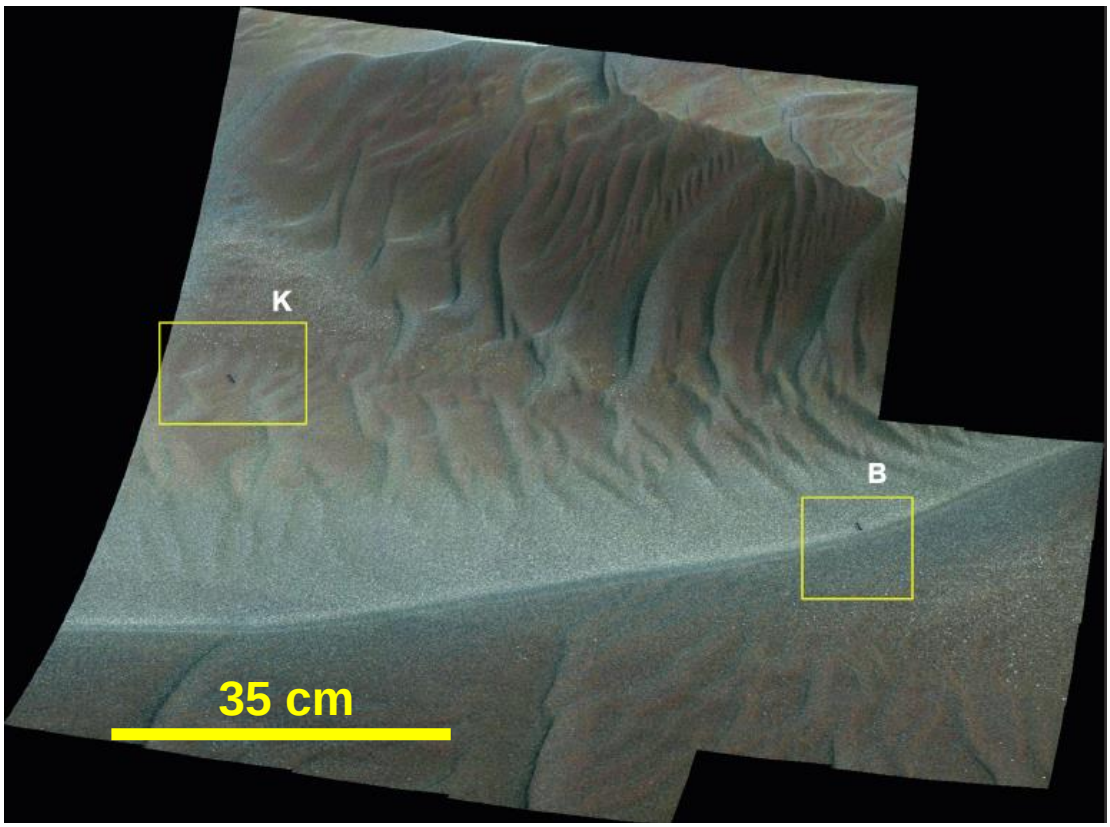

Figure 4.21: From Johnson et al. (2017), this enhanced M 100 colour Mastcam mosaic (mcam05372, sol 1184) augments the spectral characteristics of the target, highlighting changes in characteristics such as grainsize and mineralogy. The variation in colour between the crest (B) and the trough (K) indicates different soil characteristics as a result of mineral sorting.

Cooper et al., 2018; Johnson et al., 2017; Lapotre et al., 2017; O'Connell-Cooper et al., 2017; Fig. 4.21). Thus, if both Stimson localities represented different preserved dune bodies that were subjected to within-dune mineral sorting, one would expect Naukluft analyses – where samples were acquired from the top of the dune – to be richer in mafic components compared to the Emerson Plateau – where samples were analysed at the side and base (Fig. 4.20). However, a plot of mafic and felsic ChemCam clusters against height above the unconformity shows no clear correlation of mafic/felsic proportions with position in the dune outcrop (Fig. 4.22). Furthermore, dune crests are rarely preserved in the geological record (Banham et al., 2018; Nichols, 2009; Kocurek, 1991). During dune migration in periods of net sediment accumulation within the system, migrating dunes scour the area preceding the lee slope, causing erosion of the buried dune's crest stoss

slope (Kocurek, 1991; Pye and Tsoar, 2008), so ChemCam analyses are likely to have sampled the lower-most portion of the dune that is preferentially preserved.

Mineralogical similarity between the Emerson and Naukluft drilled samples suggests that they are from the same unit, whereas the difference in minerals between Stimson and the Bagnold dunes indicates different sediment source regions (Figs. 4.18 and 4.19 and Table 4.5). This similarity between the minerals that constitute the Stimson formation across both plateaus also indicates that a difference in elevation has not resulted in a substantial change in stratigraphic unit. Hence, the Stimson formation was deposited at the same geological time and within the same dune field, and has preferentially preserved its base. Therefore, no sampling bias has occurred as a result of either within dune mineral sorting or a change in stratigraphic position, so the ancient net sediment transport direction can be inferred according to the mafic-felsic mineral sorting regime within the dune field.

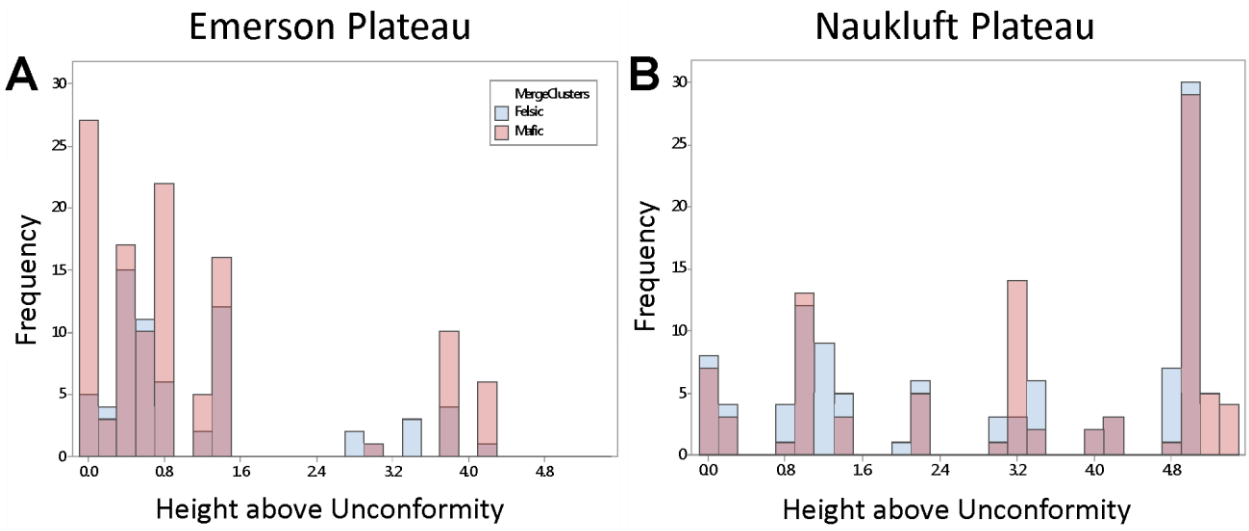

Figure 4.22: Histograms showing the distribution of mafic (Clusters 1 and 2) and felsic (Clusters 3 and 6) cluster memberships for all ChemCam analyses with respect to the analysis height above the Mt Sharp group/Stimson unconformity (as characterised by Watkins et al., 2016).

4.3.3.2. Stimson dune field mineral sorting and net sediment transport direction

Given the lack of evidence for within dune mineral sorting discussed in the previous section, the greater proportion of mafic mineral clusters and greater bulk concentration of MgO for Emerson Plateau analyses relative to the Naukluft Plateau presented in sections 4.3.1.1. and 4.3.2. is most likely to be a product of the same mafic-felsic mineral sorting regime present in terrestrial basaltic aeolian dune fields (Baratoux et al., 2011; Mangold et al., 2011; Mountney and Russell, 2004), and hypothesised for Martian dune fields (e.g., Lapotre et al., 2017; Stockstill-Cahill et al., 2008). Both terrestrial and Martian dune studies have shown that olivine and feldspar possess an inverse relationship with distance from the source (Lapotre et al., 2017). Therefore, Stimson deposited at the Naukluft Plateau, which is richer in felsic mineral abundances must have been situated closer to the sediment source than the Emerson Plateau which is higher in MgO and mafic minerals. This implies a SW-NE wind direction, which supports that determined by Banham et al. (2018), and indicates that there was a reversal in dominant transport direction between the deposition of the Stimson formation and the currently migrating Bagnold dunes shown to migrate in a NE–SW transport direction (Banham et al., 2018; Bridges et al., 2017b; Ewing et al., 2017; Lapotre et al., 2017).

4.3.4. The source regions of the Stimson formation sandstone and a comparison with other units

Mineral sorting has been shown to have a local effect on geochemical composition in relation to Al_2O_3, MgO, Na_2O and K_2O abundances (section 4.3.3.), which is the cause of the bimodality observed for Al_2O_3 in the bulk Stimson density contours (Fig. 4.5). With

the effects of mineral sorting on geochemistry constrained in section 4.3.3, this section compares the bulk Stimson major element geochemistry and mineralogical data acquired from CheMin with the modern dune deposits, and the other lithified sedimentary groups in Gale crater. This provides an indicator of how time-averaged bulk compositions of volcanic source regions have changed since a river-lake environment deposited the Bradbury and Mt Sharp Groups in Gale crater (see Chapter 3), to the dry aeolian climate on the surface today.

As discussed in section 4.3.2.2.1, the bulk chemical compositions of the Stimson formation and the Bagnold dunes are similar with the exceptions of Al_2O_3, Na_2O (slightly lower) and, CaO and FeO_T (slightly higher) at face value (Fig. 4.18). In particular, the difference in Al_2O_3 places the Bagnold dunes closer towards the mafic corner of the mineral sorting trend (Fig. 4.19). In a total alkali versus silica plot, both the ancient and modern dune deposits are situated comfortably within the subalkaline basalt field (Fig. 4.23) suggesting a predominately basaltic origin for these deposits. A basaltic origin is further supported by their primary igneous mineral assemblage dominated by plagioclase, pyroxene and olivine which, though not directly analysed in Stimson, is inferred to have been a part of the assemblage prior to diagenesis (Hausrath et al., 2018). A basaltic mineralogy is similar for many aeolian deposits across Mars that are considered to be the result of global and local scale sediment mixing (Achilles et al., 2017; Lapotre et al., 2017; Meslin et al., 2013; Hayward et al., 2007). The primary minerals found within the Stimson formation and Bagnold dunes also exist within the mineral assemblages of the fluviolacustrine sedimentary units within Gale crater (Chapter 3, Morrison et al., 2018). This could imply a common, long-lived sediment source region. However, aeolian processes are efficient at eroding underlying bedrock and incorporating the sediments into its bedforms during sediment recycling (Garzanti et al., 2013; Dott, 2003). The next

sections explore the likelihood of a common source region against sediment recycling before drawing conclusions on the sediment source region/s of the Stimson formation.

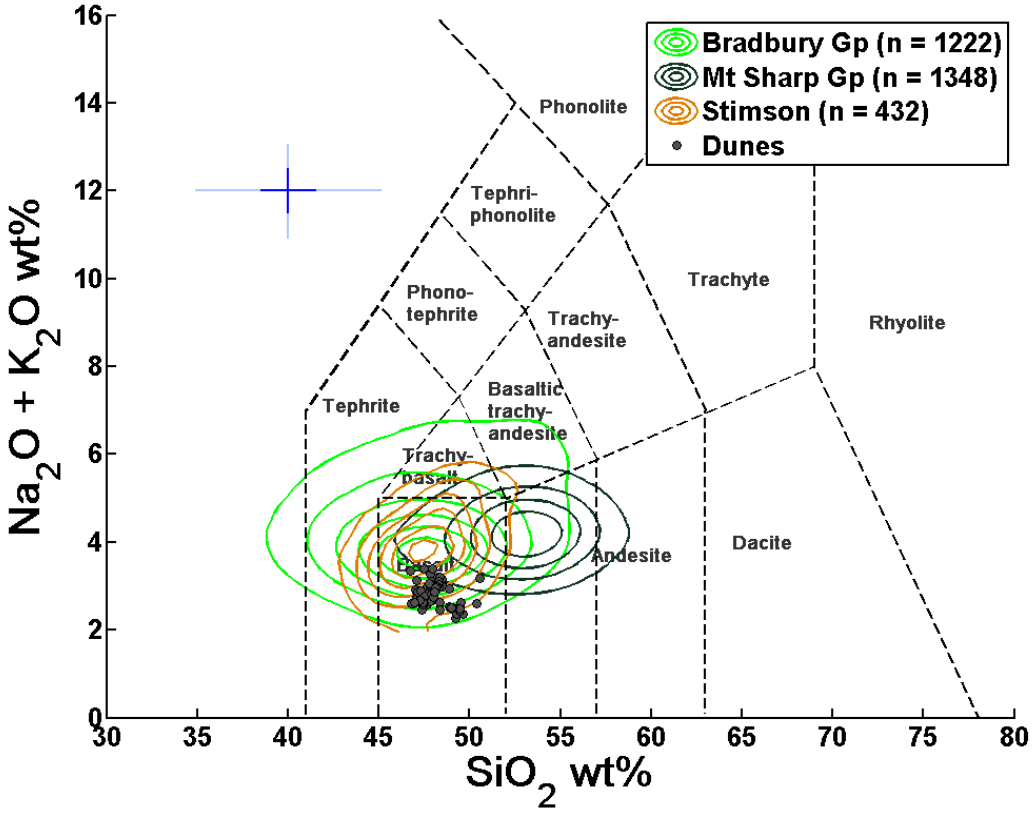

Figure 4.23: A total alkali versus silica (TAS) plot (Irvine and Barager, 1971) used to classify igneous rocks and give a preliminary understanding on sediment source region if alteration and mineral sorting processes are shown to have a minimal effect on sediment geochemistry (Chapter 3.2.2). Stimson contour level step = 0.001, bin size = 50 and smoothing factor = 30. Bradbury and Mt Sharp contour level steps = 0.0005, bin size = 100 and smoothing factor = 20. Dunes are corrected to 100% total sum of oxides.

4.3.4.1. A common source

Geochemically, the Stimson formation and Bradbury Group are similar to each other with remarkably comparable focal compositions, but have distinctive differences to the Mt. Sharp Group (Fig. 4.24) as well as the modern Bagnold dunes (Fig. 4.18). The Bagnold dunes are on average lower in Al_2O_3 and Na_2O, and higher in CaO and FeO_T

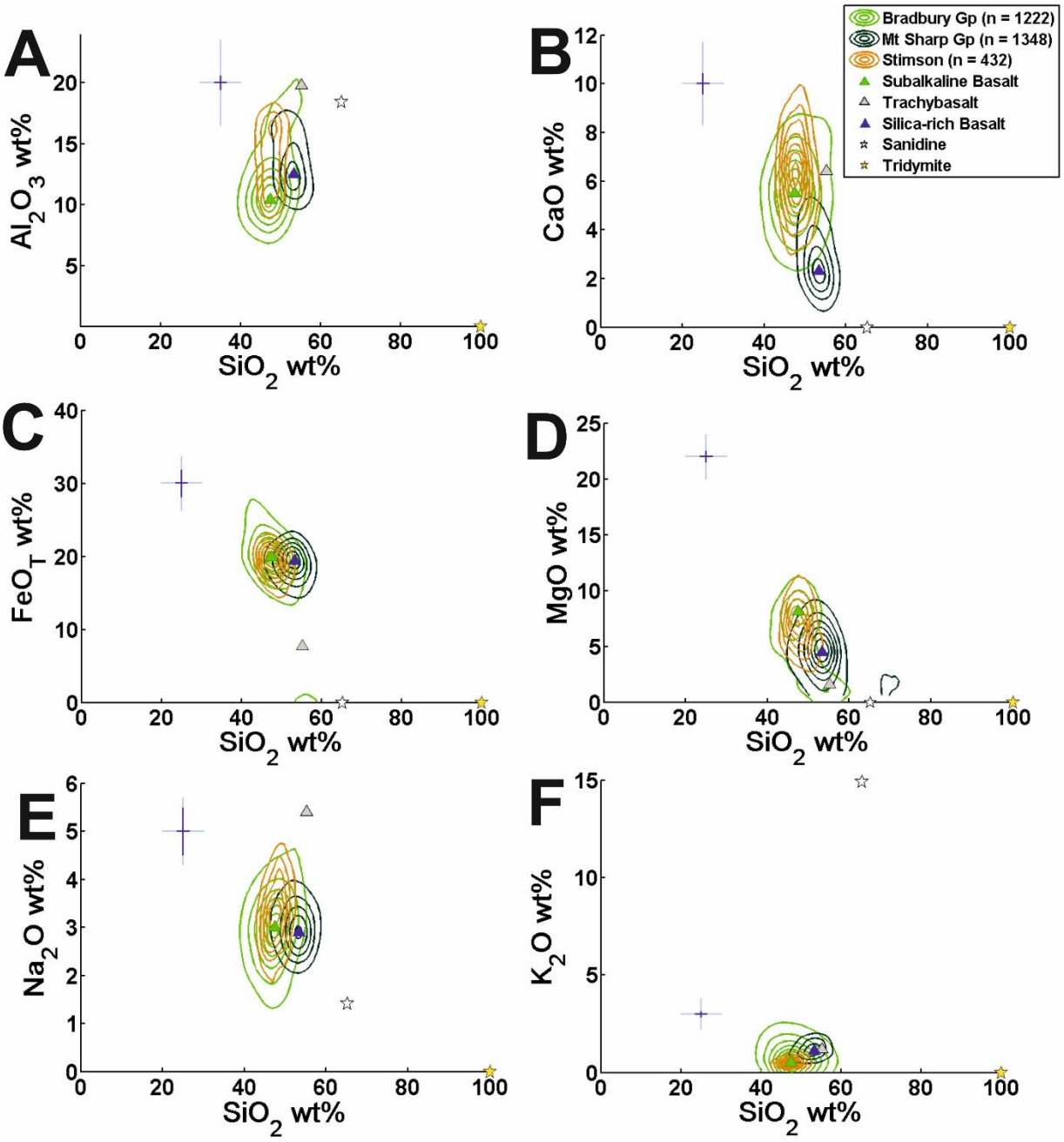

Figure 4.24: Contour plots for all the stratigraphic groups in Gale crater plotted with the endmembers calculated in Chapter 3. Bradbury and Mt Sharp Group contours have a level step of 0.0005, bin size 100 and smoothing factor of 20. Stimson formation contours have a level step of 0.001, bin size 50 and smoothing factor 30. Sanidine and tridymite mineral compositions were taken from (Morrison et al., 2018).

compared to bulk Stimson (Fig. 4.18; section 4.3.2.2.1.). Meanwhile the Stimson and Bradbury foci overlap exactly. These geochemical variations between the ancient and modern sediment deposits imply that there has been a change in source region despite the Bradbury, Stimson and Bagnold dunes all plotting within the basalt field of the TAS plot

(Fig. 4.23). This is supported by the variation in basaltic minerals such as pyroxenes and plagioclase between the ancient and modern deposits (Fig. 4.19; Morrison et al., 2018; Achilles et al., 2017). Stimson has abundant pigeonite in its crystalline component (20.5 wt%) and orthopyroxene (10.5 wt%) in comparison to the Bagnold dunes that instead have abundant augite (22.0 wt%) and less pigeonite (10.6 wt%, Table 4.5). Pyroxenes are stable phases within numerous igneous rock types from the Earth, Moon, Mars and other planetary bodies (Morrison et al., 2018; Deer, Howie and Zussman, 1992; Lindsley and Andersen, 1983). Their shared ranges in hardness (Mohs 5.5–6) and average specific gravity (3.4–3.6) make them unlikely to significantly partition during mineral sorting provided grain size is equal, hence, the variation in pyroxene minerals likely relate to different basaltic source regions between the lithified and modern aeolian deposits.

The geochemical similarity between the Stimson formation and Bradbury Group infers a similar, dominant basaltic source region for these sedimentary deposits (Fig. 4.24). In Chapter 3, I concluded that the dominant sediment source region of the Bradbury Group was a subalkaline basalt similar to the Adirondack Class subaerial lavas analysed in Gusev crater (McSween et al., 2006b) and the Gale crater basaltic igneous float and clasts studied by Edwards et al. (2017). The Stimson formation and Bradbury Group CheMin analyses from Morrison et al. (2018) also show that both units have comparable abundances of pigeonite (~21 wt% average pigeonite in Stimson, ~15 wt% average pigeonite in Bradbury sediments) and orthopyroxene (~11 wt% average Stimson and 12 wt% average Bradbury). Both the Stimson and Bradbury sedimentary units also contained olivine in the original sediments prior to diagenesis and have been subsequently altered to produce the mudstone and sandstone cement in both stratigraphic groups (Hausrath et al., 2018; Morrison et al., 2018; Siebach et al., 2017b; Treiman et al., 2016; Vaniman et al., 2014).

In addition to the overarching subalkaline basalt source region influence on the Stimson formation, Stimson also shows a weak but similar, trend to Bradbury towards trachybasalt compositions (Fig. 4.24). However, as the Stimson sandstones are well-sorted aeolian deposits, this may be a signature of the mineral sorting regime concentrating feldspar and it is therefore not possible to distinguish the source region from sediment sorting in this regard. Although there is a broad geochemical variation in Gale crater's plagioclase compositions (Morrison et al., 2018), it is also difficult to determine what has been affected by Ca^{2+} loss from the crystal into the surrounding materials during diagenesis. Hence, feldspar chemistry should not be used to determine the provenance of sedimentary units as discussed in section 4.3.2.1. The soil and dune samples have higher An contents ($An_{49[4]}$ and $An_{63[6]}$) than the average Gale crater plagioclase ($An_{40[11]}$) which places them on the high-Ca end of Martian meteorite plagioclase compositions (Morrison et al., 2018), but well within the range of compositions common for differentiated basic rocks (An_{85}–An_{30}, Deer, Howie and Zussman, 1992).

In summary, both the Stimson and Bagnold dunes stem from the erosion of basaltic source regions, though geochemical and mineralogical differences between the lithified Stimson dune deposits and modern Bagnold dunes implies a different basaltic source region. This is unsurprising given the likely extensive period of time spanning the deposition and lithification of the Stimson formation and the deposition and migration of the Bagnold dunes across the surface today (Banham et al., 2018; Ewing et al., 2017). Furthermore, different basaltic source regions between the ancient and modern dune deposits are also likely given the change in net sediment transport direction between the ancient Stimson dunes and the modern Bagnold dunes derived in section 4.3.3.2. Instead, the Stimson formation was likely derived from a similar, dominant subalkaline basaltic source region to the Bradbury Group (see Chapter 3.2.2.) due to the remarkably similar bulk geochemical compositions and similarities in basaltic mineral abundances.

4.3.4.2. The effects of sediment recycling

Aeolian processes are among the major geological processes that have shaped the surface of Mars today (Stack et al., 2014b; Hayward et al., 2007) and the current hypothesis for the formation of Mt Sharp in Gale crater involves wind excavating the 5 km high central Aeolis Mons from the sediments that had originally infilled Gale crater in the early Hesperian (see section 1.3.1.1 and Grotzinger et al., 2015; 2014). Hence, it is plausible that some of the aeolian deposits in Gale crater contain sediments that are derived from the subsequent reworking of previously deposited sedimentary material. Aeolian deposits in Gusev crater show local variations in chemistry relating to the surrounding bedrock (Ming et al., 2008). Locally derived sediments have also been shown to have contributed to the modern aeolian deposits of Gale crater as either large grains of local material in soils (Bish et al., 2013; Meslin et al., 2013), calcium-sulfate and mudstone clasts in sand dunes (Achilles et al., 2017), or Murray mudstone intraclasts incorporated into the base of the Stimson formation (Newsom et al., in rev.; Banham et al., 2018). As the Murray formation that underlies the Stimson formation is a mudstone, it is unlikely that this is preserved in the ancient Stimson sand dunes as fine grains are winnowed away in a dry-aeolian environment such as that hypothesised for the Stimson paleoenvironment of deposition (Banham et al., 2018). Therefore, the Stimson dunes may be geochemically similar to the bulk Bradbury Group due to the Stimson dunes preferentially preserving the coarser grains of Bradbury Group fluvial sandstone units during sediment recycling in a dry-aeolian environment, instead of being derived from similar source regions.

Mineralogically and geochemically, the Stimson formation is most similar to the Bradbury Group without any obvious influence of the trachyte and trachybasalt endmembers identified at the Darwin and Kimberley localities (Chapter 3.2). If this Bradbury-type geochemistry and mineralogy for Stimson is a result of the ancient Stimson dunes recycling Bradbury Group sediments, this would imply that the Bradbury Group

extends to the SW of the *Curiosity* rover traverse due to the derived SW-NE net sediment transport direction of Stimson. Furthermore, as these are dry dunes they do not incorporate sediments below a very fine sand grain size (Banham et al., 2018; Kocurek, 1991), so particles from the Mt Sharp Group and mudstone of the Bradbury Group are unlikely to be entrained in the dunes themselves before they are winnowed away by the wind. This would concentrate the mafic and felsic crystalline components of the Bradbury sandstones, to be then subjected to the mineral sorting regime described in section 4.3.3.

The only major mineralogical difference that cannot be explained by the winnowing of fine material between the Stimson formation and Bagnold dunes is the lack of sanidine from the trachytic source (Treiman et al., 2016) that was identified at the Windjana sandstone and is associated with the high concentration of K_2O observed during the traverse from the Darwin outcrop to the Kimberley formation (Le Deit et al., 2016). The Stimson formation has a minor proportion of K-feldspar (2–3 wt%; Morrison et al., 2018) that could be derived from the trachytic source. Unfortunately, this abundance, along with that of K_2O in the Stimson formation is too low to accurately define the crystalline chemistry (Morrison et al., 2018) so one can only speculate whether it is related to a Kimberley-type sandstone. Two possibilities exist that can explain this discrepancy. Either:

1) The Stimson formation was deposited far enough from the sanidine-bearing sandstone units for the sanidine to have been deposited closer to the source through the preferential transportation of mafic minerals over felsic minerals in the aeolian mineral sorting process, or
2) Sanidine – and therefore the trachytic source region – was not a component of the sediments that were previously overlying the Bradbury Group to the SW of the *Curiosity* rover traverse. Hence, it would not be eroded and incorporated

into the modern and ancient dune deposits that are derived from the NE of Gale crater.

Due to the relatively localised nature of the sanidine-bearing Kimberley sandstones (Le Deit et al., 2016; Treiman et al., 2016), hypothesis (2) is preferred to explain the lack of this source region influence in the Stimson sandstones. Although mineral sorting cannot be discounted, particularly given that the distance of the deposited Stimson formation to the exact eroded locality is unknown. As discussed in Chapter 3.2.2. mineral sorting regimes that concentrate felsic material in relation to mafic material make it difficult to discern whether a high proportion of plagioclase feldspar in a sandstone relates to the trachybasalt source region of Edwards et al. (2017), or the mineral sorting regime concentrating feldspar from the subalkaline basalt environment. Therefore, it may be that Stimson has some influence of this source region that contributed to the Bradbury Group, but it is not clear from the sandstone geochemistry and plagioclase feldspar chemistries alone.

4.4. Chapter 4 conclusions

In summary, the Stimson formation does not show any substantial evidence for open-system aqueous alteration except for calcium-sulfate mineral veins and alteration halos, with its cement having formed as the result of isochemical alteration of olivine during burial diagenesis, as suggested through hydrous alteration models (Hausrath et al., 2018; Siebach et al., 2017b). This diagenesis also formed concretions which maintain bulk composition across the affected and unaffected facies. Iron oxides are the main cement components and are the product of olivine diagenesis (Hausrath et al., 2018), though Ti-rich minerals and the early products of feldspar dissolution likely contribute to the cement at localised areas as well. Although no olivine was detected in the Stimson formation

(Morrison et al., 2018; Yen et al., 2017), it was likely present in similar proportions as in the Bagnold dune Gobabeb sample due to the similarities in MgO compositions.

Mafic-felsic mineral sorting has been identified in the Stimson formation similar to the modern dunes on the surface of Mars today (Achilles et al., 2017; Lapotre et al., 2017; Cousin et al., 2017), and in basaltic environments on the Earth (Baratoux et al., 2011; Mangold et al., 2011). In the Stimson formation, it has been seen to generate an enhanced bimodal distribution in Al_2O_3 and increase the proportions of bulk Al_2O_3, Na_2O and K_2O against MgO from the Emerson Plateau to the Naukluft Plateau. These geochemical changes indicate that the net sediment transport direction of the ancient dune field was from the SW to the NE, supporting the conclusions of Banham et al. (2018). This mineral sorting trend does not cause a substantial geochemical variation between the two localities. Therefore, the bulk Stimson formation composition maintains source region characteristics with which to compare to the other lithified units in Gale crater. The derived SW to NE net sediment transport direction for the Stimson formation is also opposite to that calculated for the Bagnold dunes (Bridges et al., 2017b; Ewing et al., 2017; Lapotre et al., 2017) indicating that prevailing wind directions have reversed since the deposition of the Stimson formation (Banham et al., 2018).

ChemCam analyses of the Stimson formation bulk geochemistry shows that it was derived from predominately ancient basaltic material, with the geochemistry and mineralogy suggesting input from a distinct basaltic source region to the modern Bagnold dunes. This difference in basaltic sediment source regions for the ancient and modern dunes is likely the result of the change in prevailing wind directions resulting in the Stimson formation sediments being derived from a source region to the SW as opposed to the Bagnold dunes that have migrated from the NE of their current locality. The remarkably comparable geochemical compositions of the Stimson formation and the

Bradbury Group suggests that they were either derived from similar mixing of the same source materials (with the exception of the trachytic source region), or that Stimson is predominately composed of recycled Bradbury material. If the Stimson formation is similar in bulk composition to the Bradbury Group as a result of sediment recycling, this implies that the Bradbury Group, from which the Stimson is derived, extended to the SW of the *Curiosity* traverse. Due to the very low abundances of K-feldspar in the Stimson sandstone, this also suggests that the Bradbury Group to the SW of the current Stimson localities likely did not contain many sediments eroded from the trachyte source region unlike the potassic sandstones of the Kimberley waypoint (Chapter 3.2.2.).

5. ChemCam analyses of alteration in the Murray formation at the Vera Rubin Ridge

The Vera Rubin Ridge (VRR), formerly known as Hematite Ridge (Fraeman et al., 2013), has been an MSL mission priority since Gale crater was selected as the landing site in July, 2011 (Grotzinger et al., 2012). As described in Chapter 1, section 1.3.4.5, VRR is a 200 m wide, ~6.5 km long erosion resistant ridge located in the NW section of Mt Sharp (Fraeman et al., 2016; 2013). Orbital detections made by the Compact Reconnaissance Imaging Spectrometer for Mars (CRISM) on-board the Mars Global Surveyor (MGS) spacecraft highlighted the unusually strong spectral signature of hematite along this ridge (Fig 5.1; Fraeman et al., 2013; Milliken et al., 2010). The presence of large quantities of hematite in sedimentary rock is of astrobiological importance as its deposition on the Earth largely occurs in habitable aqueous environments (Fraeman et al., 2013; Schwertmann and Fitzpatrick, 1992; Fischer and Schwertmann, 1975). Previous hypothesised potential environments for hematite deposition at the VRR include iron-rich groundwater encountering a redox interface (Fraeman et al., 2016; 2013), the weathering of a basaltic precursor by slightly acidic water (Fraeman et al., 2016; 2013), or repeated pulses of groundwater to generate a high water-rock ratio (Turner et al., 2019; Bridges et al., 2015b). In addition to the habitability implications for a hematite-rich locality, this site can also be of importance for the detection of organics by pyrolysis if the hematite present in VRR formed as a phase change from jarosite or goethite (Lewis et al., 2018). Jarosite forms in acidic, aqueous environments habitable for acidophiles and carries the capacity to host organic matter, but releases oxygen that can degrade organic signals in pyrolysis ovens (Lewis et al., 2018). Therefore, hematite and goethite that form from the dehydration of jarosite are more suitable for the detection of organics with pyrolysis (Lewis et al., 2018).

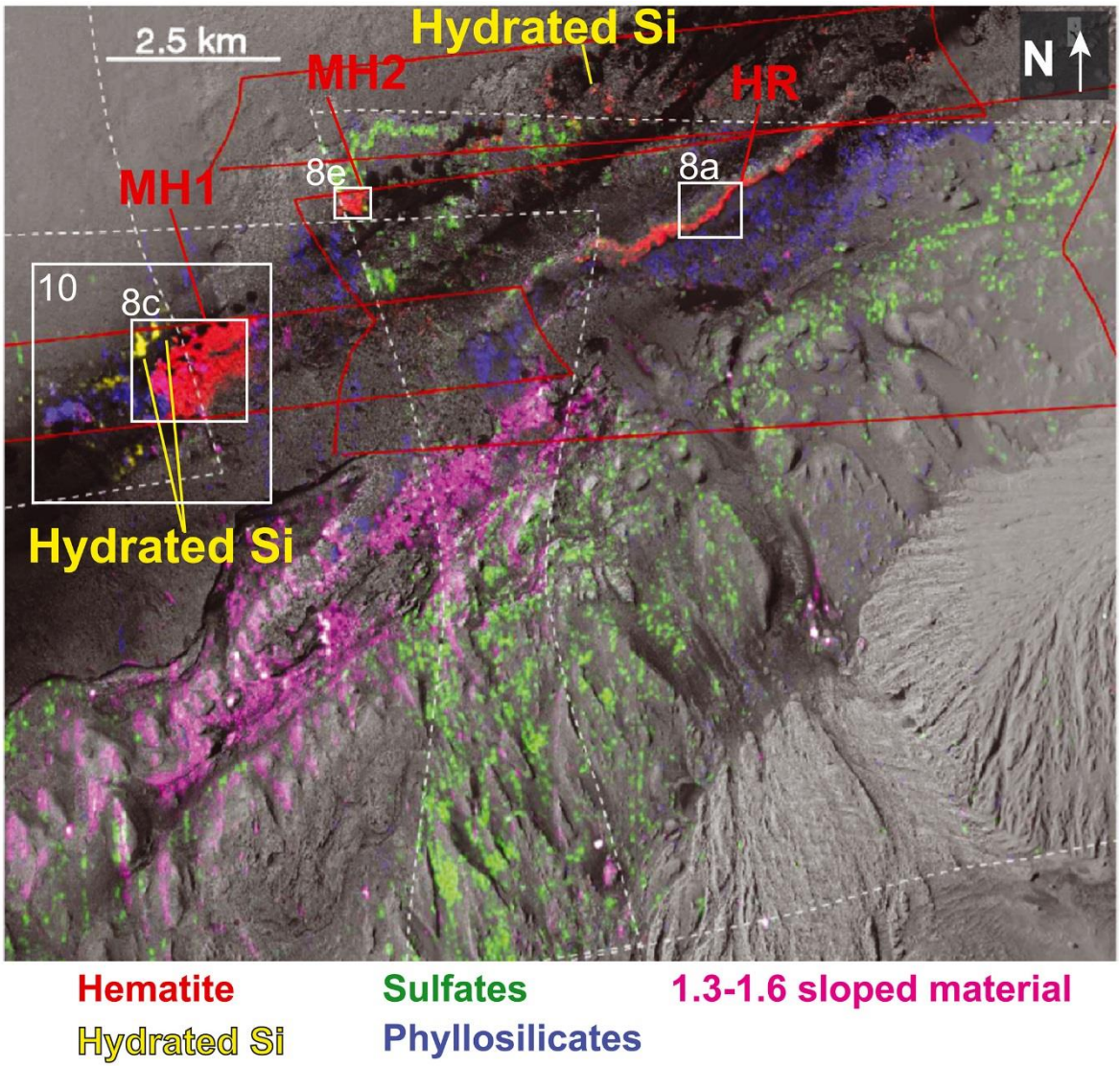

Figure 5.1: A CRISM spectral feature map from figure 6 of Fraeman et al. (2016) showing dominant secondary mineral (hematite, hydrated silica, sulfates, and phyllosilicates) endmember signatures on the lower NW portion of Mt Sharp. CRISM footprints are shown as dotted grey (full-resolution targeted) and red (along-track oversampled) lines. Annotated hematite-rich areas are MH1 (Murray Hematite 1), MH2 (Murray Hematite 2) and HR (Hematite Ridge, now known as Vera Rubin Ridge). Numbered white boxes refer to close-up images in Fraeman et al. (2016).

Curiosity reached VRR on sol 1800 (28th of August, 2017), reaching its mission goal roughly 5 years after landing in Gale crater (Edgar et al., 2018a; Fraeman et al., 2018). Since *Curiosity's* arrival at the orbitally identified hematite hotspot, multispectral analysis from the Mastcam instrument and passive imaging from ChemCam have not shown an increase in hematite abundance relative to the Murray formation mudstones analysed below the ridge (Fraeman et al., 2018; Jacob et al., 2018). Bulk geochemical

analysis from the rover's APXS instrument suite also does not show a change outside of the Murray formation's geochemical range analysed below the ridge (Thompson et al., 2018b). In order to constrain how the VRR relates to the underlying units, this chapter estimates the VRR constrained bulk geochemical compositions derived from ChemCam analyses and discusses them in relation to other Murray units using the density contour analysis methods of Chapter 2.4.1. and linear regression analysis of 2.4.2. As the formation of the characteristic hematite on the ridge is of importance to determining the paleoenvironment of deposition and post-depositional diagenetic conditions, I also discuss the geochemical variability associated with the unique alteration features on VRR, comparing these results to the previous hypotheses of VRR formation, and the sediment source regions identified in the other lithified units of Gale crater during Chapters 3 and 4.

5.1. Background

5.1.1. Vera Rubin Ridge orbital characteristics and initial hypotheses of formation

Unlike the Lower Mt Sharp Group units of the Murray formation (see section 1.3.4., for a detailed description) which are differentiated from orbit by variations in thermal inertia (Fraeman et al., 2016), the VRR has a uniformly high thermal inertia and a noticeably anhydrous, hematite spectral signature, particularly in contrast to its surrounding bedrock (Fig 5.1; Edwards et al., 2018; Fraeman et al., 2013; 2016). VRR lies conformably above the Murray formation and consists of layered bedrock with a good capacity to retain craters owing to its resilience to erosion in contrast to the underlying material (Fraeman et al., 2016). As VRR is conformable with the rest of the Mt Sharp Group stratigraphy and shares the regional northward dip (~7° ± 2.5°), the high hematite-

characteristic of this unit is likely associated with the primary deposited facies (Fraeman et al., 2016). Despite being at a similar elevation to the phyllosilicate bearing unit (PhU), the regional dip of Mt Sharp and differential erosion of the ridge compared to the over- and underlying bedrock places the VRR stratigraphically above (Fig. 1.13; Fraeman et al., 2016). PhU shows CRISM spectral signatures of an Fe/Mg phyllosilicate (Bennett et al., 2018; Fraeman et al., 2016; Thomson et al., 2011), and once the VRR campaign comes to an end, PhU will be the next section of Mt Sharp's stratigraphic record to be explored by *Curiosity* (Bennett et al., 2018).

The VRR is not the only section of Mt Sharp's stratigraphy to show strong spectral characteristics of hematite (Fig. 5.1). In addition, isolated hematite pixels have been identified within the Lower Murray formation (Fraeman et al., 2016), as well as two sections lower in the Mt Sharp stratigraphic record with high hematite CRISM absorption features (Fig. 5.1; Fraeman et al., 2016); Murray Hematite 1 (MH1) and Murray Hematite 2 (MH2). MH1 lies 4 km W of VRR, is situated in a thin, layered unit concordant with Mt Sharp stratigraphy ~250 m below VRR, and lies stratigraphically above a unit with strong phyllosilicate spectral features (Fraeman et al., 2016). MH2 lies at a similar elevation to MH1, but does not show clear evidence from orbit that it is stratigraphically constrained (Fraeman et al., 2016). The co-location of MH1 above a phyllosilicate-rich layer (similar to VRR situated above the PhU) along with hematite-rich deposits constrained to the stratigraphy led to two possible hypotheses (Fig. 5.2); either (1) hematite formed authigenically during the deposition of the Murray strata, or (2) it formed through a later diagenetic event that was restricted to the stratigraphic boundaries as a result of residual porosity in the bedrock (Fraeman et al., 2016).

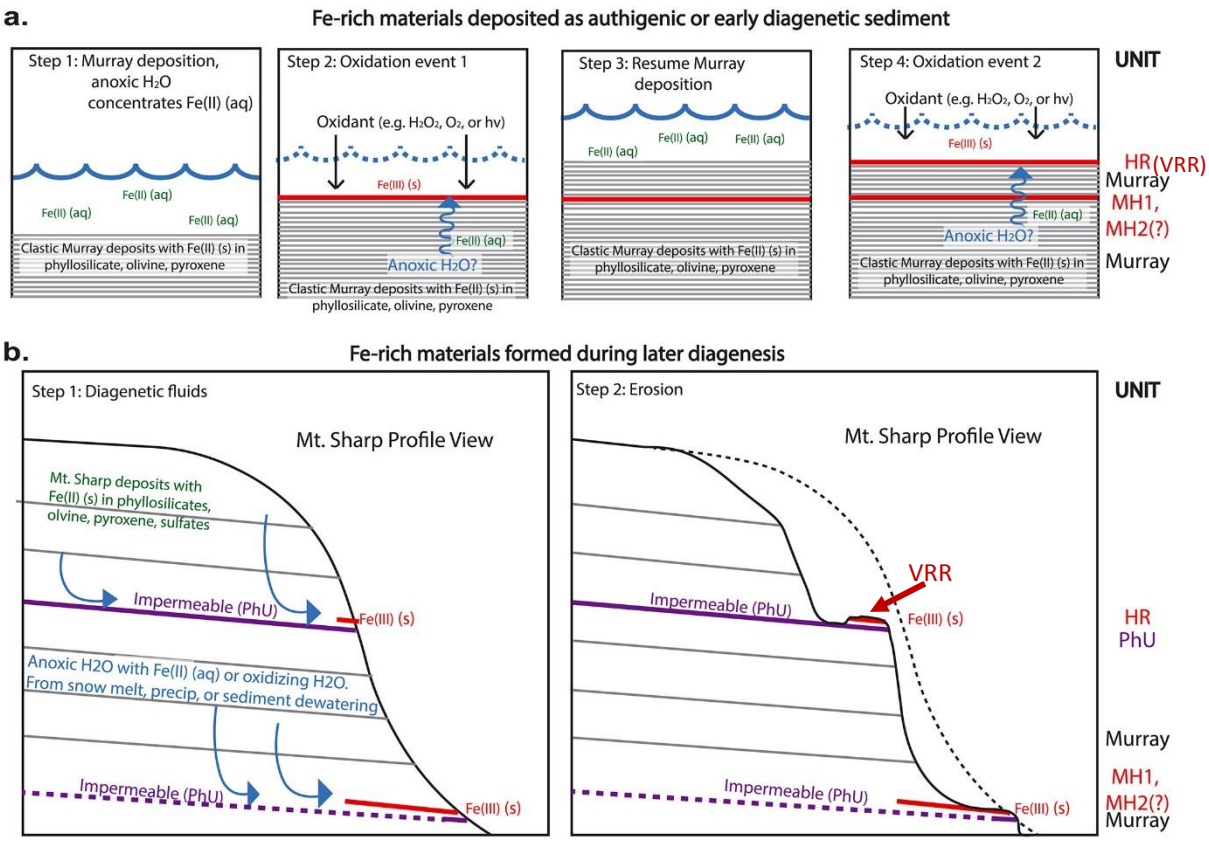

Figure 5.2: The two hypotheses of formation for the orbitally determined high hematite content of the Vera Rubin Ridge and other hematite rich areas of Gale crater (MH1 and MH2) as a cartoon schematic from Figure 14 of Fraeman et al. (2016). a) outlines the authigenic hypothesis of hematite formation whereby an oxidation event occurs during the deposition of the Murray formation leading to the precipitation of Fe^{3+} from the lake. b) details the diagenetic hypothesis where anoxic, iron-rich groundwater encounters oxidising water, possibly percolating from the surface and deposits hematite as cement in the pores of the Murray formation post-deposition.

Following the authigenic hematite formation hypothesis (1) the lacustrine setting that deposited the majority of the Murray formation would have contained waters rich in Fe^{2+}, possibly due to the interaction of the groundwater with mafic minerals and Fe-rich phyllosilicates. Then, two possible oxidation events caused the precipitation of iron as insoluble Fe^{3+} which could take the form of either: there was desiccation of the lake and UV oxidation of shallow water, or an increase of oxidants in the atmosphere via active volcanism (Fig. 5.2 A; Fraeman et al., 2016). Under the diagenetic hypothesis (2), oxidation of anoxic groundwaters saturated in Fe^{2+} would have precipitated insoluble Fe^{3+}

during the interaction of oxic groundwaters originating from a separate source (Fig 5.2 B; Fraeman et al., 2016).

Fraeman et al. (2013) also discussed the potential for hematite to be concentrated at the ridge as a result of the weathering of basaltic sediments through the interaction of slightly acidic fluids. Acidic weathering would result in the formation of a silica-rich residue which may be the source of the high-silica deposits near MH1 (Fig. 5.1). However, silica-rich deposits were not identified from orbit that are proximal to the VRR. Additionally, few minerals indicative of extensive acidic alteration have been detected in the lower Murray formation sediments suggesting minimal acidic alteration (Bristow et al., 2018; Rampe et al., 2017). Furthermore, silica-rich deposits that have been encountered along *Curiosity*'s traverse are also associated with sediments derived from a silicic volcanic source (Morris et al., 2016), or a late-stage diagenetic event that post-dates the Murray formation (Frydenvang et al., 2017; Yen et al., 2017). Therefore, the authigenic or diagenetic cause of hematite formation discussed by Fraeman et al. (2016) for VRR and MH1 and MH2 are most likely in the context of the earlier units.

5.1.2. The Vera Rubin Ridge campaign

The *Curiosity* rover started its approach of VRR on sol 1800 and has investigated over 100 m of stratigraphic thickness that constitutes the ridge (Edgar et al., 2018b). The VRR campaign is still on-going (December, 2018) and to date the rover has attempted 10 drill holes – though only 4 were successful – and made multiple ascents and descents through the stratigraphic units (Frydenvang et al., 2018a). ChemCam has analysed ~470 targets throughout the VRR campaign until November 2018 and has sampled multiple diagenetic features so far identified only at this locality such as sticks and grey patches

(Fraeman et al., 2018). This chapter presents and discusses the geochemical and data acquired by ChemCam between sols 1800–2163.

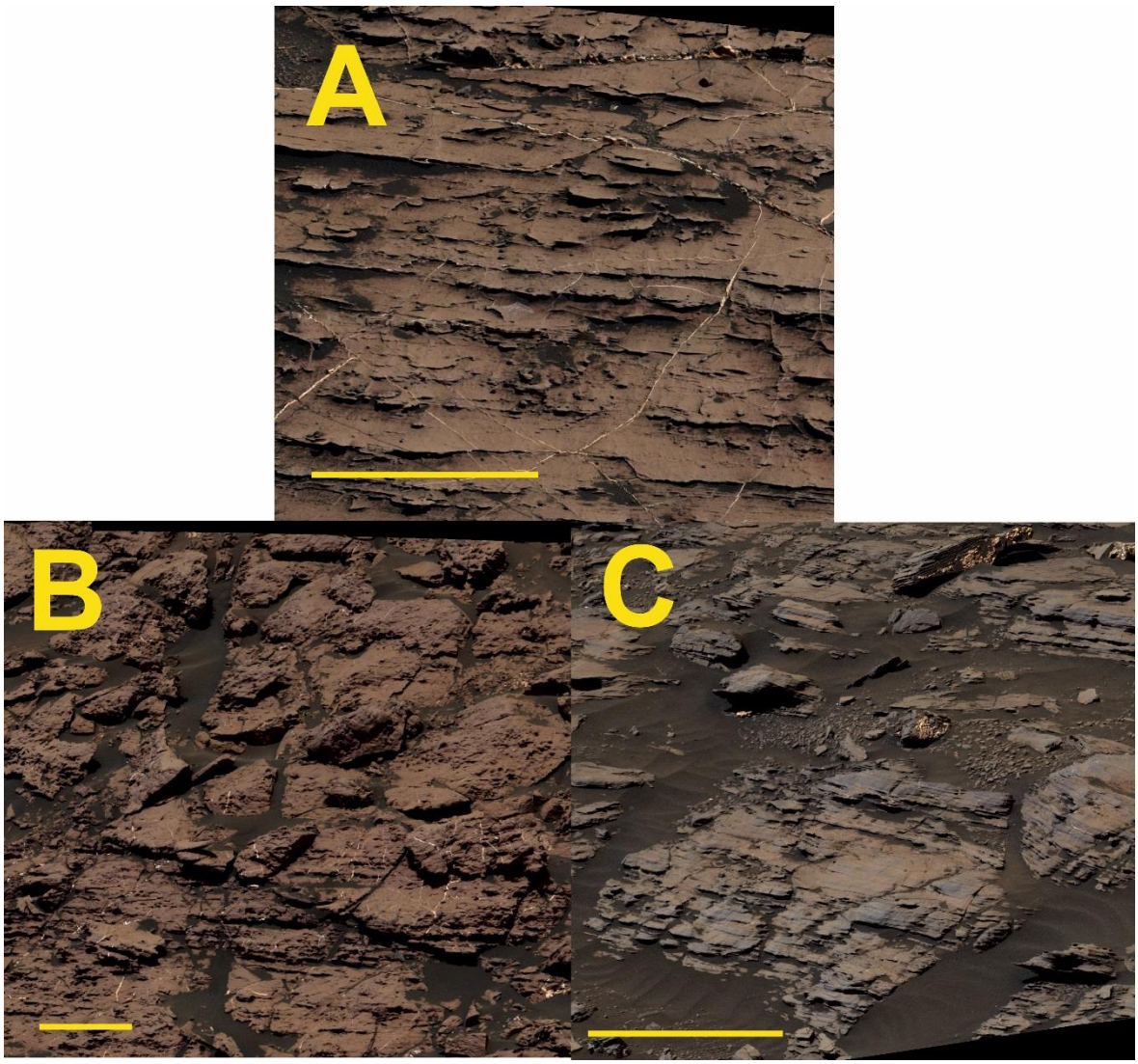

Figure 5.3: Mastcam images of A) the Blunts Point Member (mcam09314, sol 1805) that is situated stratigraphically bellow the Vera Rubin Ridge, B) the Pettegrove Point Member (mcam09462, sol 1829) which constitutes the lower ridge and C) the Jura Member (mcam10045, sol 1925) that is situated at the top of the ridge. Yellow scale bar is 25 cm for all images.

Upon investigation of the VRR, the dominant lithology was shown to be the same as the underlying Murray formation – a laminated mudstone/siltstone deposited in a low-energy lacustrine setting (Edgar et al., 2018a; Fedo et al., 2018). This observation supported earlier orbital studies that hypothesised the VRR's inclusion in the Mt Sharp Group (Fraeman et al., 2016; 2013; Anderson and Bell, 2010), and has shown that the

VRR is an extension of the Murray formation. Geochemical analyses have also suggested that VRR bedrock is a part of the Murray formation as both APXS (Thompson et al., 2018a) and ChemCam (Frydenvang et al., 2018b) report VRR compositions within the geochemical range of the previous Murray formation. Only minor enrichments and depletions have been detected for some trace elements, such as relatively high K and Cl, and low Zn, Mn, Fe and S for APXS analyses (Thompson et al., 2018a), and lower Li for ChemCam analyses (Frydenvang et al., 2018b) compared to the immediately underlying Murray formation.

The VRR has been divided into two groups (Fig. 5.3 & 5.4); Pettegrove Point and Jura, which lie conformably over the Blunts Point Member of the Murray formation exposed immediately below the ridge on the North-facing side (Edgar et al., 2018b; Fedo et al., 2018). The Blunts Point Member (Fig. 5.3 A) is composed of a recessive, fine-grained facies with planar lamination that has been cross-cut by curviplanar Ca-sulfate veins (Edgar et al., 2018a). The Pettegrove Point Member of the ridge (Fig. 5.3 B) is a thinly laminated, fine-grained facies with abundant concretions compared to the other Members at this locality. Finally, the Jura Member (Fig. 5.3 C) at the top of the VRR stratigraphic succession is also characterised by a fine-grained and planar laminated facies, but with a greater degree of variability in colour (red, purple, grey and tan), metre-scale inclined strata, and rare, diagenetic crystal moulds (Edgar et al., 2018b).

The *Curiosity* rover has successfully drilled 3 drill holes within each Member of the VRR and 1 in the Murray formation immediately below the ridge (Fig. 5.4; Morris et al., 2019). The Duluth drill hole (sol 2058) was conducted in the Blunts Point Member at the base of the VRR in a well laminated bedrock with diagenetic raised ridges and Ca-sulfate veins (Fig. 5.5 A). The Stoer drill hole (sol 2136) sampled red bedrock in the Pettegrove Point Member containing some very small scale (~1 mm in diameter) concretions

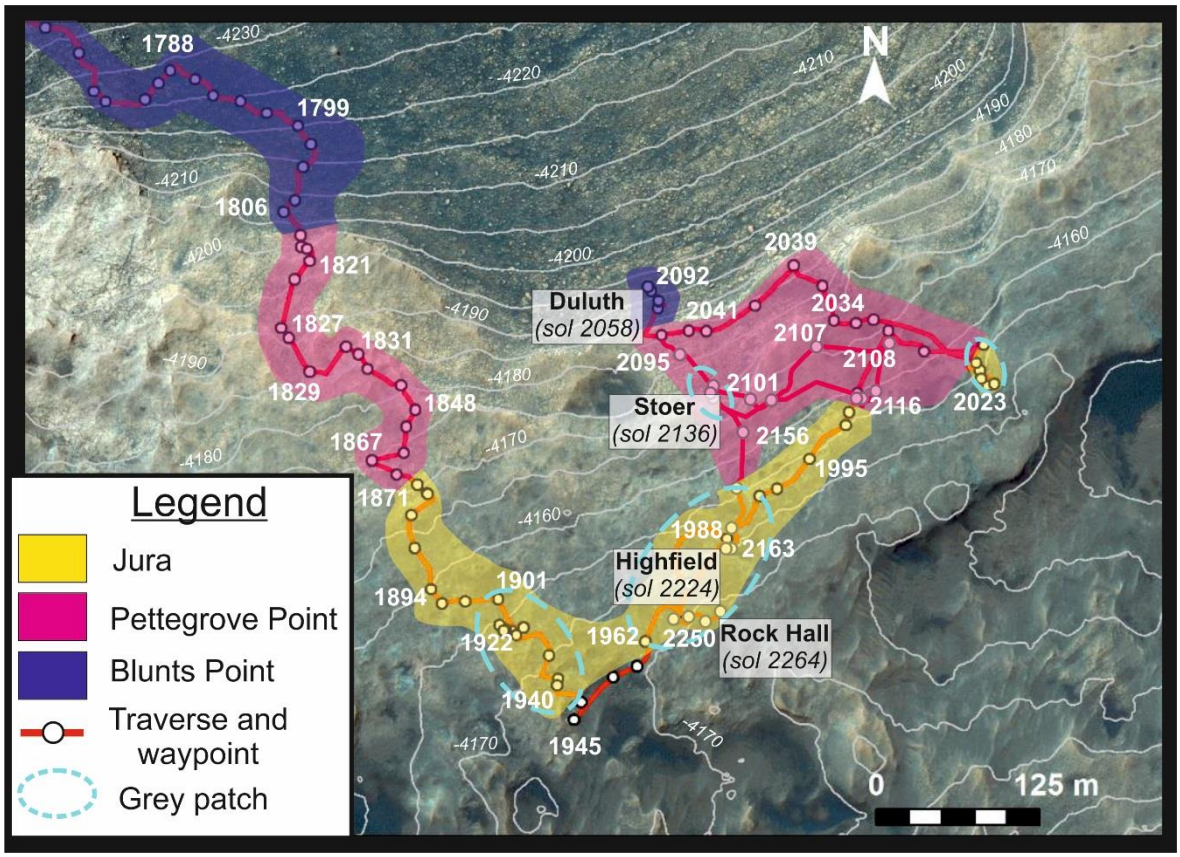

Figure 5.4: Traverse map of the Curiosity rover route along the Vera Rubin Ridge based on the current stratigraphic boundaries from the VRR working group. I have made this map based on the preliminary stratigraphic boundaries determined by the VRR working group in addition to sol numbers along the traverse, grey patch localities and the approximate locations of successful drills. Base map is a HiRISE colour map, contours are at 5 m intervals. In this chapter I present ChemCam data analysed until sol 2163.

(Fig. 5.5 B). Finally, the drilled samples 'Highfield' (sol 2224) and 'Rock Hall' (sol 2264) were acquired in the Jura Member in Grey and Red Jura respectively. The Grey Jura 'Highfield' sample was drilled at the Lake Orcadie locality (Fig. 5.4). The Lake Orcadie area on the VRR is within a diagenetic grey patch with abundant Ca-sulfate veins, Fe-rich nodules and stick diagenetic features. MAHLI images before and after drilling showed that Highfield had potentially sampled these features (Fig. 5.5 C). The Rock Hall Jura sample was acquired just south of the grey Lake Orcadie area in a patch of bedrock with an unusual, shiny, nodular appearance (Fig. 5.5 D). As of yet, only preliminary analyses of CheMin drilled samples have been determined for the VRR (Fig. 5.6; Morris et al., 2019).

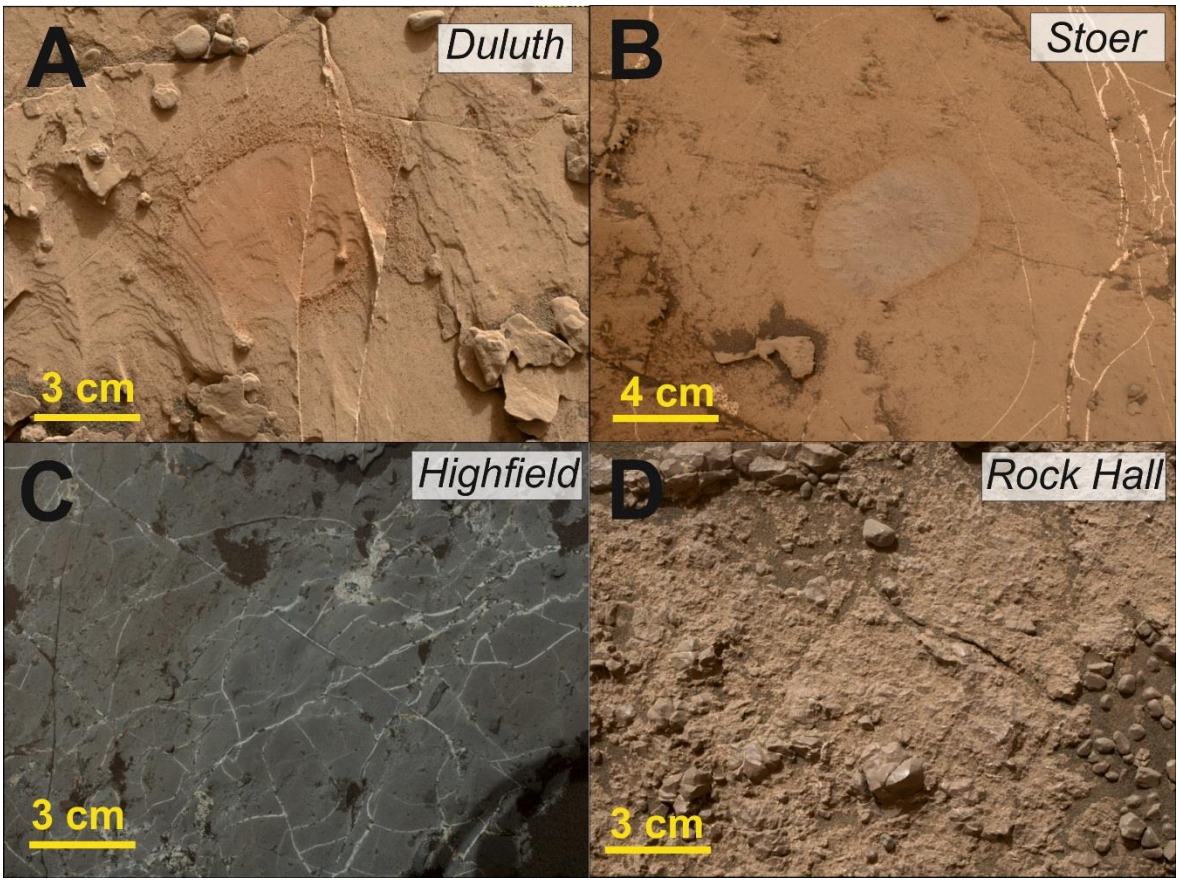

Figure 5.5: MAHLI images of the drilled bedrock targets A) Duluth (MH0007060010801832C00, 25 cm standoff) of the Blunts Point Member, B) Stoer (MH0004650010802734C00, 35 cm standoff) of red Pettegrove Point bedrock, C) Highfield (MH0007060020803168C00, 25 cm standoff) of grey Jura bedrock and D) Rock Hall (MH0001900010803528C00, 25 cm standoff) of red Jura bedrock before drilling.

This chapter, therefore, largely uses the geochemical data from ChemCam alongside earlier Murray CheMin analyses to make hypotheses on the VRR mineralogy, in addition to the mineralogical information acquired from orbit.

Aside from the successful drills, several unsuccessful drill attempts occurred on the VRR in the Pettegrove Point and Jura Members. These failed drill attempts were a result of the bedrock hardness being greater than the drill capacity of *Curiosity*'s new Feed Extended Drilling Using Percussive drill technique (Fraeman et al., 2018) and provides a testimony to the increased hardness of the Murray formation within the VRR. This hardness is likely why the ridge is such a prominent feature compared to the Mt Sharp

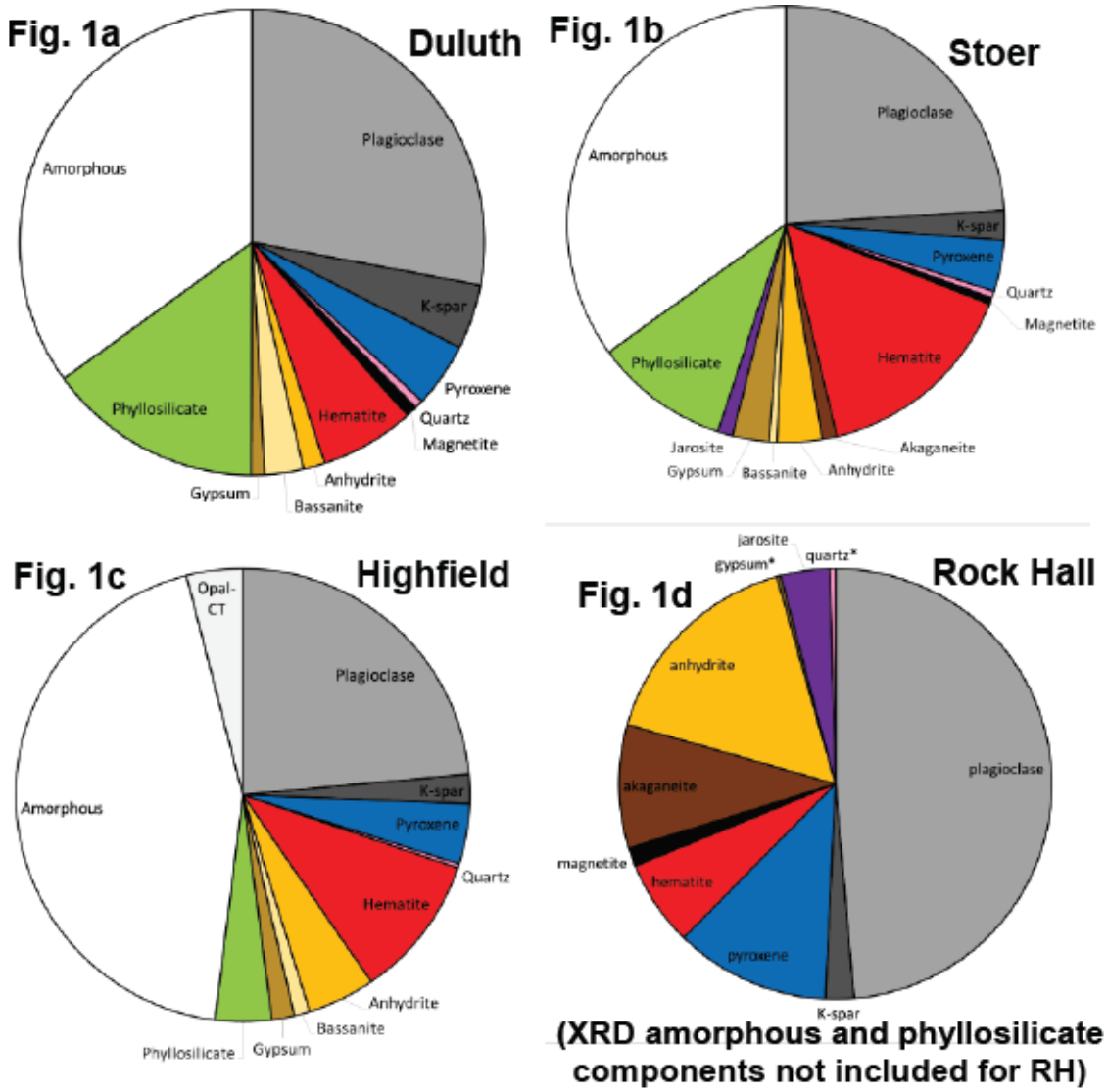

Figure 5.6: Pie charts from Morris et al. (2019) showing the preliminary results of Rietveld and FULLPAT analysis for the XRD spectra from CheMin drilled samples Duluth, Stoer, Highfield and Rock Hall. The crystalline, amorphous and phyllosilicate abundances are presented in wt %. The CheMin analysis of the Rock Hall sample was incomplete at the time of writing, therefore the amorphous and phyllosilicate abundances and compositions have yet to be determined.

Group bedrock stratigraphically situated above and below. From orbit, the VRR has a relatively homogeneous thermal inertia (TI) compared to the Murray formation below (Fraeman et al., 2016) and its TI detected by the Thermal Emission Imaging System (THEMIS) on-board the orbital spacecraft is some of the highest investigated by *Curiosity* to date (Edwards et al., 2018). Rover-detected TI from Curiosity's REMS Ground Temperature Sensor also supports an increase in TI towards the ridge (Edwards et al.,

2018), despite a lack of obvious sedimentological cause (for instance, grain size has remained constant according to MAHLI observations). This increase in TI may therefore be representative of an increase in cement abundance (Edwards et al., 2018), which may also contribute to the increase in rock hardness at this locality.

5.1.2.1. Diagenetic features on the Vera Rubin Ridge

The Murray formation has a wealth of diagenetic features (see Chapter 1.3.6 for more details). Some persist throughout the Gale crater stratigraphy such as Ca-sulfate mineral veins and silica-rich halos (see Chapter 1 section 1.3.6 and Chapter 3, sections 3.1.3 and 3.2.1). Others, such as dendritic nodules (Nachon et al., 2017), are restricted to a set stratigraphic interval or locality. In this study, I have grouped VRR diagenetic features into five categories; Ca-sulfate features (Fig. 5.7 A & F), erosion resistant features (Fig. 5.7 B), unusual textures (Fig. 5.7 C), nodules (Fig. 5.7 D) and sticks (Fig. 5.7 E). Grey patches (Fig. 5.8) up to ~10 m in diameter have also been detected along the Vera Rubin Ridge (Fraeman et al., 2018). These are currently interpreted as resulting from diagenesis (Fraeman et al., 2018), possibly from the circulation of a reducing groundwater (Jacobs et al., 2018; L'Haridon et al., 2018b; Thompson et al., 2018b), though as of yet no further interpretation stands. I have identified all diagenetic features in both VRR Members, with the exception of sticks that have only been identified in Grey Jura bedrock, as well as Ca-sulfate features, erosion resistant features, nodules and unusual textures in the underlying Blunts Point Member.

Figure 5.7 (next page): ChemCam RMI mosaics of VRR diagenetic features. A) The Driesh Ca-sulfate mineral vein (sol 2097), B) Sawtooth Bluff (sol 2067), an erosion resistant 'fin' feature, C) Dunnotar (sol 1993) targeted a transition between the typical 'smooth' bedrock texture and a 'rough' bedrock texture, D) nodule target Pongola (sol 1893), E) Stick target Haroldswick (sol 1921) analysed in a grey patch of the Jura Member, F) The Minch (sol 2163) ChemCam target taken in bedrock containing swallowtail crystal moulds (yellow box) analysed in a grey patch of the Jura Member. Yellow scale bars are 2 cm.

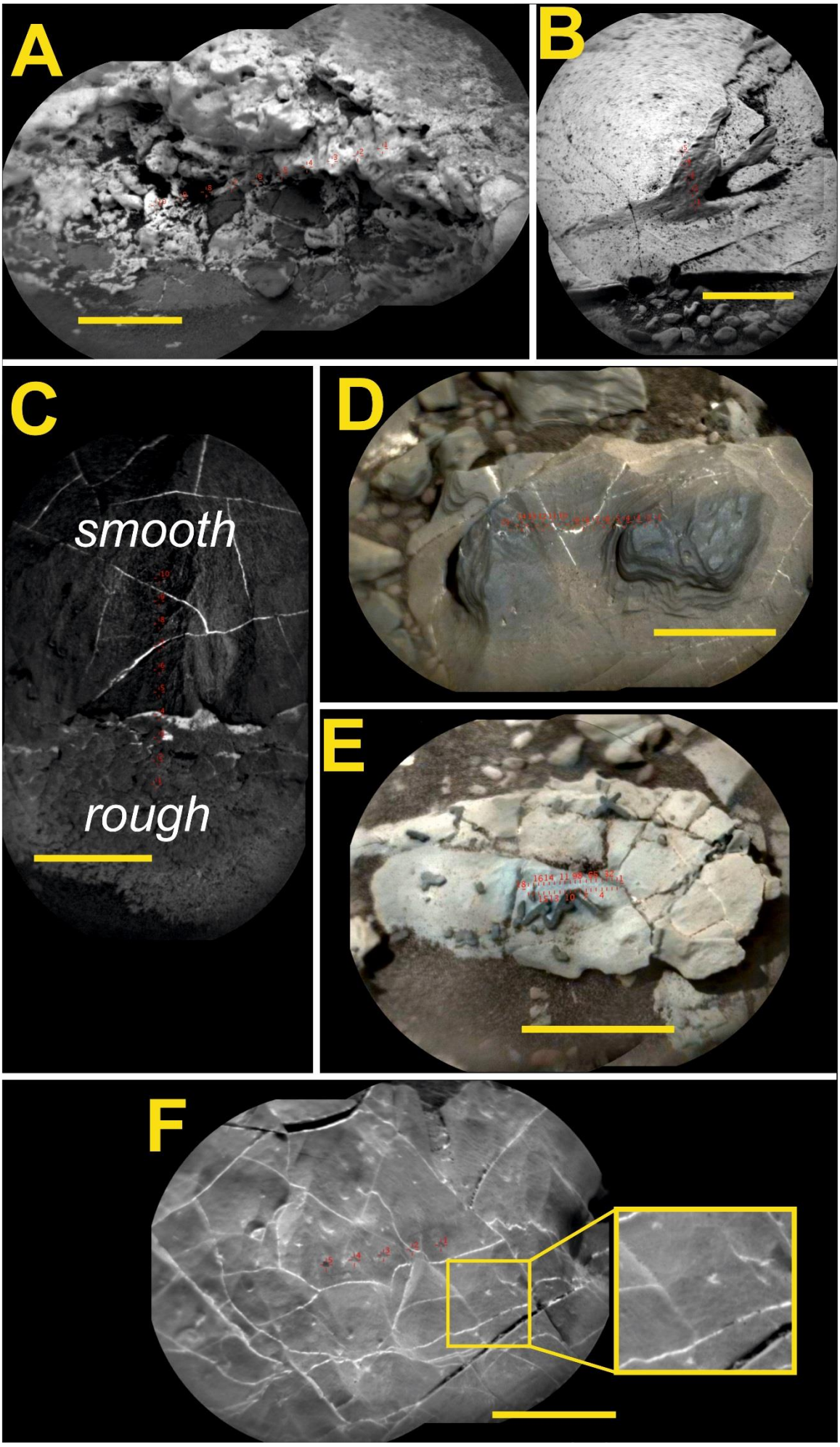
A
B
C
smooth
rough
D
E
F

The VRR has pervasive Ca-sulfate features that take the form of light-toned cement which is sometimes concentrated along bedrock edges or mineral veins that usually follow bedrock weaknesses such as fractures (Fig. 5.7 A). As discussed in Chapters 3.2.1 and 4.2.2, these Ca-sulfate-rich features were identified previously in the Bradbury Group, lower Murray formation and Stimson formation. A new Ca-sulfate related feature was also identified within the VRR Jura Member relating to mineral pseudomorphs with a swallow-tail twinning characteristic of gypsum (Fig. 5.7 F; Edgar et al., 2018b). Due to their likely origin as gypsum pseudomorphs, these have also been included within the Ca-sulfate feature group.

Erosion resistant features include anything that has a positive relief compared to the surrounding bedrock i.e., raised ridges or fins (Fig. 5.7 B). I have previously identified raised ridge and fin targets in other stratigraphic units analysed throughout the mission, such as in the Sheepbed Member (Bridges et al., 2015a; Stack et al., 2014b) and the Kimberley formation of the Bradbury Group (Chapter 3.2.1.), or at the base of the Murray formation (Chapter 3.2.2; Hurowitz et al., 2017; Nachon et al., 2017). Although nodules by definition should be classed as erosion resistant features, their high abundance throughout the stratigraphic record and in specific sites along the VRR has led me to place them within their own group. Nodules are generally mm-scale and are usually found together in the VRR bedrock (Edgar et al., 2018a). Generally, the large nodules have a smaller population density compared to the small nodules which are clustered more closely together across a given area (Edgar et al., 2018a). Nodules also possess a similar appearance to the bedrock. This is with the exception of dark nodules that are co-located with Ca-sulfate veins in the grey patches of Jura bedrock (L'Haridon et al., 2018b). As these are located within Ca-sulfate mineral veins, and as previous mineral veins have shown variations in colour (such as the dark veins at Garden City, sol 929), they have been included within the Ca-sulfate group instead of the nodule group.

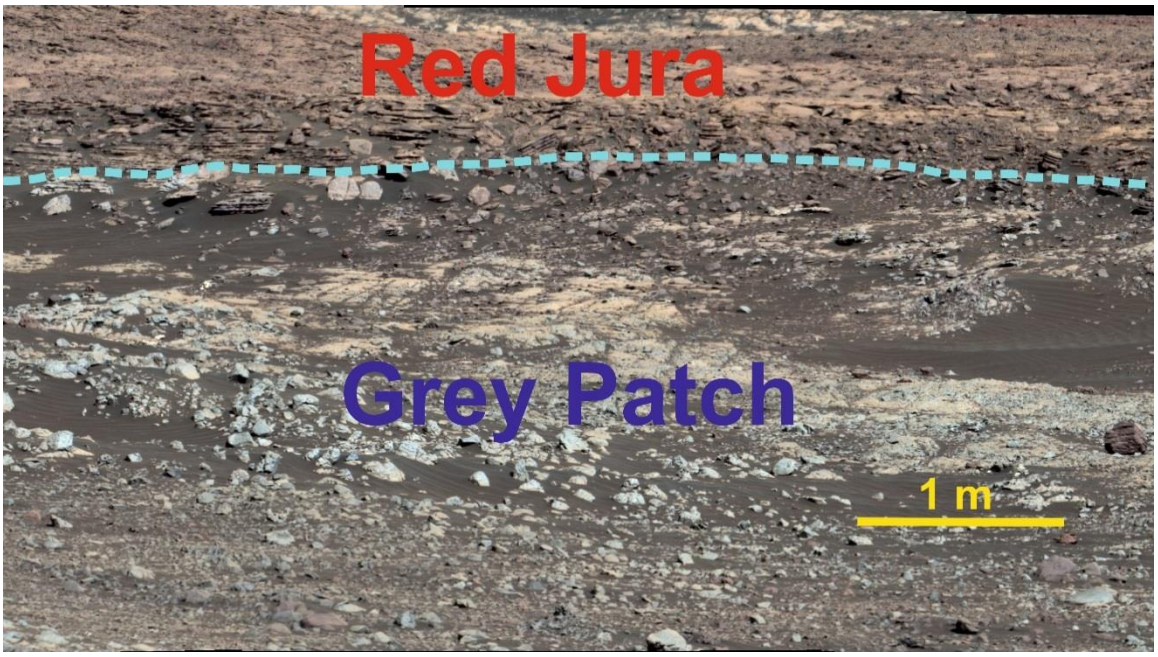

Figure 5.8: An annotated Mastcam mosaic of an example grey patch encountered along the Vera Rubin Ridge (mcam09930, sol 1898).

Unusual textures are classed as ChemCam targets that show a noticeable textural change compared to the surrounding bedrock (e.g., Fig 5.7 C). Typically, the bedrock on the VRR consists of flat, pavement-style blocks with a smooth, fine-grained texture that is either red, tan or purple in colour. Occasionally, a local transition of the typical smooth bedrock to that with a noticeably dark-toned, rough texture is observed. It is the ChemCam observation point analyses that have sampled the rough texture that constitute this group.

Finally, grey patches (Fig. 5.8) were largely investigated in the Jura Member and relate to grey-toned bedrock up to several metres in scale that are not obviously confined to the stratigraphy (Fraeman et al., 2018). Within these grey patches, diagenetic features such as nodules, Ca-sulfate veins and sticks are more common. Any diagenetic feature analysed within the grey patches are placed to their subsequent group (i.e., nodule, Ca-sulfate), however, analyses of grey bedrock not associated with an obvious diagenetic feature have been placed within a grey bedrock group for later comparison to the more common red bedrock. The sticks that are identified within the grey bedrock patches are elongate,

rectangular, dark features which usually have a positive relief (Fig. 5.7 E). Due to the uniqueness of these features, they have been placed within their own group.

Using the density contour and regression analysis methods outlined in Methods Chapter 2.4.1 and 2.4.2, this chapter investigates the bulk geochemistry of the VRR Members up to sol 2163, placing them into context with the rest of the Murray formation. This chapter also discusses the change in geochemistry from the original bulk rock composition to the diagenetic features observed. Finally, I briefly discuss the source region characteristics of the sediments that constitute the VRR and the likelihood that previous hypotheses of hematite formation are still relevant with the new observations from the ground.

5.2. Vera Rubin Ridge results

5.2.1. Vera Rubin Ridge Member compositions

Basic statistics of the VRR Member datasets (Table 5.1) and contour plots of major element oxides against SiO_2 (Fig. 5.9) show that there is minimal bulk geochemical variation between the VRR Pettegrove Point and Jura Members. In general, Pettegrove Point has foci and major element means that are slightly lower in CaO, FeO_T and TiO_2 than the Jura Member (Fig. 5.9), however, these variations are within the standard deviation of the bulk Murray formation (Fig. 5.9) and the standard deviations of the VRR Member datasets (Table 5.1). Bulk focal compositions (Table 5.2 & Fig. 5.9) and average compositions of both VRR Members (Table 5.1) also correlate with those of the Murray formation (Fig. 5.9 & Table 3.7).

Table 5.1: Basic descriptive statistics of the Vera Rubin Ridge Pettegrove Point (n = 772) and Jura Member (n = 502) datasets for each major element oxide wt% including the Mean, standard deviation (StDev), Minimum, Median, Maximum and Range.

Variable	Member	Mean	StDev	Minimum	Median	Maximum	Range
SiO_2	Jura	54.3	2.7	40.4	54.2	62.8	22.4
	Pettegrove	54.1	1.6	44.7	54.2	59.9	15.2
TiO_2	Jura	1.1	0.2	0.7	1.1	2.0	1.3
	Pettegrove	1.0	0.1	0.5	1.0	1.6	1.2
Al_2O_3	Jura	12.4	1.3	9.1	12.3	17.9	8.8
	Pettegrove	12.4	1.4	3.4	12.2	17.6	14.2
FeO_T	Jura	19.4	2.4	6.0	19.9	28.3	22.3
	Pettegrove	19.7	1.0	14.1	19.8	22.2	8.1
MgO	Jura	4.5	1.1	1.0	4.5	11.1	10.1
	Pettegrove	4.9	1.0	1.9	4.8	26.0	24.1
CaO	Jura	2.3	1.3	0.6	2.0	14.6	14.0
	Pettegrove	2.0	1.0	0.7	1.7	10.5	9.8
Na_2O	Jura	2.8	0.4	1.3	2.9	4.7	3.4
	Pettegrove	2.9	0.4	2.1	2.9	8.3	6.2
K_2O	Jura	1.5	0.4	0.5	1.4	2.8	2.3
	Pettegrove	1.5	0.4	0.1	1.4	3.0	2.9

Figure 5.9 (next page): Density contour Harker plots of the typical Pettegrove Point and Jura Member datasets of the Vera Rubin Ridge locality in the Murray formation. The contours were generated with a set bin size of 100 x 100 and smoothing factor of 20. Due to the difference in the number of points for Pettegrove Point and Jura, level steps between the Members are slightly different in order to be fully representative of the dataset (Pettegrove Point = $5x10^{-4}$, Jura = $3x10^{-4}$). The dark blue square is the focal composition of the entire Murray formation dataset and the blue lines represent the standard deviation of the bulk Murray dataset.

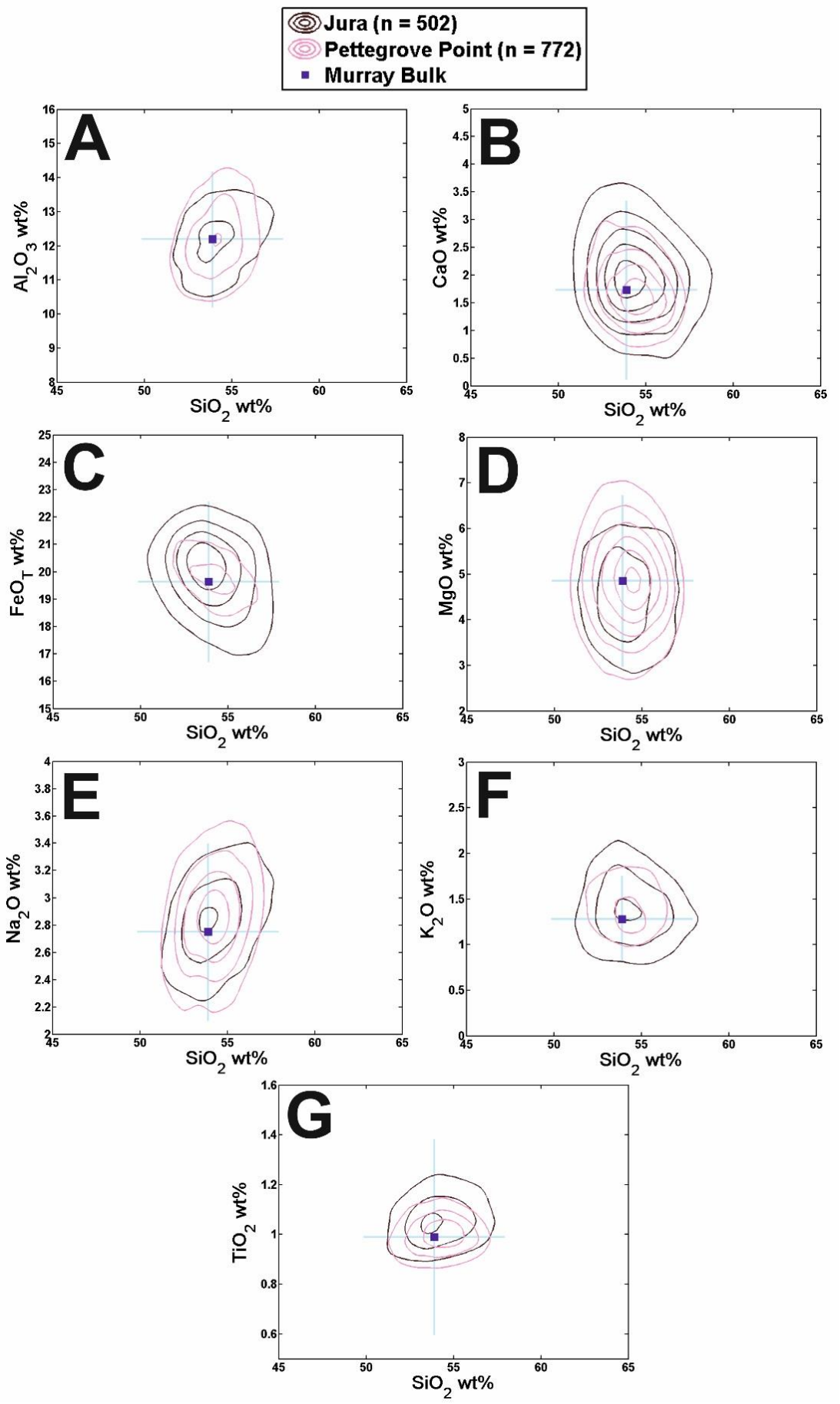
Jura (n = 502)
Pettegrove Point (n = 772)
Murray Bulk
A
B
C
D
E
F
G
Al2O3 wt%
CaO wt%
FeOT wt%
MgO wt%
Na2O wt%
K2O wt%
TiO2 wt%
SiO2 wt%

VRR Member contours cover a similar geochemical range in the Harker plots (Fig. 5.9) except for slight variations between the range for FeO_T and MgO. Jura shows FeO_T contours that encompass both higher and lower FeO_T values than Pettegrove Point (Fig. 5.9 C). In general, Jura has a larger range in FeO_T (22.3 wt%) and SiO_2 (22.4 wt%) than Pettegrove Point (range for FeO_T = 8.1 wt% and SiO_2 = 15.2 wt%) which may explain the larger spread in contours for these major element oxides in Fig. 5.9 C. Jura's density contours also show a greater geochemical range for its MgO focal composition compared to Pettegrove Point's focus (Fig. 5.9 D). The larger focal range in MgO for Jura likely reflects a lower population density between its maximum and minimum values. Respectively, Pettegrove Point has an overall significantly greater range in MgO (24.1 wt%) between its maximum and minimum values compared to Jura (10.1 wt %).

5.2.1.1. Major element correlations on the Vera Rubin Ridge

Pearson correlation coefficients were conducted on each Member of the VRR dataset using the methods outlined in Chapter 2.4.2. Very few, statistically significant ($p < 0.05$) correlations can be identified in the table of Pearson correlation coefficients across both Members (Tables A.5.1 & A.5.2 of the Appendix). Although, Jura has a greater number of significant, weak (+/- 0.25–0.50) correlations than Pettegrove Point, and slightly stronger (+/-0.50–0.75) correlations for those shared between the Members (such as CaO and SiO_2, Tables A.5.1 & A.5.2). Both Members have notable ($p < 0.05$), but weak, negative correlations between FeO_T and SiO_2 (-0.33 for Pettegrove Point, -0.54 in Jura), and Al_2O_3 against MgO (-0.25 in Pettegrove Point, -0.32 in Jura). A similar negative correlation is identified for SiO_2 and CaO in the Pettegrove Point and Jura Members (-0.48 and -0.49 respectively).

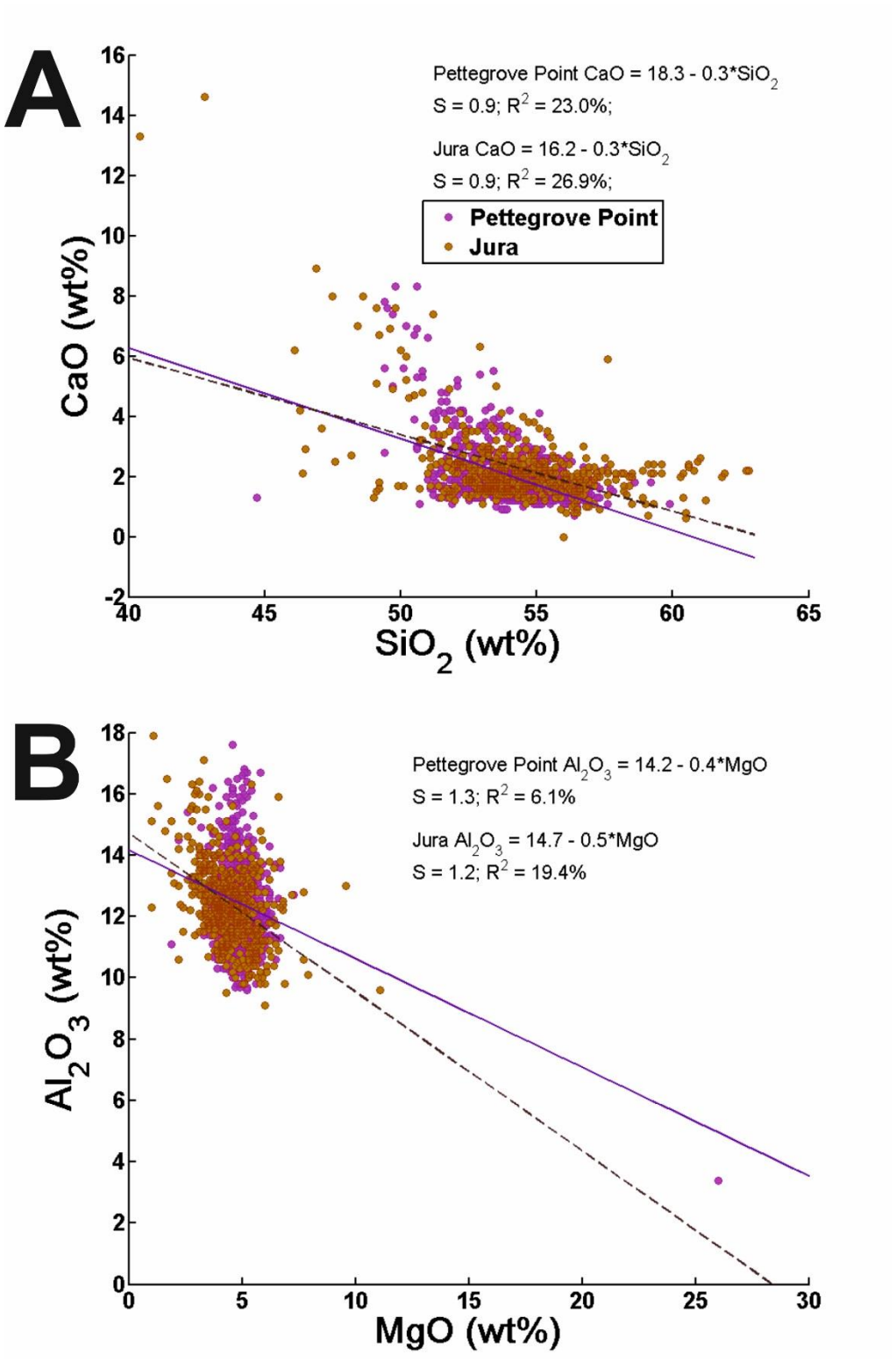

Figure 5.10: Examples of poorly fitted regression models despite strong Pearson correlations for the Pettegrove Point (n = 772) and Jura (n = 502) constrained dataset. A) CaO versus SiO_2 has a Pearson correlation coefficient of -0.48 in Pettegrove Point and -0.65 in Jura, but shows a poor fit to the data. B) Al_2O_3 versus MgO has Pearson correlation coefficients of -0.33 for Pettegrove Point and -0.44 for Jura analyses however, when plotted as a regression line, the data show no correlation (r^2 <20%). All Pearson correlation coefficients and regression lines are statistically significant ($p < 0.05$).

When significant correlations identified in the table of Pearson correlation coefficients are modelled as Simple Linear Regressions (SLR), the correlations do not provide a convincing fit to the data due to low r^2 values with high standard errors (e.g., Fig. 5.10). Most Pearson correlations instead appear to be influenced by scatter in the dataset including some outlying compositions such as that towards the outlying MgO composition for Pettegrove Point in Fig. 5.10. This lack of correlations suggests that the Member datasets are scattered about a uniform composition, which supports the contour distributions shown in Fig. 5.9.

5.2.2. Alteration trends on the Vera Rubin Ridge

At least three main classes of alteration trends exist on the VRR based on geochemical trends of the calcium-sulfate, erosion resistant, unusual texture, sticks and nodule features in the scatter and contour plots (Figs. 5.11, 5.13 & 5.14). These trends are (1) high CaO with depletions in all other major elements, (2) high FeO_T with depletions in all other major elements, and (3) high MgO. Some rare occurrences of high Al_2O_3, K_2O, Na_2O, and TiO_2 also occur in certain alteration features such as raised ridges, however these are usually restricted to specific targets and are not commonplace. Main alteration feature geochemical trends are directed away from density contours and appear to have little effect on contour shape (Figs. 5.11–5.14). The following subsections detail the geochemical trends associated with these features on the Vera Rubin Ridge, briefly comparing them to related features in the stratigraphic units of Gale crater.

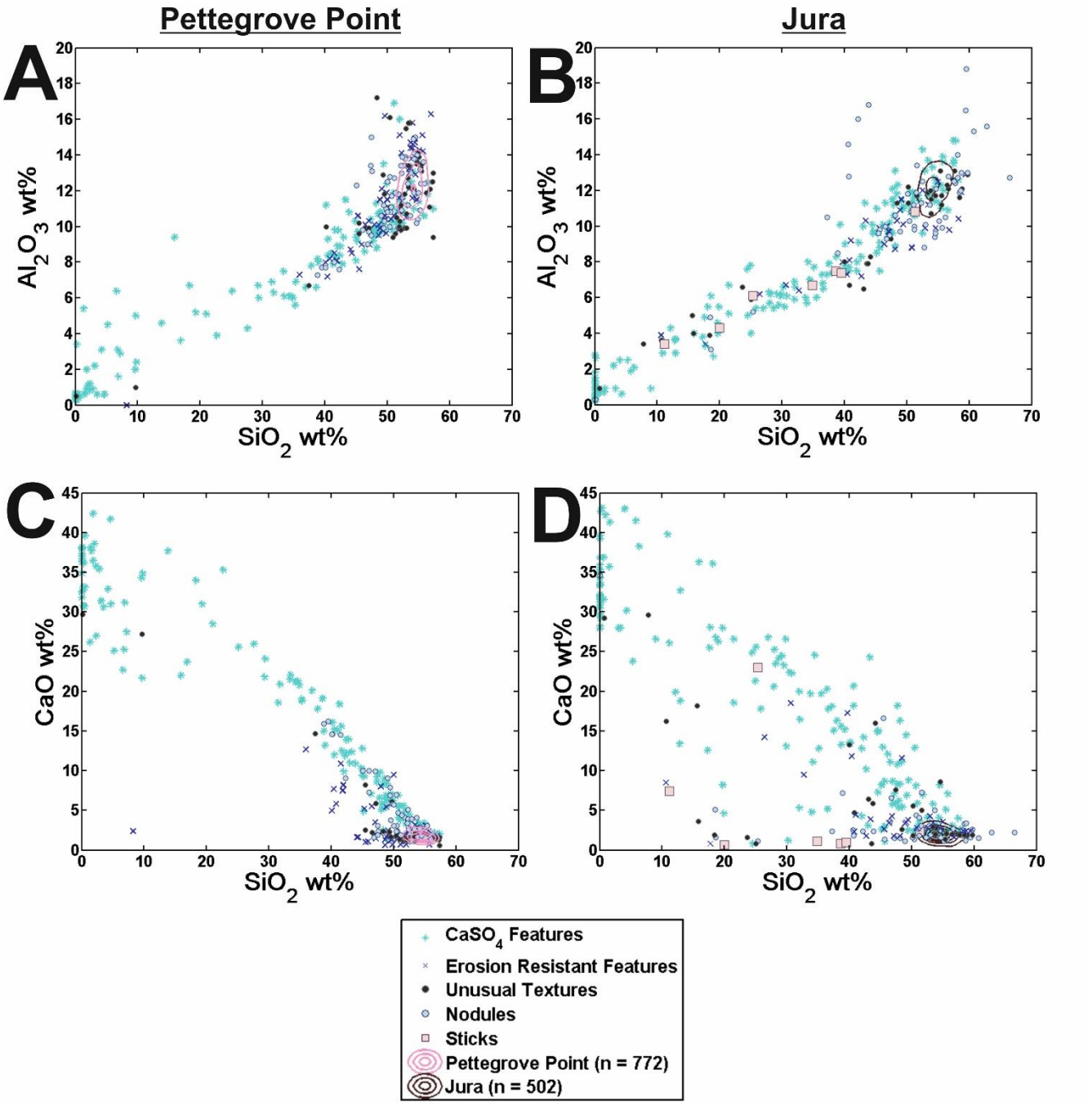

Figure 5.11: Al_2O_3 and CaO plotted against SiO_2 for the Pettegrove Point and Jura Members. These plots show the alteration feature trends for these major element oxides in relation to the density contours of the constrained ChemCam VRR dataset. Alteration features shown in both Members are Ca-sulfate mineral veins, erosion resistant features, unusual textures and nodules. Sticks are present only in the Jura Member.

5.2.2.1. Calcium-sulfate related feature trends

Similar to the calcium-sulfate features analysed earlier in the Murray formation, Bradbury Group (Chapter 3.3.2) and the Stimson formation (Chapter 4.2.2), these features exhibit the main alteration trend of (1) that shows strong depletions for all major elements except for CaO (Fig. 5.11 C & D). The maximum CaO concentration extends up to 45.0 wt% CaO and greater scatter is present for calcium-sulfate features at CaO >20.0 wt% regardless of whether the features are situated within the Jura or Pettegrove Point Members (Fig. 5.11 C & D).

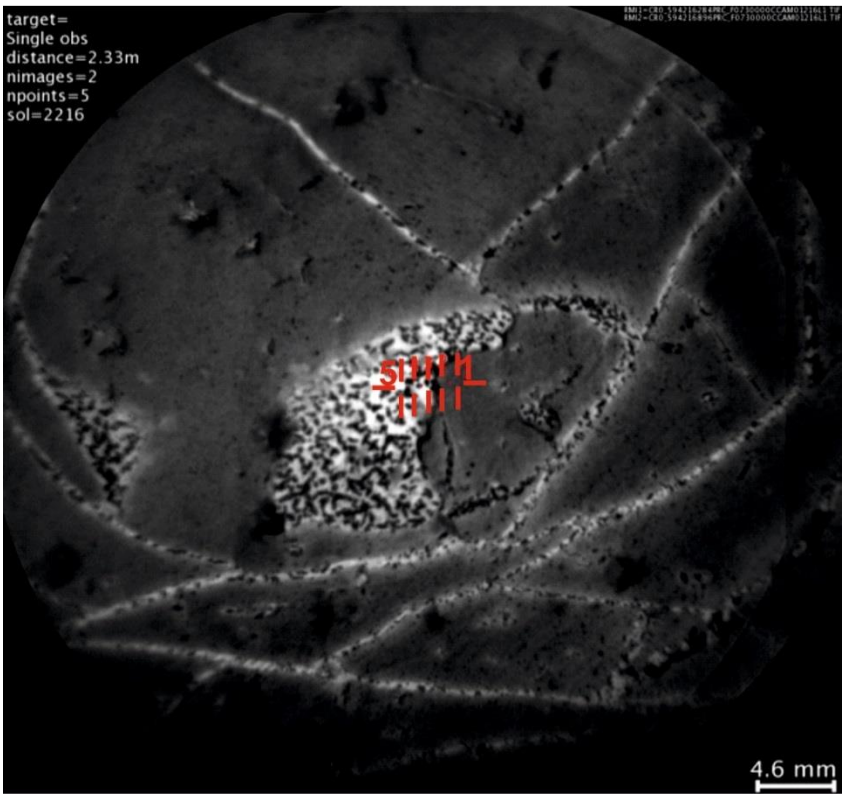

Figure 5.12: RMI mosaic of ChemCam target Grange (sol 2116) which targeted a calcium-sulfate feature that contained numerous dark nodules in the crystalline matrix. ChemCam observation point locations shown with red crosses that hit the target from right to left.

The main notable difference in the compositions of calcium-sulfate features within both VRR Members is that those in the Jura Member have a greater geochemical scatter for CaO against SiO_2 compared to those in the Pettegrove Point Member (Fig. 5.11 C &

D). The scatter in the Jura calcium-sulfate analyses relates to those that also have high concentrations of FeO_T (Fig. 5.13 B) that are predominately analysed in the Grey Jura Lake Orcadie area between sols 1965–1981 (Fig. 5.4). Several of these high FeO_T calcium-sulfate analyses also correlate with dark nodules within vein targets (e.g., sol 2216 target Grange 2216 points #3 and #4, Fig. 5.12). Only one target in the Pettegrove Point calcium-sulfate feature Driesh (sol 2097) shows high FeO_T (~37 wt%), however, unlike in the Jura calcium-sulfate features, Driesh does not appear to have dark nodules.

5.2.2.2. Erosion resistant features

Erosion resistant features follow two distinct trends in the Pettegrove Point Member; one extends towards high Al_2O_3 and K_2O, while the other exhibits a similar geochemical trend to (1) and the majority of the calcium-sulfate features with CaO-enrichment, and a depletion in all other major elements to the origin of their axis (Figs. 5.11, 5.13 & 5.14). The high Al_2O_3 and K_2O erosion resistant feature trend is solely related to the Estecourt target (sol 1861) that analysed a purple resistant ridge and can therefore be considered a rare occurrence. Meanwhile, the Pettegrove Point erosion resistant features that follow the calcium-sulfate geochemical trend share a similar bulk geochemical composition of raised ridge features analysed at the base of the Murray formation (Chapter 3.4.1).

The Jura Member erosion resistant features all trend away from the bulk contour compositions of typical bedrock towards low Al_2O_3, SiO_2, Na_2O and K_2O. Some also show enrichments in FeO_T that follow (2) which is a similar high FeO_T, low SiO_2 trend to the Jura iron-rich calcium-sulfate vein points (Fig. 5.13 B), while others extend to (1) higher CaO or (3) MgO compared to bulk Jura compositions.

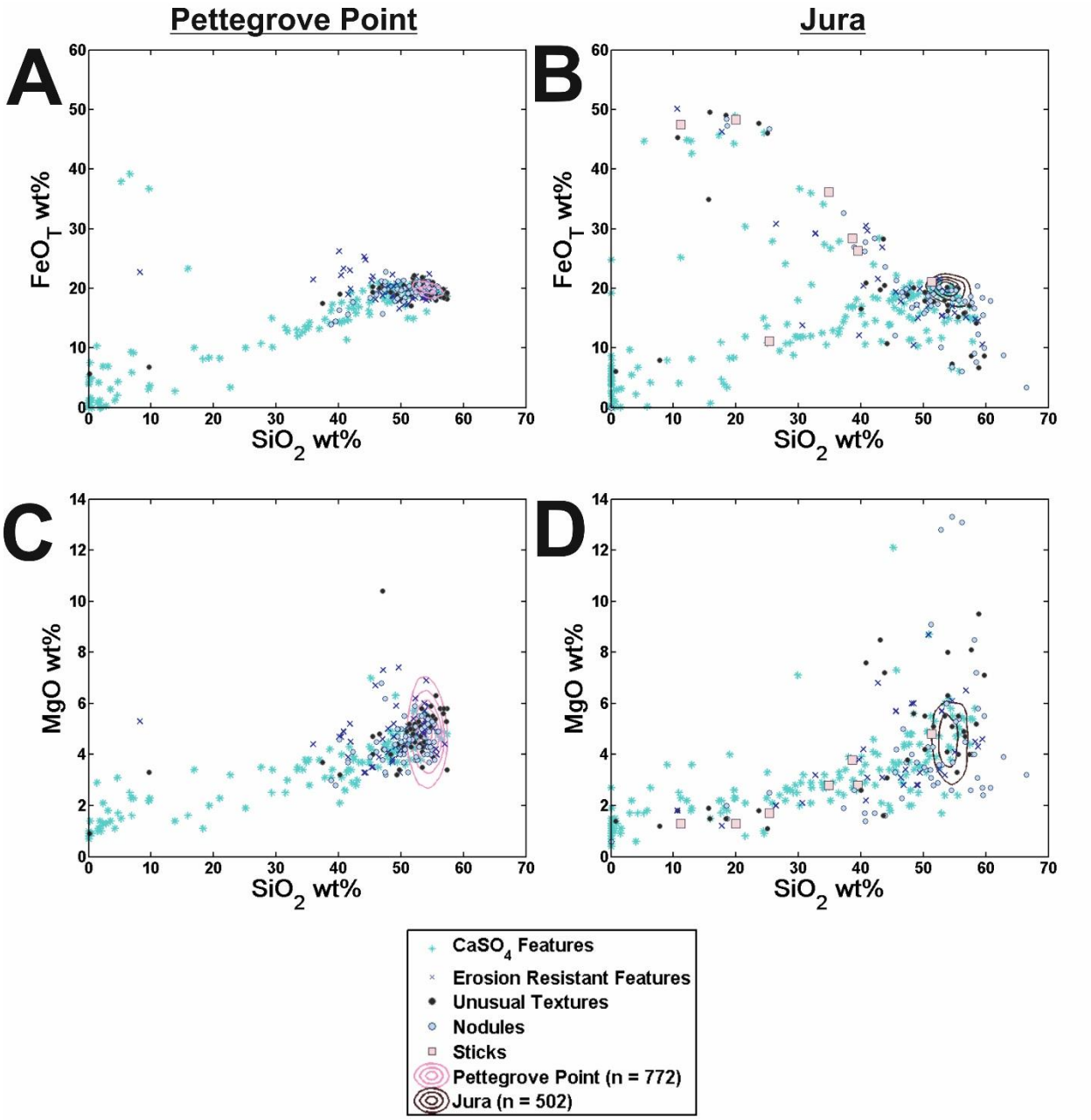

Figure 5.13: FeO_T and MgO plotted against SiO_2 for the Pettegrove Point and Jura Members. These plots show the alteration feature trends for these major element oxides in relation to the density contours of the constrained ChemCam VRR dataset. Alteration features shown in both Members are Ca-sulfate mineral veins, erosion resistant features, unusual textures and nodules. Sticks are present only in the Jura Member.

5.2.2.3. Unusual textures

Unusual textures identified between the Pettegrove Point and Jura Members both show a trend towards low Na_2O and TiO_2, with the majority also trending towards low Al_2O_3, SiO_2 and K_2O. In the Pettegrove Point Member, unusual textures either show similar CaO-enrichment with major element depletion like trend (1) for the calcium-sulfate features, or they have high Al_2O_3, and K_2O for typical bulk SiO_2, FeO_T, MgO and Na_2O compositions. Meanwhile, unusual textures in the Jura Member either follow the calcium-sulfate trend, or the high FeO_T, low SiO_2 trend identified in features relating to the grey patches.

5.2.2.4. Nodules and Sticks

Nodules show a high degree of geochemical scatter between both members on the VRR. Similar to other features, many nodules in Pettegrove Point and some in Jura show the characteristic high-CaO and low concentrations of all other major element oxides of (1) and features relating to calcium-sulfates. Many nodules in the Jura Member also share trend (2) towards high (~45 wt%) FeO_T and low concentrations of SiO_2, TiO_2, Al_2O_3, MgO, CaO, Na_2O and K_2O that is seen for several Grey Jura features. Other Jura nodules show alteration trend (3) with scatter towards high MgO (14 wt%), or have greater concentrations of SiO_2, Al_2O_3 and TiO_2 compared to bulk Jura bedrock.

So far, sticks have only been observed in Grey Jura and they also lie along alteration trend (2) towards high FeO_T and low SiO_2 that is shared by many of the other Jura nodules (Fig. 5.13 B).

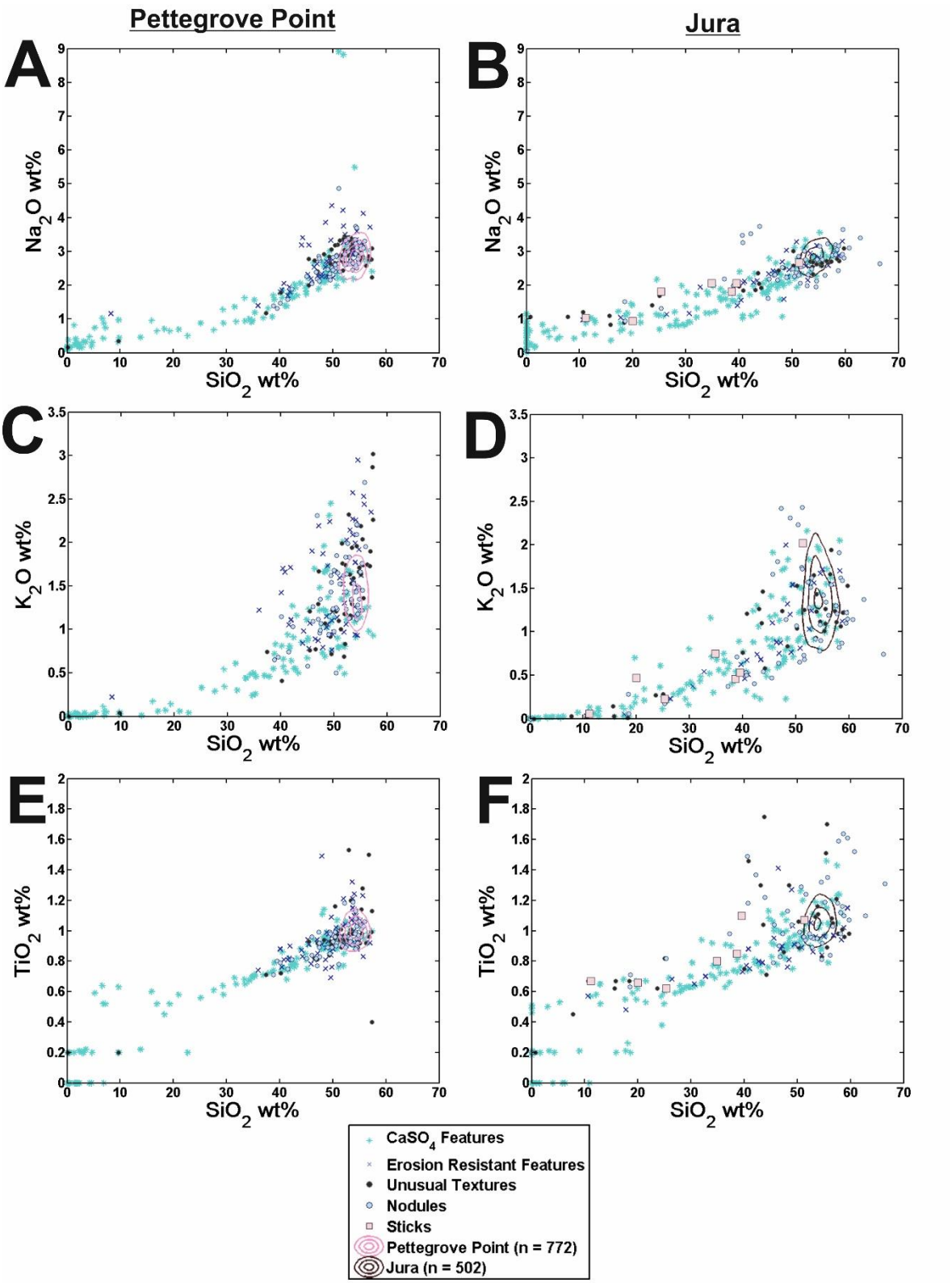

Figure 5.14: Na_2O. K_2O and TiO_2 plotted against SiO_2 for the Pettegrove Point and Jura Members. These plots show the alteration feature trends for these major element oxides in relation to the density contours of the constrained ChemCam VRR dataset. Alteration features shown in both Members are Ca-sulfate mineral veins, erosion resistant features, unusual textures and nodules. Sticks are present only in the Jura Member.

5.2.3. Geochemical variation between red and grey patches

Although both Members contain grey patches that have been sampled by ChemCam, only the Jura Member has enough 'Red' and 'Grey' ChemCam targets for density contours analysis (203 observation points analysed Red Jura, 298 analysed Grey Jura). ChemCam observation points of Grey Pettegrove Point targets are limited (n = 38) and exhibit a large standard deviation, hence, they are instead plotted as scatter points over the contours as an approximate comparison to bulk Grey Jura.

Table 5.2: Density contour focal compositions for Pettegrove Point, as well as Red and Grey Jura with their propagated 1σ errors.

	Pettegrove Point		Red Jura		Grey Jura	
	Mean	1σ	Mean	1σ	Mean	1σ
SiO_2	54.4	0.11	53.4	0.08	54.4	0.09
TiO_2	1.0	0.00	1.0	0.00	1.1	0.01
Al_2O_3	12.1	0.06	11.5	0.14	12.5	0.09
FeO_T	19.8	0.06	20.5	0.07	19.5	0.38
MgO	4.8	0.05	5.3	0.06	4.0	0.05
CaO	1.6	0.03	1.8	0.03	2.0	0.04
Na_2O	2.8	0.02	2.6	0.03	3.0	0.02
K_2O	1.4	0.03	1.6	0.03	1.3	0.02

Figure 5.15 (next page): Density contour Harker plots of Red and Grey Jura analyses of the Vera Rubin Ridge locality in the Murray formation, alongside scatter of Grey Pettegrove observation point compositions. The contours were generated with a set bin size of 50 x 50 and smoothing factor of 20. Level steps between the groups are $1x10^{-3}$. The dark blue cross is the focal composition of the entire Murray formation dataset and the blue lines represent 1σ ChemCam instrument precision.

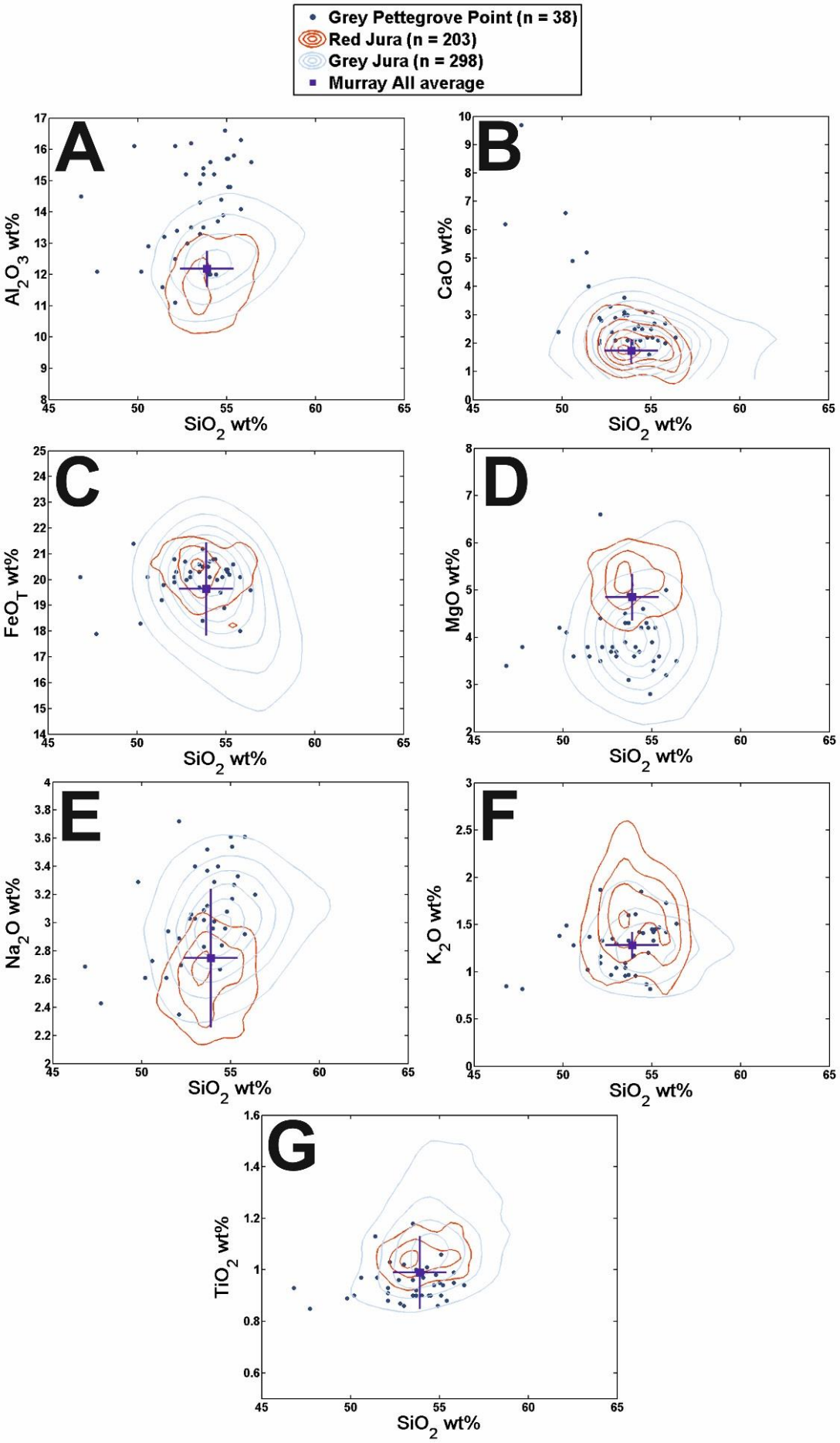
Grey Pettegrove Point (n = 38)
Red Jura (n = 203)
Grey Jura (n = 298)
Murray All average
A
B
C
D
E
F
G
Al2O3 wt%
CaO wt%
FeOT wt%
MgO wt%
Na2O wt%
K2O wt%
TiO2 wt%
SiO2 wt%

Table 5.3: Basic statistics for Red (n = 203) and Grey (n = 298) Jura targets showing the Mean, Standard Deviation (StDev), Minimum, Median, Maximum and Range values for each major element oxide wt% in the constrained ChemCam dataset.

		Mean	StDev	Min	Median	Max	Range
Red	SiO_2	53.9	2.1	47.5	53.7	59.6	12.1
	TiO_2	1.1	0.1	0.8	1.1	1.4	0.6
	Al_2O_3	11.8	1.1	9.1	11.7	15.6	6.5
	FeO_T	20.1	1.1	16.2	20.2	23.2	7.0
	MgO	4.9	0.8	2.8	5.0	7.7	4.9
	CaO	2.4	1.4	0.8	1.9	8.0	7.2
	Na_2O	2.7	0.3	2.0	2.6	4.0	1.9
	K_2O	1.6	0.4	0.7	1.6	2.7	2.0
Grey	SiO_2	54.6	3.0	40.4	54.5	62.8	22.4
	TiO_2	1.2	0.2	0.7	1.1	2.0	1.3
	Al_2O_3	12.8	1.3	9.6	12.7	17.9	8.3
	FeO_T	19.0	2.9	6.0	19.6	28.3	22.3
	MgO	4.2	1.2	1.0	4.0	11.1	10.1
	CaO	2.2	1.3	0.6	2.1	14.6	14.0
	Na_2O	3.0	0.3	1.3	3.0	4.7	3.4
	K_2O	1.4	0.4	0.5	1.3	2.8	2.3

Overall, Grey Jura has subtle bulk geochemical differences to Red Jura analyses in the density contour focal compositions (Fig. 5.15). When ChemCam instrument precision is taken into account, the variations in SiO_2, TiO_2, FeO_T, CaO and Na_2O are all within error. Only MgO and K_2O show a substantial variation in their focal compositions, with Red Jura showing higher values for both major elements (5.3 ± 0.1 wt% MgO, 1.6 ± 0.03 wt% K_2O) relative to Grey Jura (foci at 4.0 ± 0.1 wt% MgO, 1.3 ± 0.02 wt% K_2O). Meanwhile, when only the propagated standard deviation of the contour foci are considered (Table 5.2), Grey Jura is also shown to have slightly greater bulk abundances of SiO_2 (54.4 ± 0.1 wt%), Al_2O_3 (12.5 ± 0.1 wt%), CaO (2.0 ± 0.04 wt%) and Na_2O (3.0 ± 0.02 wt%) compared to Red Jura (Table 5.2). Meanwhile, Red Jura has higher bulk compositions for FeO_T (20.5 ± 0.1 wt%) compared to Grey Jura (19.5 ± 0.4 wt% FeO_T).

Grey Pettegrove Point analyses plot within the Grey Jura density contours supporting these subtle geochemical differences, though Grey Pettegrove Point analyses also exhibit notably higher Al_2O_3 compositions compared to Grey Jura. Some Grey Pettegrove Point analyses also have elevated CaO with low SiO_2 that may be a result of Ca-sulfate contamination.

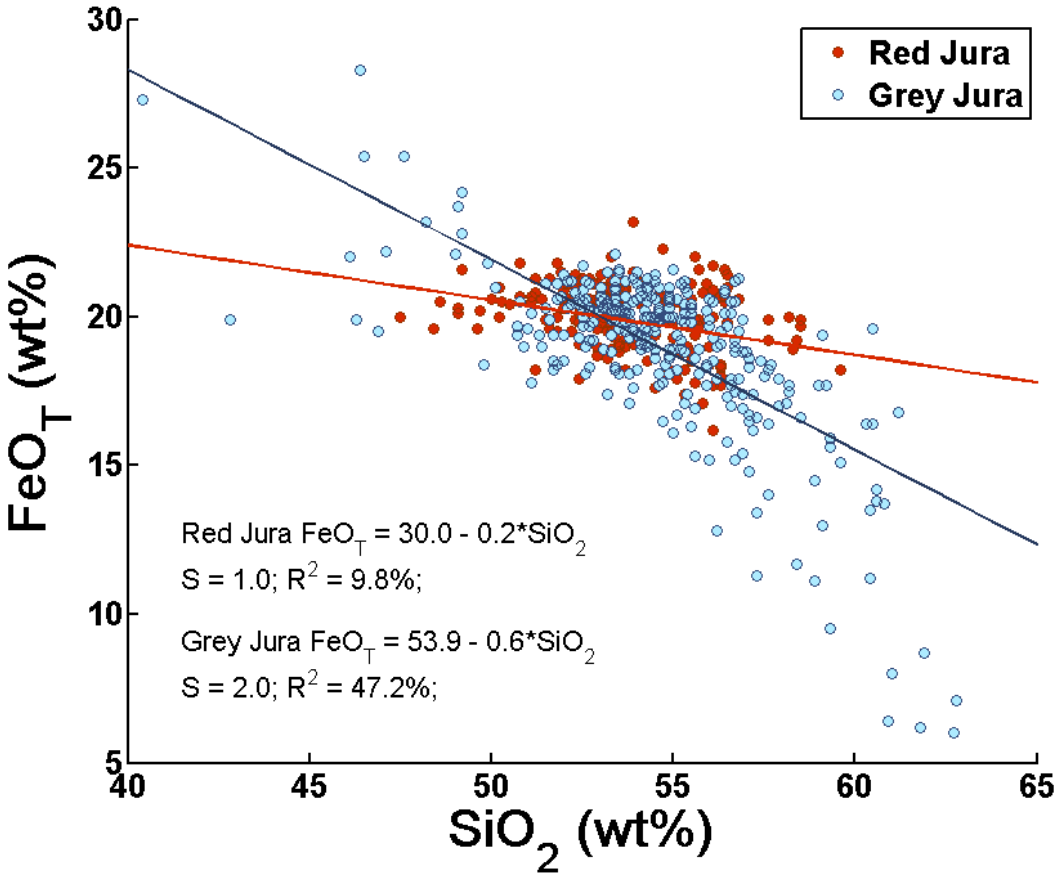

Figure 5.16: Simple linear regression model results to test the linear correlation between FeO_T and SiO_2 within the Red (red line) and Grey Jura (grey line) analyses. Straight line equation, standard error of the models (S) and the r^2 value (R^2) is provided in the bottom left hand corner of the plot. The p values for both regression lines were calculated as less than 0.05 making them statistically significant.

In general, Grey Jura patches also appear to demonstrate a greater geochemical range in compositions compared to Red Jura, which is shown by the density contours covering a much larger area of the Harker plots for all major elements (Fig. 5.15). The table of basic statistics between Red and Grey Jura (Table 5.3) also supports a larger range

for Grey Jura compared to Red, though this does not appear to have skewed the mean and median compositions in the Grey Jura dataset.

5.2.3.1. Major element correlations in the grey patches

As geochemical variation between the two VRR Members was shown to be minimal, Pearson correlation coefficients were calculated for all red targets and all grey targets across both Pettegrove Point and Jura Members (See Tables A.5.3. and A.5.4. in the Appendix). In general, grey VRR targets have a greater number of weak (+/- 0.25–0.50), but statistically significant ($p < 0.05$) major element correlations compared to red VRR targets. Most of these weak major element correlations are shared between red and grey analyses (i.e., CaO and SiO_2, or MgO and Al_2O_3), though grey targets show a stronger negative correlation for FeO_T and SiO_2 (-0.69) compared to red (-0.31). Grey targets also have significant, weak negative major element correlations for FeO_T and MgO (-0.34) and TiO_2 and K_2O (-0.25) that are not present for red targets, as well as a weak positive major element correlation for SiO_2 and TiO_2 (0.34; Appendix Tables A.5.3. and A.5.4.).

When the relatively strong FeO_T versus SiO_2 correlation is plotted as a linear regression for Grey Jura (Fig. 5.16), there is a fit of the dataset to the modelled line (r^2 = 47.2 %) in contrast to Red Jura which has no fit (r^2 = 9.8%). However, both Grey and Red Jura datasets are still largely clustered about the mean Jura compositions for SiO_2 (54.3 ± 2.7 wt%) and FeO_T (19.4 ± 2.4 wt%; Table 5.2). Therefore, some process must have generated the scatter for Grey Jura compositions between high FeO_T, low SiO_2 and low FeO_T, high SiO_2 that is not present in Red Jura.

5.3. A discussion and comparison of VRR geochemistry to previous Murray units

Overall, the results of the ChemCam derived bulk geochemical composition for the Pettegrove Point and Jura VRR Members show that they are geochemically equivalent to the underlying Murray formation (Fig. 5.9). This supports the bulk geochemical results from the APXS instrument (Thompson et al., 2018b), as well as sedimentological observations that suggest the Vera Rubin Ridge is a continuation of the lacustrine Murray formation (Edgar et al., 2018b; Fedo et al., 2018). Furthermore, no significant correlations were identified between major element oxides (section 5.2.1.1) and no subfoci were shown in the density contours (section 5.2.1). This geochemical similarity indicates that it is unlikely there has been a significant change in dominant sediment source region for the Murray formation since the Murray Buttes area, and that any alteration that has occurred has been closed system at the scale of the stratigraphic units. Therefore, the dominant source region for the Vera Rubin Ridge Jura and Pettegrove Point Members is likely to also be the silica-rich subalkaline basalt, inferred as the dominant sediment source region for the lower Murray formation in Chapter 3. So, if the lacustrine depositional environment and bulk geochemistry has not changed for VRR Murray compared to that of the earlier Murray Members, why is the Vera Rubin Ridge such a prominent feature in the Mt Sharp succession? The reasons for this may be that either:

1) There is more crystalline hematite relative to amorphous and phyllosilicate FeO_T. This would result in a greater abundance of crystalline hematite that would not increase the bulk FeO_T of the VRR Members and may therefore result in a greater spectral signature of hematite from orbit, or
2) The ridge has more favourable orbital characteristics, e.g., less dust coverage to detect the hematite present in comparison to the underlying Murray formation.

If this is correct, something other than hematite must be contributing to the increased hardness of the Murray formation at the Vera Rubin Ridge.

5.3.1. Determining the abundance of hematite on the VRR from previous CheMin analyses

The main reason the VRR was highlighted as a primary mission aim for *Curiosity* was due to the large spectral signature of hematite detected on the ridge from orbit (Fig. 5.1) which implies paleoenvironmental conditions that may have been habitable for life (Fraeman et al., 2016; 2013). Minor geochemical variations within the standard deviation of Murray compositions have been detected by ChemCam and APXS with increasing elevation in the Murray stratigraphy, such as MgO and Li (Frydenvang et al., 2018b). However, neither geochemical instrument detected substantial deviation in bulk FeO_T throughout the Murray formation (Frydenvang et al., 2018a; Thompson et al., 2018a). Additionally, ChemCam derived density contours show a similar focal composition and standard deviation to that of the bulk Murray formation (Fig. 5.9). This lack of variation for FeO_T suggests that the overall abundance of iron-bearing components in the stratigraphic units has remained the same, which indicates that changes in the relative proportions of these components may be the cause of this strong hematite spectral signal.

Three iron-bearing components have been identified in CheMin analyses of Gale crater's drilled samples; crystalline iron oxides (either hematite or magnetite; Morrison et al., 2018; Rampe et al., 2017; Morris et al., 2016; Treiman et al., 2016; Vaniman et al., 2014), Fe-rich phyllosilicates (such as Fe-saponite; Bristow et al., 2018; Morrison et al., 2018; Rampe et al., 2017; Bristow et al., 2015; Vaniman et al., 2014), and Fe-rich amorphous material (Morrison et al., 2018; Rampe et al., 2017; Treiman et al., 2016;

Dehouck et al., 2014). These iron-bearing components, though fundamentally different, have all been related to the lithified sedimentary unit cement that is considered to be either derived from the diagenetic product of olivine upon burial diagenesis (Chapter 4.3.2.2; Hausrath et al., 2018; Treiman et al., 2016), or due to the percolation of iron-rich groundwaters through the sedimentary succession (Blaney et al., 2014). Unfortunately, only preliminary quantitative abundances of the Stoer, Highfield and Rock Hall CheMin drilled samples have been determined for the ridge at the time of writing (December, 2018), with the Rock Hall analysis still incomplete (Fig. 5.6; Morris et al., 2019). Therefore, the relative mineral and amorphous abundances shown in Fig. 5.6 may change with further analysis and must be referred to with caution. Based on previous CheMin samples drilled below the ridge (Bristow et al., 2018; Rampe et al., 2017), it is likely that mineral abundances have not changed much for VRR samples, particularly given the limited geochemical variability throughout the Murray formation. As such, I discuss the varying proportions of the iron-bearing components in relation to the mineralogical trends exhibited throughout the succession below the VRR in addition to the preliminary VRR results from CheMin.

CheMin drilled samples of the Lower Mt Sharp Group were noted to have varying abundances of hematite and magnetite (Hurowitz et al., 2017; Rampe et al., 2017). Drilled samples with a greater proportion of hematite usually also contained more phyllosilicates and were classed as belonging to the hematite and phyllosilicate (HP) group (Hurowitz et al., 2017). Meanwhile, those with a greater proportion of magnetite also contained more silica and were classed as belonging to the magnetite and silica (MS) group (Hurowitz et al., 2017). APXS analyses of the Murray formation mudstones within the HP Mt Sharp Group also showed indications of Mn-oxidation with positive correlations for Zn that suggest a more oxidising environment (Hurowitz et al., 2017; Rampe et al., 2017). This has led to the development of two hypotheses by Hurowitz et al. (2017) and Rampe et al.

(2017). Either the mineralogical variation is a record of limnological stratification with the oxidised HP group deposited in shallow lake water and the more reduced MS facies deposited in a deeper lacustrine setting (Hurowitz et al., 2017). Alternatively, these mineralogical redox variations were caused from multiple influxes of short-lived, acidic pore fluids (Rampe et al., 2017). These hypotheses were discussed in Chapter 3.2.2.3, with the conclusion that the depositional hypothesis by Hurowitz et al. (2017) is the preferred formation of the HP and MS facies. This was largely due to sedimentological evidence such as interstratified cross-bedded fine sandstones in the HP facies and thin, uninterrupted mudstone laminations for the MS facies supporting variations in lake-depth deposition (Stack et al., 2018; Hurowitz et al., 2017). Furthermore, the presence of minerals such as fluorapatite that are sensitive to acidic fluids also indicate that acidic pore waters was unlikely (Rampe et al., 2017).

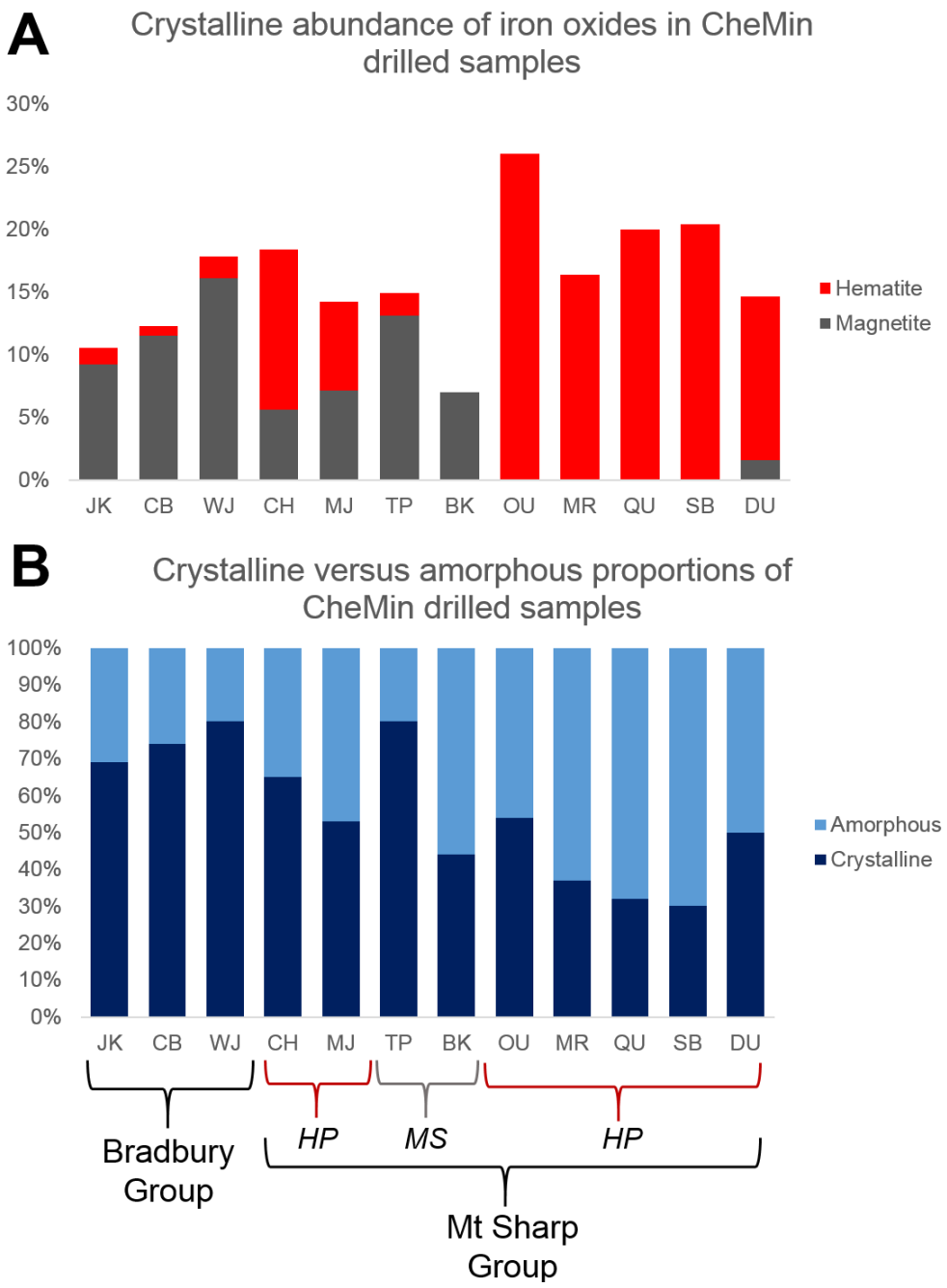

Figure 5.17: A) CheMin derived crystalline abundances of iron oxides within the drilled samples in the Bradbury and Mt Sharp Group. B) The varying proportions of amorphous and phyllosilicate (amorphous) and crystalline components of the CheMin drilled analyses within the Bradbury and Mt Sharp Groups. Overall, a transition can be seen from facies rich in magnetite to that richer in hematite with increasing elevation in the stratigraphy. However, as the amorphous and phyllosilicate component also shows an increase in B of the hematite-rich samples, this suggests that the total iron oxide has remained similar throughout the Mt Sharp succession. JK = John Klein, CB = Cumberland, WJ = Windjana, CH = Confidence Hills, MJ = Mojave, TP = Telegraph Peak, BK = Buckskin, OU = Oudam, MR = Marimba 2, QU = Quela, SB = Sebina and DU = Duluth. CheMin drilled sample data was acquired from Morrison et al. (2018) for samples JK–BK while data for OU–DU was acquired from the NASA PDS node CheMin dataset v3. HP = Hematite and phyllosilicate facies, MS = Magnetite and silica facies classifications from Hurowitz et al. (2017).

After the Marias Pass locality where the Buckskin drill hole was conducted and the MS facies ends, the Murray formation transitions into a more heterolithic assemblage (Fedo et al., 2018; Gwizd et al., 2018). Furthermore, the first evidence of desiccation cracks is found at the Old Soaker outcrop suggesting fluctuating lake levels and a shallow lake environment (Chapter 1.3.4.4; Stein et al., 2018). MnO compositions analysed along the traverse with ChemCam provide further evidence for deposition in more oxic lake waters as they show an increase in MnO concentrations within the Sutton Island and Blunt's Point Members (Lanza et al., 2018). Hence, it is likely that the HP facies closer to the VRR were deposited in shallower lake waters, potentially as a result of seasonal variations or a temporal shift towards a drier climate (Bristow et al., 2018; Lanza et al., 2018; Hurowitz et al., 2017). CheMin and SAM (Evolved Gas Analyser instrument suite on-board *Curiosity*) analysis of the phyllosilicate portion of the Marimba 2, Quela and Sebina drilled mudstone samples within the Karasberg and Sutton Island Members (see section 1.3.4 for a description of the Murray Members) also show an increasing proportion of dioctahedral smectites with increasing elevation in the Mt Sharp Group stratigraphy (Bristow et al., 2018). These greater abundances of dioctahedral clays provides further support to a transition from the MS facies at Marias Pass back to the HP facies and a shallower lake environment (Bristow et al., 2018), with decreasing distance to the Vera Rubin Ridge.

The crystalline iron oxide content of the CheMin analyses taken from the Murray Buttes locality to the base of the VRR show that hematite fully dominates the iron oxides in the crystalline assemblage (Fig. 5.17; Bristow et al., 2018). Marimba 2, Quela and Sebina contain only hematite in their crystalline component (~20 ± 1.5 wt% phyllosilicates; Fig. 5.17) in addition to the aforementioned abundance of Fe^{3+}-bearing dioctahedral smectites (Marimba 2 = ~28 ± 5 wt%; Bristow et al., 2018). The drilled Murray sample Oudam taken several hundred metres below the VRR even has the highest

hematite mineral abundance (26.0 ± 1.1 wt% of the crystalline component) and the lowest phyllosilicate abundance (3 ± 1 wt%) of the HP facies so far (Fig. 5.17; Bristow et al., 2018).

Preliminary analyses of the Stoer, Highfield and Rock Hall samples also show that hematite dominates the mineralogical assemblage on the ridge, with the red Pettegrove Point bedrock sample, Stoer possessing the largest hematite abundance on the ridge (Fig. 5.6; Morris et al., 2019). Stoer's preliminary abundance of hematite in the bulk sample (Fig. 5.6) is comparable to that of Oudam's (13.9 ± 0.4 wt%, Bristow et al., 2018) though Stoer has a notably higher phyllosilicate abundance (~15 wt%; Morris et al.) which may be a factor of different grain sizes or paleoenvironment of deposition. Oudam's drilled sample was taken from a cross-bedded unit with a fine sandstone/siltstone grain size (Bristow et al., 2018; Fedo et al., 2018) which is hypothesised to relate to deposition in an interval of aeolian or fluvial activity, not lacustrine (Bristow et al., 2018; Fedo et al., 2018). Therefore, if Murray on the VRR is an extension of the HP facies, it is more expected for there to be a similar mineralogy to that of the Marimba 2, Quela or Sebina mudstone drilled samples on the VRR, to account for the similarities in grain size and the indistinct bulk chemistry of the Murray formation below and on top of the ridge. Indeed, red VRR Murray contains a high proportion of phyllosilicates along with a high hematite abundance indicating that it formed within the HP facies. However, the quantity of hematite analysed from the VRR drilled samples is very variable, particularly between Red Pettegrove Point (Stoer) and Grey and Red Jura samples (Highfield and Rock Hall). As the hematite-rich, Stoer sample was noted to contain small-scale concretions in its bedrock before it was drilled (Fig. 5.5, section 5.1.2.), it is possible that this higher hematite concentration stems from analysing some of these millimetre-scale concretions. The nodules on the VRR are shown in section 5.2.2.2. to largely have high FeO_T concentrations. Concretions formed from iron oxides have also been previously identified at the base of Mt Sharp (Chapter

3.3.1; Nachon et al., 2017) and elsewhere in Gale crater's stratigraphy (Wiens et al., 2017b). Therefore, it is still possible that VRR Murray formation bedrock which has been relatively unaffected by concretion diagenesis (such as the majority of the Jura Member) has a comparable hematite abundance to that analysed below the ridge in the Blunts Point, Sutton Island, Karasberg and Hartmann Valley Members. If this is true, then it suggests that much of this hematite formed during deposition of the lake sediments similar to the authigenic hypothesis of Fraeman et al. (2016). Further hematite was likely to have then formed during the diagenesis of the concretions that are particularly abundant in the Pettegrove Point Member (Edgar et al., 2018b). Concretions have previously been related to preferential cementation, particularly for the Stimson sandstone, therefore, a later diagenetic event may have also bolstered the hardness of the VRR bedrock making it resilient to erosion and, in places, resistant to drilling by *Curiosity*. A diagenetic hypothesis of hematite formation on the ridge is currently under development through hydrous alteration models, preliminary results of which suggest that a high hematite abundance can occur through the repeated pulses of groundwater (Turner et al., 2019).

Although the relative abundance of hematite to magnetite is approximately equivalent on the ridge relative to the underlying Murray Blunts Point, Karasberg and Hartmanns Valley Members, a variation in the relative proportion of hematite to the iron-bearing amorphous and phyllosilicate component may also be what has caused the bulk FeO_T concentration to remain the same as that below the VRR with the increase in crystalline hematite in samples affected by the concretion diagenesis. The Marimba 2, Quela and Sebina drilled samples below the ridge all contained high abundances of amorphous and phyllosilicate components relative to the crystalline iron oxide (Fig. 5.17 B). Meanwhile, the Duluth sample immediately at the base of the ridge has a much higher proportion of crystalline material (Fig. 5.17 B) which is maintained across the Stoer and Highfield drilled samples according to the preliminary results (Fig. 5.6; Morris et al.,

2019). Therefore, this further suggests that crystalline hematite for bedrock on the ridge dominates the pore-filling cement more so than the softer, amorphous and phyllosilicate component, bolstering its hardness.

To summarise, high abundances of hematite in the VRR bedrock do not appear to be consistent across the ridge (Fig. 5.6; Morris et al., 2019) and likely relate to a later diagenetic event that formed the abundant concretions in the Pettegrove Point Member. Instead, to maintain the similar mineral assemblage and ChemCam derived bulk geochemistry of the Mt Sharp Group presented in this Chapter, it is probable that most hematite on the ridge formed authigenically in a similar paleoenvironment that deposited the HP Murray facies below the ridge. Therefore, a dominant hematite mineralogy is not restricted to the ridge, or the MH1 and MH2 localities and is in fact present throughout several hundred metres of the Murray formation HP facies below (Fig. 5.17). If this hypothesis is correct, it also suggests that the strong hematite characteristics of the ridge detected from orbit may be the result of better conditions on VRR for detecting hematite which are explored further in the next section.

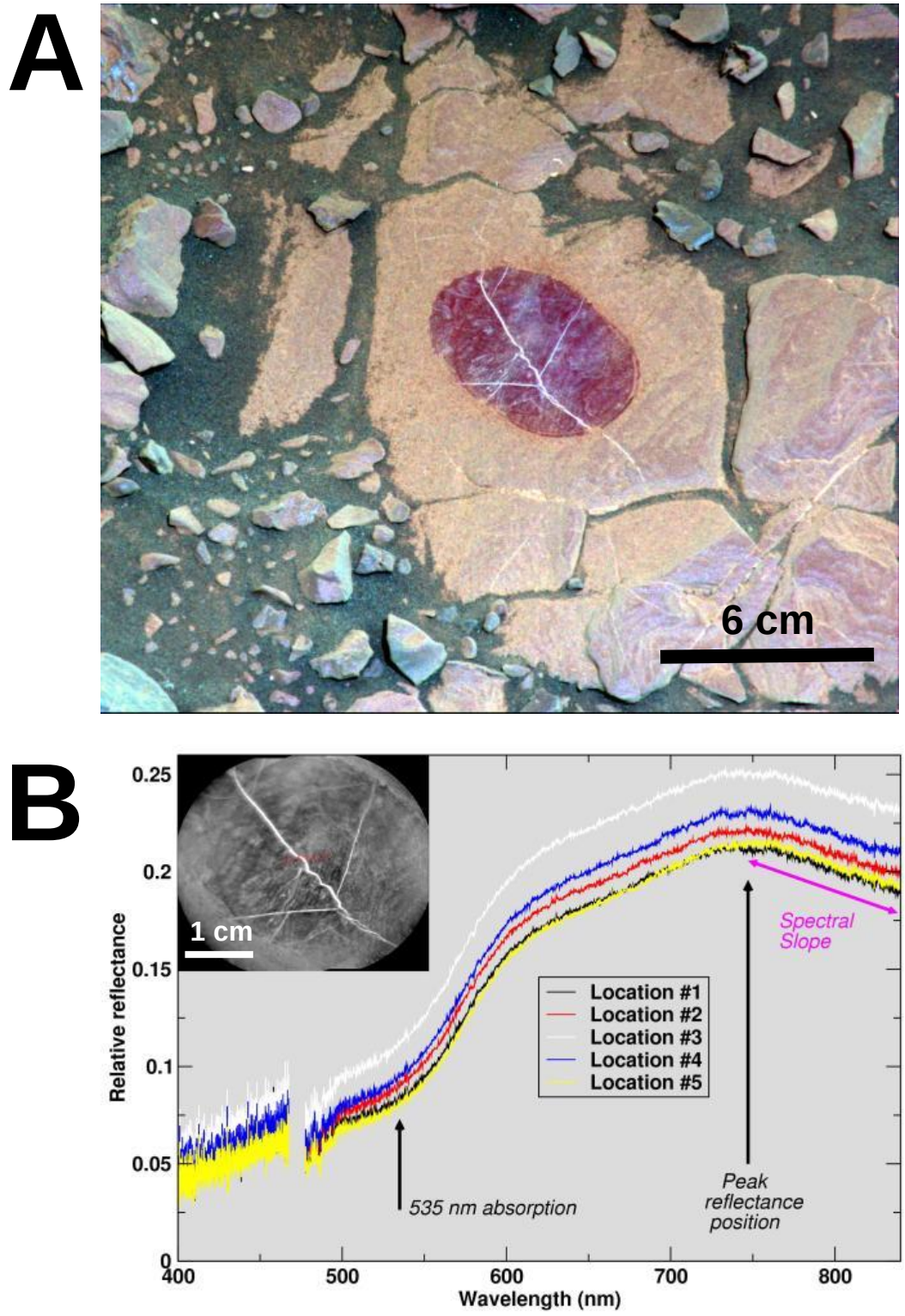

Figure 5.18: A) Multispectral target Christmas Cove of the Pettegrove Point Member of the Vera Rubin Ridge. The strong hematite absorption signatures were revealed only when dust was removed from this target using the Dust Removal Tool. B) ChemCam passive spectra of Christmas Cove with the characteristic hematite spectral features annotated.

Image credit: NASA/JPL-Caltech/LANL/CNES/IRAP/LPGNantes/CNRS/IAS

5.3.2. Ridge characteristics and the spectral capabilities to detect hematite

Certain sedimentary characteristics of the rock (such as grain size), or environmental characteristics (i.e., dust coverage) can affect the extent at which mineralogical spectral signatures are detected from orbit (Rampe et al., 2018; Dehouck et al., 2017*;* Fraeman et al., 2016; Arvidson et al., 2014; Ehlmann et al., 2013; Fraeman et al., 2013; Pelkey et al., 2007). For instance, dust coverage on the crater floor masked the absorption features of phyllosilicates present in the Yellowknife Bay locality from the CRISM instrument on-board MGO (Dehouck et al., 2017*;* Arvidson et al., 2014). This is due to CRISM being a reflectance spectroscopy technique that probes only the top microns of a sample (typically ~1–10 μm) over the area determined by its spatial resolution - typically 20 m/pixel (Pelkey et al., 2007). Hence, surface coatings, weathering rinds and textural characteristics (i.e., intimate mixing of materials) can complicate the detection of minerals from orbit (Murchie et al., 2009; Pelkey et al., 2007).

Isolated hematite-rich pixels not associated with either the VRR, HM1 or HM2 hematite-rich areas of the Mt Sharp Group (section 5.1.1) are observed which may allude to the continuation of the HP facies below the ridge discussed in section 5.3.1. However, these isolated hematite-rich pixels generally show shallower 0.86 μm band depths which can be a result of lower hematite abundances, differences in grain size, or an increase in dust cover relative to the hematite-rich area (Fraeman et al., 2016). The previous section discusses the likelihood that the VRR has a similar hematite abundance to the HP facies of the Murray formation below in relation to the other crystalline components. So, variation in hematite abundance is probably not the main cause for the obscured hematite spectral signature. It has been previously noted that the detection of hematite by CRISM is influenced by the particle size and shape within the sedimentary units (Fraeman et al.,

2016). If hematite grains are larger than ~5 μm or smaller than 5–10 μm (nanophase), the absorption band for hematite (0.86 μm) becomes obscured, possibly to the point of no detection (Fraeman et al., 2016). However, as MAHLI images do not show a systematic change in grain size with *Curiosity*'s traverse towards and over the ridge (Edwards et al., 2018), this also appears unlikely to have masked the hematite absorption feature from orbit for the lower Murray formation. It therefore appears probable that the Murray formation beneath the VRR has a greater dust coverage compared to that on top of the ridge. This would be expected given that the VRR is a prominent, resistant feature on the slopes of Mt Sharp. The ridge is therefore not only more exposed to Gale crater's variable diurnal wind regime, but may also shield the dust on the lower Murray formation from wind erosion during the downslope night time flow (Newman et al., 2017). Spectral data from Mastcam and ChemCam of the ridge also show how dust can obscure hematite detections (Fraeman et al., 2018: Jacobs et al., 2018). Even from the ground, hematite spectral signatures are clearly identified by *Curiosity*'s passive spectral instruments only along fractures (Fraeman et al., 2017) or where the dust has been brushed off the surface by the dust removal tool of the robotic arm (Fig. 5.18).

5.4. VRR diagenesis and the formation of the grey and red bedrock

The VRR has a wide variety of alteration features (section 5.1.2.) compared to the rest of the Murray formation, indicating a complex diagenetic history. Of particular interest is the colour variation from red to grey within Members on the ridge (Fig 5.8). If the VRR Members are a continuation of the HP facies identified below the ridge, then it is reasonable to assume that the dominant red colouration of the rocks (particularly in the Pettegrove Point Member) formed with the authigenic precipitation of hematite during deposition, similar to how red beds form on Earth (Eren et al., 2015; Walker et al., 1981;

Hubert and Reed, 1978; Van Houten, 1973). For terrestrial red beds such as the Tortonian red mudstones in southern Turkey (Eren et al., 2015) or the Moenkopi formation of the Colorado Plateau, USA (Walker et al., 1981), red hematite pigment is largely ascribed to authigenic precipitation when ferrous iron (Fe^{2+}) has been liberated from iron-bearing detrital minerals into neutral to alkaline pore fluids (Eren et al., 2015; Walker et al., 1981; Hubert and Reed, 1978; Van Houten, 1973). This Fe^{2+} is later converted into insoluble Fe^{3+} due to episodes of dehydration that cause a fluctuation in pH and raise the Eh of the pore fluids. Hematite authigenesis in both mud- and sandstone is usually coupled with Fe/Mg smectites as the nucleation of hematite occurs between clay flakes and continues until the pore is filled (Eren et al., 2015; Walker et al., 1981). These terrestrial examples could be somewhat analogous to the red mudstones in Gale crater, if geochemical and mineralogical variations between planets are taken into account (i.e., Martian rocks in general have a much higher FeO_T concentration and lack the quartz and limestone component found in many terrestrial sediments). Hence, if Martian 'red beds' followed the same method of formation as terrestrial red beds, this would indicate a warm climate with alternating wet and dry seasons (Eren et al., 2015; Dubiel and Smoot, 1994). A semi-arid paleoenvironment would sufficiently oxidise neutral-to-alkaline pore waters during evaporation in the dry periods, and/or cause the fluctuation in pH to precipitate hematite as the dominant oxide soon after deposition (Eren et al., 2015). A paleoenvironment with fluctuations in wet and dry periods is similar to the oxic, shallow water lake environment already inferred for the HP Murray facies from geochemical (Lanza et al., 2018*;* Mangold et al., 2019; Thompson et al., 2018a; Hurowitz et al., 2017), mineralogical (Bristow et al., 2018; Hurowitz et al., 2017) and sedimentological evidence (Edgar et al., 2018a; Stein et al., 2018). Furthermore, the preliminary CheMin analysis of the red Pettegrove Point Stoer bedrock sample and underlying, Duluth sample also drilled from red bedrock contain

phyllosilicates (Morris et al., 2019) that may have formed alongside the hematite in this scenario.

So far, Gale crater's main sedimentological evidence that show evidence of dry-periods is at the Old Soaker outcrop in the Sutton Island Member (see Chapter 1.3.4.4 for more information). Old Soaker possesses polygonal fractures interpreted as desiccation cracks that were later infilled by sediment and Ca-sulfate veins (Stein et al., 2018). The red colouration of the Old Soaker outcrop's desiccated layer (Stein et al., 2018), and dominance of hematite and dioctahedral smectites identified in the Sebina drilled sample of the Sutton Island Member (Bristow et al., 2018), further supports a similar terrestrial red bed origin of these Murray Members below the ridge. Morphological evidence of a shallow, permanent to ephemeral subaqueous environment during the deposition of the VRR Murray mudstones comes with the presence of swallowtail gypsum pseudomorphs (Fig. 5.5 F; Edgar et al., 2018b). Swallowtail gypsum precipitates in shallow, ephemeral environments on the Earth (Bachmann and Aref, 2005), therefore its presence in the Jura Member supports a hypothesis that the VRR Murray is an extension of the HP facies as discussed in section 5.3.

Only 0.1 wt% hematite cement is required to generate a red colouration in mudstones on Earth (Walker and Honea, 1969), which are more likely to become red beds in an alternating wet-and-dry climate than sandstones as they retain pore-water for longer (Eren et al., 2015). For this reason, red mudstone beds can share a sharp boundary between grey sandstone units (Eren et al., 2015). The greater porosity in sandstone units results in better drainage, so fewer iron-bearing detrital minerals are subjected to alteration (Eren et al., 2015). Furthermore, any hematite that does form is more likely to be in the coarser-grained specularite variety that is also grey in colour (Walker et al., 1981). However, grey patches in Pettegrove Point and Jura Members do not appear to be conformable with

bedding (Fig. 5.18) indicating that this change in colour did not occur syndepositionally (L'Haridon et al., 2018b). Also, as mentioned previously, MAHLI images do not show a variation in grain size along the VRR traverse (Edwards et al., 2018) so grey patches are unlikely to pertain to areas with a coarser grain size.

ChemCam derived bulk compositions for Red and Grey Jura indicate subtle geochemical differences (Fig. 5.15; section 5.2.3). Derived bulk compositions suggest that Grey Jura is slightly more enriched in Al_2O_3, SiO_2, and Na_2O, but depleted in MgO and K_2O compared to Red Jura bedrock (Table 5.2 and Fig. 5.15). Additionally, Grey Jura has a greater range in FeO_T and TiO_2 compositions (Fig. 5.15 C & G). Enrichments in Al_2O_3 and TiO_2 are usually indicative of leaching as these elements are typically the least mobile in open system settings (Nesbitt and Wilson, 1992). Furthermore, a depletion in MgO and enrichment in SiO_2 indicates the breakdown of mafic minerals that are most susceptible to alteration such as olivine and pyroxene with the subsequent remobilisation of MgO away from the grey areas (Mangold et al., 2019; Nesbitt and Wilson, 1992). This mobilised MgO may not have migrated far as the surrounding Red Jura has slightly higher MgO relative to bulk Murray (Fig. 5.15). Additionally, some Jura nodules, erosion resistant features and unusual textures show high MgO concentrations (Fig. 5.13 D). Therefore, remobilised MgO may have also partitioned into some of these alteration features by either combining with sulfates to form Mg-sulfate features similar to what is identified at the base of the Murray formation (Hurowitz et al., 2017; Nachon et al., 2017), or through the mechanism that formed the raised ridges of the Sheepbed Member mudstone in Yellowknife Bay (Bridges et al., 2015a; Leveille et al. 2014).

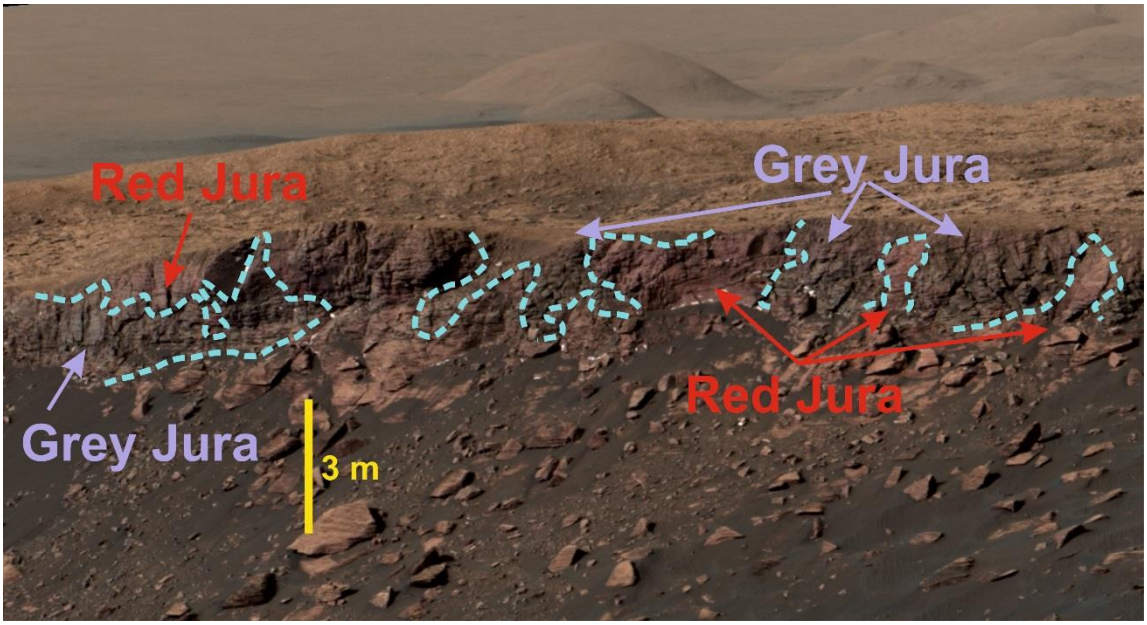

Figure 5.19: Mastcam mosaic mcam10769, sol 2038 of the Red Cliff target. This target is of exposed Pettegrove Point bedrock that shows grey patches discordant with the horizontal bedding of the Vera Rubin Ridge Member. The scale is provided with the vertical yellow line and was calculated by Dr. Steve Banham.

Another major element oxide that is likely to have experienced remobilisation in the grey patches is FeO_T. This is inferred from the large range in FeO_T concentrations for Grey Jura density contours relative to Red Jura contours (Fig. 5.15 C), the stronger negative correlation of FeO_T against SiO_2 for grey patches (section 5.2.2.1.) and the localisation of high-FeO_T alteration features to the Grey Jura patches (Fig. 5.13 B). In particular, dark-toned, Fe-rich features that are identified alongside Ca-sulfate veins in the grey patches are surrounded by low-iron, light-toned halos within the host rock. These vein-related nodular features do not correlate with any other element and are therefore assumed to relate to an enrichment of iron oxide from the surrounding bedrock (L'Haridon et al., 2018b). Ca-sulfate veins are observed throughout the Gale crater stratigraphic record (Rapin et al., 2016; Nachon et al., 2014) and are associated with late-stage, diagenetic fluids (see also Chapters 3 and 4). Therefore, given that these Fe-rich nodules are located within and surrounding veins, they likely formed contemporaneously with the Ca-sulfate veins as a late stage diagenetic feature after the formation of the grey patches (L'Haridon

et al., 2018b). Away from the high-iron features in Grey Jura, a smooth transition is also noted towards lower FeO_T concentrations to relatively higher SiO_2 (Frydenvang et al., 2018b). This low FeO_T trend may also suggest an earlier remobilisation of iron away from this area, but not to the same extent as for MgO. This could also relate to the breakdown of mafic minerals through leaching processes, which would therefore suggest that the grey patches would be richer in felsic material that is more resilient to chemical breakdown (e.g., Hausrath et al., 2008; Burns, 1993).

An enrichment in felsic minerals relative to mafic minerals in the Grey Jura compared to Red Jura would explain the elevated bulk Na_2O, SiO_2 and Al_2O_3 concentrations (Fig. 5.15 E). As Na_2O is only enriched in the bulk composition and not in alteration features this suggests that it is most likely dominantly situated within feldspar of detrital origin. Therefore, an increase in Na_2O in the Grey Jura relative to the Red could further support that these patches formed through diagenetic leaching of MgO and possibly FeO_T from the breakdown of mafic minerals away from these localities.

On the Earth, the bleaching and discoloration of red beds (e.g., Fig. 5.20) occur whenever acidic or reducing diagenetic fluids remove the authigenic hematite pore coating (Rainoldi et al., 2014; Fu et al., 2007; Schaumacher, 1996). This reaction may also form pyrite and siderite as a result of the dissolution of hematite, and leave larger grains of hematite intact in the initial sediment (Fu et al., 2007; Schaumacher, 1996). Bleaching of red beds has mostly been documented in relation to hydrocarbon seepages such as the Velma field in Oklahoma (Donovan, 1974), the Dushanzi anticline, China (Fu et al., 2007) or the Los Chihuidon High, Argentina (Rainoldi et al., 2014). In these settings, migrating hydrocarbons constitute the reducing fluid, though any reducing fluid is capable of forming grey patches in red beds (Schaumacher, 1996). Analogous to the VRR, bleaching is also

largely discordant with bedding (Fig. 5.20) and has occurred at variable scales with some discoloration visible from orbit (Rainoldi et al., 2014; Fu et al., 2007).

Figure 5.20: A terrestrial example of red bed bleaching in Argentina. This image was taken from Rainoldi et al. (2014) study tracing the upward migration of hydrocarbons in the Los Chihuidos High, Neuquén Basin, Argentina. Here, hydrocarbons were the reducing fluid that removed the pore-lining hematite from the cement and created colour variations discordant to bedding. On Mars, a different reducing fluid may have created the variation in colour seen on the Vera Rubin Ridge.

In Gale crater, discoloration of the bedrock from diagenetic fluids has already been identified previously with the silica-rich, fracture associated alteration halos (Fig 1.17 D; Frydenvang et al., 2017; Yen et al., 2017). Although these are largely related to fractures in the Stimson formation, their visual relationship to bedrock weaknesses is less obvious in the Murray formation at Marias Pass (Chapter 3.3.2; Frydenvang et al., 2017). Geochemical variations for the alteration halos in the Stimson formation show strong enrichments in SiO_2, with weak positive correlations for TiO_2 and negative correlations for all other major elements (Frydenvang et al., 2017; Yen et al., 2017). One hypothesis on the nature of these fluids is that they were neutral to alkaline which enabled the dissolution of silica from the Marias Pass tridymite-bearing mudstone locality (Frydenvang et al., 2017).

Later, the silica was deposited in the overlying Stimson formation due to a change in pH (Frydenvang et al., 2017), and it is the high concentration of silica and removal of mafic minerals that caused the light-toned colouration (Frydenvang et al., 2017; Yen et al., 2017).

Major element correlations for Grey Jura analyses show a weak positive correlation for SiO_2 and TiO_2, however they do not share the same strong SiO_2-enrichment and depletion in major element oxides (Fig. 5.15). Therefore, the remobilisation of major elements for Grey Jura patches is minimal compared to the fracture-associated halos identified in the Marias Pass and Bridger Basin areas, and unlikely to relate to the same silica-saturated fluids. However, some similarities exist such as the potential dissolution of mafic minerals, and enrichment in Na_2O from the presence of feldspar minerals that indicate some form of leaching environment (Yen et al., 2017). Additionally, the preliminary results of the CheMin Highfield analysis indicates some opal-CT in the amorphous component (Fig. 5.6; Morris et al., 2019) which was also identified in the halo-altered Stimson Lubango and Greenhorn drilled samples (Yen et al., 2017). The presence of opal-CT further supports some minor leaching in the bedrock through the interaction of a reducing fluid.

The discoloration of the Jura bedrock is likely to have occurred after the initial deposition of the VRR mudstone units. The initial Jura and Pettegrove Point Members formed their red hematite pigmentation during their deposition in a semi-arid climate. Later, the hematite cement was bolstered by repeated pulses of groundwater (Turner et al., 2019; Bridges et al., 2015b) forming the concretions, though it is not known whether this diagenesis came before, after or during the diagenesis that formed the grey patches. Grey patch diagenesis formed when a reducing groundwater fluid migrated throughout the VRR Murray units causing the dissolution of mafic minerals and remobilisation of MgO and FeO_T. Grey Jura patches are largely situated within local topographic lows indicating that

the remobilisation of MgO and FeO_T within these patches made the bedrock weaker and less resilient to erosion. The remobilisation of MgO and FeO_T from the Grey patches may have therefore also contributed to the cement and concretions in the surrounding red patches and formed the other MgO and FeO_T-rich alteration features (such as unusual textures and erosion resistant features). The preliminary CheMin analyses of the Grey Jura bedrock sample Highfield compared to the Red Pettegrove Point bedrock sample shows a lower abundance of phyllosilicates, higher abundance of the amorphous component and less hematite compared to the red Pettegrove Point analysis. The Red Jura Rock Hall sample does not have the amorphous and phyllosilicate abundances as there has not yet been sufficient analysis time (~10 hours spread over several days) to produce the 'major frame' from which these abundances are calculated (Morris et al., 2019; Morrison et al., 2018; Blake et al., 2012). The major frame is composed of all X-ray data stored as CCD images acquired during the full analysis (Blake et al., 2012) and, as this has not yet been acquired, the preliminary results presented here also have a higher uncertainty compared to the other samples (Morris et al., 2019). Preliminary results of Rock Hall do show a relatively high abundance of akagenite, anhydrite and jarosite in the sample (Fig. 5.6; Morris et al., 2019). The unique shiny and knobbly texture of the bedrock from which Rock Hall was sampled (Fig. 5.5 D) compared to the rest of the ridge indicates that this locality may have experienced a localised aqueous alteration process. Akageneite can either form from the alteration of sulphide/pyrrhotite by sulfidic/acidic aqueous fluids (Schwenzer et al., 2016b; Deer, Howie and Zussman, 1992), in a highly saline and chlorinated aqueous environment (Bibi et al., 2011: Burns, 1993) or in Cl- and Fe-rich hydrothermal systems (Holm et al., 1983). It has been identified at several locations on Mars with CRISM data, and is hypothesised to have formed from localised, mildly acidic (pH ~3–6), low temperature (< 100°C), highly saline and chlorinated aqueous environments such as those found in a retreating lagoon scenario (Carter et al., 2015). It is

possible that the Rock Hall sample was drilled in a portion of bedrock that formed in a part of the Murray formation on the shoreline where the lake waters were subject to evaporation and became saline/chlorinated as a result.

Once the grey patches formed, late-stage calcium-sulfate diagenetic fluids migrated along fractures and bedrock weaknesses to form the calcium-sulfate mineral veins observed throughout Gale crater's stratigraphic record. But, due to the more reducing conditions that generated the grey patches, the sulfate-rich fluids leached FeO_T from the surrounding bedrock and deposited it as iron oxide nodules around the veins and gypsum crystal habits (L'Haridon et al., 2018b).

5.5. Conclusions

Overall, this study into the geochemistry of the VRR shows that the Pettegrove Point and Jura Members are likely a continuation of the hematite and phyllosilicate-rich Murray facies below the ridge. The red colouration is hypothesised to be a product of the wet-and-dry shallow lake conditions under which the mudstone was initially deposited. These semi-arid conditions caused fluctuations in pH and Eh that precipitated hematite between clay sheets in the pores and generated the red colouration (Eren et al., 2014). This red bed scenario is not only applicable to the Murray formation at the VRR but also to the underlying Members, particularly to localities with other evidence of deposition in a semi-arid paleoenvironment such as the Old Soaker outcrop with desiccation cracks (Stein et al., 2018). Diagenesis along the ridge occurred in several stages, with the hardness of the VRR likely to have been formed by a later diagenetic episode that precipitated additional hematite cement in the VRR Pettegrove Point mudstone pores to form the high abundance of iron oxide concretions in this Member. Other diagenetic events that happened on the ridge include the formation of the grey patches and the precipitation of the calcium-sulfate

veins. Bulk ChemCam geochemical variations between Grey and Red Jura suggest leaching of MgO and FeO_T to form the grey patches. If leaching was the main cause of the geochemical variation and difference in colour between the Red and Grey Jura bedrock, I would expect that Red Jura has a greater proportion of the phyllosilicate component, with higher FeO_T and MgO abundances in its amorphous component relative to Grey Jura. Furthermore, if the grey patches were also formed with the interaction of a reducing fluid I would expect them to have a lower abundance of mafic minerals, pyrite to have replaced the red pore-lining hematite similar to what is observed in the terrestrial examples of red bed diagenesis, and some magnetite precipitation for iron oxides that formed under these reducing conditions. Currently, the preliminary CheMin analyses only show a lower abundance of phyllosilicates and the presence of magnetite in the Grey Jura bedrock sample relative to the Red Pettegrove Point bedrock sample (Morris et al., 2019), however, it is possible that further analysis may also reveal the differences discussed above.

The strong hematite spectral signature derived from orbit specific to the ridge is likely a result of the VRR being more exposed to the Gale crater wind regime, and therefore less likely to have surficial dust obscuring its spectral signature. Members of the Murray formation situated below the ridge after the Marias Pass area are also dominated by hematite iron oxides, have increasing proportions of dioctahedral smectites (Bristow et al., 2018), and also show variable MnO concentrations (Lanza et al., 2018) consistent with deposition in shallow lake waters. Therefore, some aspects of Fraeman et al., (2016) is consistent with the interpretation of formation for the HP facies of the Murray formation inasmuch that abundant hematite may have formed as a result of the interaction of Fe^{2+} rich lake/pore waters with an oxidation event such as ephemeral lake conditions. However, this does not solely apply to Murray on the VRR, and does not in itself explain the hardness of VRR bedrock. Instead, the alternative hypothesis of Fraeman et al. (2013) involving the mixing of groundwater with varying redox potentials post-deposition, or Turner et al.

(2019) who invokes the possibility of multiple episodes of groundwater circulation, are the most likely to have made the ridge more erosion resistant than the underlying bedrock and increased hematite precipitation in the pores of the red bedrock.

It is still uncertain why reducing fluids may have been restricted to the VRR, however, it is possible that they were prevented from migrating into the lower units due to the impermeability of the PhU (e.g., Fig. 5.2 C; Fraeman et al., 2016). These are not the only models for the formation of the Vera Rubin Ridge as ongoing work to model the thermochemical conditions required to develop a high hematite abundance in the VRR mudstones is underway (Turner et al., 2019). Furthermore, the quantification of the mineral and amorphous assemblage for VRR drilled samples by CheMin in the Grey (Highfield) and Red (Stoer, Rock Hall) Member analyses will constrain whether or not the hematite, or another cementing component is the key to unlocking why the Vera Rubin Ridge is such a prominent, orbitally identified hematite-rich and erosion resistant feature.

6. Synthesis and Further Work

6.1. Introduction

Over six years after landing in Gale crater, the *Curiosity* rover continues to generate an unrivalled chemostratigraphic dataset with the ChemCam instrument. The research presented in this thesis has provided new insight on how source region compositions and sedimentological processes relating to fluvial, lacustrine and aeolian environments have affected the geochemistry across the stratigraphic groups and units so far analysed along *Curiosity*'s traverse. Prior to *Curiosity* landing in Gale crater, geochemical variation within the Martian crust was largely attributed to variably altered, basaltic sediment provenances and minimal evidence existed for the presence of evolved magmatic crustal rocks (e.g., Buz et al., 2017; Ehlmann and Buz, 2015; Smith and Bandfield, 2012; Bibring et al., 2006). The full extent of fluviolacustrine stratigraphy preserved in Gale crater was also poorly understood, with some authors hypothesising that Gale crater contained only a thin veneer of fluviolacustrine deposits (Kite et al., 2013). Furthermore, hematite appeared to be largely isolated to the hematite-rich Vera Rubin Ridge (VRR), and few phyllosilicate bearing units were identified in the lower Mt Sharp stratigraphy (Fraeman et al., 2013). This restricted the range of geological units thought to contain information about the potentially habitable conditions within Gale, but the features seen from orbit still made it a promising candidate for the MSL mission (Grotzinger et al., 2012).

Since landing, several key waypoints and stratigraphic units such as the K-feldspar bearing Kimberley sandstones (Treiman et al., 2016) and silicic Marias Pass mudstones (Frydenvang et al. 2017; Morris et al., 2016) were shown to contain minerals indicative of an evolved magmatic source region. Furthermore, sedimentary units deposited by fluviolacustrine processes were shown to be substantially more extensive than previously recognised from orbit (Stack et al., 2016; Grotzinger et al., 2015; 2014). The research

presented in this thesis has helped to constrain the geochemical effects of mineral sorting for ancient fluvial (Bradbury Group, Chapter 3), lacustrine (Bradbury and Mt Sharp Groups, Chapter 3 & 5) and aeolian (Stimson formation, Chapter 4) processes on Mars, as well as identify the geochemical characteristics of a new sediment source region in Gale crater (Chapter 3), and how chemical weathering and alteration affected the geochemistry of these eroded sediments that were deposited and lithified in Gale crater (Chapters 3, 4 & 5). Furthermore, analysing the bulk geochemistry of Gale's stratigraphic units has shown that previously identified sediment source regions likely contributed beyond the original waypoints of identification (Chapter 3), and that the Vera Rubin Ridge locality is part of the Mt Sharp Group's Murray formation, and hence, the long-lived, habitable, lake environment that contributed to >300 m of stratigraphic succession from the base of Mt Sharp (Chapter 5).

Within the MSL science team, this work has helped support sedimentological interpretations such as geochemically identifying the prevailing NE wind direction for the ancient Stimson sandstones (Banham et al., 2018 and Chapter 4), and discussing which early hypothesis for the formation of the VRR is most likely given the most recent geochemical data from the surface (Fraeman et al., 2016 and Chapter 5). Defining the dust and alteration-free bulk compositions for each stratigraphic group will also help future MSL campaigns identify changes between main stratigraphic units through using the methodology presented in this thesis. The calculated constrained dataset compositions will additionally provide a basis for hydrous alteration models (e.g., Turner et al., 2019). The development of the density contour analytical method using ChemCam LIBS data and derived Gale crater endmember compositions will also be useful in order to compare Gale crater's geochemistry to that of SuperCam LIBS geochemical data that will be acquired in Jezero crater (Wiens et al., 2017b). The SuperCam instrument suite is a "highly evolved version" of the ChemCam instrument suite that will fly on-board the Mars2020 rover and

use LIBS, Raman, and visible and infrared passive reflectance (VISIR) spectroscopy techniques on geological targets up to 7 m from the rover mast (Wiens et al., 2017b).

With regards to global Martian geochemistry, the identification in this thesis of a new igneous compositional endmember contributing to Mt Sharp further extends the known geochemical complexity of the ancient highland crust around Gale crater. Furthermore, Gale crater is not the only crater on Mars that has a layered central mound (Bennett et al., 2016; Malin and Edgett, 2000). Nor is it the only locality on Mars that contains fluvial, lacustrine and aeolian deposits (e.g., Stack et al., 2014a; Malin and Edgett, 2000). Therefore, if the stratigraphy within Gale crater is related to a global stratigraphic record that potentially also preserved in the other craters with central mounds (Bennett et al., 2016; Kite et al., 2016; Malin and Edgett, 2000), or at other sites around Mars that contain fluviolacustrine and aeolian sedimentary deposits, such as the delta fan and lake deposits preserved in Jezero crater the landing site of the Mars2020 rover (Golombek et al., 2018; Goudge et al., 2017), then the derived geochemical effect of mineral sorting and diagenesis in this study will be applicable to these other sites on Mars as well.

In this Chapter, I synthesise the main conclusions of the thesis Chapters 3–5, and discuss the wider implications these conclusions have on the field of Martian geochemistry and future missions to the Martian surface (section 6.2), as well as the future work that can develop from this study (section 6.3).

6.2. Wider implications for Martian Geochemistry

6.2.1. Implications of this research to the geological history of Gale crater

The main results of this thesis show that the substantial geochemical variation identified within Gale's geological record has been associated with multiple stages of aqueous alteration, different mineral sorting regimes and changes in sediment source regions. As a whole, the work from this thesis has contributed to the understanding of Gale crater's geological history over the stratigraphy analysed by *Curiosity*. The following is my interpretation of Gale crater's geological history based on the results and conclusions discussed in this thesis which are illustrated in figures 6.1 and 6.2.

Sedimentary material from which the earlier Bradbury Group was derived was transported into Gale crater as part of a fluviolacustrine system (Fig. 6.1 B). This fluviolacustrine system largely eroded from the dominant subalkaline basalt endmember that has been detected elsewhere on Mars (such as Gusev crater), with lesser contributions from the trachybasalt and trachytic source regions (Fig. 6.1 C). However, as time went by, the trachytic sediment source region grew in dominance for the fluvial sandstones of the Bradbury Group, creating the high potassium abundances of the Kimberley sandstone and conglomerate units. Later, the dominant sediment source region changed to a distinct, more silica-rich subalkaline basalt with minor contributions from the trachyte source during the deposition of the Mt Sharp Group within the long-lived, paleolake (Fig. 6.1 D). Sediment contribution from this silicic, subalkaline basalt was interrupted on one known occasion by a short-lived, strongly silicic volcanic source region, the eroded products of which became more concentrated in the magnetite-silica (MS) facies representative of deeper lake deposits due to their low density and fine grain size (Fig. 6.1 C). After this short change in

sediment source regions, the silica-rich, subalkaline basalt persisted as the main sediment source for Gale's paleolake, even as the climate potentially transitioned to become more semi-arid, depositing the hematite-rich facies at, and immediately below, the VRR (Fig. 6.1 E).

Finally, once the climate in Gale crater had become too arid to support a lacustrine environment, and dry, aeolian processes started to predominate, the previous subalkaline basalt source region that deposited the early Bradbury units returned to contribute to the ancient aeolian dune sands (Figs. 6.1 F and 6.2). This contribution of the subalkaline basaltic source region was made either directly from the sediment source, or indirectly by the erosion and preferential incorporation of the earlier, coarser Bradbury Group sediments into the Stimson formation dunes (Fig. 6.2). Subtle geochemical variation within the ancient aeolian Stimson formation suggests that a change in net sediment transport direction occurred from SW-NE identified in this study and by Banham et al. (2018), to the NE-SW net sediment transport direction identified within Gale crater today (Ewing et al., 2017). The dominant sediment source region for the modern Bagnold dune deposits is also likely a subalkaline basalt. Although slight geochemical differences in Al_2O_3, Na_2O, FeO_T and CaO, and stark differences in pyroxene minerals (augite and pigeonite are present in the Bagnold dunes while pigeonite and orthopyroxene exists in the Stimson formation; Morrison et al., 2018) indicates that this basaltic source region was different to that from which the Stimson formation was derived, which is to be expected given the opposite sediment transport directions.

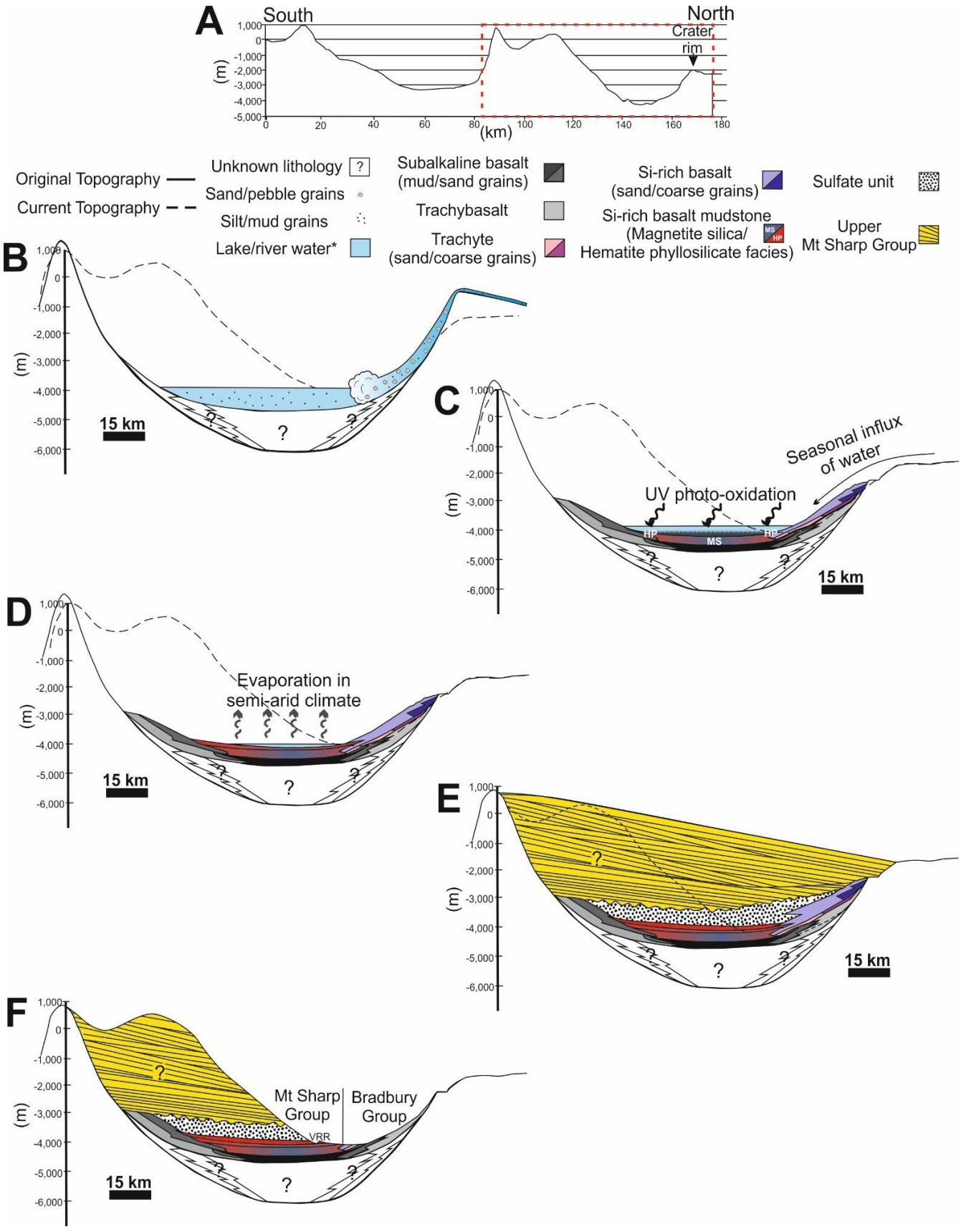
A
South
North
Crater rim
(m)
(km)
Original Topography
Current Topography
Unknown lithology
Sand/pebble grains
Silt/mud grains
Lake/river water*
Subalkaline basalt (mud/sand grains)
Trachybasalt
Trachyte (sand/coarse grains)
Si-rich basalt (sand/coarse grains)
Si-rich basalt mudstone (Magnetite silica/ Hematite phyllosilicate facies)
Sulfate unit
Upper Mt Sharp Group
B
C
Seasonal influx of water
UV photo-oxidation
HP
MS
D
Evaporation in semi-arid climate
E
F
Mt Sharp Group
Bradbury Group
VRR
15 km

Figure 6.1 (previous page): A schematic cartoon based on Grotzinger et al. (2015) (Fig. 1.16) showing the geological evolution of Gale crater's sedimentary units according to the findings of this PhD. A) A cross-section of Gale crater with the red box highlighting the area under consideration. B) A fluviolacustrine system transports sedimentary material into Gale crater, eroding the northern crater rim and deposited sediments of a sand grain size and coarser in the river deposits and silt/mud grains in the lake body. C) After the deposition of the Bradbury Group, which contains sediments derived from subalkaline basalt, trachybasalt and trachyte source regions, the Mt Sharp Group sediments were deposited in the lake environment from a largely Si-rich basaltic source. Mineralogy of the Mt Sharp Group is dependent on the depth of deposition in the lake in relation to the limnological boundary, with deposition in distal, deeper waters creating the magnetite silica (MS) facies and deposition in proximal to the shoreline, oxic waters precipitating hematite and phyllosilicates (Hurowitz et al., 2017).Although not shown here due to scale, a thin unit of tridymite-bearing mudstone was also deposited in the MS facies, likely from a rhyolitic source region, D) Later, conditions became more semi-arid resulting in shallower lake waters and a greater precipitation of hematite and phyllosilicates. E) Deposition of the sulfate units and Upper Mt Sharp Group until the crater was filled to at least the height of present day Mt Sharp. The increased pressure and temperature caused burial diagenesis to occur in the lower units, bolstering the hematite concentration in the hematite-rich Members that derive the Vera Rubin Ridge stratigraphy, F) Aeolian deflation eroded Mt Sharp to its current topographic profile.

**Lake and river water levels are exaggerated to properly illustrate the sedimentological processes. Lake depths are estimated to be between a few metres to 10s of metres (Grotzinger et al., 2015).*

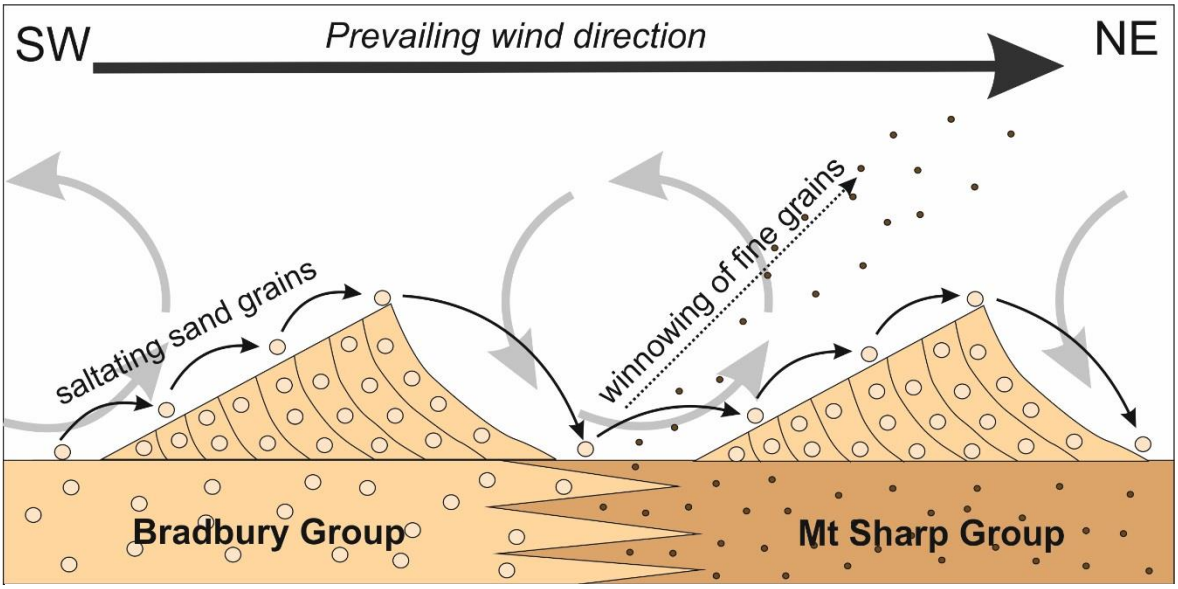

Figure 6.2: A schematic diagram illustrating the preferential transportation and preservation of the coarser Bradbury Group fluvial sediments over the fine-grained Mt Sharp Group mudstones during the migration of the Stimson formation dunes. Light grey arrows show local wind cells influenced by the dune topography.

My research suggests that chemical weathering remained low throughout the formation of Gale's sedimentary units, and post-depositional alteration occurred in a closed water-rock system at the scale of the stratigraphic units. These results differ from the interpretations of several members of the APXS (Hurowitz et al., 2017; Siebach et al., 2017a) and ChemCam (Mangold et al., 2018) teams who link APXS and ChemCam observation point geochemical variation with increased weathering at the sediment source or during deposition. My results support that chemical weathering may have increased slightly between the time during which the Bradbury Group and the Mt Sharp Groups were deposited, however, the extent of this increase is debatable within the instrument error of ChemCam (Chapter 3). Furthermore, linear regression models suggest that chemical weathering was not enough to mask source region characteristics (Chapter 3). After the deposition of the sedimentary units, burial diagenesis formed closed-system alteration features such as concretions, nodules and raised ridges, particularly in the Bradbury Group Sheepbed mudstones. Later, interactions with groundwater, particularly along bedrock

weaknesses, formed open-system alteration features such as calcium-sulfate cement, veins and nodules, as well as silica-rich alteration halos and grey patches along the VRR. The existence of open-system, aqueous alteration features in the Stimson aeolian sandstone indicates that the existence of groundwater in Gale crater outlasted the paleolake, extending the duration of time for which Gale was habitable (Frydenvang et al., 2017).

6.2.2. Implications of this research for the future of Mars exploration

The research presented in this thesis has helped to constrain the geological record for Gale crater along *Curiosity*'s traverse so far, in particular, that relating to changes in sediment provenance. *Curiosity*'s next mission aims are to explore the phyllosilicate bearing unit (PhU) and Greenheugh pediment situated beyond the Vera Rubin Ridge (Stack et al., 2019). The PhU is identified in a trough behind the VRR (Anderson and Bell, 2010) and was selected as the next area to investigate due to its strong phyllosilicate spectral signatures from orbit (Stack et al., 2019; Fraeman et al., 2016; Anderson and Bell, 2010). The orbitally derived spectral features of the PhU phyllosilicates indicate either the presence of Fe/Mg phyllosilicates or a mixture of Al and Fe/Mg phyllosilicates in the geological unit (Fraeman et al., 2016; Thomson et al., 2011). Both Al and Fe/Mg phyllosilicates have been identified in situ within the mud and sandstone units sampled from the Bradbury and Mt Sharp Groups. This work will help place the PhU into stratigraphic context by utilising bulk geochemical analysis and comparing it with the bulk compositions of previous units, similar to the work presented in Chapter 5 for the VRR. Fe/Mg smectites were most abundant in the Sheepbed Member mudstone of the Bradbury Group (Vaniman et al., 2014), while Al-bearing phyllosilicates became more dominant with elevation in the Mt Sharp Group stratigraphy (Bristow et al., 2018). Therefore, a

return to a high proportion of Fe/Mg phyllosilicates may indicate a return to a mudstone geochemistry more similar to the Sheepbed Member identified at the base of Gale crater's stratigraphic record analysed by *Curiosity*. As a result, the work from this thesis will subsequently continue to aid in understanding which sediment provenance contributed to new localities explored by *Curiosity* with the upcoming campaigns.

The Greenheugh Pediment is another feature of interest which *Curiosity* will likely investigate during the PhU campaign. The Greenheugh Pediment is hypothesised to relate to the Siccar Point Group, potentially as a contiguous deposit to the Stimson formation (Fraeman et al., 2016). This hypothesis is based on the similarities in thermophysical, spectral and morphological features of this high thermal inertia unit with the Stimson formation at the base (Fraeman et al., 2016). The inferred orbital relation of the Greenheugh pediment to the Stimson formation will be investigated thoroughly as *Curiosity* gets closer. In this instance, the work from this thesis constraining the bulk Stimson geochemistry and the geochemical effects of mineral sorting from aeolian processes will also be of use in determining the relationship of both these units.

Mars was previously thought to be a basaltic planet with little geochemical complexity in its crustal compositions. Therefore, the outcome of the work in Chapter 3 that geochemical difference between and within the stratigraphic units can be linked to at least five magmatic/volcanic source regions (subalkaline basalt, silica-rich basalt, trachybasalt, trachyte and highly silicic volcanic source) supports others that have identified evolved magmatic compositions at the surface of Mars (Edwards et al., 2017; Treiman et al., 2016; Anderson et al., 2015; Vaniman et al., 2014; Bandfield et al., 2006; 2004), and in Martian samples (e.g., Filiberto et al., 2014; Agee et al., 2013; Humayun et al., 2013). The NASA Mars2020 and ESA/Roscosmos ExoMars missions will investigate the surface of Mars at Jezero crater and Oxia Planum respectively in the near future. With

the geochemical complexity identified in Gale crater relating to at least 5 distinct source regions, in addition to the mineral sorting regimes and diagenetic processes identified in this thesis, these future missions will have a better insight into what the geochemical and mineralogical complexity of Mars can be. Future missions will also be able to compare observed geochemical variation at their landing sites to the bulk stratigraphic group compositions and defined alteration trends identified in Gale crater through this research. In particular, the NASA Mars2020 rover will have on-board the SuperCam instrument suite (Wiens et al., 2017b). SuperCam utilises both LIBS and Raman spectroscopy to get both atomic and molecular information of the geological targets (Wiens et al., 2017b). Furthermore, the paleoenvironment that deposited much of the exposed geological record in Jezero crater is hypothesised to be a prograding delta fan into a crater paleolake (Golombek et al., 2018; Goudge et al., 2017), similar to Gale crater. This suggests that the bulk density contour methods used in this research can be utilised by the SuperCam science team in the future to make direct comparisons of Jezero crater's geochemistry and geology to that observed in Gale and discussed in this thesis.

6.3. Suggestions for future work

This thesis has shown the geochemical complexity of the Ancient Highland Martian crust surrounding Gale crater, in addition to the geochemical effects sedimentological processes have on the eroded sediments during transportation, deposition and lithification. Future work can continue to investigate this geochemical complexity preserved in Mars' geological record using the methods developed in this thesis for *Curiosity*'s investigation into the PhU, and towards the Greenheugh pediment. Once the VRR campaign has come to a close, and the XRD data has been processed from CheMin,

future work can further constrain whether the hypotheses relating to the geochemical variation across the ridge made in Chapter 5 are correct.

The methods used in this thesis will also be applicable to the data that will be generated with the Mars2020 rover's SuperCam instrument suite for the fluviodeltaic environment in Jezero crater (Golombek et al., 2018; Goudge et al., 2017; Wiens et al., 2017b). This will generate an unprecedented geochemical dataset for two localities on the Martian surface that will determine whether the geochemical complexity seen within Gale crater is present at other locations on the Martian surface.

Finally, now that the estimated source region compositions of Gale's lithified units have been discerned, along with the geochemical variation associated with common alteration features, this compositional data can be used as a basis for future hydrous alteration models (e.g., Turner et al., 2019). The prevalence of diagenetic features throughout Gale's geological record, even within the dry aeolian dune deposits of the Stimson formation, suggests that groundwater was present long after the paleolake had disappeared (Frydenvang et al., 2017). This suggests that habitable conditions had continued after the climate changed towards the cold, dry climate of the Hesperian/Amazonian. Conducting hydrous alteration models from the compositions and geochemical trends defined in this thesis for Gale crater's sedimentary rocks will help to determine the habitability of the groundwater conditions that generated these diverse range of diagenetic features.

To conclude, this thesis represents a significant step towards understanding the geochemical variation in the Martian crust for the Late Noachian/Early Hesperian time period in Gale crater. My work has developed an effective method for identifying changes in sediment provenance within the geological record of Mars using LIBS observation point data from the ChemCam instrument. The results and conclusions of this thesis have further

constrained the geological history of Gale, as well as how Martian fluvial, lacustrine and aeolian paleoenvironments effect the geochemistry of the deposited sediments. The outcomes of this thesis will therefore have wider implications to global Martian geochemistry as the sedimentological processes that generated these unit in Gale (fluvial, lacustrine and aeolian) have reworked and deposited much of the material across the Martian surface which will be explored further by future missions (NASA's Mars2020 mission and ESA's ExoMars rover) to the Martian surface.

7. References

Achilles, C. N., Downs, R. T., Ming, D. W., Rampe, E. B., Morris, R. V., Treiman, A. H., Morrison, S. M., Blake, D. F., Vaniman, D. T., Ewing, R. C., Chipera, S. J., Yen, A. S., Bristow, T. F., Ehlmann, B. L., Gellert, R., Hazen, R. M., Fendrich, K. V., Craig, P. I., Grotzinger, J., Des Marais, D. J., Farmer, J. D., Sarrazin, P. C., and Morookian, J.-M., 2017, Mineralogy of an Active Eolian Sediment from the Namib Dune, Gale Crater, Mars: Journal of Geophysical Research: Planets, v. 122, no. 11, p. 2344-2361.

Acuña, M., Connerney, J., Wasilewski, P., Lin, R., Mitchell, D., Anderson, K., Carlson, C., McFadden, J., Rème, H., and Mazelle, C., 2001, Magnetic field of Mars: Summary of results from the aerobraking and mapping orbits: Journal of Geophysical Research: Planets, v. 106, no. E10, p. 23403-23417.

Acuña, M. H., Connerney, J. E. P., Wasilewski, P., Lin, R. P., Anderson, K. A., Carlson, C. W., McFadden, J., Curtis, D. W., Mitchell, D., Reme, H., Mazelle, C., Sauvaud, J. A., d'Uston, C., Cros, A., Medale, J. L., Bauer, S. J., Cloutier, P., Mayhew, M., Winterhalter, D., and Ness, N. F., 1998, Magnetic Field and Plasma Observations at Mars: Initial Results of the Mars Global Surveyor Mission: Science, v. 279, no. 5357, p. 1676-1680.

Adams, J. B., Smith, M. O., and Johnson, P. E., 1986, Spectral mixture modeling: A new analysis of rock and soil types at the Viking Lander 1 site: Journal of Geophysical Research: Solid Earth, v. 91, no. B8, p. 8098-8112.

Agee, C. B., Wilson, N. V., McCubbin, F. M., Ziegler, K., Polyak, V. J., Sharp, Z. D., Asmerom, Y., Nunn, M. H., Shaheen, R., Thiemens, M. H., Steele, A., Fogel, M. L., Bowden, R., Glamoclija, M., Zhang, Z., and Elardo, S. M., 2013, Unique Meteorite from Early Amazonian Mars: Water-Rich Basaltic Breccia Northwest Africa 7034: Science, v. 339, no. 6121, p. 780-785.

Allen, C. C., Gooding, J. L., Jercinovic, M., and Keil, K., 1981, Altered basaltic glass: A terrestrial analog to the soil of Mars: Icarus, v. 45, no. 2, p. 347-369.

Anderson, R., Bridges, J. C., Williams, A., Edgar, L., Ollila, A., Williams, J., Nachon, M., Mangold, N., Fisk, M., Schieber, J., Gupta, S., Dromart, G., Wiens, R. C., Le Mouélic, S., Forni, O., Lanza, N., Mezzacappa, A., Sautter, V., Blaney, D., Clark, B. C., Clegg, S., Gasnault, O., Lasue, J., Leveille, R., Lewin, E., Lewis, K. W., Maurice, S., Newsom, H., Schwenzer, S. P., and Vaniman, D., 2015, ChemCam results from the Shaler outcrop in Gale crater, Mars: Icarus, v. 249, p. 2-21.

Anderson, R. B., and Bell III, J. F., 2010, Geologic mapping and characterization of Gale crater and implications for its potential as a Mars Science Laboratory landing site.: Mars, v. 5, p. 76-128.

Andrews-Hanna, J. C., Zuber, M. T., Arvidson, R. E., and Wiseman, S. M., 2010, Early Mars hydrology: Meridiani playa deposits and the sedimentary record of Arabia Terra: Journal of Geophysical Research: Planets, v. 115, no. E6, p. E06002.

Andrews-Hanna, J. C., Zuber, M. T., and Banerdt, W. B., 2008, The Borealis basin and the origin of the martian crustal dichotomy: Nature, v. 453, p. 1212.

Anguita, F., Farelo, A.-F., López, V., Mas, C., Muñoz-Espadas, M.-J., Márquez, Á., and Ruiz, J., 2001, Tharsis dome, Mars: New evidence for Noachian-Hesperian thick-

skin and Amazonian thin-skin tectonics: Journal of Geophysical Research: Planets, v. 106, no. E4, p. 7577-7589.

Archer, P. D., Franz, H. B., Sutter, B., Arevalo, R. D., Coll, P., Eigenbrode, J. L., Glavin, D. P., Jones, J. J., Leshin, L. A., Mahaffy, P. R., McAdam, A. C., McKay, C. P., Ming, D. W., Morris, R. V., Navarro-González, R., Niles, P. B., Pavlov, A., Squyres, S. W., Stern, J. C., Steele, A., and Wray, J. J., 2014, Abundances and implications of volatile-bearing species from evolved gas analysis of the Rocknest aeolian deposit, Gale Crater, Mars: Journal of Geophysical Research: Planets, v. 119, no. 1, p. 237-254.

Arvidson, R. E., Bellutta, P., Calef, F., Fraeman, A. A., Garvin, J. B., Gasnault, O., Grant, J. A., Grotzinger, J. P., Hamilton, V. E., Heverly, M., Iagnemma, K. A., Johnson, J. R., Lanza, N., Le Mouélic, S., Mangold, N., Ming, D. W., Mehta, M., Morris, R. V., Newsom, H. E., Rennó, N., Rubin, D., Schieber, J., Sletten, R., Stein, N. T., Thuillier, F., Vasavada, A. R., Vizcaino, J., and Wiens, R. C., 2014, Terrain physical properties derived from orbital data and the first 360 sols of Mars Science Laboratory Curiosity rover observations in Gale Crater: Journal of Geophysical Research: Planets, v. 119, no. 6, p. 1322-1344.

Arvidson, R. E., Gooding, J. L., and Moore, H. J., 1989, The Martian surface as imaged, sampled, and analyzed by the Viking landers: Reviews of Geophysics, v. 27, no. 1, p. 39-60.

Babechuk, M. G., Widdowson, M., and Kamber, B. S., 2014, Quantifying chemical weathering intensity and trace element release from two contrasting basalt profiles, Deccan Traps, India: Chemical Geology, v. 363, p. 56-75.

Bachmann, G. H., and Aref, M. A. M., 2005, A seismite in Triassic gypsum deposits (Grabfeld Formation, Ladinian), southwestern Germany: Sedimentary Geology, v. 180, no. 1, p. 75-89.

Baker, V. R., 2001, Water and the martian landscape: Nature, v. 412, p. 228.

Baker, V. R., Strom, R. G., Gulick, V. C., Kargel, J. S., Komatsu, G., and Kale, V. S., 1991, Ancient oceans, ice sheets and the hydrological cycle on Mars: Nature, v. 352, p. 589.

Bandfield, J. L., 2006, Extended surface exposures of granitoid compositions in Syrtis Major, Mars: Geophysical Research Letters, v. 33, no. 6, p. L06203.

Bandfield, J. L., Hamilton, V. E., and Christensen, P. R., 2000, A Global View of Martian Surface Compositions from MGS-TES: Science, v. 287, no. 5458, p. 1626-1630.

Bandfield, J. L., Hamilton, V. E., Christensen, P. R., and McSween, H. Y., 2004, Identification of quartzofeldspathic materials on Mars: Journal of Geophysical Research: Planets, v. 109, no. E10, p. E10009.

Banham, S., Gupta, S., Rubin, D., Watkins, J., Sumner, D., Grotzinger, J., Lewis, K., Edgett, K., Edgar, L., and Stack, K., The Stimson Formation: Determining the Morphology of a Dry Aeolian Dune System and Its Significance in Gale Crater, Mars, *in* Proceedings 48th Lunar and Planetary Science Conference, Houston, TX, United States, 2017.

Banham, S. G., Gupta, S., Rubin, D. M., Watkins, J. A., Sumner, D. Y., Edgett, K. S., Grotzinger, J. P., Lewis, K. W., Edgar, L. A., Stack-Morgan, K. M., Barnes, R., Bell, J. F., Day, M. D., Ewing, R. C., Lapotre, M. G. A., Stein, N. T., Rivera-Hernandez, F., and Vasavada, A. R., 2018, Ancient Martian aeolian processes and palaeomorphology reconstructed from the Stimson formation on the lower slope of Aeolis Mons, Gale crater, Mars: Sedimentology, v. 65, no. 4, p. 993-1042.

Baratoux, D., Mangold, N., Arnalds, O., Bardintzeff, J. M., Platevoët, B., Grégoire, M., and Pinet, P., 2011, Volcanic sands of Iceland - Diverse origins of aeolian sand deposits revealed at Dyngjusandur and Lambahraun: Earth Surface Processes and Landforms, v. 36, no. 13, p. 1789-1808.

Bedford, C. C., Bridges, J. C., Schwenzer, S. P., Wiens, R. C., Rampe, E. B., Frydenvang, J., and Gasda, P. J., 2019, Alteration trends and geochemical source region characteristics preserved in the fluviolacustrine sedimentary record of Gale crater, Mars: Geochimica et Cosmochimica Acta, v. 246, p. 234-266.

Bell III, J. F., Godber, A., McNair, S., Caplinger, M. A., Maki, J. N., Lemmon, M. T., Van Beek, J., Malin, M. C., Wellington, D., Kinch, K. M., Madsen, M. B., Hardgrove, C., Ravine, M. A., Jensen, E., Harker, D., Anderson, R. B., Herkenhoff, K. E., Morris, R. V., Cisneros, E., and Deen, R. G., 2017, The Mars Science Laboratory Curiosity rover Mastcam instruments: Preflight and in-flight calibration, validation, and data archiving: Earth and Space Science, v. 4, no. 7, p. 396-452.

Bennett, K., Edgett, K., Fey, D., Edgar, L., Fraeman, A., McBride, M., and Edwards, C., Fine-Scale Textural Observations at Vera Rubin Ridge, Gale Crater, from the Mars Hand Lens Imager (MAHLI), *in* Proceedings Lunar and Planetary Science Conference, Houston, TX, 2018.

Bennett, K. A., and Bell, J. F., 2016, A global survey of martian central mounds: Central mounds as remnants of previously more extensive large-scale sedimentary deposits: Icarus, v. 264, p. 331-341.

Bibi, I., Singh, B., and Silvester, E., 2011, Akaganéite (β-FeOOH) precipitation in inland acid sulfate soils of south-western New South Wales (NSW), Australia: Geochimica et Cosmochimica Acta, v. 75, no. 21, p. 6429-6438.

Bibring, J.-P., Langevin, Y., Mustard, J. F., Poulet, F., Arvidson, R., Gendrin, A., Gondet, B., Mangold, N., Pinet, P., and Forget, F., 2006, Global mineralogical and aqueous Mars history derived from OMEGA/Mars Express data: Science, v. 312, no. 5772, p. 400-404.

Bindeman, I. N., Sigmarsson, O., and Eiler, J., 2006, Time constraints on the origin of large volume basalts derived from O-isotope and trace element mineral zoning and U-series disequilibria in the Laki and Grímsvötn volcanic system: Earth and Planetary Science Letters, v. 245, no. 1, p. 245-259.

Bish, D., Blake, D., Vaniman, D., Sarrazin, P., Bristow, T., Achilles, C., Dera, P., Chipera, S., Crisp, J., and Downs, R., 2014, The first X-ray diffraction measurements on Mars: IUCrJ, v. 1, no. 6, p. 514-522.

Bish, D. L., Blake, D., Vaniman, D. T., Chipera, S. J., Morris, R. V., Ming, D. W., Treiman, A. H., Sarrazin, P., Morrison, S. M., and Downs, R. T., 2013, X-ray diffraction results from Mars Science Laboratory: Mineralogy of Rocknest at Gale crater: Science, v. 341, no. 6153, p. 1238932.

Blake, D. F., Morris, R. V., Kocurek, G., Morrison, S., Downs, R., Bish, D., Ming, D., Edgett, K., Rubin, D., Goetz, W., Madsen, M. B., Sullivan, R., Gellert, R., Campbell, J. L., Treiman, A. H., McLennan, S. M., Yen, A. S., Grotzinger, J., Vaniman, D., Chipera, S. J., Achilles, C., Rampe, E. B., Sumner, D., Meslin, P. Y., Maurice, S., Forni, O., Gasnault, O., Fisk, M., Schmidt, M. E., Mahaffy, P., Leshin, L. A., Glavin, D., Steele, A., Freissinet, C., Navarro-Gonzalez, R., Yingst, A., Kah, L. C., Bridges, N., Lewis, K., Bristow, T. F., Farmer, J., Crisp, J. A., Stolper, E., Des Marais, D., and Sarrazin, P., 2013, Curiosity at Gale crater, Mars: Characterization and analysis of the Rocknest sand shadow: Science, v. 341, no. 6153, p. 1239505.

Blaney, D. L., Wiens, R. C., Maurice, S., Clegg, S., Anderson, R. B., Kah, L. C., Le Mouélic, S., Ollila, A., Bridges, N., and Tokar, R., 2014, Chemistry and texture of the rocks at Rocknest, Gale Crater: Evidence for sedimentary origin and diagenetic alteration: Journal of Geophysical Research: Planets, v. 119, no. 9, p. 2109-2131.

Bloemsma, M. R., Zabel, M., Stuut, J. B. W., Tjallingii, R., Collins, J. A., and Weltje, G. J., 2012, Modelling the joint variability of grain size and chemical composition in sediments: Sedimentary Geology, v. 280, p. 135-148.

Bogard, D. D., and Garrison, D. H., 1999, Argon-39-argon-40 “ages” and trapped argon in Martian shergottites, Chassigny, and Allan Hills 84001: Meteoritics & Planetary Science, v. 34, no. 3, p. 451-473.

Bogard, D. D., and Johnson, P., 1983, Martian Gases in an Antarctic Meteorite?: Science, v. 221, no. 4611, p. 651-654.

Borlina, C. S., Ehlmann, B. L., and Kite, E. S., 2015, Modeling the thermal and physical evolution of Mount Sharp's sedimentary rocks, Gale Crater, Mars: Implications for diagenesis on the MSL Curiosity rover traverse: Journal of Geophysical Research: Planets, v. 120, no. 8, p. 1396-1414.

Bourke, M. C., Edgett, K. S., and Cantor, B. A., 2008, Recent aeolian dune change on Mars: Geomorphology, v. 94, no. 1, p. 247-255.

Bridges, J. C., Catling, D. C., Saxton, J. M., Swindle, T. D., Lyon, I. C., and Grady, M. M., 2001, Alteration Assemblages in Martian Meteorites: Implications for Near-Surface Processes: Space Science Reviews, v. 96, no. 1, p. 365-392.

Bridges, J. C., and Grady, M. M., 2000, Evaporite mineral assemblages in the nakhlite (martian) meteorites: Earth and Planetary Science Letters, v. 176, no. 3, p. 267-279.

Bridges, J. C., Hicks, L. J., and Treiman, A. H., 2019, Chapter 5 - Carbonates on Mars, *in* Filiberto, J., and Schwenzer, S. P., eds., Volatiles in the Martian Crust, Elsevier, p. 89-118.

Bridges, J. C., and Schwenzer, S. P., 2012, The nakhlite hydrothermal brine on Mars: Earth and Planetary Science Letters, v. 359-360, p. 117-123.

Bridges, J. C., Schwenzer, S. P., Leveille, R., Westall, F., Wiens, R. C., Mangold, N., Bristow, T., Edwards, P., and Berger, G., 2015a, Diagenesis and clay mineral formation at Gale Crater, Mars: Journal of Geophysical Research: Planets, v. 120, no. 1, p. 1-19.

Bridges, J. C., Schwenzer, S. P., Leveille, R., Wiens, R. C., McAdam, A., Conrad, P., and Kelley, S. P., Martian Chemical Weathering at Hematite Ridge, Gale Crater, *in* Proceedings European Planetary Science Congress, Nantes, France, 2015b.

Bridges, J. C., Sefton-Nash, E., Vago, J., Williams, R., Balme, M., Turner, S., and Fawdon, P., Selection and Characterisation of the ExoMars 2020 Rover Landing Sites, *in* Proceedings 48th Lunar and Planetary Science, Houston, TX, 2017a.

Bridges, J. C., and Warren, P., 2006, The SNC meteorites: basaltic igneous processes on Mars: Journal of the Geological Society, v. 163, no. 2, p. 229-251.

Bridges, N. T., Calef, F. J., Hallet, B., Herkenhoff, K. E., Lanza, N. L., Le Mouélic, S., Newman, C. E., Blaney, D. L., Pablo, M. A., Kocurek, G. A., Langevin, Y., Lewis, K. W., Mangold, N., Maurice, S., Meslin, P.-Y., Pinet, P., Renno, N. O., Rice, M. S., Richardson, M. E., Sautter, V., Sletten, R. S., Wiens, R. C., and Yingst, R. A., 2014, The rock abrasion record at Gale Crater: Mars Science Laboratory results from Bradbury Landing to Rocknest: Journal of Geophysical Research: Planets, v. 119, no. 6, p. 1374-1389.

Bridges, N. T., and Ehlmann, B. L., 2018, The Mars Science Laboratory (MSL) Bagnold Dunes Campaign, Phase I: Overview and introduction to the special issue: Journal of Geophysical Research: Planets, v. 123, no. 1, p. 3-19.

Bridges, N. T., Sullivan, R., Newman, C. E., Navarro, S., van Beek, J., Ewing, R. C., Ayoub, F., Silvestro, S., Gasnault, O., Le Mouélic, S., Lapotre, M. G. A., and Rapin, W., 2017b, Martian aeolian activity at the Bagnold Dunes, Gale Crater: The view from the surface and orbit: Journal of Geophysical Research: Planets, v. 122, no. 10, p. 2077-2110.

Bristow, T. F., Bish, D. L., Vaniman, D. T., Morris, R. V., Blake, D. F., Grotzinger, J. P., Rampe, E. B., Crisp, J. A., Achilles, C. N., Ming, D. W., Ehlmann, B. L., King, P., Bridges, J., Eigenbrode, J. L., Sumner, D., Chipera, S. J., Morookian, J. M., Treiman, A. H., Morrison, S. M., Downs, R. T., Farmer, J., Des Marais, D., Sarrazin, P., Floyd, M. M., Mishna, M., and McAdam, A., 2015, The origin and implications of clay minerals from Yellowknife Bay, Gale crater, Mars: American Mineralogist, v. 100, no. 4, p. 824-836.

Bristow, T. F., Rampe, E. B., Achilles, C. N., Blake, D. F., Chipera, S. J., Craig, P., Crisp, J. A., Des Marais, D. J., Downs, R. T., Gellert, R., Grotzinger, J. P., Gupta, S., Hazen, R. M., Horgan, B., Hogancamp, J. V., Mangold, N., Mahaffy, P. R., McAdam, A. C., Ming, D. W., Morookian, J. M., Morris, R. V., Morrison, S. M., Treiman, A. H., Vaniman, D. T., Vasavada, A. R., and Yen, A. S., 2018, Clay mineral diversity and abundance in sedimentary rocks of Gale crater, Mars: Science Advances, v. 4, no. 6, p. eaar3330.

Burns, R. G., 1993, Rates and mechanisms of chemical weathering of ferromagnesian silicate minerals on Mars: Geochimica et Cosmochimica Acta, v. 57, no. 19, p. 4555-4574.

Buz, J., Ehlmann, B. L., Pan, L., and Grotzinger, J. P., 2017, Mineralogy and stratigraphy of the Gale crater rim, wall, and floor units: Journal of Geophysical Research: Planets, v. 122, no. 5, p. 1090-1118.

Calef, F., Dietrich, W., Edgar, L., Farmer, J., Fraeman, A., Grotzinger, J., Palucis, M., Parker, T., Rice, M., and Rowland, S., Geologic mapping of the Mars Science Laboratory landing ellipse, *in* Proceedings Annual Planetary Geologic Mappers Meeting, Flagstaff, AZ, 2016, Volume 1920.

Campbell, J. L., Andrushenko, S. M., Taylor, S. M., and Maxwell, J. A., 2010, A fundamental parameters approach to calibration of the Mars Exploration Rover Alpha Particle X-ray Spectrometer: 2. Analysis of unknown samples: Journal of Geophysical Research: Planets, v. 115, no. E4, p. E04009.

Carr, M. H., 2000, Martian oceans, valleys and climate: Astronomy & Geophysics, v. 41, no. 3, p. 3.20-23.26.

Carr, M. H., and Head, J. W., 2003, Oceans on Mars: An assessment of the observational evidence and possible fate: Journal of Geophysical Research: Planets, v. 108, no. E5, p. 8.

Carr, M. H., and Head, J. W., 2010, Geologic history of Mars: Earth and Planetary Science Letters, v. 294, no. 3, p. 185-203.

Carter, J., Poulet, F., Bibring, J.-P., and Murchie, S., 2010, Detection of Hydrated Silicates in Crustal Outcrops in the Northern Plains of Mars: Science, v. 328, no. 5986, p. 1682-1686.

Carter, J., Viviano-Beck, C., Loizeau, D., Bishop, J., and Le Deit, L., 2015, Orbital detection and implications of akaganéite on Mars: Icarus, v. 253, p. 296-310.

Cassanelli, J. P., and Head, J. W., 2018, Large-scale lava-ice interactions on Mars: Investigating its role during Late Amazonian Central Elysium Planitia volcanism and the formation of Athabasca Valles: Planetary and Space Science, v. 158, p. 96-109.

Chan, N. H., Perron, J. T., Mitrovica, J. X., and Gomez, N. A., 2018, New Evidence of an Ancient Martian Ocean From the Global Distribution of Valley Networks: Journal of Geophysical Research: Planets, v. 123, no. 8, p. 2138-2150.

Changela, H. G., and Bridges, J. C., 2010, Alteration assemblages in the nakhlites: Variation with depth on Mars: Meteoritics & Planetary Science, v. 45, no. 12, p. 1847-1867.

Chapman, C. R., Pollack, J. B., and Sagan, C., 1968, An Analysis of the Mariner 4 Photography of Mars: SAO Special Report, v. 268.

Chevrier, V., and Mathé, P., 2007, Mineralogy and evolution of the surface of Mars: a review: Planetary and Space Science, v. 55, no. 3, p. 289-314.

Chipera, S. J., and Bish, D. L., 2002, FULLPAT: a full-pattern quantitative analysis program for X-ray powder diffraction using measured and calculated patterns: Journal of Applied Crystallography, v. 35, no. 6, p. 744-749.

Chipera, S. J., and Bish, D. L., 2013, Fitting full X-ray diffraction patterns for quantitative analysis: a method for readily quantifying crystalline and disordered phases: Advances in Materials Physics and Chemistry, v. 3, no. 01, p. 47.

Christensen, P. R., Bandfield, J. L., Hamilton, V. E., Ruff, S. W., Kieffer, H. H., Titus, T. N., Malin, M. C., Morris, R. V., Lane, M. D., Clark, R. L., Jakosky, B. M., Mellon, M. T., Pearl, J. C., Conrath, B. J., Smith, M. D., Clancy, R. T., Kuzmin, R. O., Roush, T., Mehall, G. L., Gorelick, N., Bender, K., Murray, K., Dason, S., Greene, E., Silverman, S., and Greenfield, M., 2001, Mars Global Surveyor Thermal Emission Spectrometer experiment: Investigation description and surface science results: Journal of Geophysical Research: Planets, v. 106, no. E10, p. 23823-23871.

Clarke, J. D. A., and Stoker, C. R., 2011, Concretions in exhumed and inverted channels near Hanksville Utah: implications for Mars: International Journal of Astrobiology, v. 10, no. 3, p. 161-175.

Clegg, S. M., Wiens, R. C., Anderson, R., Forni, O., Frydenvang, J., Lasue, J., Cousin, A., Payré, V., Boucher, T., Dyar, M. D., McLennan, S. M., Morris, R. V., Graff, T. G., Mertzman, S. A., Ehlmann, B. L., Belgacem, I., Newsom, H., Clark, B. C., Melikechi, N., Mezzacappa, A., McInroy, R. E., Martinez, R., Gasda, P., Gasnault, O., and Maurice, S., 2017, Recalibration of the Mars Science Laboratory ChemCam instrument with an expanded geochemical database: Spectrochimica Acta Part B: Atomic Spectroscopy, v. 129, p. 64-85.

Clifford, S. M., and Parker, T. J., 2001, The Evolution of the Martian Hydrosphere: Implications for the Fate of a Primordial Ocean and the Current State of the Northern Plains: Icarus, v. 154, no. 1, p. 40-79.

Cousin, A., Dehouck, E., Meslin, P.-Y., Forni, O., Williams, A. J., Stein, N., Gasnault, O., Bridges, N., Ehlmann, B., Schröder, S., Payré, V., Rapin, W., Pinet, P., Sautter, V., Lanza, N., Lasue, J., Maurice, S., and Wiens, R. C., 2017a, Geochemistry of the Bagnold dune field as observed by ChemCam and comparison with other aeolian deposits at Gale Crater: Journal of Geophysical Research: Planets, v. 122, no. 10, p. 2144-2162.

Cousin, A., Sautter, V., Payré, V., Forni, O., Mangold, N., Gasnault, O., Le Deit, L., Johnson, J., Maurice, S., and Salvatore, M., 2017b, Classification of igneous rocks analyzed by ChemCam at Gale crater, Mars: Icarus, v. 288, p. 265-283.

Craddock, R. A., and Howard, A. D., 2002, The case for rainfall on a warm, wet early Mars: Journal of Geophysical Research: Planets, v. 107, no. E11, p. 21-36.

Craddock, R. A., and Maxwell, T. A., 1993, Geomorphic evolution of the Martian highlands through ancient fluvial processes: Journal of Geophysical Research: Planets, v. 98, no. E2, p. 3453-3468.

Das, B. K., Al-Mikhlafi, A. S., and Kaur, P., 2006, Geochemistry of Mansar Lake sediments, Jammu, India: implication for source-area weathering, provenance, and tectonic setting: Journal of Asian Earth Sciences, v. 26, no. 6, p. 649-668.

Davis, J. M., Balme, M., Grindrod, P. M., Williams, R. M. E., and Gupta, S., 2016, Extensive Noachian fluvial systems in Arabia Terra: Implications for early Martian climate: Geology, v. 44, no. 10, p. 847-850.

Day, M., Anderson, W., Kocurek, G., and Mohrig, D., 2016, Carving intracrater layered deposits with wind on Mars: Geophysical Research Letters, v. 43, no. 6, p. 2473-2479.

Day, M., and Kocurek, G., 2016, Observations of an aeolian landscape: From surface to orbit in Gale Crater: Icarus, v. 280, p. 37-71.

Deer, W. A., Howie, R. A., and Zussman, J., 1992, An introduction to the rock-forming minerals, Longman London.

Dehouck, E., Carter, J., Gasnault, O., Pinet, P., Daydou, Y., Gondet, B., Mangold, N., Johnson, J., Arvidson, R., and Maurice, S., Curiosity's traverse through the upper Murray formation (Gale crater): ground truth for orbital detections of Martian clay minerals, *in* Proceedings EGU, Vienna, Austria, 2017, Volume 19, p. 14867.

Dehouck, E., McLennan, S. M., Meslin, P.-Y., and Cousin, A., 2014, Constraints on abundance, composition, and nature of X-ray amorphous components of soils and rocks at Gale crater, Mars: Journal of Geophysical Research: Planets, v. 119, no. 12, p. 2640-2657.

Dera, P., Zhuravlev, K., Prakapenka, V., Rivers, M. L., Finkelstein, G. J., Grubor-Urosevic, O., Tschauner, O., Clark, S. M., and Downs, R. T., 2013, High pressure single-crystal micro X-ray diffraction analysis with GSE_ADA/RSV software: High Pressure Research, v. 33, no. 3, p. 466-484.

Dickinson, W. R., 1988, Provenance and sediment dispersal in relation to paleotectonics and paleogeography of sedimentary basins, New perspectives in basin analysis, Springer, p. 3-25.

Donovan, T. J., 1974, Petroleum microseepage at Cement, Oklahoma: evidence and mechanism: AAPG Bulletin, v. 58, no. 3, p. 429-446.

Dott, R. H., 2003, The Importance of Eolian Abrasion in Supermature Quartz Sandstones and the Paradox of Weathering on Vegetation-Free Landscapes: The Journal of Geology, v. 111, no. 4, p. 387-405.

Dubiel, R. F., and Smoot, J. P., 1994, Criteria for interpreting paleoclimate from red beds-a tool for Pangean reconstructions: Pangea: Global Environments and Resources, v. 17, p. 295-310.

Edgar, L., Fraeman, A., Gupta, S., Fedo, C., Grotzinger, J., Stack, K., Bennett, K., Sun, V., Banham, S., and Stein, N., Sedimentology and Stratigraphy Observed at Vera

Rubin Ridge by the Mars Science Laboratory Curiosity Rover, *in* Proceedings 49th Lunar and Planetary Science Conference, Houston, TX, 2018a.

Edgar, L., Fraeman, A., Gupta, S., Fedo, C., Grotzinger, J., Stack, K., Bennett, K., Sun, V., Banham, S. G., Stein, N., Edgett, K., Rubin, D., House, C. H., and Van Beek, J., A Lacustrine Environment Recorded at Vera Rubin Ridge: Overview of the Sedimentology and Stratigraphy observed by the Mars Science Laboratory Curiosity Rover, *in* Proceedings AGU, Washington, D.C., 2018b.

Edwards, C. S., Bennett, K. A., Vasavada, A. R., Piqueux, S., Hamilton, V., Fraeman, A. A., and Horgan, B., The Thermophysical Variability of the Vera Rubin Ridge as Explored by the Mars Science Laboratory, *in* Proceedings AGU, Washington, D.C., 2018.

Edwards, P. H., Bridges, J. C., Wiens, R., Anderson, R., Dyar, D., Fisk, M., Thompson, L., Gasda, P., Filiberto, J., Schwenzer, S. P., Blaney, D., and Hutchinson, I., 2017, Basalt–trachybasalt samples in Gale Crater, Mars: Meteoritics & Planetary Science, v. 52, no. 11, p. 2931-2410.

Ehlmann, B. L., 2010, Diverse aqueous environments during Mars' first billion years: the emerging view from orbital visible-near infrared spectroscopy: Geochemical News, v. 142, p. gn142.

Ehlmann, B. L., Berger, G., Mangold, N., Michalski, J. R., Catling, D. C., Ruff, S. W., Chassefière, E., Niles, P. B., Chevrier, V., and Poulet, F., 2013, Geochemical consequences of widespread clay mineral formation in Mars' ancient crust: Space Science Reviews, v. 174, no. 1-4, p. 329-364.

Ehlmann, B. L., and Buz, J., 2015, Mineralogy and fluvial history of the watersheds of Gale, Knobel, and Sharp craters: A regional context for the Mars Science Laboratory Curiosity's exploration: Geophysical Research Letters, v. 42, no. 2, p. 264-273.

Ehlmann, B. L., Edgett, K. S., Sutter, B., Achilles, C. N., Litvak, M. L., Lapotre, M. G. A., Sullivan, R., Fraeman, A. A., Arvidson, R. E., Blake, D. F., Bridges, N. T., Conrad, P. G., Cousin, A., Downs, R. T., Gabriel, T. S. J., Gellert, R., Hamilton, V. E., Hardgrove, C., Johnson, J. R., Kuhn, S., Mahaffy, P. R., Maurice, S., McHenry, M., Meslin, P. Y., Ming, D. W., Minitti, M. E., Morookian, J. M., Morris, R. V., O'Connell-Cooper, C. D., Pinet, P. C., Rowland, S. K., Schröder, S., Siebach, K. L., Stein, N. T., Thompson, L. M., Vaniman, D. T., Vasavada, A. R., Wellington, D. F., Wiens, R. C., and Yen, A. S., 2017, Chemistry, mineralogy, and grain properties at Namib and High dunes, Bagnold dune field, Gale crater, Mars: A synthesis of Curiosity rover observations: Journal of Geophysical Research: Planets, v. 122, no. 12, p. 2510-2543.

Ehlmann, B. L., Mustard, J. F., Murchie, S. L., Poulet, F., Bishop, J. L., Brown, A. J., Calvin, W. M., Clark, R. N., Marais, D. J. D., Milliken, R. E., Roach, L. H., Roush, T. L., Swayze, G. A., and Wray, J. J., 2008, Orbital Identification of Carbonate-Bearing Rocks on Mars: Science, v. 322, no. 5909, p. 1828-1832.

Eilers, P. H. C., and Goeman, J. J., 2004, Enhancing scatterplots with smoothed densities: Bioinformatics, v. 20, no. 5, p. 623-628.

Eren, M., Kadir, S., Kapur, S., Huggett, J., and Zucca, C., 2015, Colour origin of Tortonian red mudstones within the Mersin area, southern Turkey: Sedimentary Geology, v. 318, p. 10-19.

Ewing, R. C., Lapotre, M. G. A., Lewis, K. W., Day, M., Stein, N., Rubin, D. M., Sullivan, R., Banham, S., Lamb, M. P., Bridges, N. T., Gupta, S., and Fischer, W. W., 2017,

Sedimentary processes of the Bagnold Dunes: Implications for the eolian rock record of Mars: Journal of Geophysical Research: Planets, v. 122, no. 12, p. 2544-2573.

Fedo, C., Grotzinger, J., Gupta, S., Fraeman, A., Edgar, L., Edgett, K., Stein, N., Rivera-Hernandez, F., Lewis, K., and Stack, K., Sedimentology and Stratigraphy of the Murray Formation, Gale crater, Mars, *in* Proceedings 49th Lunar and Planetary Science Conference, Houston, TX, 2018.

Fedo, C. M., McGlynn, I. O., and McSween, H. Y., 2015, Grain size and hydrodynamic sorting controls on the composition of basaltic sediments: Implications for interpreting martian soils: Earth and Planetary Science Letters, v. 423, p. 67-77.

Filiberto, J., Gross, J., Trela, J., and Ferré, E. C., 2014, Gabbroic Shergottite Northwest Africa 6963: An intrusive sample of Mars: American Mineralogist, v. 99, no. 4, p. 601-606.

Filiberto, J., Treiman, A. H., and Le, L., 2008, Crystallization experiments on a Gusev Adirondack basalt composition: Meteoritics & Planetary Science, v. 43, no. 7, p. 1137-1146.

Fischer, W. R., and Schwertmann, U., 1975, The Formation of Hematite from Amorphous Iron(III)Hydroxide: Clays and Clay Minerals, v. 23, no. 1, p. 33-37.

Forni, O., Gaft, M., Toplis, M. J., Clegg, S. M., Maurice, S., Wiens, R. C., Mangold, N., Gasnault, O., Sautter, V., and Le Mouélic, S., 2015, First detection of fluorine on Mars: Implications for Gale Crater's geochemistry: Geophysical Research Letters, v. 42, no. 4, p. 1020-1028.

Fraeman, A., Bedford, C., Bridges, J., Edgar, L. A., Hardgrove, C., Horgan, B. H., Gabriel, T. S., Grotzinger, J. P., Gupta, S., and Johnson, J. R., Curiosity at Vera Rubin Ridge: Testable Hypotheses, First Results, and Implications for Habitability, *in* Proceedings AGU, New Orleans, Louisiana, 2017.

Fraeman, A., Sun, V., Edgar, L., Fedo, C., Fox, V., Grotzinger, J., Hardgrove, C., Horgan, B., House, C. H., Jacobs, S., Johnson, J. R., Johnson, S. S., Rampe, E. B., Salvatore, M., Stack, K., Thompson, L., Wellington, D. F., Wiens, R., Williams, A., and Vasavada, A. R., Curiosity at Vera Rubin Ridge: Major Findings and Implications for Habitability *in* Proceedings AGU, Washington, D.C., 2018.

Fraeman, A. A., Arvidson, R. E., Catalano, J. G., Grotzinger, J. P., Morris, R. V., Murchie, S. L., Stack, K. M., Humm, D. C., McGovern, J. A., and Seelos, F. P., 2013, A hematite-bearing layer in Gale Crater, Mars: Mapping and implications for past aqueous conditions: Geology, v. 41, no. 10, p. 1103-1106.

Fraeman, A. A., Ehlmann, B. L., Arvidson, R. E., Edwards, C. S., Grotzinger, J. P., Milliken, R. E., Quinn, D. P., and Rice, M. S., 2016, The Stratigraphy and Evolution of Lower Mt. Sharp from Spectra, Morphological, and Thermophysical Orbital Datasets: Journal of Geophysical Research, v. 121, no. 9, p. 1713-1736.

Freissinet, C., Glavin, D. P., Mahaffy, P. R., Miller, K. E., Eigenbrode, J. L., Summons, R. E., Brunner, A. E., Buch, A., Szopa, C., Archer, P. D., Franz, H. B., Atreya, S. K., Brinckerhoff, W. B., Cabane, M., Coll, P., Conrad, P. G., Des Marais, D. J., Dworkin, J. P., Fairén, A. G., François, P., Grotzinger, J. P., Kashyap, S., Kate, I. L., Leshin, L. A., Malespin, C. A., Martin, M. G., Martin-Torres, F. J., McAdam, A. C., Ming, D. W., Navarro-González, R., Pavlov, A. A., Prats, B. D., Squyres, S. W., Steele, A., Stern, J. C., Sumner, D. Y., Sutter, B., and Zorzano, M.-P., 2015, Organic molecules in the Sheepbed Mudstone, Gale Crater, Mars: Journal of Geophysical Research: Planets, v. 120, no. 3, p. 495-514.

Frydenvang, J., Gasda, P. J., Hurowitz, J. A., Grotzinger, J. P., Wiens, R. C., Newsom, H. E., Edgett, K. S., Bridges, J. C., Maurice, S., Fisk, M. R., Johnson, J. R., Rapin, W., Stein, N. T., Clegg, S. M., Schwenzer, S. P., Bedford, C. C., Edwards, P. H., Mangold, N., Cousin, A., Anderson, R. B., Payré, V., Vaniman, D., Blake, D. F., Lanza, N. L., Gupta, S., Van Beek, J., Sautter, V., Meslin, P., Rice, M., Milliken, R., Gellert, R., Thompson, L., Clark, B. C., Sumner, D. Y., Fraeman, A. A., Kinch, K. M., Madsen, M. B., Mirtofanov, I. G., Jun, I., Calef, F., and Vasavada, A. R., 2017, Diagenetic silica enrichment and late-stage groundwater activity in Gale crater, Mars: Geophysical Research Letters, v. 44, no. 10, p. 4716-4724.

Frydenvang, J., Mangold, N., Wiens, R., Clark, B., Fraeman, A., Forni, O., Meslin, P., Ollila, A., Gasda, P., and Payré, V., Geochemical variations observed with the ChemCam instrument on Vera Rubin Ridge in Gale crater, Mars, *in* Proceedings Lunar and Planetary Science Conference2018a, Volume 49.

Frydenvang, J., Mangold, N., Wiens, R., Fraeman, A., Fedo, C., L'Haridon, J., Gupta, S., Clark, B. C., Forni, O., Meslin, P. Y., Ollila, A., Gasda, P., Payre, V., Calef III, F., and Salvatore, M., Geochemical evidence from the ChemCam instrument highlighting the role of diagenesis at Vera Rubin Ridge in Gale crater, Mars, *in* Proceedings AGU, Washington, D.C., 2018b.

Fu, B., Zheng, G., Ninomiya, Y., Wang, C., and Sun, G., 2007, Mapping hydrocarbon-induced mineralogical alteration in the northern Tian Shan using ASTER multispectral data: Terra Nova, v. 19, no. 4, p. 225-231.

Gabasova, L. R., and Kite, E. S., 2018, Compaction and sedimentary basin analysis on Mars: Planetary and Space Science, v. 152, p. 86-106.

Garzanti, E., Vermeesch, P., Andò, S., Vezzoli, G., Valagussa, M., Allen, K., Kadi, K. A., and Al-Juboury, A. I. A., 2013, Provenance and recycling of Arabian desert sand: Earth-Science Reviews, v. 120, p. 1-19.

Gellert, R., and Clark, B. C., 2015, In Situ Compositional Measurements of Rocks and Soils with the Alpha Particle X-ray Spectrometer on NASA's Mars Rovers: Elements, v. 11, no. 1, p. 39-44.

Gellert, R., Rieder, R., Anderson, R. C., Brückner, J., Clark, B. C., Dreibus, G., Economou, T., Klingelhöfer, G., Lugmair, G. W., Ming, D. W., Squyres, S. W., d'Uston, C., Wänke, H., Yen, A., and Zipfel, J., 2004, Chemistry of Rocks and Soils in Gusev Crater from the Alpha Particle X-ray Spectrometer: Science, v. 305, no. 5685, p. 829-832.

Gellert, R., Rieder, R., Brückner, J., Clark, B. C., Dreibus, G., Klingelhöfer, G., Lugmair, G., Ming, D. W., Wänke, H., Yen, A., Zipfel, J., and Squyres, S. W., 2006, Alpha Particle X-Ray Spectrometer (APXS): Results from Gusev crater and calibration report: Journal of Geophysical Research: Planets, v. 111, no. E2, p. E02S05.

Gendrin, A., Mangold, N., Bibring, J.-P., Langevin, Y., Gondet, B., Poulet, F., Bonello, G., Quantin, C., Mustard, J., Arvidson, R., LeMouélic, S., Berthé, M., Bibring, J.-P., Erard, S., Forni, O., Gendrin, A., Gondet, B., Poulet, F., Soufflot, A., Combes, M., Drossart, P., Encrenaz, T., Fouchet, T., Merchiorri, R., Belluci, G., Altieri, F., Formisano, V., Bonello, G., Capaccioni, F., Cerroni, P., Coradini, A., Fonti, S., Kottsov, V., Ignatiev, N., Moroz, V., Titov, D., Zasova, L., Mangold, N., Pinet, P., Douté, S., Schmitt, B., Sotin, C., Hauber, E., Hoffmann, H., Jaumann, R., Keller, U., Arvidson, R., Mustard, J., Duxbury, T., and Forget, F., 2005, Sulfates in Martian Layered Terrains: The OMEGA/Mars Express View: Science, v. 307, no. 5715, p. 1587-1591.

Giesting, P. A., and Filiberto, J., 2016, The formation environment of potassic-chloro-hastingsite in the nakhlites MIL 03346 and pairs and NWA 5790: Insights from terrestrial chloro-amphibole: Meteoritics & Planetary Science, v. 51, no. 11, p. 2127-2153.

Golabek, G. J., Keller, T., Gerya, T. V., Zhu, G., Tackley, P. J., and Connolly, J. A. D., 2011, Origin of the martian dichotomy and Tharsis from a giant impact causing massive magmatism: Icarus, v. 215, no. 1, p. 346-357.

Golombek, M., Grant, J., Farley, K., Williford, K., Otero, R., and Chen, A., Final Three Landing Sites for the Mars 2020 Rover, *in* Proceedings Lunar and Planetary Science Conference, Houston, Texas, 2018.

Golombek, M. P., Grant, J. A., Crumpler, L. S., Greeley, R., Arvidson, R. E., Bell III, J. F., Weitz, C. M., Sullivan, R., Christensen, P. R., Soderblom, L. A., and Squyres, S. W., 2006, Erosion rates at the Mars Exploration Rover landing sites and long-term climate change on Mars: Journal of Geophysical Research: Planets, v. 111, no. E12, p. E12S10.

Goudge, T. A., Milliken, R. E., Head, J. W., Mustard, J. F., and Fassett, C. I., 2017, Sedimentological evidence for a deltaic origin of the western fan deposit in Jezero crater, Mars and implications for future exploration: Earth and Planetary Science Letters, v. 458, p. 357-365.

Green, T. H., Green, D. H., and Ringwood, A. E., 1967, The origin of high-alumina basalts and their relationships to quartz tholeiites and alkali basalts: Earth and Planetary Science Letters, v. 2, no. 1, p. 41-51.

Griffin, W. L., Belousova, E. A., O'Neill, C., O'Reilly, S. Y., Malkovets, V., Pearson, N. J., Spetsius, S., and Wilde, S. A., 2014, The world turns over: Hadean–Archean crust–mantle evolution: Lithos, v. 189, p. 2-15.

Grotzinger, J. P., Crisp, J., Vasavada, A. R., Anderson, R. C., Baker, C. J., Barry, R., Blake, D. F., Conrad, P., Edgett, K. S., Ferdowski, B., Gellert, R., Gilbert, J. B., Golombek, M., Gómez-Elvira, J., Hassler, D. M., Jandura, L., Litvak, M., Mahaffy, P., Maki, J., Meyer, M., Malin, M. C., Mitrofanov, I., Simmonds, J. J., Vaniman, D., Welch, R. V., and Wiens, R. C., 2012, Mars Science Laboratory Mission and Science Investigation: Space Science Reviews, v. 170, no. 1, p. 5-56.

Grotzinger, J. P., Gupta, S., Malin, M. C., Rubin, D. M., Schieber, J., Siebach, K., Sumner, D. Y., Stack, K. M., Vasavada, A. R., and Arvidson, R. E., 2015, Deposition, exhumation, and paleoclimate of an ancient lake deposit, Gale crater, Mars: Science, v. 350, no. 6257, p. aac7575.

Grotzinger, J. P., Sumner, D. Y., Kah, L. C., Stack, K., Gupta, S., Edgar, L., Rubin, D., Lewis, K., Schieber, J., Mangold, N., Milliken, R., Conrad, P. G., DesMarais, D., Farmer, J., Siebach, K., Calef, F., 3rd, Hurowitz, J., McLennan, S. M., Ming, D., Vaniman, D., Crisp, J., Vasavada, A., Edgett, K. S., Malin, M., Blake, D., Gellert, R., Mahaffy, P., Wiens, R. C., Maurice, S., Grant, J. A., Wilson, S., Anderson, R. C., Beegle, L., Arvidson, R., Hallet, B., Sletten, R. S., Rice, M., Bell, J., 3rd, Griffes, J., Ehlmann, B., Anderson, R. B., Bristow, T. F., Dietrich, W. E., Dromart, G., Eigenbrode, J., Fraeman, A., Hardgrove, C., Herkenhoff, K., Jandura, L., Kocurek, G., Lee, S., Leshin, L. A., Leveille, R., Limonadi, D., Maki, J., McCloskey, S., Meyer, M., Minitti, M., Newsom, H., Oehler, D., Okon, A., Palucis, M., Parker, T., Rowland, S., Schmidt, M., Squyres, S., Steele, A., Stolper, E., Summons, R., Treiman, A., Williams, R., Yingst, A., and Team, M. S. L. S., 2014, A habitable fluvio-lacustrine environment at Yellowknife Bay, Gale crater, Mars: Science (New York, N.Y.), v. 343, no. 6169, p. 1242777.

Gwizd, S., Fedo, C., Grotzinger, J., Edgett, K., Rivera-Hernandez, F., and Stein, N., Depositional History of the Hartmann's Valley Member, Murray Formation, Gale Crater, Mars, *in* Proceedings Lunar and Planetary Science Conference, Houston, TX, 2018.

Haddadi, B., Sigmarsson, O., and Devidal, J.-L., Determining intensive parameters through clinopyroxene-liquid equilibrium in Grímsvötn 2011 and Bárðarbunga 2014 basalts, *in* Proceedings EGU, Vienna, Austria, 2015.

Hallis, L. J., Taylor, G. J., Nagashima, K., Huss, G. R., Needham, A. W., Grady, M. M., and Franchi, I. A., 2012, Hydrogen isotope analyses of alteration phases in the nakhlite martian meteorites: Geochimica et Cosmochimica Acta, v. 97, p. 105-119.

Hamilton, V. E., and Christensen, P. R., 2005, Evidence for extensive, olivine-rich bedrock on Mars: Geology, v. 33, no. 6, p. 433-436.

Hammond, A. L., 1972, Mars as an Active Planet: The View from Mariner 9: Science, v. 175, no. 4019, p. 286-287.

Hanna, R. D., Hamilton, V. E., and Putzig, N. E., 2016, The complex relationship between olivine abundance and thermal inertia on Mars: Journal of Geophysical Research: Planets, v. 121, no. 7, p. 1293-1320.

Harrison, K. P., and Grimm, R. E., 2005, Groundwater-controlled valley networks and the decline of surface runoff on early Mars: Journal of Geophysical Research: Planets, v. 110, no. E12, p. E12S16.

Hausrath, E. M., Ming, D. W., Peretyazhko, T. S., and Rampe, E. B., 2018, Reactive transport and mass balance modeling of the Stimson sedimentary formation and altered fracture zones constrain diagenetic conditions at Gale crater, Mars: Earth and Planetary Science Letters, v. 491, p. 1-10.

Hausrath, E. M., Navarre-Stichler, A. K., Sak, P. B., Steefel, C. I., and Brantley, S. L., 2008, Basalt weathering rates on Earth and the duration of liquid water on the plains of Gusev Crater, Mars: Geology, v. 36, no. 1, p. 67-70.

Hayward, R. K., Fenton, L. K., and Titus, T. N., 2014, Mars Global Digital Dune Database (MGD3): Global dune distribution and wind pattern observations: Icarus, v. 230, p. 38-46.

Hayward, R. K., Mullins, K. F., Fenton, L. K., Hare, T. M., Titus, T. N., Bourke, M. C., Colaprete, A., and Christensen, P. R., 2007, Mars Global Digital Dune Database and initial science results: Journal of Geophysical Research: Planets, v. 112, no. E11.

Head, J. W., Marchant, D. R., Agnew, M. C., Fassett, C. I., and Kreslavsky, M. A., 2006, Extensive valley glacier deposits in the northern mid-latitudes of Mars: Evidence for Late Amazonian obliquity-driven climate change: Earth and Planetary Science Letters, v. 241, no. 3, p. 663-671.

Head, J. W., Marchant, D. R., Dickson, J. L., Kress, A. M., and Baker, D. M., 2010, Northern mid-latitude glaciation in the Late Amazonian period of Mars: Criteria for the recognition of debris-covered glacier and valley glacier landsystem deposits: Earth and Planetary Science Letters, v. 294, no. 3, p. 306-320.

Henares, S., Bloemsma, M. R., Donselaar, M. E., Mijnlieff, H. F., Redjosentono, A. E., Veldkamp, H. G., and Weltje, G. J., 2014, The role of detrital anhydrite in diagenesis of aeolian sandstones (Upper Rotliegend, The Netherlands): Implications for reservoir-quality prediction: Sedimentary Geology, v. 314, p. 60-74.

Herron, M. M., 1988, Geochemical classification of terrigenous sands and shales from core or log data: Journal of Sedimentary Research, v. 58, no. 5, p. 820-829.

Heydari, E., Parker, T., Calef III, F., Schroeder, J., Van Beek, J., Rowland, S., and Fairen, A., Characteristics and the Origin of the Vera Rubin Ridge, Gale Crater, Mars, *in* Proceedings Lunar and Planetary Science Conference2018.

Hicks, L. J., Bridges, J. C., and Gurman, S. J., 2014, Ferric saponite and serpentine in the nakhlite martian meteorites: Geochimica et Cosmochimica Acta, v. 136, p. 194-210.

Holm, N. G., Dowler, M. J., Wadsten, T., and Arrhenius, G., 1983, β-FeOOH · Cln (akaganéite) and Fe1-xO (wüstite) in hot brine from the Atlantis II Deep (Red Sea) and the uptake of amino acids by synthetic β-FeOOH · Cln: Geochimica et Cosmochimica Acta, v. 47, no. 8, p. 1465-1470.

Hubert, J. F., and Reed, A. A., 1978, Red-bed diagenesis in the East Berlin Formation, Newark Group, Connecticut Valley: Journal of Sedimentary Research, v. 48, no. 1, p. 175-184.

Humayun, M., Nemchin, A., Zanda, B., Hewins, R. H., Grange, M., Kennedy, A., Lorand, J. P., Göpel, C., Fieni, C., Pont, S., and Deldicque, D., 2013, Origin and age of the earliest Martian crust from meteorite NWA 7533: Nature, v. 503, p. 513.

Hurowitz, J. A., Grotzinger, J. P., Fischer, W. W., Milliken, R., Stein, N., Vasavada, A. R., Blake, D. F., Dehouck, E., Eigenbrode, J. L., Fairen, A. G., Frydenvang, J., Gellert, R., Grant, J. A., Gupta, S., Herkenhoff, K. E., McLennan, S. M., Ming, D. W., Rampe, E. B., Schmidt, M. E., Siebach, K., Stack-Morgan, K., Sumner, D. Y., and Wiens, R. C., 2017, Redox stratification of an ancient lake in Gale Crater, Mars: Science, v. 356, no. 6341, p. eeah6849.

Hynek, B. M., and Phillips, R. J., 2001, Evidence for extensive denudation of the Martian highlands: Geology, v. 29, no. 5, p. 407-410.

-, 2003, New data reveal mature, integrated drainage systems on Mars indicative of past precipitation: Geology, v. 31, no. 9, p. 757-760.

Irvine, T., and Baragar, W., 1971, A guide to the chemical classification of the common volcanic rocks: Canadian journal of earth sciences, v. 8, no. 5, p. 523-548.

Irwin, R. P., and Watters, T. R., 2010, Geology of the Martian crustal dichotomy boundary: Age, modifications, and implications for modeling efforts: Journal of Geophysical Research: Planets, v. 115, no. E11, p. E11006.

Irwin, R. P., Watters, T. R., Howard, A. D., and Zimbelman, J. R., 2004, Sedimentary resurfacing and fretted terrain development along the crustal dichotomy boundary, Aeolis Mensae, Mars: Journal of Geophysical Research: Planets, v. 109, no. E9, p. E09011.

Jacob, S., Wellington, D. F., Bell, J. F., Fraeman, A., Sun, V., Johnson, J. R., and Horgan, B., Correlating Mastcam Multispectral Data and Rock Morphology to Understand Potential Links Between Ferric Spectral Features Along Vera Rubin Ridge in Gale Crater, Mars, *in* Proceedings AGU, Washington, D.C., 2018.

Jakobsson, S. P., 1972, Chemistry and distribution pattern of recent basaltic rocks in Iceland: Lithos, v. 5, no. 4, p. 365-386.

Jin, Z., Li, F., Cao, J., Wang, S., and Yu, J., 2006, Geochemistry of Daihai Lake sediments, Inner Mongolia, north China: implications for provenance, sedimentary sorting, and catchment weathering: Geomorphology, v. 80, no. 3, p. 147-163.

Johnson, J. R., Achilles, C., Bell, J. F., Bender, S., Cloutis, E., Ehlmann, B., Fraeman, A., Gasnault, O., Hamilton, V. E., Le Mouélic, S., Maurice, S., Pinet, P., Thompson, L., Wellington, D., and Wiens, R. C., 2017, Visible/near-infrared spectral diversity from in situ observations of the Bagnold Dune Field sands in Gale Crater, Mars: Journal of Geophysical Research: Planets, v. 122, no. 12, p. 2655-2684.

Johnson, J. R., Bell III, J. F., Gasnault, O., Le Mouélic, S., Rapin, W., Bridges, J., and Wellington, D. F., First Iron Meteorites Observed By the Mars Science Laboratory (MSL) Rover Curiosity, *in* Proceedings AGU, Fall Meeting, New Orleans, Louisiana, 2014.

Jones, B. W., 2008, Mars before the Space Age: International Journal of Astrobiology, v. 7, no. 2, p. 143-155.

Kah, L. C., Kronyak, R., Van Beek, J., Nachon, M., Mangold, N., Thompson, L., Wiens, R., Grotzinger, J., Farmer, J., and Minitti, M., Diagenetic Crystal Clusters and Dendrites, Lower Mount Sharp, Gale crater, *in* Proceedings 46th Lunar and Planetary Science Conference, Houston, TX, United States, 2015.

Keith, T. E., and Muffler, L., 1978, Minerals produced during cooling and hydrothermal alteration of ash flow tuff from Yellowstone drill hole Y-5: Journal of Volcanology and Geothermal Research, v. 3, no. 3, p. 373-402.

Kite, E. S., Lewis, K. W., Lamb, M. P., Newman, C. E., and Richardson, M. I., 2013, Growth and form of the mound in Gale Crater, Mars: Slope wind enhanced erosion and transport: Geology, v. 41, no. 5, p. 543-546.

Kite, E. S., Sneed, J., Mayer, D. P., Lewis, K. W., Michaels, T. I., Hore, A., and Rafkin, S. C. R., 2016, Evolution of major sedimentary mounds on Mars: Buildup via anticompensational stacking modulated by climate change: Journal of Geophysical Research: Planets, v. 121, no. 11, p. 2282-2324.

Kocurek, G., 1991, Interpretation of Ancient Eolian Sand Dunes: Annual Review of Earth and Planetary Sciences, v. 19, no. 1, p. 43-75.

Kroonenberg, S. B., 1994, Effects of provenance, sorting and weathering on the geochemistry of fluvial sands from different tectonic and climatic environments, VSP BV, Proceedings of the 29th international geological congress, 69-81 p.:

Kutner, M. H., Nachtsheim, C. J., Neter, J., and Li, W., 2005, Applied linear statistical models (Vol. 4), McGraw-Hill Irwin New York.

L'Haridon, J., Mangold, N., Meslin, P. Y., Johnson, J. R., Rapin, W., Forni, O., Cousin, A., Payré, V., Dehouck, E., Nachon, M., Le Deit, L., Gasnault, O., Maurice, S., and Wiens, R. C., 2018, Chemical variability in mineralized veins observed by ChemCam on the lower slopes of Mount Sharp in Gale crater, Mars: Icarus, v. 311, p. 69-86.

L'Haridon, J., Mangold, N., Rapin, W., Cousin, A., Johnson, J., Fraeman, A., Meslin, P., Gasnault, O., Maurice, S., and Wiens, R., Diagenetic Iron Enrichments Observed by ChemCam on Vera Rubin Ridge, Gale Crater, Mars, *in* Proceedings Lunar and Planetary Science Conference2018, Volume 49.

Lakens, D., 2017, Equivalence Tests:A Practical Primer for t Tests, Correlations, and Meta-Analyses: Social Psychological and Personality Science, v. 8, no. 4, p. 355-362.

Lanza, N., Gasda, P., Clark, B. C., Clegg, S., Fairen, A. G., Fischer, W. W., Forni, O., L'Haridon, J., Hurowitz, J., Lamm, S., Maurice, S., Meslin, P. Y., Newsom, H., Rivera-Hernandez, F., Sumner, D., Stein, N., Wiens, R., and Frydenvang, J.,

Evidence for Shallow, Oxic Waters in the Gale Crater Lake, *in* Proceedings AGU, Washington, D.C., 2018.

Lanza, N. L., Wiens, R. C., Arvidson, R. E., Clark, B. C., Fischer, W. W., Gellert, R., Grotzinger, J. P., Hurowitz, J. A., McLennan, S. M., Morris, R. V., Rice, M. S., Bell, J. F., Berger, J. A., Blaney, D. L., Bridges, N. T., Calef, F., Campbell, J. L., Clegg, S. M., Cousin, A., Edgett, K. S., Fabre, C., Fisk, M. R., Forni, O., Frydenvang, J., Hardy, K. R., Hardgrove, C., Johnson, J. R., Lasue, J., Le Mouélic, S., Malin, M. C., Mangold, N., Martìn-Torres, J., Maurice, S., McBride, M. J., Ming, D. W., Newsom, H. E., Ollila, A. M., Sautter, V., Schröder, S., Thompson, L. M., Treiman, A. H., VanBommel, S., Vaniman, D. T., and Zorzano, M.-P., 2016, Oxidation of manganese in an ancient aquifer, Kimberley formation, Gale crater, Mars: Geophysical Research Letters, v. 43, no. 14, p. 7398-7407.

Lanza, Nina L., Wiens, Roger C., Clegg, Samuel M., Ollila, Ann M., Humphries, Seth D., Newsom, Horton E., and Barefield, James E., 2010, Calibrating the ChemCam laser-induced breakdown spectroscopy instrument for carbonate minerals on Mars: Applied Optics, v. 49, no. 13, p. C211-C217.

Lapotre, M. G. A., Ehlmann, B. L., Minson, S. E., Arvidson, R. E., Ayoub, F., Fraeman, A. A., Ewing, R. C., and Bridges, N. T., 2017, Compositional Variations in Sands of the Bagnold Dunes, Gale Crater, Mars, from Visible-Shortwave Infrared Spectroscopy and Comparison to Ground-Truth from the Curiosity Rover: Journal of Geophysical Research: Planets, v. 122, p. 2489-2509.

Lapotre, M. G. A., and Rampe, E. B., 2018, Curiosity's Investigation of the Bagnold Dunes, Gale Crater: Overview of the Two-Phase Scientific Campaign and Introduction to the Special Collection: Geophysical Research Letters, v. 45, no. 19, p. 10,200-210,210.

Le Bas, M. J., Maitre, R., Streckeisen, A., and Zanettin, B., 1986, A chemical classification of volcanic rocks based on the total alkali-silica diagram: Journal of petrology, v. 27, no. 3, p. 745-750.

Le Deit, L., Mangold, N., Forni, O., Cousin, A., Lasue, J., Schröder, S., Wiens, R. C., Sumner, D., Fabre, C., and Stack, K. M., 2016, The potassic sedimentary rocks in Gale Crater, Mars, as seen by ChemCam on board Curiosity: Journal of Geophysical Research: Planets, v. 121, no. 5, p. 784-804.

Lee, M. R., Tomkinson, T., Hallis, L. J., and Mark, D. F., 2015, Formation of iddingsite veins in the martian crust by centripetal replacement of olivine: Evidence from the nakhlite meteorite Lafayette: Geochimica et Cosmochimica Acta, v. 154, p. 49-65.

Leveille, R. J., Bridges, J., Wiens, R. C., Mangold, N., Cousin, A., Lanza, N., Forni, O., Ollila, A., Grotzinger, J., and Clegg, S., 2014, Chemistry of fracture-filling raised ridges in Yellowknife Bay, Gale Crater: Window into past aqueous activity and habitability on Mars: Journal of Geophysical Research: Planets, v. 119, no. 11, p. 2398-2415.

Lewis, J. M. T., Najorka, J., Watson, J. S., and Sephton, M. A., 2018, The Search for Hesperian Organic Matter on Mars: Pyrolysis Studies of Sediments Rich in Sulfur and Iron: Astrobiology, v. 18, no. 4, p. 454-464.

Lindsley, D. H., and Andersen, D. J., 1983, A two-pyroxene thermometer: Journal of Geophysical Research: Solid Earth, v. 88, no. S02, p. A887-A906.

Lucchitta, B. K., Ferguson, H. M., and Summers, C., 1986, Sedimentary deposits in the Northern Lowland Plains, Mars: Journal of Geophysical Research: Solid Earth, v. 91, no. B13, p. E166-E174.

MacArthur, J. L., Bridges, J. C., Hicks, L. J., Burgess, R., Joy, K. H., Branney, M. J., Hansford, G. M., Baker, S. H., Schwenzer, S. P., Gurman, S. J., Stephen, N. R., Steer, E. D., Piercy, J. D., and Ireland, T. R., 2019, Mineralogical constraints on the thermal history of martian regolith breccia Northwest Africa 8114: Geochimica et Cosmochimica Acta, v. 246, p. 267-298.

Maki, J., Thiessen, D., Pourangi, A., Kobzeff, P., Litwin, T., Scherr, L., Elliott, S., Dingizian, A., and Maimone, M., 2012, The Mars Science Laboratory Engineering Cameras: Space Science Reviews, v. 170, no. 1, p. 77-93.

Malin, M., Caplinger, M., Edgett, K., Ghaemi, F., Ravine, M., Schaffner, J., Baker, J., Bardis, J., DiBiase, D., and Maki, J., The Mars Science Laboratory (MSL) mast-mounted cameras (Mastcams) flight instruments, *in* Proceedings Lunar and Planetary Science Conference2010, Volume 41, p. 1123.

Malin, M., Caplinger, M., Edgett, K., Ghaemi, F., Ravine, M., Schaffner, J., Maki, J., Willson, R., Bell, J., and Cameron, J., The mars science laboratory (msl) mars descent imager (mardi) flight instrument, *in* Proceedings Lunar and Planetary Science Conference2009, Volume 40.

Malin, M. C., and Edgett, K. S., 1999, Oceans or seas in the Martian northern lowlands: High resolution imaging tests of proposed coastlines: Geophysical Research Letters, v. 26, no. 19, p. 3049-3052.

-, 2000, Sedimentary Rocks of Early Mars: Science, v. 290, no. 5498, p. 1927-1937.

-, 2001, Mars Global Surveyor Mars Orbiter Camera: Interplanetary cruise through primary mission: Journal of Geophysical Research: Planets, v. 106, no. E10, p. 23429-23570.

Mangold, N., Baratoux, D., Arnalds, O., Bardintzeff, J. M., Platevoet, B., Grégoire, M., and Pinet, P., 2011, Segregation of olivine grains in volcanic sands in Iceland and implications for Mars: Earth and Planetary Science Letters, v. 310, no. 3, p. 233-243.

Mangold, N., Dehouck, E., Fedo, C., Forni, O., Achilles, C. N., Bristow, T. F., Frydenvang, J., Gasnault, O., L'Haridon, J., Le Deit, L., Maurice, S., McLennan, S. M., Meslin, P. Y., Morrison, S. M., Newsom, H., Rampe, E. B., Rivera-Hernandez, F., Salvatore, M., and Wiens, R., 2019, Open-system weathering on Mars from the chemistry of mudstones at Gale crater: Icarus, v. 321, p. 619-631.

Mangold, N., Forni, O., Dromart, G., Stack, K., Wiens, R. C., Gasnault, O., Sumner, D. Y., Nachon, M., Meslin, P. Y., and Anderson, R. B., 2015, Chemical variations in Yellowknife Bay formation sedimentary rocks analyzed by ChemCam on board the Curiosity rover on Mars: Journal of Geophysical Research: Planets, v. 120, no. 3, p. 452-482.

Mangold, N., Quantin, C., Ansan, V., Delacourt, C., and Allemand, P., 2004, Evidence for Precipitation on Mars from Dendritic Valleys in the Valles Marineris Area: Science, v. 305, no. 5680, p. 78-81.

Mangold, N., Schmidt, M. E., Fisk, M. R., Forni, O., McLennan, S. M., Ming, D., Sautter, V., Sumner, D., Williams, A. J., and Clegg, S. M., 2017, Classification scheme for sedimentary and igneous rocks in Gale crater, Mars: Icarus, v. 284, p. 1-17.

Mangold, N., Thompson, L. M., Forni, O., Williams, A. J., Fabre, C., Le Deit, L., Wiens, R. C., Williams, R., Anderson, R. B., and Blaney, D. L., 2016, Composition of conglomerates analyzed by the Curiosity rover: Implications for Gale Crater crust and sediment sources: Journal of Geophysical Research: Planets, v. 121, no. 3, p. 353-387.

Masursky, H., Batson, R. M., McCauley, J. F., Soderblom, L. A., Wildey, R. L., Carr, M. H., Milton, D. J., Wilhelms, D. E., Smith, B. A., Kirby, T. B., Robinson, J. C., Leovy, C. B., Briggs, G. A., Duxbury, T. C., Acton, C. H., Murray, B. C., Cutts, J. A., Sharp, R. P., Smith, S., Leighton, R. B., Sagan, C., Veverka, J., Noland, M., Lederberg, J., Levinthal, E., Pollack, J. B., Moore, J. T., Hartmann, W. K., Shipley, E. N., De Vaucouleurs, G., and Davies, M. E., 1972, Mariner 9 Television Reconnaissance of Mars and Its Satellites: Preliminary Results: Science, v. 175, no. 4019, p. 294-305.

Maurice, S., Clegg, S. M., Wiens, R. C., Gasnault, O., Rapin, W., Forni, O., Cousin, A., Sautter, V., Mangold, N., and Le Deit, L., 2016, ChemCam activities and discoveries during the nominal mission of the Mars Science Laboratory in Gale crater, Mars: Journal of Analytical Atomic Spectrometry, v. 31, no. 4, p. 863-889.

Maurice, S., Wiens, R. C., Saccoccio, M., Barraclough, B., Gasnault, O., Forni, O., Mangold, N., Baratoux, D., Bender, S., and Berger, G., 2012, The ChemCam instrument suite on the Mars Science Laboratory (MSL) rover: science objectives and mast unit description: Space science reviews, v. 170, no. 1-4, p. 95-166.

McCauley, J. F., Carr, M. H., Cutts, J. A., Hartmann, W. K., Masursky, H., Milton, D. J., Sharp, R. P., and Wilhelms, D. E., 1972, Preliminary mariner 9 report on the geology of Mars: Icarus, v. 17, no. 2, p. 289-327.

McCleese, D. J., and Mars Expeditions Strategy Group, 2001, The Search for Life on Mars.

McCubbin, F. M., Nekvasil, H., Harrington, A. D., Elardo, S. M., and Lindsley, D. H., 2008, Compositional diversity and stratification of the Martian crust: Inferences from crystallization experiments on the picrobasalt Humphrey from Gusev Crater, Mars: Journal of Geophysical Research: Planets, v. 113, no. E11, p. E11013.

McEnroe, S. A., Brown, L. L., and Robinson, P., 2004, Earth analog for Martian magnetic anomalies: remanence properties of hemo-ilmenite norites in the Bjerkreim-Sokndal intrusion, Rogaland, Norway: Journal of Applied Geophysics, v. 56, no. 3, p. 195-212.

McGill, G. E., and Dimitriou, A. M., 1990, Origin of the Martian global dichotomy by crustal thinning in the Late Noachian or Early Hesperian: Journal of Geophysical Research: Solid Earth, v. 95, no. B8, p. 12595-12605.

McKinley, J. M., Atkinson, P. M., Lloyd, C. D., Ruffell, A. H., and Worden, R. H., 2011, How Porosity and Permeability Vary Spatially With Grain Size, Sorting, Cement Volume, and Mineral Dissolution In Fluvial Triassic Sandstones: The Value of Geostatistics and Local Regression: Journal of Sedimentary Research, v. 81, no. 12, p. 844-858.

McLennan, S. M., 2012, Geochemistry of sedimentary processes on Mars: Sedimentary Geology of Mars, v. 102, p. 119-138.

McLennan, S. M., Anderson, R., Bell, J., Bridges, J., Calef, F., Campbell, J. L., Clark, B., Clegg, S., Conrad, P., and Cousin, A., 2014, Elemental geochemistry of sedimentary rocks at Yellowknife Bay, Gale crater, Mars: Science, v. 343, no. 6169, p. 1244734.

McSween, H. Y., Ruff, S. W., Morris, R. V., Bell, J., Herkenhoff, K., Gellert, R., Stockstill, K. R., Tornabene, L. L., Squyres, S. W., and Crisp, J. A., 2006a, Alkaline volcanic rocks from the Columbia Hills, Gusev crater, Mars: Journal of Geophysical Research: Planets, v. 111, no. E9, p. 2156-2202.

McSween, H. Y., and Stolper, E. M., 1980, Basaltic Meteorites: Scientific American, v. 242, no. 6, p. 54-63.

McSween, H. Y., Stolper, E. M., Taylor, L. A., Muntean, R. A., O'Kelley, G. D., Eldridge, J. S., Biswas, S., Ngo, H. T., and Lipschutz, M. E., 1979, Petrogenetic relationship between Allan Hills 77005 and other achondrites: Earth and Planetary Science Letters, v. 45, no. 2, p. 275-284.

McSween, H. Y., Taylor, G. J., and Wyatt, M. B., 2009, Elemental composition of the Martian crust: Science, v. 324, no. 5928, p. 736-739.

McSween, H. Y., Wyatt, M. B., Gellert, R., Bell, J., Morris, R. V., Herkenhoff, K. E., Crumpler, L. S., Milam, K. A., Stockstill, K. R., and Tornabene, L. L., 2006b, Characterization and petrologic interpretation of olivine-rich basalts at Gusev Crater, Mars: Journal of Geophysical Research: Planets, v. 111, no. E2, p. E02S10.

Meslin, P.-Y., Gasnault, O., Forni, O., Schröder, S., Cousin, A., Berger, G., Clegg, S., Lasue, J., Maurice, S., and Sautter, V., 2013, Soil diversity and hydration as observed by ChemCam at Gale Crater, Mars: Science, v. 341, no. 6153, p. 1238670.

Meslin, P. Y., Johnson, J. R., Forni, O., Beck, P., Cousin, A., Bridges, J., Rapin, W., Cohen, B. A., Newsom, H., Sautter, V., Lewin, E., Nachon, M., Wiens, R., Payré, V., Gasnault, O., Maurice, S., Fairen, A. G., Schroder, S., Mangold, N., and Thomas, N., Egg rock encounter: Analysis of an iron-nickel meteorite found in Gale crater by Curiosity, *in* Proceedings 48th Lunar and Planetary Science, Texas, USA, 2017.

Milliken, R. E., Fischer, W. W., and Hurowitz, J. A., 2009, Missing salts on early Mars: Geophysical Research Letters, v. 36, no. 11, p. L11202.

Milliken, R. E., Grotzinger, J. P., and Thomson, B. J., 2010, Paleoclimate of Mars as captured by the stratigraphic record in Gale Crater: Geophysical Research Letters, v. 37, no. 4, p. L04201.

Ming, D. W., Gellert, R., Morris, R. V., Arvidson, R. E., Brückner, J., Clark, B. C., Cohen, B. A., d'Uston, C., Economou, T., Fleischer, I., Klingelhöfer, G., McCoy, T. J., Mittlefehldt, D. W., Schmidt, M. E., Schröder, C., Squyres, S. W., Tréguier, E., Yen, A. S., and Zipfel, J., 2008, Geochemical properties of rocks and soils in Gusev Crater, Mars: Results of the Alpha Particle X-Ray Spectrometer from Cumberland Ridge to Home Plate: Journal of Geophysical Research: Planets, v. 113, no. E12, p. E12S39.

Mittlefehldt, D. W., 1994, ALH84001, a cumulate orthopyroxenite member of the martian meteorite clan: Meteoritics, v. 29, no. 2, p. 214-221.

Montgomery, D. C., Peck, E. A., Vining, G. G., and Vining, G. G., 2012, Introduction to Linear Regression Analysis, Hoboken, United States, John Wiley & Sons, Incorporated.

Morad, S., and Aldahan, A. A., 1982, Authigenesis of titanium minerals in two Proterozoic sedimentary rocks from southern and central Sweden: Journal of Sedimentary Research, v. 52, no. 4, p. 1295-1305.

Morris, R. V., Bristow, T. F., Rampe, E. B., Yen, A., Vaniman, D., Tu, V., Treiman, A. H., Thorpe, M. T., Peretyazhko, T. S., Morrison, S. M., Ming, D. W., Hazen, R. M., Downs, R. T., Downs, G. W., Des Marais, D. J., Craig, P. I., Chipera, S. J., Castle, N., Blake, D. F., and Achilles, C. N., Mineralogy and formation processes for the Vera Rubin Ridge at Gale crater, Mars, from CheMin XRD analyses., *in* Proceedings 50th Lunar and Planetary Science, Houston, TX, 2019.

Morris, R. V., Golden, D. C., Bell, J. F., Shelfer, T. D., Scheinost, A. C., Hinman, N. W., Furniss, G., Mertzman, S. A., Bishop, J. L., Ming, D. W., Allen, C. C., and Britt, D. T., 2000, Mineralogy, composition, and alteration of Mars Pathfinder rocks and soils: Evidence from multispectral, elemental, and magnetic data on terrestrial analogue, SNC meteorite, and Pathfinder samples: Journal of Geophysical Research: Planets, v. 105, no. E1, p. 1757-1817.

Morris, R. V., Golden, D. C., Ming, D. W., Shelfer, T. D., Jørgensen, L. C., Bell, J. F., Graff, T. G., and Mertzman, S. A., 2001, Phyllosilicate-poor palagonitic dust from Mauna Kea Volcano (Hawaii): A mineralogical analogue for magnetic Martian dust?: Journal of Geophysical Research: Planets, v. 106, no. E3, p. 5057-5083.

Morris, R. V., Vaniman, D. T., Blake, D. F., Gellert, R., Chipera, S. J., Rampe, E. B., Ming, D. W., Morrison, S. M., Downs, R. T., Treiman, A. H., Yes, A. S., Grotzinger, J. P., Achilles, C. N., Bristow, T. F., Crisp, J. A., Des Marais, D., Farmer, J. D., Fendrich, K. V., Frydenvang, J., Graff, T. G., Morookian, J.-M., Stolper, E. M., and Schwenzer, S. P., 2016, Silicic volcanism on Mars evidenced by tridymite in high-SiO2 sedimentary rock at Gale crater: Proceedings of the National Academy of Sciences, v. 113, no. 26, p. 7071-7076.

Morrison, S. M., Downs, R. T., Blake, D. F., Vaniman, D. T., Ming, D. W., Rampe, E. B., Bristow, T. F., Achilles, C. N., Chipera, S. J., Yen, A. S., Morris, R. V., Treiman, A. H., Hazen, R. M., Sarrazin, P. C., Gellert, R., Fendrich, K. V., Morookian, J.-M., Farmer, J. D., Des Marais, D., and Craig, P. I., 2018, Crystal chemistry of martian minerals from Bradbury Landing through Naukluft Plateau, Gale crater, Mars: American Mineralogist, v. 103, p. 857-871.

Mouginot, J., Pommerol, A., Beck, P., Kofman, W., and Clifford, S. M., 2012, Dielectric map of the Martian northern hemisphere and the nature of plain filling materials: Geophysical Research Letters, v. 39, no. 2, p. L02202.

Mountney, N. P., and Russell, A. J., 2004, Sedimentology of cold-climate aeolian sandsheet deposits in the Askja region of northeast Iceland: Sedimentary Geology, v. 166, no. 3, p. 223-244.

Murchie, S. L., Mustard, J. F., Ehlmann, B. L., Milliken, R. E., Bishop, J. L., McKeown, N. K., Noe Dobrea, E. Z., Seelos, F. P., Buczkowski, D. L., Wiseman, S. M., Arvidson, R. E., Wray, J. J., Swayze, G., Clark, R. N., Des Marais, D. J., McEwen, A. S., and Bibring, J.-P., 2009, A synthesis of Martian aqueous mineralogy after 1 Mars year of observations from the Mars Reconnaissance Orbiter: Journal of Geophysical Research: Planets, v. 114, no. E2, p. E00D06.

Mustard, J. F., Murchie, S. L., Pelkey, S. M., Ehlmann, B. L., Milliken, R. E., Grant, J. A., Bibring, J. P., Poulet, F., Bishop, J., Dobrea, E. N., Roach, L., Seelos, F., Arvidson, R. E., Wiseman, S., Green, R., Hash, C., Humm, D., Malaret, E., McGovern, J. A., Seelos, K., Clancy, T., Clark, R., Marais, D. D., Izenberg, N., Knudson, A., Langevin, Y., Martin, T., McGuire, P., Morris, R., Robinson, M., Roush, T., Smith, M., Swayze, G., Taylor, H., Titus, T., and Wolff, M., 2008, Hydrated silicate minerals on Mars observed by the Mars Reconnaissance Orbiter CRISM instrument: Nature, v. 454, p. 305.

Nachon, M., Clegg, S. M., Mangold, N., Schröder, S., Kah, L. C., Dromart, G., Ollila, A., Johnson, J. R., Oehler, D. Z., and Bridges, J. C., 2014, Calcium sulfate veins characterized by ChemCam/Curiosity at Gale crater, Mars: Journal of Geophysical Research: Planets, v. 119, no. 9, p. 1991-2016.

Nachon, M., Mangold, N., Forni, O., Kah, L. C., Cousin, A., Wiens, R. C., Anderson, R., Blaney, D., Blank, J. G., and Calef, F., 2017, Chemistry of diagenetic features

analyzed by ChemCam at Pahrump Hills, Gale crater, Mars: Icarus, v. 281, p. 121-136.

Nesbitt, H. W., Fedo, C., and Young, G. M., 1997, Quartz and Feldspar Stability, Steady and Non-steady-State Weathering, and Petrogenesis of Siliciclastic Sands and Muds: The Journal of Geology, v. 105, no. 2, p. 173-192.

Nesbitt, H. W., and Wilson, R. E., 1992, Recent chemical weathering of basalts: American Journal of Science, v. 292, no. 10, p. 740-777.

Nesbitt, H. W., and Young, G. M., 1982, Early Proterozoic climates and plate motions inferred from major element chemistry of lutites: Nature, v. 299, no. 5885, p. 715-717.

Newman, C. E., Gómez-Elvira, J., Marin, M., Navarro, S., Torres, J., Richardson, M. I., Battalio, J. M., Guzewich, S. D., Sullivan, R., Torre, M. d. l., Vasavada, A. R., and Bridges, N. T., 2017, Winds measured by the Rover Environmental Monitoring Station (REMS) during the Mars Science Laboratory (MSL) rover's Bagnold Dunes Campaign and comparison with numerical modeling using MarsWRF: Icarus, v. 291, p. 203-231.

Newsom, H., Belgacem, I., Jackson, R., Ha, B., Vaci, Z., Wiens, R., Frydenvang, J., Gasda, P., Lanza, N., and Clegg, S., The materials at an unconformity between the Murray and Stimson formations at Marias Pass, Gale crater, Mars, *in* Proceedings 47th Lunar and Planetary Science Conference, Houston, TX, 2016, Volume 47, p. 2397.

Newsom, H., Belgacem, I., Jackson, R., Ha, B., Vaci, Z., Wiens, R., Frydenvang, J., Gasda, P., Lanza, N., Clegg, S., Gasnault, O., Maurice, S., Cousin, A., Rapin, W., Edgett, K., Banham, S. G., Gupta, S., William, A., Grotzinger, J., Watkins, J. A., Stein, N., Blaney, D., Schroeder, J., Calef, F., Francis, R., Ehlmann, B. L., Yen, A. S., Rubin, D., Bridges, N., Johnson, J. R., Lewis, K., Payré, V., Mangold, N., Fey, D. M., Fisk, M., Gellert, R., Thompson, L., Schmidt, M. E., Perrett, G. M., Kah, L. C., Kronyak, R., Anderson, R., Herkenhoff, K., Bridges, J., and Hurowitz, J., in rev., Deposition and diagenesis at an erosional unconformity in the ancient Martian rock record between Murray and Stimson Units at Marias Pass in Gale Crater, Mars.

Newsom, H., Edgett, K., Fey, D., Wiens, R., Frydenvang, J., Banham, S., Gupta, S., Williams, A., Grotzinger, J., and Mangold, N., A Buried Aeolian Lag Deposit at an Unconformity Between the Murray and Stimson Formations at Marias Pass, Gale Crater, Mars, *in* Proceedings 49th Lunar and Planetary Science Conference, Houston, TX, 2018, Volume 49.

Newsom, H., Jackson, R., Wiens, R., Frydenvang, J., Gasada, P., Lanza, N., Ollila, A., Clegg, S., Gasnault, O., and Maurice, S., Increasing occurrence of sandstone cemented with calcium sulfate on Mount Sharp, Gale Crater, Mars, *in* Proceedings 48th Lunar and Planetary Science Conference, Houston, TX, 2017.

Nichols, G., 2009, Sedimentology and stratigraphy, John Wiley & Sons.

Nimmo, F., and Tanaka, K., 2005, Early crustal evolution of Mars: Annual Review of Earth and Planetary Sciences, v. 33, no. 1, p. 133-161.

Nyquist, L. E., Bogard, D. D., Shih, C.-Y., Greshake, A., Stöffler, D., and Eugster, O., 2001, Ages and geologic histories of Martian meteorites, Chronology and evolution of Mars, Springer, p. 105-164.

O'Connell-Cooper, C. D., Spray, J. G., Thompson, L. M., Gellert, R., Berger, J. A., Boyd, N. I., Desouza, E. D., Perrett, G. M., Schmidt, M., and VanBommel, S. J., 2017,

APXS-derived chemistry of the Bagnold dune sands: Comparisons with Gale Crater soils and the global Martian average: Journal of Geophysical Research: Planets, v. 122, no. 12, p. 2623-2643.

O'Connell-Cooper, C. D., Thompson, L. M., Spray, J. G., Berger, J. A., VanBommel, S. J., Gellert, R., Boyd, N. I., and DeSouza, E., 2018, Chemical Diversity of Sands Within the Linear and Barchan Dunes of the Bagnold Dunes, Gale Crater, as Revealed by APXS Onboard Curiosity: Geophysical Research Letters, v. 45, no. 18, p. 9460-9470.

Parker, T. J., Mapping of Possible" Oceanus Borealis" Shorelines on Mars: A Status Report, *in* Proceedings 29th Lunar and Planetary Science Conference, Houston, TX, 1998.

Pe-Piper, G., Karim, A., and Piper, D. J., 2011, Authigenesis of titania minerals and the mobility of Ti: new evidence from pro-deltaic sandstones, Cretaceous Scotian Basin, Canada: Journal of Sedimentary Research, v. 81, no. 10, p. 762-773.

Pearson, K., 1896, Mathematical Contributions to the Theory of Evolution. III. Regression, Heredity, and Panmixia: Philosophical Transactions of the Royal Society of London. Series A, Containing Papers of a Mathematical or Physical Character, v. 187, p. 253-318.

Pelkey, S. M., Mustard, J. F., Murchie, S., Clancy, R. T., Wolff, M., Smith, M., Milliken, R., Bibring, J.-P., Gendrin, A., Poulet, F., Langevin, Y., and Gondet, B., 2007, CRISM multispectral summary products: Parameterizing mineral diversity on Mars from reflectance: Journal of Geophysical Research: Planets, v. 112, no. E8, p. E08S14.

Perrett, G. M., Maxwell, J. A., and Campbell, J. L., 2017, Combined X-ray diffraction and alpha particle X-ray spectrometer analysis of geologic materials: X-Ray Spectrometry, v. 46, no. 3, p. 171-179.

Pettijohn, F., 1954, Classification of sandstones: The Journal of Geology, v. 62, no. 4, p. 360-365.

Pettijohn, F. J., Potter, P. E., and Siever, R., 1972, Sand and Sandstones, 1-618, Springer, Berlín.

Pike, R. J., 1980, Formation of complex impact craters: Evidence from Mars and other planets: Icarus, v. 43, no. 1, p. 1-19.

Poulet, F., Bibring, J. P., Mustard, J. F., Gendrin, A., Mangold, N., Langevin, Y., Arvidson, R. E., Gondet, B., Gomez, C., The Omega, T., Berthé, M., Bibring, J. P., Langevin, Y., Erard, S., Forni, O., Gendrin, A., Gondet, B., Manaud, N., Poulet, F., Poulleau, G., Soufflot, A., Combes, M., Drossart, P., Encrenaz, T., Fouchet, T., Melchiorri, R., Bellucci, G., Altieri, F., Formisano, V., Fonti, S., Capaccioni, F., Cerroni, P., Coradini, A., Korablev, O., Kottsov, V., Ignatiev, N., Titov, D., Zasova, L., Mangold, N., Pinet, P., Schmitt, B., Sotin, C., Hauber, E., Hoffmann, H., Jaumann, R., Keller, U., Arvidson, R., Mustard, J., and Forget, F., 2005, Phyllosilicates on Mars and implications for early martian climate: Nature, v. 438, p. 623.

Poulet, F., Mangold, N., Loizeau, D., Bibring, J.-P., Langevin, Y., Michalski, J., and Gondet, B., 2008, Abundance of minerals in the phyllosilicate-rich units on Mars: A&A, v. 487, no. 2, p. L41-L44.

Pye, K., and Tsoar, H., 2008, Aeolian sand and sand dunes, Springer Science & Business Media.

Quantin-Nataf, C., Thollot, P., Carter, J., Mandon, L., and Dehouck, E., The Unique and Diverse Record of Noachian Aqueous Activity in Oxia Planum, Mars, *in* Proceedings 49th Lunar and Planetary Science Conference, Houston, TX, 2018.

Rainoldi, A. L., Franchini, M., Beaufort, D., Patrier, P., Giusiano, A., Impiccini, A., and Pons, J., 2014, Large-Scale Bleaching of Red Beds Related To Upward Migration of Hydrocarbons: Los Chihuidos High, Neuquén Basin, Argentina: Journal of Sedimentary Research, v. 84, no. 5, p. 373-393.

Rampe, E. B., Lapotre, M. G. A., Bristow, T. F., Arvidson, R. E., Morris, R. V., Achilles, C. N., Weitz, C., Blake, D. F., Ming, D. W., Morrison, S. M., Vaniman, D. T., Chipera, S. J., Downs, R. T., Grotzinger, J. P., Hazen, R. M., Peretyazhko, T. S., Sutter, B., Tu, V., Yen, A. S., Horgan, B., Castle, N., Craig, P. I., Des Marais, D. J., Farmer, J., Gellert, R., McAdam, A. C., Morookian, J. M., Sarrazin, P. C., and Treiman, A. H., 2018, Sand Mineralogy Within the Bagnold Dunes, Gale Crater, as Observed In Situ and From Orbit: Geophysical Research Letters, v. 45, no. 18, p. 9488-9497.

Rampe, E. B., Ming, D. W., Blake, D. F., Bristow, T. F., Chipera, S. J., Grotzinger, J. P., Morris, R. V., Morrison, S. M., Vaniman, D. T., and Yen, A. S., 2017, Mineralogy of an ancient lacustrine mudstone succession from the Murray formation, Gale crater, Mars: Earth and Planetary Science Letters, v. 471, p. 172-185.

Rapin, W., Meslin, P.-Y., Maurice, S., Vaniman, D., Nachon, M., Mangold, N., Schröder, S., Gasnault, O., Forni, O., Wiens, R. C., Martinez, G. M., Cousin, A., Sautter, V., Lasue, J., and Rampe, E. B., 2016, Hydration state of calcium sulfates in Gale crater, Mars: Identification of bassanite veins: Earth and Planetary Science Letters, v. 452, p. 197-205.

Reese, C. C., Solomatov, V. S., Baumgardner, J. R., Stegman, D. R., and Vezolainen, A. V., 2004, Magmatic evolution of impact-induced Martian mantle plumes and the origin of Tharsis: Journal of Geophysical Research: Planets, v. 109, no. E8, p. E08009.

Rieder, R., Economou, T., Wänke, H., Turkevich, A., Crisp, J., Brückner, J., Dreibus, G., and McSween, H. Y., 1997, The Chemical Composition of Martian Soil and Rocks Returned by the Mobile Alpha Proton X-ray Spectrometer: Preliminary Results from the X-ray Mode: Science, v. 278, no. 5344, p. 1771-1774.

Rieder, R., Gellert, R., Brückner, J., Klingelhöfer, G., Dreibus, G., Yen, A., and Squyres, S. W., 2003, The new Athena alpha particle X-ray spectrometer for the Mars Exploration Rovers: Journal of Geophysical Research: Planets, v. 108, no. E12, p. 7.

Rivera-Hernández, F., Sumner, D. Y., Mangold, N., Stack, K. M., Forni, O., Newsom, H., Williams, A., Nachon, M., L'Haridon, J., Gasnault, O., Wiens, R., and Maurice, S., 2019, Using ChemCam LIBS data to constrain grain size in rocks on Mars: Proof of concept and application to rocks at Yellowknife Bay and Pahrump Hills, Gale crater: Icarus, v. 321, p. 82-98.

Roser, B. P., and Korsch, R. J., 1986, Determination of tectonic setting of sandstone-mudstone suites using content and ratio: The Journal of Geology, v. 94, no. 5, p. 635-650.

Rubin, D., Edgar, L., and Lewis, K., 2014, Physical Sedimentology in Gale Crater, Mars: Search and Discovery, v. 50991.

Sallé, B., Mauchien, P., and Maurice, S., 2007, Laser-Induced Breakdown Spectroscopy in open-path configuration for the analysis of distant objects: Spectrochimica Acta Part B: Atomic Spectroscopy, v. 62, no. 8, p. 739-768.

Santos, A. R., Agee, C. B., McCubbin, F. M., Shearer, C. K., Burger, P. V., Tartèse, R., and Anand, M., 2015, Petrology of igneous clasts in Northwest Africa 7034: Implications for the petrologic diversity of the martian crust: Geochimica et Cosmochimica Acta, v. 157, p. 56-85.

Sautter, V., Toplis, M., Wiens, R., Cousin, A., Fabre, C., Gasnault, O., Maurice, S., Forni, O., Lasue, J., and Ollila, A., 2015, In situ evidence for continental crust on early Mars: Nature Geoscience, v. 8, no. 8, p. 605-609.

Schieber, J., Bish, D., Coleman, M., Reed, M., Hausrath, E. M., Cosgrove, J., Gupta, S., Minitti, M., Edgett, K., Malin, M. C., and Sheldon, N., 2017, Encounters with an unearthly mudstone: Understanding the first mudstone found on Mars: Sedimentology, v. 64, no. 2, p. 311-358.

Schuenemeyer, J. H., and Drew, L. J., 2011, Statistics for earth and environmental scientists, John Wiley & Sons.

Schuirmann, D. J., 1987, A comparison of the Two One-Sided Tests Procedure and the Power Approach for assessing the equivalence of average bioavailability: Journal of Pharmacokinetics and Biopharmaceutics, v. 15, no. 6, p. 657-680.

Schulte, M., Meyer, M., Grant, J., and Golombek, M., The Mars 2020 Rover Mission Landing Site Candidates, *in* Proceedings Second International Mars Sample Return, Berlin, Germany, 2018, Volume 2071.

Schultz, P. H., and Glicken, H., 1979, Impact crater and basin control of igneous processes on Mars: Journal of Geophysical Research: Solid Earth, v. 84, no. B14, p. 8033-8047.

Schumacher, D., 1996, Hydrocarbon-induced alteration of soils and sediments, *in* schumacher, D., and Abrams, M., eds., Hydrocarbon Migration And Its Near-Surface Expression Memoir 66, The American Association of Petroleum Geologists, p. 71-89.

Schwenzer, S., Bridges, J., McAdam, A., Steer, E., Conrad, P., Kelley, S., Wiens, R., Mangold, N., Grotzinger, J., and Eigenbrode, J., Modeling of sulphide environments on Mars, *in* Proceedings 47th Lunar and Planetary Science Conference, Houston, Texas, 2016a.

Schwenzer, S. P., Abramov, O., Allen, C. C., Bridges, J. C., Clifford, S. M., Filiberto, J., Kring, D. A., Lasue, J., McGovern, P. J., Newsom, H. E., Treiman, A. H., Vaniman, D. T., Wiens, R. C., and Wittmann, A., 2012, Gale Crater: Formation and post-impact hydrous environments: Planetary and Space Science, v. 70, no. 1, p. 84-95.

Schwenzer, S. P., Bridges, J. C., Wiens, R. C., Conrad, P. G., Kelley, S. P., Leveille, R., Mangold, N., Martín-Torres, J., McAdam, A., and Newsom, H., 2016b, Fluids during diagenesis and sulfate vein formation in sediments at Gale crater, Mars: Meteoritics & Planetary Science, v. 51, no. 11, p. 2175-2202.

Schwenzer, S. P., and Kring, D. A., 2009, Impact-generated hydrothermal systems capable of forming phyllosilicates on Noachian Mars: Geology, v. 37, no. 12, p. 1091-1094.

Schwertmann, U., and Fitzpatrick, R. W., 1993, Iron minerals in surface environments: Catena Supplement, v. 21, p. 7-7.

Shinohara, Y., and Kohyama, N., 2004, Quantitative Analysis of Tridymite and Cristobalite Crystallized in Rice Husk Ash by Heating: Industrial health, v. 42, no. 2, p. 277-285.

Siebach, K., McLennan, S., and Fedo, C., Geochemistry of the Stimson Sandstone, Gale Crater, Mars, *in* Proceedings Lunar and Planetary Science Conference, Houston, TX, 2017a, Volume 48, p. 2499.

Siebach, K. L., Baker, M. B., Grotzinger, J. P., McLennan, S. M., Gellert, R., Thompson, L. M., and Hurowitz, J. A., 2017b, Sorting out Compositional Trends in Sedimentary Rocks of the Bradbury Group (Aeolus Palus), Gale Crater, Mars: Journal of Geophysical Research: Planets, v. 122, no. 2, p. 295-328.

Smith, M. R., and Bandfield, J. L., 2012, Geology of quartz and hydrated silica-bearing deposits near Antoniadi Crater, Mars: Journal of Geophysical Research: Planets, v. 117, no. E6, p. E06007.

Soderblom, L., and Bell III, J., 2008, Exploration of the Martian surface: 1992-2007: The Martian Surface-Composition, Mineralogy, and Physical Properties, v. 1, p. 3.

Stack, K. M., Edwards, C. S., Grotzinger, J. P., Gupta, S., Sumner, D. Y., Calef, F. J., Edgar, L. A., Edgett, K. S., Fraeman, A. A., Jacob, S. R., Le Deit, L., Lewis, K. W., Rice, M. S., and Rubin, D., 2016, Comparing orbiter and rover image-based mapping of an ancient sedimentary environment, Aeolis Palus, Gale crater, Mars: Icarus, v. 280, p. 3-21.

Stack, K. M., Grotzinger, J. P., Griffes, J. L., and Farley, R. N., 2014a, Global Distribution of Stratified Deposits on Mars, *in* Rocha, R., Pais, J., Kullberg, J. C., and Finney, S., eds., STRATI 2013: First International Congress on Stratigraphy At the Cutting Edge of Stratigraphy: Cham, Springer International Publishing, p. 361-364.

Stack, K. M., Grotzinger, J. P., Kah, L. C., Schmidt, M. E., Mangold, N., Edgett, K. S., Sumner, D. Y., Siebach, K. L., Nachon, M., Lee, R., Blaney, D. L., Deflores, L. P., Edgar, L. A., Fairén, A. G., Leshin, L. A., Maurice, S., Oehler, D. Z., Rice, M. S., and Wiens, R. C., 2014b, Diagenetic origin of nodules in the Sheepbed member, Yellowknife Bay formation, Gale crater, Mars: Journal of Geophysical Research: Planets, v. 119, no. 7, p. 1637-1664.

Stack, K. M., Grotzinger, J. P., Lamb, M. P., Gupta, S., Rubin, D. M., Kah, L. C., Edgar, L. A., Fey, D. M., Hurowitz, J. A., McBride, M., Rivera-Hernández, F., Sumner, D. Y., Van Beek, J. K., Williams, R. M. E., and Yingst, R. A., 2018, Evidence for plunging river plume deposits in the Pahrump Hills member of the Murray formation, Gale crater, Mars: Sedimentology.

Stein, N., Grotzinger, J. P., Schieber, J., Mangold, N., Hallet, B., Newsom, H., Stack, K. M., Berger, J. A., Thompson, L., Siebach, K. L., Cousin, A., Le Mouélic, S., Minitti, M., Sumner, D. Y., Fedo, C., House, C. H., Gupta, S., Vasavada, A. R., Gellert, R., Wiens, R. C., Frydenvang, J., Forni, O., Meslin, P. Y., Payré, V., and Dehouck, E., 2018, Desiccation cracks provide evidence of lake drying on Mars, Sutton Island member, Murray formation, Gale Crater: Geology, v. 46, no. 6, p. 515-518.

Stockstill-Cahill, K. R., Anderson, F. S., and Hamilton, V. E., 2008, A study of low-albedo deposits within Amazonis Planitia craters: Evidence for locally derived ultramafic to mafic materials: Journal of Geophysical Research: Planets, v. 113, no. E7, p. E07008.

Stolper, E., and McSween, H. Y., 1979, Petrology and origin of the shergottite meteorites: Geochimica et Cosmochimica Acta, v. 43, no. 9, p. 1475-1498.

Sullivan, R., Banfield, D., Bell Iii, J. F., Calvin, W., Fike, D., Golombek, M., Greeley, R., Grotzinger, J., Herkenhoff, K., Jerolmack, D., Malin, M., Ming, D., Soderblom, L. A., Squyres, S. W., Thompson, S., Watters, W. A., Weitz, C. M., and Yen, A., 2005, Aeolian processes at the Mars Exploration Rover Meridiani Planum landing site: Nature, v. 436, p. 58.

Swindle, T. D., Caffee, M. W., and Hohenberg, C. M., 1986, Xenon and other noble gases in shergottites: Geochimica et Cosmochimica Acta, v. 50, no. 6, p. 1001-1015.

Tanaka, K. L., 1986, The stratigraphy of Mars: Journal of Geophysical Research: Solid Earth, v. 91, no. B13, p. E139-E158.

Tanaka, K. L., Skinner, J. A., and Hare, T. M., 2005, Geologic map of the northern plains of Mars: U.S. Geological Survey.

Thompson, L., Fraeman, A., Berger, J., Boyd, N., Desouza, E., Gellert, R., O'Connell-Cooper, C., Spray, J., and Yen, A., APXS determined chemistry of the Vera Rubin (Hematite) Ridge, Gale Crater, Mars: Implications for hematite signature origin, *in* Proceedings Lunar and Planetary Science Conference, Houston, TX, 2018a, Volume 49.

Thompson, L., Fraeman, A., Berger, J., Boyd, N., Gellert, R., O'Connell-Cooper, C., Spray, J. G., VanBommel, S. J., and Yen, A. S., Alpha Particle X-ray Spectrometer-Derived Compositional Characteristics of the Vera Rubin Ridge, Gale Crater, Mars and its Origin, *in* Proceedings AGU, Washington, D.C., 2018b.

Thompson, L. M., Schmidt, M. E., Spray, J. G., Berger, J. A., Fairén, A. G., Campbell, J. L., Perrett, G. M., Boyd, N., Gellert, R., and Pradler, I., 2016, Potassium-rich sandstones within the Gale impact crater, Mars: The APXS perspective: Journal of Geophysical Research: Planets, v. 121, no. 10, p. 1981-2003.

Thomson, B. J., Bridges, N. T., Milliken, R., Baldridge, A., Hook, S. J., Crowley, J. K., Marion, G. M., de Souza Filho, C. R., Brown, A. J., and Weitz, C. M., 2011, Constraints on the origin and evolution of the layered mound in Gale Crater, Mars using Mars Reconnaissance Orbiter data: Icarus, v. 214, no. 2, p. 413-432.

Tolosana-Delgado, R., and von Eynatten, H., 2009, Grain-size control on petrographic composition of sediments: compositional regression and rounded zeros: Mathematical geosciences, v. 41, no. 8, p. 869-886.

Toulmin, P., Baird, A. K., Clark, B. C., Keil, K., Rose, H. J., Christian, R. P., Evans, P. H., and Kelliher, W. C., 1977, Geochemical and mineralogical interpretation of the Viking inorganic chemical results: Journal of Geophysical Research, v. 82, no. 28, p. 4625-4634.

Treiman, A. H., Barrett, R. A., and Gooding, J. L., 1993, Preterrestrial aqueous alteration of the Lafayette (SNC) meteorite: Meteoritics, v. 28, no. 1, p. 86-97.

Treiman, A. H., Bish, D. L., Vaniman, D. T., Chipera, S. J., Blake, D. F., Ming, D. W., Morris, R. V., Bristow, T. F., Morrison, S. M., and Baker, M. B., 2016, Mineralogy, provenance, and diagenesis of a potassic basaltic sandstone on Mars: CheMin X-ray diffraction of the Windjana sample (Kimberley area, Gale Crater): Journal of Geophysical Research: Planets, v. 121, no. 1, p. 75-106.

Tsoar, H., Greeley, R., and Peterfreund, A. R., 1979, MARS: The North Polar Sand Sea and related wind patterns: Journal of Geophysical Research: Solid Earth, v. 84, no. B14, p. 8167-8180.

Turbet, M., and Forget, F., 2019, The paradoxes of the Late Hesperian Mars ocean: Scientific Reports, v. 9, no. 1, p. 5717.

Turner, S., Schwenzer, S. P., Bridges, J. C., Bedford, C. C., Rampe, E. B., Mangold, N., and L'Haridon, J., Thermochemical modelling of fluid-rock reactions in Vera Rubin Ridge, Gale crater., *in* Proceedings 50th Lunar and Planetary Science, Houston, TX, 2019.

Van Houten, F. B., 1973, Origin of Red Beds A Review-1961-1972: Annual Review of Earth and Planetary Sciences, v. 1, no. 1, p. 39-61.

Vaniman, D., Bish, D., Ming, D., Bristow, T., Morris, R., Blake, D., Chipera, S., Morrison, S., Treiman, A., and Rampe, E., 2014, Mineralogy of a mudstone at Yellowknife Bay, Gale crater, Mars: Science, v. 343, no. 6169, p. 1243480.

Vaniman, D., Dyar, M. D., Wiens, R., Ollila, A., Lanza, N., Lasue, J., Rhodes, J. M., Clegg, S., and Newsom, H., 2012, Ceramic ChemCam calibration targets on Mars Science Laboratory: Space science reviews, v. 170, no. 1-4, p. 229-255.

Vasavada, A. R., Grotzinger, J. P., Arvidson, R. E., Calef, F. J., Crisp, J. A., Gupta, S., Hurowitz, J., Mangold, N., Maurice, S., and Schmidt, M. E., 2014, Overview of the Mars Science Laboratory mission: Bradbury landing to Yellowknife Bay and beyond: Journal of Geophysical Research: Planets, v. 119, no. 6, p. 1134-1161.

Veizer, J., and Jansen, S. L., 1979, Basement and sedimentary recycling and continental evolution: The Journal of Geology, v. 87, no. 4, p. 341-370.

Walker, T. R., and Honea, R. M., 1969, Iron Content of Modern Deposits in the Sonoran Desert: A Contribution to the Origin of Red Beds: GSA Bulletin, v. 80, no. 3, p. 535-544.

Walker, T. R., Larson, E. E., and Hoblitt, R. P., 1981, Nature and origin of hematite in the Moenkopi Formation (Triassic), Colorado Plateau: A contribution to the origin of magnetism in red beds: Journal of Geophysical Research: Solid Earth, v. 86, no. B1, p. 317-333.

Wänke, H., Brückner, J., Dreibus, G., Rieder, R., and Ryabchikov, I., Chemical Composition of Rocks and Soils at the Pathfinder Site, Dordrecht, 2001, Springer Netherlands, p. 317-330.

Watkins, J. A., Grotzinger, J., Stein, N., Banham, S. G., Gupta, S., Rubin, D., Stack, K. M., and Edgett, K. S., Paleotopography of Erosional Unconformity, Base of Stimson Formation, Gale Crater, Mars, *in* Proceedings 47th Lunar and Planetary Science Conference, Houston, TX, United States, 2016, Volume 47, p. 2939.

Wellek, S., 2010, Testing statistical hypotheses of equivalence and noninferiority, Chapman and Hall/CRC.

Weltje, G. J., 2012, Quantitative models of sediment generation and provenance: state of the art and future developments: Sedimentary Geology, v. 280, p. 4-20.

Wiens, R. C., Maurice, S., Barraclough, B., Saccoccio, M., Barkley, W. C., Bell Iii, J. F., Bender, S., Bernardin, J., Blaney, D., and Blank, J., 2012, The ChemCam instrument suite on the Mars Science Laboratory (MSL) rover: Body unit and combined system tests: Space Science Reviews, v. 170, no. 1-4, p. 167-227.

Wiens, R. C., Maurice, S., Lasue, J., Forni, O., Anderson, R. B., Clegg, S., Bender, S., Blaney, D., Barraclough, B. L., and Cousin, A., 2013, Pre-flight calibration and initial data processing for the ChemCam laser-induced breakdown spectroscopy instrument on the Mars Science Laboratory rover: Spectrochimica Acta Part B: Atomic Spectroscopy, v. 82, p. 1-27.

Wiens, R. C., Maurice, S., and Rull Perez, F., 2017a, The SuperCam remote sensing instrument suite for the Mars 2020 rover mission: A preview: Spectroscopy, v. 32, p. 50-55.

Wiens, R. C., Rubin, D. M., Goetz, W., Fairén, A. G., Schwenzer, S. P., Johnson, J. R., Milliken, R., Clark, B., Mangold, N., Stack, K. M., Oehler, D., Rowland, S., Chan, M., Vaniman, D., Maurice, S., Gasnault, O., Rapin, W., Schroeder, S., Clegg, S., Forni, O., Blaney, D., Cousin, A., Payré, V., Fabre, C., Nachon, M., Le Mouelic, S., Sautter, V., Johnstone, S., Calef, F., Vasavada, A. R., and Grotzinger, J. P., 2017b, Centimeter to decimeter hollow concretions and voids in Gale Crater sediments, Mars: Icarus, v. 289, p. 144-156.

Wilhelms, D. E., and Squyres, S. W., 1984, The martian hemispheric dichotomy may be due to a giant impact: Nature, v. 309, p. 138.

Williams, J.-P., Nimmo, F., Moore, W. B., and Paige, D. A., 2008, The formation of Tharsis on Mars: What the line-of-sight gravity is telling us: Journal of Geophysical Research: Planets, v. 113, no. E10, p. E10011.

Wilson, L., Scott, E. D., and Head, J. W., 2001, Evidence for episodicity in the magma supply to the large Tharsis volcanoes: Journal of Geophysical Research: Planets, v. 106, no. E1, p. 1423-1433.

Wittmann, A., Korotev, R. L., Jolliff, B. L., Irving, A. J., Moser, D. E., Barker, I., and Rumble, D., 2015, Petrography and composition of Martian regolith breccia meteorite Northwest Africa 7475: Meteoritics & Planetary Science, v. 50, no. 2, p. 326-352.

Wray, J. J., 2013, Gale crater: the Mars Science Laboratory/Curiosity Rover Landing Site: International Journal of Astrobiology, v. 12, no. 1, p. 25-38.

Yen, A. S., Ming, D. W., Vaniman, D. T., Gellert, R., Blake, D. F., Morris, R. V., Morrison, S. M., Bristow, T. F., Chipera, S. J., and Edgett, K. S., 2017, Multiple stages of aqueous alteration along fractures in mudstone and sandstone strata in Gale Crater, Mars: Earth and Planetary Science Letters, v. 471, p. 186-198.

Zhong, S., and Zuber, M. T., 2001, Degree-1 mantle convection and the crustal dichotomy on Mars: Earth and Planetary Science Letters, v. 189, no. 1, p. 75-84.

8. Appendix

A.1. Figure reference list

Table A.1: A figure reference list of publically released images used in this thesis that were acquired from the url links provided.

Figure	Reference URL
1.1	https://planetarymaps.usgs.gov/mosaic/Mars_MGS_MOLA_ClrShade_merge_global_463m.tif
1.5 B	https://photojournal.jpl.nasa.gov/catalog/PIA14305
1.15	https://photojournal.jpl.nasa.gov/catalog/PIA21850
2.1	https://photojournal.jpl.nasa.gov/catalog/PIA14304
2.2 A	https://photojournal.jpl.nasa.gov/catalog/PIA15106
2.2 B	http://www.msl-chemcam.com/doc/images/259/image020.jpg
2.2 C	http://www.msl-chemcam.com/doc/images/259/image016.jpg
2.3	https://photojournal.jpl.nasa.gov/browse/PIA16089.jpg
2.4	https://photojournal.jpl.nasa.gov/browse/PIA17594.jpg
5.18 A	https://photojournal.jpl.nasa.gov/catalog/PIA22066
5.18 B	https://photojournal.jpl.nasa.gov/catalog/PIA22068

A.2. Supplementary information for Chapter 2

Table A.2.1: Descriptions of Minitab's regression model output, alongside the formulas used to calculate each output variable.

Minitab output variable	**Code name**	**Formula**	**Notation**	**Brief description**
Sum of squares (SS) Regression, Error, and Total	Regression Error Total	$SSR = \sum(\hat{y}_i - \bar{y})^2$ $SSE = \sum(y_i - \hat{y})^2$ $SST = \sum(y_i - \bar{y})^2$	y_i = ith observed response value $\hat{y}$ = ith fitted response $\hat{y}$ = mean response	The sum of squared distances that describe the total variation in the data (SST), the portion of the variation explained by the model (SSR), and the proportion of data variation attributed to error (SSE).
Degrees of Freedom	DF	$Regression\ DF = p$ $Error\ DF = n - p - 1$ $Total\ DF = n - 1$	n = number of observations p = number of terms in the model	The degrees of freedom represents the number of independent pieces of information in the dataset
Sequential sum of squares	Seq SS	$SS(AB) = SST - SSE - SS(A) - SS(B)$ $SS\ (A) = nb\sum_i(\bar{y}_i - \bar{y}\ ...)^2$ $SS(B) = n\sum_i\sum_j(\bar{y}_{ij} - \bar{y}_i\ ...)^2$	a = number of levels in factor A, b = number of levels in factor B, n = number of trials, y_i = mean of ith factor of A, $y\ldots$ = mean of all observations, y_j = mean of the jth factor level of B, y_{ij} = mean of observations at the ith level of A and jth level of B.	The sequential sum of squares gives the proportion of the regression sum of squares as explained by a predictor, taking into account all previous predictors in the model. This is used to calculate the predictor contribution.

Minitab output variable	Code name	Formula	Notation	Brief description
Adjusted sum of squares	Adj SS	Formula for the adjusted sum of squares for X3 given X1 and X2 are in the model: $SSR(X3\|X1,X2) = SSE(X1,X2) - SSE(X1,X2,X3)$ Formula for the adjusted sum of squares of X2 and X3 given X1 is in the model: $SSR(X2,X3\|X1) = SSE(X1) - SSE(X1,X2,X3)$	The three factors in the formula; X1, X2, X3	Unlike the Sequential sum of squares, the adjusted sum of squares does not depend on the order predictors were entered into the model. This describes the unique portion of regression sum of squares for the predictor, taking into account all other predictors in the model.
Adjusted mean square	Adj MS	$Adj\ MS = Adj\ SS/DF$		The mean square for each model component
F	F-Value	$F = Adj\ MS/MSE$ Whereby, $MSE = Adj\ SS\ Error/DF\ Error$	MSE = the mean square error term	F is used to test the model for statistical significance, providing all the factors in the model are fixed, and follows the F distribution. The Mean square error term is the variance of the data around the fitted regression line
t	T-Value	$t = r\sqrt{\frac{n-2}{1-r^2}}$	r = Pearson's correlation coefficient, n = number of observations,	A test to determine the significance of the predictor to the model. t is compared to the t-distribution.
p	P-Value	$p - value = 2P(T > \|t\|)$ For, $\alpha = 0.05$	α = significance level	Tests the null hypothesis of no correlation (H_0:ρ = 0) between the predictor and response, against the alternative hypothesis that a correlation exists (H_A:ρ ≠ 0).

Minitab output variable	Code name	Formula	Notation	Brief description
Standard deviation	S	$S = \sqrt{MSE}$		An estimate of the standard deviation of the model's error
r^2	R-sq	$r^2 = 1 - \frac{SSE}{SST}$		The coefficient of determination that measures how much variation in the response is measured by the model
Adjusted r^2	R-sq(adj)	$r^2(adj) = 1 - \frac{MSE}{SST/DF\ Total}$		The calculated r2 value that takes into account the number of predictors in the model. Only useful for multiple regression models and comparing models with different numbers of predictors.
	PRESS	$PRESS = \sum_{1}^{n} (\frac{e_i}{1 - h_i})^2$	e_i = ith residual, h_i = ith diagonal element of $\mathbf{X}(\mathbf{X}'\mathbf{X})^{-1}\mathbf{X}'$ where **x** is the predictor matrix	
Predicted r^2	R-sq (pred)	$r^2(pred) = 1 - \frac{PRESS}{SST}$		Determines how well the model can predict responses for new observations
Standard error of the coefficients	SE Coeff	$SE\ Coeff = \sqrt{(\boldsymbol{X}'\boldsymbol{X})^{-1}S^2}$	**X** = the design matrix	This provides the estimated standard deviation of the coefficient

Minitab output variable	Code name	Formula	Notation	Brief description
95% Confidence Interval	95% CI	$\hat{Y}_0 \pm t_{(1-\alpha/2,n-p)} * S(\hat{Y}_0)$ $s(\hat{Y}_0) = \sqrt{MSE(\boldsymbol{x'}_o(\boldsymbol{x'x})^{-1}\boldsymbol{x}_o}$	$\hat{Y}_0$ = fitted response value for a given set of predictor values, α = significance level, p = number of model parameters, n = number of observations, **x** = design matrix $\mathbf{x}_o$ = design matrix for the predictor values	Equates the range within which the estimated mean response for a given set of predictor values is expected to fall
Variance Inflation Factor	VIF	$VIF = \frac{1}{1 - r^2(x_1)}$		A method that determines how much correlation exists between the predictors.

A.3 Supplementary information for Chapter 3

Table A.3.1: Chemical compositions of the CheMin minerals used in this study. Aug. = Augite, Ol. = Olivine, Plag. = plagioclase, Kspar = K-feldspar, Am. and Phyll. = Amorphous and Phyllosilicate component.

	CaO	MgO	FeO_T	SiO_2	Na_2O	Al_2O_3	TiO_2	K_2O	Analysis	Ref.
Aug.	20.45	18.56	6.22	54.77	0.00	0.00	0.00	0.00	Rocknest	1
Ol.	0.00	27.67	36.46	35.87	0.00	0.00	0.00	0.00	Rocknest	1
Plag.	10.38	0.00	0.00	55.59	5.73	28.3	0.00	0.00	Rocknest	1
Kspar	0.00	0.00	0.00	65.25	1.46	18.46	0.00	14.83	Windjana	1
Am. and Phyll.	6.99	10.90	19.59	41.76	2.86	6.97	1.41	0.69	John Klein	2
	5.63	11.48	22.21	43.15	2.97	6.96	1.16	0.55	Cumberland	2
	0.9	21.6	33.8	14.20	2.9	4.7	2.6	-1.6	Windjana	3
	1.05	5.46	15.55	52.61	2.89	6.27	2.30	0.31	Confidence Hills	4
	0.02	5.59	12.72	55.39	2.91	7.73	2.15	0.57	Mojave2	4
	0.43	1.78	19.56	55.04	4.45	5.97	3.14	0.21	Telegraph Peak	4
	1.54	1.26	4.71	77.01	1.58	0.04	2.54	0.69	Buckskin	5

[1]Morrison et al. (2018)

[2]Vaniman et al. (2014),

[3]Treiman et al. (2016),

[4]Rampe et al. (2017)

[5]Morris et al. (2016).

Tables of Pearson correlation coefficients for the Bradbury and Mt Sharp (lower Murray formation to sol 1482) Groups

The following tables show the Pearson correlation coefficients (r-values) and associated p-values (grey number) for the silica-rich diagenetic halos, Murray formation with Marias Pass removed, and Sheepbed Member discussed in Chapter 3. Numbers are highlighted according to the strength of their correlations: bright yellow = very strong positive; orange = moderately strong positive; dark blue is moderately strong negative; bright blue = strong negative. Red, highlighted p-values show statistical insignificance.

Table A.3.2: Pearson correlation coefficients and calculated r values for ChemCam observation points that targeted diagenetic halo features in the Marias Pass and Bridger Basin localities.

Halos	SiO_2	TiO_2	Al_2O_3	FeO_T	MgO	CaO	Na_2O
TiO_2	0.29						
	0.0000						
Al_2O_3	-0.44	-0.31					
	0.0000	0.0000					
FeO_T	-0.72	-0.04	0.29				
	0.0000	0.3040	0.0000				
MgO	-0.35	-0.17	0.04	0.30			
	0.0000	0.0000	0.2870	0.0000			
CaO	-0.63	-0.37	0.05	0.18	0.12		
	0.0000	0.0000	0.1920	0.0000	0.0020		
Na_2O	-0.34	-0.11	0.79	0.33	-0.01	-0.05	
	0.0000	0.0060	0.0000	0.0000	0.9060	0.1810	
K_2O	-0.03	-0.04	0.48	-0.02	-0.12	-0.20	0.40
	0.4860	0.3260	0.0000	0.6880	0.0020	0.0000	0.0000

Table A.3.3. The Murray formation (excluding Marias Pass analyses) Pearson correlation coefficients and associated p-values (grey numbers). Black outlined boxes are correlations that match with the Sheepbed member (Table A.3.3.).

Murray formation (excluding Marias Pass)							
	SiO_2	TiO_2	Al_2O_3	FeO_T	MgO	CaO	Na_2O
TiO_2	0.04						
	0.19						
Al_2O_3	-0.09	-0.16					
	0.00	0.00					
FeO_T	-0.55	0.10	-0.39				
	0.00	0.00	0.00				
MgO	-0.22	-0.15	-0.23	0.08			
	0.00	0.00	0.00	0.01			
CaO	-0.45	-0.07	0.23	-0.21	-0.20		
	0.00	0.01	0.00	0.00	0.00		
Na_2O	0.03	0.00	0.61	-0.27	-0.40	0.12	
	0.37	0.90	0.00	0.00	0.00	0.00	
K_2O	0.29	-0.06	0.09	-0.09	-0.14	-0.33	0.22
	0.00	0.03	0.00	0.00	0.00	0.00	0.00

Table A.3.4. Sheepbed member mudstone Pearson correlation coefficients and associated p-values (grey numbers). Black outlined boxes are correlations that match with the Murray formation excluding Marias Pass analyses (Table A.3.2).

Sheepbed							
	SiO_2	TiO_2	Al_2O_3	FeO_T	MgO	CaO	Na_2O
TiO_2	-0.26						
	0.00						
Al_2O_3	0.17	0.06					
	0.00	0.28					
FeO_T	-0.30	0.35	-0.35				
	0.00	0.00	0.00				
MgO	0.12	-0.40	-0.63	0.10			
	0.04	0.00	0.00	0.07			
CaO	-0.16	-0.05	0.60	-0.32	-0.62		
	0.00	0.40	0.00	0.00	0.00		
Na_2O	0.26	0.17	0.53	-0.27	-0.58	0.18	
	0.00	0.00	0.00	0.00	0.00	0.00	
K_2O	0.14	0.33	0.34	-0.09	-0.42	-0.02	0.66
	0.01	0.00	0.00	0.13	0.00	0.75	0.00

Linear regression models for major elements against Chemical Indices of Alteration (CIA)

Linear regression models for the constrained, mudstone unit dataset were conducted for CIA values to determine whether their differences in SiO_2, MgO and FeO_T major element geochemistry is related to chemical weathering. In this dataset, obvious diagenetic features have been removed and the sedimentary units are of a uniform mudstone/siltstone grain size. Therefore, if geochemical variation does relate to chemical weathering, then both the Sheepbed and Murray analyses will plot along the calculated linear regression line with minimal scatter. If not, then it is hypothesised that differences in composition at the sediment source region/s are the main cause of geochemical variation for the constrained ChemCam dataset.

CIA versus SiO_2 linear regression model

Simple Linear Regression model output for SiO_2 against CIA for the Gale Crater mudstone units Sheepbed and Murray. The residual plots are shown below for normal probability and residuals versus order. Overall, the residuals show a relatively normal distribution, though there are more outlying compositions at the start of the analysis (for ChemCam observation point compositions in the Pahrump Hills area). See section 3.2.1.3. of the main text for a discussion on this model. The Sheepbed analyses are the first 350 observation points and show a closer fit to the model than the Murray formation mudstones in the residuals versus order plot.

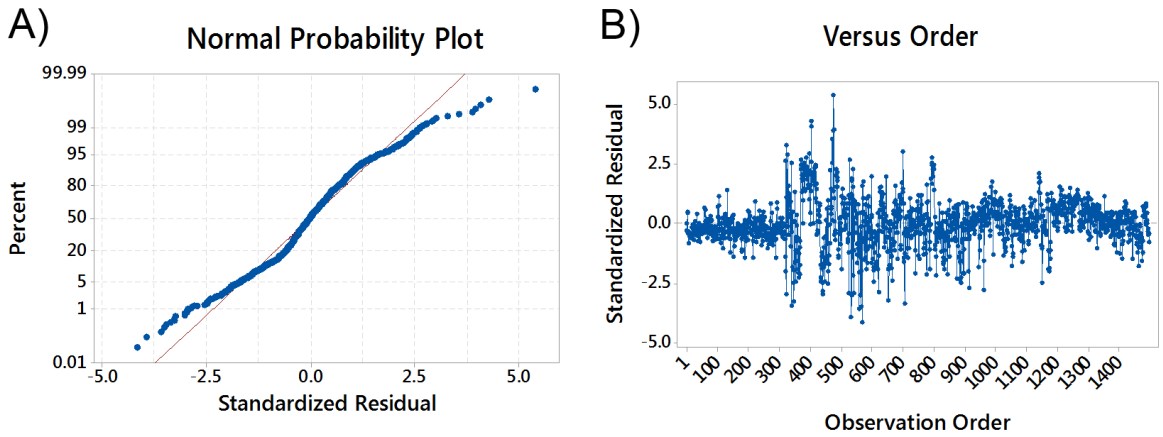

Figure A.3.1: Residual plots from the CIA against SiO_2 simple linear regression model of Sheepbed and Murray formation constrained ChemCam datasets A) Normal probability of the standardized residuals, and B) standardized residuals versus observation order for SiO_2 as a response to CIA, and Group as the categorical predictors.

Table A.3.5: Minitab v17 model output for SiO_2 as a response to predictor CIA for Sheepbed or Murray formation mudstones. Output demonstrates how well the model fits the data with calculated student t-test p-values, error (both pure and lack-of-fit), standard error (S), r^2 percentages (R-sq), and adjusted r^2(R-sq(adj)). The model is built around the null hypothesis that there is no fit between the response and predictors (H_0: $\rho = 0$).

Model output also displays the degrees of freedom (DF), Sequential Sum of Squares (Seq SS), Percentage contribution of the predictors to the model (Contribution), Adjusted Sum of Squares (Adj SS), Adjusted Mean Squares (Adj MS) and F-value which are used to calculate the regression.

Analysis of Variance

Source	DF	Seq SS	Contribution	Adj SS	Adj MS	F-Value	P-Value
Regression	1	5887.0	25.54%	5887.0	5886.96	512.81	0.000
CIA	1	5887.0	25.54%	5887.0	5886.96	512.81	0.000
Error	1495	17162.3	74.46%	17162.3	11.48		
Lack-of-Fit	1492	17162.3	74.46%	17162.3	11.50	*	*
Pure Error	3	0.0	0.00%	0.0	0.00		
Total	1496	23049.2	100.00%				

Model Summary

S	R-sq
3.38818	25.54%

Regression Equation

SiO2 = 38.140 + 0.2647 CIA

CIA versus MgO linear regression model

Simple Linear Regression model output for MgO against CIA for the Gale Crater mudstone units Sheepbed and Murray. The residual plots are shown below. The residuals show an approximate normal distribution, though there is a substantial skew in the residuals histogram and normal probability plots inferring that the Sheepbed observation point analyses (1 – 300) have anomalously high MgO content, while the majority of the Murray formation has low MgO (analyses 300+). Although it is worth noting that the MgO content is seen to increase along the traverse towards the Murray Buttes area (analyses 1200+). The residuals versus order plot suggests that there is a strong dependency of MgO on stratigraphic position, particularly between the Bradbury group Sheepbed mudstones and Mt Sharp group Murray mudstones. See section 4.4.2 of the main text for a discussion on this model.

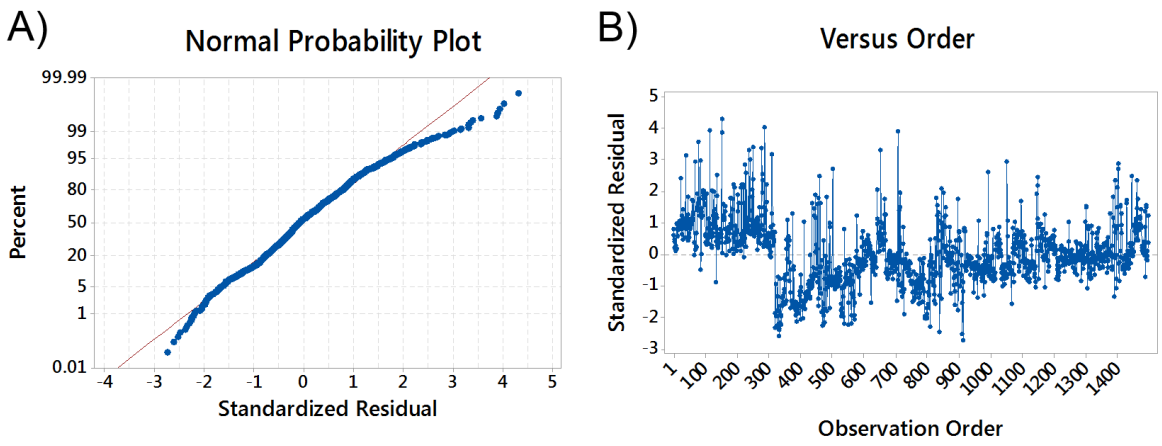

Figure A.3.2: Residual plots from the CIA against MgO simple linear regression model of Sheepbed and Murray formation constrained ChemCam datasets A) Normal probability of the standardized residuals, and B) standardized residuals versus observation order for MgO as a response to CIA, and Group as the categorical predictors distinguishing between the Sheepbed member and Mt Sharp group, Murray formation mudstones.

Table A.3.6: Minitab v17 linear regression model output for MgO versus CIA for the Sheepbed member mudstones and Murray formation mudstones groups. Output demonstrates how well the model fits the data with calculated student t-test p-values, error (both pure and lack-of-fit), standard error (S), r^2 percentages (R-sq), and adjusted r^2(R-sq(adj)). The model is built around the null hypothesis that there is no fit between the response and predictors (H_0: $\rho = 0$).

Model output also displays the degrees of freedom (DF), Sequential Sum of Squares (Seq SS), Percentage contribution of the predictors to the model (Contribution), Adjusted Sum of Squares (Adj SS), Adjusted Mean Squares (Adj MS) and F-value which are used to calculate the regression.

Analysis of Variance

Source	DF	Seq SS	Contribution	Adj SS	Adj MS	F-Value	P-Value
Regression	1	906.99	11.08%	906.99	906.986	186.30	0.000
CIA	1	906.99	11.08%	906.99	906.986	186.30	0.000
Error	1495	7278.40	88.92%	7278.40	4.868		
Lack-of-Fit	1492	7278.40	88.92%	7278.40	4.878	*	*
Pure Error	3	0.00	0.00%	0.00	0.000		
Total	1496	8185.39	100.00%				

Model Summary

S	R-sq
2.20647	11.08%

Regression Equation

MgO = 10.725 - 0.10390 CIA

CIA versus FeO_T linear regression model

Simple Linear Regression model output for FeO_T against CIA for the Gale Crater mudstone units Sheepbed and Murray. The residual plots are shown below. Residuals show a very poor fit with the model which is highlighted by the high p-value showing that there is no correlation between CIA and FeO_T content. The residuals versus order plot shows that there is a high degree of variation in iron content for the Pahrump Hills area. Aside from this location, FeO_T is relatively constant for the mudstone units. See section 4.4.2 of the main text for a discussion on this model.

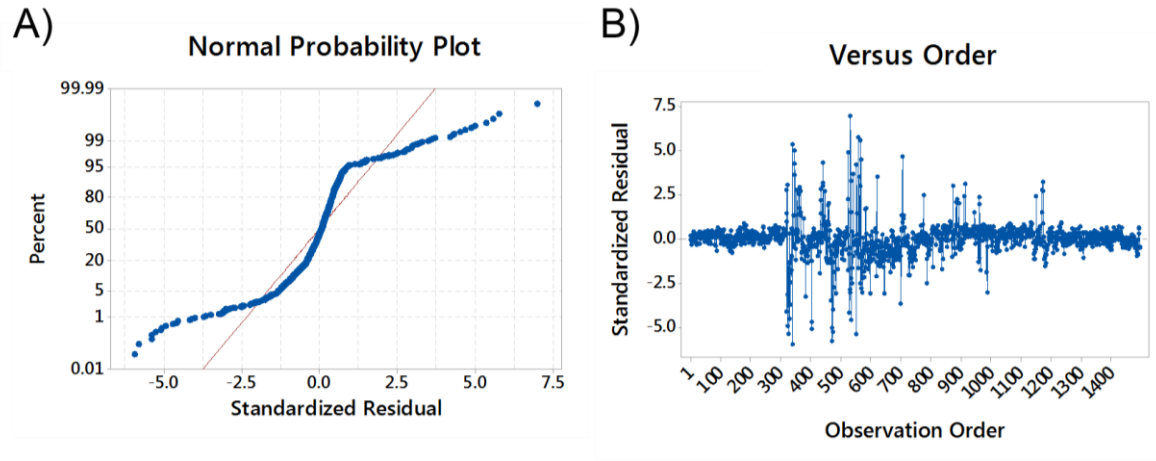

Figure A.3.3: Residual plots from the CIA against FeO_T simple linear regression model of Sheepbed and Murray formation constrained ChemCam datasets A) Normal probability of the standardized residuals, and B) standardized residuals versus observation order for FeO_T as a response to CIA, and Group (Sheepbed or Murray) as the categorical predictors.

Table A.3.7: Minitab v17 output for the linear regression model of FeO_T versus CIA for the Sheepbed and Murray mudstones. Output demonstrates how well the model fits the data with calculated student t-test p-values, error (both pure and lack-of-fit), standard error (S), and r^2 percentages (R-sq). The model is built around the null hypothesis that there is no fit between the response and predictors (H_0: $\rho = 0$).

Model output also displays the degrees of freedom (DF), Sequential Sum of Squares (Seq SS), Percentage contribution of the predictors to the model (Contribution), Adjusted Sum of Squares (Adj SS), Adjusted Mean Squares (Adj MS) and F-value which are used to calculate the regression.

Analysis of Variance

Source	DF	Seq SS	Contribution	Adj SS	Adj MS	F-Value	P-Value
Regression	1	1.9	0.01%	1.9	1.9127	0.18	0.669
CIA	1	1.9	0.01%	1.9	1.9127	0.18	0.669
Error	1495	15600.4	99.99%	15600.4	10.4351		
Lack-of-Fit	1492	15600.4	99.99%	15600.4	10.4561	*	*
Pure Error	3	0.0	0.00%	0.0	0.0000		
Total	1496	15602.3	100.00%				

Model Summary

S	R-sq
3.23034	0.01%

Regression Equation

FeOT = 19.413 - 0.0048 CIA

A.4 Supplementary information for Chapter 4

Stimson formation Cluster Analysis output

Here I provide the Minitab v17 model output of the Multivariate Cluster Analysis (variables SiO_2, TiO_2, Al_2O_3, FeO_T, MgO, CaO, Na_2O, K_2O) conducted on all Stimson formation ChemCam observation point analyses within the 95–105 % total sum of oxide range. In this model, the variables were standardised to ensure that Minitab weighs all variables equally and does not give precedence to variables with larger average wt% abundances (e.g., SiO_2). The Manhattan distance and complete linkage methods were identified as the best methods to calculate distance for the Stimson dataset (see section 2.4.3.). The final partition was identified when the difference between similarity levels exceeded 6.00. See Chapters 2.4.3. and 4.1.4. for more details.

Table 4.1: Model output of the Stimson formation Cluster analysis calculated using Manhattan distance and complete linkage methods on standardised variables SiO_2, TiO_2, Al_2O_3, FeO_T, MgO, CaO, Na_2O, K_2O.

Amalgamation Steps

Step	Number of clusters	Similarity level	Distance level	Clusters joined		New cluster	Number of obs. in new cluster
1	403	98.2978	0.6274	272	274	272	2
2	402	98.0623	0.7143	48	49	48	2
3	401	97.7112	0.8437	360	361	360	2
4	400	97.4622	0.9355	69	162	69	2
5	399	97.2977	0.9961	167	324	167	2
6	398	97.1995	1.0323	66	160	66	2
7	397	97.1511	1.0501	264	355	264	2
8	396	97.0932	1.0715	70	277	70	2
9	395	96.9795	1.1134	131	193	131	2
10	394	96.9571	1.1217	147	154	147	2
11	393	96.9073	1.1400	157	215	157	2
12	392	96.8537	1.1598	156	354	156	2
13	391	96.8484	1.1617	132	329	132	2
14	390	96.7118	1.2120	292	321	292	2
15	389	96.4983	1.2907	273	278	273	2
16	388	96.4822	1.2967	128	182	128	2
17	387	96.4069	1.3245	108	148	108	2
18	386	96.3378	1.3499	221	290	221	2
19	385	96.3258	1.3543	153	358	153	2
20	384	96.3023	1.3630	169	310	169	2
21	383	96.2818	1.3706	85	236	85	2
22	382	96.2337	1.3883	76	237	76	2
23	381	96.2160	1.3948	171	285	171	2
24	380	96.1824	1.4072	157	214	157	3
25	379	96.1674	1.4127	319	391	319	2
26	378	96.1520	1.4184	129	293	129	2

27	377	96.0250	1.4652	145	325	145	2
28	376	95.9855	1.4798	106	188	106	2
29	375	95.9605	1.4890	67	107	67	2
30	374	95.9592	1.4895	21	63	21	2
31	373	95.9530	1.4918	37	168	37	2
32	372	95.9396	1.4967	256	257	256	2
33	371	95.8453	1.5315	98	109	98	2
34	370	95.8364	1.5347	309	318	309	2
35	369	95.7798	1.5556	190	334	190	2
36	368	95.6418	1.6065	164	217	164	2
37	367	95.5397	1.6441	301	330	301	2
38	366	95.5167	1.6526	92	173	92	2
39	365	95.5110	1.6547	256	404	256	3
40	364	95.4686	1.6703	131	138	131	3
41	363	95.4643	1.6719	220	242	220	2
42	362	95.4608	1.6732	91	133	91	2
43	361	95.4256	1.6861	84	174	84	2
44	360	95.4057	1.6935	17	59	17	2
45	359	95.4002	1.6955	147	264	147	4
46	358	95.3507	1.7138	245	382	245	2
47	357	95.3455	1.7157	260	263	260	2
48	356	95.3137	1.7274	85	94	85	3
49	355	95.2397	1.7547	7	9	7	2
50	354	95.2354	1.7563	36	167	36	3
51	353	95.2343	1.7567	52	62	52	2
52	352	95.2304	1.7581	21	178	21	3
53	351	95.1684	1.7810	116	146	116	2
54	350	95.1533	1.7865	28	46	28	2
55	349	95.1453	1.7895	254	298	254	2
56	348	95.1373	1.7924	137	268	137	2
57	347	95.1329	1.7941	155	300	155	2
58	346	95.1312	1.7947	45	223	45	2
59	345	95.0354	1.8300	314	337	314	2
60	344	95.0240	1.8342	292	342	292	3
61	343	95.0156	1.8373	195	196	195	2
62	342	95.0007	1.8428	100	234	100	2
63	341	94.9643	1.8562	347	400	347	2
64	340	94.9514	1.8610	233	333	233	2
65	339	94.9490	1.8618	232	351	232	2
66	338	94.9143	1.8747	175	284	175	2
67	337	94.8162	1.9108	152	360	152	3
68	336	94.8144	1.9115	186	197	186	2
69	335	94.7621	1.9307	20	69	20	3
70	334	94.7504	1.9351	38	105	38	2
71	333	94.7463	1.9366	83	114	83	2
72	332	94.7141	1.9484	2	320	2	2
73	331	94.7007	1.9534	89	130	89	2
74	330	94.6773	1.9620	207	328	207	2
75	329	94.6656	1.9663	88	212	88	2
76	328	94.6486	1.9726	208	211	208	2
77	327	94.6350	1.9776	23	134	23	2
78	326	94.6297	1.9795	161	213	161	2
79	325	94.6053	1.9885	190	194	190	3
80	324	94.5801	1.9978	96	117	96	2
81	323	94.5316	2.0157	315	388	315	2
82	322	94.5274	2.0173	176	312	176	2
83	321	94.5074	2.0246	157	206	157	4
84	320	94.4898	2.0311	272	273	272	4
85	319	94.4449	2.0476	135	365	135	2
86	318	94.3852	2.0697	271	349	271	2
87	317	94.3480	2.0834	149	153	149	3
88	316	94.2986	2.1016	297	326	297	2
89	315	94.2850	2.1066	106	113	106	3
90	314	94.2267	2.1281	199	219	199	2
91	313	94.2188	2.1310	339	362	339	2
92	312	94.2137	2.1329	87	95	87	2
93	311	94.1817	2.1447	184	286	184	2
94	310	94.1650	2.1508	92	209	92	3
95	309	94.1608	2.1524	192	341	192	2
96	308	94.1545	2.1547	72	141	72	2
97	307	94.1277	2.1646	132	350	132	3

98	306	94.1101	2.1711	50	56	50	2
99	305	94.1035	2.1735	231	261	231	2
100	304	94.0799	2.1822	287	389	287	2
101	303	94.0624	2.1887	83	112	83	3
102	302	93.9854	2.2170	84	229	84	3
103	301	93.9678	2.2235	151	158	151	2
104	300	93.9180	2.2419	22	239	22	2
105	299	93.8779	2.2567	397	398	397	2
106	298	93.8619	2.2626	5	198	5	2
107	297	93.7898	2.2891	216	317	216	2
108	296	93.7418	2.3068	288	359	288	2
109	295	93.7353	2.3092	147	221	147	6
110	294	93.6975	2.3232	323	347	323	3
111	293	93.6582	2.3376	11	29	11	2
112	292	93.6516	2.3401	149	152	149	6
113	291	93.6512	2.3402	7	8	7	3
114	290	93.5903	2.3627	186	294	186	3
115	289	93.5653	2.3719	171	308	171	3
116	288	93.5338	2.3835	230	276	230	2
117	287	93.5222	2.3878	23	295	23	3
118	286	93.3750	2.4420	175	184	175	4
119	285	93.3628	2.4465	251	368	251	2
120	284	93.3543	2.4497	128	292	128	5
121	283	93.3371	2.4560	42	85	42	4
122	282	93.3354	2.4566	232	394	232	3
123	281	93.3290	2.4590	265	266	265	2
124	280	93.3008	2.4694	54	226	54	2
125	279	93.2616	2.4838	155	299	155	3
126	278	93.2596	2.4846	119	120	119	2
127	277	93.2483	2.4887	200	205	200	2
128	276	93.2427	2.4908	26	352	26	2
129	275	93.2274	2.4964	37	48	37	4
130	274	93.2015	2.5060	10	18	10	2
131	273	93.1942	2.5087	254	275	254	3
132	272	93.1360	2.5301	84	270	84	4
133	271	93.1197	2.5361	208	311	208	3
134	270	93.1012	2.5430	156	304	156	3
135	269	93.0735	2.5532	64	72	64	3
136	268	93.0439	2.5641	161	281	161	3
137	267	92.9942	2.5824	159	210	159	2
138	266	92.9826	2.5867	143	157	143	5
139	265	92.9300	2.6060	20	313	20	4
140	264	92.9153	2.6115	33	90	33	2
141	263	92.9106	2.6132	58	71	58	2
142	262	92.9041	2.6156	247	345	247	2
143	261	92.8928	2.6198	55	335	55	2
144	260	92.8308	2.6426	14	16	14	2
145	259	92.8033	2.6528	100	338	100	3
146	258	92.7435	2.6748	260	393	260	3
147	257	92.7329	2.6787	118	390	118	2
148	256	92.7033	2.6896	172	190	172	4
149	255	92.6811	2.6978	66	108	66	4
150	254	92.6734	2.7006	41	131	41	4
151	253	92.6578	2.7064	32	179	32	2
152	252	92.6541	2.7077	5	332	5	3
153	251	92.6357	2.7145	177	289	177	2
154	250	92.5862	2.7328	258	319	258	3
155	249	92.5736	2.7374	36	67	36	5
156	248	92.5524	2.7453	137	207	137	4
157	247	92.5305	2.7533	74	88	74	3
158	246	92.5265	2.7548	191	302	191	2
159	245	92.5221	2.7564	102	283	102	2
160	244	92.5195	2.7574	259	272	259	5
161	243	92.4591	2.7797	82	199	82	3
162	242	92.4266	2.7916	187	315	187	3
163	241	92.3465	2.8212	380	383	380	2
164	240	92.3429	2.8225	104	106	104	4
165	239	92.3373	2.8245	6	11	6	3
166	238	92.3364	2.8249	135	195	135	4
167	237	92.3242	2.8294	3	98	3	3
168	236	92.3160	2.8324	21	60	21	4

169	235	92.3112	2.8342	186	336	186	4
170	234	92.2464	2.8580	136	228	136	2
171	233	92.2309	2.8638	89	116	89	4
172	232	92.2269	2.8652	238	303	238	2
173	231	92.1755	2.8842	166	246	166	2
174	230	92.1528	2.8925	64	401	64	4
175	229	92.0783	2.9200	145	216	145	4
176	228	92.0681	2.9238	25	180	25	2
177	227	92.0512	2.9300	309	327	309	3
178	226	91.9949	2.9508	111	151	111	3
179	225	91.9894	2.9528	282	378	282	2
180	224	91.9758	2.9578	17	24	17	3
181	223	91.9067	2.9833	185	253	185	2
182	222	91.8746	2.9951	181	260	181	4
183	221	91.8475	3.0051	28	52	28	4
184	220	91.7849	3.0281	396	397	396	3
185	219	91.6836	3.0655	92	220	92	5
186	218	91.6143	3.0910	20	65	20	5
187	217	91.5941	3.0985	2	316	2	3
188	216	91.5854	3.1017	51	58	51	3
189	215	91.5787	3.1042	227	357	227	2
190	214	91.5021	3.1324	129	164	129	4
191	213	91.4679	3.1450	34	375	34	2
192	212	91.4581	3.1486	256	291	256	4
193	211	91.4054	3.1681	305	307	305	2
194	210	91.3982	3.1707	84	128	84	9
195	209	91.3589	3.1852	271	331	271	3
196	208	91.3379	3.1929	169	208	169	5
197	207	91.3240	3.1980	91	100	91	5
198	206	91.2473	3.2263	44	45	44	3
199	205	91.2375	3.2299	79	244	79	2
200	204	91.2209	3.2360	126	369	126	2
201	203	91.0792	3.2883	68	161	68	4
202	202	90.9483	3.3365	176	346	176	3
203	201	90.9431	3.3384	288	301	288	4
204	200	90.8445	3.3748	42	104	42	8
205	199	90.8294	3.3804	121	399	121	2
206	198	90.7922	3.3941	150	374	150	2
207	197	90.7631	3.4048	159	280	159	3
208	196	90.7338	3.4156	144	165	144	2
209	195	90.7260	3.4185	189	202	189	2
210	194	90.7207	3.4204	222	339	222	3
211	193	90.6019	3.4642	137	230	137	6
212	192	90.4506	3.5200	224	225	224	2
213	191	90.4468	3.5214	149	155	149	9
214	190	90.4033	3.5374	132	256	132	7
215	189	90.3832	3.5448	296	356	296	2
216	188	90.3814	3.5455	99	252	99	2
217	187	90.3724	3.5488	70	96	70	4
218	186	90.2854	3.5809	21	33	21	6
219	185	90.1930	3.6149	14	262	14	3
220	184	90.1735	3.6221	122	218	122	2
221	183	90.0945	3.6513	41	233	41	6
222	182	90.0337	3.6737	176	323	176	6
223	181	90.0296	3.6752	7	12	7	4
224	180	89.9995	3.6863	13	15	13	2
225	179	89.9806	3.6932	5	186	5	7
226	178	89.9508	3.7042	373	386	373	2
227	177	89.9118	3.7186	83	118	83	5
228	176	89.8795	3.7305	2	259	2	8
229	175	89.8145	3.7544	254	258	254	6
230	174	89.8017	3.7592	147	288	147	10
231	173	89.7920	3.7628	124	250	124	2
232	172	89.7450	3.7801	255	287	255	3
233	171	89.7191	3.7896	74	171	74	6
234	170	89.6158	3.8277	135	140	135	5
235	169	89.6120	3.8291	92	145	92	9
236	168	89.5580	3.8490	111	314	111	5
237	167	89.5309	3.8590	348	371	348	2
238	166	89.5241	3.8615	192	297	192	4
239	165	89.5089	3.8671	176	403	176	7

240	164	89.4261	3.8976	25	26	25	4
241	163	89.3585	3.9225	73	240	73	2
242	162	89.3335	3.9318	84	172	84	13
243	161	89.0847	4.0235	282	377	282	3
244	160	89.0736	4.0275	93	142	93	2
245	159	89.0394	4.0402	37	50	37	6
246	158	89.0336	4.0423	97	103	97	2
247	157	88.9961	4.0561	143	175	143	9
248	156	88.8706	4.1024	248	279	248	2
249	155	88.8570	4.1074	1	115	1	2
250	154	88.7764	4.1371	129	137	129	10
251	153	88.7201	4.1579	125	127	125	2
252	152	88.6578	4.1808	203	396	203	4
253	151	88.6412	4.1870	38	79	38	4
254	150	88.5497	4.2207	61	166	61	3
255	149	88.5145	4.2337	36	254	36	11
256	148	88.5088	4.2357	54	222	54	5
257	147	88.4924	4.2418	243	379	243	2
258	146	88.4726	4.2491	381	384	381	2
259	145	88.4673	4.2510	55	231	55	4
260	144	88.4112	4.2717	28	156	28	7
261	143	88.3103	4.3089	41	232	41	9
262	142	88.1921	4.3525	53	139	53	2
263	141	88.1137	4.3814	44	89	44	7
264	140	88.0808	4.3935	23	51	23	6
265	139	88.0015	4.4228	64	149	64	13
266	138	87.9827	4.4297	28	34	28	9
267	137	87.7804	4.5042	102	163	102	3
268	136	87.7278	4.5237	19	387	19	2
269	135	87.6422	4.5552	4	42	4	9
270	134	87.6363	4.5574	76	309	76	5
271	133	87.4535	4.6247	21	70	21	10
272	132	87.4070	4.6419	40	238	40	3
273	131	87.3666	4.6568	82	204	82	4
274	130	87.3294	4.6705	39	101	39	2
275	129	87.3005	4.6811	271	363	271	4
276	128	86.9958	4.7935	20	74	20	11
277	127	86.9329	4.8166	22	373	22	4
278	126	86.9282	4.8184	75	80	75	2
279	125	86.9101	4.8251	36	143	36	20
280	124	86.8646	4.8418	66	83	66	9
281	123	86.7944	4.8677	129	177	129	12
282	122	86.7866	4.8706	91	192	91	9
283	121	86.7820	4.8723	235	267	235	2
284	120	86.6448	4.9228	81	340	81	2
285	119	86.5925	4.9421	5	111	5	12
286	118	86.5717	4.9498	93	176	93	9
287	117	86.5445	4.9598	251	385	251	3
288	116	86.5389	4.9619	84	169	84	18
289	115	86.5275	4.9661	43	181	43	5
290	114	86.4559	4.9925	135	305	135	7
291	113	86.2705	5.0608	55	147	55	14
292	112	86.2547	5.0667	31	87	31	3
293	111	86.2326	5.0748	170	370	170	2
294	110	86.0774	5.1320	2	37	2	14
295	109	85.8060	5.2320	102	372	102	4
296	108	85.6443	5.2917	25	28	25	13
297	107	85.6166	5.3018	13	183	13	3
298	106	85.6048	5.3062	35	367	35	2
299	105	85.5712	5.3186	3	21	3	13
300	104	85.4699	5.3559	136	271	136	6
301	103	85.2519	5.4363	81	366	81	3
302	102	85.2457	5.4386	55	265	55	16
303	101	85.2167	5.4492	126	376	126	3
304	100	85.1942	5.4575	119	150	119	4
305	99	85.1147	5.4869	125	245	125	4
306	98	85.0831	5.4985	92	187	92	12
307	97	85.0528	5.5097	227	322	227	3
308	96	85.0244	5.5201	30	86	30	2
309	95	85.0028	5.5281	121	395	121	3
310	94	84.9624	5.5430	191	282	191	5

311	93	84.9147	5.5606	251	381	251	5
312	92	84.8084	5.5997	4	17	4	12
313	91	84.7432	5.6238	269	348	269	3
314	90	84.6128	5.6719	68	159	68	7
315	89	84.6030	5.6755	25	41	25	22
316	88	84.5796	5.6841	32	57	32	3
317	87	84.5327	5.7014	44	64	44	20
318	86	84.3367	5.7736	185	392	185	3
319	85	84.2399	5.8093	61	99	61	5
320	84	84.2190	5.8170	132	135	132	14
321	83	84.2021	5.8233	243	380	243	4
322	82	84.0172	5.8914	20	224	20	13
323	81	83.9070	5.9320	4	23	4	18
324	80	83.6225	6.0369	5	36	5	32
325	79	83.4123	6.1144	170	269	170	5
326	78	83.2811	6.1627	22	255	22	7
327	77	83.0934	6.2319	6	7	6	7
328	76	83.0224	6.2581	243	364	243	5
329	75	82.8266	6.3303	189	200	189	4
330	74	82.4246	6.4785	55	129	55	28
331	73	82.4063	6.4852	27	32	27	4
332	72	82.3475	6.5069	249	344	249	2
333	71	82.3325	6.5124	2	91	2	23
334	70	81.9447	6.6553	13	97	13	5
335	69	81.9085	6.6687	93	122	93	11
336	68	81.8867	6.6767	39	47	39	3
337	67	81.7071	6.7429	54	92	54	17
338	66	81.5425	6.8036	68	84	68	25
339	65	81.4705	6.8301	75	241	75	3
340	64	81.4658	6.8319	14	66	14	12
341	63	81.4139	6.8510	19	248	19	4
342	62	81.4087	6.8529	343	402	343	2
343	61	81.2242	6.9209	110	296	110	3
344	60	81.0291	6.9928	124	125	124	6
345	59	80.8722	7.0507	38	189	38	8
346	58	80.3986	7.2252	5	82	5	36
347	57	80.3716	7.2352	76	203	76	9
348	56	80.3620	7.2388	40	235	40	5
349	55	80.3266	7.2518	30	43	30	7
350	54	79.9602	7.3868	25	44	25	42
351	53	79.7508	7.4640	136	191	136	11
352	52	79.5647	7.5326	14	31	14	15
353	51	79.1202	7.6965	110	243	110	8
354	50	79.0544	7.7207	61	126	61	8
355	49	78.7771	7.8230	78	353	78	2
356	48	78.7350	7.8385	20	185	20	16
357	47	78.4070	7.9593	2	4	2	41
358	46	77.7529	8.2005	61	247	61	10
359	45	77.7188	8.2130	2	132	2	55
360	44	77.2453	8.3876	19	119	19	8
361	43	77.0144	8.4727	54	76	54	26
362	42	76.5372	8.6486	20	68	20	41
363	41	76.3846	8.7048	25	55	25	70
364	40	76.2464	8.7558	35	170	35	7
365	39	76.0589	8.8249	124	251	124	11
366	38	75.6681	8.9689	10	19	10	10
367	37	75.6083	8.9910	13	14	13	20
368	36	75.5943	8.9962	53	144	53	4
369	35	75.3220	9.0965	30	102	30	11
370	34	75.2167	9.1353	2	5	2	91
371	33	75.1228	9.1700	40	306	40	6
372	32	74.8273	9.2789	39	73	39	5
373	31	74.6803	9.3331	20	22	20	48
374	30	74.1206	9.5394	38	136	38	19
375	29	73.8387	9.6433	6	35	6	14
376	28	73.0208	9.9448	54	121	54	29
377	27	73.0197	9.9452	2	3	2	104
378	26	72.9553	9.9689	123	124	123	12
379	25	72.3259	10.2009	40	93	40	17
380	24	71.7631	10.4084	201	227	201	4
381	23	71.1857	10.6212	75	81	75	6

382	22	70.8360	10.7501	53	77	53	5
383	21	70.6626	10.8140	6	61	6	24
384	20	70.4833	10.8801	13	249	13	22
385	19	70.0448	11.0417	30	110	30	19
386	18	68.1874	11.7264	25	38	25	89
387	17	67.6726	11.9162	2	20	2	152
388	16	66.0073	12.5300	25	54	25	118
389	15	64.6966	13.0131	75	343	75	8
390	14	64.4746	13.0950	25	39	25	123
391	13	62.9283	13.6650	2	6	2	176
392	12	62.2967	13.8978	30	40	30	36
393	11	59.7595	14.8330	1	13	1	24
394	10	57.1173	15.8069	25	30	25	159
395	9	56.6199	15.9903	2	10	2	186
396	8	53.9630	16.9696	75	78	75	10
397	7	53.1816	17.2577	27	123	27	16
398	6	47.8043	19.2398	2	25	2	345
399	5	44.2791	20.5392	53	201	53	9
400	4	41.8173	21.4466	1	27	1	40
401	3	37.6635	22.9778	2	53	2	354
402	2	28.8881	26.2125	1	2	1	394
403	1	0.0000	36.8609	1	75	1	404

Final Partition

Number of clusters: 7

	Number of observations	Within cluster sum of squares	Average distance from centroid	Maximum distance from centroid
Cluster1	24	108.019	1.87770	4.43136
Cluster2	186	741.190	1.84593	5.45472
Cluster3	159	755.463	2.02536	4.67190
Cluster4	16	141.688	2.72923	4.89245
Cluster5	5	24.657	2.16300	3.15498
Cluster6	10	85.431	2.72777	4.33647
Cluster7	4	19.115	2.01244	3.49088

Cluster Centroids

Variable	Cluster1	Cluster2	Cluster3	Cluster4	Cluster5	Cluster6	Cluster7
SiO2	-0.22976	-0.263790	0.136102	1.22096	-1.18046	2.84794	-2.29332
TiO2	-0.22589	-0.160233	0.062635	2.10124	-0.94004	-0.16097	-0.51103
Al2O3	-1.75197	-0.438501	0.783742	-1.04096	-0.19919	1.59366	0.17701
FeOT	0.57265	0.266724	-0.268218	0.52270	-1.27891	-3.47602	3.02098
MgO	2.05496	0.335650	-0.474651	-0.85875	-0.39604	-1.80934	-0.61675
CaO	-0.56012	0.097165	-0.018974	-0.69785	4.58728	-1.23931	-0.24766
Na2O	-1.40651	-0.433329	0.619933	-0.32542	-1.01338	2.86851	-0.65639
K2O	-0.74128	-0.153125	0.165498	-0.06065	-0.50871	2.48495	-0.34447

Distances Between Cluster Centroids

	Cluster1	Cluster2	Cluster3	Cluster4	Cluster5	Cluster6	Cluster7
Cluster1	0.00000	2.55055	4.35597	4.26250	6.32179	9.00777	4.69155
Cluster2	2.55055	0.00000	1.96738	3.13465	5.00540	7.21591	3.64954
Cluster3	4.35597	1.96738	0.00000	3.29259	5.39188	5.66185	4.40224
Cluster4	4.26250	3.13465	3.29259	0.00000	6.91312	6.96948	5.22974
Cluster5	6.32179	5.00540	5.39188	6.91312	0.00000	9.21163	6.60551
Cluster6	9.00777	7.21591	5.66185	6.96948	9.21163	0.00000	9.67519
Cluster7	4.69155	3.64954	4.40224	5.22974	6.60551	9.67519	0.00000

Equivalence test results for the Emerson Plateau and Naukluft Plateau localities

This section of the supplementary material shows the Minitab v17 model output for two-sample equivalence tests that are designed to test how equivalent the compositions of the Emerson Plateau and Naukluft plateau are while taking into account 1σ ChemCam precision. Emerson Stimson was used as the reference mean to compare the mean and standard deviation of Stimson compositions at the Naukluft plateau. N = sample number, StDev = standard deviation, SE Mean = Standard Error of the Mean, 95% CI = 95% Confidence interval (α = 0.05). The test statements and result is given in each table.

Table A.4.2: Mode output for the SiO_2 two-sample equivalence test for observation point analyses in the Emerson and Naukluft plateaus constrained dataset. The constrained data used in this equivalence test show no obvious alteration and are not members of outlying clusters 4, 5, and 7 likely associated with diagenesis (section 4.2.1.1., pp.##).

Method

```
Test mean = mean of Naukluft
Reference mean = mean of Emerson
Equal variances were not assumed for the analysis.
```

Descriptive Statistics

```
Comments    N    Mean   StDev  SE Mean
Naukluft  193  48.504  2.9001  0.20875
Emerson   183  48.238  2.5312  0.18711


Difference: Mean(Naukluft) - Mean(Emerson)

Difference       SE         95% CI        Equivalence Interval
   0.26592  0.28034  (-0.19635, 0.72819)       (-1.5, 1.5)

CI is within the equivalence interval. Can claim equivalence.
```

Test

```
Null hypothesis:         Difference ≤ -1.5 or Difference ≥ 1.5
Alternative hypothesis:  -1.5 < Difference < 1.5
α level:                 0.05

Null Hypothesis     DF  T-Value  P-Value
Difference ≤ -1.5  371   6.2993    0.000
Difference ≥ 1.5   371  -4.4021    0.000

The greater of the two P-Values is 0.000. Can claim equivalence.
```

Table A.4.3: Model output of the TiO_2 two-sample equivalence test for observation point analyses in the Emerson and Naukluft plateaus constrained dataset. The constrained data used in this equivalence test show no obvious alteration and are not members of outlying clusters 4, 5, and 7 likely associated with diagenesis (section 4.2.1.1., pp.##).

Method

```
Test mean = mean of Naukluft
Reference mean = mean of Emerson
Equal variances were not assumed for the analysis.
```

Descriptive Statistics

Comments	N	Mean	StDev	SE Mean
Naukluft	193	0.88694	0.12372	0.0089059
Emerson	183	0.93546	0.18045	0.013339

Difference: Mean(Naukluft) - Mean(Emerson)

Difference	SE	95% CI	Equivalence Interval
-0.048521	0.016039	(-0.074980, 0)	(-0.14, 0.14)

CI is within the equivalence interval. Can claim equivalence.

Test

Null hypothesis:	Difference ≤ -0.14 or Difference ≥ 0.14
Alternative hypothesis:	-0.14 < Difference < 0.14
α level:	0.05

Null Hypothesis	DF	T-Value	P-Value
Difference ≤ -0.14	320	5.7035	0.000
Difference ≥ 0.14	320	-11.754	0.000

The greater of the two P-Values is 0.000. Can claim equivalence.

Table A.4.4: Model output of the Al_2O_3 two-sample equivalence test for observation point analyses in the Emerson and Naukluft plateaus constrained dataset. The constrained data used in this equivalence test show no obvious alteration and are not members of outlying clusters 4, 5, and 7 likely associated with diagenesis (section 4.2.1.1., pp.##).

Method

```
Test mean = mean of Naukluft
Reference mean = mean of Emerson
Equal variances were not assumed for the analysis.
```

Descriptive Statistics

Comments	N	Mean	StDev	SE Mean
Naukluft	193	14.159	2.7526	0.19813
Emerson	183	13.444	2.9721	0.21970

Difference: Mean(Naukluft) - Mean(Emerson)

Difference	SE	95% CI	Equivalence Interval
0.71481	0.29585	(0, 1.2027)	(-0.57, 0.57)

CI is not within the equivalence interval. Cannot claim equivalence.

Test

Null hypothesis:	Difference ≤ -0.57 or Difference ≥ 0.57
Alternative hypothesis:	-0.57 < Difference < 0.57
α level:	0.05

Null Hypothesis	DF	T-Value	P-Value
Difference ≤ -0.57	367	4.3428	0.000
Difference ≥ 0.57	367	0.48946	0.688

The greater of the two P-Values is 0.688. Cannot claim equivalence.

Table A.4.5: Model output of the FeO_T two-sample equivalence test for observation point analyses in the Emerson and Naukluft plateaus constrained dataset. The constrained data used in this equivalence test show no obvious alteration and are not members of outlying clusters 4, 5, and 7 likely associated with diagenesis (section 4.2.1.1., pp.##).

Method

```
Test mean = mean of Naukluft
Reference mean = mean of Emerson
Equal variances were not assumed for the analysis.
```

Descriptive Statistics

Comments	N	Mean	StDev	SE Mean
Naukluft	193	18.573	2.5665	0.18474
Emerson	183	18.656	2.3125	0.17095

Difference: Mean(Naukluft) - Mean(Emerson)

Difference	SE	95% CI	Equivalence Interval
-0.083745	0.25170	(-0.49878, 0.33129)	(-1.8, 1.8)

CI is within the equivalence interval. Can claim equivalence.

Test

Null hypothesis:	Difference ≤ -1.8 or Difference ≥ 1.8
Alternative hypothesis:	-1.8 < Difference < 1.8
α level:	0.05

Null Hypothesis	DF	T-Value	P-Value
Difference ≤ -1.8	373	6.8187	0.000
Difference ≥ 1.8	373	-7.4841	0.000

The greater of the two P-Values is 0.000. Can claim equivalence.

Table A.4.6: Model output of the MgO two-sample equivalence test for observation point analyses in the Emerson and Naukluft plateaus constrained dataset. The constrained data used in this equivalence test show no obvious alteration and are not members of outlying clusters 4, 5, and 7 likely associated with diagenesis (section 4.2.1.1., pp.##).

Method

```
Test mean = mean of Naukluft
Reference mean = mean of Emerson
Equal variances were not assumed for the analysis.
```

Descriptive Statistics

Comments	N	Mean	StDev	SE Mean
Naukluft	193	6.3777	2.1201	0.15261
Emerson	183	7.6437	2.8447	0.21029

Difference: Mean(Naukluft) - Mean(Emerson)

Difference	SE	95% CI	Equivalence Interval
-1.2660	0.25983	(-1.6946, 0)	(-0.49, 0.49)

CI is not within the equivalence interval. Cannot claim equivalence.

Test

Null hypothesis:	Difference ≤ -0.49 or Difference ≥ 0.49
Alternative hypothesis:	-0.49 < Difference < 0.49
α level:	0.05

Null Hypothesis	DF	T-Value	P-Value
Difference ≤ -0.49	335	-2.9866	0.998
Difference ≥ 0.49	335	-6.7583	0.000

The greater of the two P-Values is 0.998. Cannot claim equivalence.

Table A.4.7: Model output of the CaO two-sample equivalence test for observation point analyses in the Emerson and Naukluft plateaus constrained dataset. The constrained data used in this equivalence test show no obvious alteration and are not members of outlying clusters 4, 5, and 7 likely associated with diagenesis (section 4.2.1.1., pp.##).

Method

```
Test mean = mean of Naukluft
Reference mean = mean of Emerson
Equal variances were not assumed for the analysis.
```

Descriptive Statistics

Comments	N	Mean	StDev	SE Mean
Naukluft	193	6.0617	1.7840	0.12842
Emerson	183	6.3956	1.5466	0.11433

Difference: Mean(Naukluft) - Mean(Emerson)

Difference	SE	95% CI	Equivalence Interval
-0.33397	0.17193	(-0.61748, 0)	(-0.42, 0.42)

CI is not within the equivalence interval. Cannot claim equivalence.

Test

Null hypothesis:	Difference ≤ -0.42 or Difference ≥ 0.42
Alternative hypothesis:	-0.42 < Difference < 0.42
α level:	0.05

Null Hypothesis	DF	T-Value	P-Value
Difference ≤ -0.42	371	0.50037	0.309
Difference ≥ 0.42	371	-4.3853	0.000

The greater of the two P-Values is 0.309. Cannot claim equivalence.

Table A.4.8: Model output of the Na_2O two-sample equivalence test for observation point analyses in the Emerson and Naukluft plateaus constrained dataset. The constrained data used in this equivalence test show no obvious alteration and are not members of outlying clusters 4, 5, and 7 likely associated with diagenesis (section 4.2.1.1., pp.##).

Method

Test mean = mean of Naukluft
Reference mean = mean of Emerson
Equal variances were not assumed for the analysis.

Descriptive Statistics

Comments	N	Mean	StDev	SE Mean
Naukluft	193	3.6252	0.77559	0.055829
Emerson	183	3.2538	0.88683	0.065556

Difference: Mean(Naukluft) - Mean(Emerson)

Difference	SE	95% CI	Equivalence Interval
0.37146	0.086107	(0, 0.51346)	(-0.49, 0.49)

CI is not within the equivalence interval. Cannot claim equivalence.

Test

Null hypothesis:	Difference ≤ -0.49 or Difference ≥ 0.49
Alternative hypothesis:	-0.49 < Difference < 0.49
α level:	0.05

Null Hypothesis	DF	T-Value	P-Value
Difference ≤ -0.49	361	10.005	0.000
Difference ≥ 0.49	361	-1.3766	0.085

The greater of the two P-Values is 0.085. Cannot claim equivalence.

Table A.4.9: Model output of the K_2O two-sample equivalence test for observation point analyses in the Emerson and Naukluft plateaus constrained dataset. The constrained data used in this equivalence test show no obvious alteration and are not members of outlying clusters 4, 5, and 7 likely associated with diagenesis (section 4.2.1.1., pp.##).

Method

Test mean = mean of Naukluft
Reference mean = mean of Emerson
Equal variances were not assumed for the analysis.

Descriptive Statistics

Comments	N	Mean	StDev	SE Mean
Naukluft	193	0.70917	0.45306	0.032612
Emerson	183	0.60071	0.47337	0.034993

Difference: Mean(Naukluft) - Mean(Emerson)

Difference	SE	95% CI	Equivalence Interval
0.10846	0.047833	(0, 0.18734)	(-0.14, 0.14)

CI is not within the equivalence interval. Cannot claim equivalence.

Test

Null hypothesis: Difference ≤ -0.14 or Difference ≥ 0.14
Alternative hypothesis: -0.14 < Difference < 0.14
α level: 0.05

Null Hypothesis	DF	T-Value	P-Value
Difference ≤ -0.14	370	5.1943	0.000
Difference ≥ 0.14	370	-0.65936	0.255

The greater of the two P-Values is 0.255. Cannot claim equivalence.

A.5 Supplementary information for Chapter 5

A.5. Tables of Pearson correlation coefficients for the Vera Rubin Ridge

In this supplementary material section, I provide tables of Pearson correlation coefficients (r-values) for all major element oxide combinations in the constrained Vera Rubin Ridge Member ChemCam datasets. These tables include their Pearson correlation coefficient t-test results (p-values) for a null hypothesis where there is no correlation (H_0:$\rho = 0$) between the two variables against the alternative hypothesis that there is a correlation (H_A:$\rho \neq 0$; see section 2.4.2). Numbers are highlighted according to the strength of their correlations: bright yellow = very strong positive; orange = moderately strong positive; dark blue is moderately strong negative; bright blue = strong negative. Red, highlighted p-values show statistical insignificance.

Table A.5.1: A table of Pearson correlation coefficients and associated p-value derived from the student's t-test statistic for Pettegrove Point analyses of the Vera Rubin Ridge. Boxes outlined in black show correlations that also exist within the Jura Member (Table A.5.2).

Pettegrove	SiO_2	TiO_2	Al_2O_3	FeO_T	MgO	CaO	Na_2O
TiO_2	0.14						
	0.0000						
Al_2O_3	0.24	0.03					
	0.0000	0.4740					
FeO_T	-0.33	0.12	-0.15				
	0.0000	0.0010	0.0000				
MgO	-0.18	-0.12	-0.25	-0.08			
	0.0000	0.0010	0.0000	0.0200			
CaO	-0.48	-0.19	0.02	-0.19	-0.21		
	0.0000	0.0000	0.6080	0.0000	0.0000		
Na_2O	0.14	-0.21	0.34	-0.25	-0.17	0.06	
	0.0000	0.0000	0.0000	0.0000	0.0000	0.1030	
K_2O	0.12	0.06	0.06	0.10	-0.09	-0.12	0.10
	0.0010	0.0980	0.1150	0.0040	0.0120	0.0010	0.0080

Table A.5.2: A table of Pearson correlation coefficients and associated p-value derived from the student's t-test statistic for Jura analyses of the Vera Rubin Ridge. Boxes outlined in black show correlations that also exist within the Pettegrove Point Member (Table A.5.1).

Jura	SiO_2	TiO_2	Al_2O_3	FeO_T	MgO	CaO	Na_2O
TiO_2	0.27						
	0.0000						
Al_2O_3	0.26	0.10					
	0.0000	0.0010					
FeO_T	-0.54	-0.11	-0.20				
	0.0000	0.0000	0.0000				
MgO	-0.09	-0.18	-0.32	-0.16			
	0.0010	0.0000	0.0000	0.0000			
CaO	-0.49	-0.19	-0.02	-0.03	-0.18		
	0.0000	0.0000	0.4110	0.3270	0.0000		
Na_2O	0.16	-0.06	0.37	-0.15	-0.17	-0.07	
	0.0000	0.0480	0.0000	0.0000	0.0000	0.0140	
K_2O	-0.05	-0.13	0.04	0.14	-0.04	-0.06	0.07
	0.0620	0.0000	0.1160	0.0000	0.1420	0.0290	0.0100

Table A.5.3: A table of Pearson correlation coefficients and associated p-value derived from the student's t-test statistic for "Red" target analyses for both Members on the Vera Rubin Ridge. Boxes outlined in black show correlations that also exist within the Grey bedrock (Table A.5.4.).

Red	SiO_2	TiO_2	Al_2O_3	FeO_T	MgO	CaO	Na_2O
TiO_2	0.18						
	0.0000						
Al_2O_3	0.25	-0.01					
	0.0000	0.6720					
FeO_T	-0.31	0.13	-0.12				
	0.0000	0.0000	0.0000				
MgO	-0.15	-0.07	-0.27	-0.14			
	0.0000	0.0220	0.0000	0.0000			
CaO	-0.54	-0.19	0.00	-0.11	-0.22		
	0.0000	0.0000	0.8910	0.0000	0.0000		
Na_2O	0.18	-0.21	0.39	-0.22	-0.16	-0.04	
	0.0000	0.0000	0.0000	0.0000	0.0000	0.2150	
K_2O	0.07	0.09	0.05	0.12	-0.06	-0.09	0.04
	0.0370	0.0050	0.1050	0.0000	0.0490	0.0070	0.2640

Table A.5.4: A table of Pearson correlation coefficients and associated p-value derived from the student's t-test statistic for Grey analyses of the Pettegrove Point and Jura Members on the Vera Rubin Ridge. Boxes outlined in black show correlations that also exist within the Red bedrock (Table A.5.3.).

Grey	SiO_2	TiO_2	Al_2O_3	FeO_T	MgO	CaO	Na_2O
TiO_2	0.34						
	0.0000						
Al_2O_3	0.22	0.00					
	0.0000	0.9930					
FeO_T	-0.69	-0.13	-0.21				
	0.0000	0.0180	0.0000				
MgO	0.06	-0.06	-0.36	-0.34			
	0.3030	0.2980	0.0000	0.0000			
CaO	-0.50	-0.31	-0.08	0.08	-0.07		
	0.0000	0.0000	0.1290	0.1600	0.2150		
Na_2O	0.12	-0.03	0.38	-0.04	-0.15	-0.20	
	0.0320	0.6350	0.0000	0.4460	0.0050	0.0000	
K_2O	-0.17	-0.25	0.10	0.12	-0.13	-0.02	0.20
	0.0020	0.0000	0.0560	0.0320	0.0140	0.6970	0.0000